HEDL - TC-160-11

ALLOY DEVELOPMENT PROGRAM
QUARTERLY TECHNICAL PROGRESS
LETTER
OCTOBER-NOVEMBER-DECEMBER 1976

INFORMATION CONCERNING USE OF THIS DOCUMENT

APPLIED TECHNOLOGY

Any further distribution by any holder of this document or of the data therein to third parties representing foreign interests, foreign governments, foreign companies and foreign subsidiaries, or foreign divisions of U. S. companies should be coordinated with the Director, Division of Reactor Development and Demonstration, United States Energy Research and Development Administration.

This document is
PUBLICLY RELEASABLE
Janis Hardal, Richland
Authorizing Official
Date: 9-15-08

Hanford Engineering Development Laboratory

Operated by the Westinghouse Hanford Company | A Subsidiary of Westinghouse Electric Corporation | for the United States Energy Research and Development Administration Contract No. EY-76-C-14-2170

DISTRIBUTION OF THIS DOCUMENT IS LIMITED
No Automatic Distribution Announcement
Refer all requests to

DISCLAIMER

This report was prepared as an account of work sponsored by an agency of the United States Government. Neither the United States Government nor any agency Thereof, nor any of their employees, makes any warranty, express or implied, or assumes any legal liability or responsibility for the accuracy, completeness, or usefulness of any information, apparatus, product, or process disclosed, or represents that its use would not infringe privately owned rights. Reference herein to any specific commercial product, process, or service by trade name, trademark, manufacturer, or otherwise does not necessarily constitute or imply its endorsement, recommendation, or favoring by the United States Government or any agency thereof. The views and opinions of authors expressed herein do not necessarily state or reflect those of the United States Government or any agency thereof.

DISCLAIMER

Portions of this document may be illegible in electronic image products. Images are produced from the best available original document.

Operated by
Westinghouse
Hanford Company
for the USERDA

A Subsidiary of
Westinghouse Electric
Corporation

Contract No.
EY-76-C-14-2170

P.O. Box 1970
Richland,WA 99352

Hanford Engineering Development Laboratory

INFORMATION CONCERNING USE OF THIS DOCUMENT

CONTROLLED DISTRIBUTION DOCUMENT

This is a working document required for internal HEDL laboratory use and program distribution in order to perform, direct or integrate the work of the LMFBR/FFTF program. Distribution is limited to HEDL, ERDA, and ERDA contractors who require the document in order to perform work required by HEDL or ERDA. Its contents should not be published, further disseminated, or used for other purposes until approval for such release or use has been secured from HEDL Records Accountability.

PATENT STATUS

This document copy, since it is transmitted in advance of patent clearance, is made available in confidence solely for use in performance of work under contracts with the U.S. Energy Research and Development Administration. This document is not to be published nor its contents otherwise disseminated or used for purposes other than specified above before patent approval for such release or use has been secured, upon request, from the RL Patent Attorney, Richland Operations Office, U.S. ERDA, Richland, Washington 99352.

NOTICE

This document was prepared as an account of work sponsored by the United States Government. Neither the United States nor the United States Energy Research and Development Administration, nor any of their employees, nor any of their contractors, subcontractors, or their employees, makes any warranty, express or implied, or assumes any legal liability or responsibility for the accuracy, completeness or usefulness of any information, apparatus, product or process disclosed, or represents that its use would not infringe privately owned rights.

PRELIMINARY DOCUMENT

This document contains information of a preliminary nature prepared in the course of work under U.S. ERDA Contract EY-76-C-14-2170. This information is subject to corrections or modification upon the collection and evaluation of additional data.

HEDL - TC-160-11

ALLOY DEVELOPMENT PROGRAM 3rd QUARTERLY TECHNICAL PROGRESS LETTER OCTOBER-NOVEMBER-DECEMBER 1976

Compiled by
J. J. Laidler

April 1977

NOTICE
This report was prepared as an account of work sponsored by the United States Government. Neither the United States nor the United States Energy Research and Development Administration, nor any of their employees, nor any of their contractors, subcontractors, or their employees, makes any warranty, express or implied, or assumes any legal liability or responsibility for the accuracy, completeness or usefulness of any information, apparatus, product or process disclosed, or represents that its use would not infringe privately owned rights.

Based upon contributions from the following laboratories:

General Electric Company
Fast Breeder Reactor Department
Hanford Engineering Development Laboratory
Naval Research Laboratory
Oak Ridge National Laboratory
Westinghouse Electric Corporation
Advanced Reactors Division
Research Laboratory

Hanford Engineering Development Laboratory

Operated by the Westinghouse Hanford Company | A Subsidiary of Westinghouse Electric Corporation | for the United States Energy Research and Development Administration Contract No. EY-76-C-14-2170

This document is
PUBLICLY RELEASABLE
Janis Aardal, Richland
Authorizing Official
Date: 9-15-08

DISTRIBUTION OF THIS DOCUMENT IS LIMITED
No Automatic Distribution or Announcement
Refer all requests to HEDL EB

CONTENTS

Contents (Cont'd)

Contents (Cont'd)

Contents (Cont'd)

Contents (Cont'd)

FIGURES

Figures (Cont'd)

Figures (Cont'd)

Figures (Cont'd)

Figures (Cont'd)

Figures (Cont'd)

Figures (Cont'd)

Figures (Cont'd)

Figures (Cont'd)

Figures (Cont'd)

Figures (Cont'd)

Figures (Cont'd)

TABLES

Tables (Cont'd)

Tables (Cont'd)

REPORTABLE ADVANCED ALLOY DEVELOPMENT 189a PROGRAMS

189a No.	Reported in Section	189a Title	RDD Lead Branch
CW065	III	Component Materials Compatibility	TM
CW071	I, II	FBR Advanced Alloy Development	TF
CX008		Correlation of Substructure with Mechanical Properties of LMFBR Cladding and Structural Materials	TF
FF101	I, II	Advanced Clad/Duct Development	TF
FF129	III	Advanced Alloy Sodium Compatibility	TM
HH016	I	Advanced Alloy Development	TF
OH037	I, II	FBR Advanced Alloy Development	TF
SG013	I	FBRD Advanced Alloy Development	TF
SX004		Subgrain Refinement Strengthening	TF

CHAPTER I.

SWELLING AND CREEP

1. DENSITY CHANGES IN NEUTRON-IRRADIATED COMMERCIAL ALLOYS

W. V. Cummings, J. J. Laidler, R. R. Borisch and M. K. Korenko
Hanford Engineering Development Laboratory

1.1 OBJECTIVE

The objective of this investigation is to characterize the swelling behavior of candidate commercial alloys from irradiation test AA-I, utilizing immersion density measurements.

1.2 SUMMARY

Immersion density swelling data were obtained for a number of candidate commercial alloys, each irradiated to fluences of 3.3 to 5.9 x 10^{22} n/cm^2 (E>0.1 MeV) at eight different temperatures ranging from 400 to 650°C. The results confirm the expected swelling resistance of HT-9, 330 and Inconel 706. In general, the swelling behavior of the alloys examined is in good agreement with the current design equations[1]. Exceptions to this are shown by A-286 and Nimonic PE16, in which cases the variance from predicted swelling is attributed to heat-to-heat variability in swelling behavior.

1.3 ACCOMPLISHMENTS AND STATUS

1.3.1 Introduction

The AA-I test consists of four B-7a capsules (B-113, B-115, B-116 and B-117) and is the principal irradiation vehicle for evaluating the swelling behavior of commercial alloys of interest to the National Advanced Alloy Development Program. The test was fabricated in 1974, prior to the time at which the eight candidate commercial alloys were selected. The test therefore includes a rather wide variety of commercial alloys[2], among which are all of the alloys subsequently selected as candidate alloys; however, two of the candidate alloys, AISI 310 and 330, are not present in the thermomechanical treatment condition (20% cold-work) identified as the prime condition for these particular alloys. Specimens with that cold-work level are included in the AA-VII test[2]. The M-813 specimens in the AA-I test may not be fully representative of commercially-prepared M-813, since the material was prepared by hot isostatic pressing of a powder mixture. Arc-melted M-813 specimens were included in a later test, AA-XI[2]. The balance of the alloys and conditions in the AA-I test are completely representative of the candidate alloys and require no backup or supplementary tests.

The AA-I capsules are designed for discharges and specimen examination at peak fluences ranging from 6 x 10^{22} to 20 x 10^{22} n/cm^2 (E>0.1 MeV), with examinations to include immersion density measurements and transmission electron microscopy. Density changes have been determined for the candidate alloys after the first discharge of Capsule B-113, and the results of the measurements are reported here. Immersion density measurements on the remaining alloys contained in Capsule B-113 have been deferred indefinitely.

1.3.2 Experimental Details

Capsule B-113, containing eight subcapsules with design operating temperatures of 399, 427, 454, 482, 510, 538, 593 and 649°C, received a total exposure of 20,862 megawatt-days in Row 2 of EBR-II. This resulted in specimen fluences ranging from 3.3×10^{22} to 5.9×10^{22} n/cm^2 (E>0.1 MeV) as shown in Table 1.

TABLE 1

FLUENCE/TEMPERATURE DATA FOR CAPSULE B-113

Subcapsule Designation	Design Temperature (°C/°F)	Fluence, 10^{22} n/cm^2 (E>0.1 MeV)
M	399/750	4.0
L	427/800	5.0
E	454/850	3.3
F	482/900	4.5
K	510/950	5.7
G	538/1000	5.4
J	593/1100	5.9
H	649/1200	5.9

A summary of the pre-irradiation candidate alloy specimen history, including alloy designation, manufacturer, manufacturer's heat number, heat treatments and pre-irradiation densities, is presented in Table 2.

Irradiation-induced volume changes were determined by comparison of pre- and postirradiation density measurements, using a minimum of two averaged measurements. The accepted maximum variation between individual measurements was ±0.05%. Thermal control tests are also being conducted at temperatures spanning the range of irradiation temperatures; data have been obtained after an exposure of 100 hours.

1.3.3 Results and Discussion

The density change data for the candidate alloys, expressed as percent swelling ($\Delta V/V_o$ or $\Delta\rho/\rho_o$), are presented in Table 3.

1.3.3.1 Ferritic Alloy. Figure 1 presents the immersion density change data for the neutron-irradiated candidate ferritic alloy, HT-9. The volume change is small under all irradiation conditions, in agreement with the predictions of good swelling resistance established by electron[3] and iron ion[4] irradiation experiments. Also shown in Figure 1 are the 100-hour thermal control data. The swelling at this fluence is so low at all temperatures as to preclude any conclusions regarding the peak swelling temperature. The predicted swelling from the current Alloy Properties Databook[1] HT-9 swelling equation is also plotted in Figure 1, and is seen to be an adequate representation of the swelling behavior at these fluences and well within the uncertainty limits related to actual irradiation temperatures and neutron fluences.

1.3.3.2 Solid Solution Alloys. Swelling data for the candidate alloy, 20% cold-worked AISI 310 stainless steel, have been reported previously[5] for specimens contained in the AA-Ia test (Capsule B-109), which received a fluence comparable to that of Capsule B-113. Those data indicated very little swelling in this alloy, although preliminary transmission electron microscopy results[6] indicate the impending onset of high swelling rates, as expected from charged-particle irradiation experiments[7,8].

TABLE 2

SPECIMEN HISTORY OF COMMERCIAL ALLOYS--IRRADIATION TEST AA-I (PIN B-113)

Material	Source		Heat Treatment Condition	Preirradiation Density gm/cm^3
	Heat No.	Manufacturer		
M-813 STA	R74073	Federal Mogul	1079°C/4 hr/AC + 899°C/1 hr/AC + 749°C/8 hr/AC	7.9290
AISI 316 20% CW	81513	CarTech	As-Received	7.9614
Inconel 706 ST	48C5HK	Huntington Alloys	1066°C/1 hr/WQ	8.0620
AISI 330 ST	X-14726	Rolled Alloys	1066°C/1 hr/WQ	7.9819
HT-9 STA	-	Combustion Engineering	1052°C/30 min/AC + 780°C/2.5 hr/AC	7.7606
Inconel 706 STA	48C5HK	Huntington Alloys	954°C/1 hr/WQ + 843°C/3 hr/AC + 718°C/8 hr/FC to 621°C, Hold at 621°C/18 hr total/AC	8.0985
Nimonic PE16 STA	C-07206	CarTech	1079°C/4 hr/AC + 899°C/1 hr/AC + 749°C/8 hr/AC	8.0409
A-286 STA	L-2724K11	Universal Cyclops	982°C/1 hr/OQ + 718°C/16 hr/AC	7.9478

ST - Solution treated
STA - Solution treated and aged
CW - Cold worked

TABLE 3

IRRADIATION CONDITIONS AND PERCENT SWELLING
IN COMMERCIAL ALLOYS IRRADIATION TEST AA-I (B-113)

Irrad. Temp., °C →		399	427	454	482	510	538	593	649
$\phi t \times 10^{22}$ →		4.0	5.0	3.3	4.5	5.7	5.4	5.9	5.9
Alloy	H.T. Code	Percent Swelling							
M-813 STA	00	+0.43	+0.55	+0.14	+0.47	+0.79	+0.76	+0.32	-0.23
AISI 316 20% CW	46	-0.10	-0.09	-0.09	-0.12	+0.67	+0.85	+1.34	+0.08
Inconel 706 ST	80	-0.12	-0.30	-0.43	-0.44	-0.46	-0.50	-0.47	-0.51
AISI 330 ST	89	-0.19	-0.20	-0.22	-0.19	+0.03	-0.03	+0.04	+0.01
HT-9 STA	97	+0.09	+0.04	+0.11	+0.04	+0.10	+0.04	+0.07	+0.03
Inconel 706 STA	0B	-0.01	-0.08	-0.03	-0.02	+0.15	+0.04	0.00	-0.06
Nimonic PE16 STA	5H	0.00	-0.05	+0.04	+0.26	+0.78	+0.89	+1.36	-0.12
A-286 STA	7E	+1.63	+1.33	+0.14	+0.12	-0.10	-0.09	-0.02	-0.15

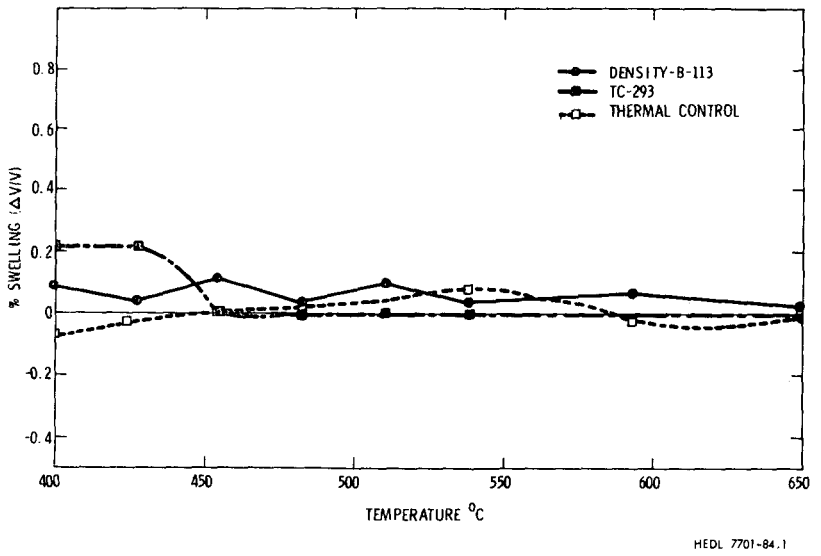

FIGURE 1. Immersion density change data for alloy HT-9 from the AA-I reactor test and the 100-hour thermal control specimens compared to the predictions from TC-293 (Rev. 2).

Figure 2 shows the density change results for alloy 330 in the solution-annealed condition, for both neutron-irradiated and thermally-aged specimens. Swelling is negligible at these fluences; there is some indication of irradiation-induced densification in the 400-500°C temperature range, but the difference may be a consequence of incomplete ex-reactor densification after 100 hours aging as compared to the 8,000-hour duration of the reactor test. The current swelling prediction[1] for 20% cold-worked 330 is seen in Figure 2 to be satisfactory for the B-113 irradiation conditions.

A comparison which serves to place the advanced alloy development effort in the correct perspective is shown in Figure 3, which contrasts the swelling behavior of solution-annealed 330 with that of 20% cold-worked AISI 316 (BB lot) specimens irradiated in the same

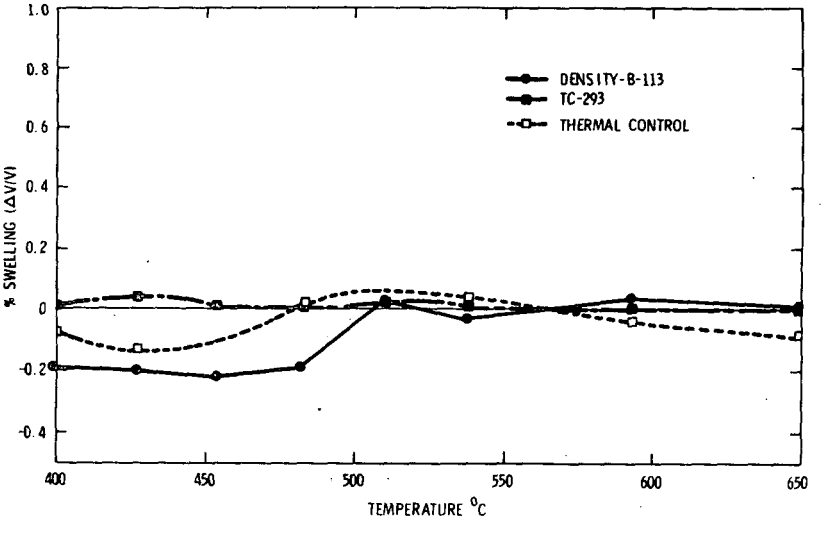

FIGURE 2. Immersion density change data for solution annealed 330 from the AA-I reactor test and the 100-hour thermal control specimens, compared to the predictions for cold-worked 330 appearing in TC-293 (Rev. 2).

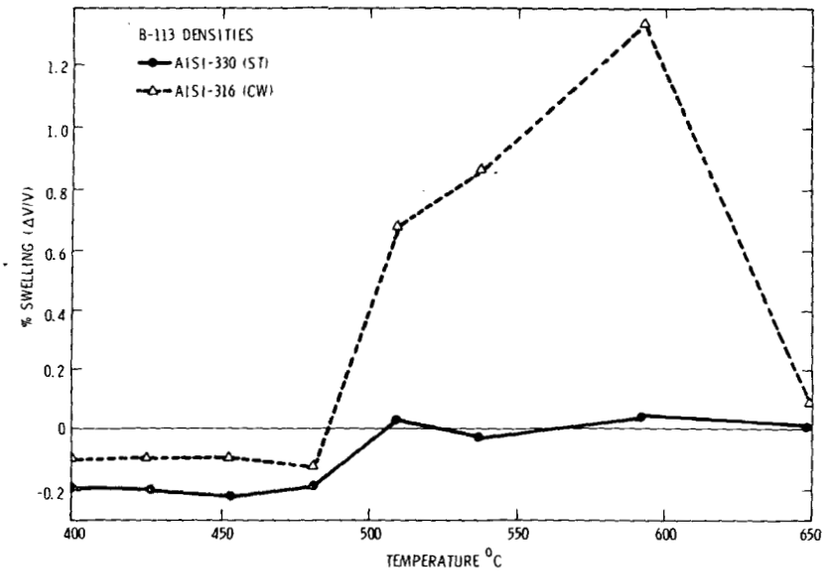

HEDL 7701-223.4

FIGURE 3. Immersion density change data comparing the swelling behavior of annealed 330 and 20% CW AISI 316 specimens included in Capsule B-113 of the AA-I test.

subcapsules. The peak swelling in the reference steel occurs at approximately 600°C and is consistent with the predictions of the Rev. 5 NSM Handbook equation for an incubation parameter (τ) of 5. Swelling of solution-annealed AISI 316 would be expected to be on the order of 6% or so under similar conditions. The steady-state swelling rate for alloy 330 is probably much lower than that for AISI 316[7], and it also appears that the incubation parameter, τ, is larger for annealed 330 than for annealed 316. If the effects of cold-working are the same for the two materials, which is reasonable to expect, then the swelling of 20% cold-worked 330 at higher fluences should be much less than that of the reference material.

1.3.3.3 γ'-Strengthened Alloys. The swelling behavior of the candidate γ'-strengthened commercial alloys (A-286, M-813 and Nimonic PE16) is illustrated in Figure 4. While the fluence levels in this case are still too low to support anything but speculation on alloy performance capabilities, it is appropriate to note that the observed swelling in two of the alloys (A-286 and Nimonic PE16) did not follow the expectations represented by the current swelling equations[4].

Alloy A-286 exhibited high swelling at the lowest irradiation temperatures, as predicted[1]; at higher temperatures, however, the swelling is substantially less than expected, as shown in Figure 5. The swelling of similarly-treated A-286 specimens from the AA-Ia (B-109) test[5,6], on the other hand, agrees quite well with the predictions of TC-293. This discrepancy may be attributed to heat-to-heat variability of swelling behavior in A-286, since the specimens in the AA-Ia and AA-I tests were derived from different heats of this alloy. It would appear from Figure 5 that this variability is expressed in the form of variable breadth of the swelling/temperature profile, which is related to the "b" coefficient in the swelling equation[1]. The results of a separate evaluation[6] of the AA-Ia results for A-286 suggest, however, that the absence of significant swelling in the AA-I specimens at

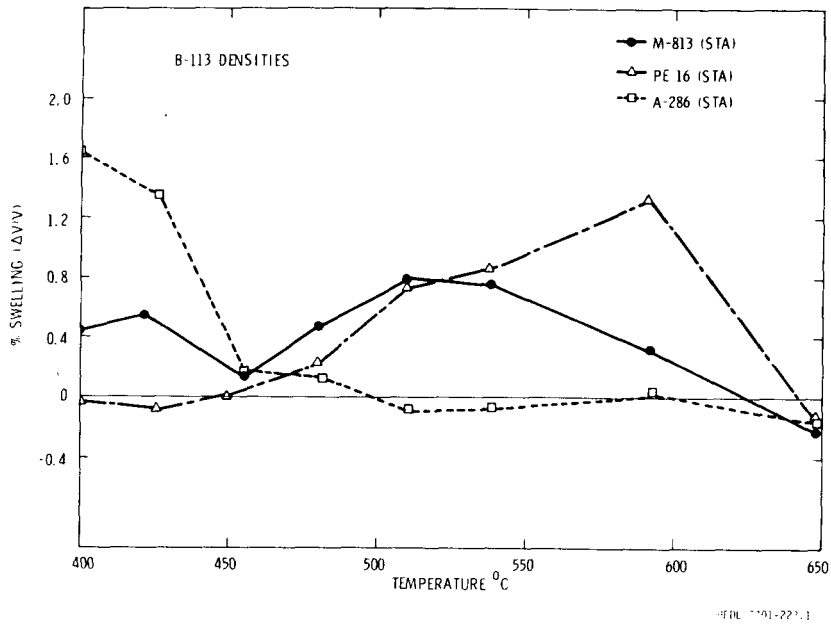

FIGURE 4. Immersion density change data comparing the swelling behavior of the candidate γ' strengthened alloys, as contained in the AA-I test.

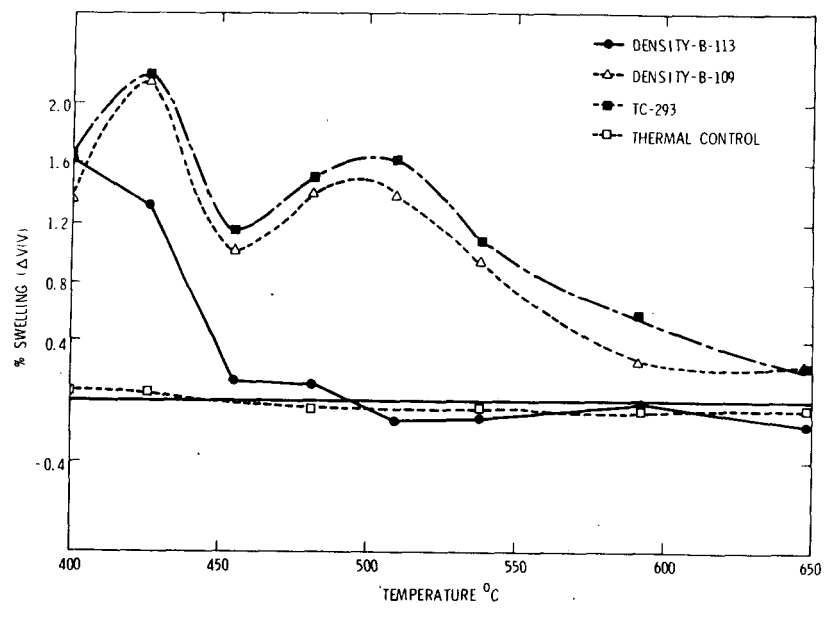

FIGURE 5. Immersion density change data for aged A-286 from the AA-I reactor test and the 100-hour thermal control specimens compared to the behavior from a different heat of A-286 from the AA-I test and with the predictions from TC-293 (Rev. 2).

higher temperatures may be related to the matrix composition. Comparison of the compositions of the two A-286 heats, Table 4a, could lead to this rationalization but would imply high sensitivity to minor compositional variations. Clearly this is a question with far-reaching implications, which will require higher-fluence data for resolution.

TABLE 4

CHEMICAL COMPOSITIONS * OF COMMERCIAL ALLOYS A-286 AND NIMONIC PE16
USED IN IRRADIATION TESTS AA-I (B-113) AND AA-Ia (B-109)

a. A-286		Fe	Cr	Ni	Mo	Ti	Al	Mn	Si	C	Nb	Co	B	V	Cu	S	Other
AA-I (B-113) Lot C2724K11	Vendor	Bal	14.15	24.6	1.21	2.2	0.17	1.22	0.54	0.053	-	-	0.0057	0.25	-	0.008	
	Overcheck	Bal	14.15	24.6	1.15	2.4	0.16	1.25	0.69	0.045	+Ta 0.02	0.62	-	-	0.065	-	
AA-Ia (B-109) Lot C-51644	Vendor	Bal	15.01	25.51	1.26	2.16	0.18	1.34	0.55	0.05	-	-	0.007	0.27	-	0.004	0.009 N_2
	Overcheck	Bal	15.25	25.00	1.34	2.10	0.25	1.40	0.53	0.084	+Ta 0.01	0.037	-	-	0.075	-	0.0025 N_2
b. Nimonic PE16		Fe	Cr	Ni	Mo	Ti	Al	Mn	Si	C	Nb	Co	B	V	Cu	S	Other
AA-I (B-113) Lot C-07206	Vendor	Bal	16.5	43.37	3.15	1.27	1.20	<0.01	<0.01	0.082	-	0.03	0.05	<0.01	<0.01	0.001	0.05 Zr
	Overcheck	Bal	16.88	44.45	3.08	1.38	1.35	0.005	-	0.067	+Ta 0.01	0.038	0.0032	-	0.02	-	<0.01 Zr
AA-Ia (B-109) Lot FZ-2213	Vendor	Bal	16.35	43.5	3.32	1.16	1.10	0.03	0.10	0.06	-	0.05	0.0015	-	0.04	0.003	0.035 Zr
	Overcheck	Bal	16.70	44.75	3.20	1.20	1.30	0.025	0.08	0.059	+Ta <0.01	0.012	-	-	0.027	-	

*Weight percent

The density change data for Nimonic PE16 represent another case of heat-to-heat variability in swelling behavior, as shown in Figure 6. The temperature profiles of swelling are similar for the AA-I and AA-Ia specimens, but the magnitude of swelling in the AA-I material is substantially greater. The compositions of the two heats are compared in Table 4b; the principal difference between the two is the higher silicon content of the AA-Ia heat. The lower swelling of the AA-Ia heat may reflect the anticipated general beneficial effect of silicon additions in imparting resistance to swelling, but an additional difference between the two materials which cannot be discounted at this time is the higher pre-irradiation dislocation density[9] in the AA-Ia material. Both factors, higher silicon content and higher dislocation density, might be expected to increase the incubation fluence for the onset of swelling and produce the observed behavior.

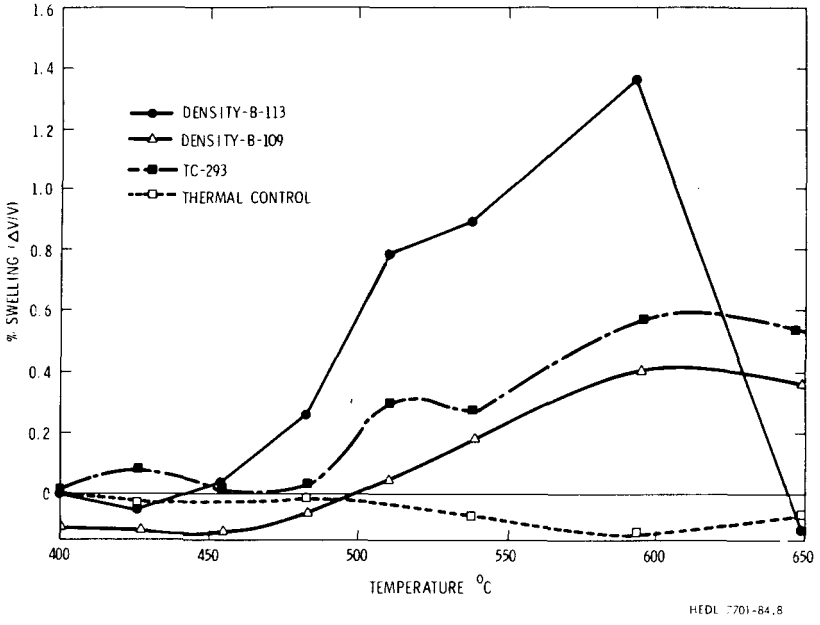

FIGURE 6. Immersion density change data for aged Nimonic PE16 from the AA-I reactor test and the 100-hour thermal control specimens compared to the behavior from a different heat of Nimonic PE16 from the AA-Ia reactor test and with the predictions from TC-293 (Rev. 2).

The good agreement between the TC-293 swelling equations and the observed swelling in the AA-Ia A-286 and PE16 specimens, as contrasted with the apparently discrepant AA-I data, should not be taken as indicative that the AA-I heats of A-286 and Nimonic PE16 can be expected to display anomalous swelling behavior. In point of fact, the AA-Ia (B-109) data were the primary data available at the time and strongly influenced the formulation of the current[1] swelling equations.

The observed swelling of M-813 is compared to the TC-293 swelling equation predictions in Figure 7. The good agreement between data and prediction is verification of the peak swelling temperature and peak breadth assumed in TC-293. These parameters, it should be noted, were based strictly on the results of charged-particle simulation experiments.

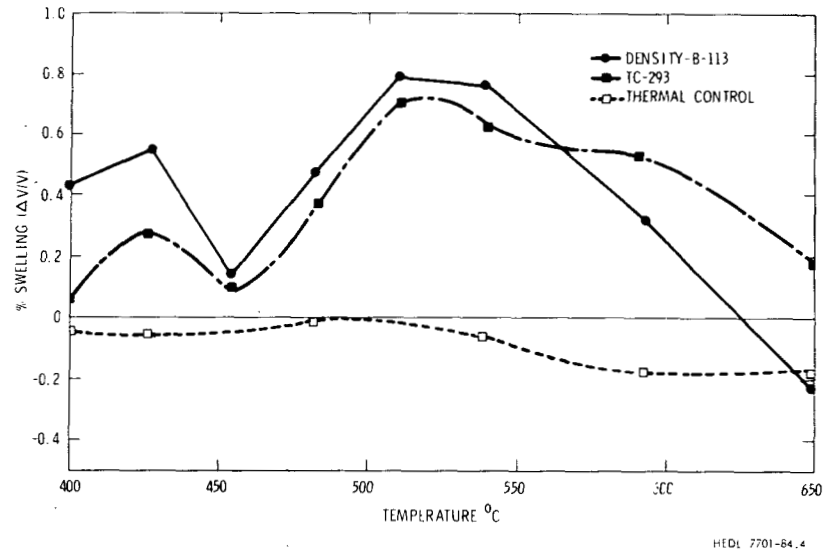

FIGURE 7. Immersion density change data for aged M-813 from the AA-I reactor test and the 100-hour thermal control specimens, compared to the predictions from TC-293 (Rev. 2).

1.3.3.4 γ'/γ"-Strengthened Alloys. Swelling behavior of the candidate alloy Inconel 718 has been reported previously[5], for neutron fluences comparable to those obtained with Capsule B-113, and the measurement of density changes for the B-113 specimens was therefore not assigned a high priority for completion. These data will be obtained at a later time.

Density change results for two heat treatment conditions (solution treated, fully aged) of the candidate alloy Inconel 706 are shown in Figure 8. The swelling observed in Inconel 706 is the lowest yet measured in the commercial alloys, confirming the expected

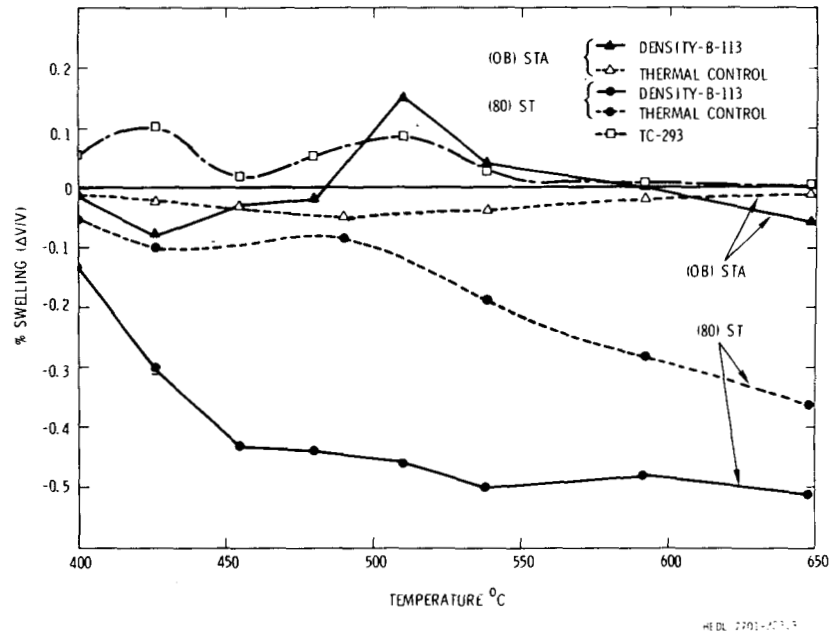

FIGURE 8. Immersion density change data for the solution treated and aged conditions of Inconel 706 from the AA-I reactor test and the 100-hour thermal control specimens, compared to the prediction of TC-293 (Rev. 2) for the fully-aged condition.

swelling resistance of this alloy. The fluences available at this stage are obviously too low to ascertain the peak swelling temperature. An interesting aspect of the irradiation response of Inconel 706 is the extensive densification observed in specimens irradiated in the solution-treated condition. The densification is most probably due to the precipitation of a combination of carbonitrides, γ', γ'' and delta phases. The thermal control density change data show similar densification reactions. As seen in Figure 8, there are indications that the densification process is enhanced by irradiation in the lower range of irradiation temperatures. Examination of the microstructure of irradiated solution-treated specimens should prove particularly illuminating.

1.3.4 Conclusions

1. In general, the current[1] swelling equations for the commercial alloys are adequate representations of the swelling behavior of these materials, insofar as the equations can be confirmed at fluences ranging from 3.3 to 5.9 x 10^{22} n/cm^2 (E>0.1 MeV).

2. The possibility of significant heat-to-heat variations in swelling cannot be ignored.

1.4 EXPECTED ACHIEVEMENTS IN THE NEXT REPORTING PERIOD

The candidate commercial alloys from B-113 will be examined by transmission electron microscopy and subjected to charged-particle irradiation to assess swelling behavior at high fluences. Further density measurements on the AA-I commercial alloys will be conducted as resources permit.

1.5 REFERENCES

1. Alloy Properties Databook, TC-293, Rev. 2, June, 1976.

2. Alloy Development Program Irradiation Experiments, TC-286 (as revised), May, 1975.

3. Gelles, D. S., and Thomas, L. E., Alloy Development Program Quarterly Technical Progress Letter, TC-160-3 (10-12/74), p. 15.

4. Smidt, F. A., Jr., Alloy Development Program Quarterly Technical Progress Letter, TC-160-5 (4-6/75), p. 77.

5. Borisch, R. R., and Powell, R. W., Alloy Development Program Quarterly Technical Progress Letter, TC-160-9 (4-6/76), p. 7.

6. Powell, R. W., this report.

7. Thomas, L. E., and Gelles, D. S., Alloy Development Program Quarterly Technical Progress Letter, TC-160-8 (1-3/76), p. 28.

8. Lauritzen, T., et al, Alloy Development Program Quarterly Technical Progress Letter, TC-160-9 (4-6/76), p. 32.

9. Bates, J. F., et al, Alloy Development Program Quarterly Technical Progress Letter, TC-160-1 (4-6/74), p. 13.

2. THE SWELLING AND MICROSTRUCTURAL CHARACTERIZATION OF NICKEL ION BOMBARDED COMMERCIAL ALLOYS

T. Lauritzen and W. L. Bell
General Electric Company

2.1 OBJECTIVE

The objective of the nickel-ion bombardment studies on advanced commercial alloys is to characterize the high-dose swelling behavior and assess the microstructural stability of prospective LMFBR core structural materials in the absence of similar in-reactor data. The work is intended to simulate in-reactor behavior and thus provide a basis for predicting the type and magnitude of swelling and microstructural changes that could be expected in service. Ultimately, the results of this study are expected to provide guidance for the selection of alloys for specific in-reactor applications.

2.2 SUMMARY

The swelling behavior and microstructural stability of a number of commercial austenitic alloys were evaluated from results of transmission electron microscopy examination of nickel-ion bombarded foils. Included were the solid solution grades Type 310 and Type 330 and the precipitation-hardenable grades Nimonic PE16, Inconel 706, Inconel 718 and M-813. Specimens of the several alloys in various commercial heat-treated conditions were bombarded with 4 and 5 MeV nickel ions over a range of temperatures to doses as high as 250 displacements per atom. Although marked differences in the temperature dependence of swelling were observed among the alloys, none but the solid solution alloys exhibited swelling in excess of two percent at their respective peak swelling temperatures. Microstructural examination revealed a general acceleration in precipitation kinetics and enhanced overaging in alloys with high titanium to aluminum ratios. In the less complex alloys, microstructural changes were slight. The results demonstrate that valid simulation of in-reactor microstructural behavior can be produced by nickel-ion bombardment and suggest that, except for Types 310 and 330, all of the alloys studied exhibit acceptable swelling, i.e., $\leq$5 percent, to doses typical of goal LMFBR fluence.

2.3 ACCOMPLISHMENTS AND STATUS

2.3.1 Introduction

One of the life-limiting factors in present LMFBR systems is the response of prospective core materials to the effects of high neutron fluences and high sodium temperatures. Alloys selected as cladding for the reactor fuel must, for example, be capable of maintaining strength, dimensional stability and integrity at temperatures and doses as high as 700°C and 150 displacements per atom. The maintenance of adequate strength depends primarily upon compositional and microstructural stability; the resistance of material to irradiation-induced creep and swelling governs dimensional stability, and integrity is measured largely by the compatibility of the cladding tube to liquid sodium on the outside and solid fuels and fission products on the inside. Although all are affected to some degree by the nuclear environment, only the phenomena of swelling and irradiation creep can be related directly to the exposure of materials to high energy particle irradiation.

Thus, the development of an appropriate material for such applications involves an arduous series of both thermal and irradiation tests that extend, or can be extrapolated, to a projected end of life. Aside from the inconvenience of long aging times, thermal testing is rather straightforward. In-reactor irradiation testing, on the other hand, is hampered by substantially longer exposures, generally poor experimental control and limited facility availability. Realizing the constraint that in-reactor testing posed to prompt materials development, experimenters early sought techniques whereby such testing could be simulated. The work of Nelson, Mazey and Hudson[1] on heavy ion bombardment in an accelerator introduced such a simulation technique and was instrumental in initiating a large-scale experimental effort both here and abroad to study irradiation effects on LMFBR structural materials[2].

General Electric interest in this experimental approach began in 1969 with a modest company-funded program using high energy deuterons as the bombarding species[3]. This effort evolved into the highly successful joint FBRD-CR&D program of the early 1970s, in which a large number of potential LMFBR materials was screened for swelling, and the significant effects of alloy composition on swelling were discussed[4,5]. The bombarding species in that work was 5 MeV nickel ions.

2.3.2 Description of Materials

Eleven grades of six commercial austenitic alloys are being evaluated in the present program. They include annealed (ST) and commercially heat-treated (STA) Nimonic PE16 and Inconel 706, commercially heat-treated (STA) Inconel 718 and M-813, annealed (ST) Type 310 steel, annealed (ST) and 20 percent cold-worked (CW) Type 330 steel, and thermomechanically-treated (AU) Nimonic PE16 and Inconel 706. Heat treatment details and chemical compositions of the several alloys are given in Tables 5 and 6, respectively.

All alloys were procured by HEDL and were provided in the form of as-heat-treated 3 mm diameter rods or as 0.25 mm thick, 3 mm diameter wafers. All wafering was performed by abrasive cutting. The disks were subsequently surfaced by wet grinding and metallographic polishing.

Prebombardment microstructural characterization of the alloys was performed by HEDL[6]. Results of this characterization are summarized below to provide the basis for an assessment of the effect of bombardment on microstructural stability.

Of the alloy types used in this study, four are precipitation hardenable; the remaining two are solid solution alloys that are hardenable principally by solid solution strengthening and by cold working. Precipitation in Nimonic PE16, Inconel 706, Inconel 718 and M-813 depends primarily upon alloy composition, and, in particular, upon the contents of the alloying elements aluminum, titanium and niobium[7]. Aluminum and titanium combine with nickel to form the cuboidal gamma prime (γ') precipitate $Ni_3(Ti,Al)$; niobium precipitates in the gamma double prime (γ'') phase Ni_3Nb. As shown in Table 6, Inconel 706 contains the most titanium and has the highest titanium-to-aluminum ratio (Ti/Al = 6.15), a parameter that influences the overaging characteristics of these alloys[8]. Inconel 718, M-813 and Nimonic PE16 contain decreasing ratios of titanium to aluminum; in PE16, the ratio is roughly one. The γ' precipitate formed in all four alloys is cuboidal; the average length of a cube edge is generally used to specify the precipitate size. In those alloys containing more than trace amounts of niobium (Inconel 706 and Inconel 718), both γ' and γ'' are formed in the aging heat

TABLE 5
HEAT TREATMENTS OF BASE COMMERCIAL ALLOYS

Alloy	Heat. No.	Heat Treatment
ST Nimonic PE16	C-07206	1080°C/4 hr/AC
STA Nimonic PE16	C-07206	1080°C/4 hr/AC + 890°C/1 hr/AC + 750°C/8 hr/AC
ST Inconel 706	48C5HK	1066°C/1 hr/WQ
STA Inconel 706	48C5HK	954°C/1 hr/WQ + 843°C/3 hr/AC + 720°C/8 hr/FC to 620°C, hold for 18 hr total/AC
STA Inconel 718	44F9EY) 55F1EY)	954°C/1 hr/WQ + 718°C/8 hr/FC to 621°C, hold for 18 hr total/AC
CW Type 310	X-14342	1066°C/1 hr/WQ + 20% CW
ST Type 330	X-14726	1066°C/1 hr/WQ
CW Type 330	X-14726	1066°C/1 hr/WQ + 20% CW
STA M-813	R74073	1080°C/4 hr/AC + 900°C/1 hr/AC + 750°C/8 hr/AC
AU Nimonic PE16	C-07206	1100°C/2 hr/AC + 30% CW + 900°C/ 1 hr/ AC + 800°C/16 hr/AC + 700°C/2 hr/AC
CWA Inconel 706	48C5HK	1100°C/1 hr/WQ + 30% CW + 720°C/8 hr/ FC to 620°C, hold for 18 hr total/AC

AC = Air Cool
WQ = Water Quench
FC = Furnace Cool
CW = Cold Work (as measured by reduction in cross-sectional area)

TABLE 6

CHEMICAL COMPOSITIONS OF BASE COMMERCIAL ALLOYS
(VENDOR ANALYSIS UNLESS OTHERWISE INDICATED)

	Nimonic PE16	Inconel 706	Inconel 718 59F1EY	Inconel 718 44F9EY	Type 310	Type 330	M-813
Carbon	0.082	0.03	0.02	0.04	0.06	0.05	0.034
Manganese	<0.01	0.10	0.10	0.10	1.52	1.58	0.022*
Iron	Bal	Bal	Bal	Bal	Bal	Bal	Bal
Sulfur	0.001	0.002	0.005	0.007	0.022	0.013	-
Silicon	<0.01	0.10	0.18	0.23	0.56	1.27	-
Copper	<0.01	0.02	0.14	0.12	0.33	0.25	0.027*
Nickel	43.37	41.49	53.81	52.83	19.65	36.05	34.1
Chromium	16.5	16.09	18.23	18.57	24.7	19.05	18.35
Aluminum	1.20	0.27	0.58	0.5	-	-	1.59
Titanium	1.27	1.66	0.95	0.92	-	0.03*	2.38
Molybdenum	3.15	-	3.05	2.83	0.30	0.22*	4.26
Cobalt	0.03	0.048*	0.03	0.03	-	0.3*	0.02
Niobium + Tantalum	0.01*	2.95	5.16	5.28	-	-	-
Vanadium	<0.01	-		-	-	-	-
Phosphorus	0.001	-		-	0.027	0.021	-
Other	<0.01Zr 0.0032B	-		-	-	0.01Sn	-

* Overcheck analysis

treatment. Body-centered tetragonal γ'' occurs as disk-like platelets, for which an average thickness and an average diameter is commonly used to specify size. Both γ' and γ'' are metastable and overaging will result in their dissolution and replacement by stable phases which habit {111} planes in the austenite matrix. Overaging of γ' results in plates of eta (η) phase, hexagonal Ni_3Ti, while overaging of γ'' results in plates of delta (δ) orthorhombic Ni_3Nb[7].

In the solid solution alloys Type 310 and Type 330, the only precipitate species are carbides which, incidentally, exist in all six alloys to varying degrees. Specific second-phase data on the several alloys in their various microstructural conditions are given below, as derived from transmission electron microscopy (TEM) examination at HEDL. The letters prefixing the alloy types indicate the heat treatment to which the alloy has been subjected. Actual treatments are given in Table 5.

- ST Nimonic PE16 contains a large number of blocky intragranular carbides and a moderate dislocation density. No observable γ' precipitation occurred.

- In addition to the intragranular carbides, STA Nimonic PE16 contained a heavy grain boundary carbide precipitation, a low dislocation density, and intragranular γ' with an average particle size of 15.5 nm. The STA heat treatment used on this alloy is similar to the manufacturer's recommended heat treatment for optimum properties.

• The AU heat treatment on Nimonic PE16--developed in an attempt to optimize in-reactor behavior--produced a completely recrystallized microstructure with a very low dislocation density. A fairly uniform distribution of γ' was formed, with an average particle size of 39 nm.

• ST Inconel 706 contained a low to medium dislocation density and, with the exception of a few scattered intragranular carbides, the material was clean.

• STA Inconel 706 represents the manufacturer's recommended condition for optimum mechanical properties. It contained γ' precipitates averaging 39 nm, γ'' platelets averaging 5 nm thick and 16 nm in diameter, and a grain boundary phase identified as delta (δ), the orthorhombic phase Ni_3Nb. In addition, the microstructure revealed a medium dislocation density and scattered large blocky carbides at grain boundaries.

• CWA Inconel 706 is a thermomechanical modification of the commercial grade, developed in an effort to optimize in-reactor properties of this alloy.

• In the manufacturer's recommended heat treatment condition, STA Inconel 718 contains γ', γ'', δ and carbides. According to the HEDL characterization, the two heats used in this study exhibited similar microstructure: extensive precipitation of lenticular δ platelets at grain boundaries, fine intragranular γ' and γ'', and scattered carbides. In the Heat 59F1EY material all γ' and γ'' particles were estimated to be less than 10 nm. In Heat 44F9EY, the γ' precipitates averaged 10 nm and the γ'' platelets measured 5 nm thick and 15 nm in diameter.

• The STA M-813 used in this study was produced by the powder metallurgy process. It contained carbide-coated grain boundaries, a low dislocation density, and a bimodal γ' distribution. Average sizes of the two populations were 15 and 55 nm.

• In its solution-treated condition, Type 310 exhibited a clean microstructure with only scattered carbide precipitates, and a low dislocation density. Except for an obviously high dislocation density, the cold-worked material looked much the same.

• Both grain boundary carbides and a fine dispersion of intragranular carbides were observed in ST Type 330 steel. The microstructure revealed a medium dislocation density with substantial dislocation-carbide interaction. Similar precipitate distributions were noted in the high dislocation density cold-worked material.

2.3.3 Experimental Details

Heavy ion bombardment techniques have been used for a number of years to simulate the type and magnitude of void formation that occurs in metals and alloys with high temperature fast neutron irradiation[2,9,10]. In the present investigation, positively-charged nickel ions were used to bombard thin-foil disks of test materials. Initial work was done with 5 MeV ions on the High Voltage Engineering Corporation's tandem Van de Graaff accelerator; later bombardments were made with 4 MeV ions in the State University of New York-Albany Dynamitron.

Prior to bombardment, the disks were implanted with 5 to 15 atom parts per million of helium by alpha particle bombardment in a cyclotron. The lower helium level was selected to represent that concentration produced by the (n-α) reaction during the initial period of in-reactor void nucleation. Helium implantation was performed at the research facilities of

Medi-Physics, Inc., of Emeryville, California, following the technique developed by FBRD in an earlier swelling simulation program[3]. Bombardment utilized an external beam of 24.6 MeV alpha particles. Uniform depth deposition of helium was achieved by degrading the beam energy in a continuous manner with a rotating aluminum wedge installed in the beam path. Mass spectrometric analysis performed by H. Farrar IV of Atomics International on representative implanted disks demonstrated that an accuracy of ±20% in desired helium level was achieved with the FBRD implantation technique.

After implantation, disks with comparable residual activities (resulting from alpha particle bombardment) were selected for final preparation for nickel-ion bombardment. Preparation included a 10-15 minute oxidation heat treatment at 350°C in air followed by electropolishing of the ion entry surface. Oxidation of the back side of the disk was used to minimize sticking of the disk to the bombardment furnace fixture; electropolishing removed structurally-deformed material resulting from wafering and grinding and cleansed the ion entry surface.

Nickel-ion bombardment was performed on individual disks fitted into an eight-position carousel, each containing a small independently controlled furnace. This assembly was described in detail by Johnston, et al[11]. Bombardment temperatures were selected to span the estimated peak swelling temperature of each alloy. A nickel-ion flux of 1.3×10^{13} ions/cm^2-sec was used with both 4 and 5 MeV ions, the flux producing a displacement rate of roughly 2×10^{-2} dpa/sec at the peak position in the displacement damage curve. Doses ranging from 30 to 250 dpa were used to assess the dose dependence of swelling. Alpha particle and nickel-ion bombardment parameters are summarized in Table 7.

Selected specimens--particularly those bombarded to high nickel-ion doses--were fitted with partial surface masks to selectively shield portions of sample from the ion beam[5]. Profilometry measurement of the boundary between the swelled and shielded region provided a direct measurement of the total integrated swelling along the ion path in those specimens in which swellings greater than approximately 5 percent occurred. In the majority of the specimens, however, steps were too shallow for meaningful measurement and all swelling data were collected by transmission electron microscopy techniques.

TABLE 7

BOMBARDMENT PARAMETERS

Helium Implantation	
Alpha Particle Energy:	24.6 MeV
Maximum Implantation Depth:	23.9 μm
Helium Content:	
Inconel 718 (Heat No. 59F1EY):	15 ± 3 appm
Inconel 718 (Heat No. 44F9EY):	5 ± 0.8 appm
All Other Alloys:	5 ± 0.8 appm
Nickel-Ion Bombardment	
Nickel-Ion Energy:	4 and 5 MeV
Nickel-Ion Flux:	1.3×10^{13}/cm^2-sec
Damage Rate:	2×10^{-2} dpa/sec
Peak Damage Depth, 4 MeV:	760 nm
Peak Damage Depth, 5 MeV:	920 nm

Preparation of the bombarded specimens for TEM examination included the calibrated removal of material from the ion entry surface and backthinning to perforation. Since 4 and 5 MeV nickel ions have a range of about 1100 and 1400 nm respectively in these materials and the zone of principal interest--the peak damage zone--lies only 760 and 900 nm respectively from the ion entry surface, TEM foils must be carefully prepared to produce a final foil thickness that lies within the peak damage zone. Calibrated polishing of the ion entry surface was performed by argon ion milling (using a commercial ion micro-milling apparatus) in which a sputtering rate of roughly 200 nm per minute was possible. A portion of the sample surface shielded from the ion beam (masked with protective lacquer) during milling provided a baseline from which to measure the depth of material removed. Once the required depth was attained, the entire ion-milled surface was masked with protective lacquer and the specimen perforated by electropolishing from the back side. [The above experimental procedures were developed in earlier ion bombardment simulation programs and were discussed in some detail in previous publications[5,11].] Following perforation, the ion-bombarded regions of the thinned foils were examined in a JEM 6A electron microscope operated at 100 kV.

2.3.4 Results

2.3.4.1 Nimonic PE16. The microstructural damage produced by high energy nickel-ion bombardment was evaluated in three lots of Nimonic PE16: solution treated (ST), solution-treated and aged (STA), and a thermomechanically-treated condition designated AU. All were produced from the same metallurgical heat, C-07206. Details of the swelling and microstructural characterization performed after bombardment are discussed below.

Swelling. ST Nimonic PE16 was found to be highly resistant to void formation. In the initial bombardment sequence performed to establish the peak swelling temperature, it was observed that the 116 dpa bombardment dose produced a peak swelling of less than 0.1 percent over the 100-degree temperature range selected for evaluation. Since this swelling occurred at the lowest bombardment temperature (625°C), it could not be used to pinpoint the peak swelling temperature. An additional series of bombardments was thus run to a substantially higher dose, over a lower temperature range. These 248 dpa bombardments produced voids at all temperatures, but only at 625°C was the distribution uniform. This temperature was thus assigned as the peak swelling temperature of ST Nimonic PE16, of the HEDL heat C-07206.

The temperature dependence of swelling in STA Nimonic PE16 was evaluated from 116 dpa bombardment data at 625, 675 and 725°C on the HEDL heat C-07206, and corroborated with earlier data[4] at similar doses and temperatures on material from another commercial heat, DAB664. Because of the extremely low step heights observed in the earlier evaluation, the bombardments of the HEDL alloy were performed on unmasked surfaces. Transmission electron microscopy examination of foils prepared in the peak damage region revealed that void formation had occurred at all temperatures (Figure 9), but only at the intermediate temperature was the void distribution sufficiently uniform to yield reliable swelling values. It was thus determined that the peak swelling temperature of this heat of STA Nimonic PE16 lies near 675°C. This determination is supported by the earlier data, particularly as regards the low-temperature swelling behavior of the alloy. The somewhat lower general swelling in

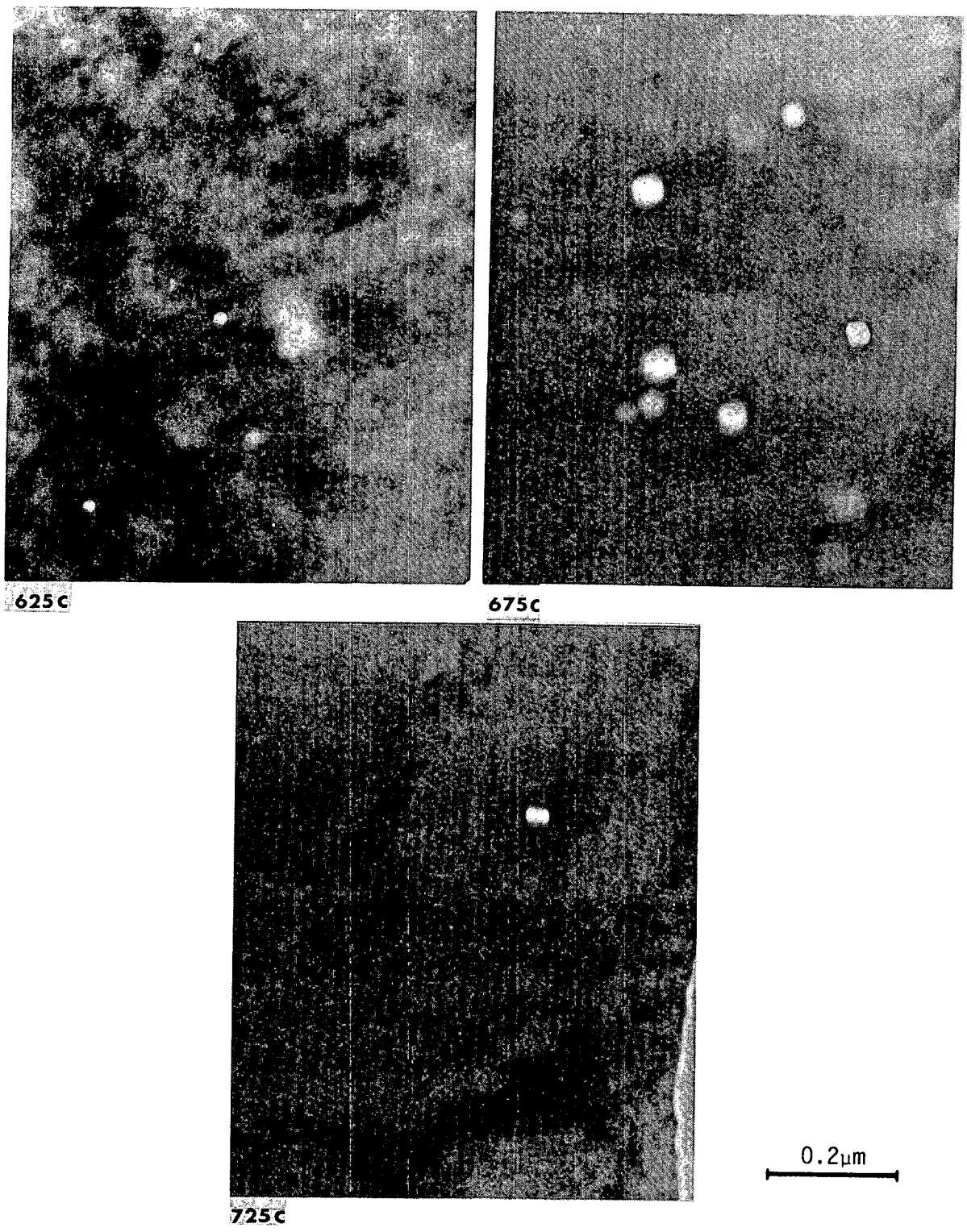

FIGURE 9. Void distributions in STA Nimonic PE16 after nickel-ion bombardment to 116 dpa.

DAB664 (Table 8) is likely related to the substantially higher levels of silicon and manganese in this alloy (0.27 and 0.11 percent, respectively) compared with <0.01 Si and 0.005 Mn in the HEDL alloy.*

TABLE 8

SWELLING IN STA NIMONIC PE16, HEATS DAB664 AND C-07206, BOMBARDED WITH 5 MeV NICKEL IONS TO 116 DPA

	Average Void Density, cm^{-3}	Average Void Size, nm	Average Swelling, $\%\Delta V/V_o$
575°C			
DAB664	1.0×10^{13}	29	0.01
C-07206	-	-	-
625°C			
DAB664	$<3.0 \times 10^{13}$	39	<0.1
C=07206	2.3×10^{13}	22	0.01
675°C			
DAB664	2.6×10^{12}	92	0.18
C-07206	1.3×10^{14}	43	0.58
725°C			
DAB664	4.7×10^{13}	37	0.17
C-07206	1.0×10^{13}	40	<0.01

AU Nimonic PE16, the thermomechanically-modified lot of this alloy heat, is clearly the least swelling resistant of the three lots tested. Although the magnitudes of swelling observed were not high, the generally uniform void distributions at 625 and 675°C and the virtual absence of voids at 575 and 725°C showed the peak swelling temperature of AU Nimonic PE16 to occur in the range 650-675°C. Representative void distributions are shown in Figure 10. The relative temperature dependence of swelling in Nimonic PE16 in the three material conditions tested is shown in Figure 11.

Two techniques were used to provide dose dependence of swelling data. In the early phases of the program, the conventional method of examining only the peak damage zone in each foil was used. This required individual bombardments to each dose level selected for evaluation. In later work, a foil preparation technique was developed to permit the examination of discrete zones along the ion path in a single foil, using conventional (low-voltage) TEM techniques. Details of this technique are given in the appendix. In the examination of Nimonic PE16, this latter technique was used in the determination of dose dependence of swelling in the AU condition, whereas the conventional "peak" determination was used in the other two grades. Results shown in Figure 12 indicate an upward shift in the incubation dose from the AU to the ST condition, but a comparable secondary swelling rate in all. Values of the two parameters are given below:

*Johnston, et al[5] have shown that silicon and manganese can inhibit swelling in Fe-Cr-Ni alloys.

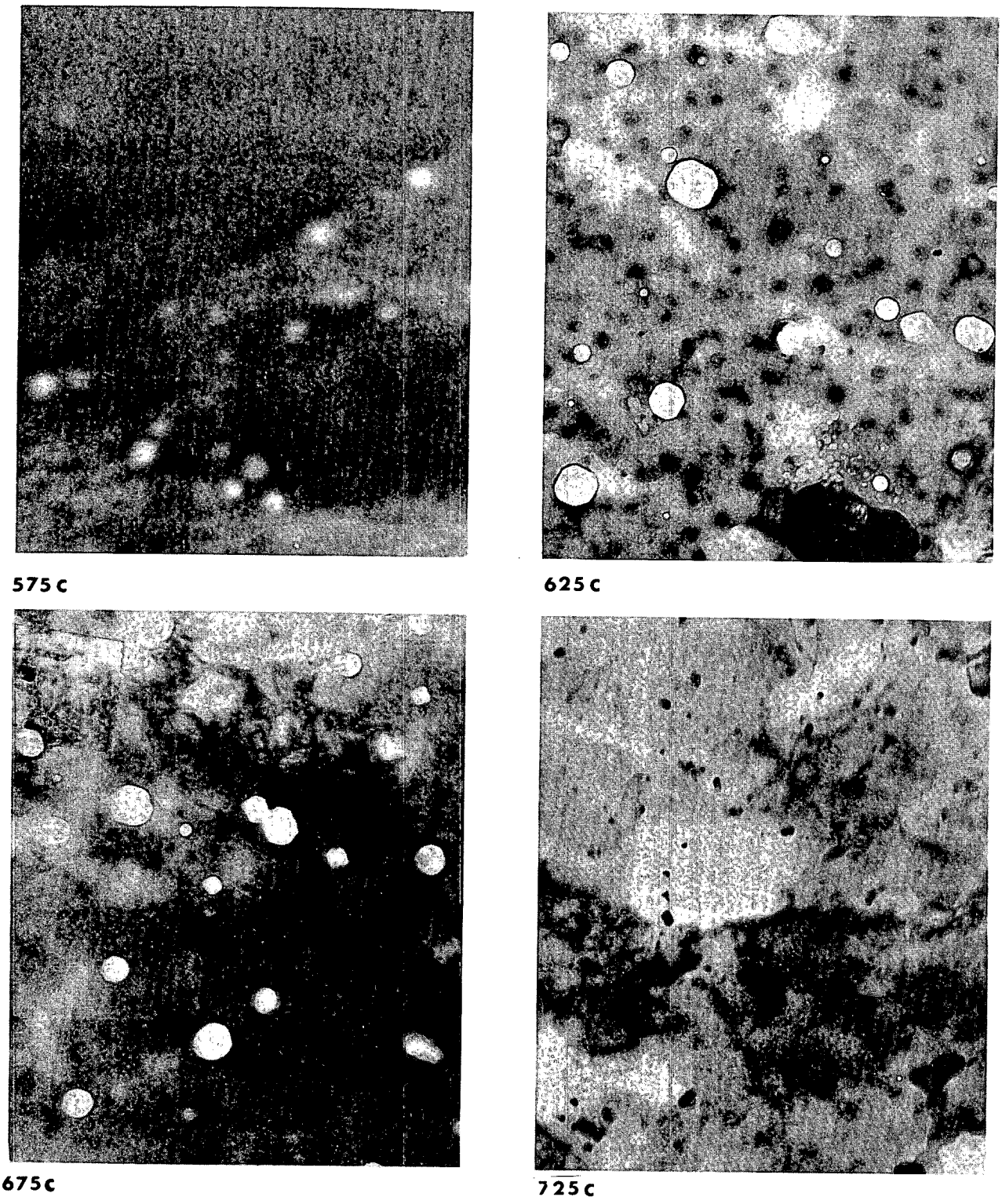

FIGURE 10. Void distributions in AU Nimonic PE16 after nickel-ion bombardment to 248 dpa.

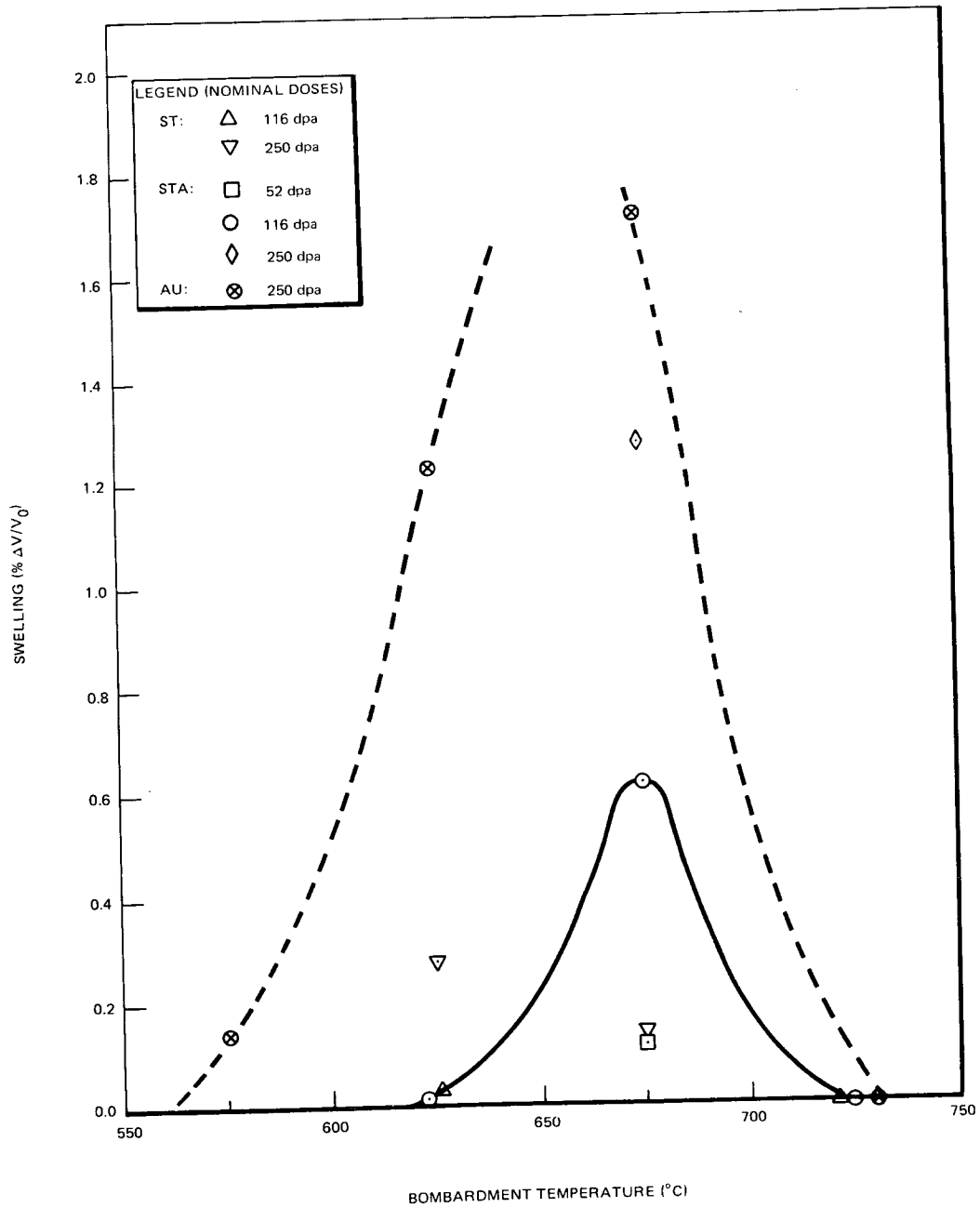

FIGURE 11. Temperature dependence of swelling in Nimonic PE16, bombarded with high energy nickel ions.

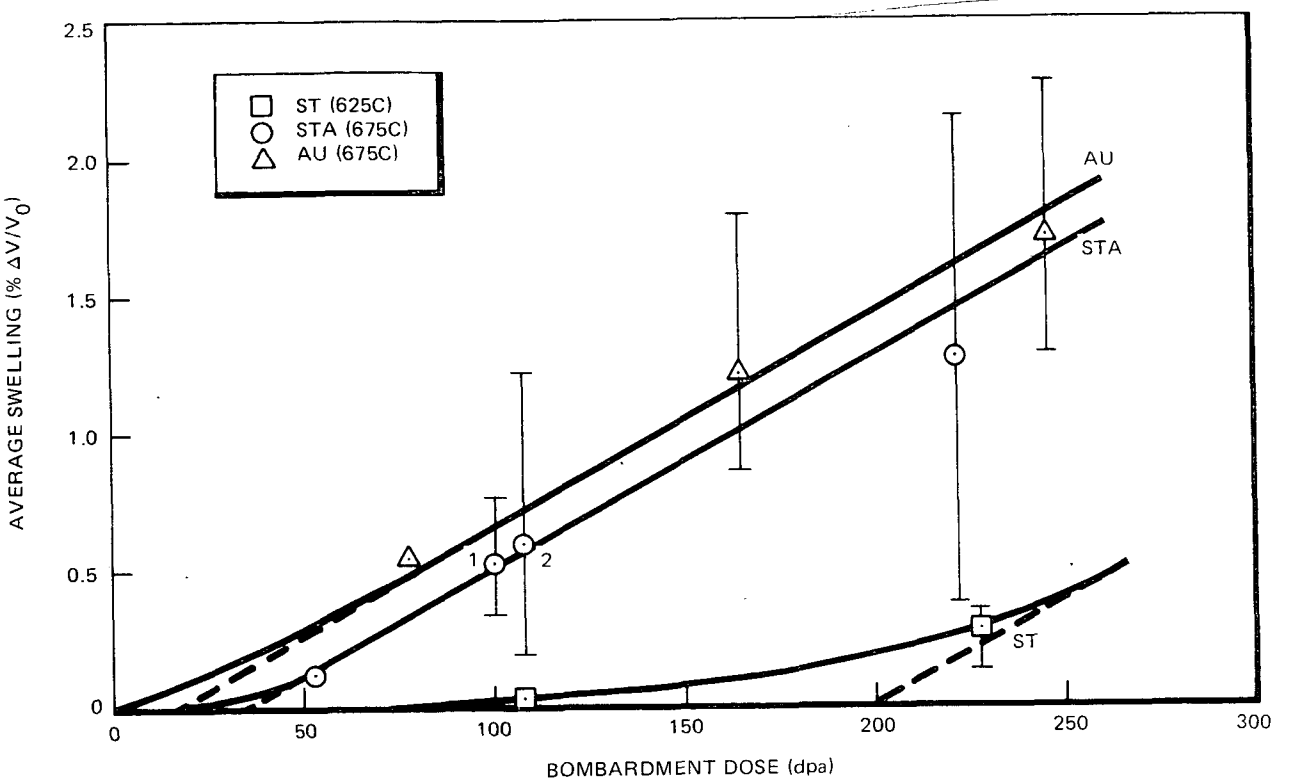

FIGURE 12. Dose dependence of swelling in Nimonic PE16, bombarded with high energy nickel ions. The AU Nimonic PE16 data points represent the surface, intermediate and peak damage zones in the same bombardment foil; STA Nimonic PE16 points 1 and 2 represent the intermediate and peak damage zones, respectively, in different foils. All other data were collected from peak damage zones.

Condition or Lot	Approximate Peak Swelling Temperature	Approximate Incubation Dose, τ	Secondary Swelling Rate
ST	625°C	200 dpa	0.008%/dpa*
STA	675°C	50 dpa	0.008%/dpa
AU	675°C	15 dpa	0.008%/dpa

*In view of the long incubation shown by ST Nimonic PE16, a definitive secondary swelling rate could not be determined without substantially higher dose data. The values shown here are based on the assumption that, once τ has been obtained, all three alloys will swell at a comparable rate.

In addition to the data collected from the peak damage zone of STA Nimonic PE16, swelling determinations were made at two points along the ion path in the 222 dpa bombardment specimen. Swelling measured at an intermediate position (99 dpa) was similar to that measured at the peak in a 106 dpa bombardment (see Figure 12). However, examination of the bombarded surface of the former sample revealed an order of magnitude higher swelling than expected. This anomaly has not yet been resolved. These and all other data collected in the examination of the three lots of Nimonic PE16 are given in Table 9.

Microstructural Changes. A general statement about the behavior of Nimonic PE16 during ion bombardment is that no strong evidence of changes in precipitate microstructures were noted. In aged (STA and AU) materials, the gamma prime distribution appears to be much the same after ion bombardment as before. In annealed materials, no tendency was noted for the formation of gamma prime during bombardment to 116 dpa at the lower temperatures. Very faint gamma prime reciprocal lattice points could be detected after this dose at 725°C and also after 248 dpa at lower temperatures. Dislocation arrays appeared to be more fully developed in ST and AU materials than in the aged PE16 at comparable doses and temperatures. Stacking faults could be observed in annealed material, their sizes and numbers varying with dose and temperature as shown in Figure 13. With the density of defects occurring in Figure 13(a), faint, short relrods were produced in the diffraction patterns much as though a platelike precipitate were present. However, coarsening with increased bombardment temperature did not occur and these defects are most likely faulted loops and thermally unstable.

Unusual grain boundary effects were noticed in all materials bombarded to 248 dpa. Figure 14(a) and 14(b) show that grain boundary regions are well marked in very thin and very thick regions, making it unlikely to be a surface relief phenomenon and more of an electron transparency effect. In AU material bombarded at 675°C, these electron dense regions are physically quite close to actual grain boundary positions [Figure 14(c)] and respond more slowly to electrochemical attack and/or ion milling [Figure 14(d)]. Selected area diffraction from these regions reveals only austenite and gamma prime diffraction spots, so apparently no phase change or precipitation is involved. After 625°C bombardment the opaque strips in AU PE16 are separated from the grain boundary positions by their approximate width ($\sim$1 μm) as shown in Figure 15. Stereoanalysis of Figure 15(b) indicates the opaque regions are no thicker than the surrounding material. However, there appears to be a slight change in void population: slightly more large voids and slightly fewer small voids seem to occur in these regions. A tentative explanation of this grain boundary behavior is that segregation effects are occurring in these regions, changing the chemistry, electron transparency and swelling behavior.

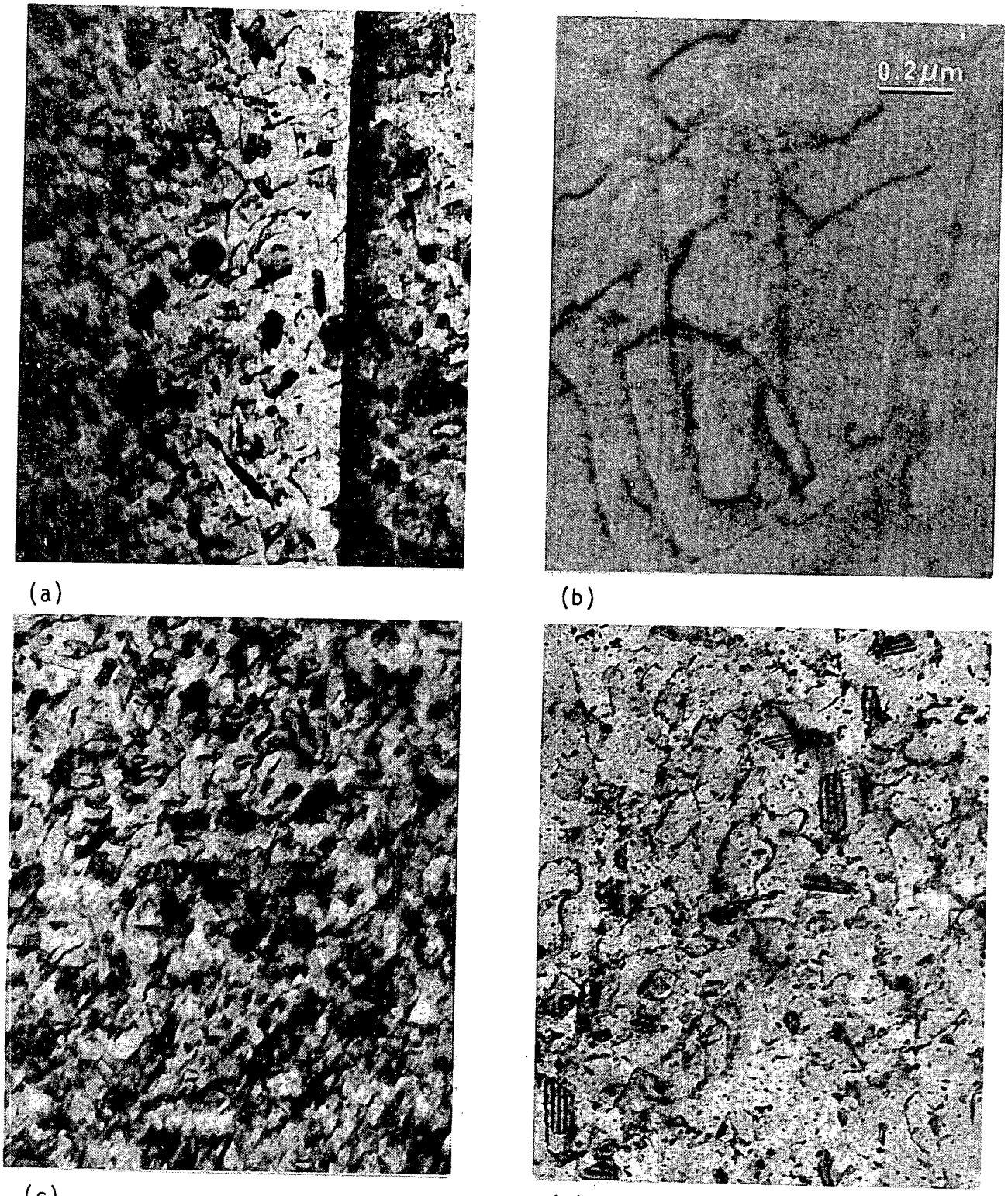

FIGURE 13. Microstructures of STA Nimonic PE16 after (a) 116 dpa at 625°C; (b) 116 dpa at 725°C; (c) 248 dpa at 575°C, and (d) 248 dpa at 625°C.

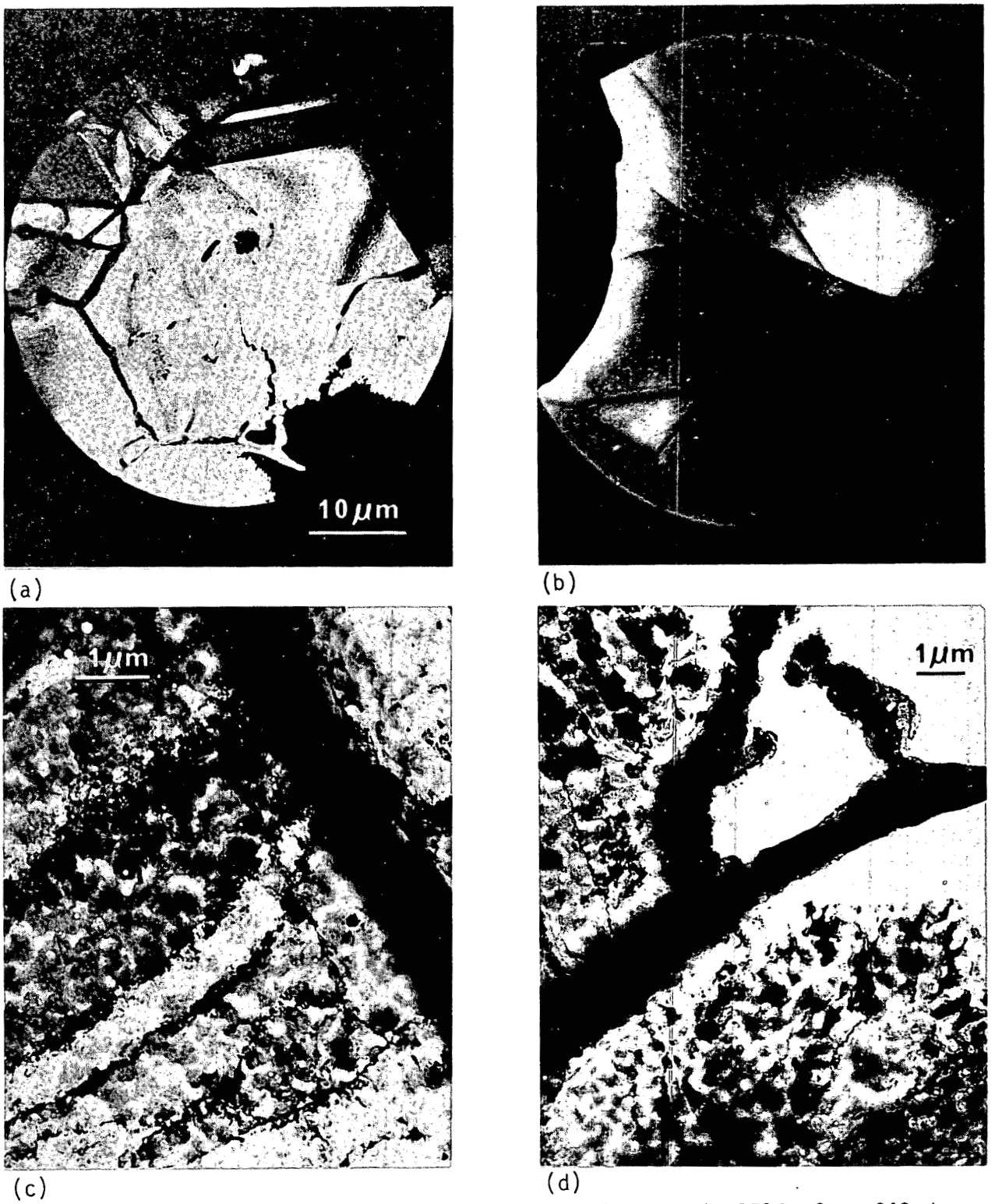

FIGURE 14. Grain boundary opacity effects in AU Nimonic PE16 after 248 dpa nickel-ion bombardment at 675°C: (a) and (b) low-magnification diffuse-dark-field images, (c) and (d) bright-field images.

(a)

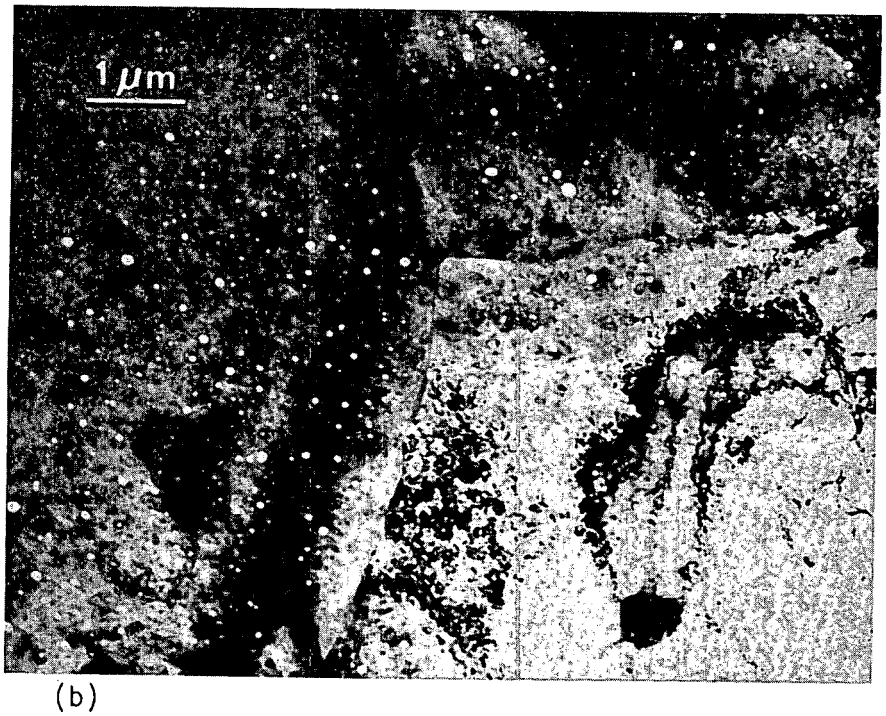

(b)

FIGURE 15. Electron opacity effects near grain boundaries in AU Nimonic PE16 after ion bombardment to 248 dpa at 625°C.

TABLE 9

SWELLING DATA ON NICKEL-ION BOMBARDED NIMONIC PE16

Heat Treatment	Temp., °C	Dose dpa	Average Void Parameters: Density Voids/cm^3	Diameter, nm	Swelling, %$\Delta V/V_o$	Remarks
ST	575	243	1.7×10^{13}	59	<0.1	Local concentration of voids, to 1.5 percent
	625	106	4.6×10^{13}	20	0.03	
		227	2.1×10^{14}	29	0.28	Uniform void distribution
	675	26	-	-	-	No voids
		60	-	-	-	No voids
		224	2.3×10^{13}	50	0.15	Non-uniform void distribution
	725	110	-	-	-	No voids
STA	625	114	2.3×10^{13}	22	0.01	
	675	52	6.1×10^{13}	33	0.11	Peak
		78	7.2×10^{13}	78	1.83	Bombarded surface(a)
		99	3.2×10^{13}	69	0.52	Not peak(a)
		106	1.3×10^{14}	43	0.58	Peak
		222	3.7×10^{13}	92	1.28	Peak(a)
	725	96	1.0×10^{13}	40	<0.01	
AU	575	247	1.7×10^{13}	55	0.14	
	625	78	5.2×10^{13}	58	0.48	Bombarded surface(b)
		247	1.2×10^{14}	57	1.22	Peak(b)
	675	76	4.1×10^{13}	59	0.55	Bombarded surface(c)
		164	8.4×10^{13}	65	1.22	Not peak(c)
		247	1.2×10^{14}	64	1.71	Peak(c)
		?	3.6×10^{13}	52	0.29	Beyond peak(c)
	725	241	-	-	-	No voids

* (a): same foil, (b) same foil, (c) same foil

2.3.4.2 Inconel 706. Inconel 706, like Nimonic PE16, was bombarded in three microstructural conditions; solution treated (ST), the commercially aged condition (STA) and a thermomechanical treatment designated CWA. All were prepared from HEDL heat 48C5HK. Although comparable to Nimonic PE16 in base alloy composition, Inconel 706 contains niobium as well as titanium and aluminum. The alloy is therefore susceptible to both gamma prime and gamma double prime precipitation and their respective overaging forms, delta and eta. Details of the swelling and microstructural studies on the three lots are given below.

Swelling. All three Inconel 706 grades (Heat No. 48C5HK) exhibited a high degree of swelling resistance. In the solution-treated alloy, only trace swellings (<0.001 percent) could be detected over a 225-degree temperature range, at doses as high as 231 dpa. In the cold worked and aged alloy, a peak swelling of 0.008 percent was measured at

575°C at a bombardment dose of 236 dpa; higher and lower temperature bombardments at similar doses produced no voids. Swelling in the commercially aged material was substantially larger but the void distribution was so irregular that assigned swelling values are likely to be highly pessimistic.

Two void distributions were identified in STA Inconel 706. At 475°C, small (<10 nm) voids were observed in the matrix and adjacent to second-phase precipitates. The small matrix voids were also noted at 550°C along with the larger voids (~44 nm) clustered near precipitates. The void populations at 575 and 625°C were composed primarily of the larger voids. Electron micrographs representative of these distributions are shown in Figure 16.

In view of the vanishingly small swelling that can be attributed to the smaller voids and the predominance of the large but non-uniformly distributed voids at the higher temperatures, it was decided that assignment of a peak swelling temperature be based on maximum swelling values computed from the latter distribution. The data compiled in Table 10 pertain predominantly to this distribution. These admittedly sparse data indicate a peak

TABLE 10

SWELLING DATA ON NICKEL-ION BOMBARDED INCONEL 706

Heat Treatment	Temp., °C	Dose dpa	Average Void Parameters			Remarks
			Density Voids/cm^3	Diameter, nm	Swelling, $\%\Delta V/V_o$	
ST	500	106	2.3×10^{13}	8	<0.001	
	550	120	-	-	-	No voids
		202	-	-	-	No voids
	600	116	5.7×10^{12}	11	<0.001	
	625	116	-	-	-	No voids
		231	-	-	-	No voids (HVEM)
	675	114	-	-	-	No voids
	725	119	-	-	-	No voids
STA	475	116	5.5×10^{13}	7	0.001	
	550	116	4.0×10^{13}	19	0.051	
	575	64	3.9×10^{13}	25	0.045	Not peak*
		236	1.5×10^{13}	82	0.435	Local islands of voids*
	625	120	1.4×10^{13}	41	0.051	
	675	103	-	-	-	No voids
	725	116	-	-	-	No voids
CWA	525	229	-	-	-	No voids
	575	238	8.6×10^{12}	20	0.008	
	625	238	-	-	-	No voids

* Same foil

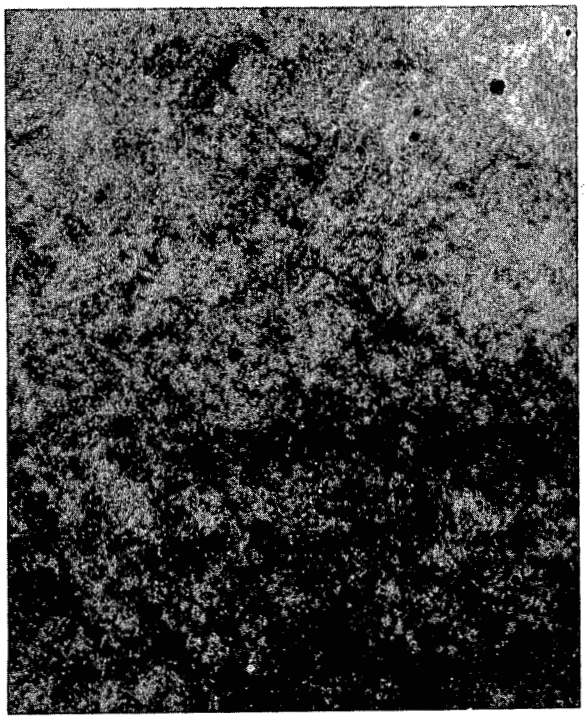

475 c

625c

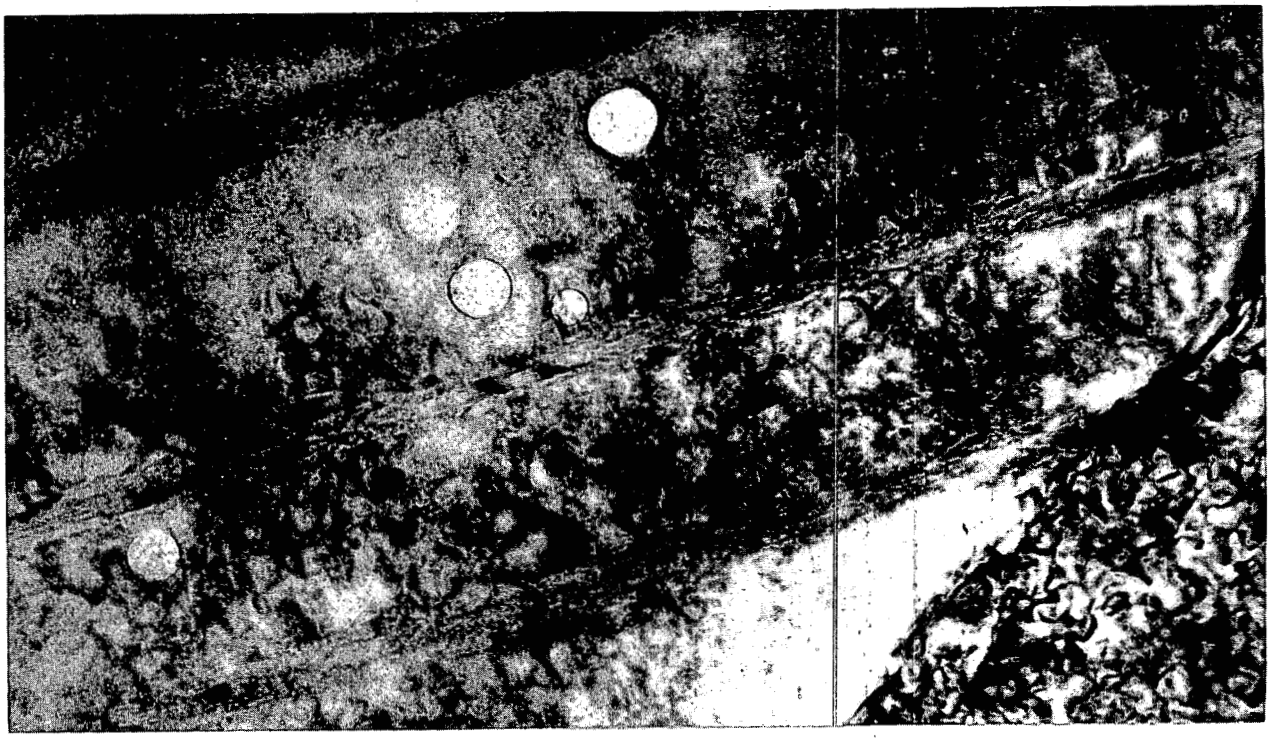

550c

FIGURE 16. Void distributions in STA Inconel 706 after nickel-ion bombardment to 116 dpa.

0.1μm

swelling temperature of 575°C, a peak swelling rate of 0.002%/dpa and a dose intercept of 44 dpa. Earlier GE results[4] on an aged Inconel 706 heat of almost identical composition showed swelling of <0.1% at 625°C and <<0.1% at 675°C and 725°C at a nominal dose of 116 dpa.

All that can be said of ST Inconel 706 is that its peak swelling temperature lies within the 500-600°C range and its swelling rate is <0.0001%/dpa. A similar swelling rate is shown by the TEM data on the CWA alloy at its 575°C peak swelling temperature. The temperature dependence of swelling of all three alloys and the dose dependence of swelling of STA Inconel 706 are shown in Figure 17.

Microstructural Changes. Figure 18 shows the microstructures of STA Inconel 706 after 116 dpa bombardments at temperatures between 550 and 725°C. Representative selected area diffraction patterns are shown in Figure 19 where streaks due to thin precipitates can be detected even for the material bombarded at the lowest temperature. Faint streaks were also observed in diffraction patterns of an additional specimen bombarded at 475°C. The obvious effects of increasing the bombardment temperature are the enhanced coarsening of the precipitate platelets and the appearance of intensity maxima on relrods (reciprocal lattice rods arising from thin platelets in real space) due to the development of stronger form factor effects with the coarser plates.

The precipitates habit {111} planes of the matrix and relrods in diffraction patterns pass through, and eventually connect, matrix reciprocal lattice points along <111> directions. However, even with the coarsest plates the intensity maxima developing along the relrods are not localized enough to allow accurate interplanar spacings to be determined.

It is not possible to identify the precipitates produced in Inconel 706 by ion bombardment solely on the basis that they habit {111} planes, since both δ and η phases have this characteristic and both are stable phases produced by overaging. Distinction between the two possibilities must be accomplished using interplanar spacings. However, relrod intersections with diffraction patterns of arbitrary orientations will not allow correct interplanar spacings to be determined and, even when the relrods lie in the diffraction patterns, the diffuse nature of the intensity maxima makes difficult the measurements required to obtain interplanar spacings accurate enough to identify the proper phase. One way to avoid these problems is to use a <111> matrix orientation and determine the positions of the intersections of relrods which are normal to the electron diffraction pattern. These intersections will then be in the proper positions for reflections belonging to the zone axis of the precipitate parallel with the <111> matrix direction, the <001> for the η phase or the <010> for the δ phase. Figure 20 is a <111> diffraction pattern from the material containing the coarsest platelets, aged Inconel 706 bombarded at 725°C. The weak interior spots have sixfold symmetry with corresponding interplanar spacings of 0.221 nm in agreement with published values for $\{2\bar{0}20\}$ Planes of hexagonal Ni_3Ti[12]. To match published data on orthorhombic Ni_3Nb, these spots would need to correspond to {002} and {201} planes with spacings of 0.228 nm and 0.223 nm respectively[13], with interplanar angles of 61° and 58°; the measured angles are all within half degrees of 60°. It is thus clear that the better choice of precipitate species, based upon experimental evidence, is η phase, the hexagonal form of Ni_3Ti.

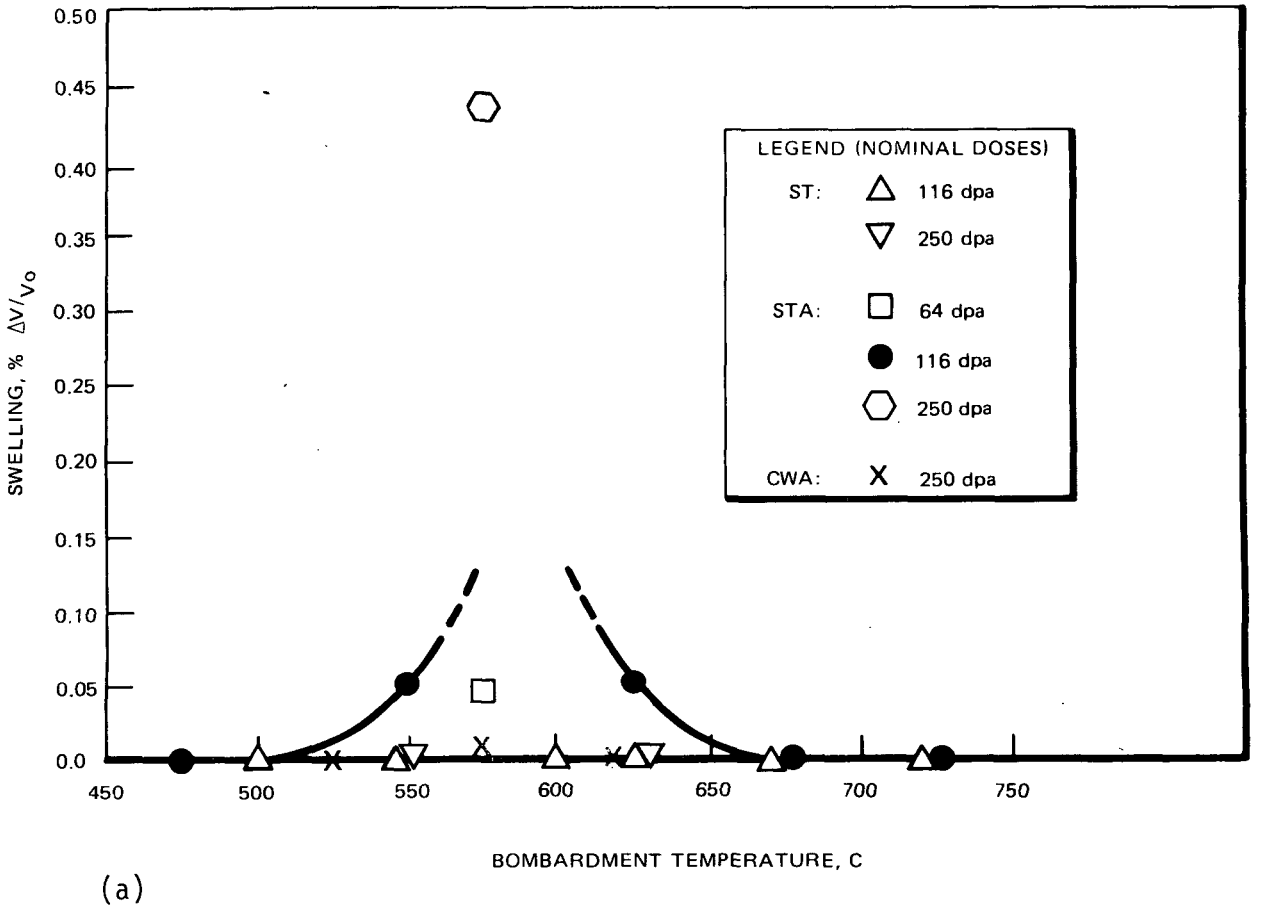

(a)

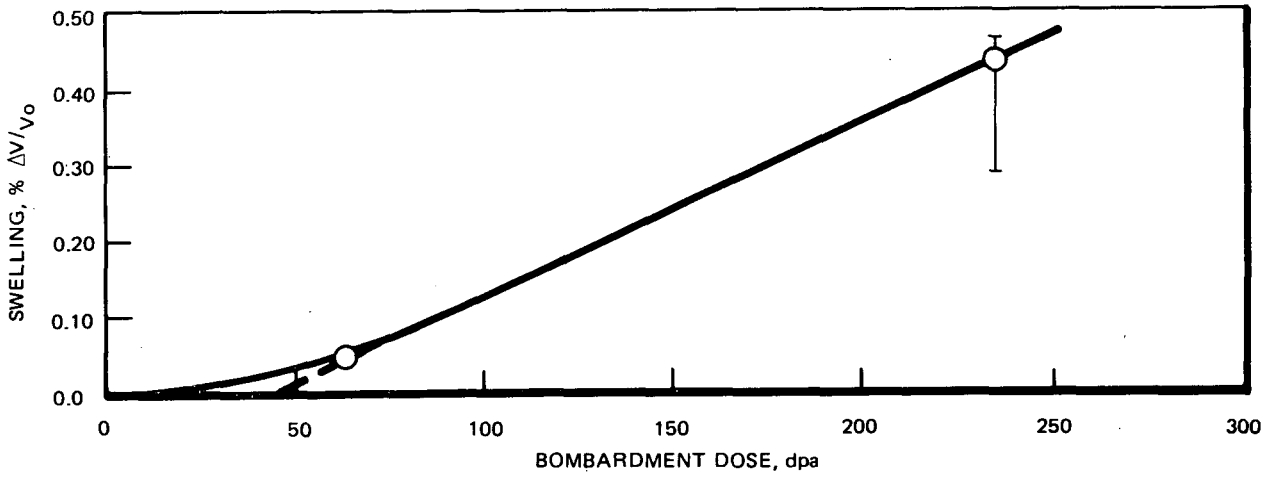

(b)

FIGURE 17. Temperature and dose dependence of swelling in Inconel 706, bombarded with high energy nickel ions: (a) temperature dependence of swelling, and (b) dose dependence of swelling in STA Inconel 706 at 575°C.

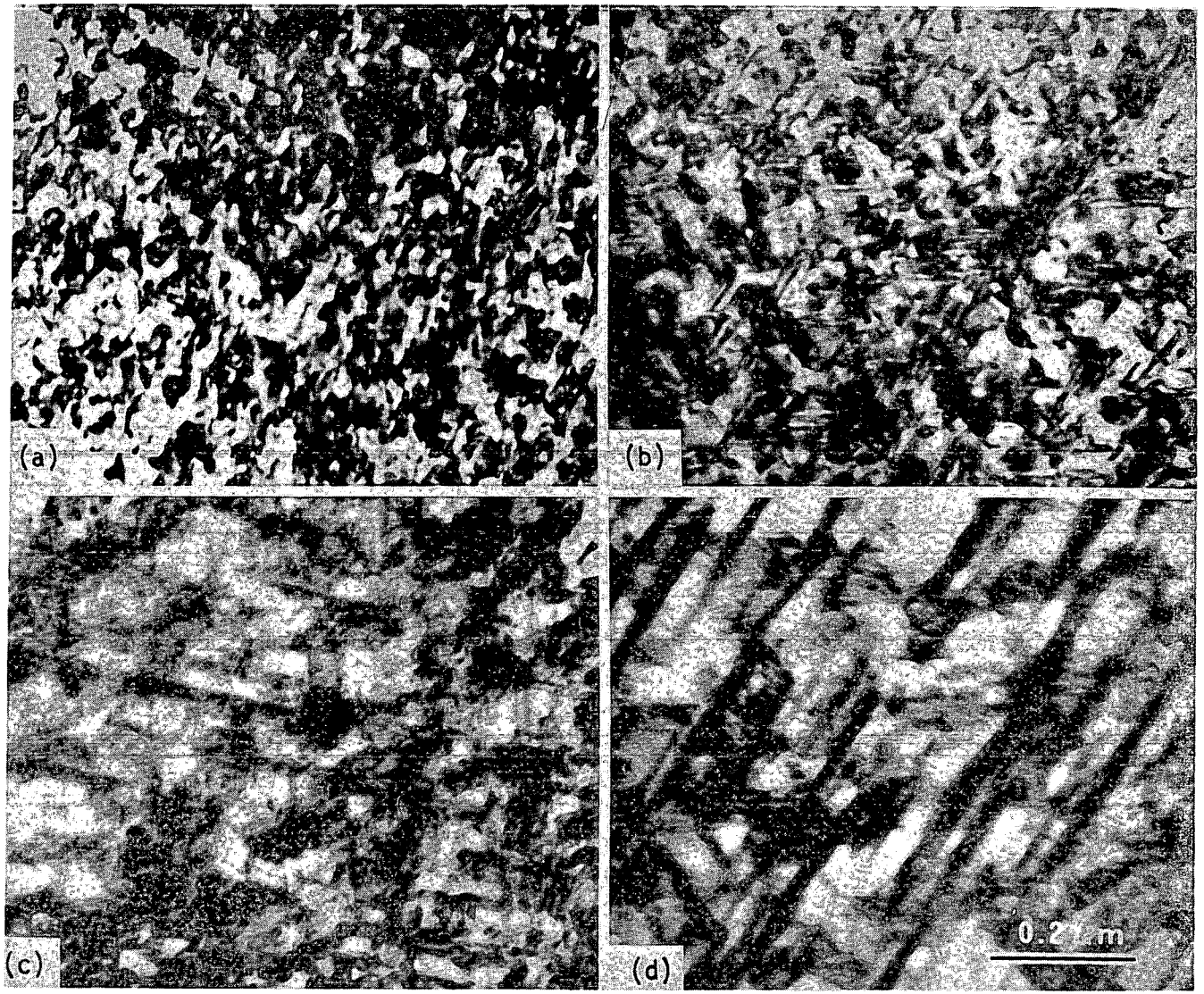

FIGURE 18. TEM images of STA Inconel 706, bombarded with 5 MeV nickel ions to 116 dpa: (a) 550°C, dark-field image; (b) 625°C, dark-field image; (c) 675°C, bright-field image, and (d) 725°C, bright-field image.

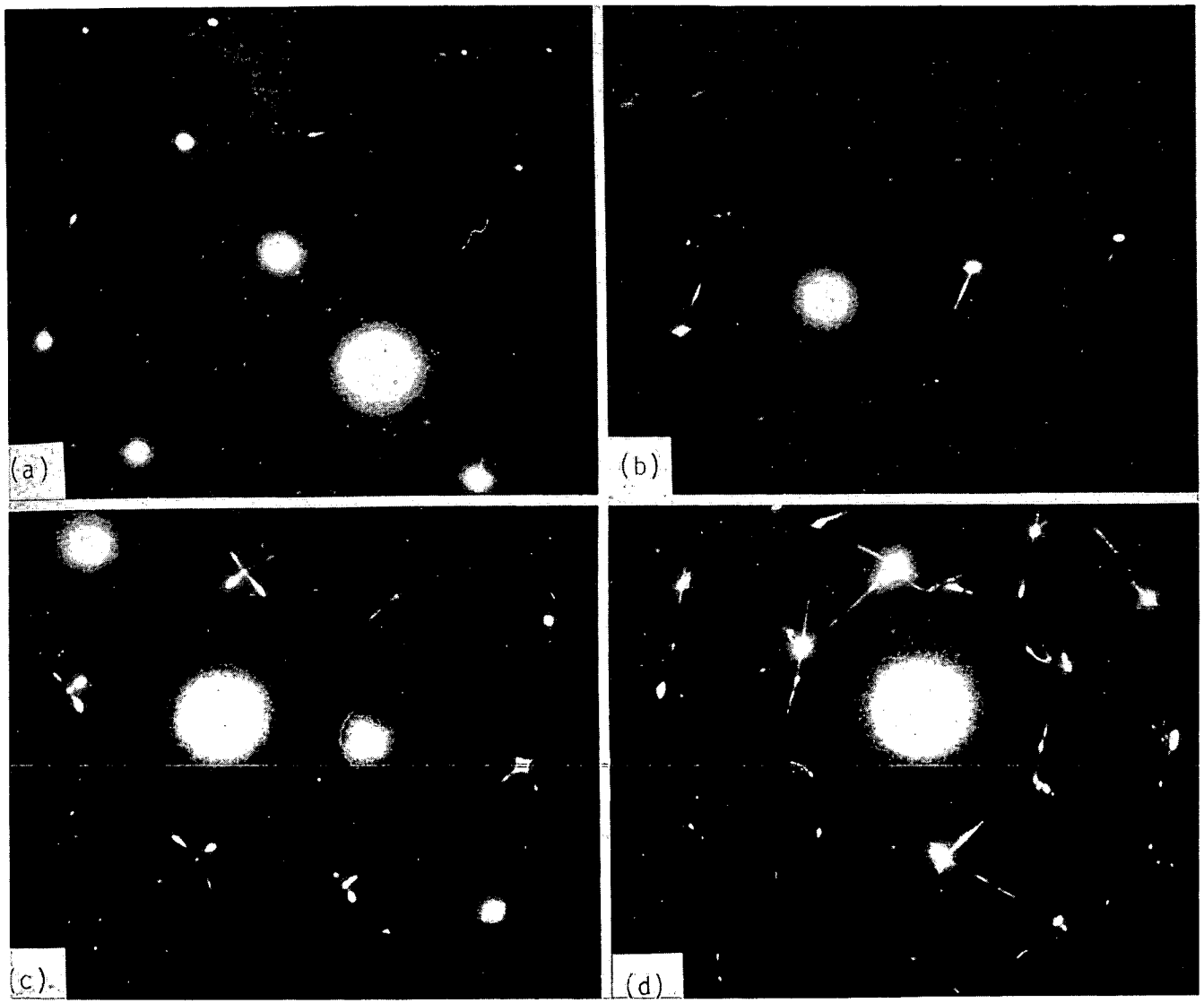

FIGURE 19. Representative selected area electron diffraction patterns from STA Inconel 706 after 5 MeV nickel-ion bombardment to 116 dpa: (a) 550°C; (b) 625°C; (c) 675°C, and (d) 725°C.

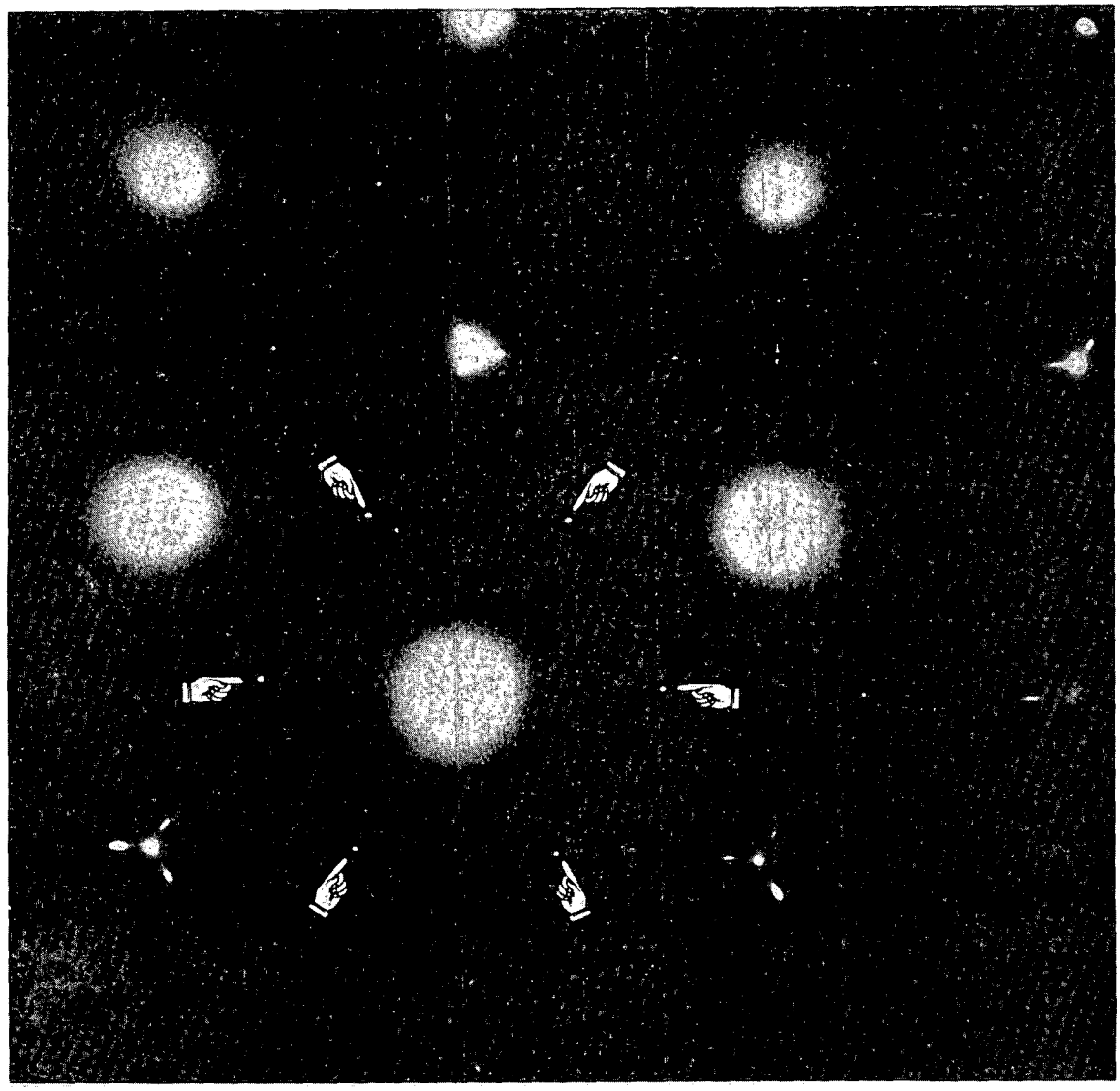

FIGURE 20. Selected area <111> electron diffraction pattern from Inconel 706 bombarded at 725°C. The reflections indicated correspond to {2020} planes of hexagonal eta phase platelets in the plane of the specimen. Satellite spots around outer reflections are caused by relrods produced by thin precipitates on inclined {111} planes.

The pre-irradiation precipitate phases, γ' and γ'', are degraded or dissolved during ion bombardment. With increasing bombardment temperature the superlattice reflections became weakened and dark-field imaging disclosed fewer particles.

ST Inconel 706 was studied after similar ion bombardments and precipitate platelets were also observed as shown in Figure 21. However, in both images and diffraction patterns, it appeared that the degree of coarsening of the platelets was lower than observed in aged material bombarded at similar temperatures. In addition to the relrods due to the platelets, superlattice spots corresponding to γ' or γ'' were observed in the diffraction patterns. Since neither of the metastable precipitate phases were present during the pre-irradiation characterization, ion bombardment must also have produced these in addition to the coarser platelet phase. However, in dark-field images using the superlattice reflections, the metastable precipitates could not be easily detected or distinguished from the diffuse background.

To emphasize the difference in coarsening between ST and STA Inconel 706 during heavy ion bombardment, Figure 22 shows typical grain boundaries in the materials bombarded at 625°C. Characteristic overaging behavior is exhibited by the aged material[7] and cellular precipitation is advanced at the grain boundaries. In contrast, the annealed material still has straight grain boundaries and no noticeably greater coarsening of precipitate plates in these regions.

Bombardments to higher doses were made only for a limited number of temperatures, so further analysis of overaging behavior could not be carried out for many of the cases studied after 116 dpa. However, after 248 dpa it was very clear that 600°C is still the approximate boundary between sluggish and rapid overaging behavior during ion bombardment. Figure 23 shows the general features of ST, STA and CWA Inconel 706 after 248 dpa below 600°C; platelet features are generally difficult to identify. The representative selected area diffraction patterns of Figure 24 exhibit corresponding weak relrod features.

A very dramatic difference can be observed in CWA material after 248 dpa at 625°C where there is extensive precipitation of coarse platelets. Figure 25 shows a bright-field image and a dark-field image of the same area obtained using a precipitate reflection. The selected area diffraction pattern, showing the objective aperture position for dark-field imaging, is shown in Figure 26(a). Since the volume of precipitate material is large, the structure factors are no longer dominated by form factor effects and complete precipitate diffraction patterns can be observed and analyzed. The diffraction pattern is straightforwardly indexed in Figure 26(b) as a hexagonal pattern with zone axis $[\bar{8}176]$ superposed on the austenite pattern near the zone axis $[3\bar{7}\bar{6}]$. After tilting the foil a few degrees, a slightly different pattern is obtained from the same austenite grain as shown and indexed in Figures 26(c) and (d). A $[\bar{5}143]$ hexagonal pattern is now superposed on an austenite pattern near $[3\bar{6}\bar{5}]$. Both patterns are required to demonstrate that there are unit changes in the c-axis indices (i.e., $20\bar{2}5$ and $20\bar{2}6$ are neighboring points in the reciprocal lattice of the precipitate) and hence there is a real lattice parameter corresponding to C = 0.828 nm. This effectively identifies the eta phase and justifies the hexagonal indexing used. Further evidence of this can be seen along directions connecting austenite reflections away from the pattern centers where the relrods along $[1\bar{1}1]$, an alternate habit plane, exhibit intensity maxima corresponding to one quarter of the <111> translation vector.

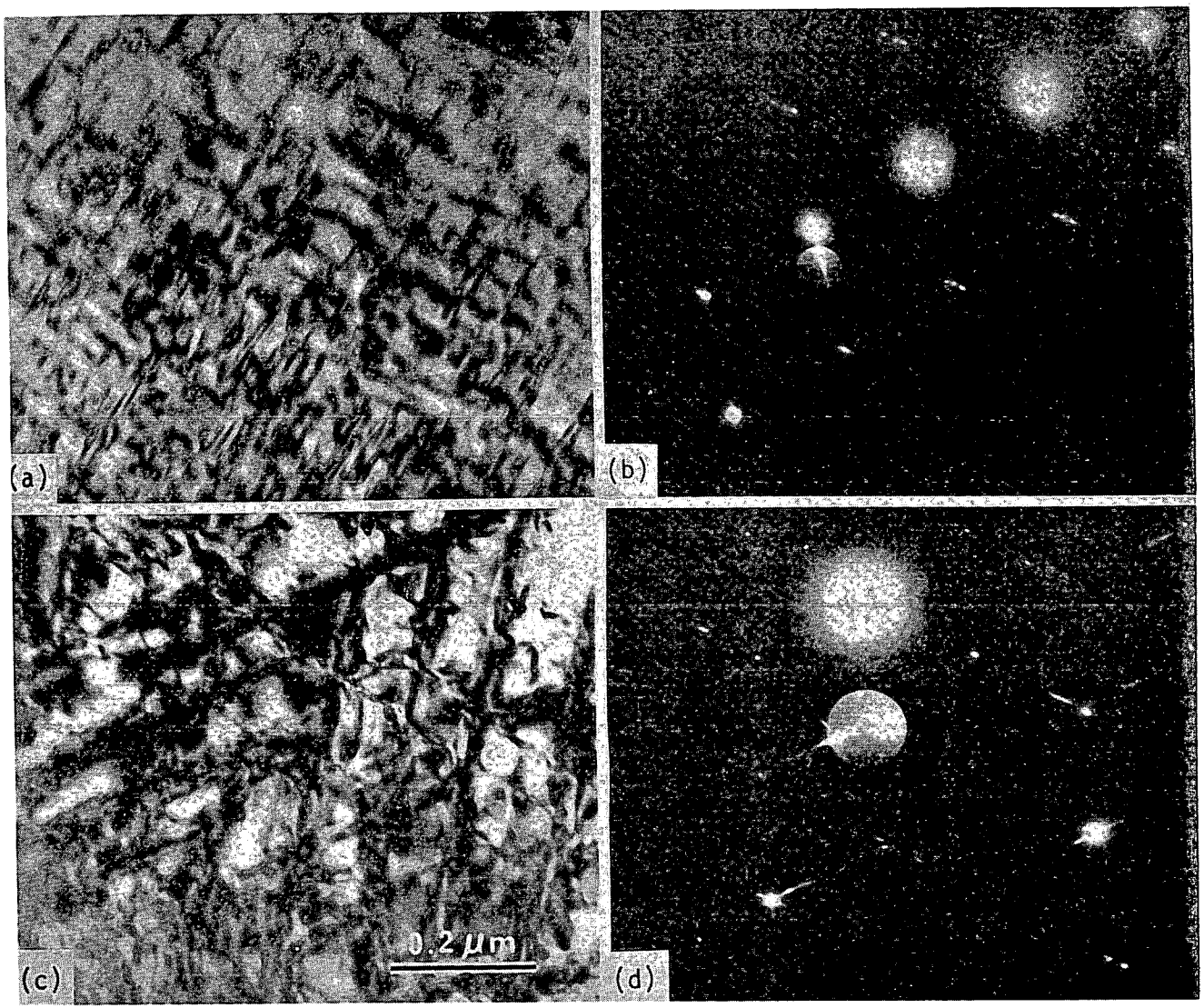

FIGURE 21. Bright-field images and representative selected area diffraction patterns from ST Inconel 706 after 5 MeV nickel-ion bombardment to 116 dpa: top, 625°C; bottom, 725°C.

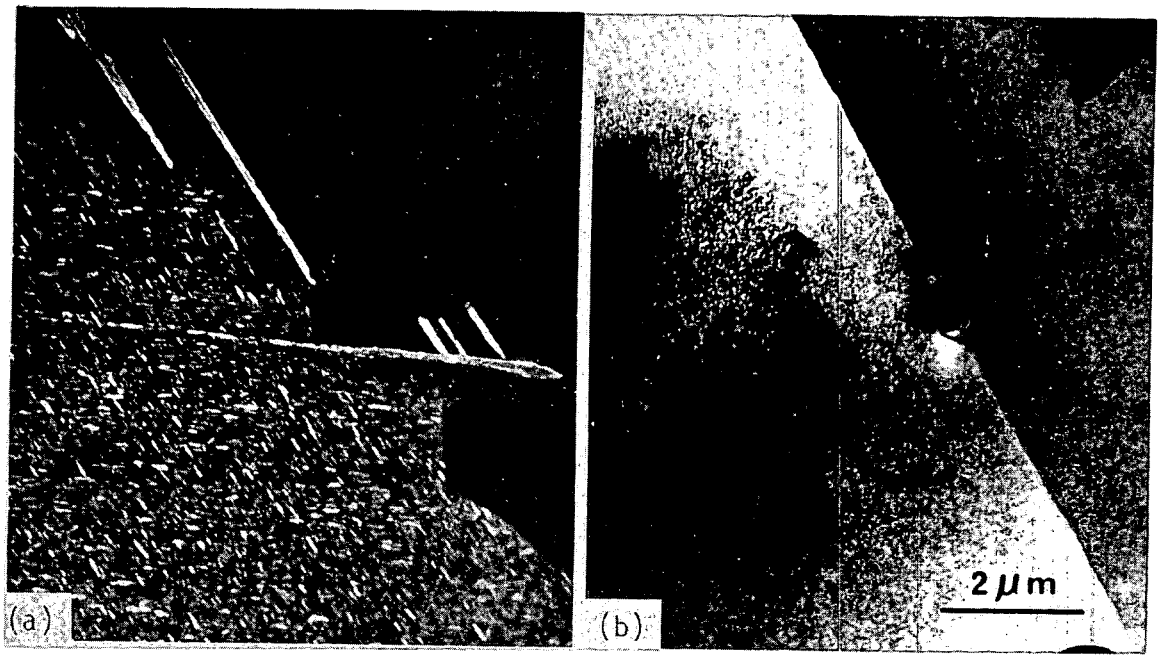

FIGURE 22. Dark-field images of grain boundary regions in (a) STA and (b) ST Inconel 706, after 5 MeV nickel-ion bombardment to 116 dpa.

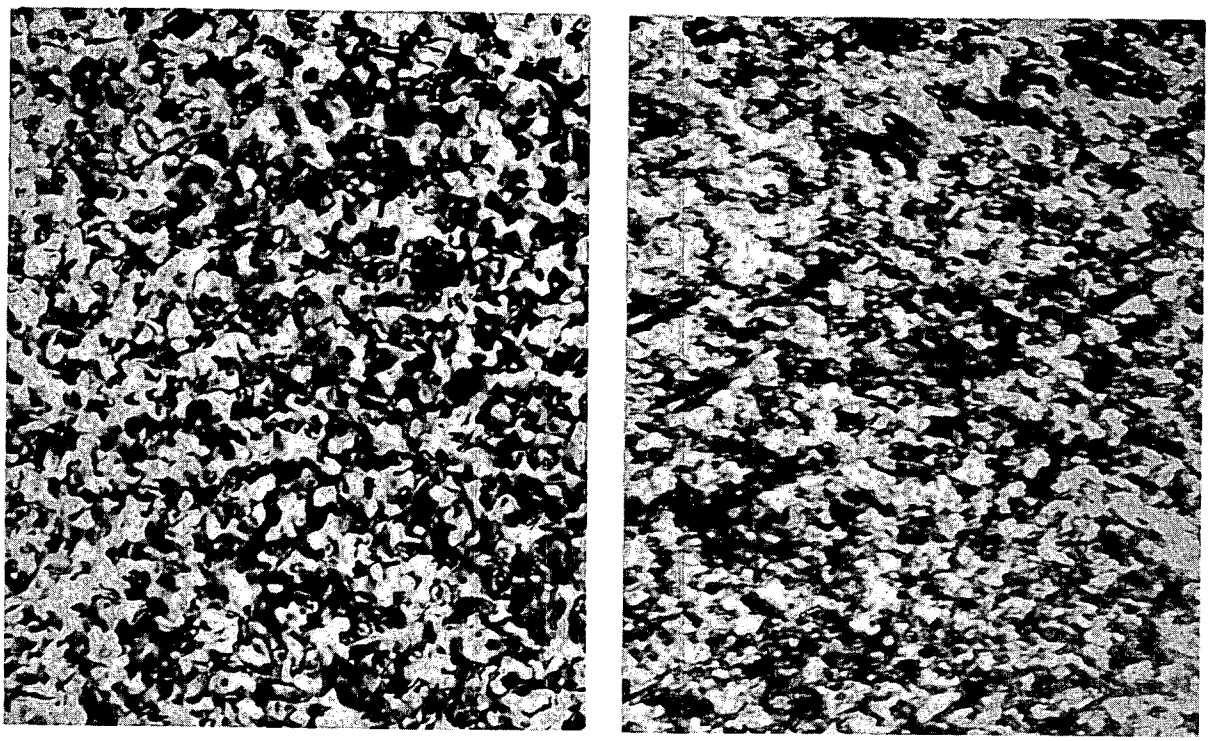

(a) (b)

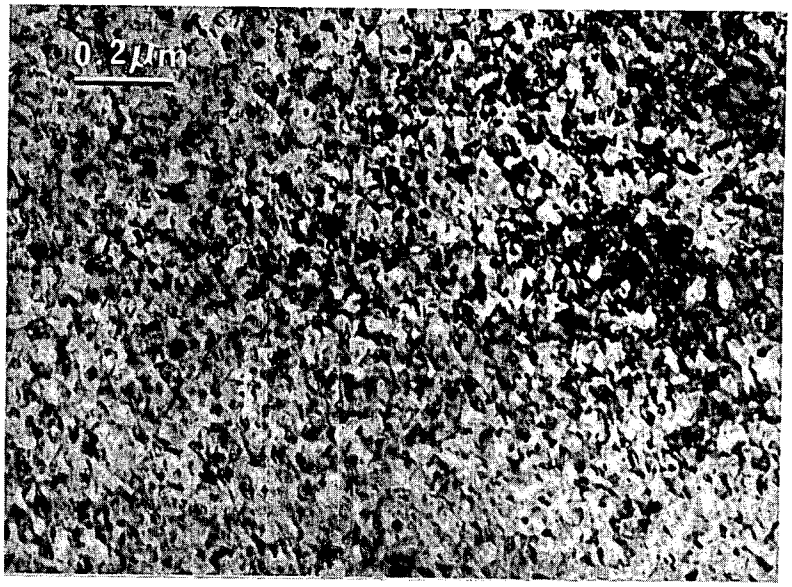

(c)

FIGURE 23. Bright-field images of Inconel 706 ion bombarded to 248 dpa: (a) ST, 550°C; (b) STA, 575°C, and (c) CWA, 575°C.

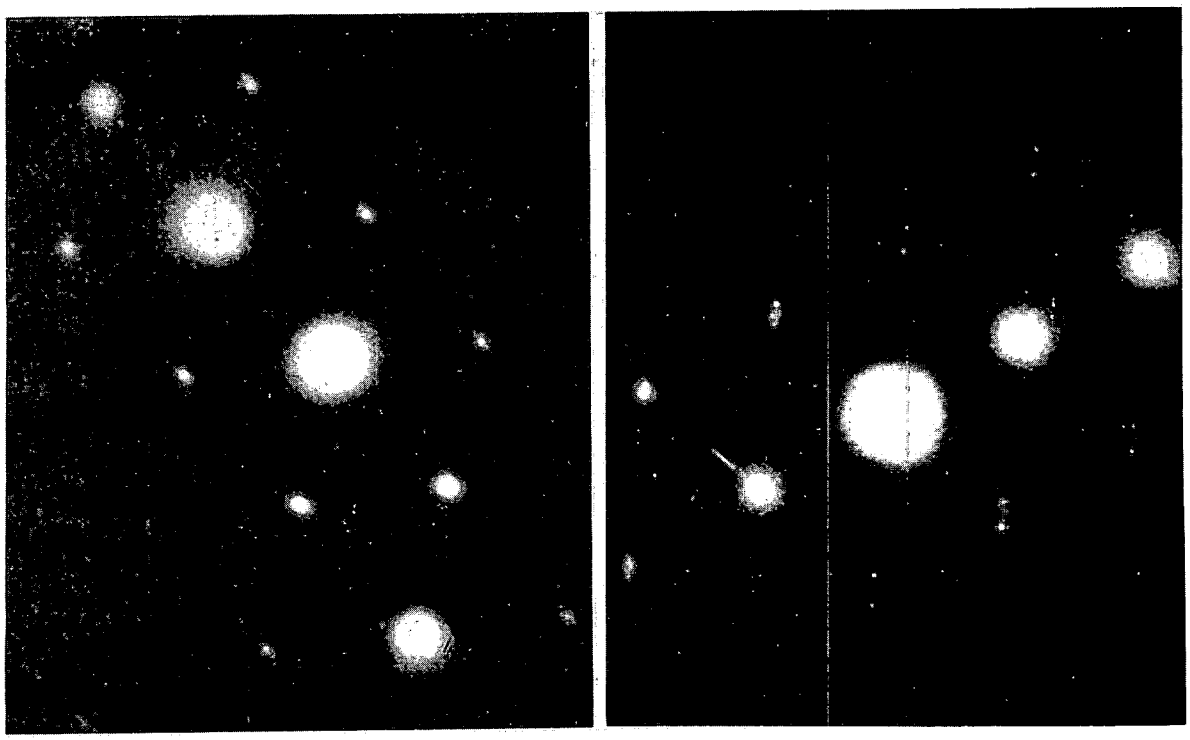

(a) (b)

(c)

FIGURE 24. Representative selected area electron diffraction patterns from Inconel 706 ion bombarded to 248 dpa: (a) ST, 550°C, (b) STA, 575°C, and (c) CWA, 575°C.

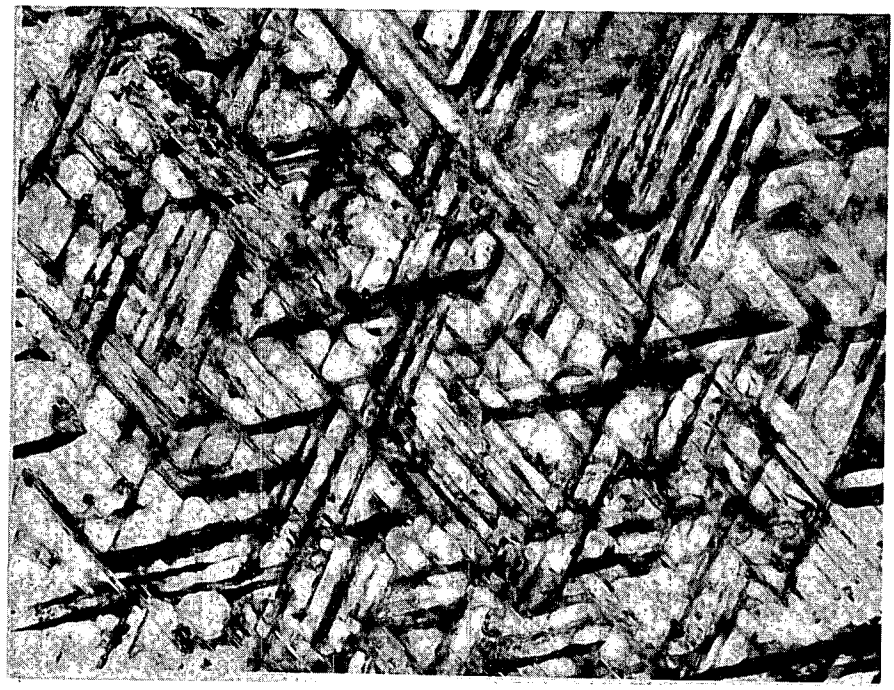

(a)

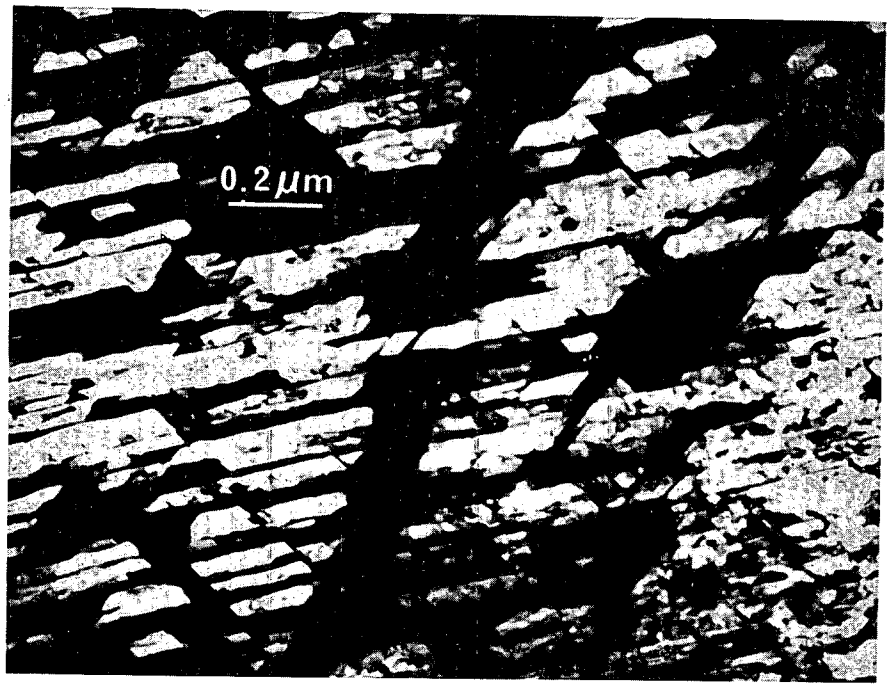

(b)

FIGURE 25. Bright-field (a) and dark-field (b) image pair of CWA Inconel 706 after ion bombardment to 248 dpa at 625°C.

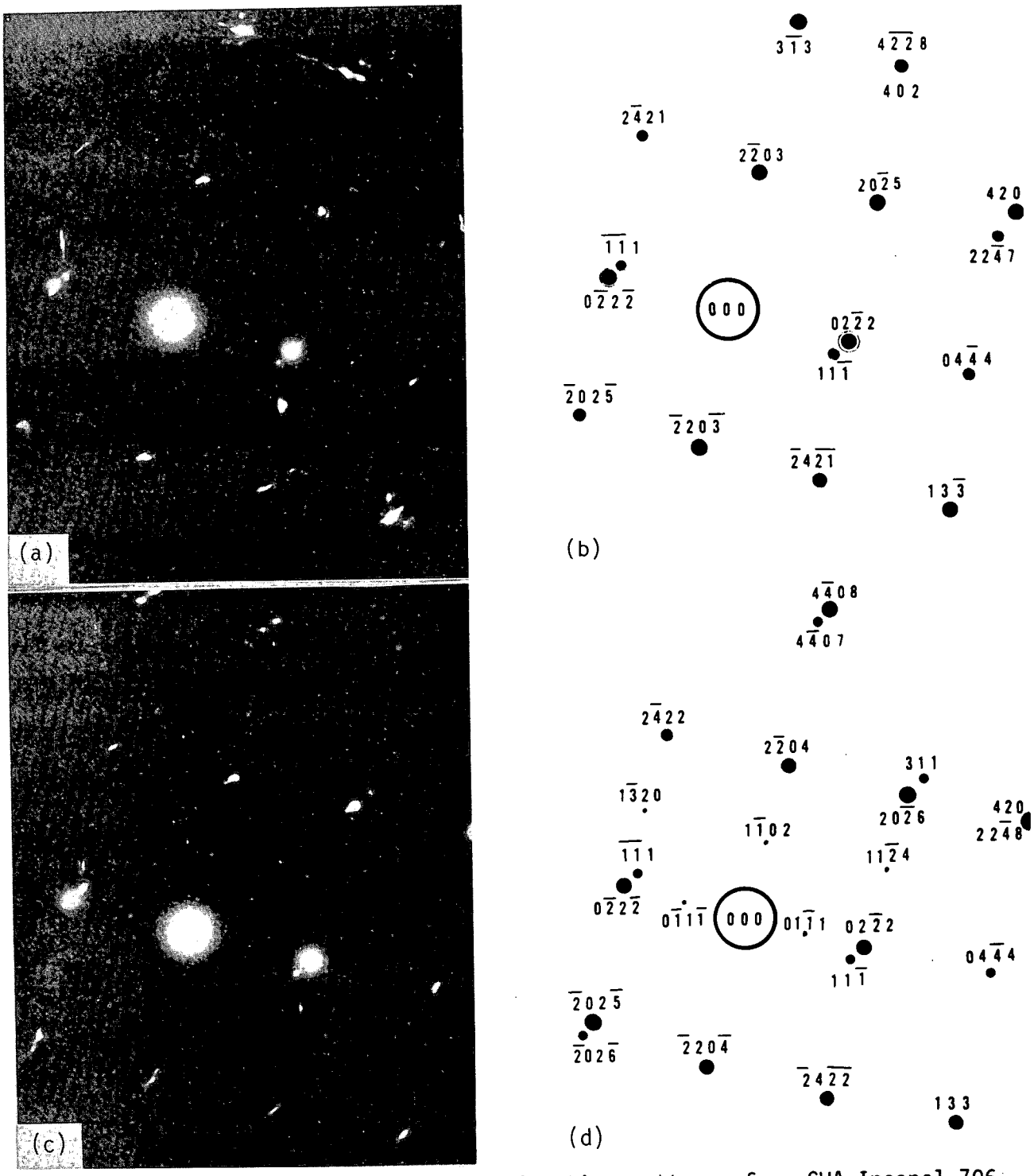

FIGURE 26. Selected area electron diffraction patterns from CWA Inconel 706 after ion bombardment to 248 dpa at 625°C: (a) Pattern of area shown in Fig 25; (b) hexagonal (4 digit) and fcc (3 digit) indexing of one precipitate orientation, (c) and (d) pattern and indexing from the same region after tilting the foil slightly.

Figure 26(c) also exhibits weak first-order reflections, $(01\bar{1}1)$, $(1\bar{1}02)$ and $(11\bar{2}4)$, which fit into the hexagonal indexing. Other weak spots not indexed belong to precipitates habiting other {111} planes. A listing of interplanar spacings of the precipitating phase, obtained from diffraction patterns of CWA Inconel 706 after 248 dpa ion bombardment, is compared in Table 11 to x-ray diffraction data of the eta and delta phases taken from the ASTM card index file. The ASTM card data has been supplemented, in brackets, to account for reflections that would be expected in electron diffraction patterns arising from double diffraction. Except for planes of the type $\{10\bar{1}0\}$ and $\{20\bar{2}0\}$, there is rather a complete correspondence with eta phase data. The {2020} interplanar spacing has previously been observed in lower dose STA Inconel 706 (Figure 20).

TABLE 11

X-RAY DIFFRACTION DATA FOR η AND δ PHASES

Ni_3Ti (η) ASTM CARD 5-723			Observed	Ni_3Nb (δ) ASTM CARD 15-101		
hkil	I/I_1	d(Å)	d(Å)	d(Å)	I/I_1	hkl
$10\bar{1}0$	10	4.39				
$10\bar{1}1$	10	3.90	3.90			
				3.403	2	101
				3.262	10	110
$(10\bar{1}2)$		(3.02)	3.02			
$11\bar{2}0$	10	2.56	2.55	2.568	4	200
				2.27	20	002
$20\bar{2}0$	20	2.21		2.23	35	201
$(11\bar{2}2)$		(2.17)	2.19			
$20\bar{2}1$	50	2.13	2.12	2.12	100	020
0004	50	2.07	2.07	2.07	8	102
				2.00	75	012
				1.97	75	211
$20\bar{2}2$	100	1.95	1.95	1.95	6	120
				1.80	2	121
$20\bar{2}3$	20	1.72	1.73	(1.70)		(202)
$(12\bar{3}0)$		(1.66)	1.66	1.55	6	022
$12\bar{3}2$	10	1.54	1.53	1.54	8	221
$20\bar{2}4$	20	1.51	1.51			
$20\bar{2}5$	20	1.33	1.33	(1.33)		(222)
				1.30	16	203
$22\bar{4}0$	50	1.28	1.27	1.28	8	400
$(22\bar{4}1)$		(1.26)	1.25	(1.24)		(230)
$(22\bar{4}2)$		(1.22)	1.22			
				1.20	8	032
$20\bar{2}6$	20	1.17	1.16			
				1.13	4	004
$40\bar{4}0$	-	1.11		1.11	16	223
$40\bar{4}1$	10	1.10		1.10	10	420

There is also fair, but incomplete, correspondence of the observed interplanar spacings with delta phase data. However, the weak reflections observed in Figure 26(c), $\{10\bar{1}1\}$, $\{10\bar{1}2\}$, and $\{12\bar{3}0\}$, provide a further indication to those already specified that eta is the precipitating phase in ion bombarded Inconel 706, since no reasonable inaccuracies in measurements and calculations would account for the lack of correspondence with the delta phase data.

The austenite-to-eta transformation conforms to the following transformations of planes:

$$(111)_\gamma \rightarrow (0004)_\eta$$

$$(1\bar{1}0)_\gamma \rightarrow (2\bar{1}\bar{1}0)_\eta$$

$$(01\bar{1})_\gamma \rightarrow (\bar{1}2\bar{1}0)_\eta$$

Thus the transformation of planes with arbitrary Miller indices can be written as:

$$\begin{pmatrix} h \\ k \\ i \\ l \end{pmatrix}_\eta = \frac{1}{3} \begin{pmatrix} 3 & -3 & 0 \\ 0 & 3 & -3 \\ -3 & 0 & 3 \\ 4 & 4 & 4 \end{pmatrix} \begin{pmatrix} h \\ k \\ l \end{pmatrix}_\gamma$$

The indexing used in Figure 26 was made consistent with this transformation matrix. For example, the very strong $(02\bar{2}2)_\eta$ reflection occurs at the austenite reciprocal lattice position of $(11\bar{1}) + 1/6\ (111) = 1/6\ (77\bar{5})$, i.e., one sixth the distance between $(11\bar{1})$ and (220) along the [111] relrqd. The transformation matrix accounts for all reflections which are coincident in the cubic and hexagonal lattices [e.g., $(402)_\gamma$ transforms to $(4\bar{2}\bar{2}8)_\eta$ in Figure 26] and maintains the correct interplanar spacings and interplanar angles.

In view of the excellent correspondence obtained in CWA Inconel 706 with the nature and morphology of the intragranular platelike hexagonal phase precipitate, there can remain no doubt that it is eta phase that is produced by ion bombardment.

No grain boundary effects were observed in ST or CWA Inconel 706 bombarded to the higher doses. STA material, however, exhibited faint grain boundary delineation. This material also contained platelets of grain boundaries which are of much greater size than the intragranularly precipitating eta phase. These boundary effects are illustrated in Figure 27.

In all cases that could be analyzed, the grain boundary precipitates proved also to be eta phase, so the cellular precipitation behavior (Figure 22) continues at the higher doses. No evidence at all has been obtained that delta plates are present, either intra or intergranularly, after nickel ion bombardment.

No traces of gamma prime could be found in STA Inconel 706 after 248 dpa at 625°C but faint {001} reflections from this phase could still be observed after the same dose at 575°C. Gamma prime reflections were also observed after high dose bombardment of ST Inconel 706 at 550°C. In the CWA material, extremely weak gamma prime reflections were present after 248 dpa at 575°C and no trace of this phase was found after 625°C bombardment.

One further precipitation event was found to occur in Inconel 706 below 600°C where eta precipitation is sluggish. Very weak reflections can be found on diffraction patterns radially just inside the austenite reflections. This is illustrated in Figure 28 for ST and CWA materials after 248 dpa. The diffracting positions occupied are characteristic of TiC and an agreeing lattice parameter of .436 nm can be calculated from the reflections observed. No such features were observed in STA material after high dose bombardments.

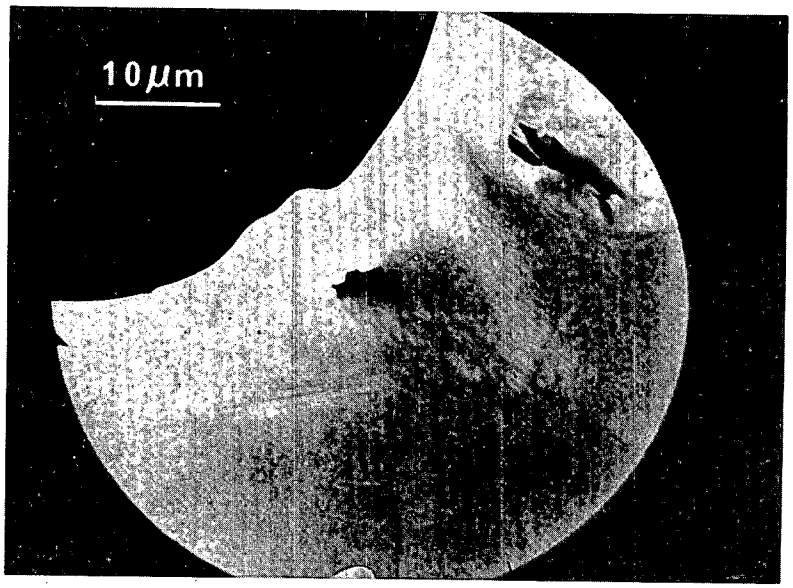

(a)

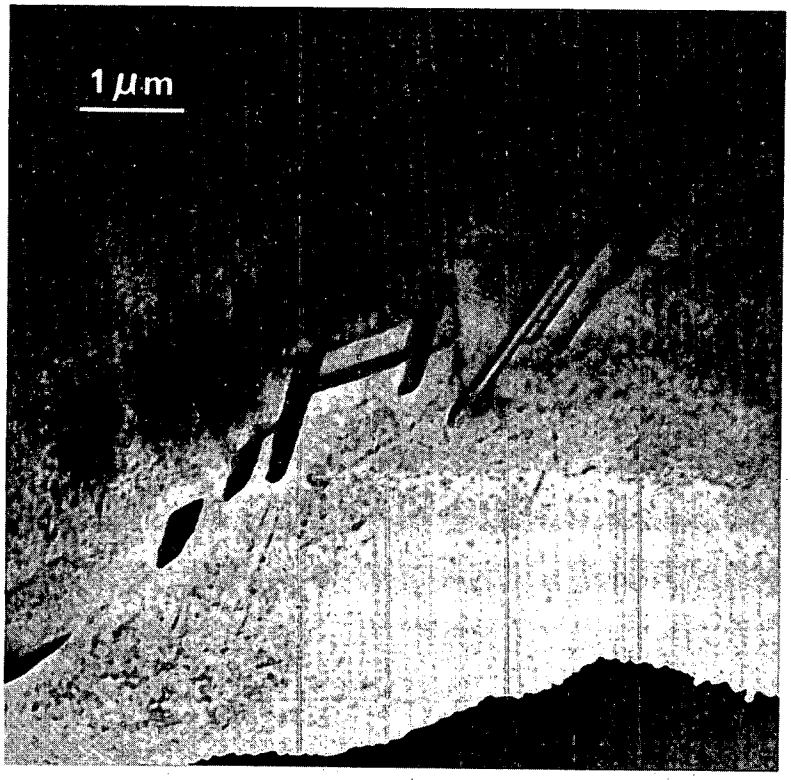

(b)

FIGURE 27. Diffuse-dark-field images showing grain boundary effects in STA Inconel 706 after ion bombardment to 248 dpa: (a) after 575°C bombardment, faint grain boundary delineation represents the strongest effect observed in Inconel 706; (b) after 625°C bombardment, coarse eta plate precipitation more or less characteristic of the cellular growth occurring at grain boundaries.

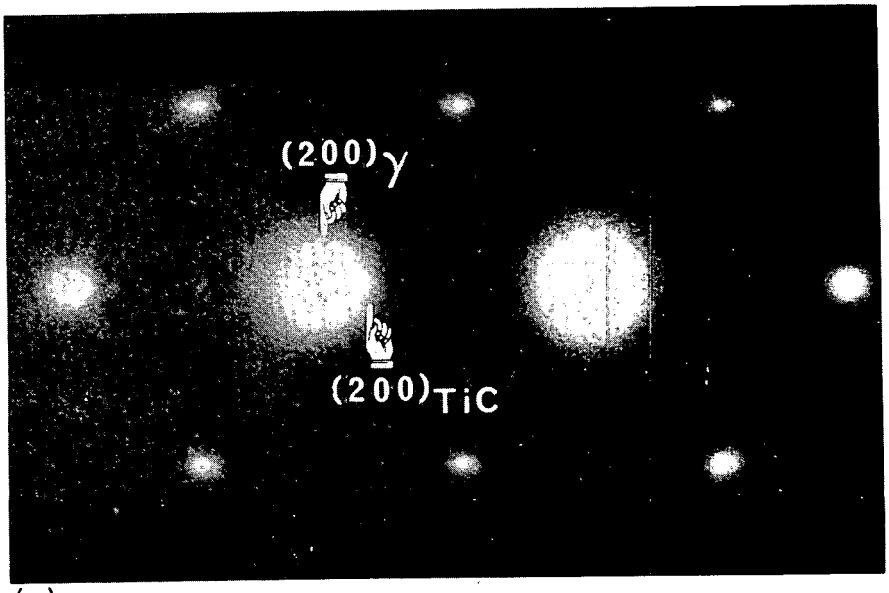

(a)

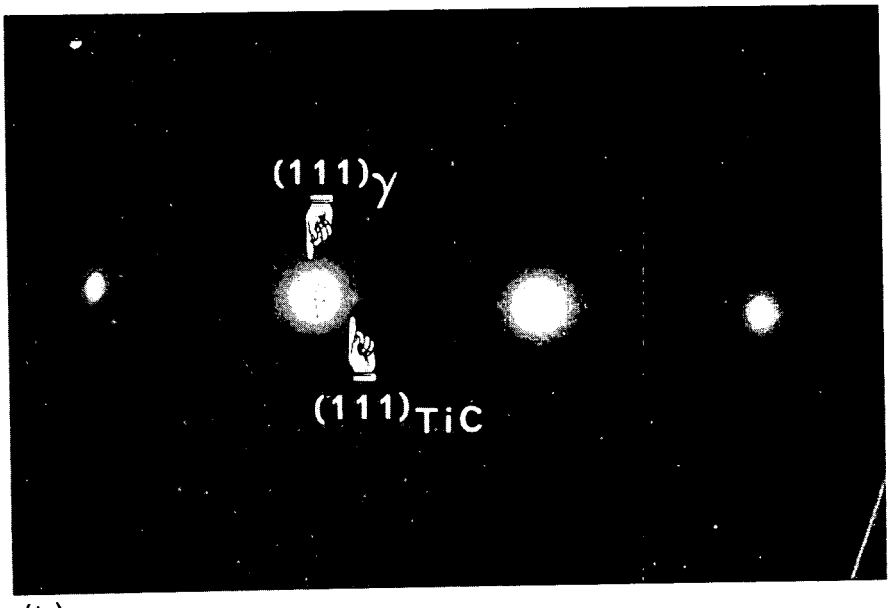

(b)

FIGURE 28. Selected area electron diffraction patterns from Inconel 706 bombarded to 248 dpa which contains spots in positions characteristic of TiC: (a) ST, 550°C, and (b) CWA, 575°C.

2.3.4.3 Inconel 718. Inconel 718 is one of a family of high-nickel superalloys that is hardenable by high-temperature aging. Like Inconel 706, alloy 718 contains alloying elements for both gamma prime and gamma double prime formation and is susceptible to over-aging by the transformation of these precipitates to delta and eta. Because of its inherently high mechanical strength and attractive wear characteristics, Inconel 718 is being considered in a number of LMFBR in-core applications. Its stability in a fast reactor environment is thus of great practical concern. In the present study, the alloy was bombarded in its commercially-aged condition, designated by the acronym STA (for solution treated and aged). Its swelling and microstructural behavior are characterized in the following discussion.

Swelling. The temperature dependence of swelling in STA Inconel 718 was evaluated from 116 dpa bombardments at 50-degree increments from 525 to 725°C. Peak swelling occurred at 625°C. This observation was confirmed by higher-dose bombardments, which produced uniform void distributions at both 575 and 625°C, and a peak swelling of 2.04 percent at the higher temperature. Typical foil microstructures are shown in Figure 29. Confirmation of both lower-dose bombardments with higher-dose runs also provided data for dose dependence of swelling at peak and off-peak locations. These results show swelling rates of 0.015 and 0.004%/dpa and dose intercepts of 105 and 120 dpa, respectively, for 625 and 575°C bombardments. The STA Inconel 718 data are shown graphically in Figure 30 and listed in Table 12.

Two heats of STA Inconel 718 were used in the present study. In the initial phase of the work, material from Heat No. 59F1EY, implanted with 15 ppm of helium, was used to establish the temperature dependence of swelling. However, since bombardments at the upper two temperatures of the three-temperature matrix failed to produce voids, the assessment could not pinpoint the swelling peak. Lower temperature work with material from Heat No. 44F9EY, implanted with 5 ppm of helium, confirmed the 625°C peak at the nominal 116 dpa level. Similar results were subsequently collected at twice this dose, using the 5 ppm helium material exclusively. Although the effect of the higher helium level is unclear, the consistently low swelling observed in this alloy at the lower dose level using both 5 and 15 ppm of helium suggest that the effect was minor. (The two heats of Inconel 718 used here received identical heat treatments.)

Microstructural Changes. The microstructural features of STA Inconel 718 (Heat No. 59F1EY) after 116 dpa bombardments are shown in Figure 31 where the coarsening of precipitate platelets, similar to those observed in Inconel 706, can be seen to increase with increasing bombardment temperature. Molybdenum masks had been used to shield certain areas of the target specimens from ion bombardment for purposes of obtaining step heights which can be correlated to swelling behavior. In each specimen, perforations were made in the ion bombarded region and also in an area that had been shielded. Thus thermal control information could be obtained from the same specimen that had undergone bombardment. In all cases, the unirradiated material appeared as characterized in the pre-irradiation study and γ'' could be imaged using appropriate dark-field techniques. The appearance of the material under the masked area of the 725°C bombarded specimen is also shown in Figure 31 and is representative of that observed in specimens bombarded at lower temperatures.

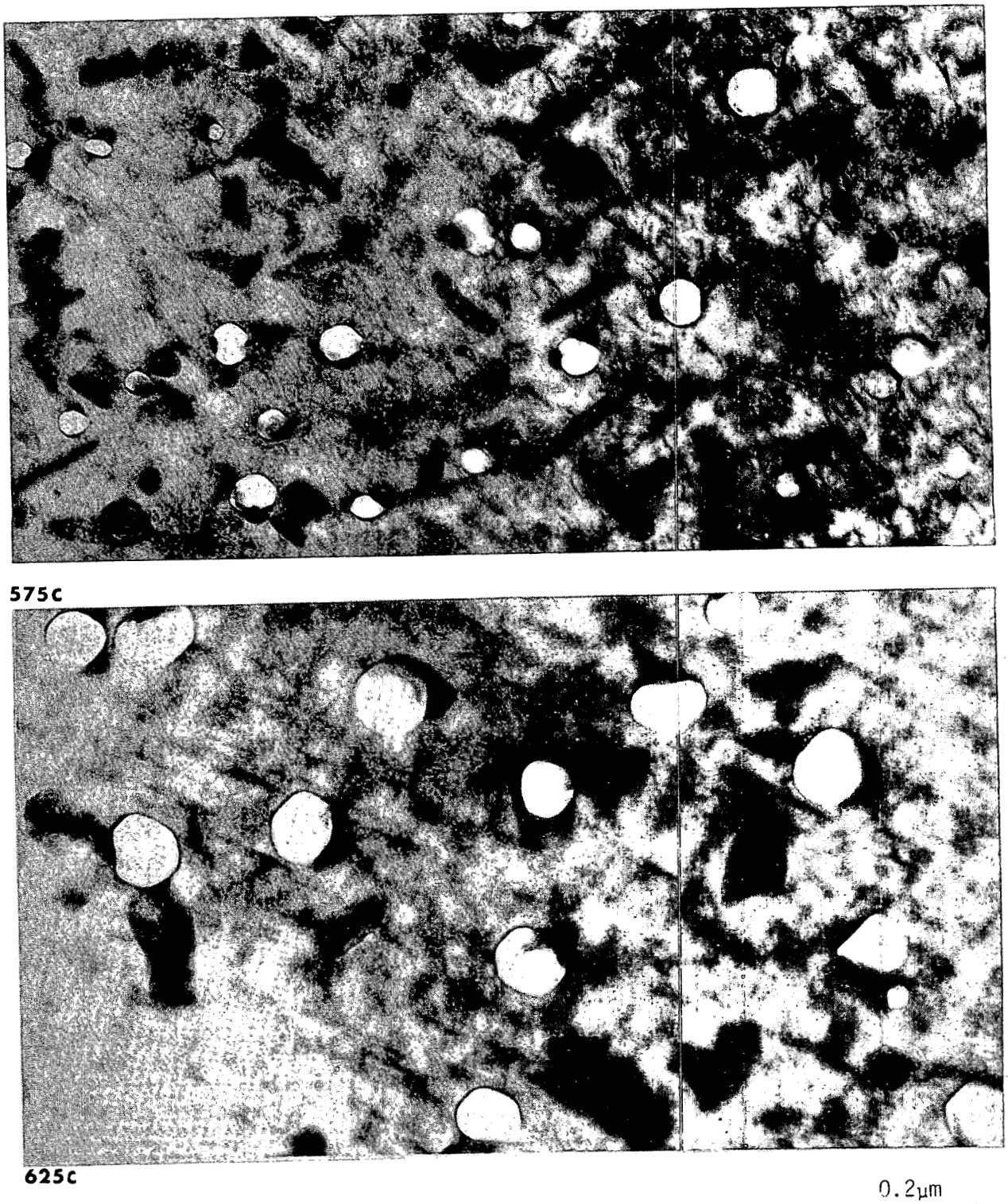

FIGURE 29. Void distribution in STA Inconel 718 after nickel ion bombardment to 239 dpa.

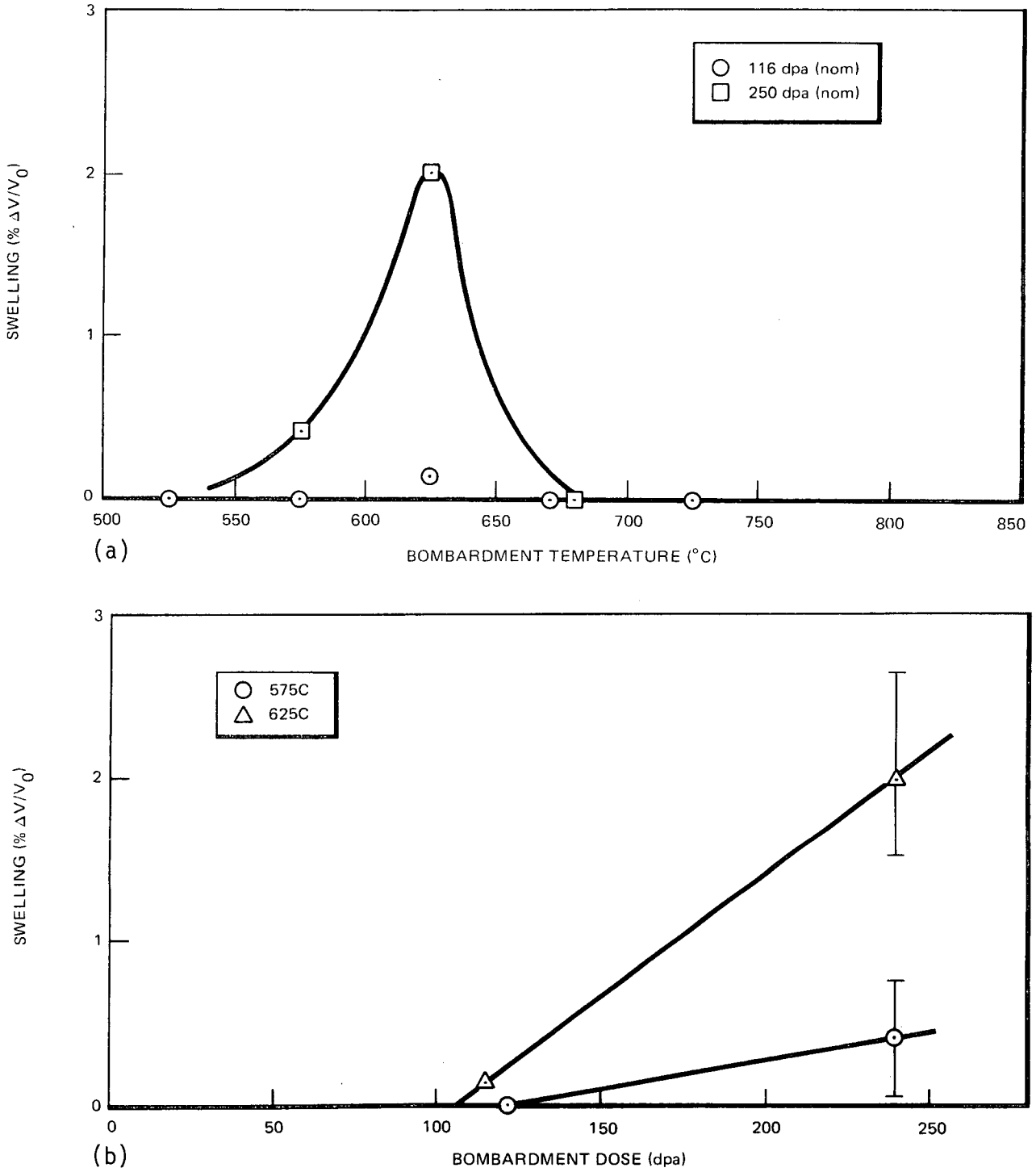

FIGURE 30. Temperature and dose dependence of swelling in STA Inconel 718, bombarded with high energy nickel ions: (a) temperature dependence of swelling, and (b) dose dependence of swelling.

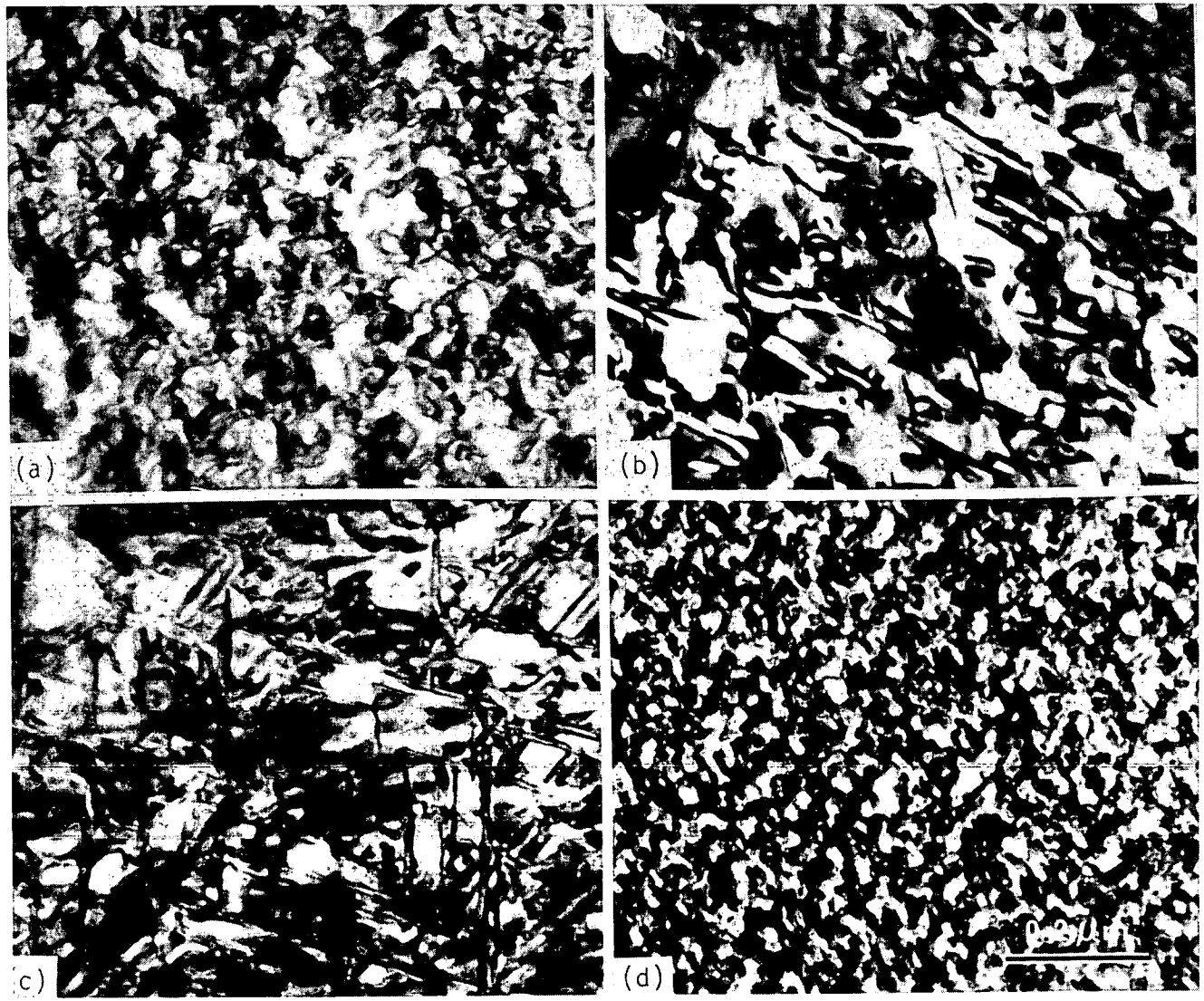

FIGURE 31. STA Inconel 718, ion bombarded to 116 dpa: (a) 625°C, dark-field image; (b) 675°C, dark-field image; (c) 725°C, bright-field image, and (d) 725°C, under mask, dark-field image.

TABLE 12

SWELLING DATA ON NICKEL-ION BOMBARDED INCONEL 718

Condition	Temp., °C	Dose dpa	Average Void Parameters			Remarks
			Density Voids/cm^3	Diameter nm	Swelling %	
STA	525	122	-	-	-	No voids
	575	122	2.5×10^{13}	19	<0.01	
		239	7.7×10^{13}	44	0.04	
	625	115	4.0×10^{13}	41	0.15	15 ppm helium
		239	5.8×10^{13}	88	2.00	
	675	109	-	-	-	15 ppm helium) No voids
		231	-	-	-	No voids (HVEM)
	725	107	-	-	-	15 ppm helium) No voids

Figure 32 shows representative selected area diffraction patterns obtained from STA Inconel 718 after ion bombardments. After the 625°C bombardment, only very faint streaks can be detected along {111} directions due to the thin nature of the precipitating platelets. After 675°C bombardment, relrods are clearly evident although no tendency exists to exhibit intensity maxima along the streaks. After bombardment at 725°C, diffuse intensity maxima are appearing on the streaks, indicating that form factor effects are becoming stronger as the platelets thicken. In the masked areas of the specimens, no streaks along {111} directions could be detected in the diffraction patterns and only the characteristic superlattice reflections of the precipitates produced by the double aging treatment were observed.

After bombardment to 248 dpa below 600°C, an extremely sluggish platelet precipitation occurs, characterized primarily by very weak and short relrods in selected area diffraction patterns. The platelets themselves are very difficult to observe but can be seen faintly in the background of Figure 29(a). As observed in Inconel 706, platelet precipitation is much more pronounced above 600°C [Figure 29(b)]. The precipitates are now coarse enough to be clearly imaged in bright-field, matrix dark-field and precipitate dark-field (from relrods) as shown in Figure 33. Diffraction patterns exhibit a corresponding development in relrod effects as shown in Figure 34. Comparisons with the lower dose results (Figures 31, 32) show the precipitation to be well advanced at 625°C and roughly comparable to what occurred at 725°C after 116 dpa.

Structure analysis and precipitate identification are still complicated by the fact that strong, well localized intensity maxima are not present on the relrods. Without observations of the weak first order reflections seen in Inconel 706, it is difficult to distinguish between eta and delta phases with only approximate values of interplanar spacings. Perhaps the best evidence that bombardment of Inconel 718 results in eta platelets is that the relrods connect austenite reciprocal lattice points. This is basically inconsistent with delta phase precipitation since the cubic and orthorhombic lattices cannot be spatially coherent.

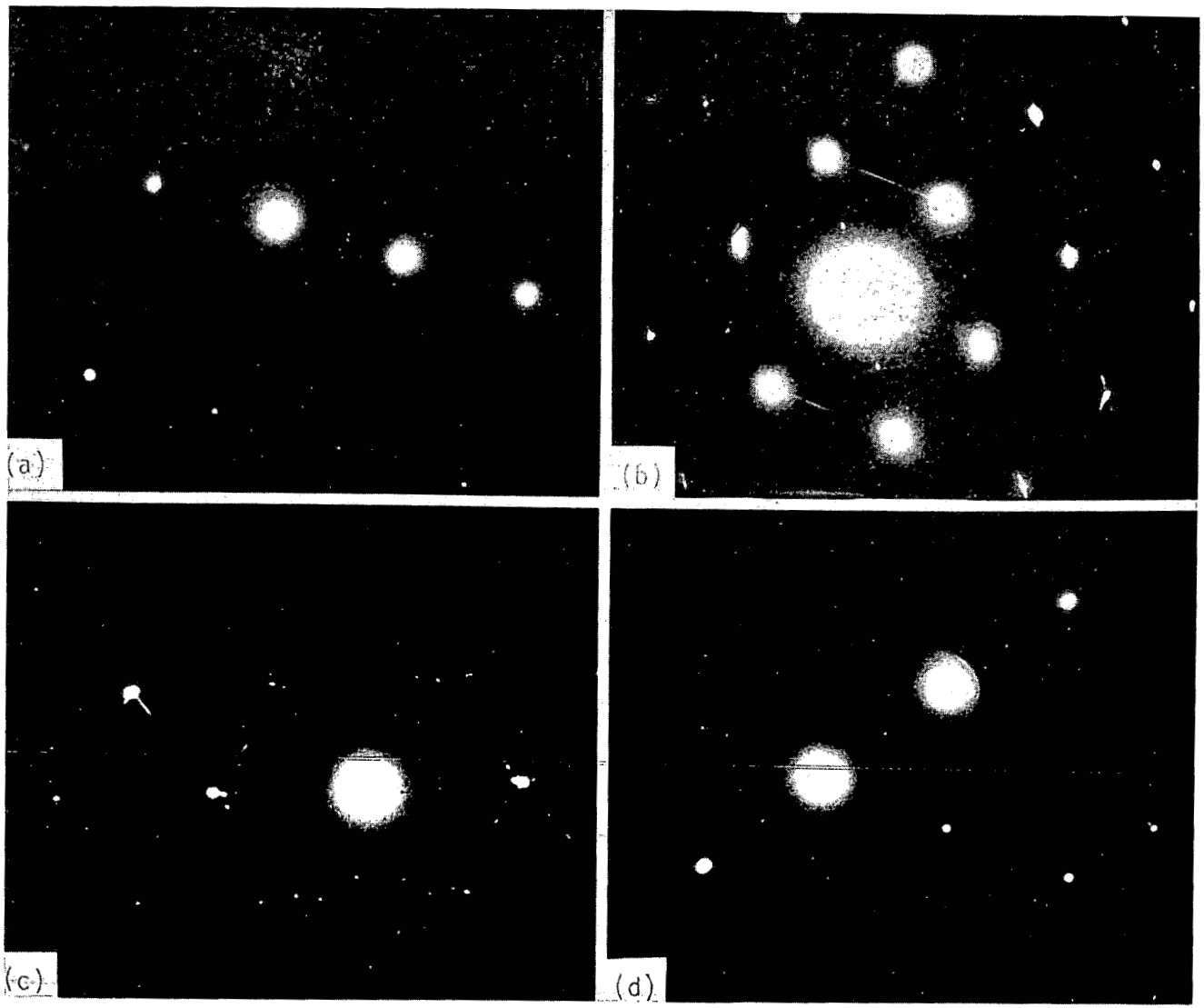

FIGURE 32. Representative selected area electron diffraction patterns from STA Inconel 718 after nickel-ion bombardment to 116 dpa: (a) 625°C; (b) 675°C; (c) 725°C, and (d) 725°C, under mask.

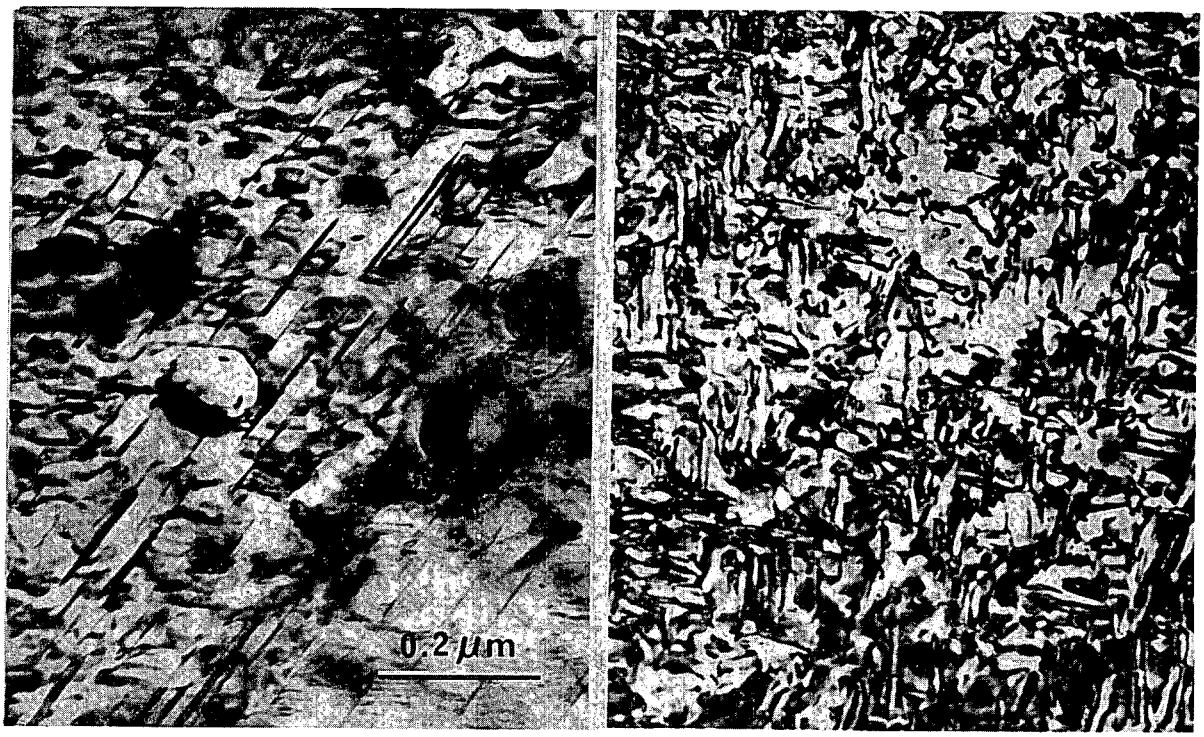

(a) (b)

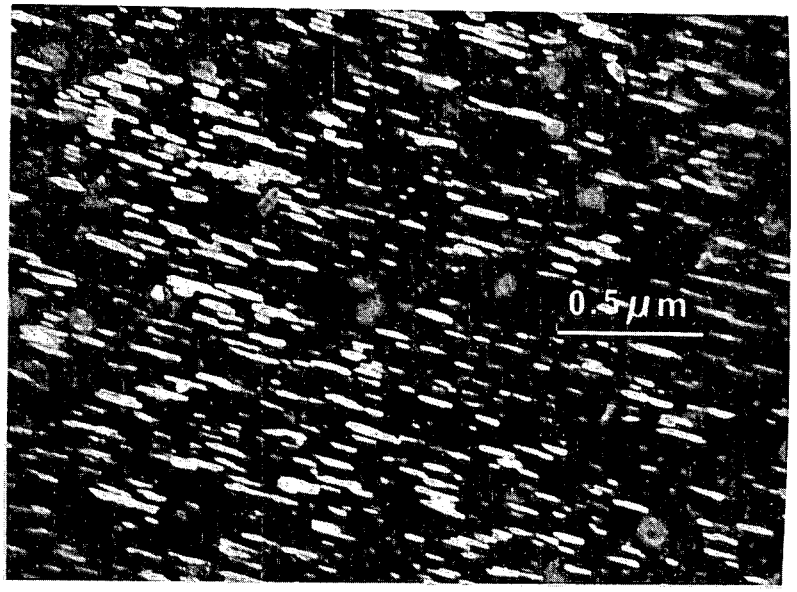

(c)

FIGURE 33. Platelet precipitation in STA Inconel 718 after ion bombardment to 248 dpa at 625°C: (a) bright-field image; (b) matrix dark-field image, and (c) precipitate dark-field image (from relrod).

(a)

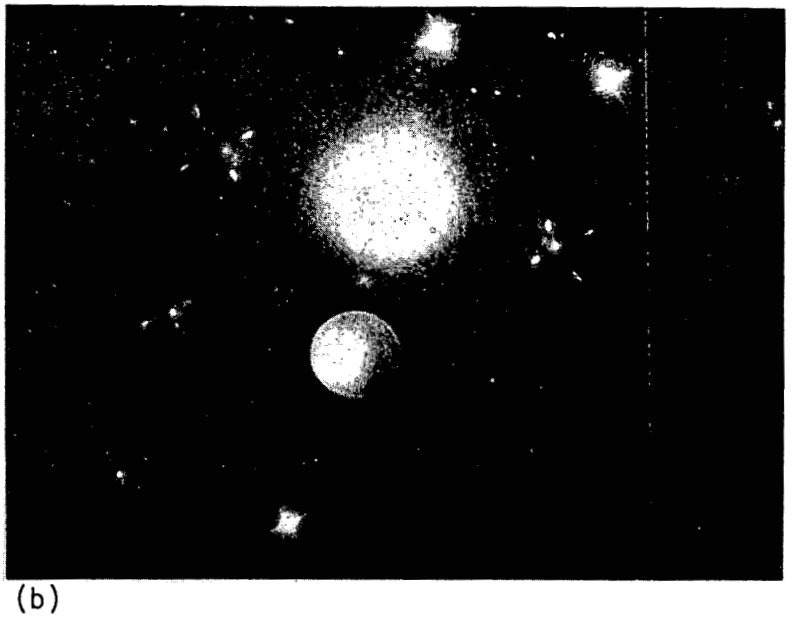

(b)

FIGURE 34. Representative selected area electron diffraction patterns from STA Inconel 718 after ion bombardment to 248 dpa at 625°C.

It has been fairly firmly established that eta phase is produced in Inconel 706 by ion bombardment, hence essentially an overaging process occurs. The more sluggish behavior of Inconel 718 is consistent with its much lower Ti/Al ratio but nevertheless, eta phase is also expected with overaging[7]. The similarities between the precipitating platelets in the two Inconels are too close to allow serious consideration that they are entirely different phases.

Reactor irradiated Inconel 718 has recently been studied. The results will be reported elsewhere but it is worthwhile to mention here that a platelike precipitating phase was observed which produced <111> relrods and which coarsened with increasing irradiation temperature at a fluence of 5 x 10^{22}n/cm^2 (E>0.1 MeV) (roughly equivalent to 38 dpa heavy ion dose). Figure 35 is a <111> zone axis austenite diffraction pattern obtained from material irradiated at 454°C which contains, in addition to strong gamma prime reflections, weak reflections at the same positions observed in Figure 20 for Inconel 706 for the $\{20\bar{2}0\}$ reflections of the eta phase. Thus, it is likely that eta platelets are being produced in both ion bombarded and neutron irradiated Inconel 718.

Imaging in 2½-D was used extensively in the studies of the gamma prime alloys as an aid in characterizing the platelet phases that occurred[14]. After 116 dpa bombardment, the greatest coarsening in the Inconels occurred at the highest temperature while faulted loops appeared in PE16 at 625°C. The comparisons used in Figure 36 illustrate that eta phase develops less rapidly in Inconel 718 than in either STA or ST Inconel 706. After 248 dpa at 625°C, the comparison with CWA Inconel 706 shows even less rapid overaging response as illustrated in Figure 37. This figure also allows comparisons of the high dose ion bombardment effects with those produced by the relatively low dosage accumulated in EBR-II at 510°C.

The much coarser chunky and rodlike precipitates observed after high doses (Figure 29), often associated with the voids that were present, could not be analyzed due to insufficient diffraction data. Spotty rings [Figure 34(a)] were often observed and may be due to this phase. Diffraction pattern evidence for TiC was observed after low doses at 525°C but the larger precipitates are not believed to be this precipitate.

Gamma prime or gamma double prime reflections appear weakened on diffraction patterns of high dose Inconel 718, consistent with the overaging that is occurring. The diffraction pattern of Figure 34(b) shows that these reflections are streaked in <111> directions the same as are the matrix reflections. This could be due to double diffraction or alternately it may be an indication that gamma prime is reprecipitating upon the platelets habiting {111} planes. Similar redistribution has been reported for Inconel 718, neutron irradiated at 650°C, where gamma prime is thought to be redistributed on faulted loops[15].

Much stronger grain boundary effects are present in Inconel 718 than were observed in Inconel 706. The unbombarded natures of the grain boundaries are shown in Figure 38 as obtained from thin areas under the masked regions of specimens bombarded to 116 dpa. Regular grain boundaries and only few boundary plates (delta phase) can be observed. At 116 dpa the boundary regions are apparently more strongly delineated at the lower bombardment temperatures as shown in Figure 39. This delineation consists of a mixture of plate precipitation and a somewhat spotty electron opacity similar to that observed in PE16. Figure 40 shows that the plates seem coarser and the grain boundaries more irregular as

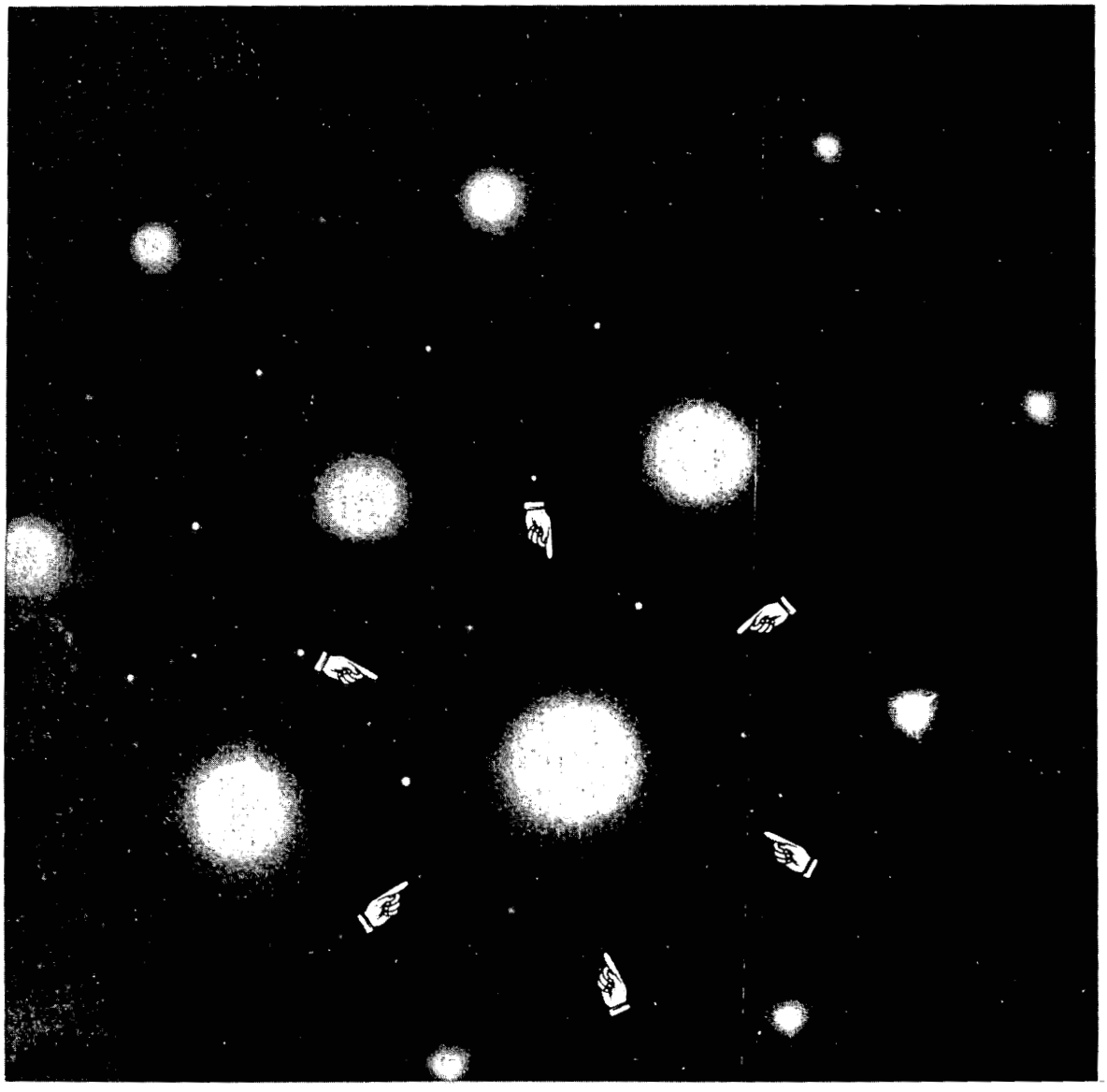

FIGURE 35. Selected area <111> electron diffraction pattern from STA Inconel 718 after neutron irradiation to 5 x 10^{22} n/cm^2 (E>0.1 MeV) at 454°C. The weak reflections indicated correspond to {20$\bar{2}$0} planes of hexagonal eta phase platelets in the plane of the specimen. Compare with Figure 20.

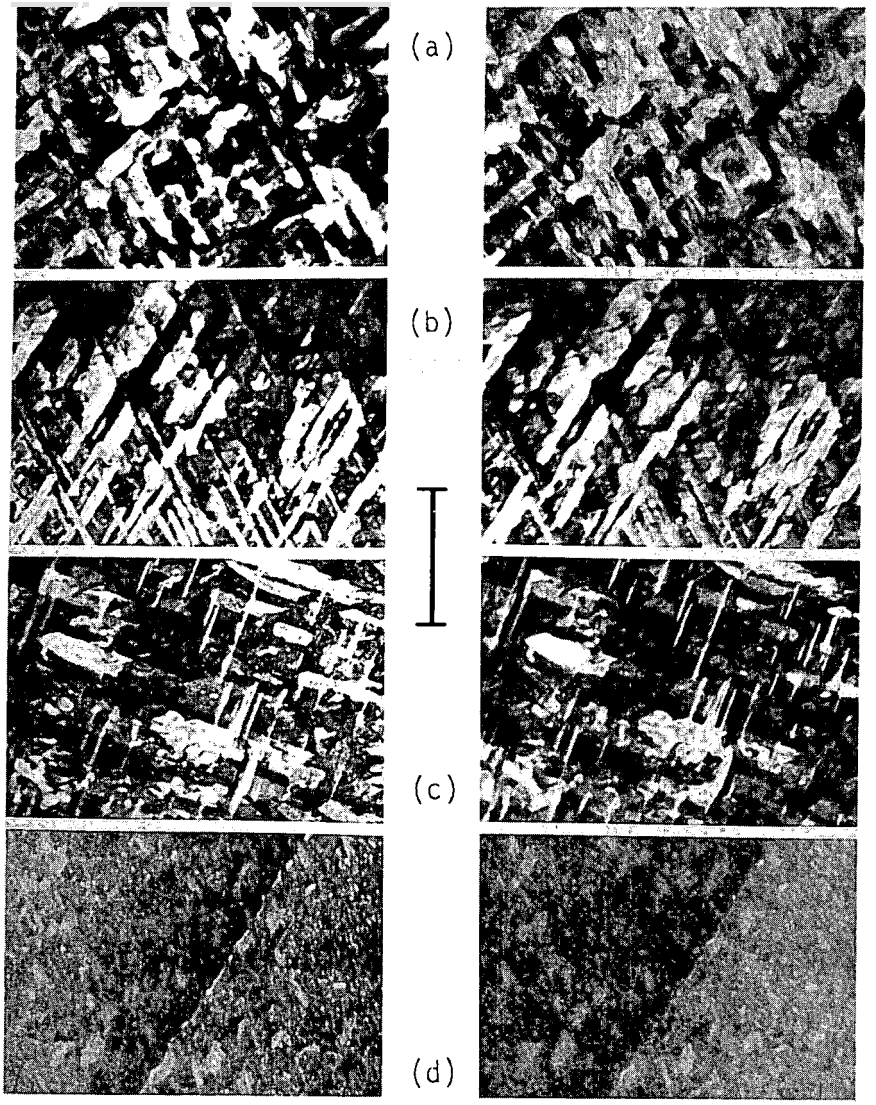

FIGURE 36. 2½-D stereo image pairs of precipitates in the Inconel alloys and faulted loops in Nimonic PE16 after ion bombardment to 116 dpa: (a) STA Inconel 706, 725°C; (b) ST Inconel 706, 725°C; (c) STA Inconel 718, 725°C, and (d) ST Nimonic PE16, 625°C. In-focus images are on the left and defocused images on the right. Scale mark indicates 0.5 μm.

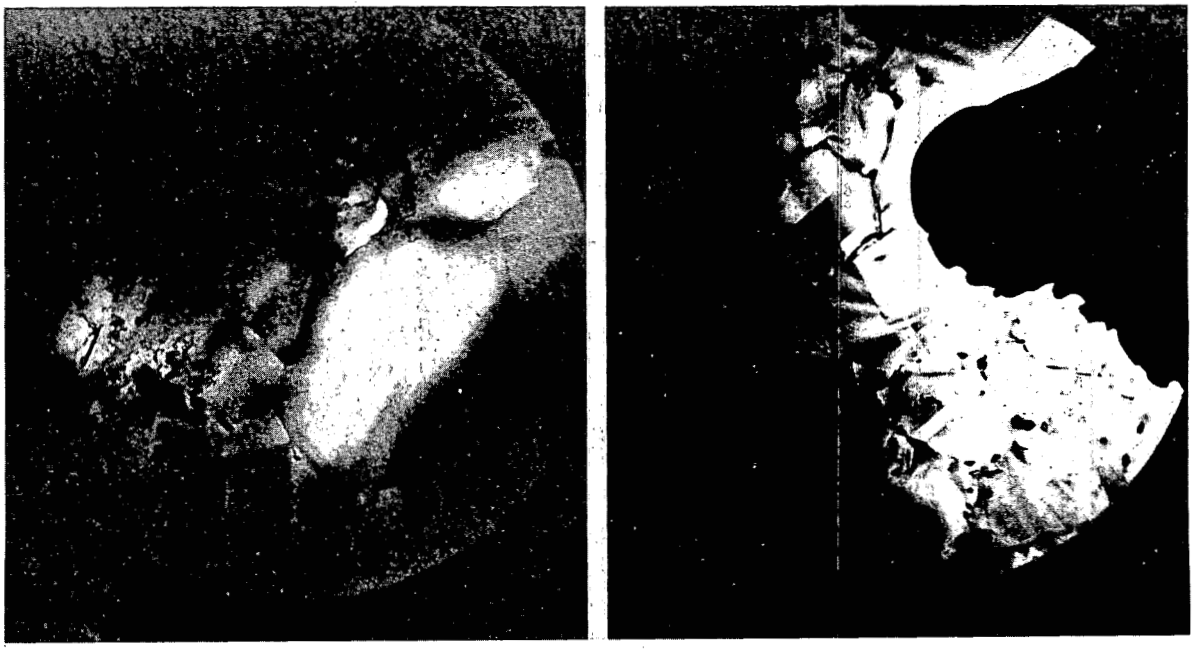

(a) (b)

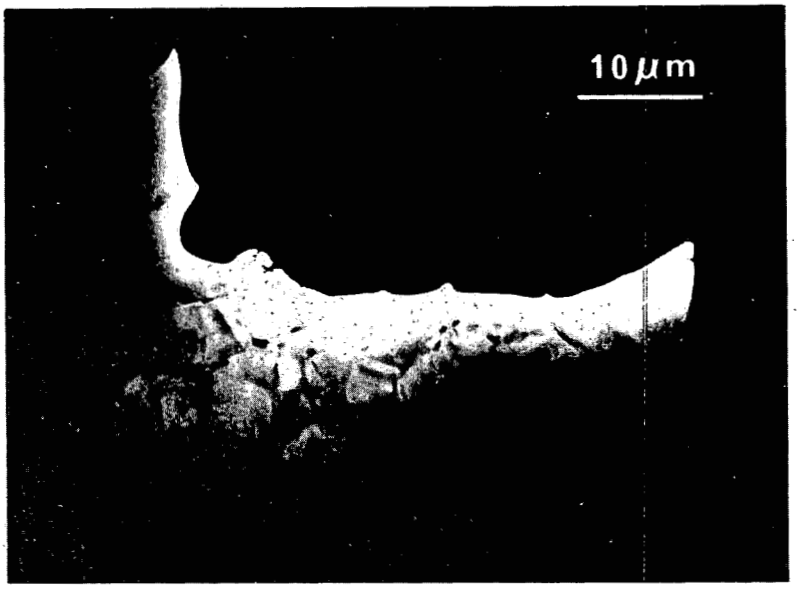

(c)

FIGURE 39. Low magnification diffuse-dark-field images showing spotty electron opacity effects near grain boundaries in STA Inconel 718 ion bombarded to 116 dpa at: (a) 625°C; (b) 575°C, and (c) 525°C.

(a)

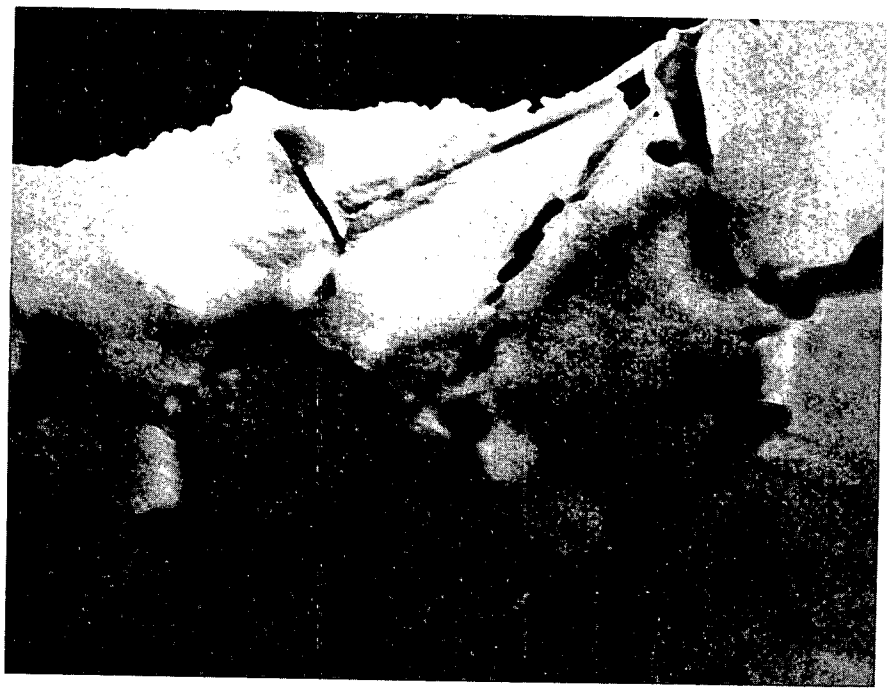

(b)

FIGURE 40. Diffuse-dark-field images of grain boundary effects in STA Inconel 718 ion bombarded to 116 dpa at: (a) 575°C, and (b) 525°C.

bombardment temperature increases. Figure 41 illustrates that with increasing dose the opacity effect becomes stronger and still tends to be more noticeable at the lower bombardment temperature. As seen in PE16 at 625°C, the opaque regions are parallel to grain boundaries but separated from them by approximately 1 μm.

Grain boundary opacity effects therefore seem to correlate to some extent with overaging. Nimonic PE16 does not overage during bombardment and develops the strongest boundary effects. Inconel 718 overages slowly, particularly below 600°C, and exhibits noticeable opaque regions. Inconel 706 exhibits only slight delineation of grain boundaries.

The grain platelets that can be analyzed in this alloy are delta phase. This precipitation behavior contrasts with that of Inconel 706 wherein only eta phase was found on grain boundaries.

2.3.4.4 M-813. M-813 is an intermediate-nickel austenitic alloy that is hardenable by precipitation of gamma prime. Its similarity in base alloy composition to the solid solution alloy Type 330 offers the opportunity to assess the relative swelling propensity of these two alloy classes and perhaps to gain insight into the effects of compositional variables on swelling. M-813 was bombarded in the solution treated and aged condition with 4 MeV nickel ions. Observed swelling and microstructural changes produced by high dose bombardment are discussed below.

Swelling. STA M-813 was bombarded at 575, 625, 675 and 725°C to a nominal peak dose of 119 dpa. These parameters were selected on the basis of predictions which suggested a peak swelling temperature in the range of 610-700°C and a swelling greater than 17 percent for a matrix composition in which the principal swelling inhibitor, titanium, is lost in gamma prime precipitation[16]. In view of this expected high swelling, all bombardments were made with the aid of partial surface masks. Examination of the surfaces of all foils after bombardment revealed, however, that swelling was too low to be measured by the step height technique. This indicated a peak swelling of substantially less than 5 percent at all temperatures. This observation was confirmed by TEM examination, which revealed a peak swelling of 0.28 percent at 625°C. Although void distributions were uniform at both 575 and 625°C, only local concentrations of voids could be detected at 675°C. No voids were observed at 725°C. Representative void distributions are shown in Figure 42. The temperature and dose dependence of swelling in STA M-813 are shown in Figure 143. Dose dependence data were collected from two depths in the 625°C foil. These data indicate a maximum swelling rate of 0.005%/dpa with a dose intercept of 47 dpa and a minimum swelling rate (assuming no incubation) of 0.002%/dpa. Swelling data collected at all temperatures are compiled in Table 13.

Microstructural Changes. Bimodal distributions of gamma prime were observed in STA M-813 as illustrated in Figure 44. Below 600°C the distribution appears similar to that existing prior to bombardment[6] while at 675°C the numbers and sizes of the larger particles appear to have increased.

Bombardment at 575°C produced a precipitate giving diffraction spots similar to those thought to be due to TiC in the Inconels. Figure 45 shows this precipitate and its diffraction effects. Assuming cubic structure, the lattice parameter can be determined as 0.424 nm or that of TiN. Higher temperature bombardments did not apparently produce this precipitate.

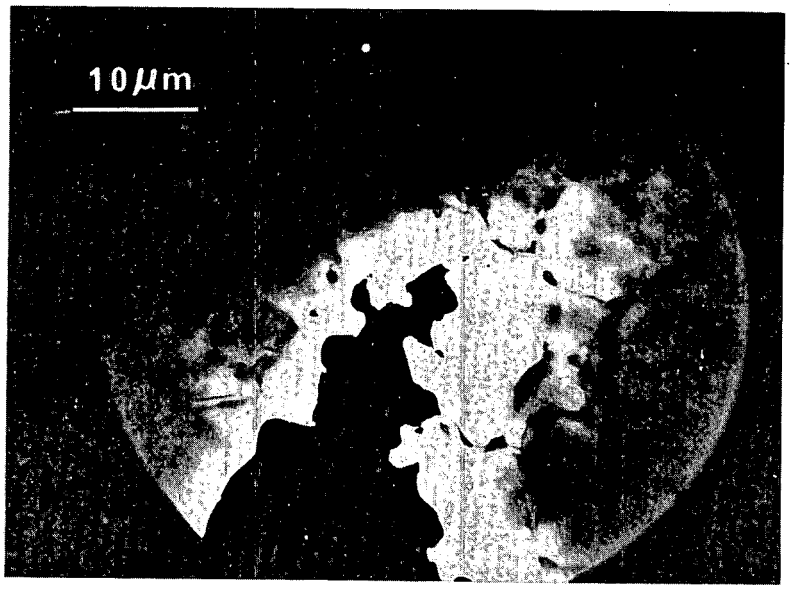

(a)

(b)

FIGURE 41. Low magnification diffuse-dark-field images showing spotty electron opacity near grain boundaries in STA Inconel 718 ion bombarded to 248 dpa at: (a) 625°C and (b) 575°C.

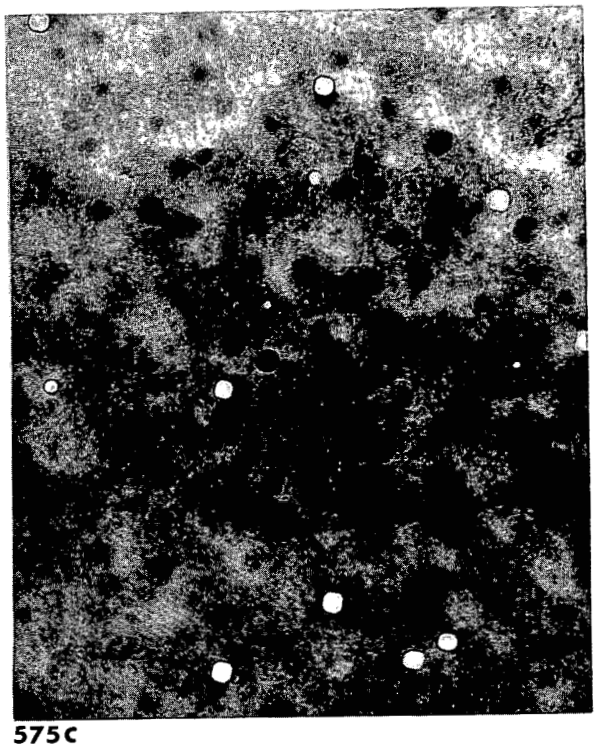

575c

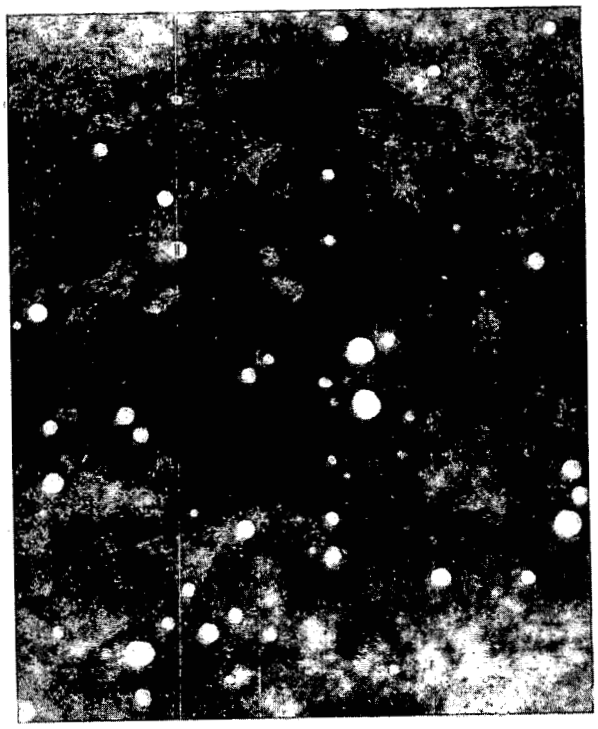

625c

675c

725c

0.2μm

FIGURE 42. Void distributions in STA M-813 after nickel-ion bombardment to 116 dpa.

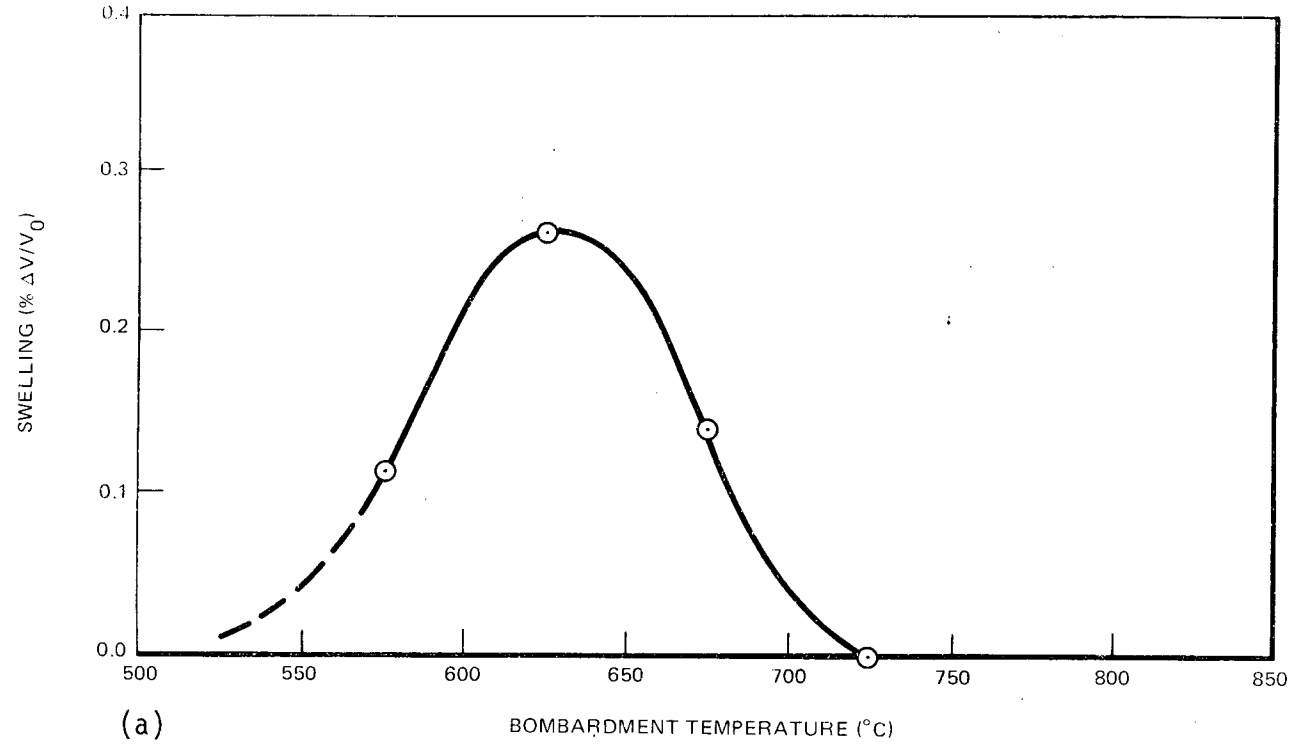

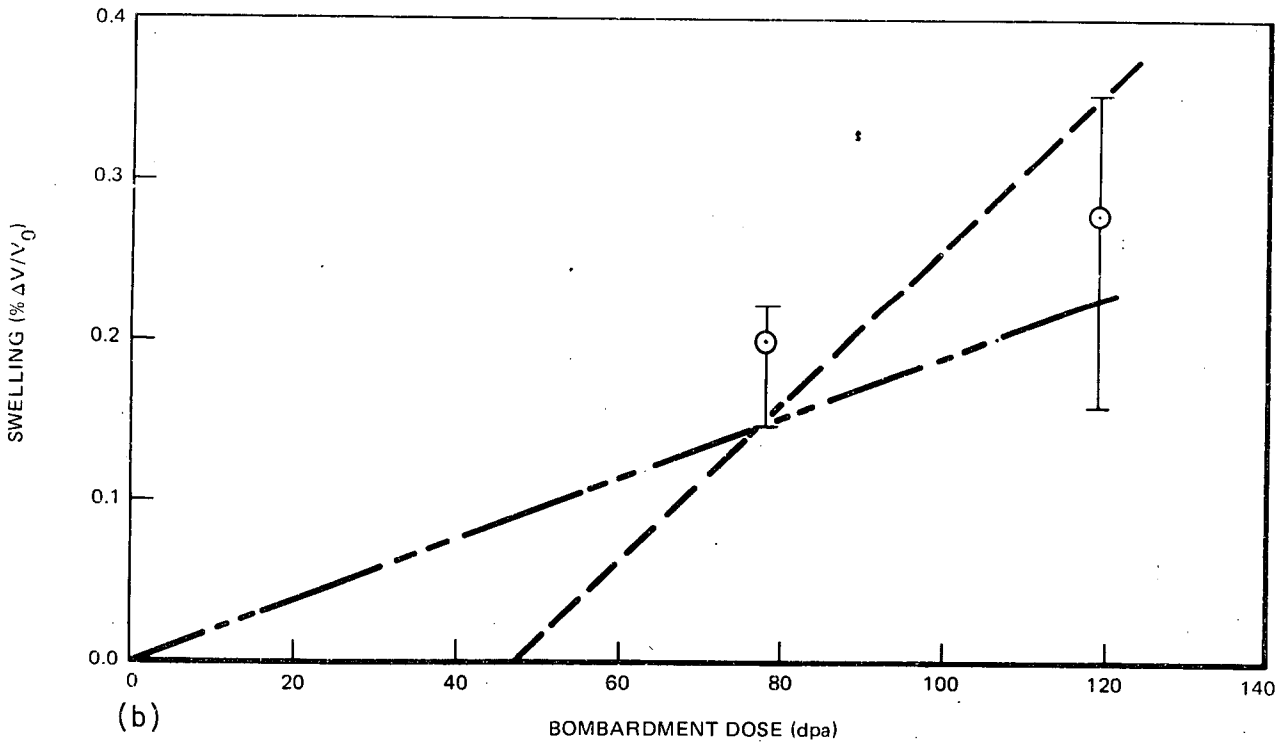

FIGURE 43. Temperature and dose dependence of swelling in STA M-813, bombarded with 4 MeV nickel ions: (a) temperature dependence of swelling and (b) dose dependence of swelling at 625°C.

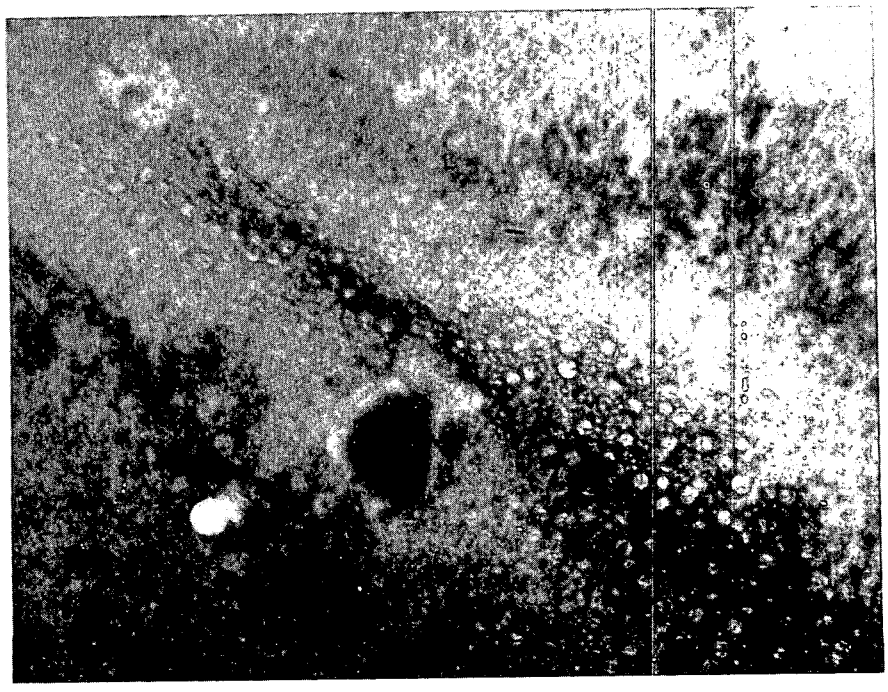

(a)

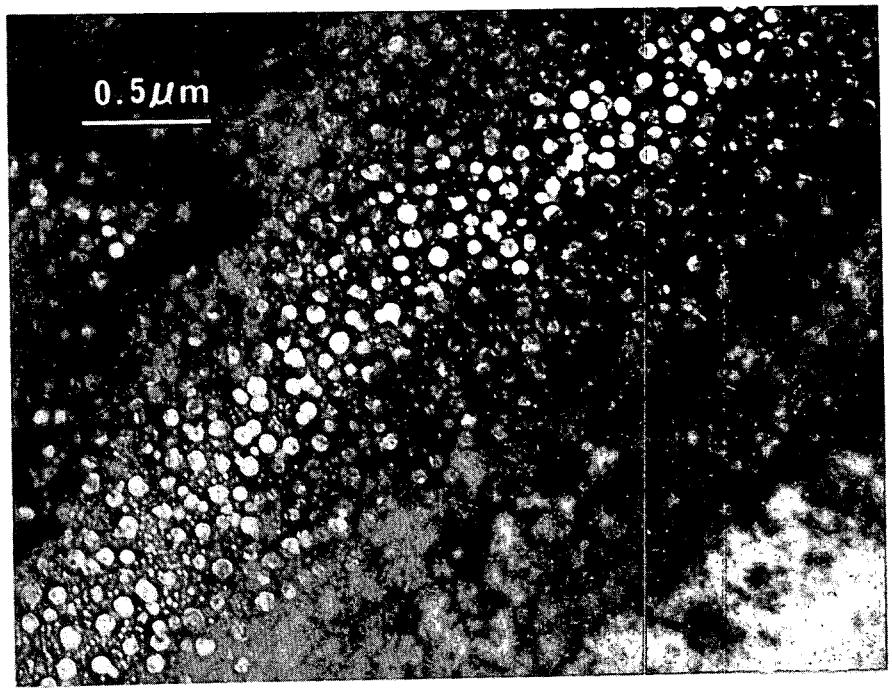

(b)

FIGURE 44. Precipitate dark-field images of bimodal γ' distributions in STA M-813 ion bombarded to 116 dpa at (a) 575°C and (b) 675°C.

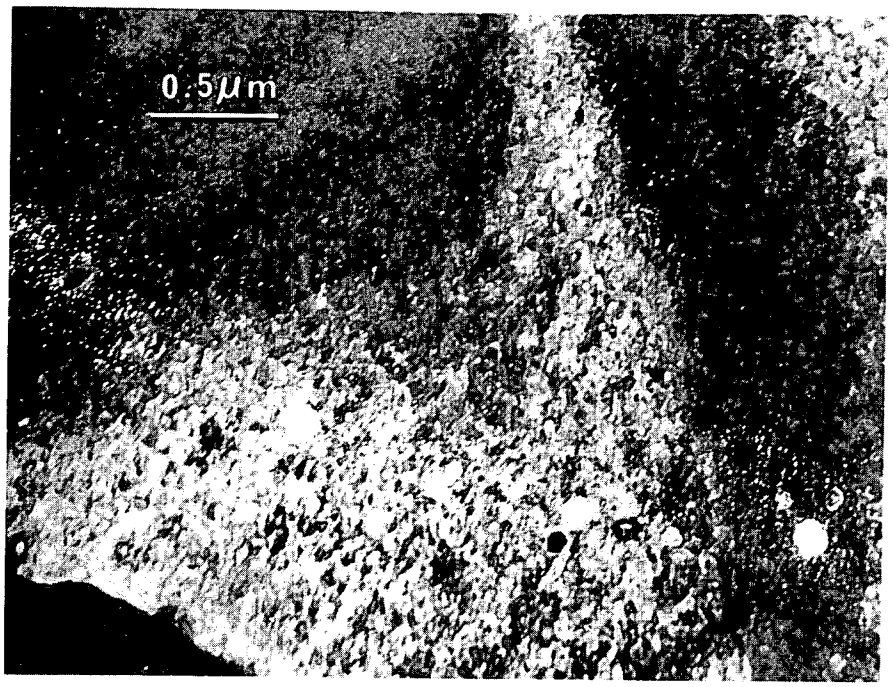

(a)

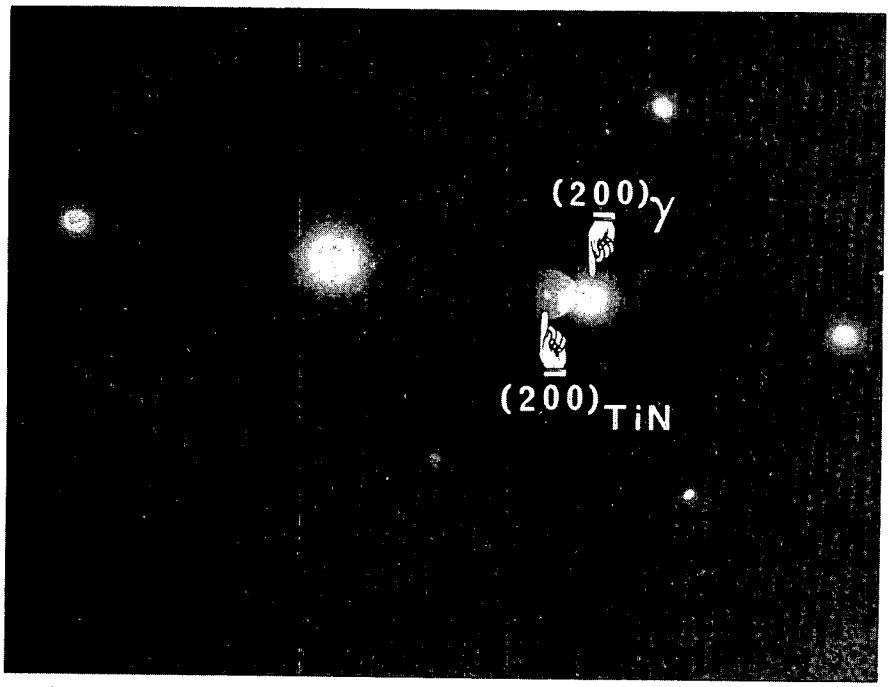

(b)

FIGURE 45. Precipitate dark-field image and selected area electron diffraction pattern exhibiting spots characteristic of TiN in STA M-813 after ion bombardment to 116 dpa at 575°C.

TABLE 13

SWELLING DATA ON NICKEL-ION BOMBARDED M-813

Condition	Temp., °C	Dose, dpa	Average Void Parameters			Remarks
			Density voids/cm^3	Diameter, nm	Swelling %	
STA	575	117	6.2×10^{13}	32	0.11	
	625	78	9.7×10^{13}	34	0.20	Intermediate(a)
		119	1.1×10^{14}	34	0.28	Peak(a)
	675	119	1.1×10^{14}	30	0.14	Non-uniform void distribution
	725	119	-	-	-	No voids

(a) = same foil

Grain boundary delineation also occurred in this alloy as shown in Figure 46. Figure 47 shows this delineation is due to a combination of the carbides on the boundaries and electron opacity effects. The noticeable tendency for larger voids in the grain boundary regions seems more due to the carbides than the electron dense regions.

2.3.4.5 Type 310 Steel

Swelling. Experiments performed in an earlier phase of the current program showed that ST Type 310 steel underwent gross swelling when bombarded with 5 MeV nickel ions at the relatively moderate dose of 116 dpa. Swellings were so large at the peak swelling temperature that the surface of a foil bombarded at 700°C had expanded as much as 300 nm above an adjacent surface that was shielded from the ion beam. According to the empirical relation developed by Johnston, et al[4], for bombardments using the technique applied in this work, such a "step height" represented a swelling of almost 50 percent.

From a purely metallurgical standpoint, however, Type 310 remains an attractive candidate for in-core structural applications, as evidenced by the inclusion of a cold-worked grade in the current evaluation. (The selection of a 20 percent cold work treatment is based on earlier studies which showed that cold working imparts some swelling resistance to austenitic alloys.)(e.g., 17)

Guided by the experimental results on annealed material, and the realization that high levels of swelling cannot be easily or reliably evaluated by TEM techniques, the principal bombardments of CW Type 310 were made at 56 dpa. Temperatures of 625, 675 and 725°C were selected to span the swelling peak. A uniform distribution of voids was observed at all temperatures, Figure 48. Analysis of selected micrographs yielded an average peak swelling of just over one percent; interpolation of the temperature dependence of swelling curve (Figure 49) places the peak at approximately 640°C.

An evaluation of the dose dependence of swelling was performed on specimens bombarded at the two lower temperatures, using the single-sample technique described in the appendix. In the case of the 625°C bombardment specimen, a single electropolishing operation produced a series of holes scattered over a region that included a portion of the foil that was shielded from the ion beam, and surfaces representing three depths along the ion path

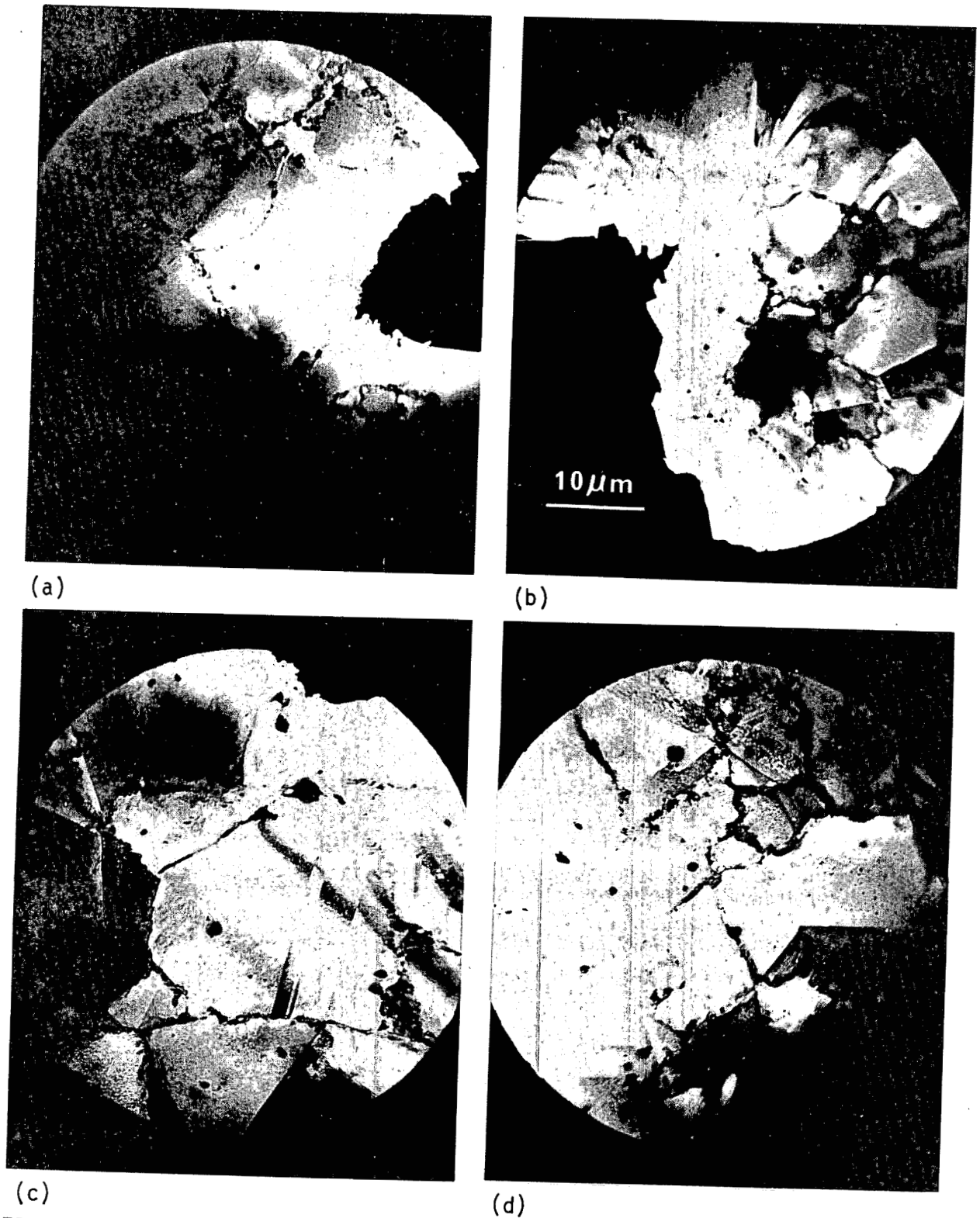

FIGURE 46. Low magnification diffuse-dark-field images showing spotty grain boundary effects in STA M-813 ion bombarded to 116 dpa at: (a) 575°C; (b) 625°C; (c) 675°C and (d) 725°C.

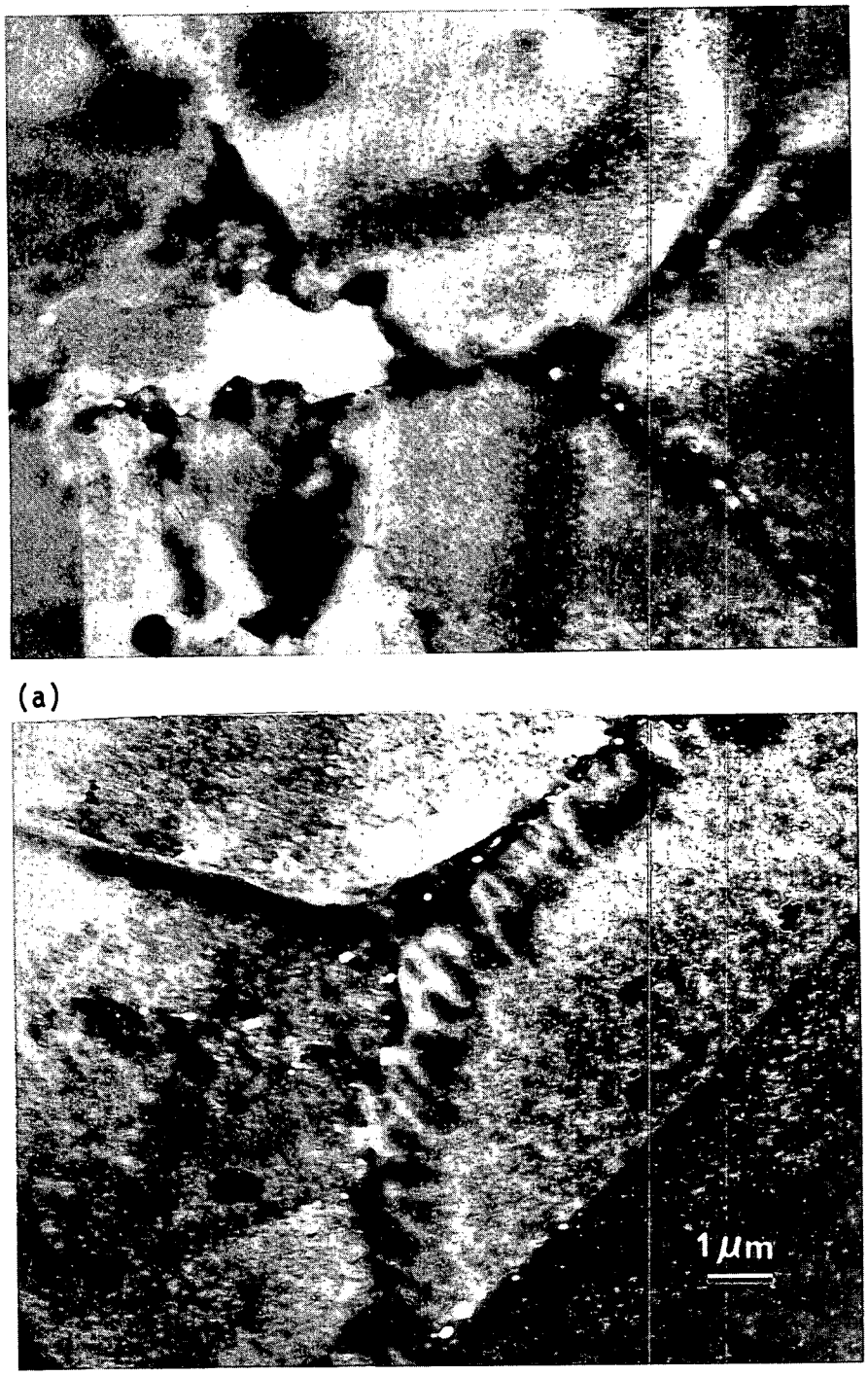

FIGURE 47. Diffuse-dark-field images illustrating grain boundary regions in STA M-813 after ion bombardment to 116 dpa at: (a) 575°C and (b) 675°C.

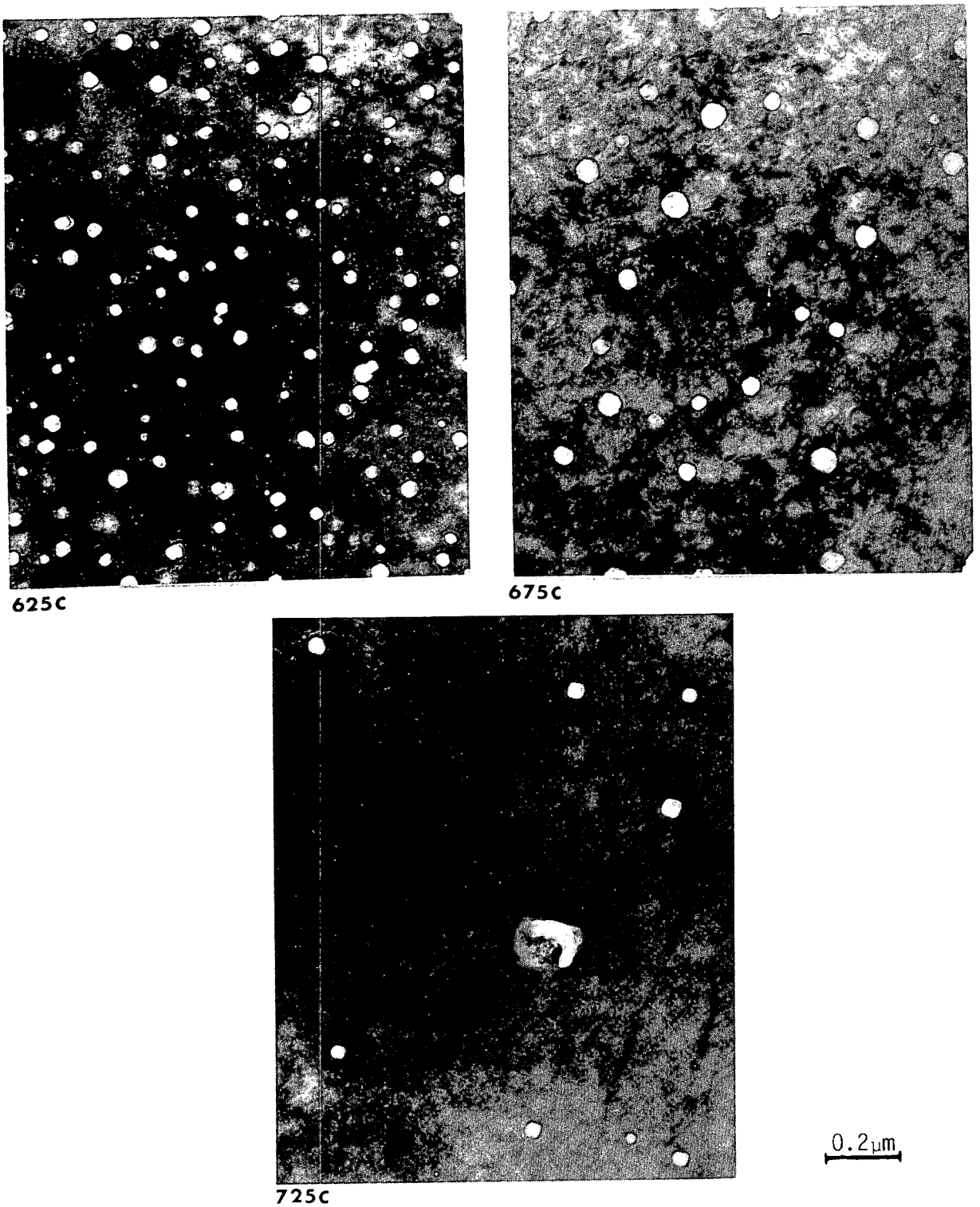

FIGURE 48. Void distributions in CW Type 310 steel after nickel-ion bombardment to 58 dpa.

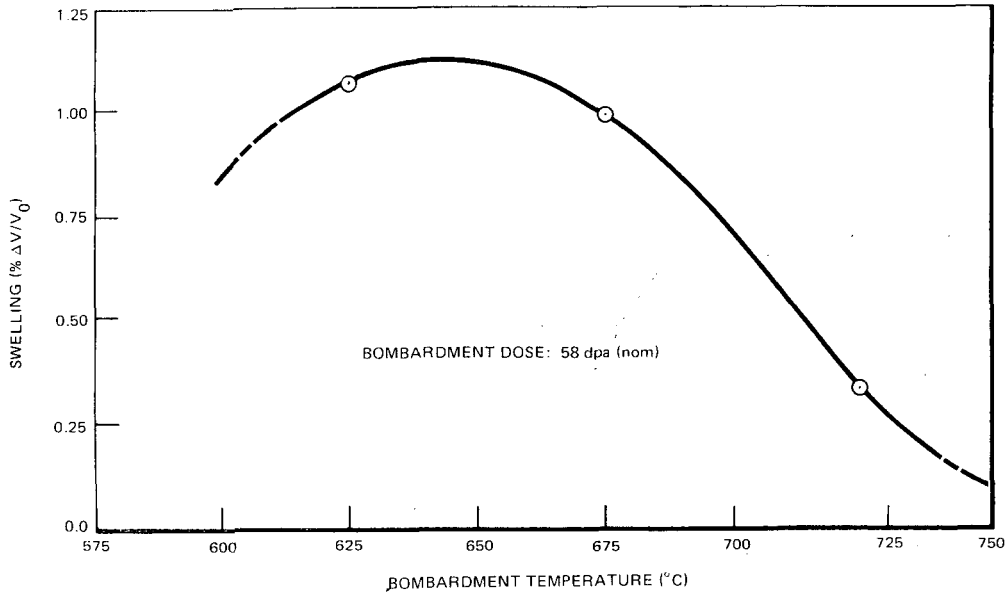

FIGURE 49. Temperature dependence of swelling in CW Type 310 steel, bombarded with 4 MeV nickel ions.

(produced by consecutive ion milling). A composite electron micrograph of this region is shown in Figure 50. The void distributions in individual bombarded regions in both the 625 and 675°C foils are shown in Figures 51 and 52, and results of TEM analysis in Figures 53 and 54. Extrapolation of the swelling curves of Figure 53 give a swelling rate of 0.04%/dpa and a dose intercept of 37 dpa for the 675°C bombardment. Although the swelling behavior at 625°C was not explored beyond 54 dpa, the complementary lower dose data at both temperatures suggest that the dose dependence of swelling is essentially the same.

A compilation of all swelling data, including the earlier results on the solution-treated alloy, is given in Table 14.

TABLE 14

SWELLING DATA ON NICKEL-ION BOMBARDED TYPE 310 STEEL

Condition	Temp., °C	Dose, dpa	Average Void Parameters			Remarks
			Density voids/cm^3	Diameter, nm	Swelling %	
ST	600	98	6.0×10^{14}	62	7.9	
	650	116	-	-	26	Step height
	700	116	-	-	46	Step Height
20% CW	625	16	5.3×10^{13}	23	0.03	)
		26	2.5×10^{14}	24	0.19	) Same foil
		54	5.0×10^{14}	34	1.06	)
	675	16	3.9×10^{13}	34	0.10	(a)
		31	1.3×10^{14}	55	1.10	(b)
		56	1.3×10^{14}	53	.99	(a)
		120	1.1×10^{14}	83	3.64	(b)
	725	59	3.7×10^{13}	56	0.34	

(a) Same foil
(b) Same foil

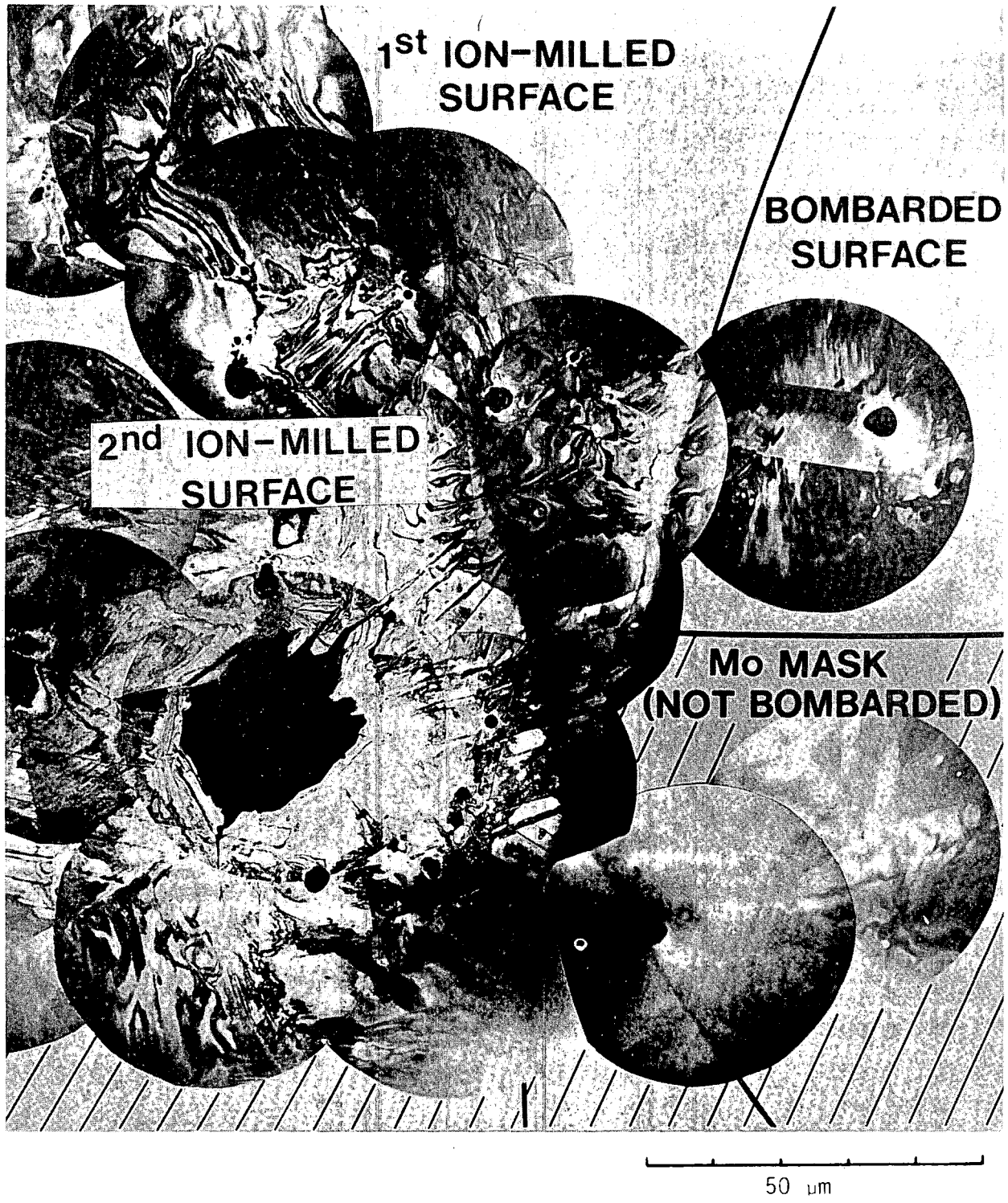

FIGURE 50. Electron micrograph composite of CW Type 310 steel foil bombarded at 625°C with 4 MeV nickel ions. Doses in each region are as follows: No mask (0 dpa), bombarded surface (16 dpa), 1st-ion milled surface (26 dpa) and 2nd ion-milled surface (54 dpa).

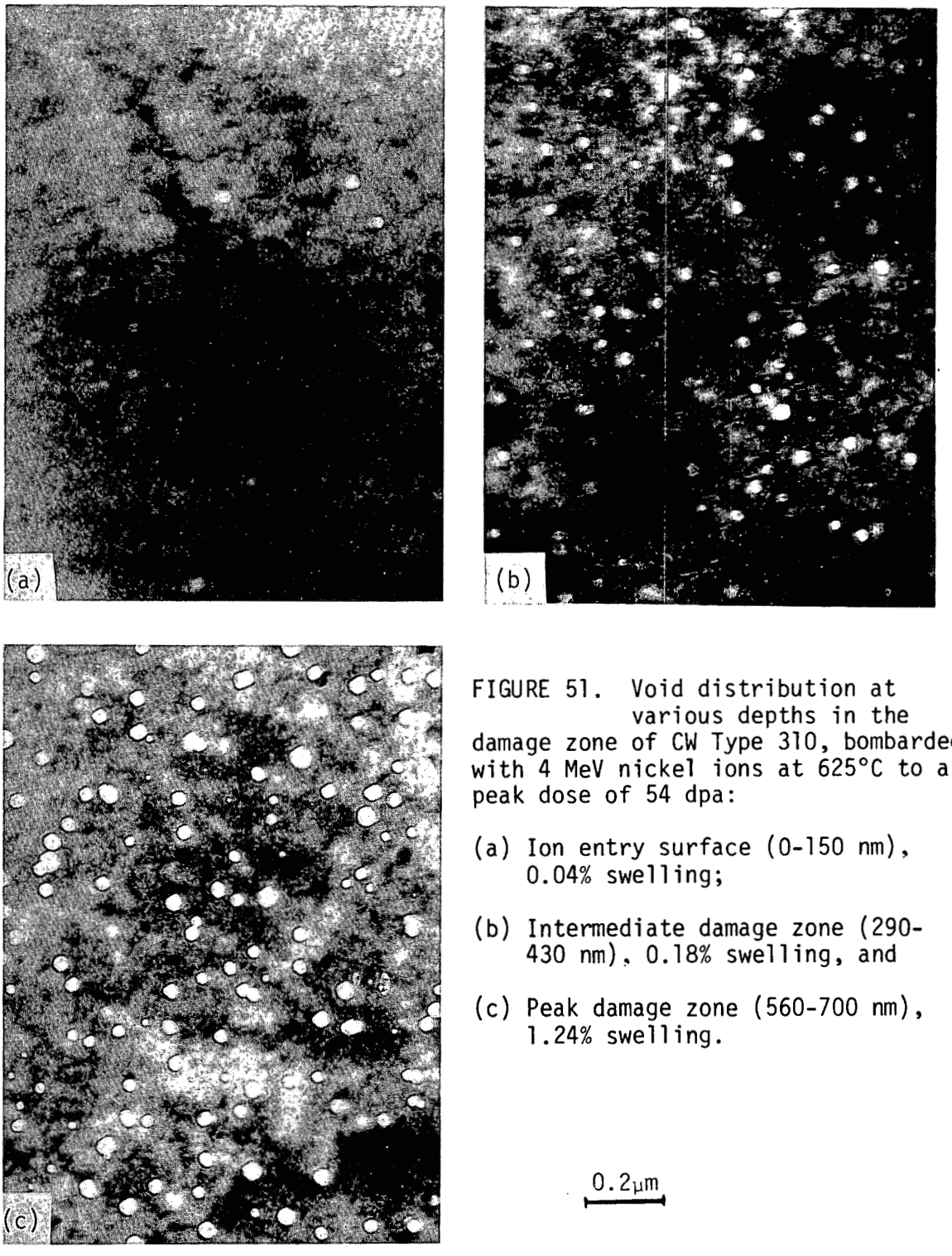

FIGURE 51. Void distribution at various depths in the damage zone of CW Type 310, bombarded with 4 MeV nickel ions at 625°C to a peak dose of 54 dpa:

(a) Ion entry surface (0-150 nm), 0.04% swelling;

(b) Intermediate damage zone (290-430 nm), 0.18% swelling, and

(c) Peak damage zone (560-700 nm), 1.24% swelling.

0.2μm

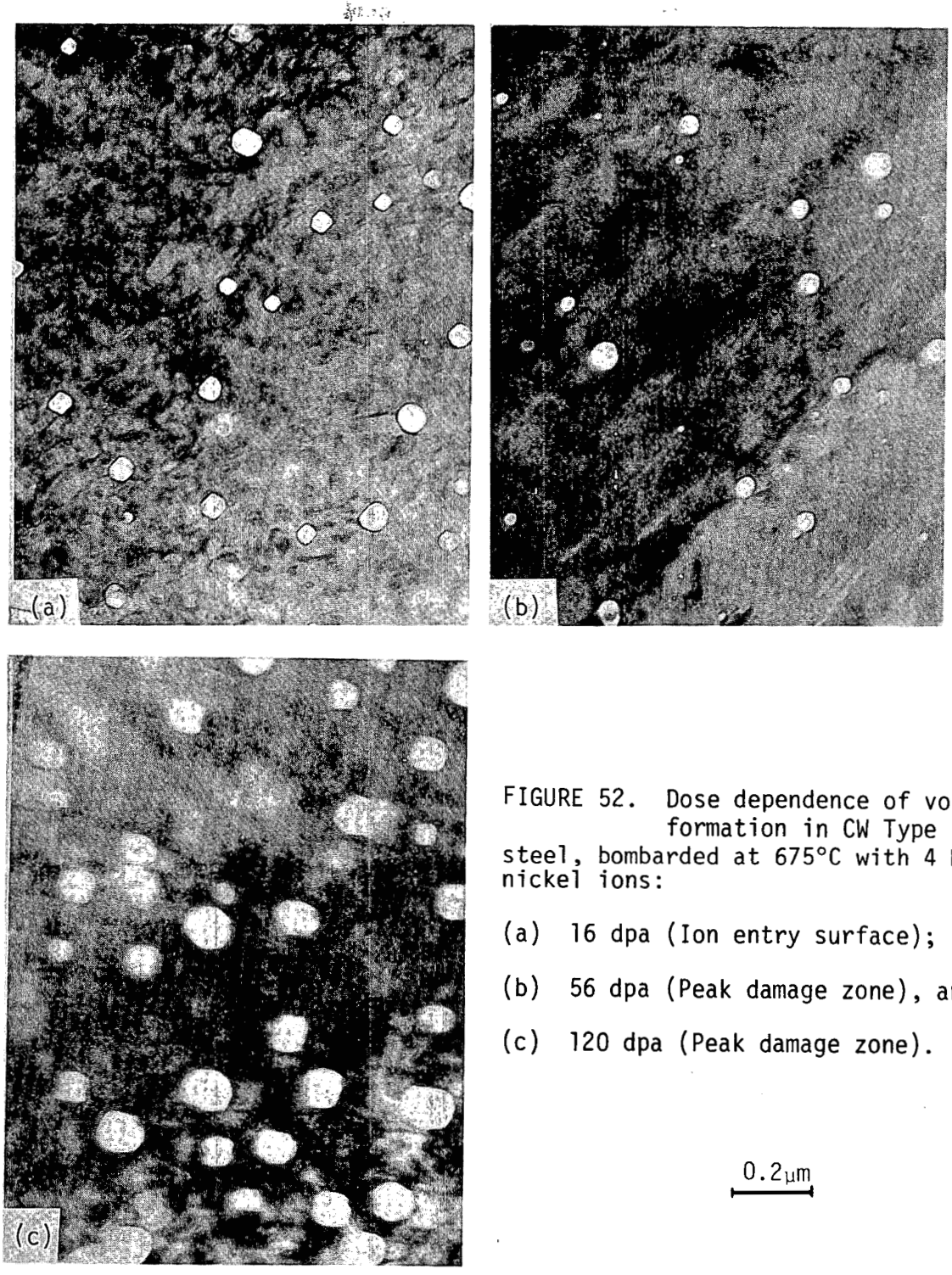

FIGURE 52. Dose dependence of void formation in CW Type 310 steel, bombarded at 675°C with 4 MeV nickel ions:

(a) 16 dpa (Ion entry surface);

(b) 56 dpa (Peak damage zone), and

(c) 120 dpa (Peak damage zone).

0.2μm

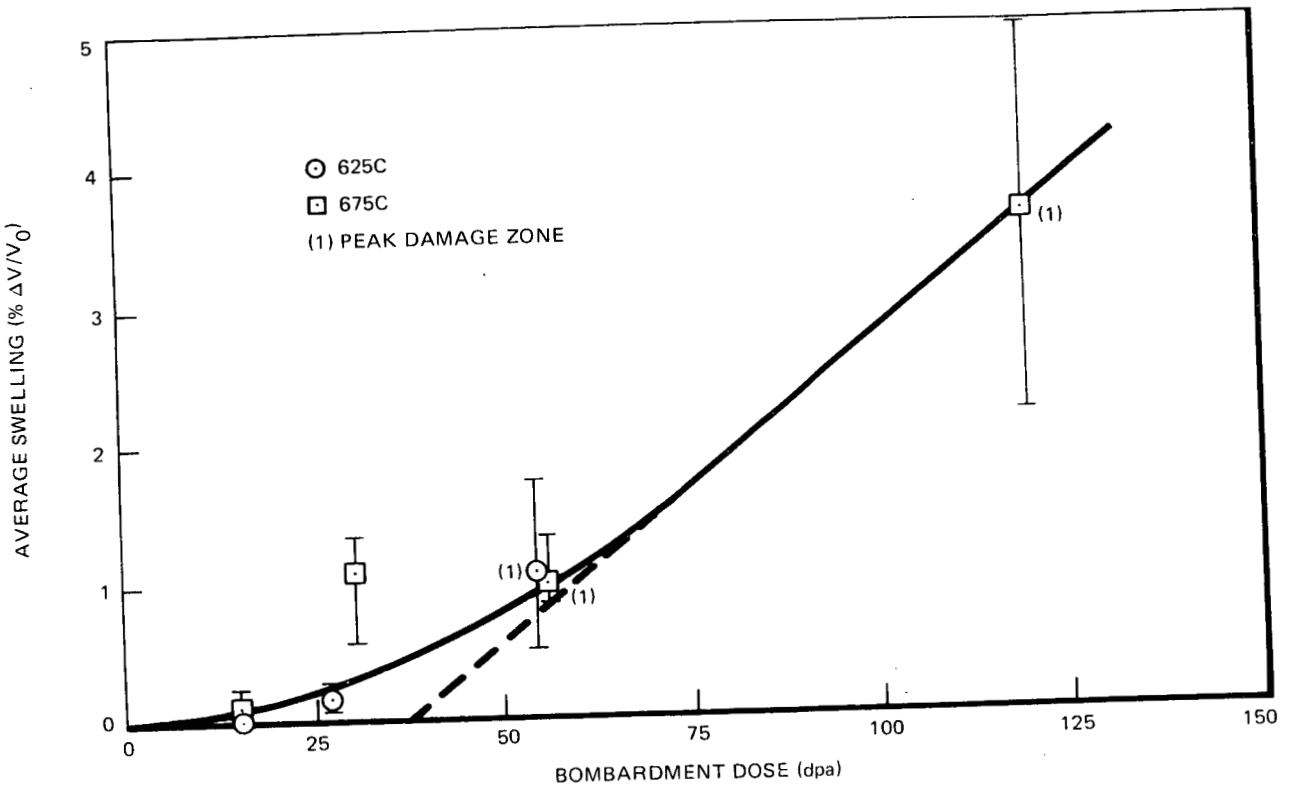

FIGURE 53. Dose dependence of swelling in CW Type 310 steel, bombarded with 4 MeV nickel ions.

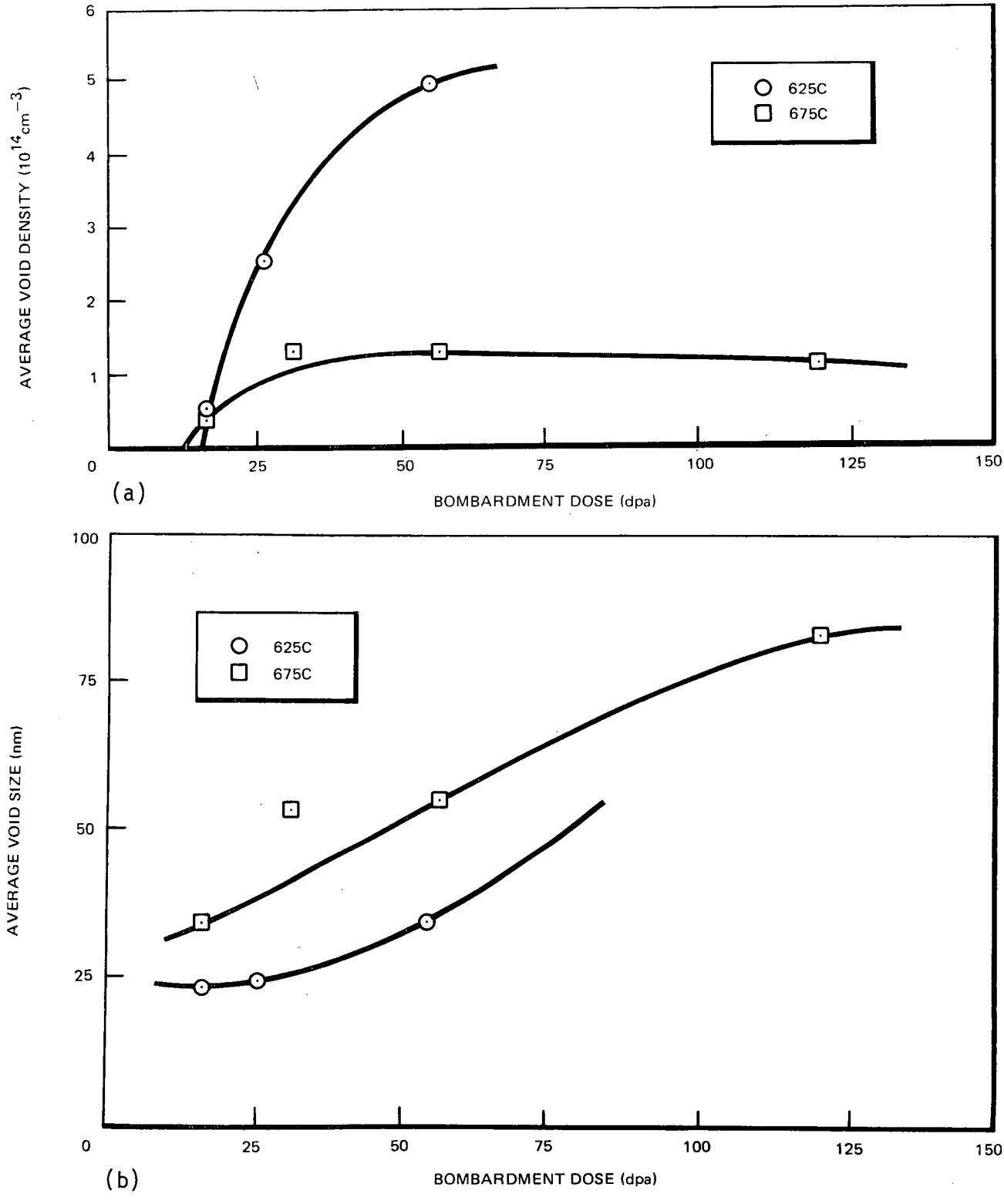

FIGURE 54. Dose dependence of void formation in CW Type 310 steel, bombarded with 4 MeV nickel ions: (a) void density and (b) void diameter.

Microstructural Changes. No noticeable development of any precipitation effects was observed in CW Type 310 steel, and no grain boundary delineation was observed. Only dislocation arrangements were observed to change with dose and temperature as illustrated in Figure 55.

2.3.4.6 Type 330 Steel. Type 330 steel is a solid-solution alloy, similar in base composition to age-hardenable M-813. It is a relatively simple alloy, the minor additions being limited to carbon, manganese and silicon. Interest in Type 330 as a potential LMFBR core structural material stems from its attractive high temperature strength and the potential swelling resistance offered by a moderately high matrix nickel content. The swelling and microstructural stability of both solution-treated (ST) and 20% cold worked (CW) Type 330 were evaluated. Results are presented below.

Swelling. The initial bombardment matrix selected for the evaluation of swelling in both ST and CW Type 330 steel consisted of 550, 600 and 650°C bombardments to a nominal dose of 248 dpa. These parameters were based on an expected peak swelling temperature of 600°C and an expectation of moderately low peak swelling at 116 dpa. Although the latter trend was confirmed at these temperatures, it was clear from the results of TEM examination of the bombarded foils that the peak swelling temperature was not lower than 650°C in either grade of the Type 330 material used in these studies. An additional bombardment of ST Type 330 at 700°C confirmed this observation and showed a sharp increase in swelling. Representative void distributions in both grades are shown in Figures 56 and 57.

Although the present results still cannot firmly establish the swelling peak, we can be assured that this peak occurs at a temperature not lower than 700°C. TEM data in Figure 58 illustrate the temperature dependence of swelling in both alloy grades and demonstrate the beneficial effect of cold working in controlling swelling in Type 330 steel. The data summarized in Table 15 shows as much as 40% reduction in swelling at 650°C, with substantially higher reductions at the lower temperatures.

Swelling rates of both Type 330 grades are listed below. These rates are based on an assumption of zero incubation dose in all cases. This assumption was judged to be valid in view of the high swelling measured at an intermediate depth in two of the ST foils.

	Swelling Rate, %/dpa	
	ST	CW
550°C	0.001	<0.001
600°C	0.002	<0.001
650°C	0.006	0.003
700	0.024	-

Microstructural Changes. Although extensive intragranular precipitation occurred below 600°C in both ST and CW materials, insufficient diffraction data was obtained to allow identification of the precipitating phase. The precipitate produces strong reflections in the 0.2 ± 0.02 nm range and could easily be imaged in a dark field as illustrated in Figure 59. The precipitates are rods rather than plates: streaks in electron diffraction patterns were consistently parallel with traces of {100} austenite planes, a characteristic of a relplate rather than a relrod. The axes of the rods lie along <100>

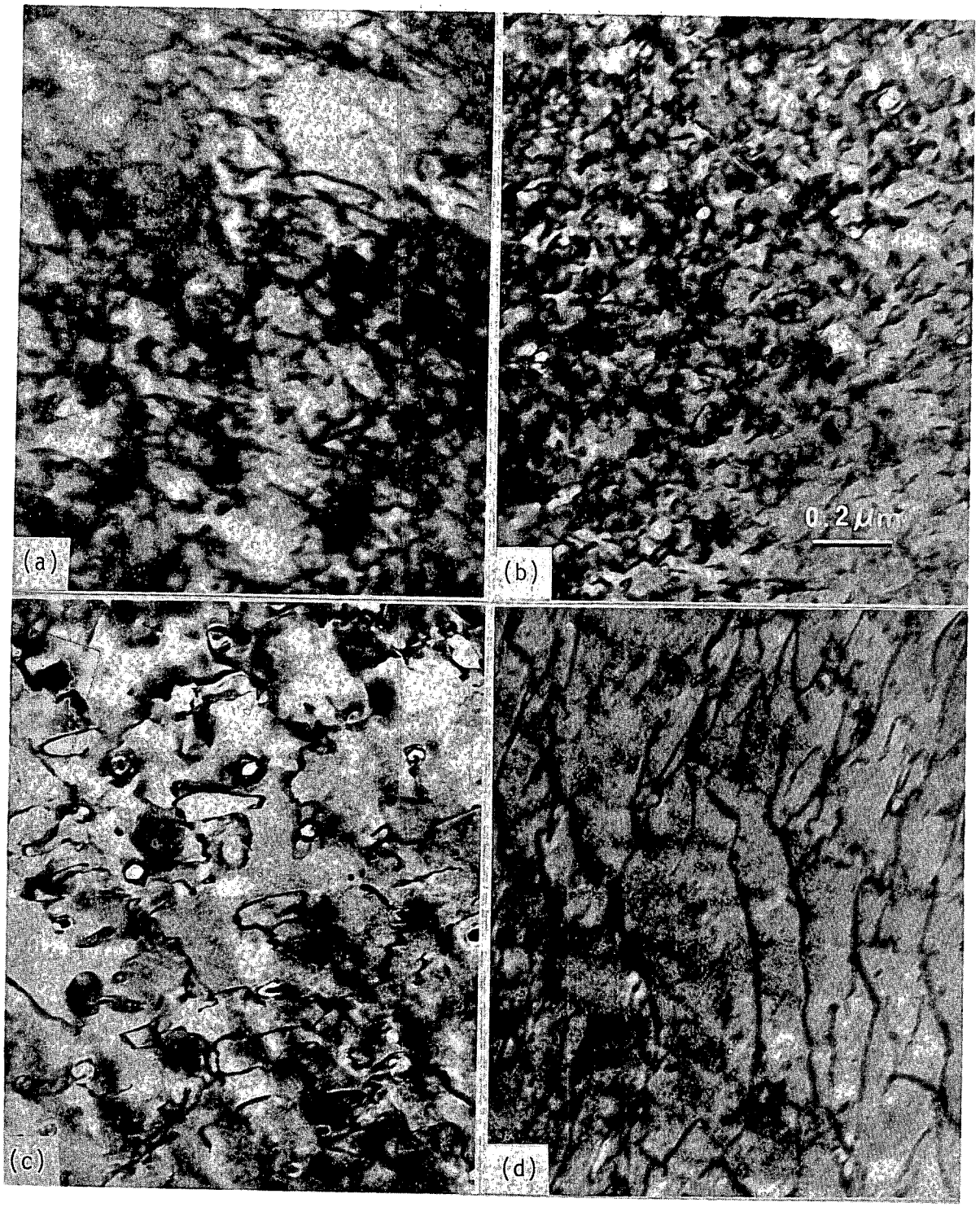

FIGURE 55. Dislocation arrangements in CW Type 310 steel after ion bombardment to: (a) 0 dpa (under mask) at 625°C; (b) 58 dpa at 675°C; (c) 116 dpa at 675°C, and (d) 58 dpa at 725°C.

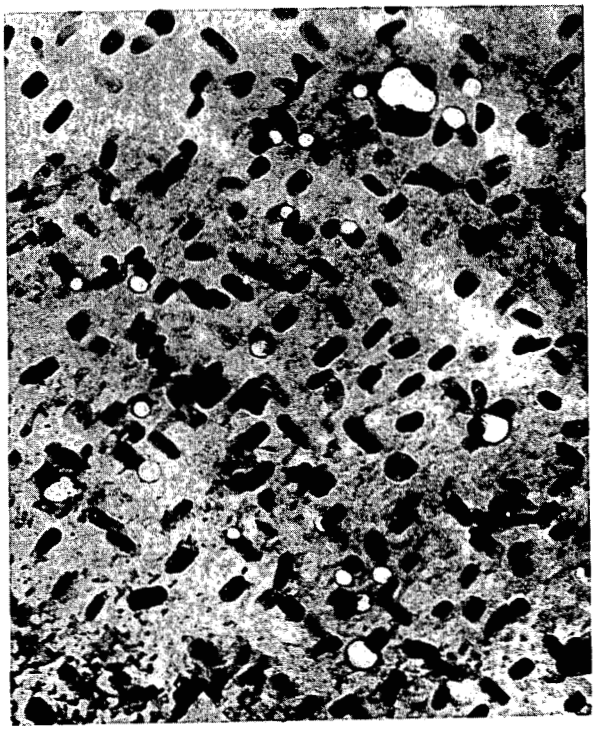

550C

600C

0.2μm

650C

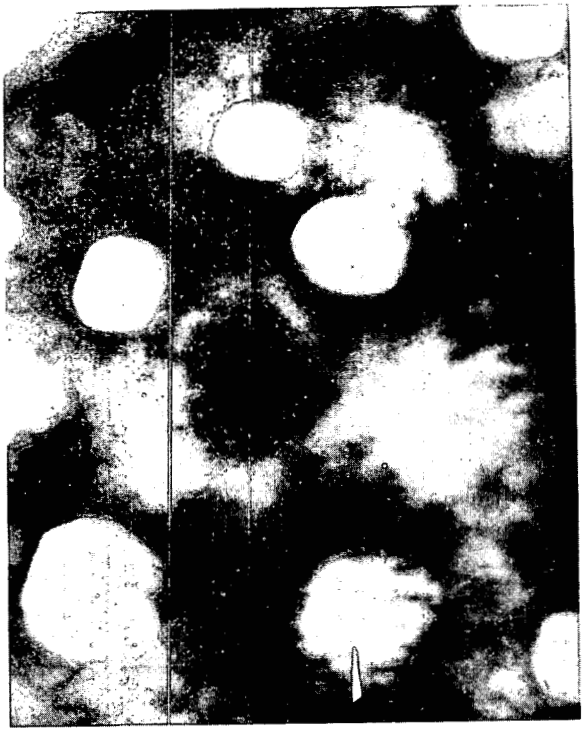

700C

FIGURE 56. Void distributions in ST Type 330 steel after nickel-ion bombardment to 248 dpa.

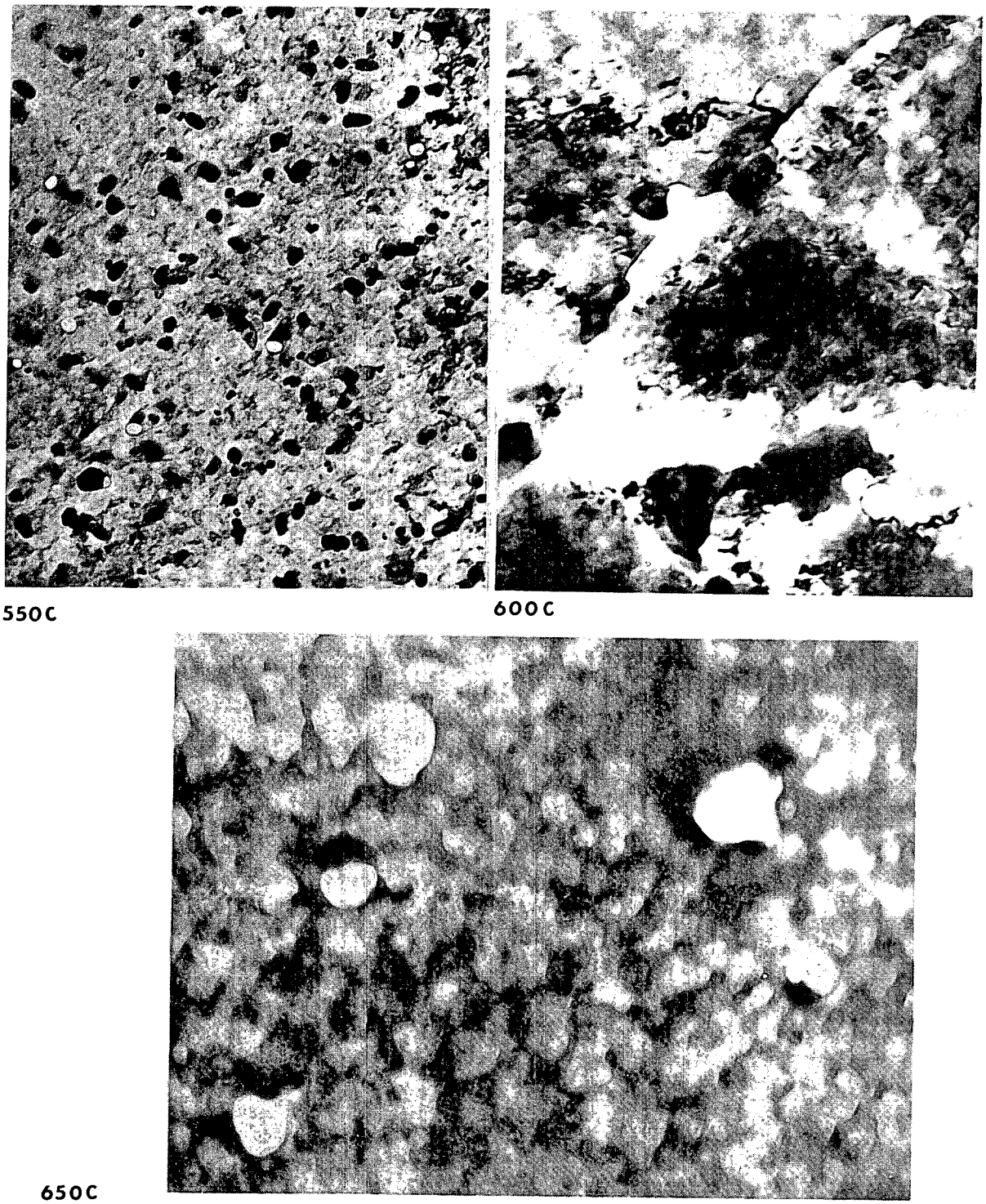

FIGURE 57. Void distributions in CW Type 330 steel after nickel-ion bombardment to 248 dpa.

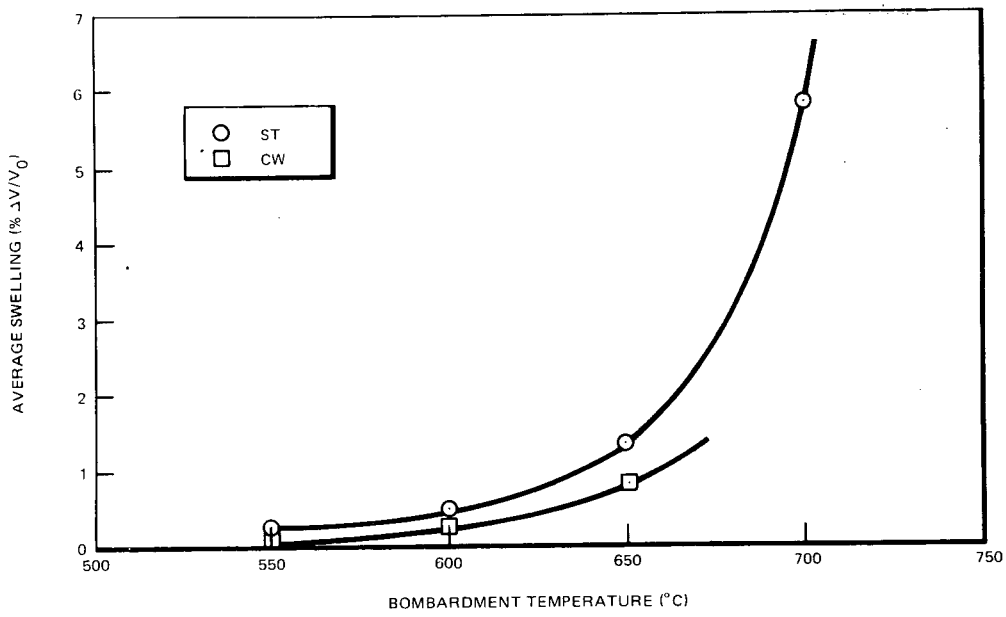

FIGURE 58. Temperature dependence of swelling in Type 330 steel, bombarded with 4 MeV nickel ions to a dose of 250 dpa.

TABLE 15

SWELLING DATA ON NICKEL-ION BOMBARDED TYPE 330 STEEL

Heat Treatment	Temp., °C	Dose, dpa	Average Void Parameters			Remarks
			Density, voids/cm^3	Diameter, nm	Swelling %	
ST	550	229	9.4×10^{13}	36	0.24	
	600	64	7.6×10^{12}	81	0.22	
	600	224	2.4×10^{13}	73	0.46	
	650					
	650	234	1.4×10^{13}	122	1.33	
	700	247	1.7×10^{13}	192	5.82	
20% CW	550	247	2.9×10^{13}	30	0.04	Uniform distribution
	600	247	7.7×10^{12}	88	0.23	Non-uniform distribution
	650	247	2.2×10^{12}	194	0.80	Non-uniform distribution

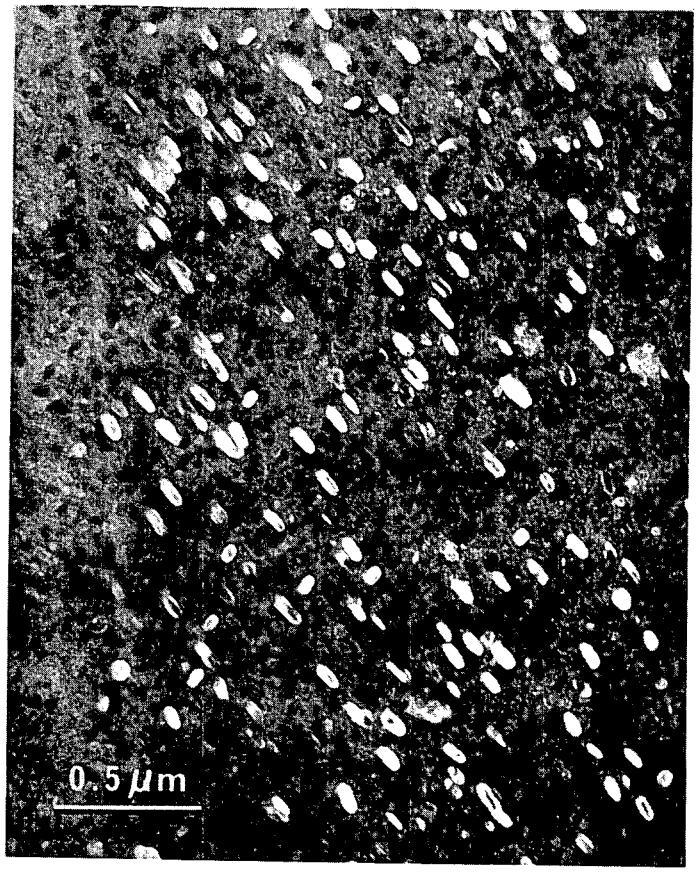

FIGURE 59. Dark-field image of precipitates, possibly silicides, in ST Type 330 steel after ion bombardment to 248 dpa at 550°C.

directions of the matrix. The precipitates are not $M_{23}C_6$ since the characteristic diffraction patterns were not detected at any time. The spacings of intensity maxima along rel-streaks indicate that one lattice parameter is in the 2.5-3.0 nm range. The best fit with a limited and hardly definitive amount of diffraction data is that a manganese silicide ($Mn_{0.815}Si_{0.185}$, ASTM card No. 24-737) appears during 550°C bombardment.

During 600°C to 700°C bombardments, these precipitates do not appear. The common carbide $M_{23}C_6$ is the only second phase found, and an intragranular distribution existed prior to bombardment. The carbides, however, do appear to coarsen with increasing bombardment temperature.

At most, only slight grain boundary delineation was observed in annealed material as shown in Figure 60 where there can also be seen some tendency for voids to prefer grain boundary sites.

2.3.5 Discussion

The six commercial austenitic alloys studied in this program exhibited a broad range of swelling behavior. As shown in the comparative listings in Table 16, peak swellings ranged from virtually zero to far in excess of 5 percent, the projected design limit for an end-of-life dose of 150 dpa. Predictably, the highest swelling occurred in the intermediate-nickel solid solution alloys, Types 310 and 330, and the lowest in the high-nickel precipitation-hardenable alloys. These trends are consistent with results from earlier simulation testing[4], which revealed a sharp reduction in swelling of Fe-Cr-Ni alloys with increasing nickel content.

TABLE 16

SUMMARY OF SWELLING DATA: COMPARATIVE SWELLING BEHAVIOR

Alloy	Secondary Swelling Rate, %/dpa	Peak Temperature, °C	Dose Intercept, τ(dpa)	Predicted Swelling at 250 dpa, % $\Delta V/V_o$
ST Type 310	0.4*	700	0	100
CW Type 310	0.04	675	37	8.9
ST Type 330	0.024*	700	0	6.0
STA Inconel 718	0.015	625	105	2.2
AU Nimonic PE16	0.008	675	15	1.9
STA Nimonic PE16	0.008	675	50	1.6
STA M-813	0.005	625	47	1.0
CW Type 330	0.003*	≥675	0	0.8
ST Nimonic PE16	0.008	625	200**	0.4
STA Inconel 706	0.002	575	44	0.4
CWA Inconel 706	0.0001*	575	0	<0.1
ST Inconel 706	0.0001*	500-600	0	<0.1

* Minimum swelling rate, based on assumption of zero incubation dose, i.e., primary or first-stage swelling.

** Dose intercept based on the attainment of a secondary swelling rate of 0.008%/dpa after approximately 250 dpa.

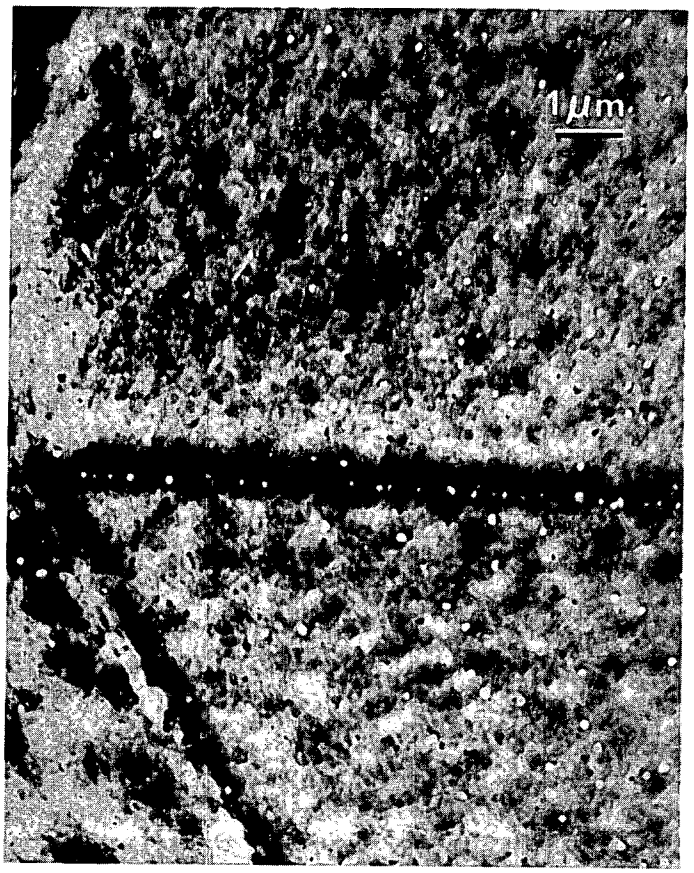

FIGURE 60. Diffuse-dark-field image of grain boundary regions in ST Type 330 steel after ion bombardment to 248 dpa at 650°C.

However, as the listing shows, variations in swelling behavior occurred not only between alloy types but within a given alloy type that had been modified by mechanical working or heat treatment. The effect of cold working, for example, is readily apparent in the order of magnitude reduction in swelling in both types 310 and 330 with 20-percent cold worked structures, compared with that of annealed material. In the precipitation-hardenable alloys Nimonic PE16 and Inconel 706, on the other hand, the annealed material exhibited the lowest swelling of the three microstructural conditions tested.

Although it is generally accepted that the high dislocation density accounts for the swelling inhibition shown by cold worked materials, no such straightforward explanation suffices to explain the differences noted in the complex precipitation-hardenable alloys. It is widely believed, however, that swelling resistance in Fe-Cr-Ni alloys is a sensitive function of the solid solution composition and any changes in that composition, particularly with regard to established swelling inhibitors, are expected to modify the swelling behavior.

Since the precipitation-hardenable alloys owe their unique mechanical properties to microstructural changes produced by high-temperature aging, it is perhaps predictable that such modifications will indeed alter the swelling of this family of alloys, much like cold working affects swelling in a predominantly solid solution material. Indeed, such predictions made on a number of the alloys studied in this program were found to be qualitatively correct, and were helpful in selecting bombardment parameters for alloys whose swelling behavior was, for the most part, empirically unknown. The relative swelling resistance of annealed versus aged materials, for example, was correctly predicted by Johnston, et al[16], on the basis of anticipated changes in solid solution composition of these alloys. Similarly, an upward shift in peak swelling temperature with aging was predicted and was shown to be at least qualitatively true in relation to the two alloys examined in both annealed and aged conditions in this program.

The fact that empirical results did not generally show close quantitative agreement with predicted behavior is likely due in part to the highly complex microstructure of these superalloys. As shown by Bell, et al[18], in an earlier publication and confirmed in this work, the response of the precipitation-hardenable alloys to a combination of overaging and irradiation could be expected to range from virtually zero, in the case of Nimonic PE16, to the sophisticated microstructural changes noted in Inconel 718. It would be somewhat difficult in the latter case to predict swelling response from considerations of solid solution composition without some prior knowledge of the microstructural stability of the alloy in the anticipated service environment. It was precisely this kind of information that the present work was directed to produce by simulation testing. Moreover, the fact that similar microstructural response was noted in reactor-irradiated Inconel 718 lends considerable credence to the application of the ion simulation technique for valid characterization of swelling and microstructural response of prospective materials to LMFBR core environments.

Although the swelling resistance of Inconel 706 is the most favorable of all the alloys studied, there may be some cause for concern about a possible loss of mechanical properties due to overaging. The less rapid overaging behavior of Inconel 718, on the other hand, indicates that the greater stabilities of the primary hardening phases, γ' and γ'', combined with the fineness of the secondary hardening η phase, should guarantee long-lived mechanical properties in this alloy.

Both Inconels exhibited a temperature boundary, at approximately 600°C, between sluggish and rapid overaging behavior during ion bombardment. With the more rapid overaging of Inconel 706, this temperature effect was observed after 116 dpa and was the most significant microstructural feature after 248 dpa. In Inconel 718, however, this temperature influence could be identified only after the higher dose.

Below 600°C, conditions seem to be favorable for other precipitation reactions to occur. Titanium carbides or nitrides were observed in M-813. Type 330 stainless steel, without the titanium and aluminum of the superalloys, exhibits similar precipitation features involving primarily silicides below 600°C and coarsening of carbides above this temperature.

The Ti/Al ratios of the superalloys can be correlated with the stabilities of the pre-bombardment precipitate phases. No noticeable changes occur in PE16; slight changes with increasing temperature occur in M-813, and the Inconels overage. The grain boundary opacity effects observed correlate in a reverse manner: Inconel 706 exhibits the least grain boundary delineation and PE16 the most, with Inconel 718 and M-813 showing intermediate effects. What causes these effects has not been defined, but segregation effects may be involved since, without involving phase changes, these areas seem to exhibit different response to electrochemical attack and their swelling behavior may be slightly different than surrounding matrix material. Thickness variations due to surface relief effects on the ion milled sides of specimens are not thought responsible but, even if they were, their origin could only be explained by some unusual properties of these areas. The grain boundaries themselves are in many instances separated from the electron-opaque regions but clearly form the pattern which the narrow regions adopt. The influences of such grain boundary effects upon mechanical and corrosion stabilities cannot be assessed but it would seem likely that some changes in properties would occur.

2.3.6 Conclusions

2.3.6.1 Swelling

(a) Nickel-ion bombardments at peak swelling temperatures to doses comparable to goal LMFBR fluences produced acceptably low swelling (based on the criterion of ≤5 percent swelling in 150 dpa) in nine of the twelve alloys tested: ST, STA and AU Nimonic PE16, ST, STA and CWA Inconel 706, STA Inconel 718, M-813 and CW Type 330 steel. Similar bombardments revealed unacceptably high swelling behavior in ST and CW Type 310 and ST Type 330.

(b) Swelling ratings of the several alloys arranged from best to worst, are given below:

ST Inconel 706 (best)
CWA Inconel 706
STA Inconel 706
ST Nimonic PE16
CW Type 330
STA M-813
STA Nimonic PE16
AU Nimonic PE16
STA Inconel 718
ST Type 330
CW Type 310
ST Type 310 (worst)

(c) General trends indicate that solution-treated precipitation-hardenable materials swell less and at a lower temperature than comparable aged material. In solid solution alloys, swelling is substantially higher in the solution-treated condition than in the 20 percent cold-worked state.

2.3.6.2 Microstructural Effects

(a) Bombardment with 4 and 5 MeV nickel ions accelerates overaging in the Inconel alloys 706 and 718; the overaging is similar to that produced by fast neutron irradiation.

(b) Pre-existing metastable precipitates of γ' and γ'' are degraded or dissolved in the two Inconel alloys during accelerated overaging caused by ion bombardment above 600°C. The stable overaging precipitate produced under these conditions is thin platelets of the η phase, Ni_3Ti. Pre-existing delta phase plates at grain boundaries disappear during bombardment of Inconel 706 but continue to form and grow in Inconel 718.

(c) Aged Inconel 706 overages more rapidly than does solution treated material bombarded under similar conditions.

(d) The degree of coarsening of η platelets can be correlated with the Ti/Al ratio of the alloys Inconel 706, Inconel 718 and Nimonic PE16. The latter alloy, with a Ti/Al ratio of one, does not overage during ion bombardment, nor does pre-existing γ' noticeably change as a result of high dose bombardments between 625 and 725°C.

(e) Undefined grain boundary effects are produced in the precipitation hardenable alloys by ion bombardment. The tendency to form electron-opaque grain boundary regions decreases with increasing Ti/Al ratio.

(f) Both M-813 and Type 330 steels experienced precipitate reactions at lower bombardment temperatures that involved carbides and nitrides in M-813 and silicides in Type 330. Higher temperature effects were restricted in coarsening of γ' in the former and carbides in the latter. No unusual microstructural changes were noted in bombarded Type 310 steel.

2.4 REFERENCES

1. Nelson, R. S., Mazey, D. J., and Nelson, J. A., J. Nuclear Materials 37, 1 (1970).

2. Corbett, J. W., and Ianniello, L. C., Editors, Radiation-Induced Voids in Metals, AEC Symposium Series No. 26 (1972).

3. Armijo, J. S., and Lauriten, T., Reference 1, p. 479.

4. Johnston, W. G., Rosolowski, J. H., Turkalo, A. M., and Lauritzen, T., J. Nuclear Materials 54 (1974), p. 24.

5. Johnston, W. G., Lauritzen, T., Rosolowski, J. H., and Turkalo, A. M., J. Met (June 1976).

6. Cummings, W. V., Gelles, D. S., and Bates, J. F., Alloy Development Program Quarterly Technical Progress Letter, TC-160-2 (8-10/74), p. 26.

7. Sullivan, C. P., and Donachie, M. J., Jr., Metals Engineering Quarterly, November 1971, p. 1.

8. Milhalisin, J. R., and Decker, R. F., Trans. TMS-AIME 218 (1960), p. 507.

9. Wheeler, J. B., Editor, Effects of Radiation on Substructure and Mechanical Properties of Metals and Alloys, ASTM STP 529 (1973).

10. Wheeler, J. B., Editor, Properties of Reactor Structural Alloys after Neutron or Particle Irradiation, ASTM STP 570 (1975).

11. Johnston, W. G., Rosolowski, J. H., Turkalo, A. M., and Lauritzen, T., J. Nuclear Materials 47 (1973), p. 155.

12. Beattie., M. J., Jr., and Hagel, W. C., Trans. TMS-AIME, 211 (1957), p. 911.

13. Bohm, H., Ehrlich, K., and Kramer, K. H., Metall., 2 (1970), p. 139.

14. Bell, W. L., J. Appl. Phys. 47 4 (1976), p. 1676.

15. Gelles, D. S., Ward, A. L., Steichen, J. M., and Knecht, R. L., Alloy Development Program Quarterly Technical Progress Letter, TC-160-9 (4-6/76), p. 22.

16. Johnston, W. G., Lauritzen, T., Rosolowski, J. H., and Turkalo, A. M., GE-CR&D Report 76CRD019, January 1976.

17. Challenger, K. D., and Lauritzen, T., Reference 10, p. 388.

18. Bell, W. L., Lauritzen, T., Darlin, E. S., and Warner, R. W., ASTM STP 611 (1976).

2.5 APPENDIX

2.5.1 Depth Distribution of Swelling by Conventional TEM

The nature of the damage zone in ion-bombarded materials, i.e., the variation in displacement damage with depth, presents a compelling argument for evaluating the damage distribution as a function of depth into the foil. Although such specimens have generally been examined (by conventional TEM techniques) in the region of the peak damage zone, there exists the potential for considerable economic gain in the recovery of swelling and microstructural data from not only the peak damage zone but from shallower depths, i.e, at intermediate doses, within the same bombardment sample. Such data are typically collected by bombarding a series of specimens to a range of doses and examining a single dose level in each. This obviously requires more material, more beam time and more TEM preparation than is required for a single specimen. Since the latter operations represent a substantial fraction of the costs associated with ion-bombardment experiments, the potential for cost savings is an attractive incentive toward the development of a technique for recovering such data from a single TEM disk. A further incentive in ion bombardment studies using preconditioned (reactor-irradiated) materials is the desire to conserve material and minimize the handling of highly radioactive specimens.

A number of investigators have demonstrated the feasibility of single-specimen studies of depth distribution of damage. Wolff, et al[A1], working with deuterons and Spurling and Rhodes[A2], who used protons, showed results of conventional TEM examinations on foils prepared parallel to the ion beam. However, although these demonstrations proved to be successful, the unique sample preparation procedures did not lend themselves to routine utilization of the techniques. Later work by Johnston, et al[A3], on nickel-ion bombarded materials showed depth distribution of damage in foils prepared parallel to the bombarded surface. More recently, the so-called full-range technique for examining a conventionally-prepared TEM foil has been demonstrated by Diamond, et al[A4]. This is perhaps the most straightforward technique that is presently available. One must simply back-thin a bombarded foil to its ion entry surface and stereographically image the damage zone (nominally 700 nm

in this application) with 0.6 - 1.0 MeV electrons. However, the dependence of this technique upon high voltage microscopy facilities and sophisticated data analysis programs effectively limit its application to national laboratories' programs.

To counter the impact of this valuable tool in the handling of ion-bombarded foils, a technique for gathering similar data on a single TEM disk using conventional sample preparation procedures and conventional TEM capabilities was demonstrated. Using a standard ion-bombarded TEM foil (i.e., a 3-mm diameter disk nominally 0.15 mm thick), the technique involves the stepped removal of material from the ion entry surface by sequential masking and ion milling, followed by targeted perforation by back thinning. Figure 61 shows an idealized schematic drawing of (a) the central region of a prepared foil with ion milling masks applied to the ion entry surface and (b) a cross-section of the portion of the foil indicated. Preparation of the ion-bombarded surface thus requires a multi-step ion-milling process, rather than the single-step process normally used, and a somewhat broader masked region to assure an adequate surface area for perforation. In the work discussed here, the 1 mm-diameter central region of the 3 mm-diameter disk is generally reserved for TEM examination. This region represents the circular unmasked portion of a disk bombarded with a partial mask of the geometry developed by Johnston, et al[A5]. The first ion-milling mask (a commercial lacquer) is applied to an elliptical region that overlaps approximately 0.2 mm into the central region. After the required argon ion milling, the mask is dissolved away, the step is measured and an accurate milling rate is established. The second mask is then applied above and overlapping the originally masked region and extending an additional distance into the central region. The ion milling-measurement sequences are then repeated. Although a number of consecutive milling operations can theoretically be performed, we have found it convenient (i.e., ease of step height measurement and multiple perforations) to restrict the number of steps to two. This would provide three dose levels: the bombarded surface, an intermediate zone and the peak zone, as shown in Figure 61. Thus, in this work, each ion milling sequence aimed for the removal of roughly 325 nm for a total removal of 650 nm in the central region. In the latter case, a 150 nm foil thickness after perforation would provide a region ranging from 650 nm to 800 nm, the peak damage depth being 760 nm.

Initial perforation of the foil is performed in the usual manner: the ion-milled surfaces are protected by translucent stop-off lacquer and a film of commercial polyvinylidene chloride; perforation is performed with a Fischione twin jet apparatus, using an electrolyte of 10 percent perchloric in acetic acid. Although no attempt is made during the first electropolishing to bias the location of the first perforation, the hole generally occurs in the peak damage zone in specimens that had been given a lightly dished electropolished surface before bombardment.

After TEM examination, the back surface of the original hole, as well as the surface away from the ion-masked regions, is coated with opaque lacquer; the front surface is prepared in the usual manner and the second electropolishing performed. This sequence is repeated until all areas of interest have been adequately perforated and examined. Results of this procedure were given in Section 2.3.6. The reader is directed particularly to the work on CW Type 310, Section 2.3.6.1.

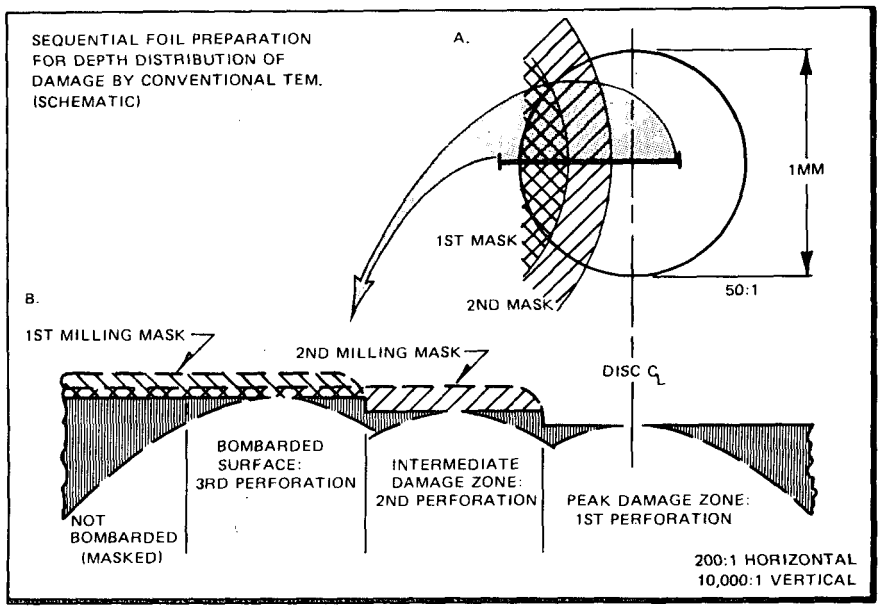

FIGURE 61. Sequential foil preparation for depth distribution of damage by conventional TEM (schematic).

2.5.2 References

A1. Wolff, U. E., Lauritzen, T., and Rosenbaum, H. S., 29th Annual Proceedings, Electron Microscope Society of America, C. J. Arceneaux, ed (1971).

A2. Spurling, R. A., and Rhodes, C. G., J. Nuclear Mat. 44 (1972), p. 341.

A3. Johnston, W. G., Lauritzen, T., Rosolowski, J. H., and Turkalo, A. M., "The Depth Distribution of Void Swelling Produced by 5 MeV Nickel Ions," in publication.

A4. Diamond, S., Baron, M., Bleiberg, M. L., Bajaj, R., and Chickering, R., "HVEM Quantitative Stereoscopy Through the Full Damage Range of an Ion-Bombarded Fe-Ni-Cr Alloy," Proceedings of the International Conference on Radiation Effects and Tritium Technology, October 1975 (in publication).

A5. Johnston, W. G., Rosolowski, J. H., Turkalo, A. M., and Lauritzen, T., "Nickel-Ion Bombardment of Type 304 Stainless Steel: Comparison with Fast Reactor Swelling Data," J. Nuclear Mat. 47 (1973), p. 161.

3. HVEM IRRADIATION OF REACTOR-CONDITIONED COMMERCIAL ALLOYS

L. E. Thomas, D. S. Gelles and J. J. Laidler

Hanford Engineering Development Laboratory

3.1 OBJECTIVE

The objective of this work is to assess the effect of prior neutron irradiation on swelling under HVEM electron irradiation, in order to provide guidance for the conduct of subsequent charged-particle irradiations of the candidate commercial and developmental alloys.

3.2 SUMMARY

Neutron irradiated specimens of fully-aged and solution-treated Nimonic PE16, 20% cold-worked 310 stainless steel and aged A-286 were electron irradiated at 500 to 700°C in the HVEM to determine the effect of reactor-conditioning on the simulation of void swelling at high neutron fluences.

For aged PE16 it was found that the swelling behavior under electron irradiation was unaffected by prior neutron irradiation. Specimens from four different reactor temperature/fluence conditions showed similar temperature-dependent swelling rates in the HVEM irradiations. Aged A-286 and 20% cold-worked 310 also appear insensitive to prior neutron irradiation, although the data available for these alloys is too limited for a firm conclusion. The swelling behavior of aged PE16, A-286 and cold-worked 310 was also consistent with previous results on helium-injected (not reactor-conditioned) specimens of slightly different composition. However, reactor-conditioning did alter the swelling response of solution-treated PE16 under electron irradiation, and this effect is attributed to the irradiation-enhanced precipitation of γ' which occurs in-reactor.

It is concluded that void and dislocation substructures generated in-reactor exert only second-order control over void swelling during electron irradiation. Reactor-conditioning experiments can be better described as temperature change experiments, provided that the alloy in question remains stable during neutron irradiation.

Based on these findings, procedures for conducting swelling simulation tests with reactor-conditioned specimens are recommended. These procedures combine limited simulation tests on reactor-conditioned specimens, comparison of results with simulation studies on virgin material, screening of neutron-irradiated specimens by TEM examination for microstructural evidence of phase and swelling instabilities, and interpretation of "reactor-conditioning" results in terms of temperature change experiments. The use of such procedures will permit maximum effective utilization of resources, enabling the experimenter to eliminate tests which would otherwise prove in the long run to have been unnecessary.

3.3 ACCOMPLISHMENTS AND STATUS

3.3.1 Introduction

In view of the many differences between neutron and charged particle irradiations, it is almost incredible that charged particle irradiations should provide the ability for successful simulation of void swelling at high neutron fluences. Exact translation from the reactor timescale of months to the hours or so required under electron or nickel ion irradiation, simultaneously involving kinetics of helium production and irradiation-enhanced diffusion of various chemical species and lattice defects, is difficult to envision. Yet with few exceptions, simulation of reactor swelling behavior by means of charged particle bombardment appears remarkably successful. For example, the latest post-neutron irradiation examinations[1-3] qualitatively confirm simulation-based swelling predictions[4] for commercial alloys, including AISI 310, A-286, M-813, Nimonic PE16, AISI 330, Inconel 706 and Inconel 718.

To lend increased confidence to quantitative swelling predictions, simulation tests using reactor-conditioned, i.e., previously neutron-irradiated, specimens have been proposed[5]. Such tests cover two distinct possibilities. First, it seems unlikely that simulation methods can reproduce exactly the same microstructures present in the void nucleation stage of swelling in-reactor. Reactor-conditioning overcomes this difficulty by ensuring that irradiation-induced (or accelerated) precipitation, transmutation products (especially helium) and defects such as dislocations, bubbles and voids are co-generated in a manner characteristic of the reactor environment.

Second, a few alloys have been found for which swelling predicted from charged-particle irradiations clearly differs from that produced in reactor. For example, the AISI 316-derivative alloy LS-1, with relatively high titanium, zirconium and silicon additions, showed considerably better swelling resistance than 316 under both nickel ion[6] and electron irradiation[7]. However, after only 2.7×10^{22} neutrons/cm^2 (E>0.1 MeV), 0.8% swelling was observed[8] in LS-1 alloy specimens. Electron microscopy revealed that a phase instability was promoted by neutron irradiation and that the void swelling was associated with irradiation-induced precipitation. As another example, the experimental Fe-15Cr-25Ni alloy, E48, containing titanium and aluminum additions, also showed low swelling after nickel ion bombardment[9] and it was suggested that the swelling was suppressed by the Ti and Al additions. This alloy also developed high swelling at a relatively low neutron fluence[10].

These examples reflect exceptional swelling behavior which is apparent during postirradiation examination after low neutron fluences. The reactor-conditioning experiments cover the possibility that irradiation-induced instabilities may also develop at intermediate neutron fluences.

The basic aim of charged-particle irradiation experiments in the simulation of in-reactor swelling behavior is determination of the peak swelling rate and the neutron irradiation temperature at which the peak rate occurs. Thus, it is essential not only to obtain a correlation between neutron and charged-particle doses, but to establish an equivalency of irradiation temperatures as well. It is the latter consideration which is the principal concern of the series of experiments reported here.

The conventional assumption regarding simulation experiments is that the void growth rate is related to the void density, dislocation density, irradiation temperature and instantaneous point defect supersaturation. As a consequence of the different supersaturations which prevail during typical neutron and charged-particle irradiation conditions, the peak swelling rate is presumed to occur at a higher temperature under charged-particle irradiation than in the case of neutron irradiation. This effect is commonly termed a "temperature shift", and has been observed frequently in experiments with a variety of pure metals and stainless steels[11]. In cases where void density and dislocation density are the only parameters which control void growth, peak swelling under charged-particle irradiation should occur when a specimen irradiated at the peak swelling temperature in-reactor is bombarded with charged particles at a higher temperature reflecting the appropriate temperature shift. The charged-particle peak swelling temperature should then be the same for both reactor-conditioned and virgin specimens. Knowing the peak swelling temperature for virgin specimens, the correct temperature shift (and hence the true temperature of peak swelling in the reactor-irradiated material) can be determined by irradiating reactor-conditioned specimens from several reactor irradiation temperatures at the charged-particle peak temperature. The in-reactor peak is then that condition for which the peak swelling rate is observed under charged-particle irradiation.

Assessment of expected high-fluence swelling behavior of certain alloys may be complicated in the event that the void growth rates are dominated by factors other than void density and dislocation density. Of particular concern is the case in which solute redistribution occurs during neutron irradiation, as typified by the behavior of alloys LS-1 and E48. This solute redistribution may take the form of solute clustering, short-range order, precipitation of new phases, or increased volume fraction of precipitate phases present prior to irradiation. If, as is suspected[12], the major effect of such solute redistribution is to alter the swelling behavior of the matrix, then the peak swelling rate for charged-particle irradiation of reactor-conditioned specimens will occur in specimens for which the reactor irradiation conditions were such as to maximize the change in matrix composition. In this case, deduction of the peak swelling temperature for reactor irradiation can be very difficult and it may be necessary to await reactor test data at higher neutron fluences before the true swelling behavior can be determined.

A further complication may exist in the event that the reactor-conditioned specimen has not received sufficient neutron fluence to exceed the swelling incubation fluence. While low fluences are considered sufficient to establish representative solute redistribution effects, void nucleation may still be incomplete and the response to charged-particle irradiation may reflect the extent of completion of nucleation.

At the time the present study was undertaken, only three candidate commercial alloys were available in the neutron-irradiated condition. These alloys, Nimonic PE16, A-286 and AISI 310, in several different heat-treatment conditions had been irradiated in EBR-II, pin B-109 of the AA-Ia test at eight temperature/fluence conditions, up to 5.4×10^{22} n/cm^2 (E>0.1 MeV) and 650°C. Most of the HVEM irradiation experiments described in this report concentrate on fully aged Nimonic PE16 to determine the effects of different neutron-irradiation temperatures on subsequent swelling in the HVEM. Solution-treated Nimonic PE16 was included to determine the effect of in-reactor precipitation on subsequent swelling. Aged

A-286 and 20% cold-worked AISI 310 were included mainly to determine if their swelling rates were comparable to those found in material not subjected to prior neutron irradiation and to investigate the microstructural changes which occur in the presence of different initial structures.

3.3.2 Experimental Details

The experimental procedure and conditions are similar to those described previously[4]. Disk specimens, prepared for TEM by jet electropolishing, were electron-irradiated in the heating-tilting stage of a JEOL 1000 KV electron microscope, using beam conditions which produce 15 dpa/hour and a 70°C temperature rise in the center of an irradiated region about 6 μm in diameter. The irradiation time totalled one hour (15 dpa), and irradiations were interrupted every fifteen minutes to take stereo micrographs of the irradiated region. Analysis of the stereo micrographs allows the evolution of the void structure, starting from the initial neutron-irradiated state, to be followed in three dimensions through an entire run. For analysis, the polyhedral shapes of the voids were determined and used to compute void volumes accurately. Irradiation conditions for the specimens subjected to electron irradiation are summarized in Table 17.

TABLE 17

SPECIMEN CONDITIONS FOR HVEM REACTOR-CONDITIONING EXPERIMENTS

Alloy	Condition	Heat ID	Subcapsule ID	Reactor Conditions (E>0.1 MeV)
Nimonic PE16	Fully Aged	FZ2213	L	4.3×10^{22} n/cm^2 at 427°C
			K	5.1×10^{22} n/cm^2 at 510°C
			J	5.4×10^{22} n/cm^2 at 593°C
			H	5.4×10^{22} n/cm^2 at 650°C
Nimonic PE16	Solution Treated	FZ2213	L	4.3×10^{22} n/cm^2 at 427°C 5.4×10^{22} n/cm^2 at 593°C
AISI 310	20% CW	33567	J	5.4×10^{22} n/cm^2 at 593°C
A-286	Fully Aged	C51644	L	4.3×10^{22} n/cm^2 at 427°C

3.3.3 Results

To describe the electron irradiation results, it will be convenient to refer to the four neutron-irradiation temperature/fluence conditions by irradiation subcapsule designation, L, K, J and H (see Table 17).

3.3.3.1 Aged Nimonic PE16. Figure 62 illustrates representative changes in void structure for aged PE16, condition J, under electron irradiation at 650°C. The voids created in PE16 by neutron irradiation are nearly perfect cubes, and in Figure 62(a) the crystal orientation, [112], is such that the projected images show all the cube corners and edges. Electron irradiation produces an order-of-magnitude increase in void density with the new voids distributed much more uniformly than the original ones. Both new and original voids grow under electron irradiation, but the voids created in-reactor remain nearly cubic while the new voids are nearly octahedral, suggesting that the two populations formed and grew under different conditions of solute flux. At 15 dpa [Figure 62(e)], local specimen bending due to the swelling is apparent. The new voids account for most of the total void volume.

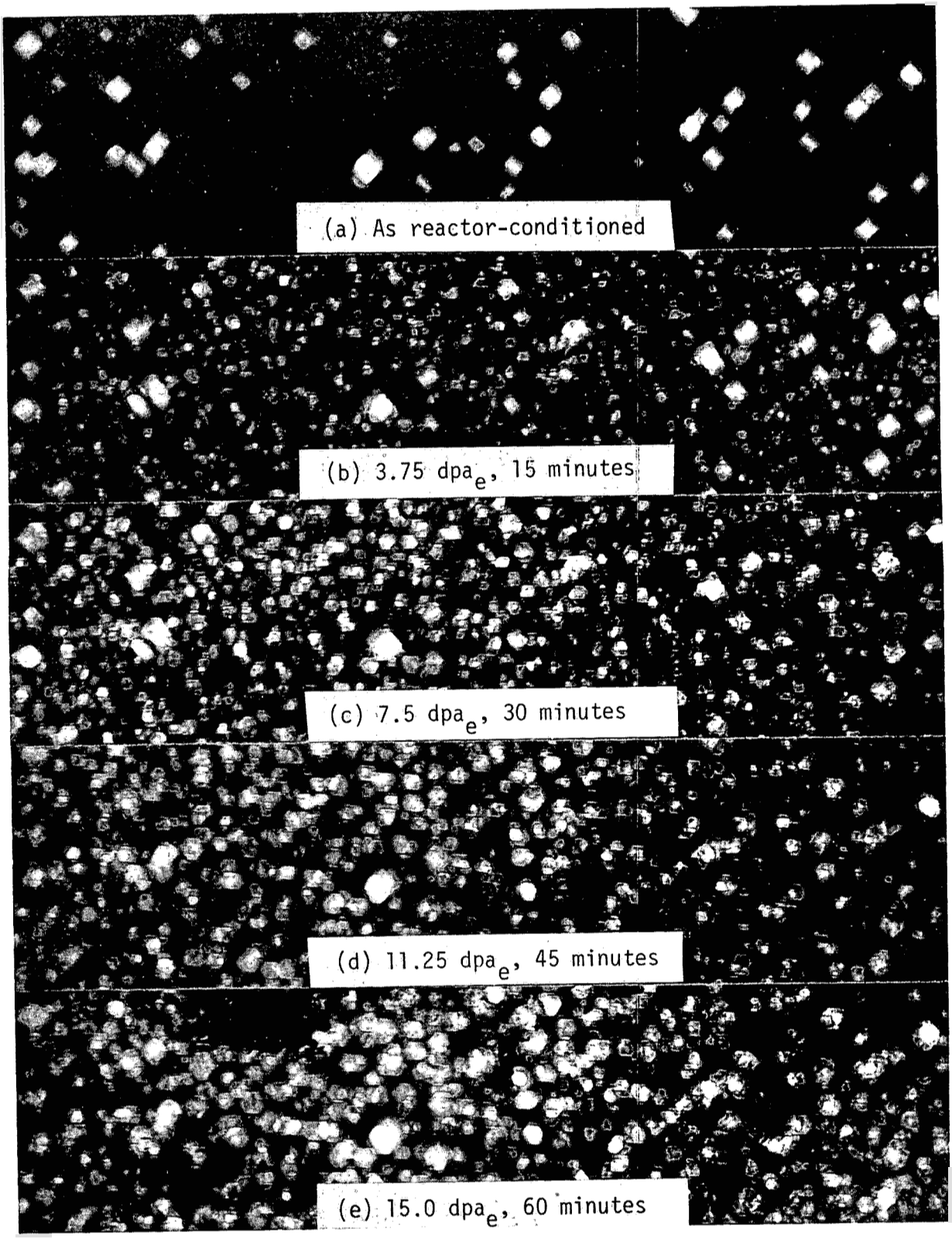

FIGURE 62. HVEM generated void swelling at 650°C in aged Nimonic PE16, reactor-conditioned to 5.4 x 10^{22} n/cm^2 at 593°C; irradiation conditions as shown.

As indicated in Table 18, all four reactor conditions of aged Nimonic PE16 (L, K, J and H) were electron-irradiated at 500 to 700°C. Table 18 also lists initial and final void densities and swelling data. As shown by these results, the increase in void densities at the onset of electron irradiation depended strongly on electron irradiation temperature. Thus, reactor generated microstructural features had little effect on void nucleation behavior in the HVEM. Only at the highest HVEM irradiation temperatures did the voids created in reactor dominate the swelling microstructure.

As shown by Figure 63, the swelling rates for all four reactor conditions of aged Nimonic PE16 exhibit similar temperature dependent behavior with the peak of 0.4%/dpa at 650°C. Changes in reactor conditioning temperature or fluence have little effect on subsequent swelling behavior in the HVEM. Only at 700°C is a large variation with reactor conditions observed. Although this variation may be symptomatic of experimental problems at the highest possible microscope operating temperature, it is more likely due to effects caused by void nucleation difficulties. An example is provided with two irradiations at 650°C on material from subcapsule L which gave a factor of two difference in swelling rates and very different void nucleation behavior. The higher swelling rate accompanied a large increase in void density at the onset of electron irradiation, whereas the lower rate, 0.25%/dpa, corresponded to the only instance observed at 650°C where no new voids formed during electron irradiation. This same behavior is reflected at 700°C, the L condition developing no increase in void density with the lowest swelling rate, and the J and H conditions behaving in the opposite manner.

Two electron irradiations were also performed on aged PE16 (J condition) which was prepared for TEM by electropolishing at -40°C. Contrary to results reported by Buswell, et al[13], the swelling rates and void densities in the specimens polished at low temperature were similar to those from specimens polished at room temperature. Buswell, et al, report differences in void densities and swelling at different electropolishing temperatures, and attribute this to hydrogen pick-up during specimen preparation. Present results, however, support the continued use of room-temperature polishing.

3.3.3.2 Solution-Treated Nimonic PE16. Results for solution-treated Nimonic PE16 are also presented in Table 18. Morphologically, the HVEM swelling behavior was similar to that in aged Nimonic PE16. The voids produced during HVEM irradiation accounted for most of the swelling observed. However, void nucleation in the HVEM was absent for the L condition run at 650°C and the resultant swelling rate was unusually low.

Solution-treated Nimonic PE16, condition J, showed a peak swelling rate at a lower temperature, 600°C, and an apparently higher peak rate, 0.7%/dpa (see Figure 64) than did aged Nimonic PE16. Solution-treated condition L gave 0.4% swelling/dpa at 600°C, but the data available are insufficient to conclude that this is the peak swelling temperature. Figure 64 therefore provides the first indication that variations in reactor conditioning can cause variation in HVEM reactor conditioned experiments. The effect is attributed to differences in the extent of γ' precipitation during reactor conditioning.

TABLE 18

EXPERIMENTAL PARAMETERS AND RESULTS ON NIMONIC PE16, AISI 310 AND A-286
REACTOR-CONDITIONED IRRADIATIONS

Specimen ID/Run	Reactor Condition	HVEM Temp., (°C)	Swelling at 0 dpa (%)	Initial Void Density (cm^{-3})	Initial Void Diameter* (nm)	Swelling at 15 dpa (%)	Final Void Density (cm^{-3})	Swelling Rate (%/dpa)
Nimonic PE16								
STA 7L/538A	4.3×10^{22}, 427°C	500	0.08	2.6×10^{14}	14.4	0.56	1.3×10^{16}	0.03
486A		525	NM	NM	NM	NM	NM	NM
538B		550	0.24	4.4×10^{14}	20.6	1.2	1.8×10^{16}	0.08
484B		600	0.07	2.0×10^{14}	18.1	4.7	4.6×10^{15}	0.33
516A		650	0.06	3.4×10^{14}	11.1	2.3	5.0×10^{14}	0.24
538C		650	0.10	3.0×10^{14}	15.8	5.4	3.6×10^{15}	0.46
516B		700	0.13	2.6×10^{14}	19.9	0.8	2.5×10^{14}	0.06
STA 7K/540	5.1×10^{22}, 510°C	550	NM	NM	NM	0.2	3.3×10^{15}	0.015
STA 7J/533	5.4×10^{22}, 593°C	550		1.3×10^{14}	39.8		2.7×10^{15}	0.026
482A		600	0.3	3.2×10^{14}	37.4	5.1	4.0×10^{15}	0.36
483		650	0.5	1.2×10^{14}	39.4	6.2	2.0×10^{15}	0.40
482B		700	0.2	2.0×10^{14}	33.9	3.8	3.3×10^{14}	0.33
539A	5.4×10^{22}, 593°C	600	0.7	1.6×10^{14}	41.2	3.1	6.1×10^{15}	0.20
539B	Polished at -40°C	650	0.4	9.0×10^{13}	41.3	6.3	2.9×10^{15}	0.44
STA 7H/535A	5.4×10^{22}, 650°C	650	0.6	8.6×10^{13}	49.3	4.7	8.0×10^{14}	0.37
535B		700	0.6	5.8×10^{13}	61.3	6.6	1.1×10^{14}	0.48
ST 6L/515A	4.3×10^{22}, 427°C	600	0.4	2.8×10^{14}	30.3	6.3	5.0×10^{15}	0.40
515B		650	0.3	2.0×10^{14}	27.5	2.0	3.0×10^{14}	0.12
ST6J/530	5.4×10^{22}, 593°C	550	0.0	NM	NM	0.6	4.0×10^{15}	0.04
486A		600	0.4	1.5×10^{14}	36.3	8.1	3.7×10^{15}	0.72
499		650	0.2	1.0×10^{14}	35.9	3.1	1.2×10^{15}	0.20
AISI 310, 20% CW								
PJ/506A	5.4×10^{22}, 593°C	600	0.275	8.7×10^{13}	31.5	16.3	2.5×10^{15}	1.06
		700	0.10	1.1×10^{14}	24.6	6.0	1.2×10^{15}	0.41
A-286 (STA)								
5L/	4.3×10^{22}, 427°C	550	2.4	4.0×10^{15}	21.3	5.5	4.0×10^{15}	0.2
501		600	2.2	3.0×10^{15}	22.6	7.7	3.0×10^{15}	0.42
503A		650	2.4	4.0×10^{15}	22.1	7.4	3.0×10^{15}	0.8
503B		700	2.1	4.0×10^{15}	21.1	1.2	2.0×10^{15}	-

* Equivalent Sphere Diameter
NM = Not Measured

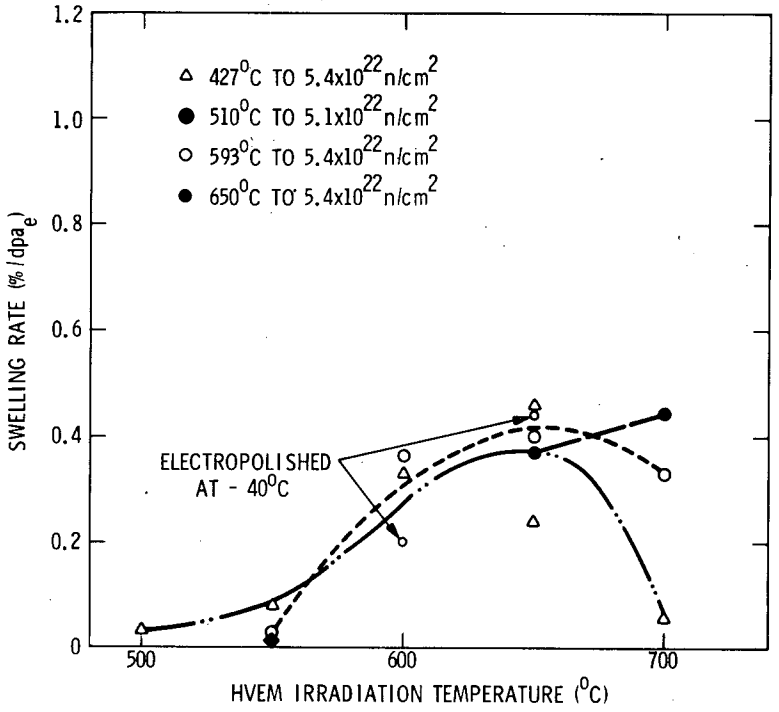

FIGURE 63. Electron irradiation swelling rates obtained in aged Nimonic PE16 after reactor conditioning.

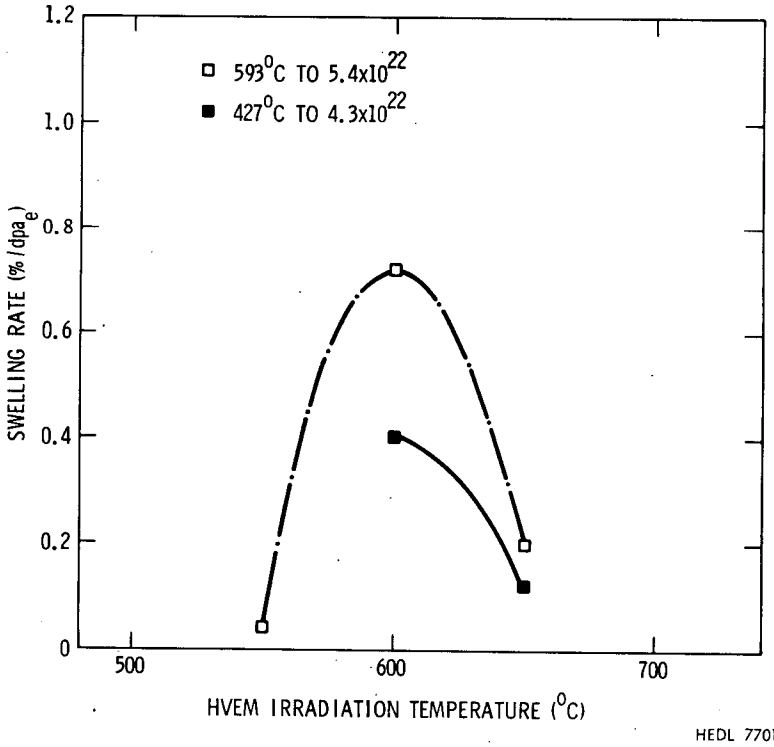

FIGURE 64. Electron irradiation swelling rates obtained in solution treated Nimonic PE16 after reactor conditioning.

3.3.3.3 Comparison with Previous Results. Figure 65 compares the swelling rates for reactor-conditioned Nimonic PE16 with rates for helium-injected PE16 without reactor conditioning. To make this comparison note that different heats of material were involved. Although the peak swelling rate for the aged, helium-injected material is nearly three times that of reactor-conditioned material, the peak swelling temperatures are the same. Moreover, immersion density results for both heats of PE16 (at a comparable fluence) are now available[1,2], and these also show three times the swelling at the same peak temperature, 600°C in reactor, for the heat which shows higher swelling under HVEM irradiations. The swelling behavior for helium injected solution treated PE16 appears significantly different from that in reactor-conditioned material, and this can again be attributed to the extensive precipitation of γ' during reactor conditioning. Figure 66 shows the void densities obtained, as a function of electron irradiation temperature, for all the reactor-conditioned specimens of Nimonic PE16. The void densities of reactor-conditioned material are generally similar to those obtained for the helium-injected heat which was electron-irradiated without prior neutron irradiation.

3.3.3.4 AISI 310, 20% CW. The 310 stainless steel specimens subjected to electron irradiation were cold-worked material which had received 5.4×10^{22} n/cm^2 at 593°C. Electron irradiations were performed at two temperatures, 600 and 700°C.

The effect of electron irradiation at 600°C, the peak swelling temperature, is illustrated by the micrograph series in Figure 67. Small voids which may be visible in the background of Figure 67(a) formed during initial examination at the irradiation temperature and reflect an unusually sensitive response to electron irradiation at a fluence of approximately 0.05 dpa$_e$. Figures 67(b) through 67(e) follow the development of voids in the same region through 15 dpa. As in Nimonic PE16, electron irradiation produced an order-of-magnitude increase in void density, and although both the original and new voids quickly become indistinguishable during subsequent void growth, the voids formed during electron irradiation accounted for most of the swelling. At 15 dpa [Figure 67(e)] the void volume fraction reached 0.16.

The irradiation parameters summarized in Table 18 demonstrate increases in void density at both irradiation temperatures. Swelling rates found are similar to those determined for Type 316 stainless steel. Comparison (in Figure 68) with previous electron irradiation results for solution-treated, helium-injected 310 stainless steel without prior reactor irradiation indicates similar swelling behavior, despite the difference in the initial conditions of the specimens.

3.3.3.5 A-286. The A-286 chosen for electron irradiations was aged material which received 4.3×10^{22} n/cm^2 at 627°C, the peak swelling temperature according to immersion density measurements. Transmission electron microscopy observations of the specimens used for electron irradiation yielded 2.2% swelling, in good agreement with the macroscopic density measurements, despite changes in the γ' precipitates under neutron irradiation. The initial void structure shown in Figure 69(a) consisted of 4×10^{15} voids/cm^2, with a mean void diameter of 21 nm.

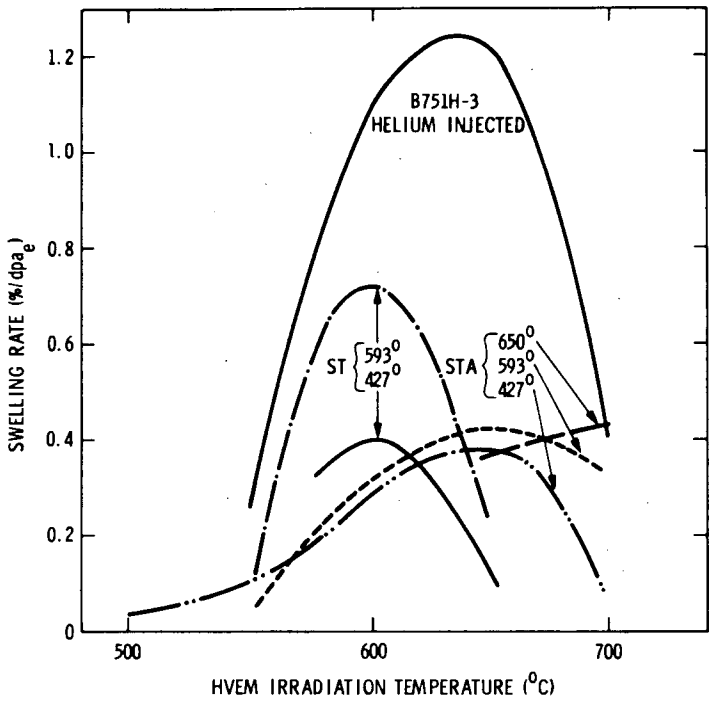

FIGURE 65. Comparison of reactor conditioning results for Nimonic PE16 with previous results on helium-injected specimens of a different heat.

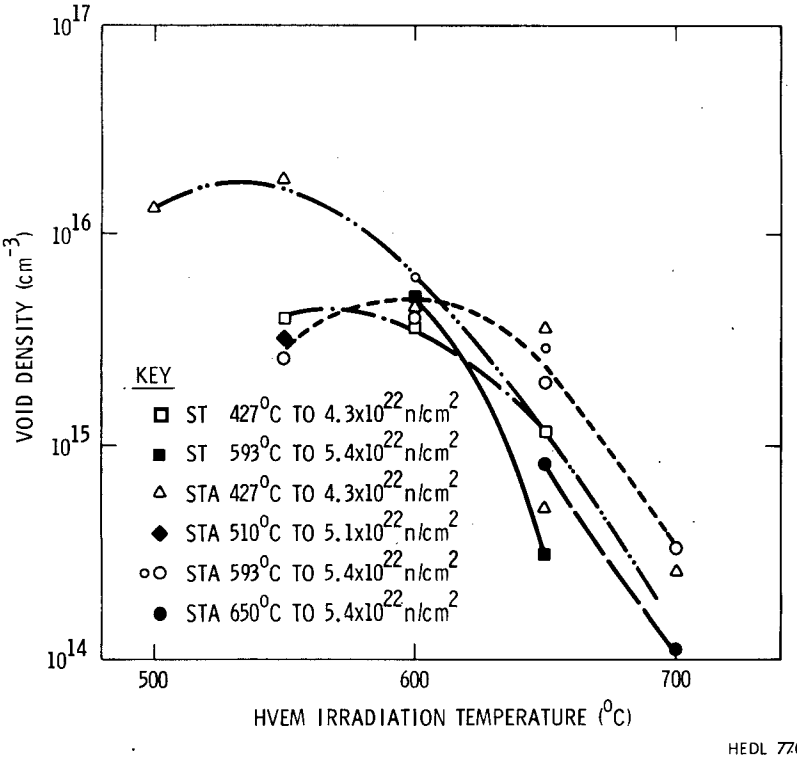

FIGURE 66. Void densities for reactor-conditioned Nimonic PE16 after 15 dpa (electron).

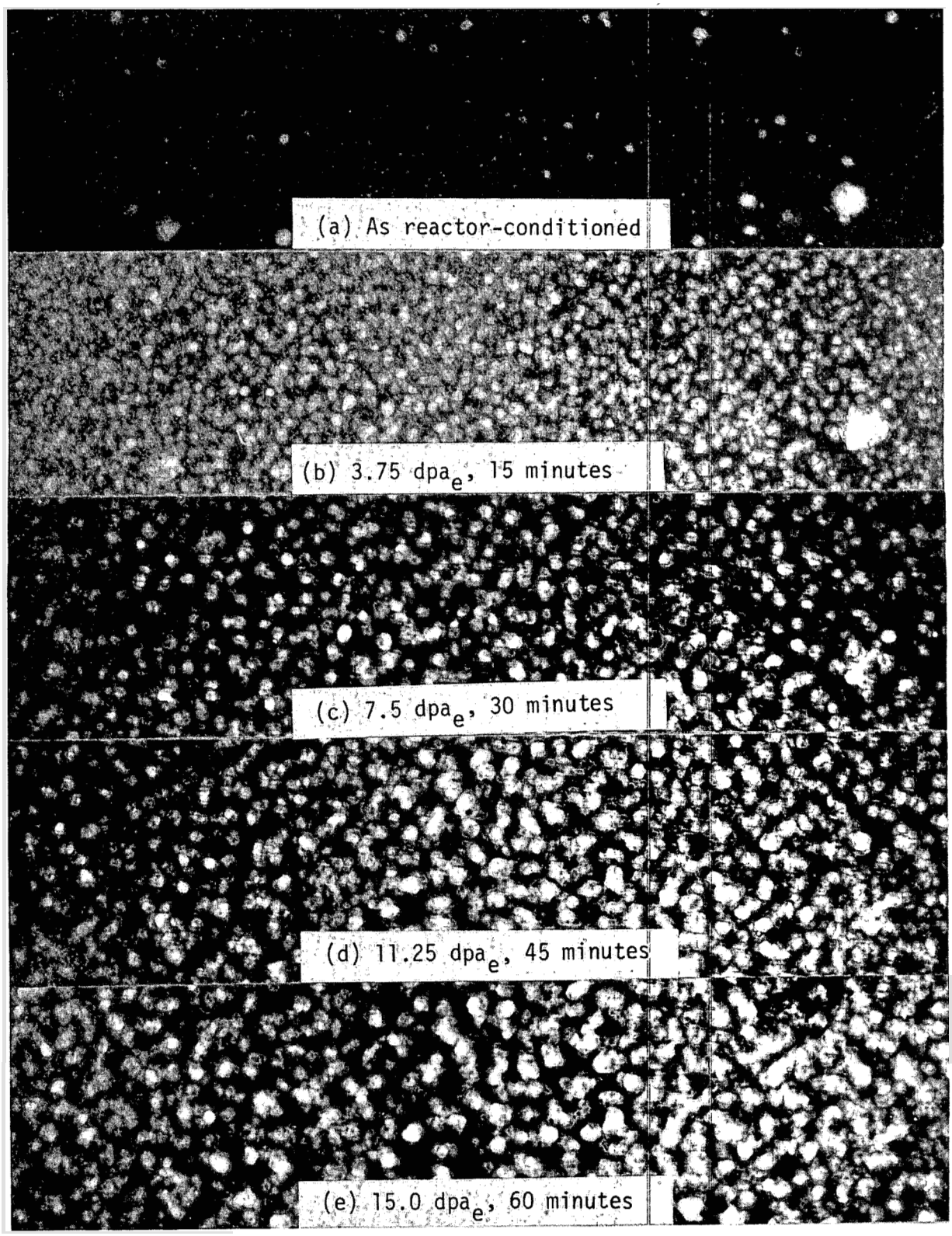

FIGURE 67. HVEM generated void swelling at 600°C in 20% CW 310 stainless steel, reactor-conditioned to 5.4 x 10^{22} n/cm^2 at 593°C; irradiation conditions as shown.

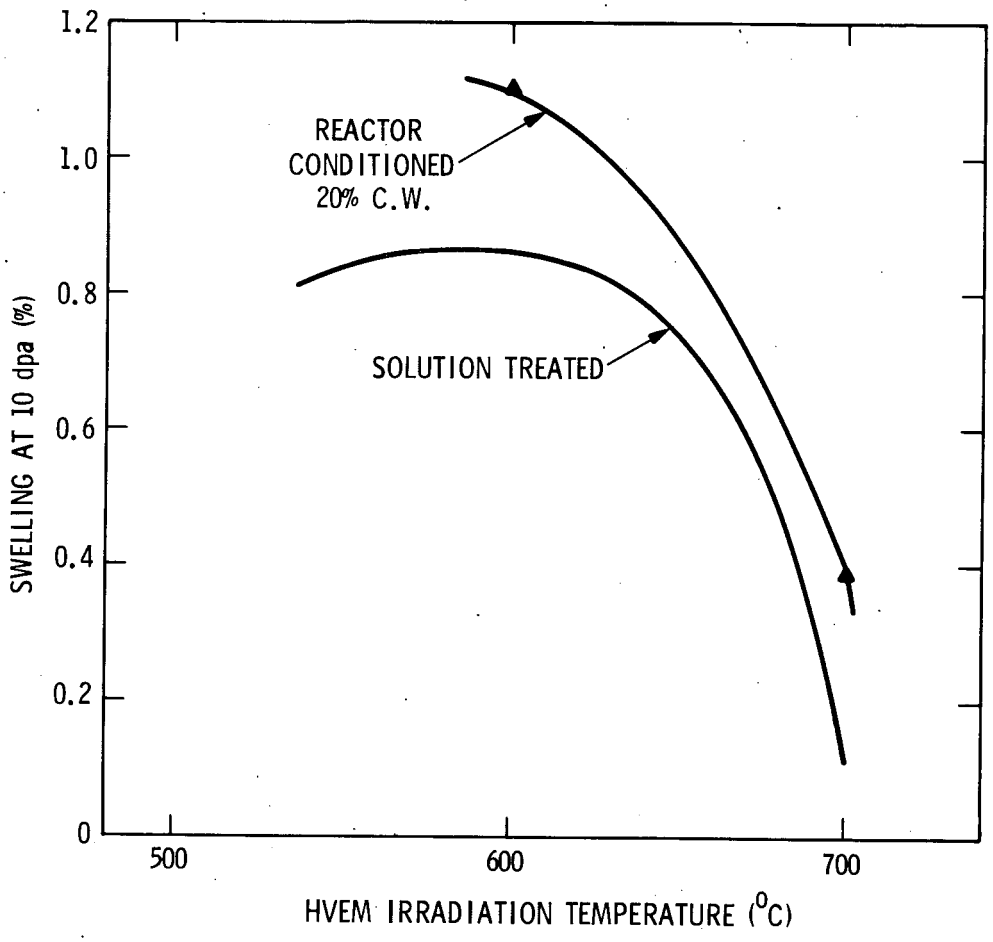

FIGURE 68. Comparison of reactor-conditioning results for 20% CW 310 with previous results on solution-treated helium-injected specimens of a different heat.

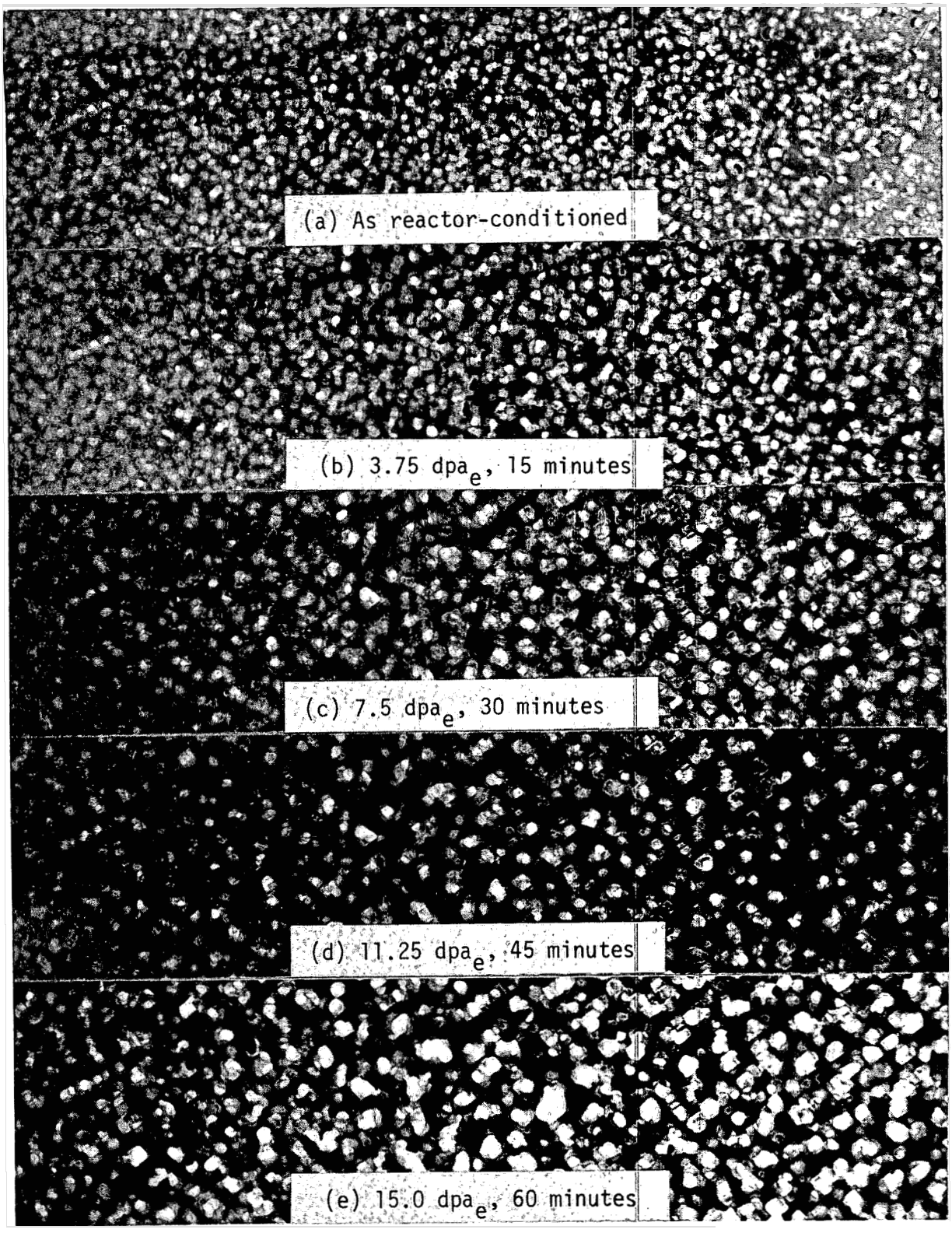

FIGURE 69. HVEM generated void swelling at 650°C in fully aged A-286, reactor-conditioned to 4.3 x 10^{22} n/cm^2 at 427°C; irradiation conditions as shown.

Unlike Nimonic PE16 and 310 stainless steel, A-286 underwent decreases in void density at each of the four electron irradiation temperatures used (see Table 18). The original voids grew or coalesced with neighboring voids, as indicated in the micrograph series of Figure 69, producing relatively high swelling rates. The precipitates associated with voids also grew during electron irradiation. (These precipitates had also been present in HVEM irradiations of helium-injected A-286.)

The swelling behavior in reactor-conditioned A-286 was similar to helium injected material of a different heat. A comparison of swelling rates is provided in Figure 70, showing similar temperature dependences. The peak swelling temperature of the reactor-conditioned material is about 50°C higher, but the swelling rates are similar in magnitude for these two heats. Thus, the HVEM generated swelling obtained on reactor-conditioned aged A-286 is consistent with earlier results from HVEM irradiations of helium injected material. This similar temperature dependence of swelling rates indicates that reactor conditioning has little effect on swelling in A-286 under electron irradiation.

Void density behavior in reactor-conditioned aged A-286 was significantly different from that of earlier helium injected specimens. Figure 71 demonstrates that for aged A-286 the void density generated in-reactor at 427°C is four times larger than observed in helium injected material of a different heat. Irradiation at 550°C maintained the void density but higher irradiation temperatures resulted in a decreasing void density during irradiation. Nonetheless voids were still present at 700°C. But from previous results in helium injected A-286, no swelling resulted at 650°C because voids failed to develop. An apparent difference in peak swelling temperature results. Thus reactor conditioning is expected to overcome conditions where lack of voids adversely affects irradiation experiments.

3.3.4 Discussion

3.3.4.1 Swelling Behavior in Reactor-Conditioned Alloys. Aged Nimonic PE16 showed a similar temperature-dependence of swelling rate for each of four different neutron-irradiation conditions. Since the neutron irradiations involved only small differences in fluence, it can be concluded that varying the neutron irradiation temperature has no effect on subsequent swelling behavior under electron irradiation. It can also be concluded that the void and dislocation structures generated in reactor exert at most only second-order control over void swelling during electron irradiation.

Solution-treated Nimonic PE16, on the other hand, exhibited a lower peak swelling temperature and higher peak swelling rate than the aged, reactor-conditioned material. The swelling behavior of solution-treated Nimonic PE16 also differs from that observed without prior neutron irradiation and suggests that the extensive precipitation of γ' which occurs in solution-treated PE16 during irradiation in-reactor strongly influences subsequent swelling. The difference is one of stability with respect to second-phase formation under reactor-irradiation conditions.

As in aged Nimonic PE16, the swelling behavior of reactor-conditioned 20% cold-worked 310 stainless steel and aged A-286 is consistent with that observed in the same alloys without prior reactor irradiation. Because of the limited data, however, no firm conclusion regarding the effects of reactor conditioning on swelling in these two materials is warranted at this time.

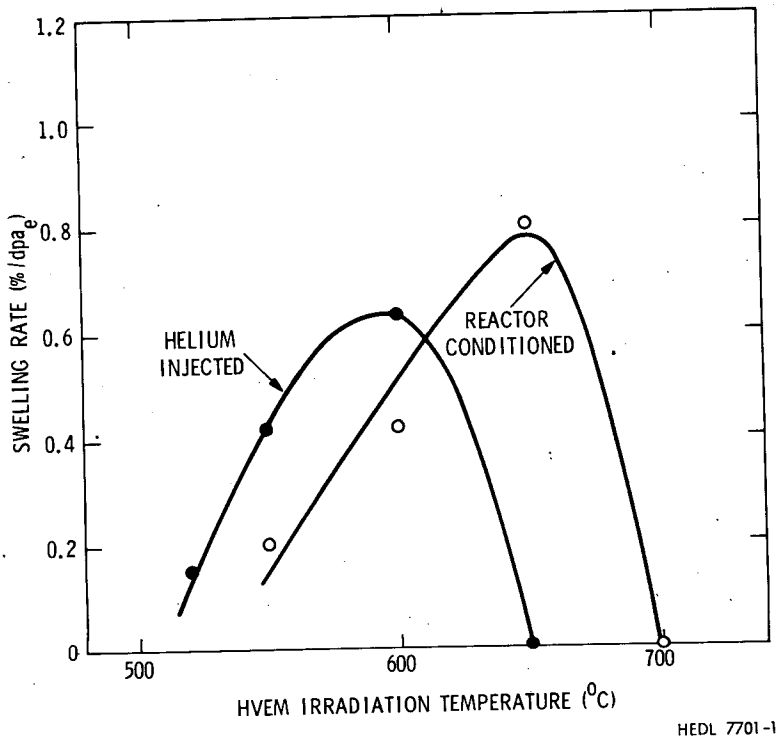

FIGURE 70. Comparison of reactor-conditioning results for A-286 with previous results on helium-injected specimens of a different heat.

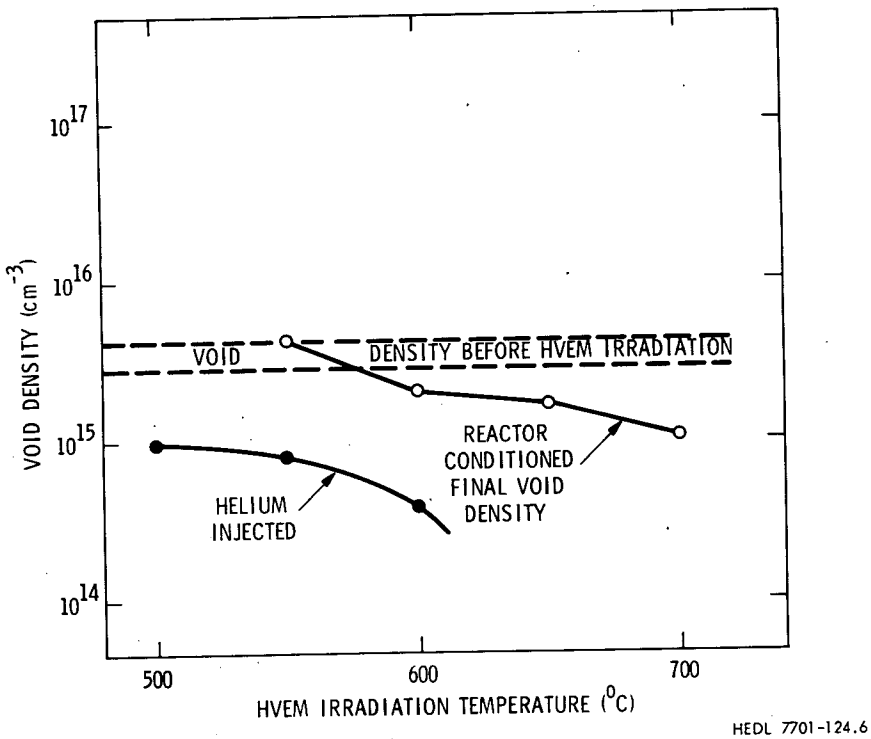

FIGURE 71. Void densities for A-286 irradiations after 15 dpa (electron).

3.3.4.2 Temperature-change Analysis. At the beginning of the present experimental study it was considered likely that swelling initiated under neutron-irradiation would continue under HVEM electron irradiation at a rate characteristic of the initial (i.e., neutron) irradiation conditions. For example, a series of electron irradiations at different temperatures for each of several different reactor temperature conditions would yield a family of swelling rate vs. (electron irradiation) temperature curves, related by the temperature shift between HVEM and reactor swelling regimes.

This is an important concept which is essential to the interpretation of future charged-particle irradiation experiments with reactor-conditioned specimens. Since the results with aged Nimonic PE16 appear to represent the special case where the swelling rate curves are superimposed, the concept is best illustrated schematically, beginning with Figure 72. This figure shows two curves of swelling rate, R, as a function of irradiation temperature. The solid curve represents the temperature dependence of R as determined by charged-particle irradiation of virgin material; the broken curve represents the unknown temperature dependence of R for neutron-irradiated material. Establishment of the nature of the latter curve is the objective of the present series of experiments. It is assumed for the present that the curve for charged-particle irradiation can be normalized to that for neutron irradiation through intercorrelation studies such as the USP experiment[14]. The goal, then, is to discern the temperature-dependence of R for the case of neutron irradiation. For the purposes of this illustration, three neutron irradiation (reactor conditioning) temperatures (T_1, T_2, T_3) and three charged-particle irradiation temperatures (τ_1, τ_2, τ_3) will be considered, as shown in Figure 72.

If it is assumed for simplicity that the temperature shift associated with charged-particle irradiation is constant for all irradiation temperatures, then it should be possible to map the swelling rates for charged-particle irradiation onto the neutron irradiation curve as shown in Figure 73. A more complex temperature shift relationship simply requires an asymmetric mapping function. For the purposes of this illustration, it will be assumed that T_1/τ_1, T_2/τ_2 and T_3/τ_3 are equivalent effective temperatures. Since the swelling rates at T_1, T_2 and T_3 are unknown, charged-particle irradiations are performed at three temperatures for each of the reactor conditioning temperatures. The experiment then becomes in effect a temperature-change experiment, and important information is at hand to aid in the interpretation of such experiments. Simulation experiments, involving temperature changes during HVEM electron irradiation of stainless steel[15,16] provided the insight shown schematically in Figure 74. In the case of a temperature decrease, the new swelling rate is characteristic of the lower temperature, regardless of whether the change takes place before or after the attainment of steady-state (linear with dose) swelling at the original (higher) temperature. The response to a temperature increase, on the other hand, depends on the dose at which the increase takes place. When the increase comes before steady-state swelling is attained, the new swelling rate is characteristic of the higher temperature. However, when the temperature is increased after reaching steady-state swelling, the new swelling rate is unchanged from that characteristic of the original temperature.

Treating the charged-particle irradiation as a temperature-change experiment, it is possible to construct a relationship as shown in Table 19, which shows the effect of different (T, τ) combinations on the predicted R values for neutron irradiated material.

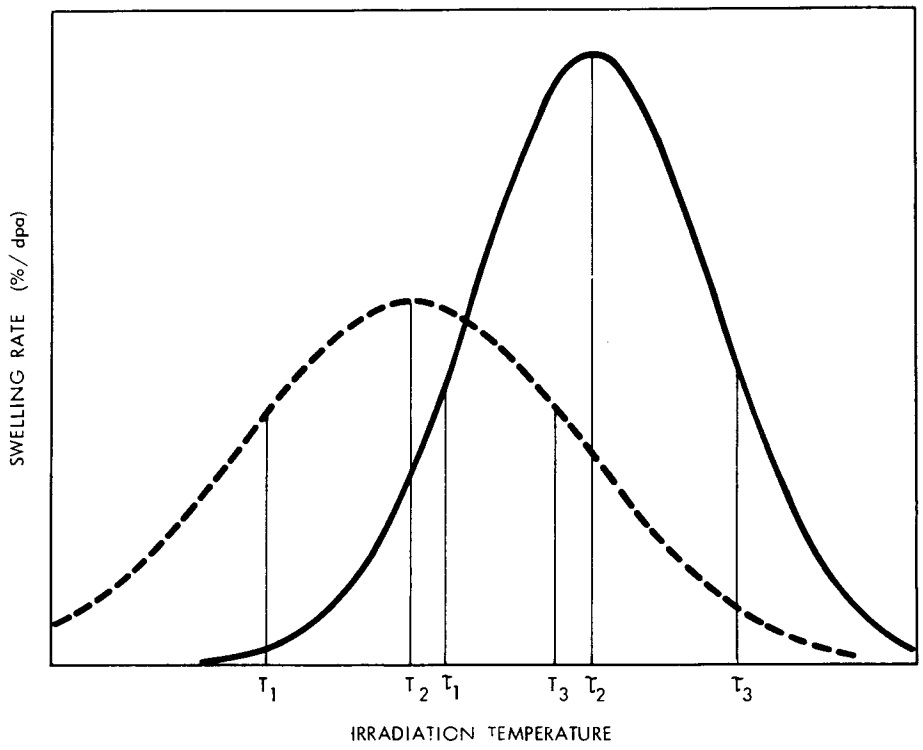

HEDL 7702-101.1

FIGURE 72. Schematic temperature-dependence of swelling rate for neutron irradiation (broken curve) and charged-particle irradiation (solid curve).

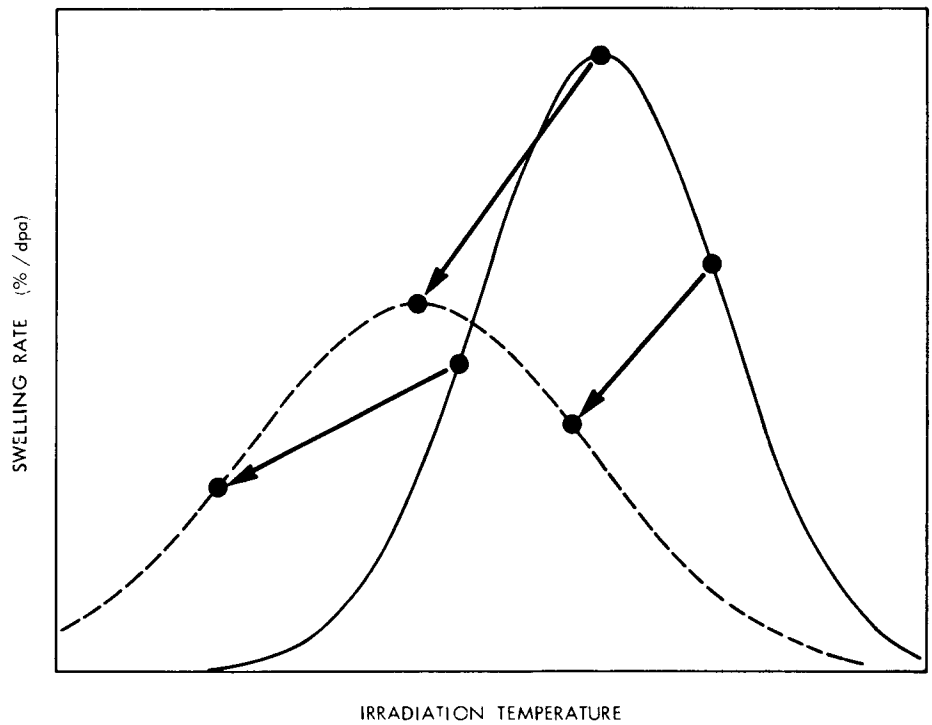

HEDL 7702-101.2

FIGURE 73. Schematic mapping of charged-particle irradiation swelling rates to those for neutron irradiation.

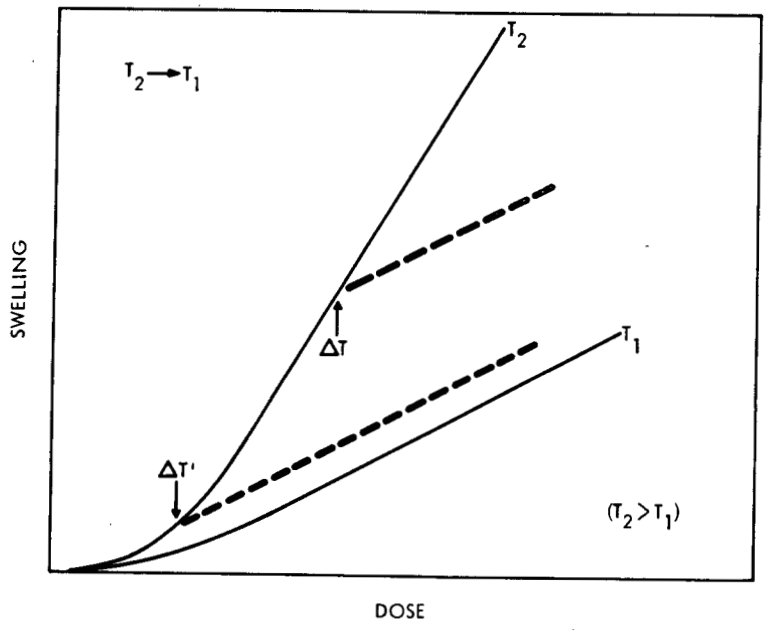

(a)

HEDL 7702-101.4

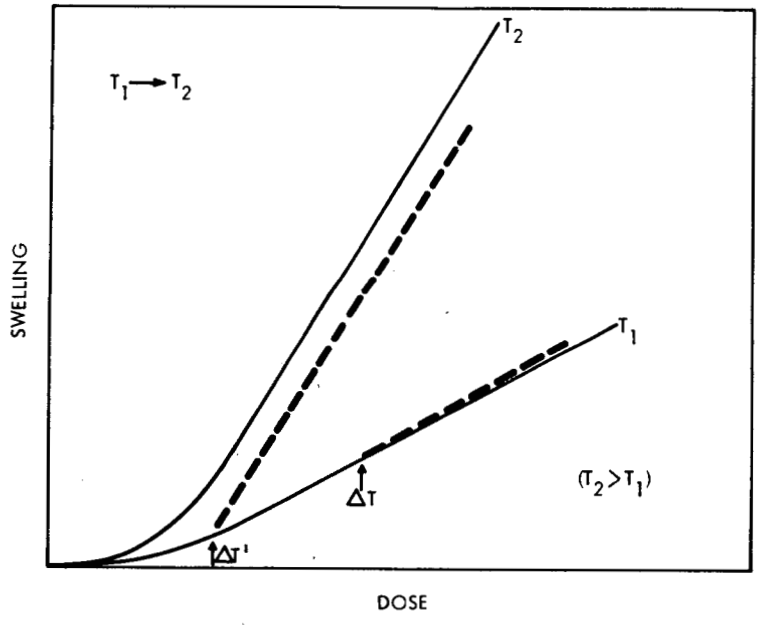

HEDL 7701-101.3

(b)

FIGURE 74. The effect on swelling of temperature changes in HVEM experiments based on the work of Makin and Walters (16): (a) for a temperature decrease, and (b) for a temperature increase, both before and after steady-state void swelling is obtained.

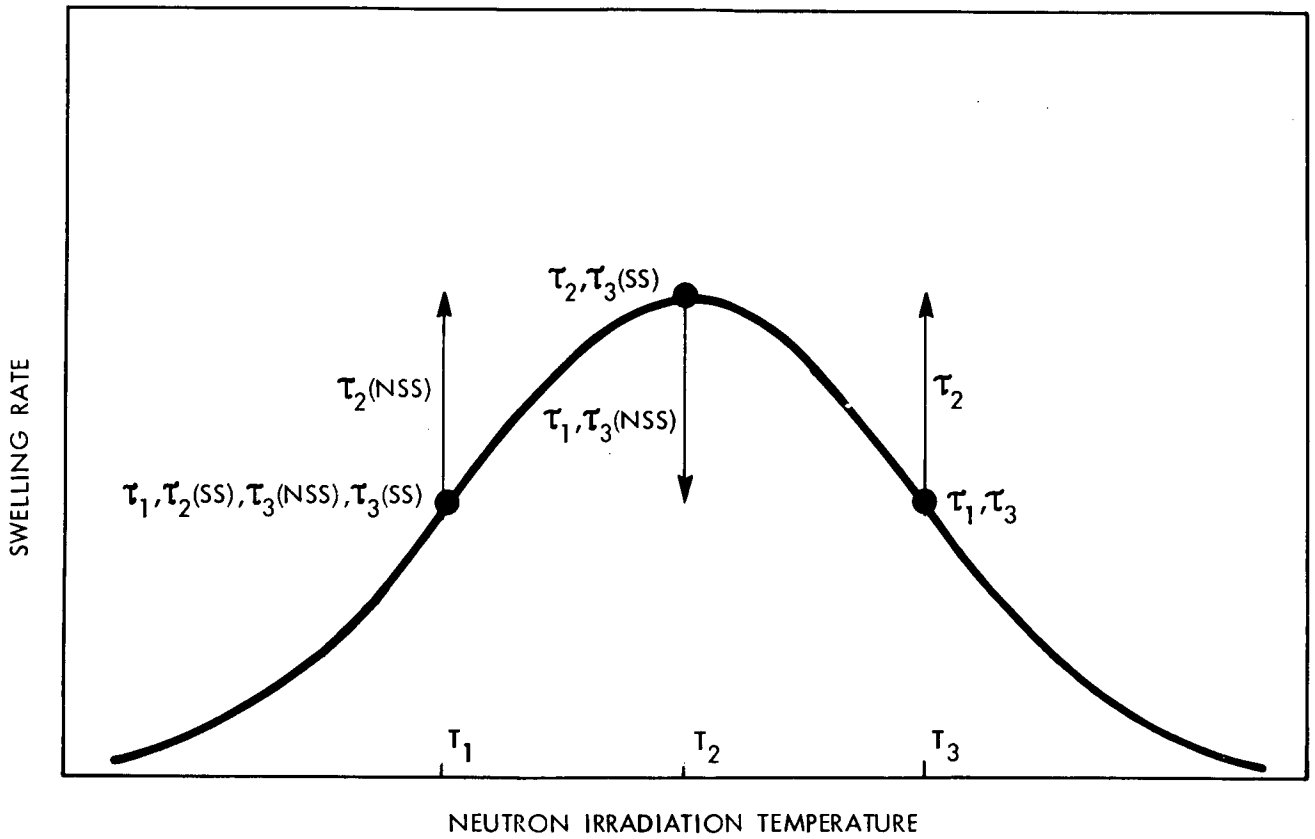

HEDL 7702-101.6

FIGURE 75. Schematic illustration of shifts in predicted swelling rate (arrows) from the true value of the neutron irradiation swelling rate, for various combinations of reactor irradiation temperature and charged-particle irradiation temperature. Refer to Figure 72.

TABLE 19

VARIATION IN PREDICTED STEADY-STATE SWELLING RATE (R) FOR VARIOUS COMBINATIONS OF NEUTRON IRRADIATION TEMPERATURE (T) AND CHARGED-PARTICLE IRRADIATION TEMPERATURE (τ)

Neutron Irradiation Temperature	Charged-Particle Irradiation Temperature	Effective Temperature Change	Results
T_1	τ_1	None	True R
T_1	τ_2	Temp. Increase	Higher R if NSS* Correct R if SS
T_1	τ_3	Temp. Increase	Probably correct R
T_2	τ_1	Temp. Decrease	Lower R
T_2	τ_2	None	True R
T_2	τ_3	Temp. Increase	Lower R if NSS Correct R if SS
T_3	τ_1	Temp. Decrease	Correct R
T_3	τ_2	Temp. Decrease	Higher R
T_3	τ_3	None	True R

* NSS: Non-steady state swelling condition
SS: Steady-state swelling condition

These effects are shown grapically in Figure 75, and it can be seen that the effect of various combinations is simply to shift R values along the R vs. T curve. Recasting the effects shown in Table 19 and Figure 75 in terms of the swelling rate which would be observed for charged-particle irradiation at various reactor conditioning temperatures yields Figure 76. Note that this figure also pertains to a situation in which the peak swelling temperature for charged-particle irradiation of preconditioned material may not be the same as that for irradiation of virgin material, due to changes in matrix composition during neutron irradiation. This would require successive iterations to locate the peak precisely. In any event, as shown in Figure 76b, the expected behavior depends on whether or not the steady-state swelling condition has been achieved during neutron irradiation.

Comparison of the predictions of Figure 76a with the results for reactor-conditioned aged Nimonic PE16 (Figure 63) reveals good agreement and suggests that steady-state swelling has not been achieved in this alloy. In the absence of data for a reactor-conditioning temperature of 510°C, it is difficult to determine the peak temperature shift; the parameters which appear to most closely approximate the T_2/τ_2 condition of the preceding schematic argument are T_2 = 593°C, τ_2 = 650°C. This amounts to a temperature shift of about 60°C. Using as "correct" those HVEM swelling rates corresponding to a ΔT of 60°C (to the extent possible) and comparing with swelling rates used for Nimonic PE16 in the TC-293[17] equation yields good agreement. This agreement is taken as verification of the technique since the TC-293 equation adequately represents[2] the observed swelling in the B-109 (AA-Ia) material used here.

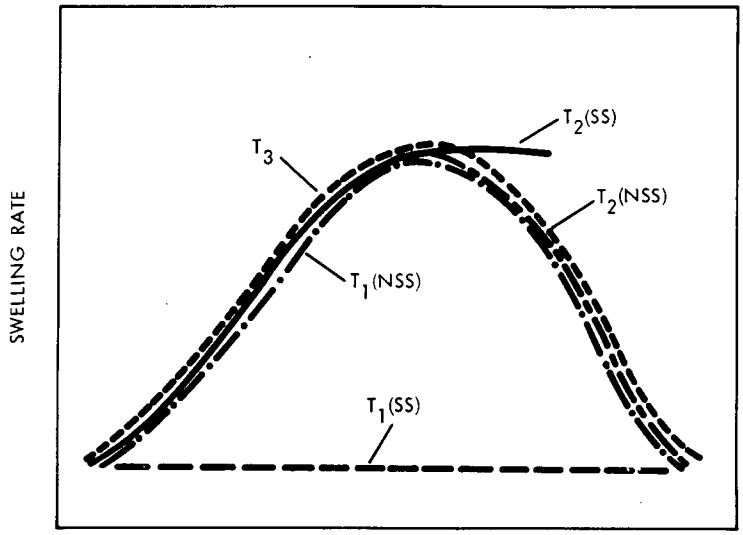

HEDL 7702-101.5

(a)

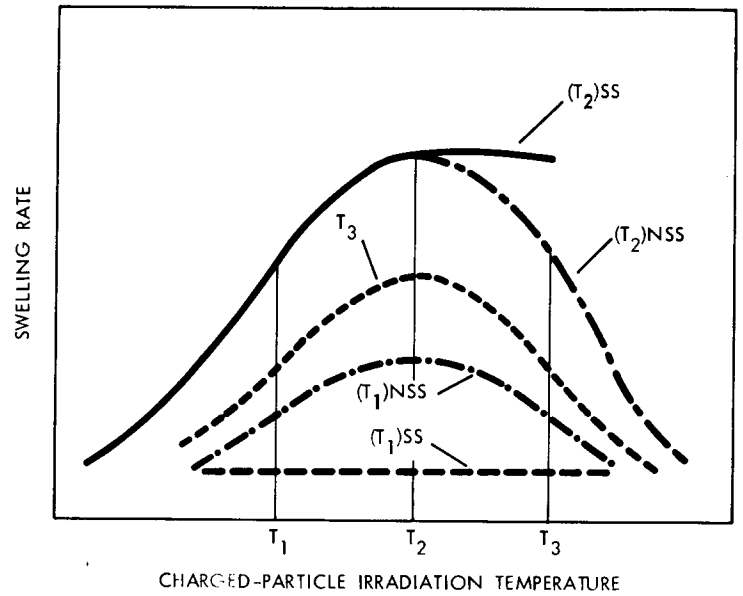

HEDL 7702-101.7

(b)

FIGURE 76. Schematic illustration of expected temperature-dependence of swelling rate for charged-particle irradiation of specimens reactor-conditioned at various temperatures: (a) insignificant microchemical segregation, and (b) reactor induced microchemical segregation.

The results for reactor-conditioned solution-treated Nimonic PE16 (Figure 64) are also consistent with the predictions of Figure 76, and indicate non-steady state swelling behavior, despite the limited data available. It is of interest to note that the peak swelling temperature is about 50°C lower in this case than for aged PE16; this may be a consequence of degree of matrix composition change.

As stated above, the aim of this discussion is to provide a framework for general interpretation of reactor-conditioning experiments. Alloys which show greater sensitivity to reactor-conditioning would be expected to provide a more conclusive test of the analysis.

3.3.4.3 Effect of Reactor-conditioning on Microstructure. A subsequent report is planned on the detailed analysis of microstructural evolution during irradiation of reactor-conditioned materials; however, several aspects of the microstructural behavior observed warrant discussion here. For example, it was found that the voids in neutron-irradiated Nimonic PE16 differed in shape from those produced in the same specimens under electron irradiation. Also, the initial void shapes in aged PE16 changed little under electron irradiation. It was further observed that electron irradiations in which only neutron-irradiation induced voids grew yielded lower swelling rates than electron irradiations which produced extensive void nucleation. These differences in void growth behavior may be caused by the γ' which precipitates at void surfaces in-reactor. While the quantities of solute involved in void coatings are too small to change alloy matrix chemistry, the possibility exists that void growth may be altered in the presence of irradiation-induced redistribution of solute.

It also appears that not all phase transformations influence swelling. Most of the γ' in A-286 transformed to η phase during irradiation in-reactor, but this irradiation-induced transformation appears to have little effect on subsequent swelling under electron irradiation. This observation may be explained by the fact that the transformation from metastable γ' to stable η involves no chemical change, to a first approximation. Second order effects on matrix chemistry may arise from solubility differences in the two phases. Nevertheless, it is tempting to speculate that neither the $\gamma' \rightarrow \eta$ transformation nor the $\gamma'' \rightarrow \delta$ transformation will influence swelling in γ' or γ'' hardened alloys.

3.3.4.4 Recommendations for Charged-particle Irradiations of Reactor-conditioned Alloys. The results obtained in these initial irradiation tests on reactor-conditioned alloys indicate that many of the alloys scheduled for further testing are likely to show the same swelling behavior with or without prior neutron irradiation. Testing of reactor-conditioned specimens is needed to identify alloys which, through neutron-irradiation induced changes in matrix chemistry, exhibit a different swelling response after reactor conditioning. The number of such tests which must be performed can be limited, however, by relying on comparison of simulation results obtained from one reactor condition, preferably the peak swelling condition identified by immersion density, with simulation results from virgin material. In cases where the results disagree or where TEM observations of specimens from different reactor conditions indicate irradiation-induced precipitation or other solute redistribution effects likely to influence swelling, additional simulation tests should be undertaken. Then in the event that reactor conditioning proves to significantly influence swelling under subsequent

8. Bates, J. F., Thomas, L. E., Borisch, R. R., Garner, F. A., and Caplinger, W. H., Alloy Development Program Quarterly Technical Progress Letter, TC-160-7 (10-12/1975), 31.

9. Diamond, S., and Chickering, R., Alloy Development Program Quarterly Technical Progress Letter, TC-160-5 (4-6/1975), 319.

10. Thomas, L. E., Alloy Development Program Quarterly Technical Progress Letter, TC-160-9 (4-6/1976), 79.

11. See several papers in CONF-710601, Proceedings of the 1971 International Conference on Radiation-Induced Voids in Metals, U.S.A.E.C., 1972.

12. Johnston, W. G., et al, Alloy Development Program Quarterly Technical Progress Letter, TC-160-5 (4-6/1975), p. 259.

13. Buswell, J. T., Fisher, S. B., Harbottle, J. E., and Norris, D. I. R., Physical Metallurgy of Reactor Fuel Elements, Proceedings of an International Conference, Berkeley, U.K., September 2-7, 1973.

14. Garner, F. A., "Design and Analysis of Intercorrelation Experiments," this report.

15. Norris, D. I. R., and Buswell, J. T., J. Nucl. Mat., 59 (1976), 316.

16. Makin, M. J., and Walters, G. P., US/UK Cladding and Structural Materials Information Exchange, November 5-7, 1975.

17. Alloy Properties Databook, TC-293 (Rev. 2), June, 1976.

4. MICROSTRUCTURAL CHANGES IN NEUTRON-IRRADIATED A-286

R. W. Powell

Hanford Engineering Development Laboratory

4.1 OBJECTIVE

The general objective of this work is to characterize the microstructural response to neutron irradiation of the candidate commercial alloys. This information will be used to assess the relative merits of each alloy as a potential cladding or duct material and to provide a basis for estimating the performance capabilities of the various alloys over the full range of service conditions.

4.2 SUMMARY

Transmission electron microscopy examination and analysis has been completed on fully-aged A-286 irradiated at five temperatures in the AA-Ia test to a peak fluence of 5.4 x 10^{22} n/cm^2 (E>0.1 MeV). Details of the void analysis indicate that the temperature dependence of the incubation fluence given in TC-293[1] is qualitatively correct while the transition to steady-state swelling is probably more gradual than predicted. The swelling behavior of aged A-286 can be described by the superposition of two swelling regimes; one at low temperatures dominated by precipitates and one at high temperatures dominated by the matrix. The alloy behavior would be significantly improved if the precipitate phase which tends to be associated with voids were eliminated.

4.3 ACCOMPLISHMENTS AND STATUS

4.3.1 Introduction

Immersion density measurements[2] on neutron irradiated A-286 have indicated high swelling at low temperatures for the solution treated and aged (STA) condition and high swelling at all temperatures for the overaged (OA) condition. The low temperature swelling casts doubts on the viability of A-286 as a candidate duct alloy, and the broad temperature dependence of swelling for the OA condition suggests potentially low performance in cladding applications. Transmission electron microscopy examination was performed to correlate the observed density changes with the various microstructural changes and gain some degree of insight as to the processes which led to the relatively high swelling observed.

4.3.2 Experimental Procedures

Cylindrical specimens, 3 mm in diameter by 1.25 cm long, were irradiated in EBR-II at eight temperatures in capsule B-109. The design temperature and fluence for each of the eight subcapsules are given in Table 20.

Following neutron irradiation, immersion density measurements were made on all specimens; the results of these measurements have been previously reported[2]. The specimens were then sliced into disks of approximately 0.3 mm thickness using a Buehler Isomet saw

equipped with nine ganged diamond blades. The disks were cleaned and deburred by electropolishing and prepared for transmission electron microscopy examination using either a Fischione or a Metalthin Electropolisher.

TABLE 20

SUBCAPSULE DESIGN CONDITIONS FOR B-109

Subcapsule ID	Temperature (°C)	Fluence (10^{22} n/cm^2, E>0.1 MeV)
M	399	3.4
L	427	4.4
E	454	3.3
F	482	4.2
K	510	5.1
G	538	5.0
J	593	5.4
H	650	5.4

Transmission electron microscopy examinations were performed using either the HVEM or the JEM 200a operated at 1000 kV and 200 kV, respectively. Void analyses were performed in specific orientations taking account of void shape to accurately define the void volume.[3]

4.3.3 Results and Discussions

4.3.3.1 Voids. Microstructural analysis was performed on A-286 specimens following neutron irradiation. Five different temperature/fluence conditions have been examined for the solution treated and aged (STA) heat treatment while one temperature/fluence condition has been examined for both the solution treated (ST) and the overaged (OA) specimens.

The variation of swelling with irradiation temperature is shown in Figure 78 for the STA specimens. Swelling determined from immersion densitometry was, in all cases, within the experimental uncertainty of the swelling determined by electron microscopy (±30%). This shows that any precipitation which occurred during irradiation did not produce a significant volume change. The lower swelling observed at 454°C is indicative of the lower fluence received by that subcapsule.

Figures 79 and 80, which describe the void density and the void size as a function of temperature, provide more information on the processes occurring at the different temperatures. The two cases in which there was a deviation from the usual temperature dependence of these parameters may be significant. Considering Figure 79, the void density in the specimen irradiated at 454°C is lower than would be expected when compared to the data at 427°C and 482°C. Therefore, it appears that the transition to steady-state swelling for A-286 at 454°C has not been completed at the fluence received by subcapsule E, 3.3 x 10^{22} n/cm^2 (E>0.1 MeV). Judging from the smooth variation of void density with temperature for the adjacent subcapsules, L (427°C), F (482°C) and K (510°C), it is likely that void nucleation is essentially over by the time the corresponding fluences are achieved, 4.4 x 10^{22} n/cm^2, 4.2 x 10^{22} n/cm^2, and 5.1 x 10^{22} n/cm^2(E>0.1 MeV), respectively. Thus, the transition to steady-state swelling for A-286 (STA) at 454°C is probably completed between 3.3 x 10^{22} n/cm^2 and 4.4 x 10^{22} n/cm^2 (E>0.1 MeV).

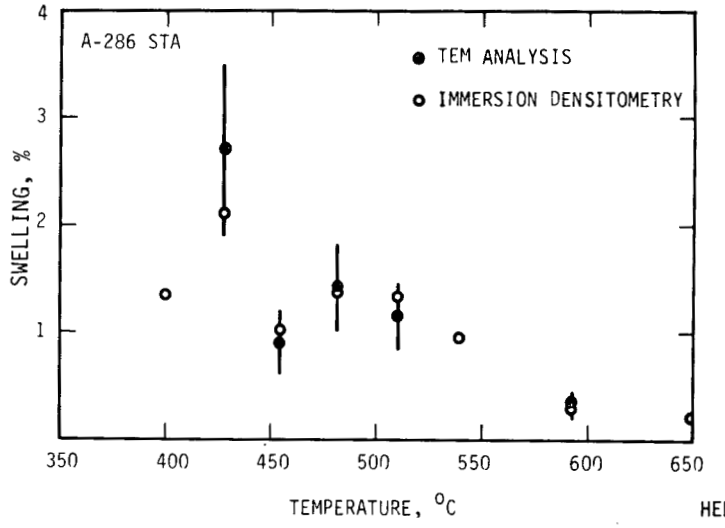

FIGURE 78. Swelling as determined from transmission electron microscopy and immersion densitometry for A-286 (STA).

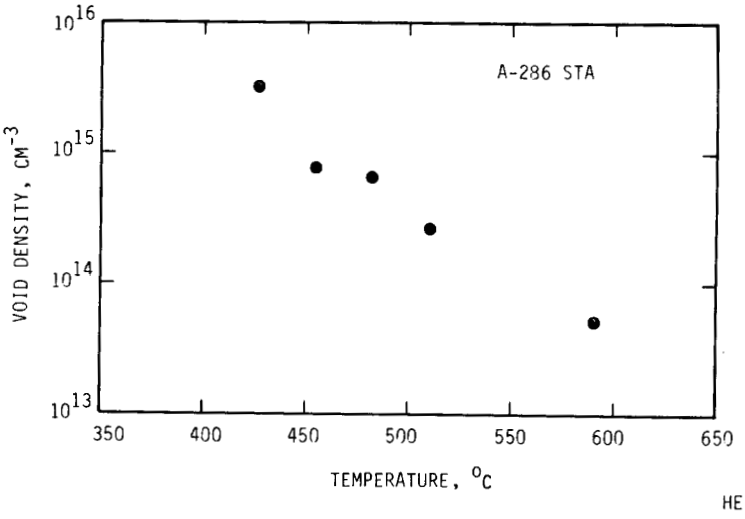

FIGURE 79. Void density as a function of temperature for A-286 (STA).

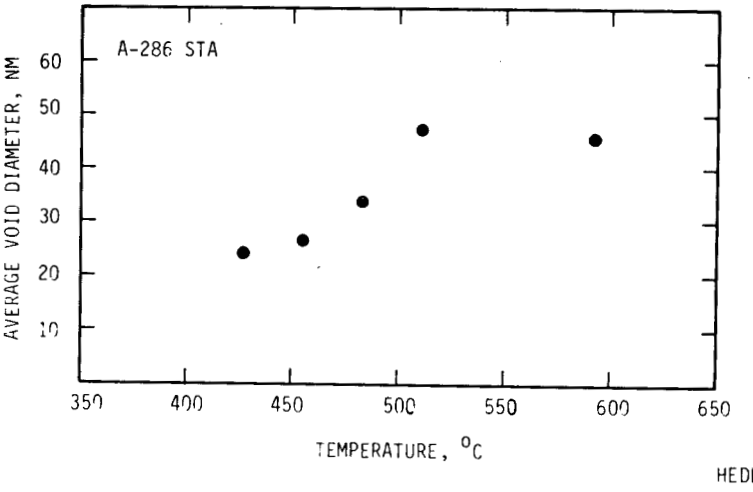

FIGURE 80. Temperature dependence of the average void size for A-286 (STA).

Further information on the projected swelling curves in A-286 (STA) can be obtained by considering Figure 80, which shows the temperature dependence of the void size. The average void size at 593°C is less than the void size at 510°C, even though the fluence is slightly higher at the higher temperature. This indicates that the incubation fluence is larger at 593°C than at 510°C. Assuming a smooth temperature dependence of the incubation fluence (τ) implies that τ increases with increasing temperature (at least above 510°C).

These observations on the form of the swelling curves for A-286 (STA) can be compared with swelling equations contained in TC-293 (Alloy Properties Databook)[1] for this material. The temperature dependence of the incubation fluence given in TC-293 is consistent with the observation made here (τ increases with T above 510°C) in that an upward concave parabola centered at 400°C is used. On the other hand, the transition from zero swelling to steady-state swelling inherent in the fluence dependent swelling equation given in the Databook is probably too short. The equation indicates that steady-state swelling would be achieved by approximately 2×10^{22} n/cm^2 (E>0.1 MeV), whereas the data given here imply that 4×10^{22} n/cm^2 (E>0.1 MeV) is a better estimate. This is not a major deviation from the equation and would require only a slight decrease in α (see Reference 1) and/or a slight increase in τ. In either case, there would be little, if any, change in the predicted swelling at high fluences.

As reported previously[2], a striking result from immersion density measurements on the three heat treatments for A-286 was the very high swelling ($\sim$2%) at high temperatures observed for the overaged specimens. Detailed microstructural analyses were performed on STA, ST and OA specimens from the J subcapsule (593°C) to provide information on the reason for this variation in swelling behavior with preirradiation heat treatment.

Table 21 describes the void populations for the STA, ST and OA specimens that were irradiated at 593°C. It is evident from the void densities and average void sizes that the reduced swelling in ST, compared to STA specimens, is due to a smaller average void size in ST material. Higher fluence data are required to determine if the difference in size is due to a difference in void growth rate, a difference in incubation fluence, or a change in the rate of achieving steady-state swelling.

TABLE 21

TEM RESULTS OF VOID ANALYSES FOR VARIOUS CONDITIONS OF A-286 FROM J SUBCAPSULE (593°C)

Parameter	Heat Treatment Condition		
	STA	ST	OA
Swelling (%)	0.35	0.18	1.6
Void Density (cm^{-3})	5.5×10^{13}	4.3×10^{13}	2.7×10^{14}
Average Void Size (nm)	46	35	46

The most significant effect of heat treatment on swelling is represented by the comparison of the STA and the OA specimens irradiated at 593°C. It is clear from Table 21 that the fivefold higher swelling in the OA specimen is due to a fivefold increase in the void number density. The void density for the OA specimen is the same as that for the STA specimen

irradiated at a 70°C lower temperature (510°C). This indicates that the overaging process produced an increased void nucleation rate during high temperature (593°C) neutron irradiation. The higher nucleation rate could be due to the production of more heterogeneous nucleation sites or a precipitation reaction producing a significantly changed matrix composition. These possible mechanisms will be examined further in the next section.

4.3.3.2 Precipitates. One of the major aspects of the microstructure of A-286 following neutron irradiation is the precipitate structure which has developed. There are a number of phases which are present in A-286 following neutron irradiation but three are the most important: γ', η and a third phase which is as yet unidentified.

The main strengthening component in superalloys such as A-286 is γ', an ordered fcc precipitate, and its response to neutron irradiation is, therefore, important. A characteristic feature of A-286 following neutron irradiation is the low intensity of γ' superlattice spots in the electron diffraction patterns. This indicates that the volume fraction of γ' was reduced during irradiation. Dark field micrographs using the γ' superlattice reflections did not have sufficient contrast for publishing due to the low intensity of the superlattice spots, but qualitative features of the γ' structure can be determined from the negatives and indicate a similarity with Nimonic PE16 reported previously by Gelles[4]. There is evidence that a small amount of γ' coated voids, while other features suggest that γ' precipitated at spiral dislocations. The extent to which these processes occurred is less than is found in Nimonic PE16.

The reason for the reduced volume fraction of γ' following neutron irradiation may be the formation of η (γ' transforms to η). This phase is hexagonal close packed and forms semicoherently with the matrix with its basal plane parallel to the {111} matrix planes. Thin platelets of η are very similar in appearance to extrinsic faulted loops, which also form on {111} planes with a Burgers vector perpendicular to the plane of the loop. Since the strain in the matrix is qualitatively the same for a faulted loop and a thin η platelet, distinguishing between these two entities depends on the thickness of the precipitate and its corresponding ability to produce crystallite shape effects (i.e., a characteristic associated with the precipitate rather than the matrix). In the general case it is possible to identify η platelets (if they are large enough), but impossible to state conclusively, solely from electron diffraction information, that η is not present when extrinsic faulted loops are observed.

Neutron irradiation produced a relatively high density of fringed (under appropriate electron-optical imaging conditions) planar defects in all the A-286 STA specimens examined. Examples of these are shown in Figure 81 for a specimen irradiated at 593°C. Similar structures were observed at lower irradiation temperatures, with the average size of the defect decreasing with decreasing temperature. Solution treated A-286 irradiated at 593°C developed the same type of planar features, as illustrated in Figure 82. A selected area diffraction pattern taken at the [110] zone axis is also shown in Figure 82 for the ST specimen. The presence of streaks along <111> directions indicates the presence of thin strain-free disks on {111} planes or planar defects producing a strain in <111> directions (or any combination of the two). The presence of streaks through the matrix spot would normally indicate the presence of small strain-free disks, but in this case the multiple

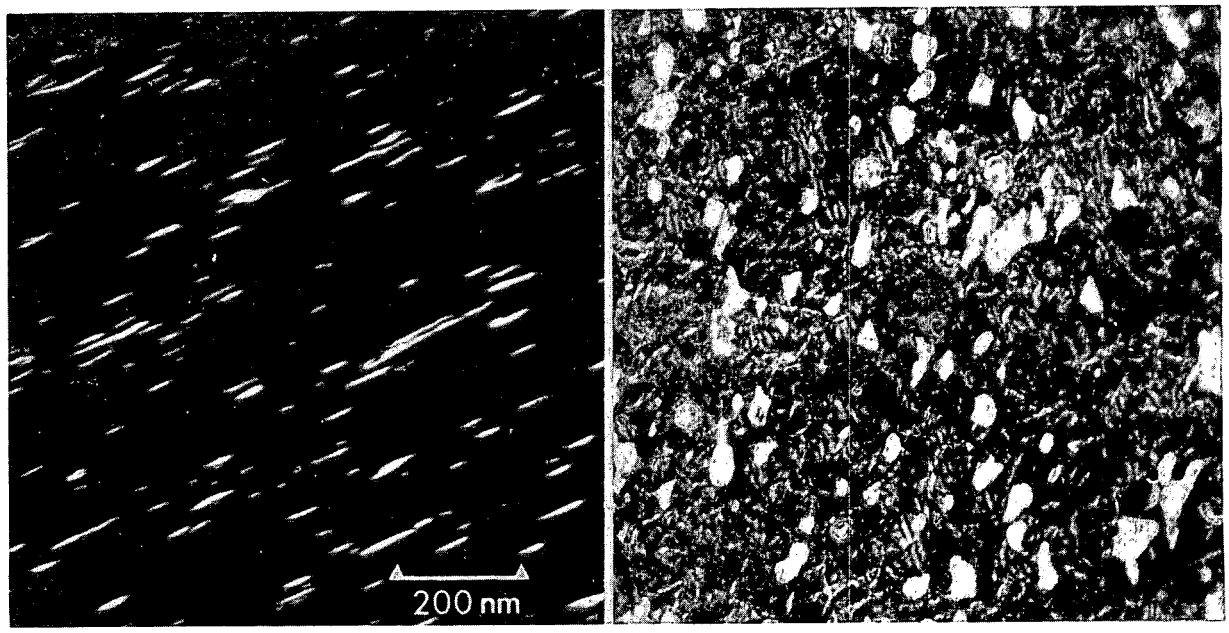

FIGURE 81. Dark field micrographs illustrating high density of fringed planar defects in A-286 (STA) after irradiation to 5.4 x 10^{22} n/cm^2 (E>0.1 MeV) at 593°C. In (a) the defects are nearly parallel to the beam while in (b) they are less inclined.

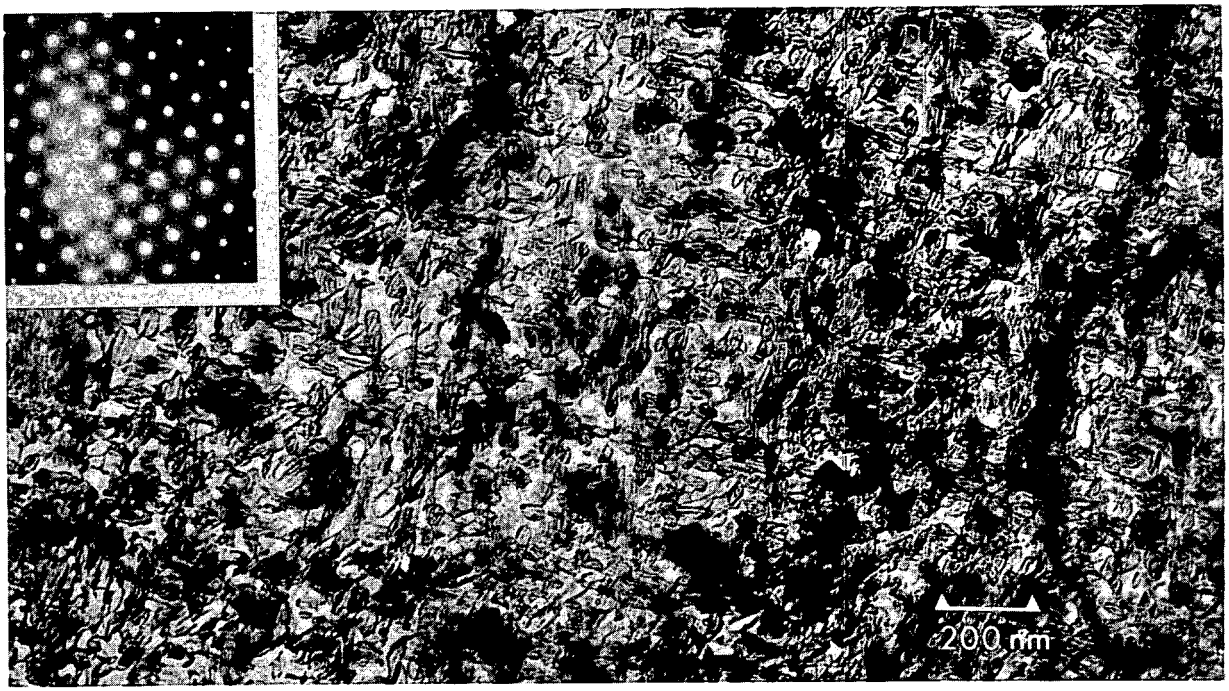

FIGURE 82. Bright field HVEM micrograph showing high density of planar defects in A-286 (ST) after irradiation at 593°C. A (110) diffraction pattern is inset to illustrate the relrods.

diffraction which is occurring would produce the same effect. As is evident from the length of the streaks and the fact that there are no intensity maxima along them, the corresponding planar defect is very thin. This is exactly the case mentioned above in which it is not possible to distinguish between Frank loops and η from electron diffraction effects alone.

Other aspects of the structure indicate that the planar defects in Figures 81 and 82 are thin platelets of η rather than faulted loops. The first indication is the high density of planar features at the irradiation temperature of 593°C. Very rarely are Frank loops observed in 316 stainless steel irradiated at this temperature[5]; the occurrence of Frank loops is also infrequent in a Nimonic PE16 specimen irradiated in the same subcapsule as A-286[4]. Another indication that these are η platelets rather than faulted loops is the appearance of the fringes in Figure 81(b). The wavy character of the fringes associated with the defects indicates that either the specimen surface is very uneven or the defect is actually a platelet of varying thickness or orientation. Since it is unlikely that the specimen surface is wavy on such a fine scale, the observed appearance of the fringes is believed to be due to a precipitate with small variations in thickness. Considering all these factors, it is felt that thin platelets of η have formed extensively at all temperatures in A-286 (STA) and this transformation is responsible for the decreased volume fraction of γ' present after irradiation.

The third major feature of the precipitate structure of irradiated A-286 is the presence of unidentified precipitates which are associated with many of the voids. Figures 83 and 84 show these precipitates for a low temperature irradiation (427°C) and a high temperature irradiation (593°C), respectively. The apparent association between the precipitates and the voids has been verified by stereomicroscopy. It should be noted that the precipitates are incoherent with the matrix and therefore not all the precipitates are visible in any given orientation. It is obvious from comparing the two micrographs that the precipitate density decreases with increasing temperature (Figure 84 is a thicker foil than Figure 83) in much the same way that the void density varies.

These precipitates were not present before irradiation in any of the A-286 heat treatment conditions included in the AA-Ia test[6]. It is apparent that the precipitates formed during irradiation and the precipitation process (i.e., density) was dependent on the irradiation temperature.

A similar precipitate/void association has been observed during electron irradiation of 316 and is reported elsewhere in this Progress Letter[7]. In the case referred to, the void was observed to grow at a significantly higher rate than nearby voids. It is asserted that if such an association occurs extensively, a high steady-state swelling rate would result. This appears to be the case for A-286 (STA) and may explain various aspects of the swelling behavior of this alloy.

The observation that the precipitate density varies with temperature and that precipitate-void association can lead to large void growth rates have impact on understanding the swelling behavior of A-286 (STA). This alloy exhibits a low temperature swelling peak which is both higher in magnitude and substantially lower in temperature than for similar candidate alloys M-813 and Nimonic PE16[8]. This behavior is believed to be controlled by the irradiation-induced precipitates which are associated with voids. The temperature

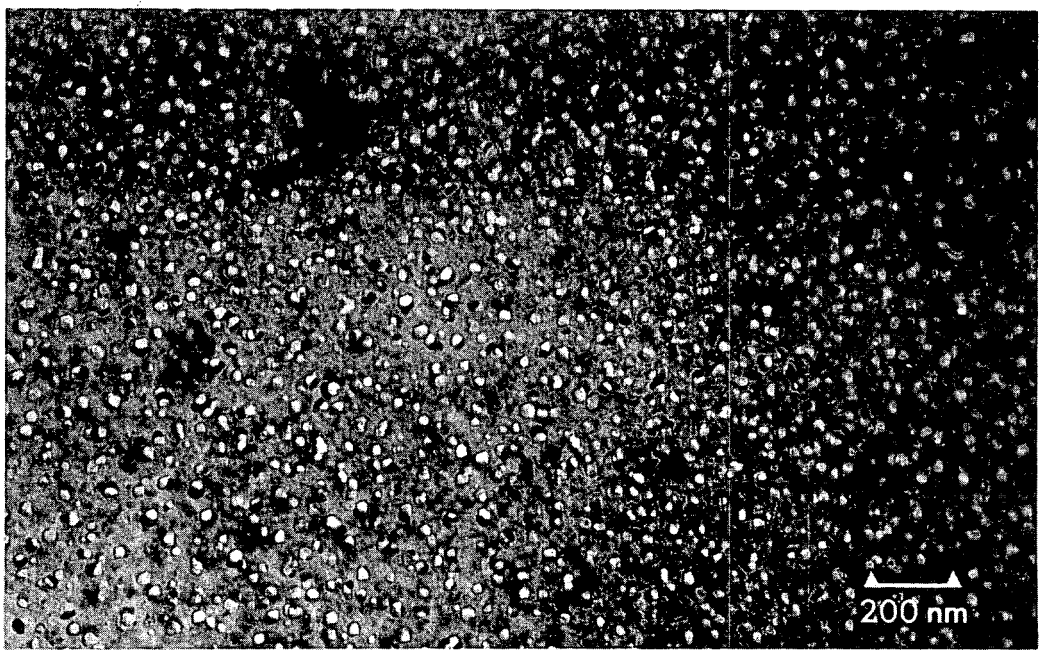

FIGURE 83. Void-precipitate association in fully-aged A-286 after irradiation at 427°C.

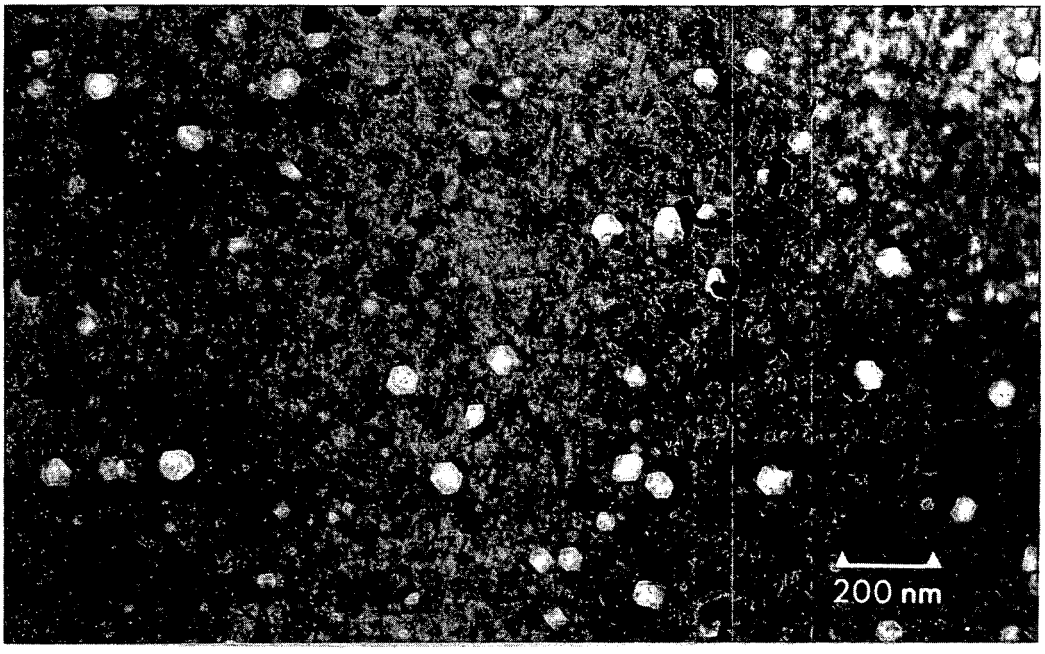

FIGURE 84. Void-precipitate association in fully-aged A-286 after irradiation at 593°C.

dependence of swelling is governed by the temperature dependence of the precipitate concentration, which leads to the low temperature swelling peak. At the low temperature (427°C) a large majority of the voids are associated with the precipitates; this leads to a high steady-state swelling rate as well as a reduced incubation fluence. At higher temperatures, where the precipitate density is low, the swelling is also low and much more comparable to M-813 and Nimonic PE16.

Similar reasoning can be applied to the similarities and differences in the swelling behavior of the STA and OA conditions of A-286. Figure 85 describes the immersion density results for these two pre-irradiation heat treatments. Both materials exhibit identical swelling at the lowest temperatures but the OA specimens showed much larger swelling

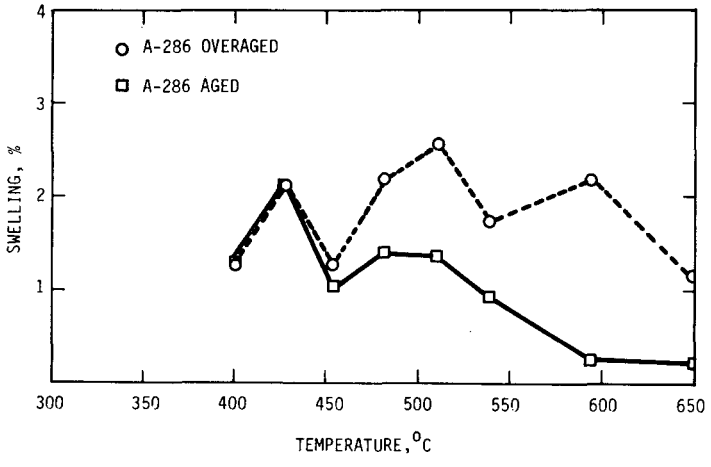

FIGURE 85. Swelling as determined by immersion densitometry for A-286 (STA) and A-286 (OA).

at the higher temperatures. As was stated in Section 4.3.3.1, the higher swelling in the overaged specimens was due to a fivefold increase in the void number density. Microstructural analysis of specimens irradiated at 593°C indicated that, for the STA and OA heat treatment conditions, there was no significant difference in the concentration of precipitates attached to voids. Pre-irradiation characterization of the overaged specimens showed that a significant amount of cellular η (Ni_3Ti) formed during the overaging process[6]. The final treatment for this condition was 500 hours at 760°C, which is expected to transform some of the existing γ' to η. Since the solvus temperature is higher for η than for γ', the extended time at temperature would result in additional precipitation of η from the matrix. This would lead to a decrease in the Ni and Ti content of the matrix, which could account for the higher swelling observed in the OA condition at the higher temperatures. The identical swelling at lower temperatures is probably due to the controlling influence of the precipitates attached to the voids. This is depicted in Figure 86 where the composite swelling curve of overaged A-286 is shown schematically as being composed of a high temperature swelling peak related to the matrix composition and a low temperature peak related to the precipitate effects. The STA A-286 composite swelling curve is shown in Figure 87 and differs from the OA condition response only in the lower magnitude of the "compositional swelling curve". If this interpretation is correct, the swelling resistance of alloys in this general class could be greatly improved by modifying the alloy composition to eliminate the formation of the precipitates which associate with voids. This would leave only the "compositional swelling curve" which is likely to be acceptably low.

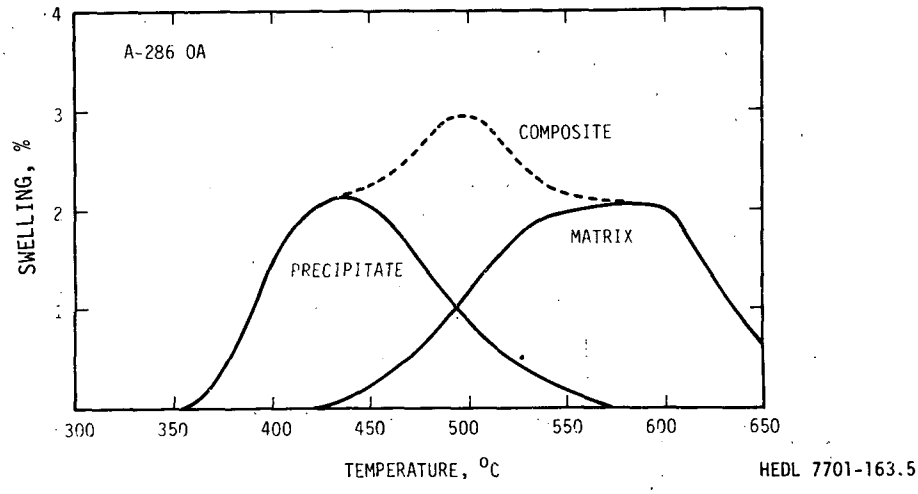

FIGURE 86. Schematic swelling behavior of A-286 (OA) illustrating two swelling curves which contribute to the total observed swelling.

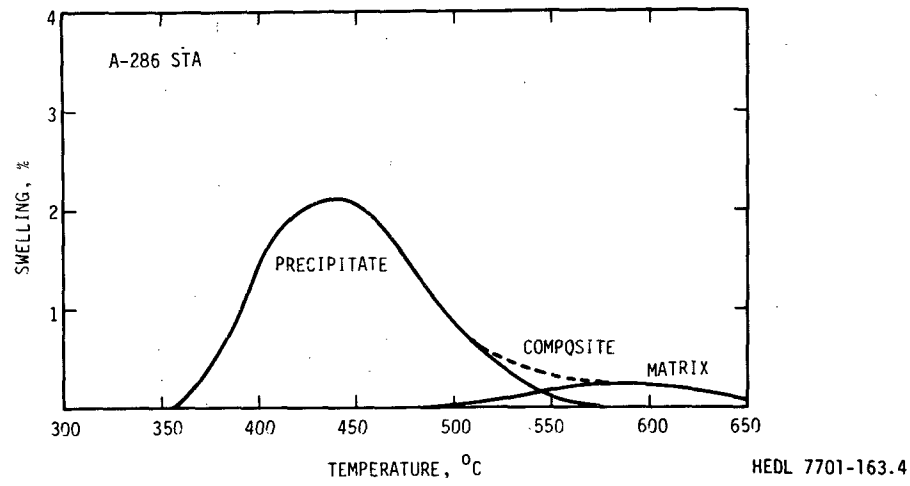

FIGURE 87. Schematic swelling behavior of A-286 (STA).

If the precipitate-related swelling peak is to be eliminated, it is first necessary to identify the precipitates in question. Figure 88 shows a bright field micrograph illustrating the voids and associated precipitates along with three dark field micrographs showing only the precipitates. Inset in each micrograph is the corresponding selected area diffraction pattern identifying the precipitate spot used to produce the dark field image of the appropriate precipitates. This gives three d_{hkl} spacings for the precipitate under study which can be compared with d_{hkl} spacings of known phases to aid in the identification of the precipitates. This portion of the work is still in progress and will be supplemented with data from energy-dispersive x-ray analysis using the scanning transmission electron microscope.

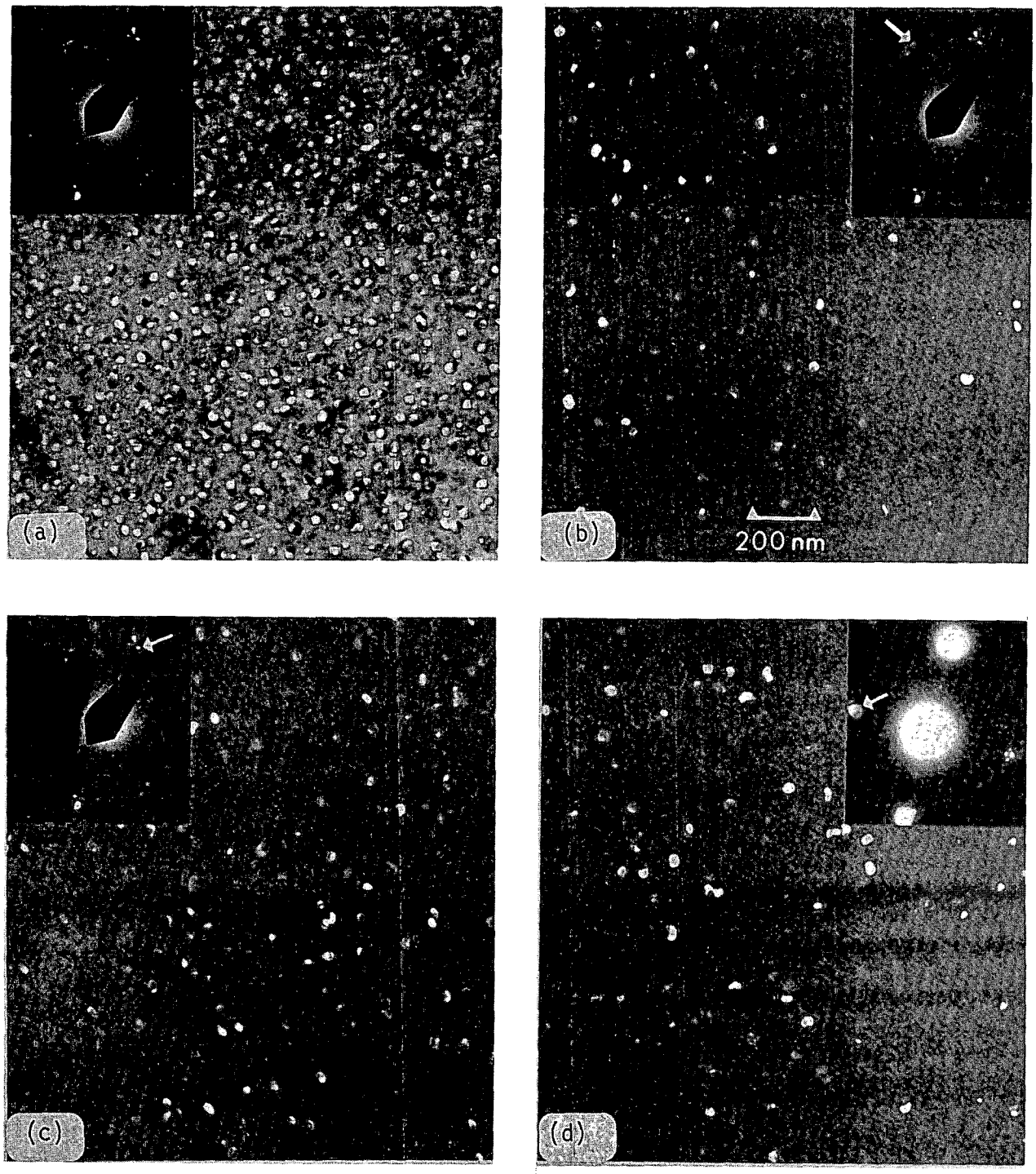

FIGURE 88. Set of micrographs illustrating the precipitates which are associated with voids in fully aged A-286 after neutron irradiation at 427°C: (a) bright field micrograph, and (b), (c) and (d) are corresponding dark field micrographs using the precipitate reflections shown in the inset diffraction patterns.

4.3.4 Conclusions

Microstructural analysis of the voids and precipitates which formed in A-286 during neutron irradiation in the AA-Ia test has led to the following conclusions:

1. The transition to steady-state swelling in A-286 (STA) at 450°C is completed between 3.3 x 10^{22} n/cm^2 (E>0.1 MeV) and 4.4 x 10^{22} n/cm^2 (E>0.1 MeV).

2. The incubation fluence for A-286 (STA) increases with increasing temperature above 510°C.

3. The larger swelling observed at high temperatures for the overaged A-286 compared to the fully-aged A-286 is probably due to a reduction of Ni and Ti in the matrix resulting from the precipitation of cellular η phase during the overaging process.

4. Gamma prime in A-286 precipitates at void surfaces and dislocations during neutron irradiation but to a lesser extent than has been observed for Nimonic PE16.

5. A significant amount of gamma prime is lost during irradiation and this is probably due to the formation of thin platelets of eta phase.

6. The low temperature swelling of A-286 in all heat treatment conditions is due to a temperature dependent precipitation of an unidentified phase which enhances void growth.

7. The swelling behavior of A-286 can be described by a low temperature swelling curve related to precipitate effects and a high temperature swelling curve related to the matrix composition.

8. The swelling resistance of alloys in the A-286 composition range can be greatly increased by eliminating the instability which causes the precipitation of the phase associated with the voids.

4.4 EXPECTED ACHIEVEMENTS IN THE NEXT REPORTING PERIOD

This work on the A-286 irradiated in the B-109 capsule will be completed following the identification of the precipitates associated with the voids.

5.5 REFERENCES

1. Alloy Properties Databook, TC-293, Rev. 2, June 30, 1976.

2. Borisch, R. R., and Powell, R. W., Alloy Development Program Quarterly Technical Progress Letter, TC-160-9 (4-6/1976), 7.

3. Thomas, L. E., Annual Information Meeting, National Alloy Development Program, October 20, 1976, TC-721, p. 544.

4. Gelles, D. S., Alloy Development Program Quarterly Technical Progress Letter, TC-160-10 (7-9/1976).

5. Brager, H. R., private communication.

6. Bates, J. F., Cummings, W. V., Gelles, D. S., Mastel, B., Alloy Development Program Quarterly Technical Progress Letter, TC-160-1 (4-6/1974), 13.

7. Powell, R. W., Alloy Development Program Quarterly Technical Progress Letter, TC-160-11.

8. Cummings, W. V., and Korenko, M. K., Alloy Development Program Quarterly Technical Progress Letter, TC-160-11.

5. VOID SWELLING IN Ni-ION IRRADIATED A-286

R. Bajaj and S. Diamond

Westinghouse Advanced Reactors Division

5.1 OBJECTIVE

The objective of this work is to determine the Ni-ion induced void swelling in A-286 and to compare it to similar γ' precipitation hardened experimental and developmental alloys.

5.2 SUMMARY

Nickel-ion induced swelling of commercial alloy A-286 (STA) was investigated. A swelling rate of 0.042%/dpa was obtained at the peak swelling temperature of 550°C with a very low incubation dose of 5 dpa. Based upon the results of these Ni-ion irradiations, combined with available neutron and electron irradiation data, the peak swelling of A-286 at 3×10^{23} nvt is 13% $\Delta V/V$. Radiation induced precipitates analyzed by electron diffraction analysis were found to be G-phase associated with voids and possibly η phase. The swelling in Ni-ion irradiated A-286 is in good agreement with that observed in neutron irradiated material assuming a dose equivalence of 100 dpa $\equiv 1 \times 10^{23}$ n/cm^2. The observed swelling is comparable with electron irradiation, however, the incubation doses are in disagreement. A comparison of heavy ion induced swelling in A-286 with experimental alloy E48 and developmental alloys D21 and D25 shows that Al additions increase the incubation dose and Cr reductions decrease the swelling rate in the FE-Ni-Cr γ'-strengthened alloys.

5.3 ACCOMPLISHMENTS AND STATUS

5.3.1 Introduction

Alloy A-286 (heat #651644) [the same heat as contained in the AA-Ia (B-109) test] obtained in the form of 3.2 cm diameter bar was sliced to about 0.75 mm thickness and given the commercial heat treatment (solution treated at 980°C for one hour and aged at 720°C for 16 hours). Specimens for nickel ion bombardment were prepared and helium injected using the standard techniques described in Reference 1. The specimens were then Ni-ion irradiated at 550°C (peak swelling temperature, see Reference 2) to a peak displacement dose of $\sim$220 dpa. These materials were irradiated in the same holder along with other developmental alloys.

One of the specimens was back thinned to the surface and examined by TEM. Figure 89 shows voids in the "near-ion-entry surface" region with a displacement dose of $\sim$83 dpa. A swelling of 3% was calculated in this region. The specimen was then sectioned by ion milling using a calibrated milling rate of 36.5 nm/min. to remove about 250 nm. Prior to ion-milling, Cu was deposited on the back side of the specimen for mechanical support and heat conduction. After ion milling, the sample was dipped in 15% HNO_3 solution to remove the Cu from the back surface. Figure 90 shows a stereo montage of voids in the specimen sectioned to 250 nm. The bottom micrograph shows large voids which are due to dissolution (or removal by gas evolution) of precipitates from the voids; however, the other micrographs taken from thicker sections do

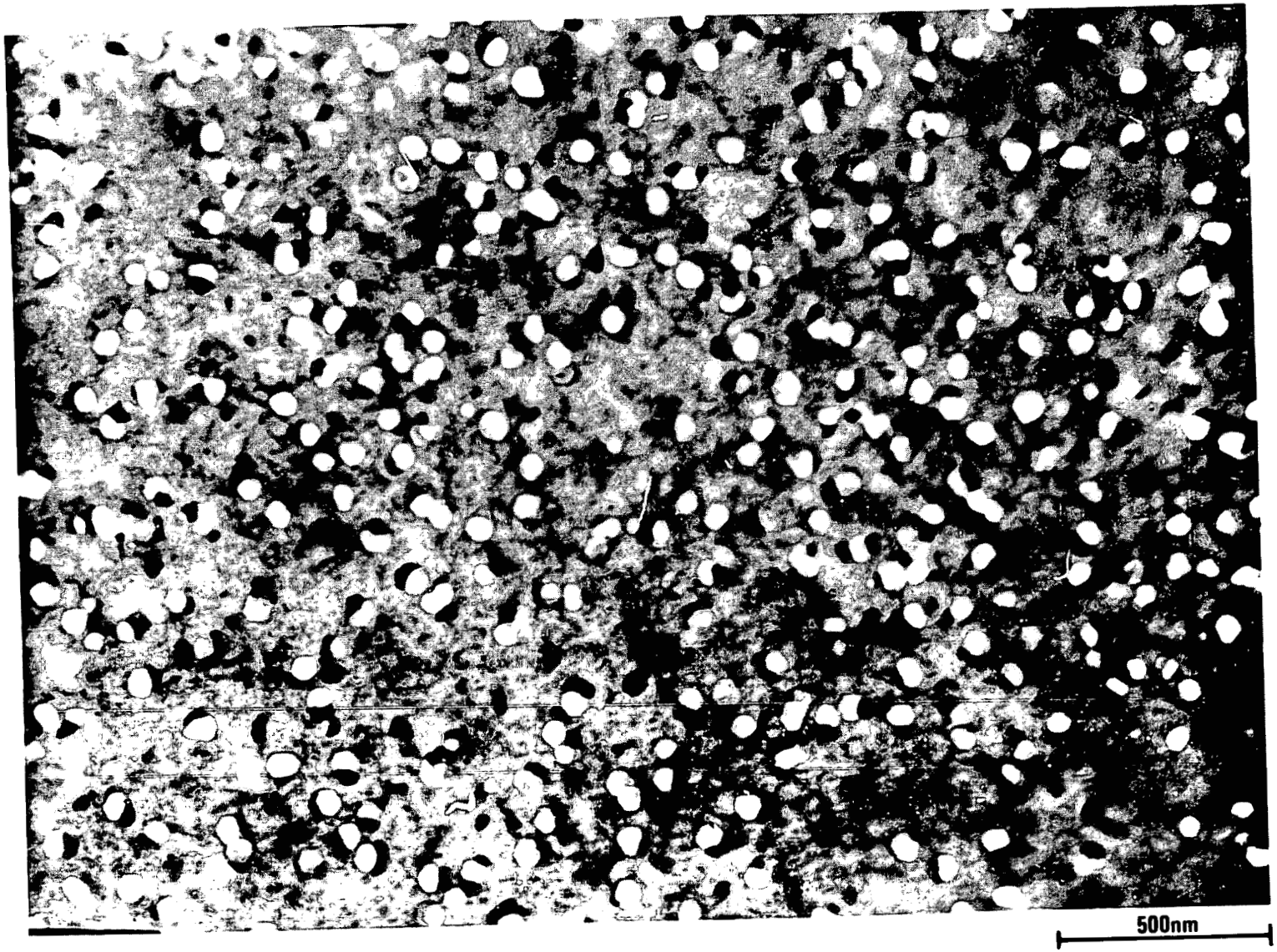

FIGURE 89. Voids in near ion entry surface region (~83 dpa) in A-286 STA irradiated at 550°C.

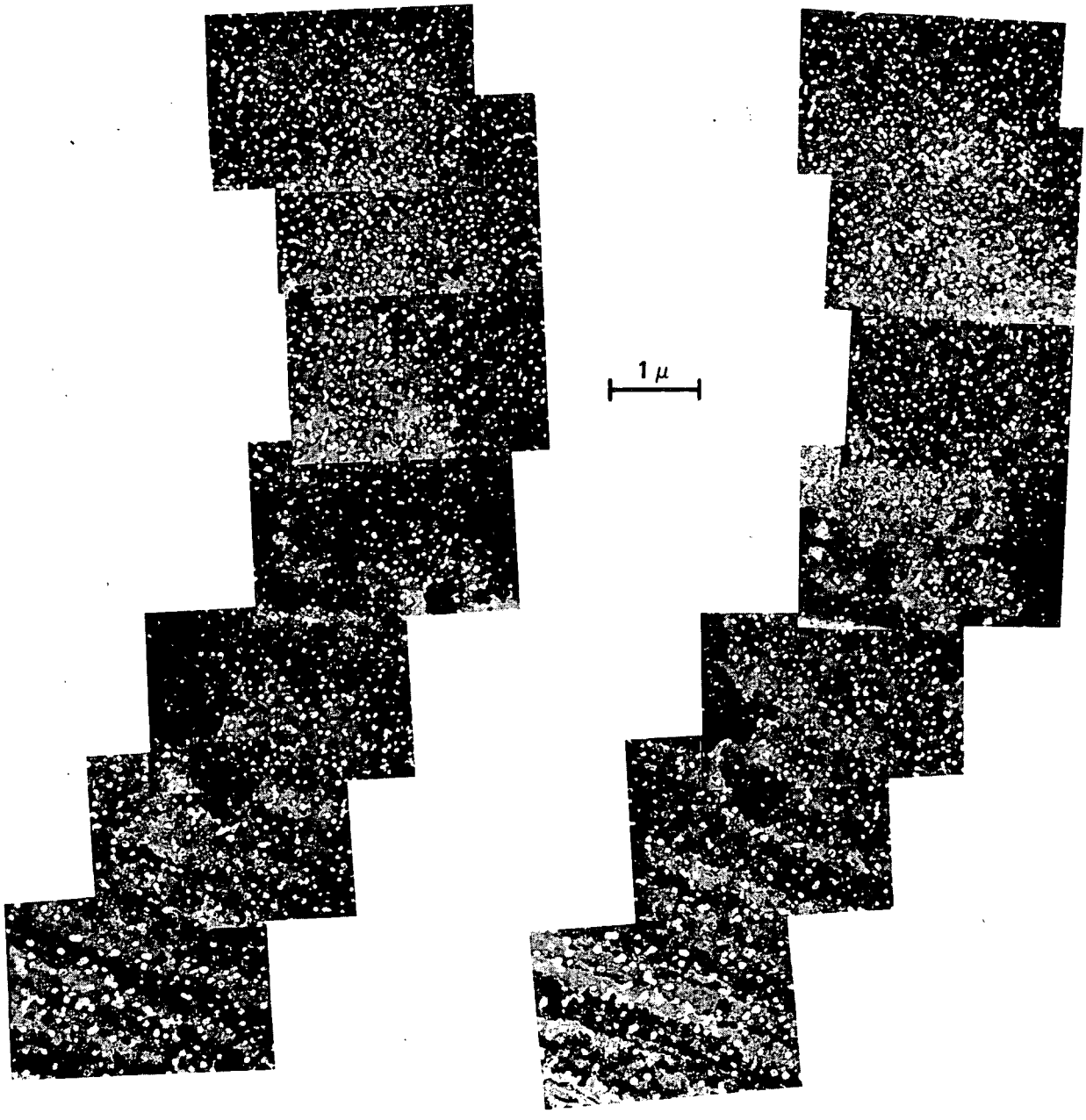

9427-17

FIGURE 90. Stereo montage of voids in irradiated A-286 STA foil sectioned 250 nm from ion entry surface.

show precipitates attached to the voids. The swelling measurements were taken from micrographs #3 and #5 (from bottom) and were calculated as 4.8% and 5.4% at 128 dpa and 132 dpa respectively. No measurements were taken from micrograph #7 because of the loss of resolution due to dislocation contrast in the thick section.

In order to determine the swelling at the highest displacement damage, a second specimen was sectioned to the peak damage region by removing 520 nm. TEM examination on this foil showed 9% swelling. Figure 91 shows a void contrast micrograph in the specimen sectioned to include the peak damage region. Figure 92 shows a high magnification micrograph in dislocation contrast, and Figure 93 shows a typical grain boundary where no significant difference in void distribution was observed. Table 22 summarizes the void swelling parameters for A-286.

Figure 94 shows a swelling versus dose plot for A-286 using a least squares fit of the data. Parameters were derived for A-286 for the swelling equations.

$$(\Delta V/V_o)_o = 0, \quad \phi < \tau$$

$$(\Delta V/V_o)_o = R(\phi-\tau), \quad \phi > \tau$$

where

$(\Delta V/V_o)_o$ = stress free swelling, %

R = steady state swelling rate, %/dpa

ϕ = displacement dose (Ni-ions) in dpa

τ = incubation dose in dpa

$R = A \exp [-b (T-T_p)^2]$

$\tau = \tau_o + P(T-T_o)^2$

where

T_p = peak swelling temperature

A, b, P = constants

τ_o = incubation doses at T_o

T = temperature in °C

τ = 5 dpa

A = 0.042%/dpa

T_p = 550°C

$b = 2.9 \times 10^{-4}$

$P = 4 \times 10^{-4}$

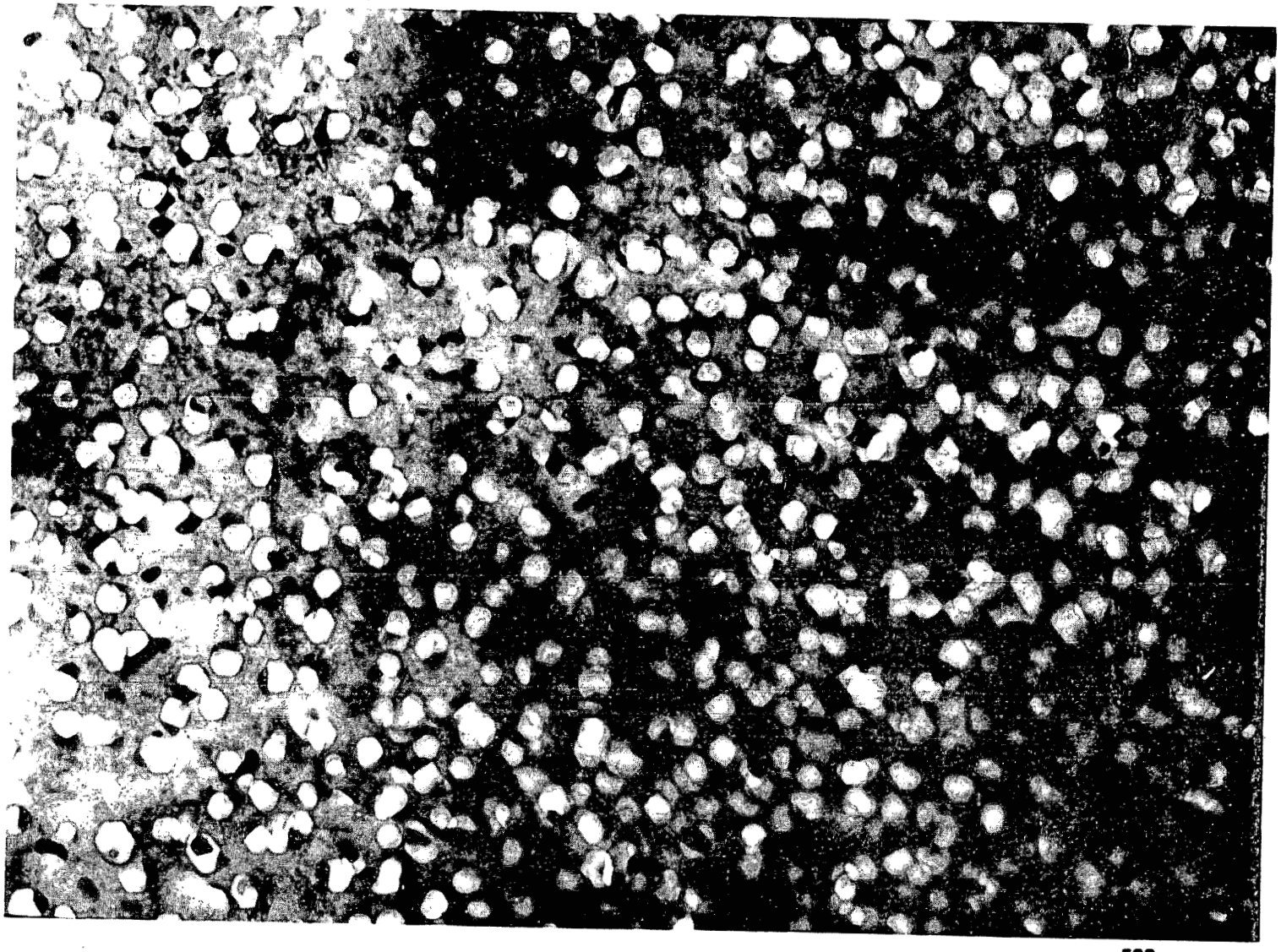

FIGURE 91. Voids in peak displacement damage region (average dose ∿200 dpa) in A-286 STA irradiated at 550°C.

FIGURE 92. Dislocation in A-286 STA irradiated at 550°C in peak displacement damage region (average dose ∿200 dpa).

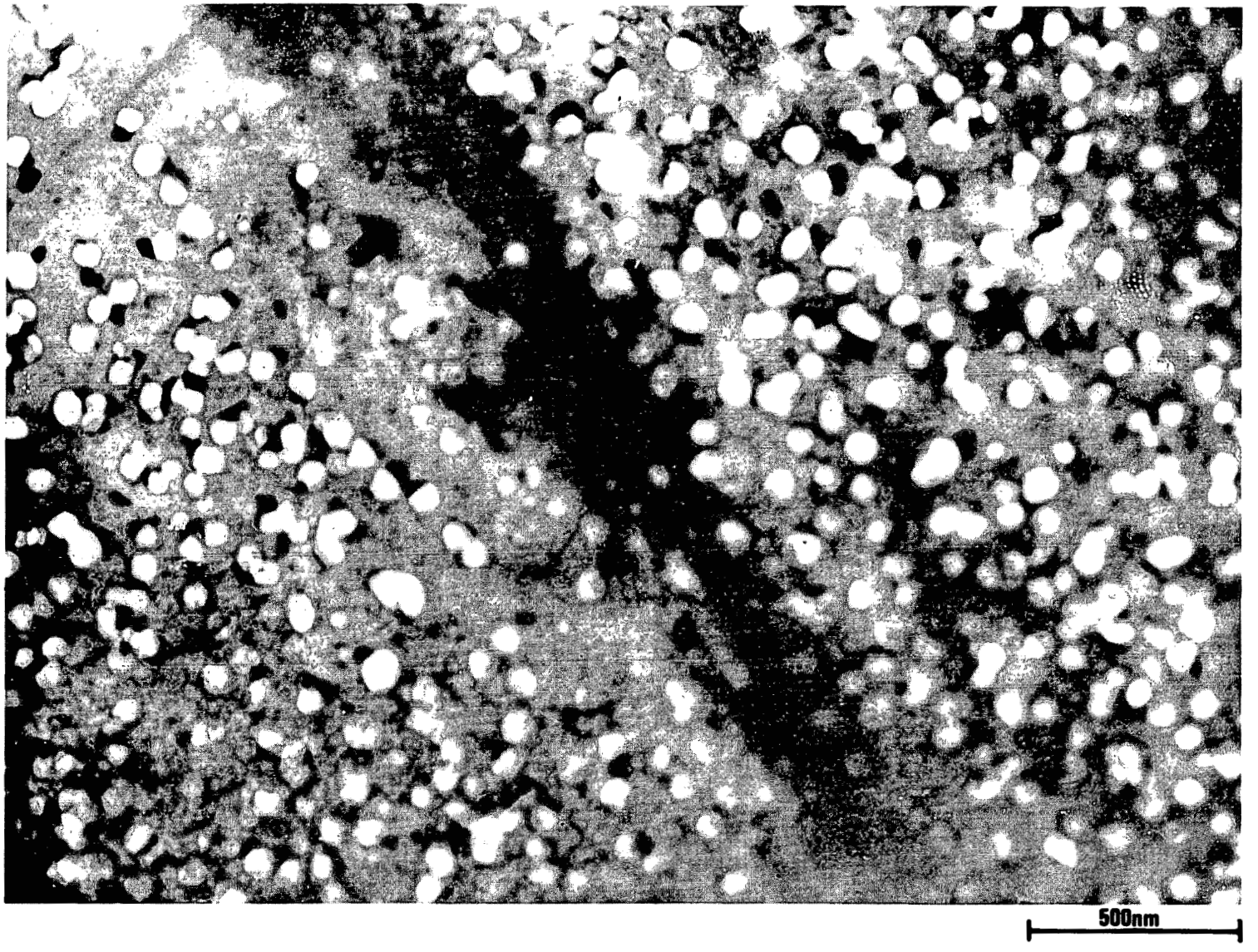

FIGURE 93. Grain boundary in A-286 STA irradiated at 550°C sectioned to peak displacement damage (average dose ∿200 dpa)

TABLE 22

SWELLING PARAMETERS IN Ni-ION IRRADIATED A-286 AT 550°C

Dose (dpa)	Average Void Size (nm)	Void Density (#/cm^3)	Swelling ($\Delta V/V_o$) %
83	52.4	2.76×10^{14}	3.1
128	56.0	4.34×10^{14}	4.8
132	53.5	5.7×10^{14}	5.4
200	60.7	6.32×10^{14}	9.0

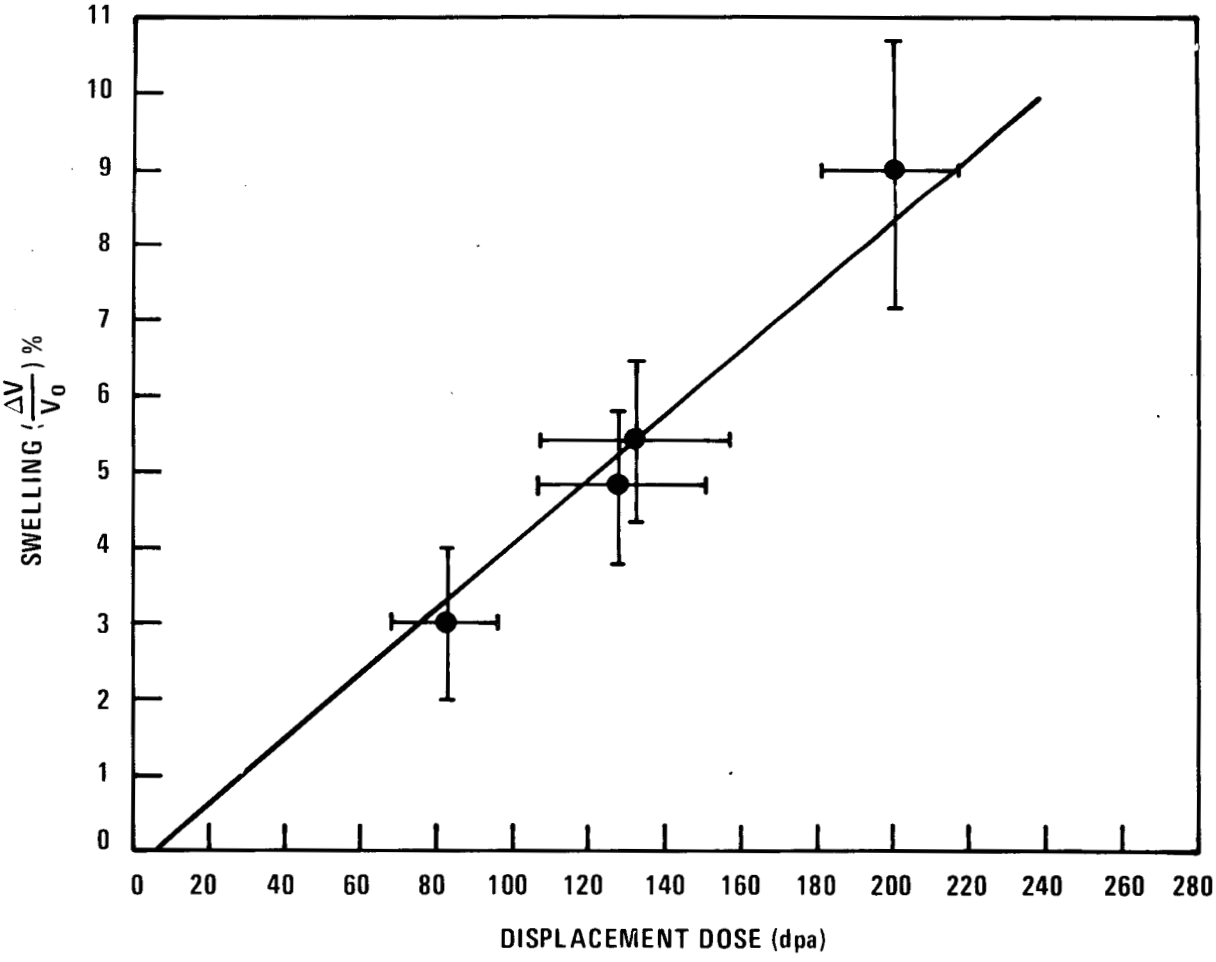

FIGURE 94. Swelling vs. displacement dose in A-286 STA irradiated peak at temperature (550°C).

5.3.2 Precipitate Identification

Radiation-induced precipitates in A-286 sectioned to the peak damage region were examined by TEM. Dark field micrographs and diffraction patterns were taken to identify the precipitates. Electron diffraction patterns were analyzed by methods described previously[3] to determine d-spacing for the precipitates.

Two kinds of precipitates could be seen in dark field. Figure 95 shows in dark field those precipitates which are associated with voids. A coating of the fine precipitates can be seen on the voids. Figure 96 shows the same area in bright field. Electron diffraction analysis of the d-spacing and comparison with published d-spacing[4] reveal that these precipitates are G phase (Table 23).

The second kind of precipitates identified were small aligned precipitates not associated with voids. These precipitates, mostly invisible in bright field, are shown in dark field in Figure 97 and were observed when the relrod of Figure 98 was used for imaging. The morphology of this precipitate suggests that it is η phase; however, no detailed diffraction analysis could be carried out because of the relatively low volume fraction of this phase.

No long needles of eta phase were observed in irradiated A-286 as were observed by Gelles et al[5] in unirradiated long term aged A-286 (solution annealed at 980°C one hour, aged 720°C 16 hours and re-aged at 764°C, 500 hours).

TABLE 23

PRECIPITATE d-SPACINGS IN IRRADIATED A-286 STA

Measured d-Spacing	Published d-Spacing for Phase G	hkl
5.55	5.604	200
3.961	3.983	220
	2.803	
	2.499	420
2.265	2.285	422
2.132	2.154	333-511
1.958	1.977	440

5.3.4 Discussion

Large error bars are associated with the swelling measurements in this alloy. The reason for this lies with the association of precipitates with the voids which inherently results in inaccuracies in size and volume measurements. The error bars associated with the dose arise from the thickness of the foil over which the dose was averaged using the energy deposition curve derived from the EDEP-I code.

Figure 99 shows relative swelling versus temperature for A-286 irradiated with neutrons, nickel ions and electrons. The neutron irradiation data are from pin B-109, reported by Borisch and Powell[6]. Electron irradiations are by Thomas and Gelles[7]. The

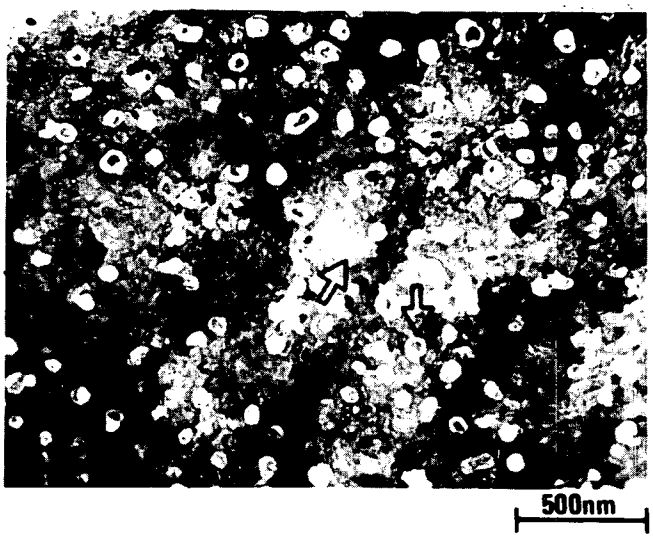

FIGURE 95. Dark-field micrograph of precipitates in irradiated A-286 (∿200 dpa) showing precipitates associated with voids.

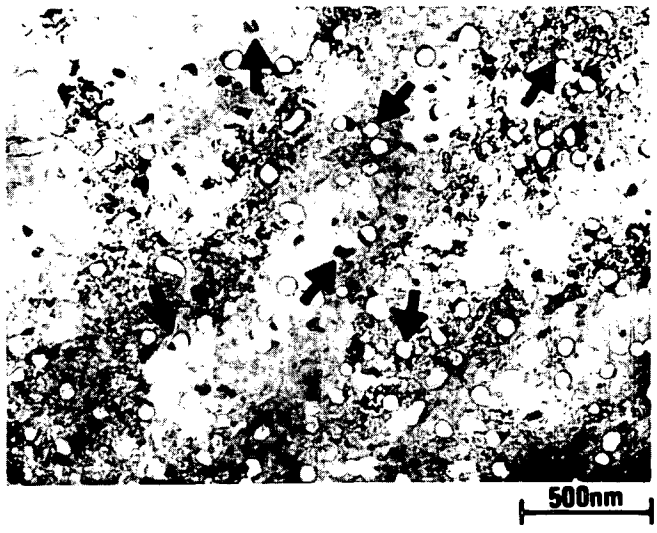

FIGURE 96. Bright-field micrograph of the same area as Figure 95.

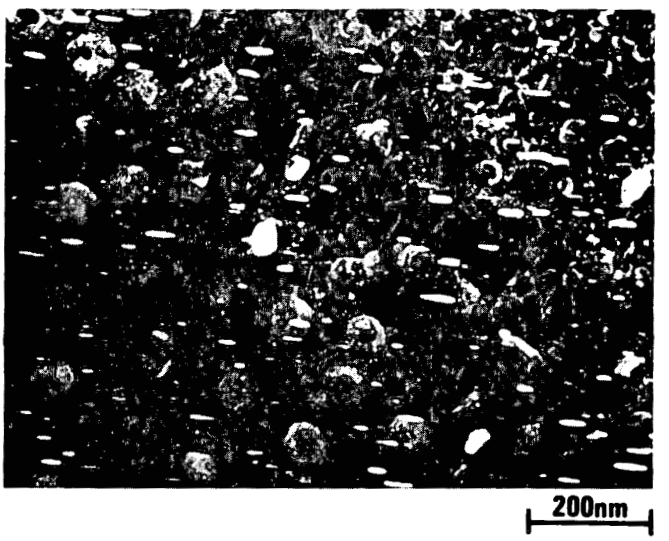

FIGURE 97. Dark-field micrograph of lenticular precipitates in irradiated A-286 (~200 dpa).

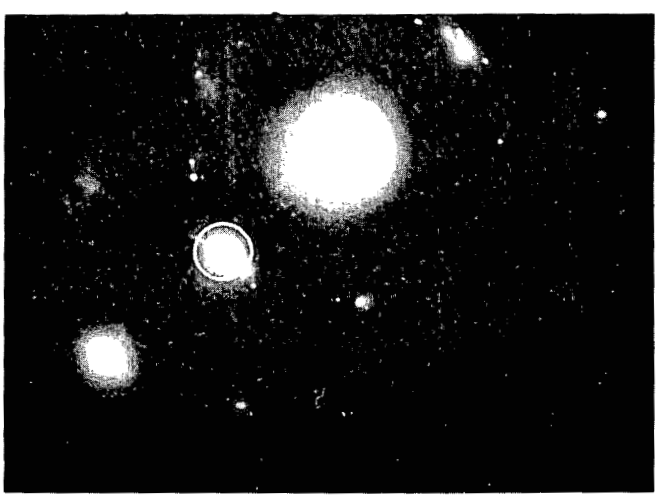

FIGURE 98. Diffraction pattern of irradiated A-286 STA (~200 dpa) showing relrod streak (under circle) used for imaging precipitates in Figure 97.

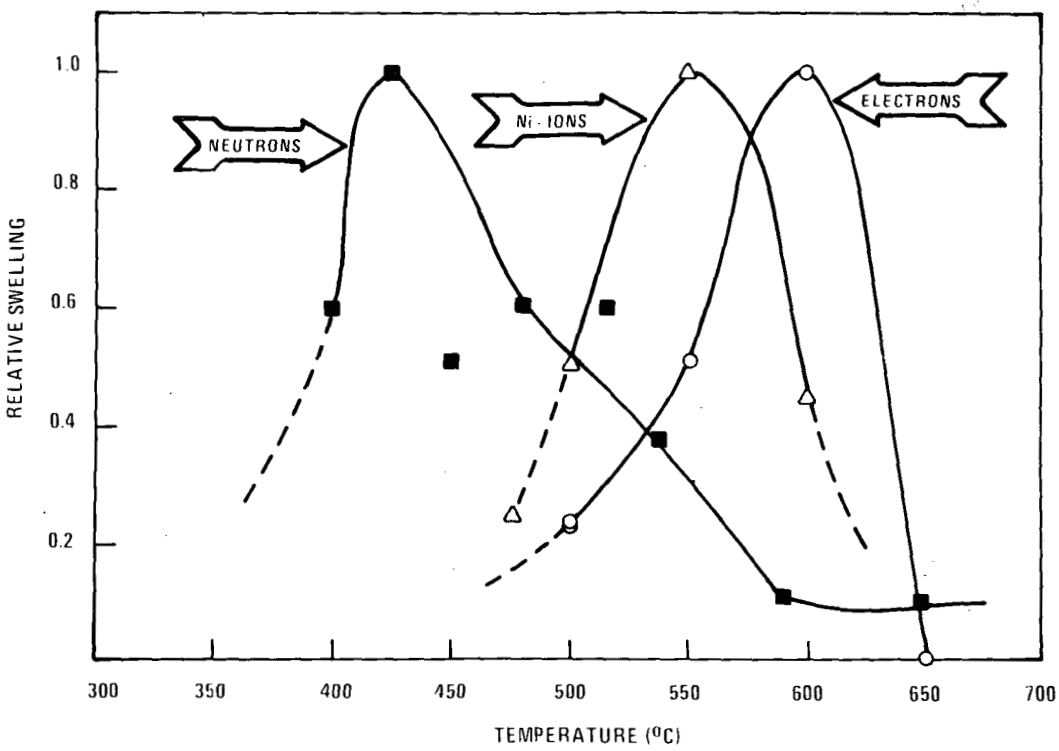

FIGURE 99. Relative swelling vs. irradiation temperature for A-286 STA irradiated with neutrons, electrons and Ni-ions.

Ni-ion data plotted in Figure 99 are from step height measurements reported by Bajaj[2]. A temperature shift of ∿125°C between neutron and Ni-ion peak swelling and a shift of ∿175°C for electrons is evident from Figure 99. A shift of 100-125°C between neutron and Ni-ion swelling is in good agreement with current theories. A relative shift of ∿50°C between electron and Ni-ion irradiations is consistent with other data[8,9].

Figure 94 shows a very low incubation dose of ∿5 dpa for swelling which is in fair agreement with neutron results. Swelling of ∿2% was observed at a neutron dose of 4.3 x 10^{22} n/cm^2[6] at a peak temperature of 425°C. Using the dose equivalence of 50 Ni-ion dpa ≡ 1 x 10^{23} n/cm^2 this corresponds to ∿21 dpa. A better agreement between neutrons and Ni-ion data is obtained using 100 Ni-ion dpa ≡ 1 x 10^{23} n/cm^2. Swelling of ∿1.7% with Ni-ions and ∿2% with neutrons with zero incubation is then obtained. The incubation dose obtained by electron irradiation, however, is 10 dpa$_e$ at peak temperature[7] which is in disagreement with Ni-ion. Figure 100 shows a plot of swelling at the peak temperature versus dose for neutrons, Ni-ion and electron irradiations using the following dose equivalencies:

100 Ni-ion dpa ≡ 1 x 10^{23} n/cm^2

10 electron dpa ≡ 15 x 10^{23} n/cm^2

Using these dose equivalencies, a good agreement is obtained between Ni-ion, neutron and electron data (30 dpa). In plotting the electron data in Figure 100, $\Delta V/V_o$ was calculated from data in Reference 7.

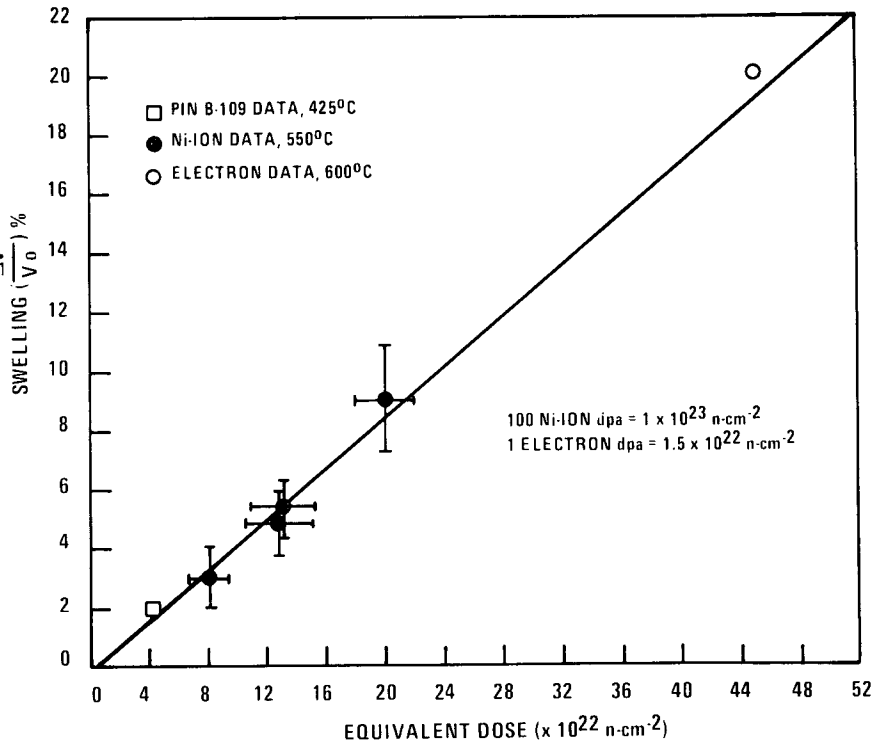

FIGURE 100. Swelling at peak temperature vs. displacement dose for A-286 STA irradiated with neutrons, electrons and Ni-ions.

Figure 101 shows a plot of swelling in A-286 STA, E48 STA, D21 STA and D25 STA at 550°C which is the peak swelling temperature for A-286 STA, E48 STA and D21 STA. In the case of D21 STA and D25 STA, full range HVEM data are plotted (open symbols) with those obtained by conventional TEM using sectioning techniques (closed symbols). These data (HVEM and TEM) are in fair agreement both in the peak damage region (D21 STA and D25 STA) and in the near ion entry surface region (D25 STA). The E48 STA swelling data plotted in Figure 101 are HVEM measurements reported by Chickering[10].

D21 STA and D25 STA exhibit a high incubation dose of about 140 to 150 dpa as compared to about 5 dpa for A-286 STA. Since all three alloys were irradiated in the same holder under identical conditions and since the swelling measurements by HVEM are in fair agreement with those by TEM, it can be concluded that the high incubation doses in the ion-bombarded developmental alloys are real. Figure 101 also shows swelling versus dose relationship for experimental alloy E48 at the peak swelling temperature (550°C)[10]. It can be seen that E48 also has an incubation dose of ∿140 dpa. The major difference between A-286 and the other three alloys is the amount of Al in the alloy. Alloy A-286 contains 2.0% Ti and 0.2% Al (a Ti/Al ratio ∿10) whereas E48 contains 3% Ti and 1.5% Al (a Ti/Al ratio of 2), D21 contains 3.3% Ti and 1.7% Al (a Ti/Al ratio of 1.9) and D25 contains 1.8% Ti and 1.3% Al (a Ti/Al ratio of 1.4). It can be concluded that Al increases the incubation dose. However, the rate of swelling is higher in E48 (0.066%/dpa) than in A-286 (0.042%/dpa). The reduction in swelling rate in A-286 can be accounted for by higher C, Si, Mn and Mo in this alloy.

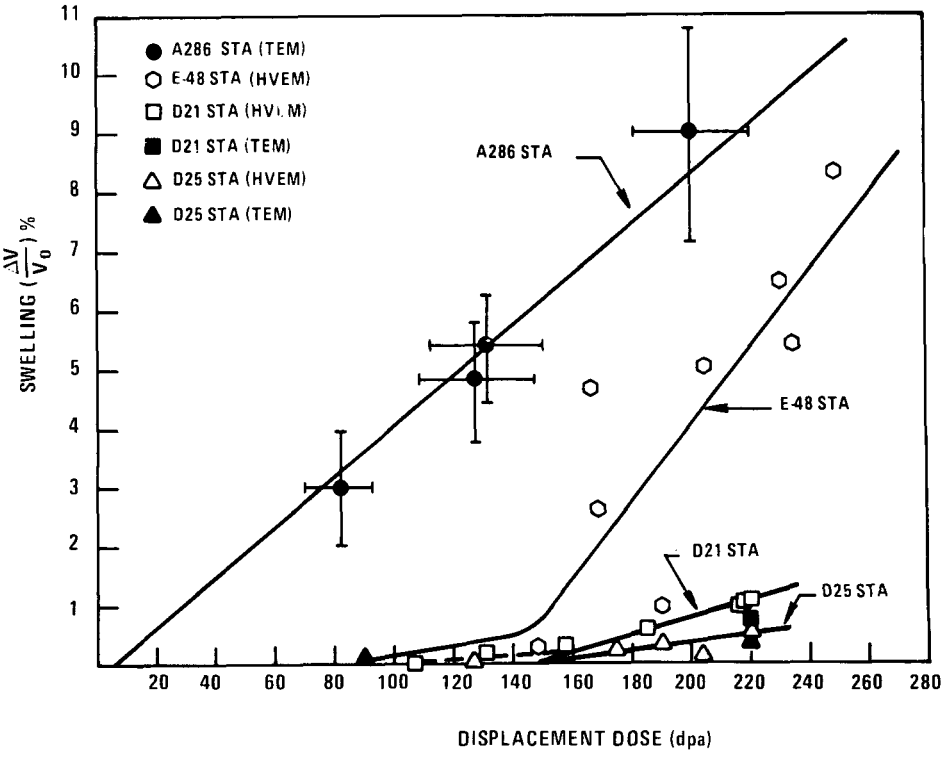

FIGURE 101. Swelling vs. displacement dose for A-286 STA, E48 STA, D21 STA and D25 STA at irradiation temperature of 550°C showing full range HVEM and TEM data for D21 STA and D25 STA.

A comparison of swelling in D21 STA and D25 STA with A-286 STA shows that D21 and D25 have both large incubation doses in swelling and much lower swelling rates. The incubation can be accounted for by the presence of larger amounts of Al (or smaller Ti/Al ratio) as described above. The decrease in swelling rate in D21 cannot be accounted for by C, Mn, Si and Mo since D21 and A-286 contain these elements in comparable amounts. It can only be the result of reduced Cr in D21 and D25 (8% and 10% respectively in D21 and D25 compared to 15% in A-286). The following conclusions about the merits of alloying elements can be drawn from comparison of heavy ion bombardments of E48, A-286, D21 and D25.

1. Aluminum increases the swelling incubation dose in Fe-Ni-Cr, γ'-strengthened alloys.

2. Reduction of Cr content has a strong effect in reducing swelling in these alloys.

3. Additions of C, Mn and Si have a small effect in reducing swelling.

4. Nickel and molybdenum additions reduce swelling (compare D21 with D25).

A comparison of microstructure produced by Ni-ion irradiation and neutron irradiation is worthwhile. Figure 102 shows micrographs of a Ni-ion irradiated specimen in the near-ion-entry-surface region ($\sim$85 dpa) and a neutron irradiated (5.4×10^{22} n/cm^2) material reproduced from Reference 11. It can be seen that very similar microstructures are produced by

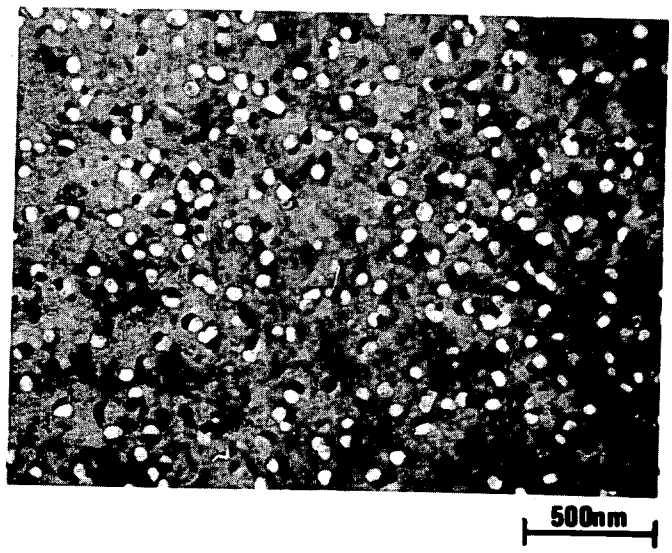

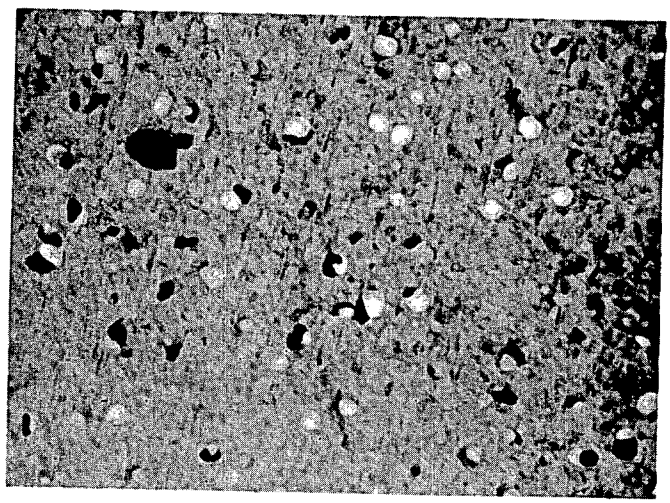

FIGURE 102. Microstructure produced by Ni-ion irradiation (83 dpa, 550°C) [top]; and by neutron irradiation (5.4×10^{22} n/cm^{-2}, 593°C) [bottom].

Ni-ion and neutron irradiations. The precipitates associated with the voids have similar morphologies. In the neutron irradiated material a lenticular precipitation can be seen which is similar to the precipitates shown in Figure 97 in dark-field. The former precipitates are believed to be G phase and the latter, η phase.

5.3.5 Conclusions

Based upon the results of these Ni-ion irradiations combined with available neutron irradiations and electron irradiations data, the peak swelling of A-286 at 3×10^{23} is 13% $\Delta V/V$. From a comparison of void swelling in Ni-ion irradiated A-286 STA with E48 STA, D21 STA and D25 STA it can be concluded that an increase in aluminum content (with a small Ti/Al ratio) and reduction in chromium level are beneficial in reducing swelling in Fe-Ni-Cr alloys. The Al appears to increase the incubation dose while the Cr reduces the swelling rate.

The microstructure produced by neutron irradiation is very similar to that produced by Ni-ion irradiation in A-286 STA. A good agreement can be obtained between swelling in neutron irradiated and Ni-ion irradiated STA A-286 when a dose equivalence of 100 dpa Ni-ion $\equiv 1 \times 10^{23}$ n/cm^{-2} is used.

5.4 EXPECTED ACHIEVEMENTS IN THE NEXT REPORTING PERIOD

This completes the work on Ni-ion irradiated A-286 alloy.

5.5 REFERENCES

1. Diamond, S., Chickering, R., and Bleiberg, M. L., Alloy Development Quarterly Technical Progress Letter, TC-160-5 (4-6/1975), p. 319.

2. Bajaj, R., and Chickering, R. W., Alloy Development Program Quarterly Technical Progress Letter, TC-160-7 (10-12/1975), p. 79.

3. Bajaj, R., Annual Information Meeting, National Advanced Alloy Development Program, October 20, 1976, TC-721, p. 511.

4. Donachie, M. J., and Kreige, O. H., J. Metals, JMLSA, Vol. 7, No. 3, September 1972, p. 269.

5. Bates, J. F., Cummings, W. V., Gelles, D. S., Mastel, B., and Laidler, J. J., Alloy Development Program Quarterly Technical Progress Letter, TC-160-1 (4-6/1974), p. 13.

6. Borisch, R. R., and Powell, R. W., Alloy Development Program Quarterly Technical Progress Letter, TC-160-9 (4-6/1976), p. 7.

7. Thomas, L. E., and Gelles, D. S., Alloy Development Program Quarterly Technical Progress Letter, TC-160-8 (1-3/1976), p. 28.

8. Lauritzen, T., Bell, W. L., Johnston, W. G., Darlin, E. S., and Konze, G. M., Alloy Development Program Quarterly Technical Progress Letter, TC-160-8 (1-3/1976).

9. Korenko, M. K., and Gelles, D. S., Alloy Development Program Quarterly Technical Progress Letter, TC-160-9 (4-6/1976), p. 21.

10. Chickering, R. W., and Diamond, S., Alloy Development Program Quarterly Technical Progress Letter, TC-160-7 (10-12/1976), p. 229.

11. Gelles, D. S., Annual Information Meeting, National Advanced Alloy Development Program, October 1976, TC-721, p. 444.

6. PHASE STABILITY OF D21 AND D25 UNDER IRRADIATION

R. Bajaj and S. Diamond
Westinghouse Advanced Reactors Division

6.1 OBJECTIVE

The objective of this work is to determine the nature of precipitates produced by Ni-ion irradiation in developmental alloys D21 and D25.

6.2 SUMMARY

Dark field micrography and electron diffraction analysis was completed on the precipitation in D21 STA and D25 STA Ni-ion irradiated at 550°C and 750°C. At 550°C, D21 STA precipitates were analyzed to be G phase with smaller quantities of η, M_7C_3 and σ present. In D25 STA, the precipitates were identified as primarily M_7C_3 and some η. At 750°C D21 STA precipitates M_6C and Laves phase. The phase analysis in D25 STA revealed the presence of M_6C carbides and an additional precipitate which could not be identified using the published d-spacing of phases commonly found in superalloys. Although these complex reactions are not understood, the precipitation is generally consistent with the reactions observed in these types of materials under thermal conditions.

6.3 ACCOMPLISHMENTS AND STATUS

In a previous quarterly progress letter[1], the precipitation produced by nickel ion-irradiation at 550°C to a maximum dose of ∿220 dpa in D21 STA and D25 STA was reported. Table 24 summarizes the interplanar d-spacing and phase identification obtained by electron diffraction analysis in D21 and D25 after this irradiation exposure. The conclusions of this analysis were that under these irradiation conditions, D21 STA predominantly precipitates G phase with smaller amounts of η, σ and M_7C_3 carbides and in D25 STA, M_7C_3 precipitates with η but no G phase could be identified[1,2].

This report describes the details of the precipitation analysis in these alloys irradiated at high temperature (750°C) to a relatively low dose (∿55 dpa). The analysis techniques used were the same as in the previous study[1], i.e., bright and dark field microscopy and electron diffraction analysis.

6.3.1 D21 STA

Figure 103 shows precipitates in D21 STA in bright field. The large precipitates appear to be uniformly distributed in the specimen. No voids were observed in the near surface region and γ' particles could not be imaged in bright or dark field.

Figure 104 shows a typical diffraction pattern showing spot and ring patterns. Diffraction patterns were taken in various crystallographic orientations and spacings between spots were measured to an accuracy of ±0.05 mm. The matrix spots were used as calibration spots for the camera constant determination. Table 25 summarizes the d-spacings obtained by

TABLE 24

INTERPLANAR SPACINGS AND PHASE IDENTIFICATIONS OBTAINED BY ELECTRON DIFFRACTION IN ALLOYS D21 STA AND D25 STA Ni-ION IRRADIATED AT 550°C TO 220 DPA

D21 STA

d_{Avg}, Å (Measured Lattice Spacing)	Phase				
	G*	σ	M_7C_3	η	γ,γ'
5.50	✓				
4.01		✓	✓		
3.97		✓			
3.92				✓	
3.60					✓
3.32 ?					
3.236 ?					
2.588		✓			
2.495	✓				
2.284	✓				
2.162	✓				
2.149			✓		
2.101	✓		✓		
2.082					✓
1.997		✓	✓		
1.977		✓			
1.955		✓		✓	
1.903	✓	✓	✓		
1.868	✓				
1.796					✓
1.696	✓				
1.604		✓		✓	✓
1.483			✓	✓	
1.449	✓		✓	✓	
1.319	✓			✓	
1.285	✓			✓	
1.257			✓	✓	
1.237	✓	✓	✓	✓	
1.204					
1.089	✓			✓	✓
1.060	✓				

D25 STA

d_{Avg}, Å (Measured Lattice Spacing)	Phase		
	M_7C_3*	η	γ,γ'
2.545		✓	✓
2.519	✓		
2.434	✓	✓	
2.183	✓	✓	
2.073			✓
2.059	✓		
2.033	✓		
1.840	✓		
1.594	✓	✓	
1.471	✓	✓	
1.273		✓	
1.190	✓	✓	
1.131		✓	
1.081	✓	✓	✓
1.032		✓	✓

* Predominant phase as determined by dark field microscopy.

FIGURE 103. Dark field micrograph of precipitates in D21 STA irradiated (∿55 dpa) at 750°C.

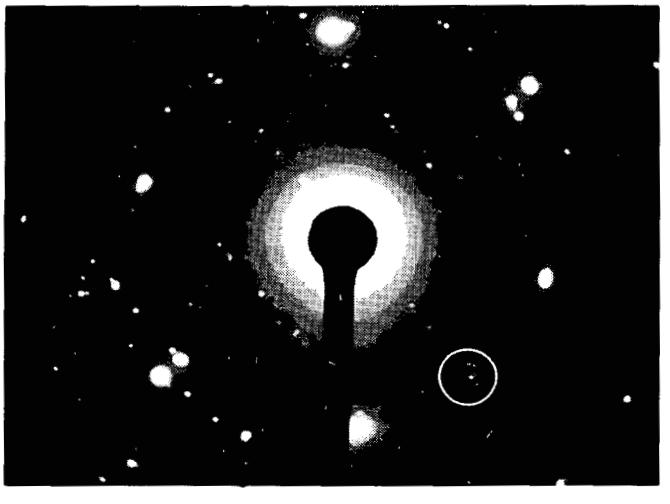

FIGURE 104. A typical diffraction pattern obtained from D21 STA irradiated (∿55 dpa) at 750°C.

TABLE 25

PHASE IDENTIFICATION IN D21 STA Ni^+ ION IRRADIATED AT 750°C TO 55 DPA

Measured d-spacings (Å)	Published d-spacings, Å[1]		Phases Present in D21	hkl	hkl
	M_6C a = 11.20	Laves a = 4.75 c = 7.90		M_6C	Laves
6.527 6.488 6.484	6.47		M_6C	111	
	5.60				
4.111 4.104		4.11	Laves		100
		3.95			
3.654 3.643		3.65	Laves		
3.453 3.410			Anomalous Anomalous		
3.40 3.392 3.389	3.38		M_6C	311	
3.235 3.20	3.23		M_6C	222	
2.816	2.80	2.85	M_6C	400	
	2.57				
2.5116 2.502					
2.154	2.29 2.16	2.38 2.22	M_6C	333	
2.057		2.06	Laves		200
2.01 1.985	1.98	2.04 1.99	M_6C, Laves	440	004
1.60	1.893 1.771 1.6888 1.61 1.568	1.975 1.824 1.78 1.62 1.526	M_6C, Laves	444	203

such measurements. These d-spacings were compared to published d-spacings and phase determination was made[2]. From Table 25 it can be seen that the best matches are obtained for M_6C type carbides and Laves phases in D21 STA.

Figure 105(a) shows a dark field micrograph of precipitates imaged using a cluster of spots under the circle in Figure 105(b). The d-spacing for the brightest spot corresponds to Laves phase. In addition to the large precipitates there is a fine dispersion of Laves phases in the interstices. The precipitates showing dark in this micrograph are probably carbide precipitates. Figure 105(c) shows a bright field micrograph of the same area.

FIGURE 105(a). Dark field micrograph of precipitates in D21 STA irradiated (∿55 dpa) at 750°C imaged by using spot under circle in Fig. 105(b).

FIGURE 105(b). Diffraction pattern of the area imaged in Fig. 105(a).

FIGURE 105(c). Bright field micrograph of the area in Fig. 105(a).

Figure 106(a) shows a dark field micrograph of precipitates imaged using the two spots under circle in Figure 104. The d-spacings corresponding to these spots are 2.057Å and 2.154Å which correspond to Laves phase and $M_{23}C_6$ type carbides respectively. Figure 106(b) is the bright field of the same area.

6.3.2 D25 STA

Figure 107(a) shows large precipitates in D25 STA in dark field which were imaged with the spot under the circle in the diffraction pattern in Figure 107(b). From the analysis of the diffraction patterns [Figure 107(b) and 107(c)] it is concluded that these precipitates are M_6C type carbides.

Another kind of precipitation was also observed in D25 as shown in Figure 108(a), with the corresponding diffraction pattern in Figure 108(b). Electron diffraction analysis of Figure 108(b) and other patterns was carried out to determine the d-spacings which are listed in Table 26 along with measured d-spacings of M_6C phase. No match could be obtained for the listed d-spacing with the published d-spacing of precipitates observed in various superalloys. At this writing, therefore, the identification of this phase remains incomplete.

TABLE 26
PHASE IDENTIFICATION IN D25 STA IRRADIATED AT 750°C TO 55 DPA

Measured d-spacing	Published d-spacing M_6C a = 11.20	hkl	Measured d-spacings (M_6C spacings excluded)
6.47	6.47	111	
			5.10
			5.15
			3.827
			3.72
			3.67
			3.64
3.244	3.23	222	3.075
2.81	2.80	400	
			2.40
2.154	2.16	333	
			2.133
			2.129
			1.82

6.3.3 Discussion

From Table 24 it is clear that the low temperature irradiation (550°C) of developmental alloys results in precipitation of M_7C_3 carbide precipitates with possibly some η. In the case of D21 STA, G phase is precipitated. At the higher irradiation temperature of 750°C however, M_6C precipitate is found to be the predominant phase. In D21 STA Laves phase was also found at 750°C.

The mechanisms of precipitation in complex superalloys are not well understood; however there is some evidence to suggest that at high temperatures M_6C carbide phase is more stable than M_7C_3 carbide. M_7C_3 is a psuedo hexagonal phase whereas M_6C is a f.c.c. phase.

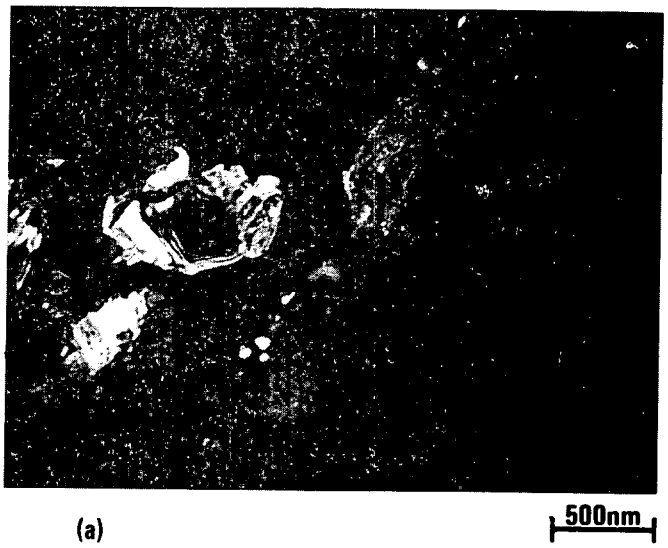

FIGURE 106(a). Dark field micrograph of precipitates in D21 STA irradiated (∿55 dpa) at 750°C imaged by using spot under circle in Figure 104.

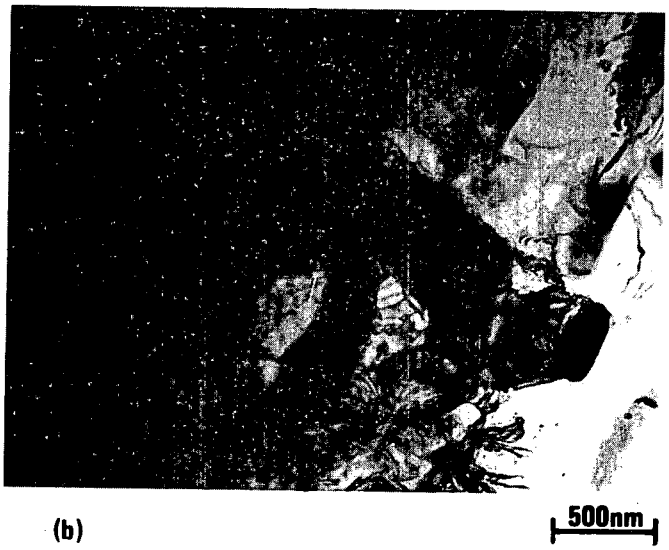

FIGURE 106(b). Bright field of same area as in Figure 106(a).

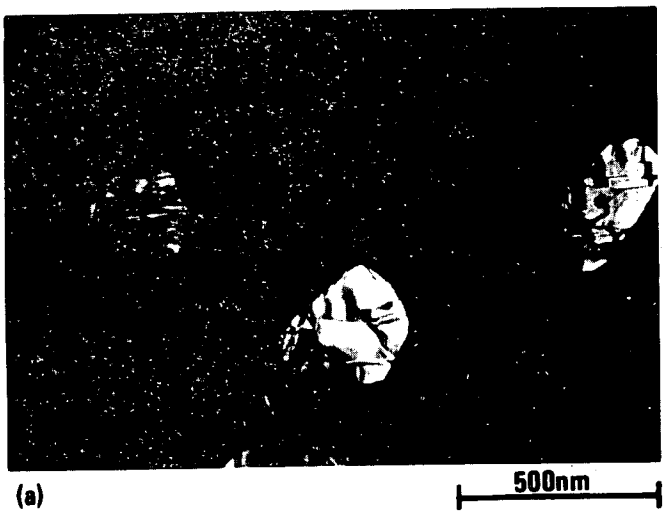

FIGURE 107(a). Dark field micrograph of precipitates in D25 STA irradiated (∿55 dpa) at 750°C imaged by using spot under circle in Fig. 107(b).

FIGURE 107(b). Diffraction pattern of the area imaged in Fig. 107(a).

FIGURE 107(c). Diffraction pattern of a typical area in D25 STA irradiated (∿55 dpa) at 750°C.

(a)

FIGURE 108(a). Dark field micrograph of precipitates in D25 STA irradiated (∿55 dpa) at 750°C imaged by using spot under circle in Fig. 108(b).

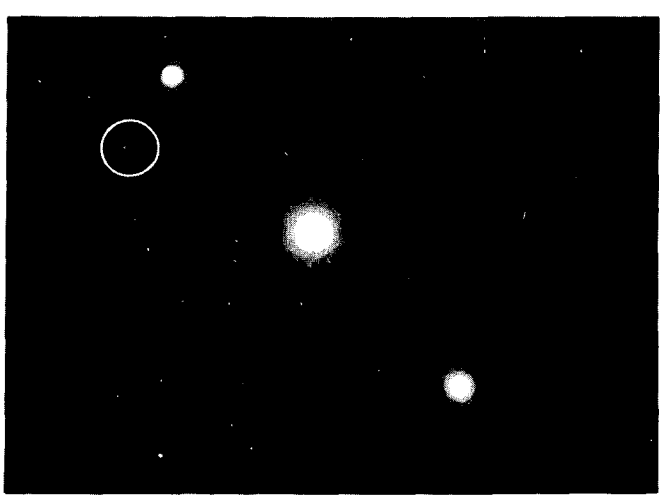

(b)

FIGURE 108(b). Diffraction pattern of the area imaged in Fig. 108(a).

In a matrix of f.c.c. γ, it can be expected that a f.c.c. phase will be more stable. Furthermore, M_7C_3 is known to transform to cubic phases. An example of this can be found in high nickel alloys such as Inconel 600[3] and Nimonic 80A[4] in which M_7C_3 transforms to $M_{23}C_6$ (where M is primarily Cr). In low Cr and low C alloys containing Mo the more probable phase is M_6C. M_6C carbides in general are more stable than $M_{23}C_6$ carbides[5] at high temperatures, therefore it is not surprising that M_6C precipitation occurred at high irradiation temperatures[5]. It is well known that the kinetics of precipitation are greatly enhanced by production of excess vacancies during irradiation resulting in precipitation at lower temperatures than thermal conditions.

At high irradiation temperature (750°C) Laves phase was also observed. This may be due to stabilization of this phase by Si as suggested by Miner and Lowell in Unitemp 718[6] and in B-1900 by Lowell and Miner[7].

At the low irradiation temperature, G phase was observed in D21 STA which is in agreement with the observations of this phase in thermally treated alloys with similar compositions by Beattie and Hagel[8]. However, the morphologies and temperatures of precipitations in the two cases are quite different due to differences in nucleation and growth processes.

6.4 EXPECTED ACHIEVEMENTS IN THE NEXT REPORTING PERIOD

A comparison will be made of the irradiation induced precipitates with those produced by long term thermal aging in D21 and D25 aged at various temperatures. The microstructural analysis of these alloys irradiated with neutrons (AA-VII test) will be carried out.

6.5 REFERENCES

1. Bajaj, R., and Diamond, S., Alloy Development Program Quarterly Technical Progress Letter, TC-160-10 (10-12/1976).

2. Donachie, M. J., and Kriege, O. H., "Phase Extraction and Analysis in Superalloys," Summary of Investigations by ASTM Committee E-4, Task Group L, Journal of Materials, JMLSA, Vol. 7, No. 3, September 1972, p. 269.

3. Collins, H. E., and Kortovich, C. S., J. Mat. 1969, 4, p. 62.

4. Fell, E. A., et al., "Structural Processes in Creep," 136, London, The Iron and Steel Institute (1961).

5. "Superalloys," C. T. Sims and W. C. Hagel, eds., John Wiley & Sons, New York, 1972, p. 52-58.

6. Lowell, C. E., and Miner, R. V., NASA TM-X-68191, January 1973.

7. Miner, R. V., and Lowell, C. I., NASA TN-D-7989, June 1975.

8. Beattie, H. J., and Hagel, W. C., Journal of Metals, July 1957, p. 911.

7. SWELLING OF SOLID SOLUTION DEVELOPMENTAL ALLOYS UNDER NICKEL ION BOMBARDMENT

A. F. Rowcliffe and P. S. Sklad
Oak Ridge National Laboratory

7.1 OBJECTIVE

The objective of this work is the development of solid solution alloys with low swelling properties suitable for use in advanced LMFBR fuel systems.

7.2 SUMMARY

Step height swelling data have been obtained on three batches of a laboratory heat of 316, alloy G7. After annealing at 1150°C, alloy G7 exhibits swelling peaks at 600 and 680°C. After annealing at 1050°C only one swelling peak at 680°C has been detected. Some possible reasons for this behavior are discussed and the data are compared with those from the X098 experiment.

7.3 ACCOMPLISHMENTS AND STATUS

7.3.1 Introduction

The swelling behavior of developmental alloys LS1, LS2, D15, D18, D9 and D11 has been investigated using nickel ion bombardment and step height measurements, and the results have been presented in earlier reports[1,2]. The bombardment technique utilized a rectangular stack of narrow specimens which were bombarded simultaneously in the same holder. In addition to continuous measurement by beam profilometry, a postbombardment assessment of beam uniformity was made by measuring the surface step on standard stainless steel specimens placed at regular intervals in the stack. Two types of stainless have been used for this purpose, a "high purity" 316 designated P7 and a laboratory heat of 316, alloy G7. Swelling data were thus accumulated for both steels in several heat treatment conditions. The data on alloy G7 were recently used to provide a comparison with the swelling behavior of alloys D9 and D11 in various metallurgical conditions[3]. It was found that at high temperatures the alloy G7 exhibited double peak swelling behavior, a phenomenon previously encountered in reactor irradiations but not in nickel ion irradiations. Over a period of about one year, data have been obtained on three different batches of G7 with varying processing histories. The data have now been brought up to date and are presented below.

7.3.2 Results

The composition of the 316 alloy G7 is shown in Table 27 together with that of the M2783 alloy used in the X098 experiments. Both the molybdenum and the combined (C + N_2) contents of the M2783 alloy are significantly higher than those of G7. Ion bombardment specimens were fabricated from G7 in three separate batches, Table 28. Final heat treatments were carried out with specimens measuring 2.5 cm long x 3 mm wide x 0.66 mm thick. The principal difference between the three batches lies in their final heat treatments. Batch A3 specimens were annealed at 1150°C ±5°C for 15 minutes in a ceramic tube furnace containing a tantalum getter under a vacuum of $\sim 5 \times 10^{-6}$ torr. Batch A4 specimens were encapsulated in quartz tubes containing a tantalum getter under a vacuum of $\sim 5 \times 10^{-6}$ torr and then backfilled

TABLE 27

ALLOY COMPOSITIONS (WEIGHT PERCENT)

	Cr	Ni	Mo	Si	Mn	Ti	C	N_2	S	P
G7	16.5	13.7	1.86	.44	2.05	<.01	.041	.004	.032	.035
M2783	16.81	12.98	2.46	.47	1.79	<.02	.058	.030	.017	.029

TABLE 28

HEAT TREATMENT HISTORY

Batch A3	Batch A4	Batch A8
Hot rolled to 3 mm		
Cold rolled to 15 mm		
1150°C 1 hr. vac. ⟶		
CR to 1 mm	CR to 0.75 mm	
1050°C 15 min. vac.	1050°C 15 min. vac.	
CR to 0.6 mm	CR to 0.6 mm	
Cut specimens	Cut specimens ⟶	
1150°C 15 min. vac.	1150°C 15 min. He	1050°C 15 min. He

with helium containing ∿1 appm O_2 and 6 appm N_2. Final annealing was the same as for Batch A3, i.e., 1150°C for 15 minutes. Batch A8 specimens were similarly encapsulated and then heat treated at 1050°C for 15 minutes. Following heat treatment, the 2.5 cm long strips were cut into pieces 4.3 mm long with a low speed diamond saw. After mounting in an ion bombardment holder, the surface to be bombarded was prepared by a polishing sequence which removed 0.2 mm from the cut surface. Ion bombardment of G7 was carried out in several different experiments in which the calculated peak displacement dose was 170 ± 20 dpa. All specimens were preinjected with 5 appm helium at room temperature.

In Figure 109, step height data are plotted as a function of temperature for all batches. When these data were presented previously[3], a single curve was drawn through data points from all three batches. With the addition of several new data points it appears that two types of swelling behavior are observed depending on whether the final heat treatment was at 1150°C or at 1050°C. At bombardment temperatures below 620°C all three batches behave similarly and may be accounted for by a single curve. Above this temperature there is a pronounced divergence in behavior. In batch A3 specimens, annealed at 1150°C in vacuum, swelling decreases sharply from a maximum at ∿680°C. Batch A4 specimens, which were also annealed at 1150°C but in a helium atmosphere, follow the swelling behavior of batch A3 quite closely up to ∿625°C, but were not bombarded at any higher temperatures. On the other hand, swelling in batch A8 specimens, annealed at 1050°C increases steadily to a single maximum at 680°C. Data on the A8 batch were obtained at 50°C intervals so that it is possible that a minimum exists between the data points. Even so, at temperatures above ∿625°C swelling is generally higher by 50 to 60% in the specimens annealed at 1050°C.

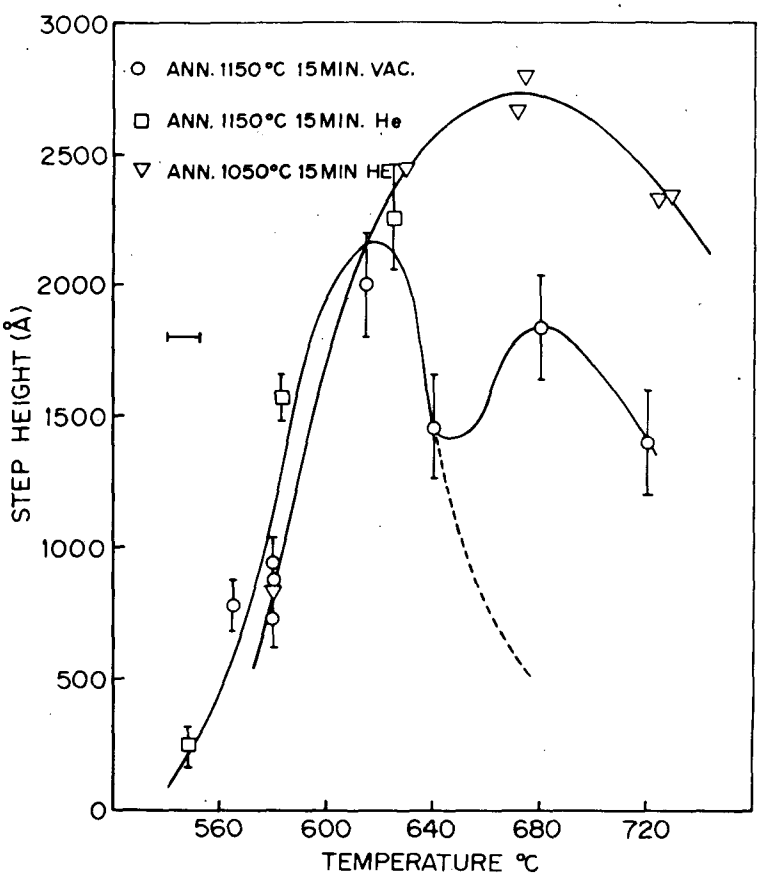

FIGURE 109. Step height swelling data for 316 heat G7 Ni ion bombarded to a peak dose of 170 dpa.

These differences in swelling behavior are not thought to be due to variations in specimen preparation technique or irradiation technique. Duplicate specimens of batch A8 were polished, helium injected, and ion bombarded at temperatures of ∿675°C and ∿725°C. Step height measurements on the duplicate specimens were in excellent agreement, i.e., (268 nm, 280 nm) and (235 nm, 236 nm) at 675°C and 725°C, respectively. For the A3 material, three separate bombardments were carried out at 580°C. The specimens had all received the same heat treatment but had undergone different final surface preparations. These were: (a) the normal final polish with 0.5 μm diamond, (b) the 0.5 μm diamond polish followed by polishing with 0.1 μm diamond, (c) the 0.5 μm diamond and 0.1 μm diamond treatments followed by an electropolish at -20°C which removed ∿2 μm. After receiving separate bombardments of 170 dpa the step heights produced in these three samples were 72 ± 4 nm, 96 ± 7 nm, and 90 ± 6 nm, respectively. Evidently, removal of the damage produced by the 0.5 μm diamond by polishing with 0.1 μm diamond increases swelling by a factor of ∿0.2. Further electropolishing to remove the 0.1 μm diamond does not result in any further swelling increase; this is not surprising since, if carefully carried out, the dislocation damage produced by the 0.1 μm diamond should not extend much more than 300 nm below the surface. Thus, the 0.5 μm diamond polishing technique inhibits swelling slightly. However, all specimens are treated in exactly the same way, and the technique consistently produces extremely smooth surfaces which are ideal for

surface profilometry. It should also be pointed out that differences in swelling behavior between annealed and 20% CW 316 are easily detected in measurements made on 0.5 μm diamond finished surfaces.

Since the reproducibility of the techniques is quite good, the differences in swelling behavior between the 1050 and 1150°C annealed specimens must be metallurgical in origin. Increasing the final annealing temperature increases the concentration of various solutes in solution at the beginning of the irradiation. In the case of 316 stainless, it is known that increasing the annealing temperature from 1050 to 1150°C will double the amount of carbon in solution. However, little is known about the distribution during processing of other important elements such as molybdenum and silicon and what effect annealing temperature has on their concentration in solution. Assuming that increasing the solution treatment temperature increases the solute concentration we may rationalize the results in the following two ways:

(a) Increasing the solute content reduces the swelling in the high temperature regime in the manner demonstrated by Johnston, et al[4], and Gessel[5] in their work on solute additions to ternary alloys. If this were the only effect then the swelling curve for the A3 material would follow the dotted line in Figure 109. However, increasing the solute supersaturation also increases the subsequent nucleation rate of carbide and intermetallic phases. It is postulated that at temperatures above 640°C precipitation occurs with an associated enhancement of void nucleation and growth giving rise to a second swelling peak at 680°C.

(b) An alternative suggestion due to Makin is that the "double peak" is really a "central depression". Above 650°C, $M_{23}C_6$ is redistributed and reprecipitated in particles sufficiently fine to be effective point defect traps or sinks and to produce a reduction in swelling. The effect of fine carbide precipitation overcomes the normal increase in swelling in this temperature regime. Swelling eventually increases again because at higher temperatures precipitation occurs on a much coarser scale and a second peak is reached at 680°C after which swelling decreases as thermal vacancy emission restricts void nucleation. Transmission electron microscopy evidence from ion bombarded specimens is not available yet to support either of these suggestions. At present, the first explanation seems more probable and the results indicate that the benefits of increased solute concentrations may be lost in temperature regimes where certain types of precipitation occur. The effects of precipitation may possibly be minimized by avoiding phases which coarsen rapidly or nucleate on a coarse scale such as $M_{23}C_6$ and the TCP phases.

The dose dependence of swelling for G7 was determined for the batch A3 material by bombarding at 580°C to peak displacement doses of 70, 170 and 340 dpa. The data are plotted in Figure 110. Specimens were preinjected with 5 appm helium at room temperature. The incubation parameter τ is 35 dpa and the steady state swelling rate is 0.13% per dpa.

7.3.3 Comparison with X098 Data

The X098B irradiation experiment has provided swelling data at four temperatures and at a fluence of 14×10^{22} n cm^{-2} on an air melted heat of 316 stainless steel. The molybdenum and the (C + N) content are both higher than in the G7 heat and a strict comparison of the data is probably not valid. However, a comparison is useful from the point of view of providing some guidance in selecting temperatures and doses for ion bombardment of the X098 material in the Unified Simulation Program.

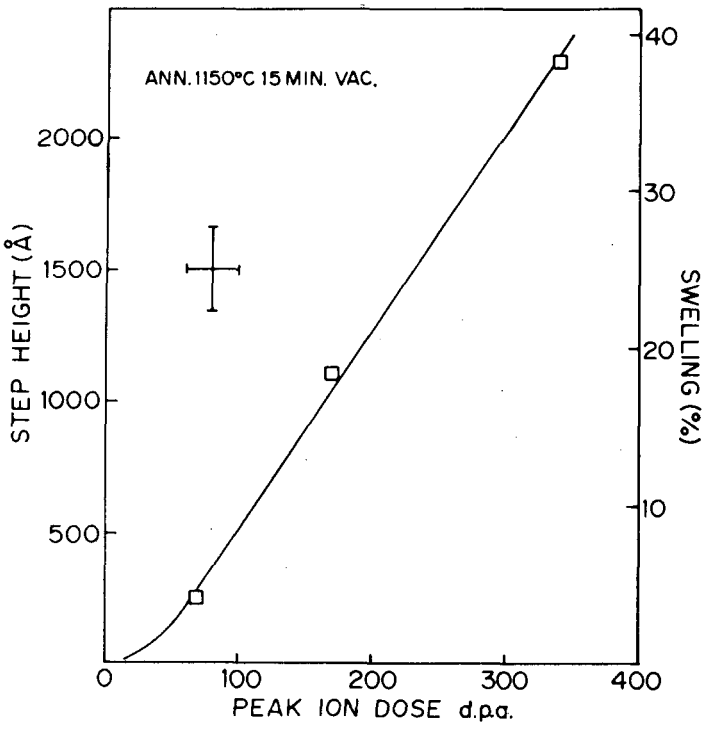

FIGURE 110. Step height swelling data for 316 heat G7 Ni ion bombarded at 580°C.

The peak swelling temperature for the G7 alloy annealed at 1050°C is 680°C after ion bombardment to 170 dpa. The heat M2783 tubing was annealed at 1093°C prior to irradiation, and after an exposure of 13 x 10^{22} the peak swelling temperature was found to be ~590°C. Thus, the peak swelling temperature shift is ~90°C. The swelling rate under ion bombardment was not measured. However, a straight line through the two neutron data points gives a value for τ of 6.5 x 10^{22} n cm^{-2} and a swelling rate of 3.5% per 10^{22} n cm^{-2}. Using these parameters, the neutron dose required to produce the 45% swelling observed in the ion experiment is 19.5 x 10^{22} n cm^{-2}. The equivalent peak ion dose is 170 dpa. At the peak swelling temperature equivalent amounts of damage are produced by 87 dpa (ions) or 10^{23} n cm^{-2}.

If we assume that the M2783 material behaves in a similar fashion to G7 after an 1150°C anneal, then the neutron dose to produce 30% swelling at the peak temperature is 15 x 10^{22} n cm^{-2} and the damage equivalence is 113 dpa (ions) ≡ 10^{23} n cm^{-2}.

At 580°C under ion bombardment the two heat treatments produce the same swelling in alloy G7, and we will therefore assume that the measured swelling rate of 0.13% per dpa applies to both conditions. The equivalent neutron temperature is 490°C, assuming the peak temperature shift applies at all temperatures. From the plots of Weiner and Boltax[4], the neutron swelling parameters for the M2783 material are τ = 6 x 10^{22} and R ~ .70% x 10^{22} n cm^{-2}. The damage equivalence obtained by equating the swelling rates is 54 dpa (ions ≡ 10^{23} n cm^{-2}. A comparison of the incubation parameters [6 x 10^{22} n cm^{-2} and 35 dpa (ions)] gives a similar value for damage equivalence. There is, however, considerable uncertainty in the neutron swelling rates since there are only four temperatures available and the value of 54 dpa ≡ 10^{23} n cm^{-2} should be considered to be a lower bound.

This comparison yields damage equivalents of 87 or 113 dpa $\equiv 10^{23}$ n cm^{-2} at the peak temperature depending upon which set of ion data is used and thus emphasizes that in any correlation experiment it is vital to use identically treated material in each irradiation experiment. It is suggested that in selecting the USP ion temperatures and doses a temperature shift of ~90°C should be expected when using an ion displacement rate of 10^{-2} dpa sec^{-1}. If it is assumed that the M2783 material will behave in a similar manner to the G7 annealed at 1050°C then it appears that an ion dose of ~75 dpa at 605°C will produce damage equivalent to that produced by a neutron fluence of 13 x 10^{22} n cm^{-2} at 515°C. At 680°C, an ion dose of ~120 dpa will be required to produce damage equivalent to that produced by a neutron fluence of 13 x 10^{22} n cm^{-2} at 590°C.

7.4 EXPECTED ACHIEVEMENTS IN THE NEXT REPORTING PERIOD

The final step height ion bombardment experiment involving compositional variants of D9 will be completed and will yield data at several more temperatures on the G7 annealed at 1050°C. Further ion bombardment work will concentrate on TEM disk specimens with emphasis on previously neutron irradiated developmental alloys.

7.5 REFERENCES

1. Rowcliffe, A. F., Sklad, P. S., and Bloom, E. E., "Development of Solid Solution Alloys," TC-160-6 (7-9/1975), p. 17.

2. Rowcliffe, A. F., Sklad, P. S., Leitnaker, J. M., and Bloom, E. E., "Development of Solid Solution Alloys," TC-160-7 (10-12/1975), p. 52.

3. Rowcliffe, A. F., Gessel, G. R., Alloy Development Program Annual Information Meeting, October 1976, TC-721, p. 526.

4. Johnston, W. G., et al., ASM Seminar on Radiation Damage in Metals, Cincinnati, November 1975.

5. Gessel, G., "The Effect of Alloying Elements on Swelling Behavior," TC-160-10 (7-9/1976), p. 145.

6. Weiner, R. A., and Boltax, A., "Comparison of High Fluence Swelling Behavior of Austenitic Stainless Steels," TC-675-2 (7-9/1976), p. 106.

8. THERMAL STABILITY OF ALLOYS D9 AND D11

J. M. Leitnaker and A. F. Rowcliffe
Oak Ridge National Laboratory

8.1 OBJECTIVE

The objective of this work is to determine the phase stability of developmental alloys D9 and D11 and to establish the feasibility of higher-stability modifications to these alloys.

8.2 SUMMARY

Aging studies on alloy D9 have shown a tendency to form Laves phase (Fe_2Mo). Although the quantities formed may not be sufficient to cause a serious deterioration in mechanical behavior, the precipitation of this phase may have an adverse effect on long term swelling behavior. Accordingly, six modified D9 alloys have been produced with variations in Mo, Ti and C content designed to improve phase stability. These will be subjected to phase stability tests both in and out of reactor and to mechanical testing.

8.3 ACCOMPLISHMENTS AND STATUS

8.3.1 Introduction

It was observed previously that the E-75 heat of developmental alloy D11 formed Laves phase (Fe_2Mo) on aging in the cold worked condition at 750°C together with a small amount of TiC. Aging studies have now been carried out on specimens from the 135 kg heats of D9 and D11 in order to assess the stability of these alloys towards intermetallic and carbide phase formation.

8.3.2 Experimental

The specimens used were prepared from D9 heat 07438 and D11 heat 77258 by a sequence of hot rolling and cold rolling with intermediate anneals at 1100°C. Specimens for aging were in the form of sheet 0.6 mm thick in two conditions: (a) annealed at 1100°C 15 minutes and (b) annealed at 1100°C 15 minutes and cold rolled 25%. Disks for TEM and rectangular pieces for precipitate extraction were encapsulated and aged at 650, 750 or 850°C for periods up to 1,000 hours. After aging, examinations were carried out by (a) optical metallography, (b) TEM, (c) electrolytic extraction and weighing of extracted precipitates, (d) chemical analysis of the liquid supernate and electron probe micro-analysis of the extracted precipitates, and (e) x-ray analysis of the extracted phases.

8.3.3 Results

Earlier work involving alloys with various Cr:Ni ratios indicated that alloy D9 should not form sigma phase[1]. Short term aging of annealed D9 between 700 and 850°C produced a small volume fraction of grain boundary carbides, mostly TiC. Longer term aging has now been completed at 650, 750 and 850°C. Figures 111 and 112 are optical micrographs of cold worked D9 after aging for 100 hours and 1,000 hours at 750°C. A considerable amount of

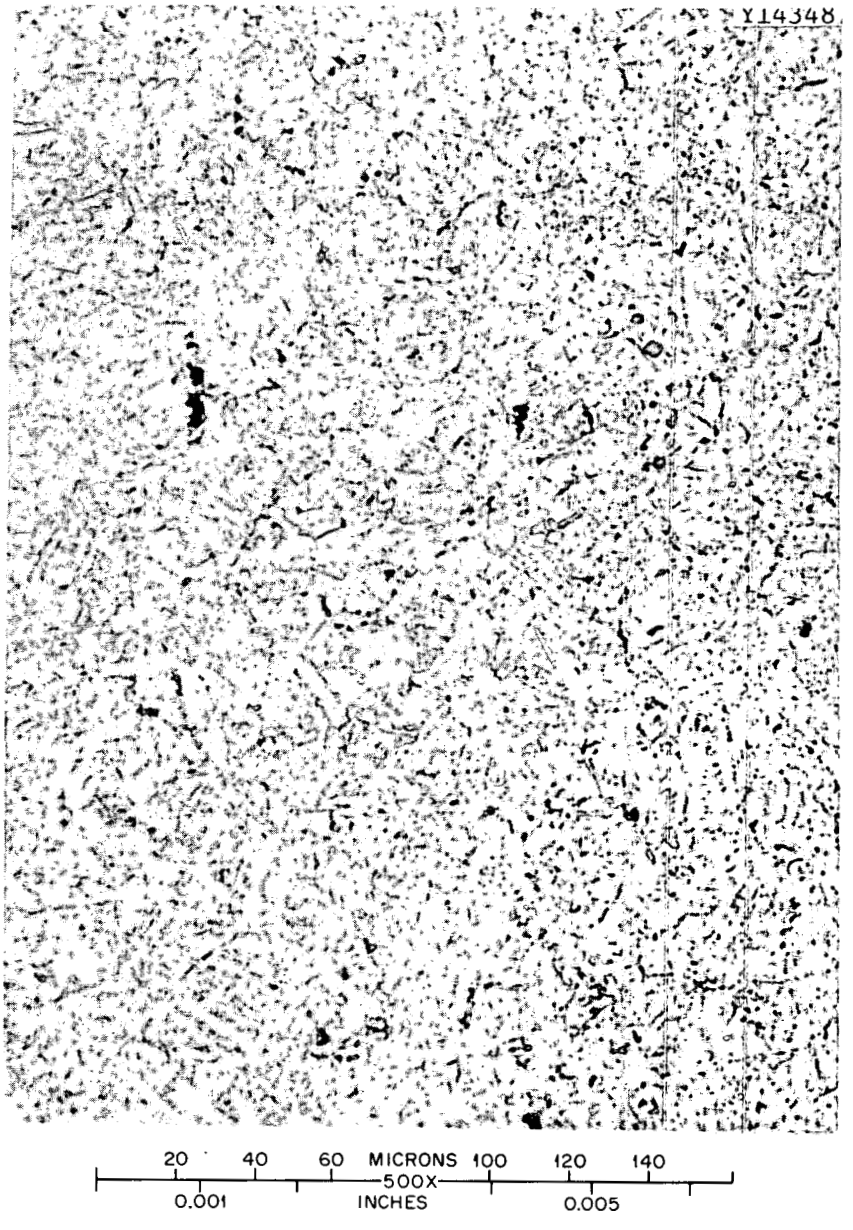

FIGURE 111. Alloy D9: 1100°C, 15 minutes, 25% CW, 750°C, 100 hours. Etched in modified aqua regia.

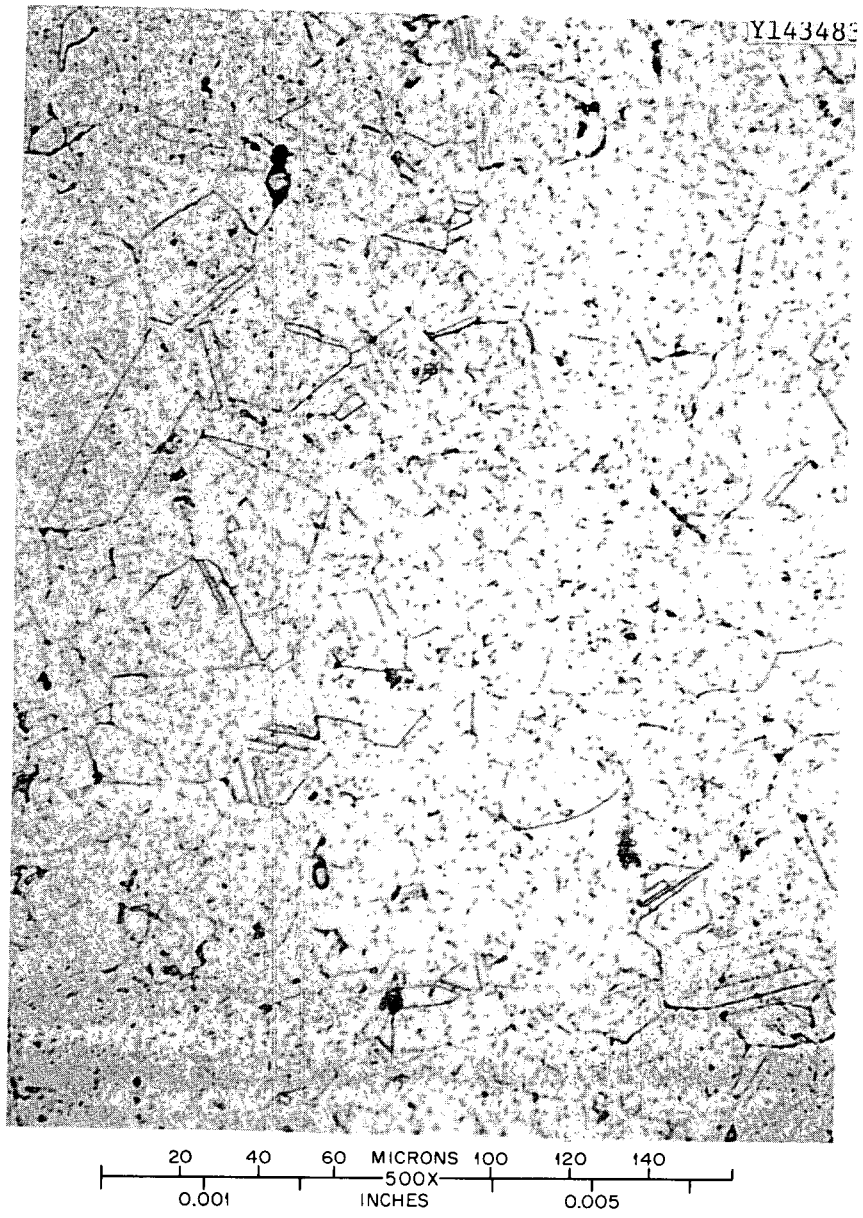

FIGURE 112. Alloy D9: 1100°C, 15 minutes, 25% CW, 750°C, 1,000 hours. Etched in modified aqua regia.

precipitation is evident both within the grains and at the grain boundaries. After 500 hours the weight fraction of precipitate determined by electrolytic extraction was 2.71%, Table 29. The weight fraction after 1,000 hours is not yet available. An x-ray analysis of the phases extracted after 500 hours at 750°C is shown in Table 30. The major phase present appears to be a Laves type compound with lattice parameters a_o = 4.748 Å and c_o = 7.735 Å. Titanium carbide is estimated to comprise only ~10% of the total precipitate extracted. The presence

TABLE 29

PRECIPITATE EXTRACTED, WEIGHT PERCENT

Alloy	Time (Hours)	Temperature (°C)		
		650	750	850
D9 annealed	100	.42	.62	.67
D9 annealed	1,000	--	2.90	1.73
D9 CW	500	1.06	2.71	--

TABLE 30

X-RAY DIFFRACTION DATA ON EXTRACTED PRECIPITATE FROM D9, COLD WORKED 25% AND AGED 500 HOURS AT 750°C

d (Å)	I (peak heights)	TiC		Laves a_o = 4.748 c_o = 7.735		
		(hkl)	I/I_o	(hkl)	I/I_o	d (calc., Å)
2.818	8			(012)		2.817
2.700	6					
2.497	23	(111)	80			
2.374	125			(110)	50	2.374
2.185	200			(013)	80	2.184
2.165	25	(200)	100			
2.056	35			(200)	14	2.056
2.023	250			(112)	100	2.023
1.988	160			(021)	95	1.987
1.932	25			(004)	20	1.934
1.815	12			(022)		1.815

TiC phase intensities listed are from ASTM Card 6-0614.

Laves phase intensities listed are from ASTM Card 7-145; other line intensities were not immediately available.

of sigma phase has not been detected. The Laves phase nucleates at grain boundaries and within the grains in cold worked specimens. Figure 113 shows the partially recrystallized structure after 500 hours at 750°C. Massive Laves phase particles have formed within the unrecrystallized areas and also at high angle boundaries. Grain boundary migration during recrystallization frequently isolates Laves particles in the center of recrystallized grains, Figure 114. Electron probe microanalysis of the extracted phases has shown that the major components are iron and molybdenum together with smaller concentrations of silicon and titanium. Quantitative measurements of the composition are in progress. Laves phase is also present after 100 hours at 850°C, but has not yet been detected at 650°C.

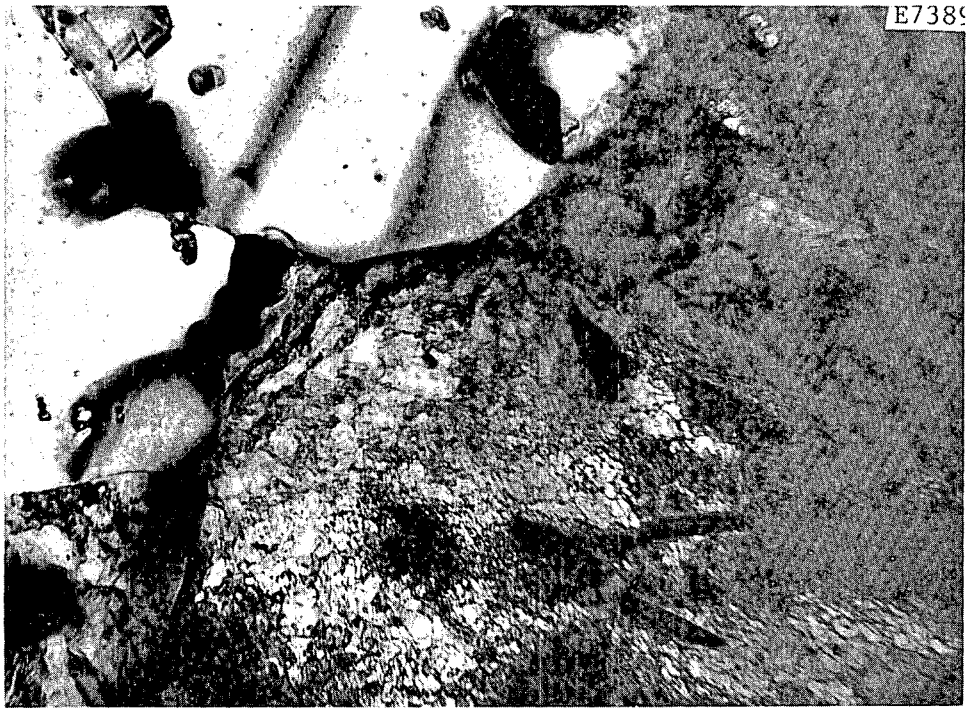

FIGURE 113. Alloy D9: 1100°C, 15 minutes, 25% CW, 750°C, 100 hours. TEM micrograph (Magn. X20,000).

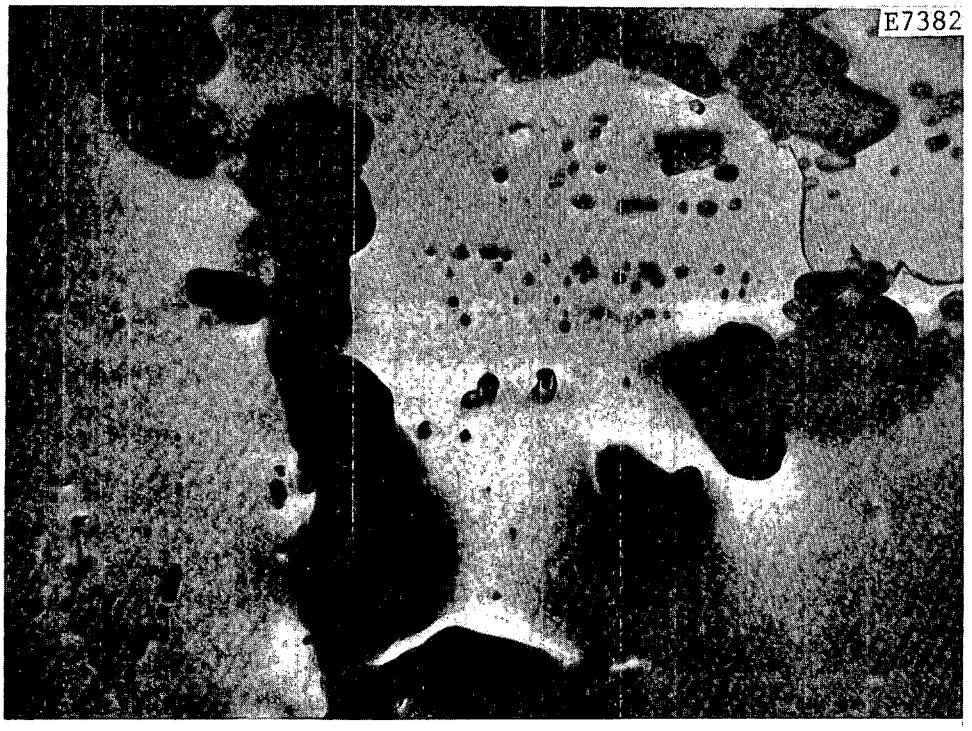

FIGURE 114. Alloy D9: 1100°C, 15 minutes, 25% CW, 750°C, 100 hours. TEM micrograph (Magn. X45,000).

Earlier work on the E-75 heat of D11 which contained 3.05 weight percent Mo had shown similar behavior[1]. After aging in the cold worked condition at 750°C for 100 hours, ~2.68 weight percent of precipitated phases were extracted and found to be predominantly Laves phase. X-ray analysis of the extracted phases from the 135 kg heat of D11 aged in the cold worked condition at 750°C for 500 hours also indicated a preponderance of Laves phase together with some TiC and eta phase, Table 31. The weight fraction was somewhat lower than in the E-75 material, 1.9% compared with 2.68%. This may be the result of the lower molybdenum content (2.47%) of the large heat material.

TABLE 31

X-RAY DIFFRACTION DATA ON EXTRACTED PRECIPITATE FROM D11, COLD WORKED 25% AND AGED 500 HOURS AT 750°C

		TiC		Laves Phase a_o = 4.748 c_o = 7.735			Eta Phase	
d (Å)	I	(hkl)	I/I_o	(hkl)	I/I_o	d (Calc., Å)	(hkl)	a_o (Calc., Å)
4.12	2			(100)		4.11		
3.87	2			(002)		3.868		
3.64	3			(011)		3.631		
3.35	4						(311)	11.11
2.819	8			(012)		2.817		
2.765	11						(400)	11.060
2.538	15						(331)	11.063
2.497	30	(111)	80					
2.375	100			(110)	50	2.374		
2.257	50						(422)	11.057
2.184	170			(013)	80	2.184		
2.164	30	(200)	100					
2.127	85						(333)	11.052
2.056	30			(200)	14	2.056		
2.024	170			(112)	100	2.023		
1.987	115			(021)	95	1.987		
1.954	20					1.954		11.053
1.933	18			(004)	20	1.934		

TiC phase intensities listed are from ASTM Card 6-0614.

Laves phase intensities listed are from ASTM Card 7-145; other line intensities were not immediately available.

Work is continuing to obtain a more complete knowledge of the extent of the Laves phase field in D9. From the point of view of mechanical properties the formation of Laves in the quantities observed so far would probably have only a small effect, providing it remained in a well dispersed blocky form. However, the main reason for concern is the observation that silicon appears to be soluble in the Laves phase. This raises the possibility of significantly depleting the matrix of an important element which is known to suppress swelling. The effect of neutron irradiation on the stability of Laves and the extent of its formation is unknown. However, experience with precipitation of other phases in nickel alloys and stainless steels suggest that phases which appear at a particular temperature during thermal aging are frequently nucleated at much lower temperatures in reactor. It has recently been reported by Korenko[2] that during neutron irradiation to a fleunce of 2×10^{22} at 510, 538 and 593°C the E-75 heat of D11 produced a copious amount of precipitation. Although swelling is low at this

fluence most of the voids appeared to be associated with precipitates. Phase identification has not yet been established, but it is evident that some improvement in phase stability is desirable. A modified version of Dll with reduced molybdenum has already been produced and has been inserted in the AA-XII experiment[2]. A series of six modified D9 alloys has now been produced which are currently undergoing preparation for insertion in the AA-VI experiment. The composition of these alloys is shown in Table 32. Alloys D9-B2, D9-B3 and D9-B4 are designed to eliminate Laves formation by reducing molybdenum. Some reduction in high temperature strength will occur as molybdenum is progressively reduced from 2.3% in D9 to zero in D9-B4. Stress rupture measurements will be used to assess this effect. In alloys D9-B5 and D9-B6, the molybdenum content is fixed at 1 weight percent and the Ti:C ratio is changed from 6:1 by weight in D9-B3 to 9:1 in D9-B5 and 12:1 in D9-B6. In D9-B5 this is accomplished by increasing titanium to 0.45 weight percent. In D9-B6 the ratio is increased by reducing the carbon level to 0.025 weight percent. The Ti:C ratio has been increased in order to promote the formation of TiC in preference to $M_{23}C_6$ which is frequently observed in massive form associated with large voids after neutron irradiation.

TABLE 32

MODIFIED D9 ALLOYS (WEIGHT PERCENT)

	Cr	Ni	Mo	Si	Mn	Ti	C	Fe
D9	14.0-14.75	14.0-15.0	2.0-2.5	0.9-1.1	1.8-2.2	.15-.30	.04-.06	Bal
D9-B2	14.5	14.5	1.5	0.9	2.0	0.30	0.05	Bal
D9-B3	14.5	14.5	1.0	0.9	2.0	0.30	0.05	Bal
D9-B4	14.5	14.5	0.0	0.9	2.0	0.30	0.05	Bal
D9-B5	14.5	14.5	1.0	0.9	2.0	0.45	0.05	Bal
D9-B6	14.5	14.5	1.0	0.9	2.0	0.30	0.025	Bal
D9-B7	14.5	14.5	1.0	0.7	2.0	0.30	0.025	Bal
Al, Nb, Ta, V, W, Cu, Zr, Co - All <.05 S - .01 Max; P - .02 Max; N - .01 Max; B - .002 Max.								

In the sixth alloy, D9-B7, the silicon level has also been reduced to improve further the stability of the alloy while still allowing it to remain in a low swelling composition regime. The alloys were made in 0.7 kg melts from high purity starting materials and melted under argon four times before drop casting into rectangular billets. Some of the problems with phase instabilities can arise directly from chemical inhomogeneities produced during processing. To overcome some of the inhomogeneity observed in earlier work on LSl and other developmental alloys a more extensive rolling and annealing sequence was adopted, Table 33. Material was retained at each stage of cold work and aged at 750°C for 100 hours to precipitate carbide and intermetallic compounds and so reveal any chemical inhomogeneities. This information will be useful in planning fabrication sequences in the future.

8.4 EXPECTED ACHIEVEMENTS IN THE NEXT REPORTING PERIOD

The six modified D9 alloys will be prepared for insertion into the AA-VI experiment. Aging studies will be completed to assess the thermal stability of these alloys. Stress rupture tests will be carried out to compare the behavior of these alloys with that of D9. An assessment will be made of the distribution of major alloying elements at various stages of processing.

TABLE 33

FABRICATION SEQUENCE FOR MODIFIED D9 ALLOYS

1.	Remelt four times and drop cast
2.	Anneal 1100°C one hour argon
	Hot roll to 6.4 mm with interpass anneals 1100°C one hour argon
3.	Chemical clean
	Anneal 1150°C one hour vacuum
4.	Reduce from 6.4 mm to 1.5 mm in five single pass reductions of 25% with interpass anneals 1100°C one-half hour vacuum
5.	Final reduction stages to give 50% cold work before final annealing treatment

N.B. for alloy D9-B5 all anneals in stages 4 and 5 are 1150°C, one-half hour.

8.5 REFERENCES

1. Rowcliffe, A. F., Sklad, P. S., and Bloom, E. E., "Development of Solid Solution Alloys," TC-160-6 (7-9/1975), p. 17.

2. Korenko, M. K., "Postirradiation Examination of Precursor Developmental Alloys," TC-160-10 (7-9/1976), p. 24.

9. SWELLING BEHAVIOR OF HT-9 IN MODIFIED HEAT TREATMENT CONDITION

F. A. Smidt, Jr.
Naval Research Laboratory

9.1 OBJECTIVE

The objective of this study is to assess the potential of commercial ferritic alloys for use as cladding or ducts in an LMFBR and to determine the optimum composition and processing parameters.

9.2 SUMMARY

The swelling resistance of HT-9 given a modified heat treatment was examined using ion irradiation with 2.8 MeV $^{56}Fe^{+}$ ions. A previous study of HT-9 showed the major portion of swelling was from voids associated with precipitates formed along grain boundaries and the modified heat treatment was designed to reduce this precipitation. The results of the swelling evaluation using TEM indicated the heat treatment was effective in reducing swelling up to about 80 dpa, after which the swelling rate was the same as for the original heat treatment.

9.3 ACCOMPLISHMENTS AND STATUS

Previous studies of the swelling behavior of ferritic alloys EM-12 and HT-9 showed the largest proportion of the swelling came from a population of large voids associated with precipitates[1]. Several modifications of the original heat treatment of HT-9 were examined to determine if a reduction in the extent of precipitation could be achieved within the normal range of heat treatments[2]. The stock material had received a heat treatment consisting of a solution anneal for 30 minutes at 1050°C/AC followed by tempering at 780°C for 2-1/2 hours which was recommended by the vendor. Tempering temperatures for the superchrome steels are selected on the basis of trade-offs between strength and toughness and commonly fall in the range 550 to 700°C when the alloy is employed in elevated temperature service. The selection of 780°C was apparently intended to provide stability of the precipitate structure under irradiation but also tends to produce an overaged structure with large precipitates (presumably $M_{23}C_6$ and M_6C) at the grain boundaries. Specimens given experimental tempering treatments at 595, 650 and 705°C for four hours were examined by transmission electron microscopy (TEM) and the intermediate treatment of 650°C for four hours was selected on the basis of the microstructures observed[2].

Specimens of HT-9 in the form of TEM disks were given a heat treatment consisting of a solution anneal at 1050°C for one hour and a temper at 650°C for four hours in a vacuum of 10^{-6} Torr. The specimens were cooled to room temperature following the solution anneal and tempering treatments by removing the furnace and permitting the samples to cool rapidly in the vacuum. The specimens were then implanted with a maximum concentration of 1 appm helium in the NRL cyclotron using a 30 MeV alpha particle beam in conjunction with an aluminum

degrader foil so as to tailor the implant profile to one half a Gaussian-shaped peak with a full width half maximum of 11.8 μm. Specimen temperature was kept below 200°C during the implant.

Ion bombardment of the specimens was performed in the NRL 5-MV Van de Graaff accelerator using a beam of 2.8 MeV $^{56}Fe^{+}$ ions using the same procedures as described for the previous irradiation of HT-9[1]. The test matrix consisted of irradiation temperatures of 500 and 550°C for doses of 40, 80, 150 and 250 dpa at a dose rate of 6×10^{-2} dpa/sec at the peak damage region in the foil. All values were calculated on the basis of a displacement energy of 40 eV, efficiency of 0.8 and use of the E-DEP-1 code. Specimens were thinned to the peak damage region using a laser interferometer to monitor removal of material from the front face and then back thinned to perforation. Specimens were examined in a JEM-200A electron microscope operating at 200 kV.

Microscopy in tempered martensitic alloys is exceedingly difficult because the magnetic specimens distort the beam, the martensitic structure is highly strained and has small grain sizes so that widely varying diffraction conditions exist in any given field of view. Stereo measurements commonly employed to measure thickness were almost impossible to apply in these specimens because of the above difficulties. The large voids present in the samples permitted an estimation of thickness that gave reasonably consistent results. A lower limit on thickness was set by the largest void completely within the foil while a maximum upper limit was set by the largest hole in the foil. A more definitive upper limit was a large void intersecting only one surface which appeared to be approximately one half in the foil so the radius equals the thickness. Visibility of small voids also proved to be a difficult problem in these specimens because of the high dislocation density and the small grains which would not permit imaging of large areas under conditions suitable for the viewing of the small voids. Fortunately the small voids contribute proportionately less to the swelling than the larger ones, so errors in swelling are small although wide variations in mean diameter and void density are evident in the statistics.

One additional problem was encountered in the experiment in that an error in the bombardment sequence at 500°C resulted in accumulation of 400 dpa in the specimen intended for 150 dpa and 0 dpa in the specimen intended for 250 dpa. This interpretation is based on the fact that no voids were observed in the "250 dpa" specimen and higher than anticipated swelling occurred in the "150 dpa" specimen. Control specimens showed no unusual recovery of microstructure and the 550°C specimens showed the expected dose dependence of swelling. Further references to the specimen in question will refer to it as the 400 dpa - 500°C specimen.

A micrograph of the thin section in the 400 dpa - 500°C specimen is shown in Figure 115. The larger voids in this section were severely truncated and possibly somewhat enlarged but the specimen is thin enough to show the dislocation structure, the presence of a few precipitates and the association of some voids with these precipitates. The precipitates do not appear to have grown appreciably during the ion bombardment. The mean diameter of the void population, void density and swelling are summarized in Table 34 and compared with the results from the previous study. Inspection of these results shows that voids of rather large sizes are observed at low doses, these voids tend to grow to doses up to 150 dpa and then new voids appear which increase the void density and may or may not decrease the mean

FIGURE 115. Micrograph of specimen of HT-9 ion bombarded to 400 dpa at 500°C showing dislocation structure precipitates and voids in a thin section of the specimen. Note the frequent association between precipitates and voids.

TABLE 34

SUMMARY OF VOID OBSERVATIONS ON HT-9

Temp., °C	dpa	$\bar{d}$ (nm)	ρ_v (cm^{-3})	$\Delta V/V$ (%)
500	40	58	1.0×10^{13}	.15
500	80	58	1.8×10^{13}	.22
500	400	154	2.7×10^{13}	7.5
550	80	70	3.3×10^{13}	.90
550	150	99	1.8×10^{13}	1.4
550	250	76	6.5×10^{13}	2.3
500*	40	92	1.9×10^{13}	1.2
500*	80	106	1.7×10^{13}	1.8
500*	150	117	3.3×10^{13}	3.7
500*	250	142	2.4×10^{13}	4.7
550*	150	76	1.7×10^{13}	0.7

* Data from previous study with aging at 780°C for 2-1/2 hours (1)

void size. The swelling increases continuously with dose as shown in Figure 116 for both the modified heat treatment at 500 and 550°C and the original heat treatment. It appears that the modified heat treatment is effective in reducing swelling up to 80 dpa but thereafter swelling occurs at approximately the same rate as observed in the stock material. Swelling is noticeably more uniform from one area of the specimen to another than in the previous experiment on stock material and standard error limits of ±30% are indicated by the error bars on the graph.

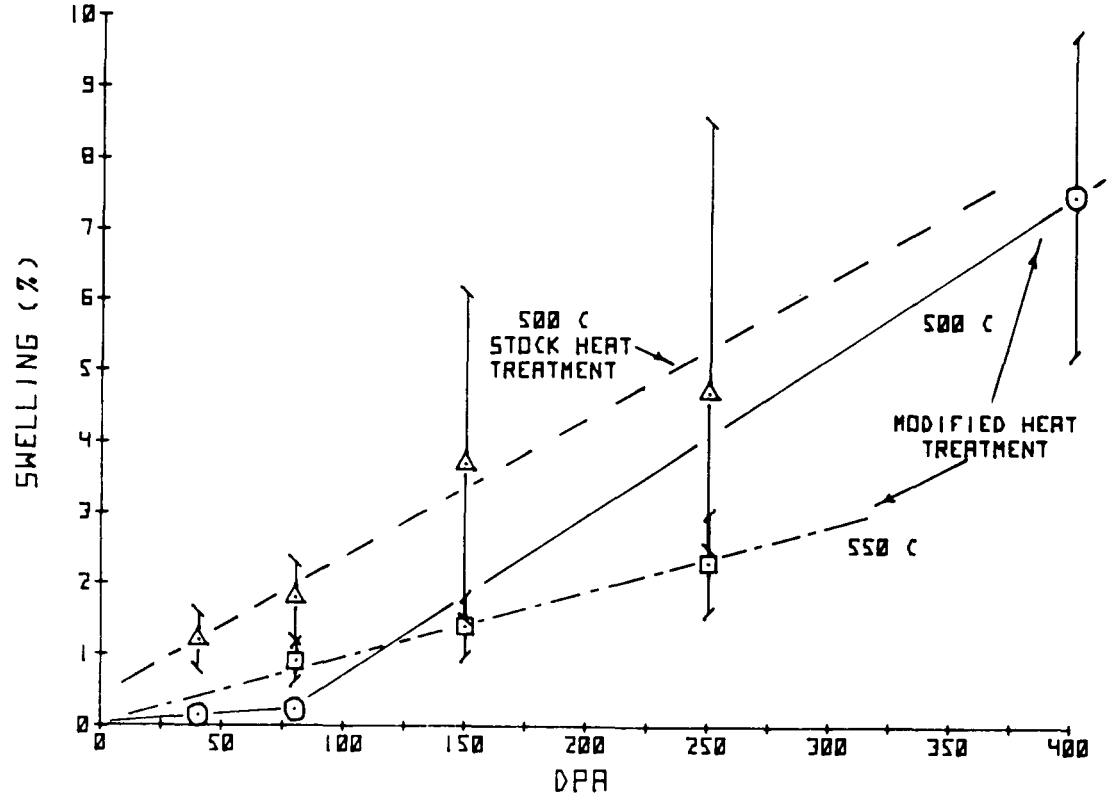

FIGURE 116. The dose dependence of swelling in HT-9 for the modified heat treatment (temper 4 hours at 650°C) is compared with the stock heat treatment (temper 2-1/2 hours at 780°C) at the peak swelling temperature of 500°C. The dose dependence of swelling at 550°C is also shown for the modified heat treatment.

It is concluded that the modification in heat treatment was partially successful in reducing precipitation and the early onset of swelling resulting from void formation in association with these precipitates. If HT-9 is selected for further study as a candidate duct alloy it would appear profitable to explore the effect of reducing the carbon content (with suitable modifications in the solution anneal temperature to avoid formation of δ ferrite).

9.4 EXPECTED ACHIEVEMENTS IN THE NEXT REPORTING PERIOD

Specimens of HT-9 irradiated in B-113 will be received from HEDL for the purpose of ion bombardment of the preconditioned specimens.

9.5 REFERENCES

1. Smidt, F. A., Jr., Malmberg, P. R., Sprague, J. A., and Westmoreland, J. E., "Swelling Behavior of Commercial Ferritic Alloys, EM-12 and HT-9 as Assessed by Ion Bombardment," TC-160-9 (4-6/1976), pp. 249-260.

2. Smidt, F. A., Jr., "Optimization of Heat Treatment of HT-9," TC-160-7 (10-12/1975), pp. 19-23.

10. OPTIMIZATION OF CANDIDATE ALLOY COMPOSITIONS

J. J. Laidler and M. K. Korenko
Hanford Engineering Development Laboratory

10.1 OBJECTIVE

The objective of this work is to provide a base of alloy performance data which can be used as guidance in optimization of developmental alloy compositions for Phase I testing in FFTF.

10.2 SUMMARY

Evaluation of the characteristics of the Series A, B and C modifications to the candidate developmental alloys is in progress, with the aim of identifying those compositional modifications which are appropriate for the first series of advanced alloy tests in FFTF. Experimentation to date has been limited to thermal aging and short-term stress-rupture tests, since these data will be relied upon for initial guidance in developing ordering specifications. The results obtained to this point suggest that minor modifications to alloys D9, D11, D21 and D25 would be beneficial to overall alloy performance, the modifications being directed primarily to improvements in phase stability.

10.3 ACCOMPLISHMENTS AND STATUS

10.3.1 Introduction

The long lead times involved in fabrication of fuel assembly components and unfueled test specimens for testing in FFTF Cycle 1 require that preparation of test materials begin in the near future. The procurement of small (250 kg) heats for production of tubing to be used in Cycle 1 MOTA and fuel tests must be initiated in June, 1977. At that time, the alloys under active consideration will be narrowed from the present sixteen candidate alloys to ten alloys showing greatest promise, these ten alloys to be known as the "leading candidate alloys." The leading candidate alloys will be processed to the point at which cladding bars are available for initiation of tube-drawing procedures. At that time, in February, 1978, a major programmatic milestone will be reached: six "prime candidate" alloys will be chosen from among the leading candidate alloys, and these six alloys will be sent through the tubing fabrication process. All six prime candidate alloys are intended for initial MOTA testing, but a further reduction of the number of alloys will take place in March, 1979, when the three "select" alloys are chosen. Initial fuel assembly tests will be limited to the select alloys.

The alloy fabrication schedule is thus such that there are two near-term requirements (in June, 1977 and February, 1978) to specify alloy compositions, and the decisions made at those times will impact the advanced alloy FFTF test program through the first six to eight reactor cycles. Those candidate commercial alloys which are selected for further investigation will be prepared according to ASME composition specifications. The

developmental alloy compositions, on the other hand, are not considered to be absolutely fixed at this time and significant performance improvements may be possible by making minor composition adjustments. To facilitate these compositional optimizations, three series (A, B and C) of modified developmental alloys have been prepared and are under test. This report describes the status of studies being conducted with modified alloys.

10.3.2 Solid Solution Alloys

The compositions of the solid solution alloys from Series A, B and C are shown in Table 35; compositions of the corresponding candidate commercial (AISI 310, 330) and developmental (D9, D11) alloys are shown for comparison.

Thermal aging studies of the candidate alloys D9 and D11 have been conducted to evaluate phase stability in these materials. Figure 117 illustrates the change in microstructure observed after aging for 1,000 hours at 700°C. The precipitate phase has been identified[1] as a Laves phase; the presence of such phases is usually considered detrimental to mechanical properties since the precipitates are incoherent and brittle. Furthermore, Laves precipitation tends to deplete the matrix of essential strengthening elements. Recent postirradiation examination[2] of the experimental alloy E75, which is only slightly richer in molybdenum than alloy D11, revealed that the Laves phase precipitates are surrounded by a shell of high-swelling matrix region. Thus, the elimination of this phase instability should improve both the mechanical properties and swelling resistance of alloys D9 and D11. Based on experience with 316 stainless steels, for which it is found[3] that increasing tendency for sigma phase formation is associated with reduced incubation period for the onset of steady-state swelling, it also appears desirable to reduce such tendencies in alloys of this class, particularly alloy D9.

Modifications to alloy D9 are included in the Series C alloy group (see Table 35), and are intended to ameliorate the D9 phase instabilities illustrated previously. The D9 Series C alloys are presently being fabricated, and aging studies will be initiated in the near future. An important adjunct to the Series C, D9 modifications is the MV-III alloy series[4], currently under irradiation in EBR-II as the AA-XI irradiation test. Long-term aging studies of the MV-III alloys are currently in progress, and the results of these studies should prove useful in setting the D9 composition.

The Series B modification to alloy D11, D11-B1, was designed to suppress Laves phase precipitation. Figure 118 shows the results of aging alloy D11-B1 for 1,000 hours at 700°C; upon comparison with the D11 aging response shown in Figure 117, it can be seen that the alloy stability has been markedly improved. The B1 modification also has a beneficial effect on mechanical properties, as indicated by short-time uniaxial creep-rupture tests. The 100 hour/650°C rupture stress of 25% cold-worked D11-B1 is 276 MPa, as compared with 245 MPa for alloy D11 (25% cold-worked) and 241 MPa for 20% cold-worked X-lot (first-core steel) 316 stainless steel. A further advantage of the D11-B1 modification is the reduced neutron absorption cross section afforded by the reduction in molybdenum content. Alloy D11-B1 is currently under irradiation in EBR-II as part of the AA-XII test.

The Series A alloy group represents wider departures from the D9 composition, and was designed to suppress sigma phase formation as well as to explore new strengthening mechanisms. Alloys MD1 through MD5, representative structures of which are shown in

TABLE 35

COMPOSITIONS* OF SOLID SOLUTION ALLOYS

Alloy Series	Designation	Fe	Ni	Cr	Mo	W	Nb	V	Si	Mn	Zr	Ti	Al	C	B
Commercial	AISI 316	Bal	13.5	17.5	2.5	-	-	-	0.6	1.75	-	-	-	0.05	<0.001
	AISI 310	Bal	21.0	25.0	-	-	-	-	-	2.0	-	-	-	0.1	-
	AISI 330	Bal	35.0	19.0	-	-	-	-	1.25	1.5	-	-	-	0.05	-
Developmental	D9	Bal	14.5	14.5	2.0	-	-	-	1.0	2.0	0.05	0.23	-	0.05	-
	D11	Bal	20.2	7.8	3.07	-	-	-	0.97	1.51	-	0.24	-	0.046	-
Series A	MD1	Bal	14.0	7.5	2.0	0.1	0.1	-	1.0	1.0	0.05	0.25	0.05	0.05	0.005
	MD2	Bal	14.0	7.5	2.0	0.1	0.9	-	1.0	1.0	0.05	0.25	0.05	0.09	0.005
	MD3	Bal	14.0	7.5	2.0	0.1	0.1	-	1.0	1.0	0.05	0.5	0.5	0.05	0.005
	MD4	Bal	14.0	7.5	2.0	0.1	0.1	-	1.0	1.0	0.05	1.0	1.0	0.05	0.005
	MD5	Bal	14.0	7.5	2.0	0.1	-	0.9	1.0	1.0	0.05	0.25	0.05	0.09	0.005
	MD6	Bal	14.0	12.0	2.0	0.1	0.1	-	1.0	1.0	0.05	0.25	0.05	0.05	0.005
	MD7	Bal	14.0	12.0	2.0	0.1	0.9	-	1.0	1.0	0.05	0.25	0.05	0.09	0.005
	MD8	Bal	14.0	12.0	2.0	0.1	0.1	-	1.0	1.0	0.05	0.5	0.5	0.05	0.005
	MD9	Bal	14.0	12.0	2.0	0.1	0.1	-	1.0	1.0	0.05	1.0	1.0	0.05	0.005
	MD10	Bal	14.0	12.0	2.0	0.1	-	0.9	1.0	1.0	0.05	0.25	0.05	0.09	0.005
Series B	D11-B1	Bal	20.0	7.5	1.5	-	-	-	0.8	1.5	0.05	0.25	-	0.05	0.005
Series C	D9-C1	Bal	15.5	13.5	1.5	-	-	-	1.0	2.0	0.05	0.23	-	0.04	-
	D9-C2	Bal	14.5	14.5	1.5	-	-	-	0.9	2.0	-	0.3	-	0.05	<0.002
	D9-C3	Bal	14.5	14.5	1.0	-	-	-	0.9	2.0	-	0.3	-	0.05	<0.002
	D9-C4	Bal	14.5	14.5	0	-	-	-	0.9	2.0	-	0.3	-	0.05	<0.002
	D9-C5	Bal	14.5	14.5	1.0	-	-	-	0.9	2.0	-	0.45	-	0.05	<0.002
	D9-C6	Bal	14.5	14.5	1.0	-	-	-	0.9	2.0	-	0.3	-	0.025	<0.002
	D9-C7	Bal	14.5	14.5	1.0	-	-	-	0.7	2.0	-	0.3	-	0.025	<0.002

*Compositions in weight percent

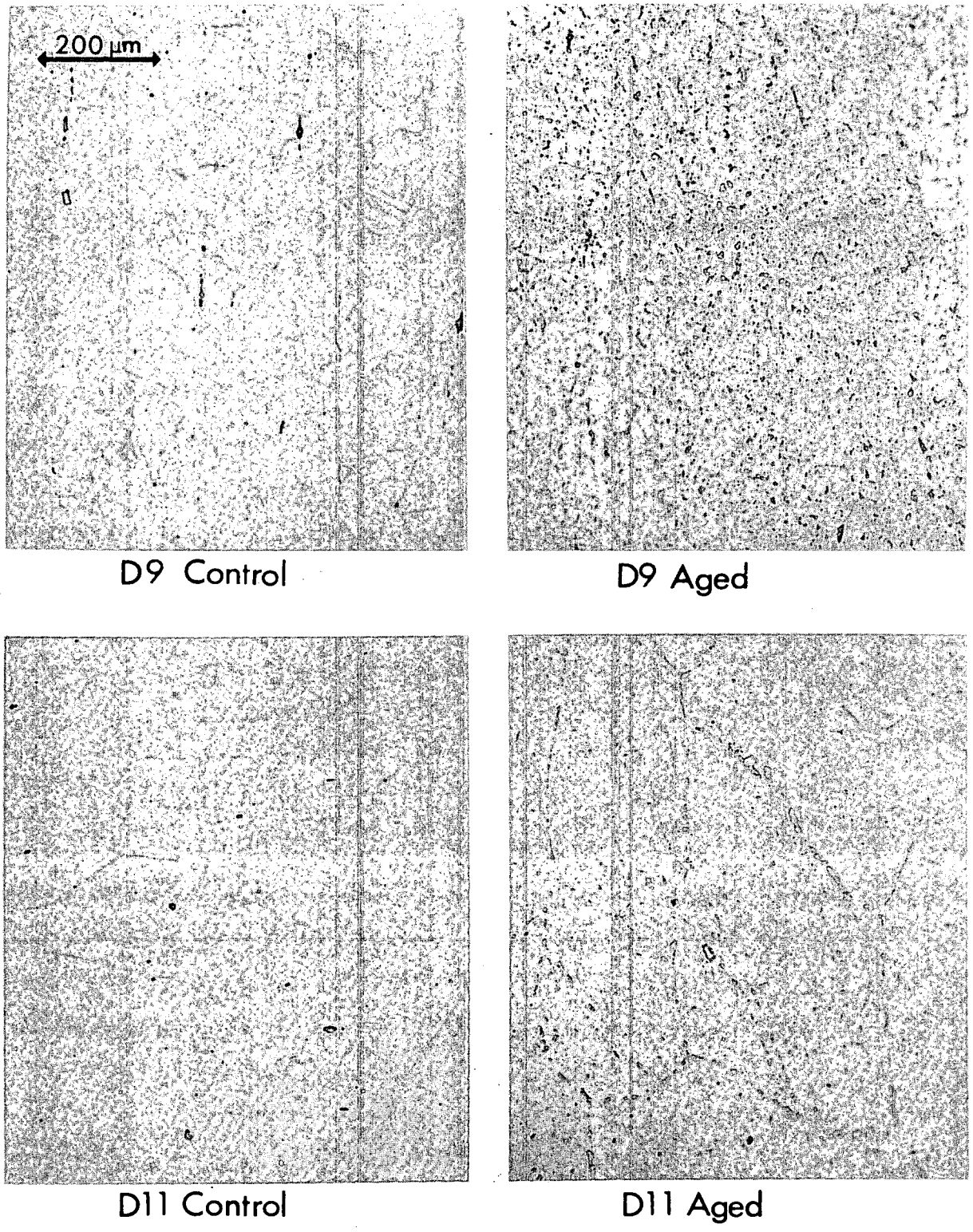

FIGURE 117. Phase stability of alloys D9 and D11 after aging 1,000 hours at 700°C.

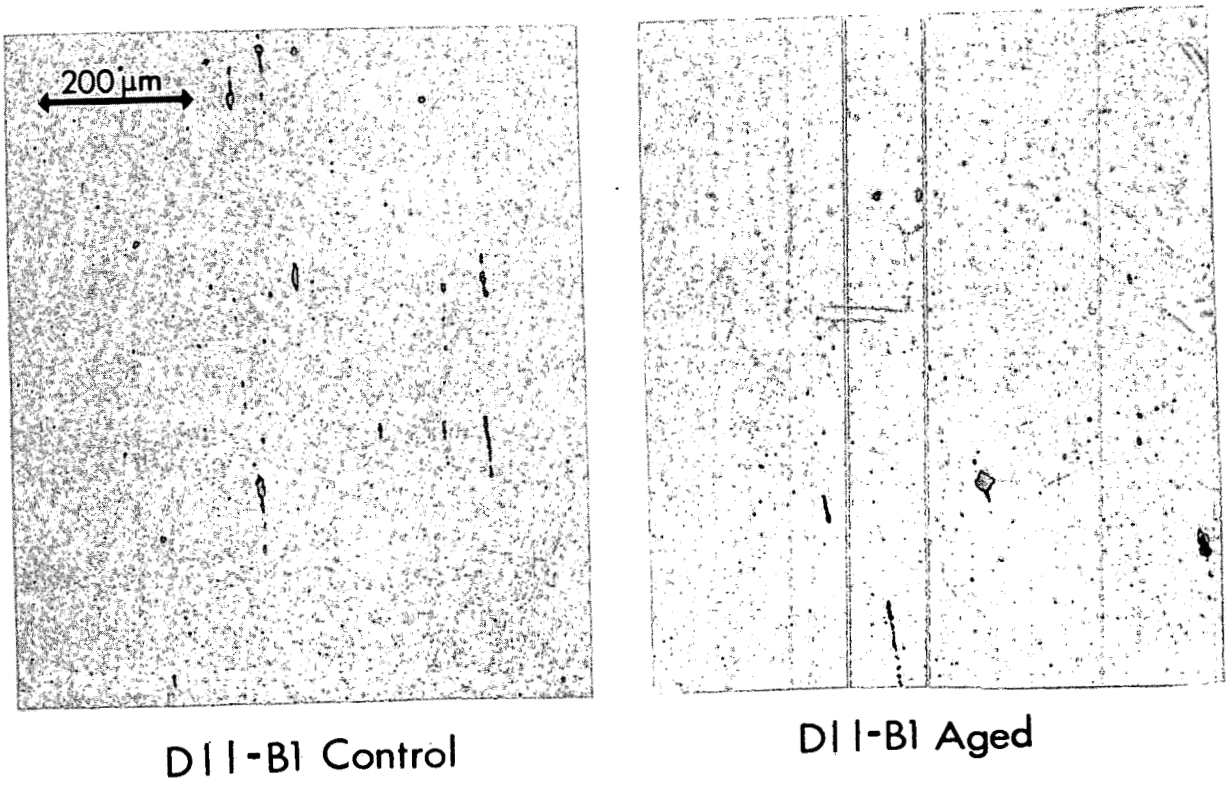

FIGURE 118. Phase stability of alloy D11-B1 after aging 1,000 hours at 700°C.

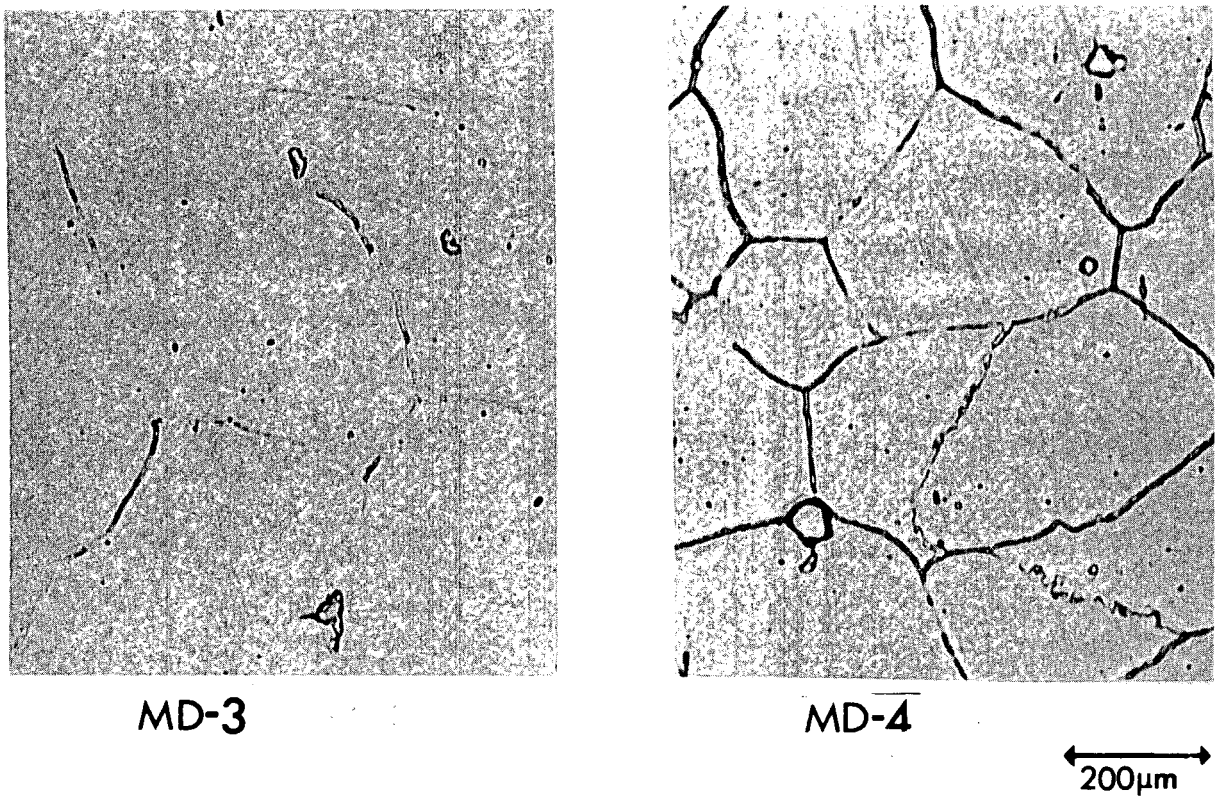

FIGURE 120. Precipitation induced by high titanium and aluminum in the low chromium-low nickel austenitic alloys.

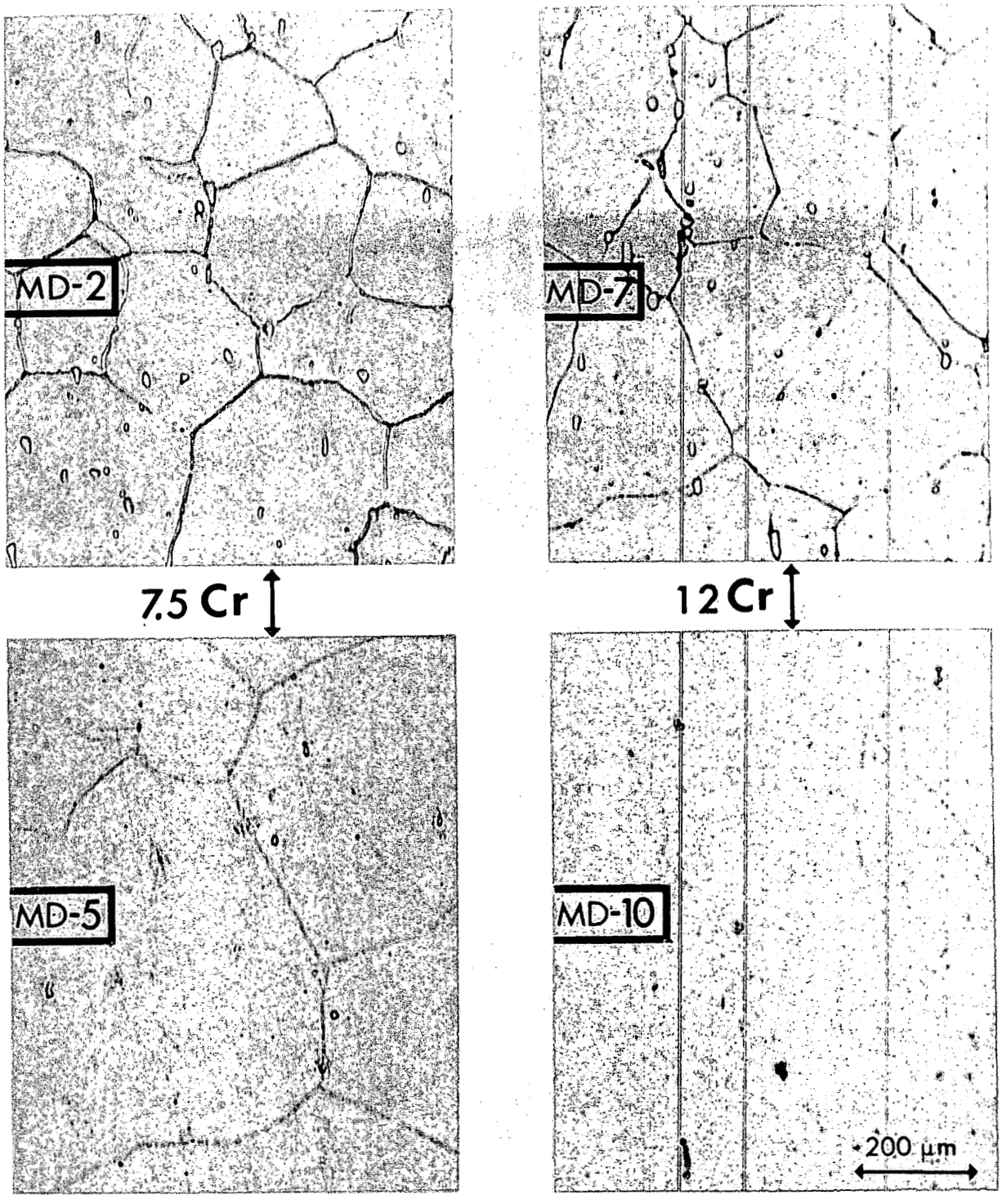

FIGURE 121. The effect of chromium content on niobium- and vanadium-related precipitation.

Alloy MD24, as illustrated in Figure 122, is an example of an attempt at niobium strengthening of a high-nickel solid solution alloy. This alloy contains a balanced distribution of solid solution strengthening agents and is potentially both swelling resistant and moderately strong. A solid solution alloy in the higher nickel range was originally thought to warrant attention, since it would be stable, low-swelling and capable of significant solution strengthening. The strength improvements necessary to offset the higher neutron absorption cross section were not attainable, however, precluding any further emphasis on such alloys.

10.3.3 γ' Strengthened Alloys

The compositions of the Series A, B and C gamma-prime strengthened alloys are shown in Table 36, with the candidate commercial (A-286, M-813, Nimonic PE16) and developmental (D21, D25, D66, D42) alloys listed for comparison.

The Series A alloys in this general class were designed with the primary purpose of determining the optimum concentrations of titanium and aluminum. The effect of increasing titanium and aluminum on the low nickel-low chromium austenitic alloys is illustrated in Figure 123. As the Ti/Al content varies from 2.0/1.0 to 3.0/1.5 to 3.0/2.5 in alloys MD11, MD12 and MD13, respectively, the grain size decreases and the amount of detrimental phase increases. Transmission electron microscopy confirmed that γ' was present in all three alloys; thus, the nickel content of this alloy class could be lowered to 20 percent and still utilize γ' strengthening. The secondary phases present were not identified quantitatively; however, subsequent work on similar alloys illustrates that the three percent molybdenum level is too high and induces Laves phase formation. The smaller intergranular precipitates appear to be β phase, based on the effects of aluminum on similar Fe-20Ni-12Cr button heats studied earlier by INCO/HEDL. The decrease in grain size is due to decreased grain boundary mobility arising from precipitate pinning. This view is supported by the irregular nature of the grain boundaries in the high (Ti+Al) alloy. Trends similar to that illustrated in Figure 122 were observed over the composition range from 20 to 30 percent nickel. Alloys with higher nickel contents, in the range of 35 to 45 percent, can tolerate much higher Ti+Al levels without phase instabilities; however, fabricability and weldability are degraded.

In general, the three percent molybdenum addition is high for this class of materials. When the molybdenum content is lowered to one percent in combination with additions of vanadium and niobium, the result is the production of large blocky carbides as illustrated in Figure 124. Thus, the effect of vanadium and niobium additions in the presence of carbon is almost identical for γ' strengthened or solid solution alloys (compare Figures 124 and 121). Electron microprobe analysis was performed on alloy D25-B5 to assess the distribution of the alloying additions. The results, summarized in Figure 125, illustrate that Fe, Ni, Cr, Mo and Al are homogeneously distributed in the matrix. The bulk of the Ti is concentrated in precipitates, presumably carbonitrides. Molybdenum tends to concentrate in the titanium-rich precipitates, while the precipitates are depleted of Fe, Ni and Cr. This behavior is similar to that observed in the solid solution alloys. The large aluminum additions had no overriding influence on the basic compound formation. There appears to be a definite reaction sequence in which the first two sets of reactions dictated by the thermodynamics[6] are oxide and carbide formation, respectively. The remaining active residual

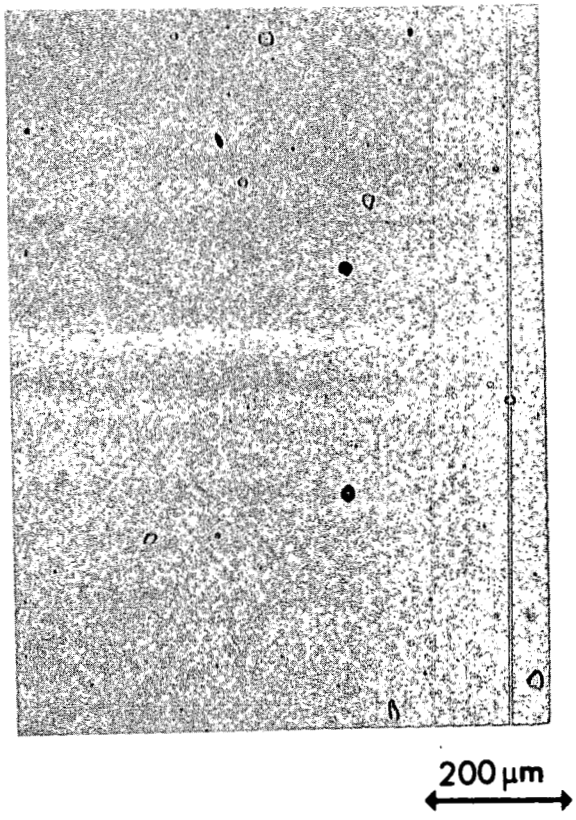

FIGURE 122. The effect of niobium additions on a high-nickel solid solution strengthened alloy, MD24.

TABLE 36

COMPOSITIONS* OF γ'-STRENGTHENED ALLOYS

Alloy Series	Designation	Fe	Ni	Cr	Mo	Si	Mn	Zr	Ti	Al	C	B	Other
Commercial	A-286	Bal	25.0	15.0	1.25	0.65	1.6	-	2.15	0.2	0.04	0.005	
	M-813	Bal	35.0	18.0	4.0	-	-	0.10	2.25	1.4	0.08	0.005	
	Nimonic PE16	Bal	43.5	16.5	3.3	0.15	0.1	-	1.2	1.2	0.05	0.010	
Developmental	D21	Bal	24.9	8.4	1.0	1.0	1.0	-	3.3	1.7	0.04	0.0005	
	D25	Bal	30.1	10.5	3.7	1.0	1.0	0.007	1.8	1.3	0.04	0.0007	
	D66	Bal	45.0	12.0	3.3	0.5	-	0.05	2.5	2.5	0.03	0.005	
	D42	Bal	60.0	15.0	5.0	0.5	-	0.03	1.5	1.5	0.03	0.01	1.5 Nb
Series A	MD11	Bal	20.0	7.5	3.0	0.5	1.0	0.05	2.0	1.0	0.05	0.005	
	MD12	Bal	20.0	7.5	3.0	0.5	1.0	0.05	3.0	1.5	0.05	0.005	
	MD13	Bal	20.0	7.5	3.0	0.5	1.0	0.05	3.0	2.5	0.05	0.005	
	MD14	Bal	25.0	7.5	3.0	0.5	1.0	0.05	3.0	1.5	0.05	0.005	
	MD15	Bal	25.0	7.5	3.0	0.5	1.0	0.05	3.0	2.0	0.05	0.005	
	MD16	Bal	25.0	7.5	3.0	0.5	1.0	0.05	3.0	2.5	0.05	0.005	
	MD17	Bal	25.0	7.5	3.0	0.5	1.0	0.05	3.0	3.0	0.05	0.005	
	MD18	Bal	25.0	7.5	1.0	0.5	1.0	0.05	3.0	1.5	0.05	0.005	0.5 V
	MD19	Bal	30.0	7.5	1.0	0.5	1.0	0.05	3.0	1.5	0.05	0.005	1.0 Nb
	MD20	Bal	30.0	7.5	1.0	0.1	1.0	0.05	2.0	1.0	0.05	0.005	0.5 V, 0.5 Nb
	MD21	Bal	35.0	10.0	3.0	0.5	1.0	0.05	2.0	1.5	0.05	0.005	
	MD22	Bal	35.0	10.0	3.0	0.5	1.0	0.05	2.5	2.0	0.05	0.005	
	MD23	Bal	35.0	10.0	3.0	0.5	1.0	0.05	3.0	2.0	0.05	0.005	
	MD24	Bal	40.0	12.0	4.0	0.5	1.0	0.05	0.2	0.1	0.05	0.005	
	MD28	Bal	45.0	12.0	3.0	0.5	-	0.05	3.0	3.0	0.03	0.005	
	MD29	Bal	45.0	12.0	3.3	0.5	-	0.05	2.5	2.5	0.03	0.005	
	MD30	Bal	45.0	12.0	3.0	0.5	-	0.05	2.5	1.6	0.03	0.005	
Series B	D21-B1	Bal	25.0	7.5	1.0	0.3	0.2	0.05	3.3	1.7	0.05	0.005	
	D21-B2	Bal	25.0	7.5	1.0	0.3	0.2	0.05	3.9	2.2	0.05	0.005	
	D21-B3	Bal	25.0	7.5	1.0	0.3	0.2	0.05	4.8	2.7	0.05	0.005	
	D25-B1	Bal	30.0	10.5	1.0	0.3	0.2	0.05	1.8	1.3	0.05	0.005	
	D25-B2	Bal	30.0	7.5	1.0	0.3	0.2	0.05	3.3	1.7	0.05	0.005	
	D25-B3	Bal	30.0	7.5	1.0	0.3	0.2	0.05	3.9	2.2	0.05	0.005	
	D25-B4	Bal	30.0	7.5	1.0	0.3	0.2	0.05	4.8	2.7	0.05	0.005	
	D25-B5	Bal	35.0	7.5	2.0	0.3	0.2	0.05	3.3	1.7	0.05	0.005	

*Compositions in weight percent

TABLE 36. COMPOSITIONS* OF γ'-STRENGTHENED ALLOYS (Continued)

Alloy Series	Designation	Fe	Ni	Cr	Mo	Si	Mn	Zr	Ti	Al	C	B	Other
Series B (Cont'd)	D66-B1	Bal	40.0	7.5	1.0	0.3	0.2	0.05	3.9	2.2	0.05	0.005	
	D66-B2	Bal	45.0	7.5	1.0	0.3	0.2	0.05	3.9	2.2	0.05	0.005	
	D66-B3	Bal	45.0	7.5	1.0	0.3	0.2	0.05	4.8	2.7	0.05	0.005	
	D66-B4	Bal	45.0	7.5	3.0	0.3	0.2	0.05	3.9	2.2	0.05	0.005	
	D66-B5	Bal	45.0	12.0	3.0	0.3	0.2	0.05	3.9	2.2	0.05	0.005	
Series C	D21-C1	Bal	25.0	7.5	1.0	1.0	0.2	0.05	3.3	1.7	0.05	0.005	
	D21-C2	Bal	25.0	7.5	1.0	-	0.2	0.05	3.3	1.7	0.05	0.005	0.2 Sc
	D21-C3	Bal	25.0	7.5	1.0	-	0.2	0.05	3.3	1.7	0.05	0.005	0.2 Y
	D21-C4	Bal	25.0	7.5	1.0	-	0.2	0.05	3.3	1.7	0.05	0.005	0.2 Hf
	D21-C5	Bal	25.0	7.5	1.0	-	0.2	0.05	3.3	1.7	0.05	0.005	0.2 La
	D21-C6	Bal	25.0	7.5	1.0	1.0	0.2	0.05	3.3	1.7	0.05	0.005	0.2 Sc
	D21-C7	Bal	25.0	7.5	1.0	1.0	0.2	0.05	3.3	1.7	0.05	0.005	0.2 Y
	D21-C8	Bal	25.0	7.5	1.0	1.0	0.2	0.05	3.3	1.7	0.05	0.005	0.2 Hf
	D21-C9	Bal	25.0	7.5	1.0	1.0	0.2	0.05	3.3	1.7	0.05	0.005	0.2 La
	D21-C10	Bal	25.0	15.0	1.25	1.0	1.6	0.05	2.15	0.8	0.04	0.005	
	D25-C1	Bal	30.0	5.0	1.0	0.3	0.2	0.05	3.9	2.2	0.05	0.005	
	D25-C2	Bal	35.0	7.5	1.0	0.3	0.2	0.05	3.9	2.2	0.05	0.005	
	D25-C3	Bal	35.0	7.5	1.0	0.3	0.2	0.05	3.3	1.7	0.05	0.005	
	D25-C4	Bal	30.0	10.5	1.0	0.7	0.2	0.05	1.8	1.3	0.05	0.005	
	D25-C5	Bal	30.0	10.5	1.0	0.3	0.2	0.05	3.3	1.7	0.05	0.005	
	D25-C6	Bal	35.0	18.0	4.0	1.0	-	0.10	2.25	1.4	0.08	0.005	
	D66-C1	Bal	40.0	7.5	1.0	0.3	0.2	0.05	3.3	1.7	0.05	0.005	
	D66-C2	Bal	45.0	7.5	1.0	0.3	0.2	0.05	3.3	1.7	0.05	0.005	
	D66-C3	Bal	45.0	10.5	3.0	0.7	0.2	0.05	3.3	1.7	0.05	0.005	
	D66-C4	Bal	40.0	10.5	2.0	0.5	0.2	0.05	3.3	1.7	0.03	0.005	
	D66-C5	Bal	43.5	16.5	3.3	1.0	0.1	0.05	1.2	1.2	0.05	0.003	
	D42-C1	Bal	60.0	15.0	5.0	0.5	0.2	0.05	1.5	1.5	0.03	0.005	1.5 Nb

*Compositions in weight percent

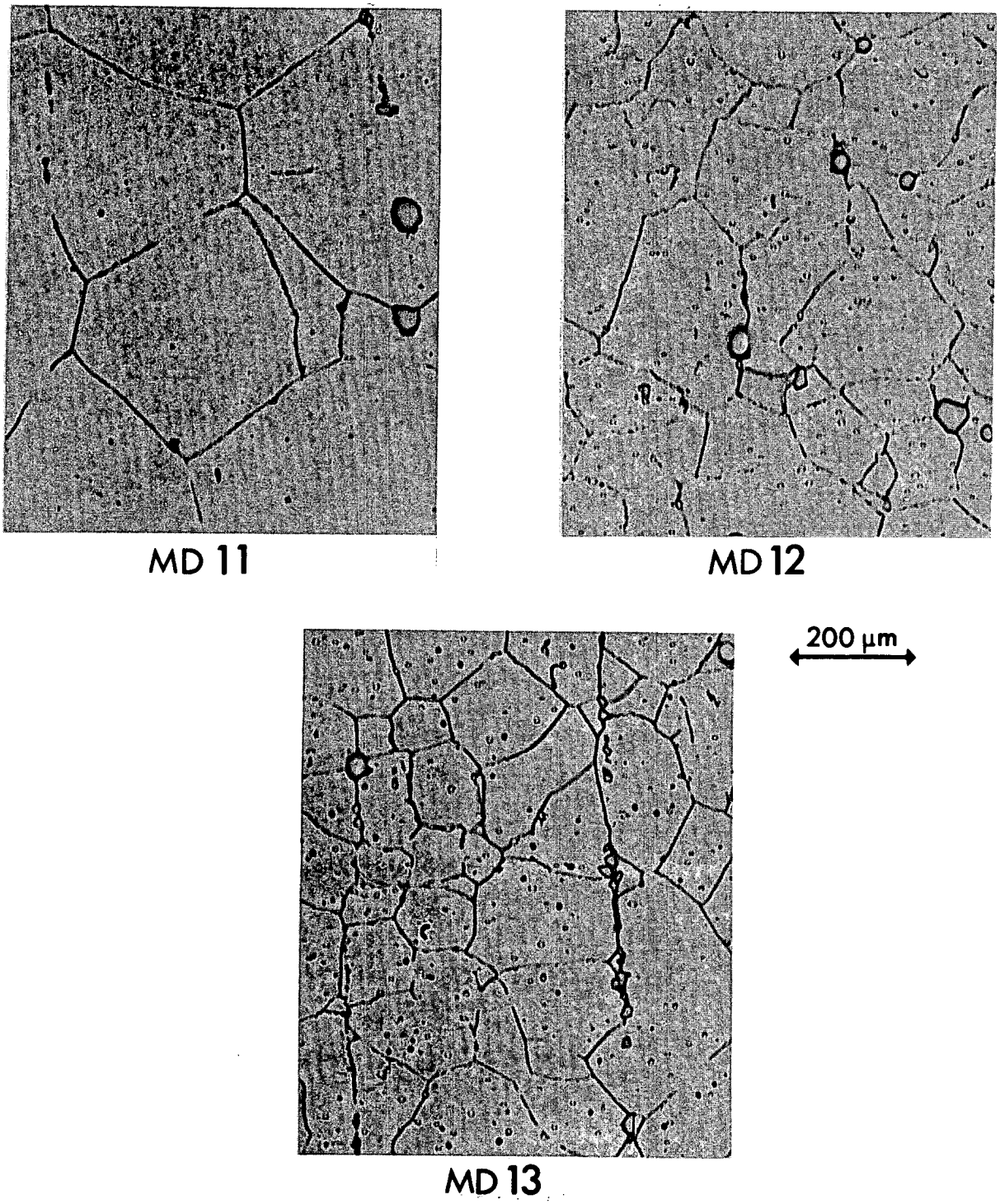

FIGURE 123. The effect of increasing the Ti+Al content in Fe-7.5Cr-20Ni alloys. Alloys MD11, MD12 and MD13 contain Ti/Al contents of 2.0/1.0, 3.0/1.5 and 3.0/2.5, respectively.

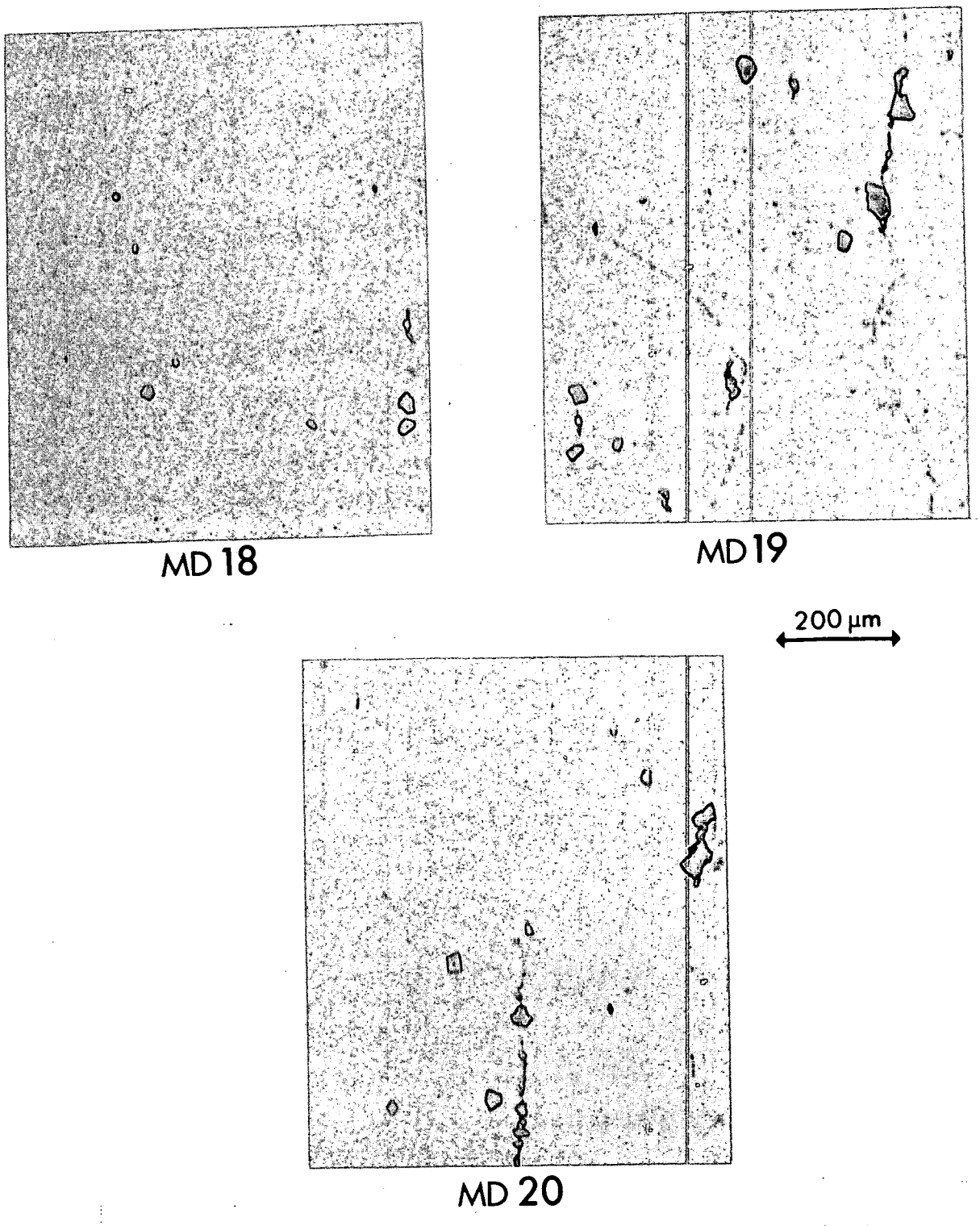

FIGURE 124. The production of vanadium and niobium carbides in γ' strengthened alloys.

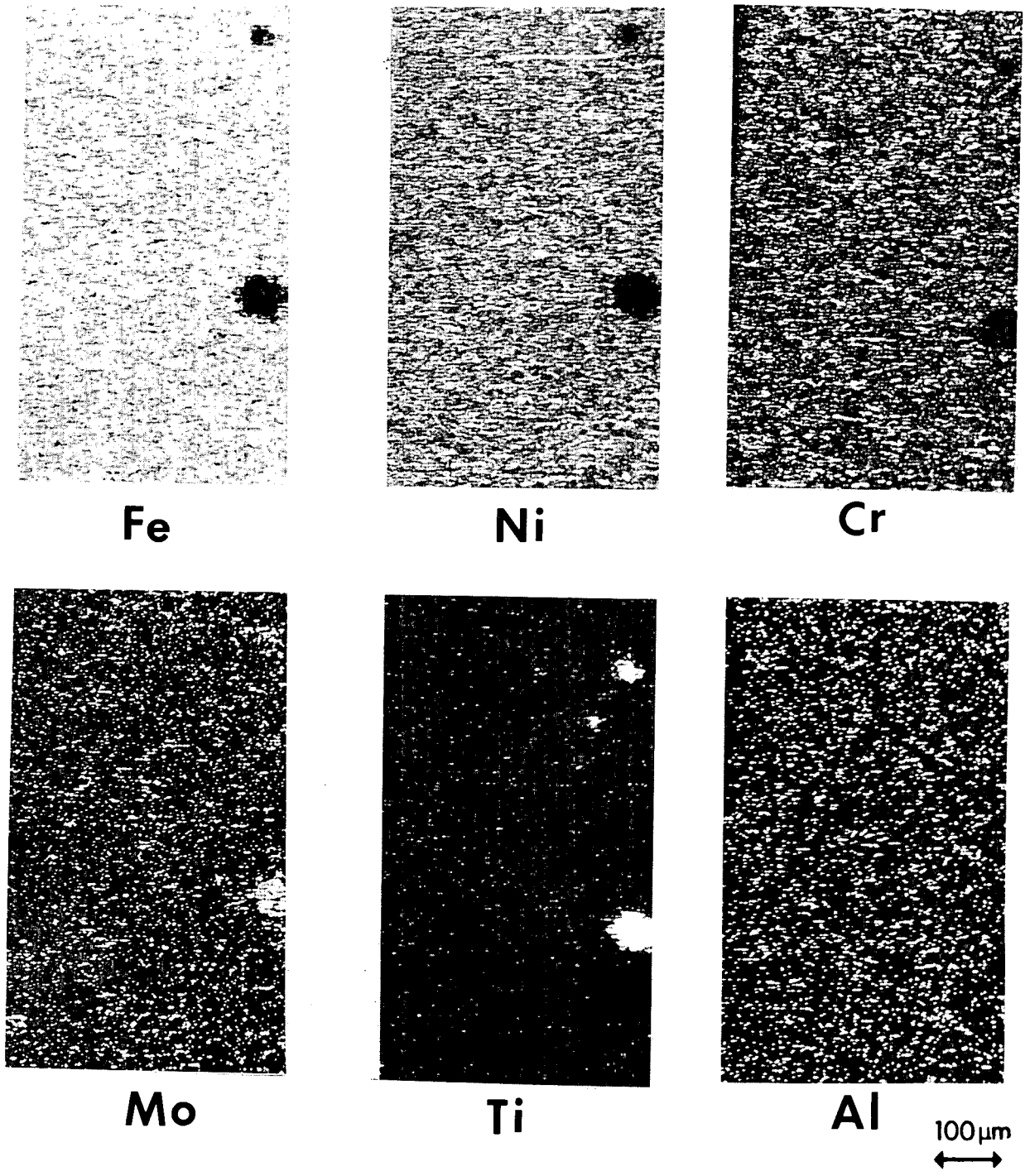

FIGURE 125. Electron microprobe scan of inclusions in γ' strengthened alloy D25-B5.

elements represent a small "unbound" fraction of the original additions. The interactions of these active elements in dynamic microcomplexes[6] and solute flows[7] are potentially very sensitive to heat-to-heat variations and processing variables. These mechanisms offer a possible explanation of the controlling factors for swelling resistance and γ' redistribution.

Although simulation experiments have shown the alloys D21, D25 and D66 to be highly resistant to swelling, all three alloys have known shortcomings which can be alleviated substantially by minor compositional modifications. Alloys D21 and D25 exhibit phase instabilities by virtue of precipitation of Laves and G phases[8], and do not possess the mechanical strength achievable within this alloy class. Fabrication and welding of alloy D66 has proven to be very difficult, due in large part to its high aluminum content. The Series B modifications to D21, D25 and D66 were designed to circumvent phase instabilities and to determine the upper limits of Ti and Al content, while the Series C versions of D66 were directed to the fabricability problem. The Series C modifications to alloy D21 include alloys intended to survey alternatives to silicon additions, in the event that silicon proves in the long run to be detrimental in some alloy performance aspects such as fuel compatibility or mass transport. Scandium, yttrium, hafnium and lanthanum additions were selected for study, since these elements are most likely to form chemically active complexes[6].

In the determination of the optimum Ti and Al levels there is a trade-off between strength and fabricability. During the production of the Series B specimens for the AA-XII reactor test, it was possible to assess the relative fabricability of a wide range of compositions. The alloys with highest (Ti+Al) content, such as D21-B3 and D25-B3, were the most difficult to roll. Alloy fabrication was possible to levels as high as 4.8 titanium and 2.7 aluminum; however, the transition from easy to difficult fabrication is between (3.3 to 3.9) Ti and (1.7 to 2.2) Al. Since tube fabrication is nominally a more difficult process than rolling, the optimum limit appears to be near 3.3 Ti and 1.7 Al. On an atom fraction basis, this is equivalent to a Ti:Al ratio of 1.09 and a (Ti+Al) content of 7.3%. This ratio is near the optimum, but this material still has a potential for strengthening by increasing the Ti to Al ratio. Materials for LMFBR applications are more restricted on the upper limit of this ratio than are superalloys for non-nuclear applications, since increasing the Ti/Al ratio leads to phase instabilities such as eta-phase precipitation during irradiation.

Phase extraction analyses and transmission microscopy confirm that the D21-B1 and D25-B2 modifications have eliminated the Laves and G phases observed in alloys D21 and D25. Alloys D21-B1 and D25-B2 contain only γ' and carbides. Figure 126 illustrates that alloy D21-B1 has the potential for development, under certain heat treatment schedules, of a cellular γ' structure which is typically nucleated at grain boundaries.

Stress rupture testing of alloys D21-B1, D21-B2, D25-B1 and D25-B2 confirmed the anticipated improvement in strength of the Series B alloys over the candidate materials D21 and D25. A 10 to 15 percent increase in 100-hour 650°C rupture strength was achieved by a combination of reduced phase instabilities and increased γ' volume fraction. The 1Mo-0.3Si-3.3Ti-1.7Al level is preferable for both the 25 and 30 percent nickel alloys. The 10.5 Cr alloy is approximately ten percent stronger than the 7.5 Cr alloy in the 30 percent nickel range. Thus, at this nickel content, the 10.5 Cr level is preferred to achieve the

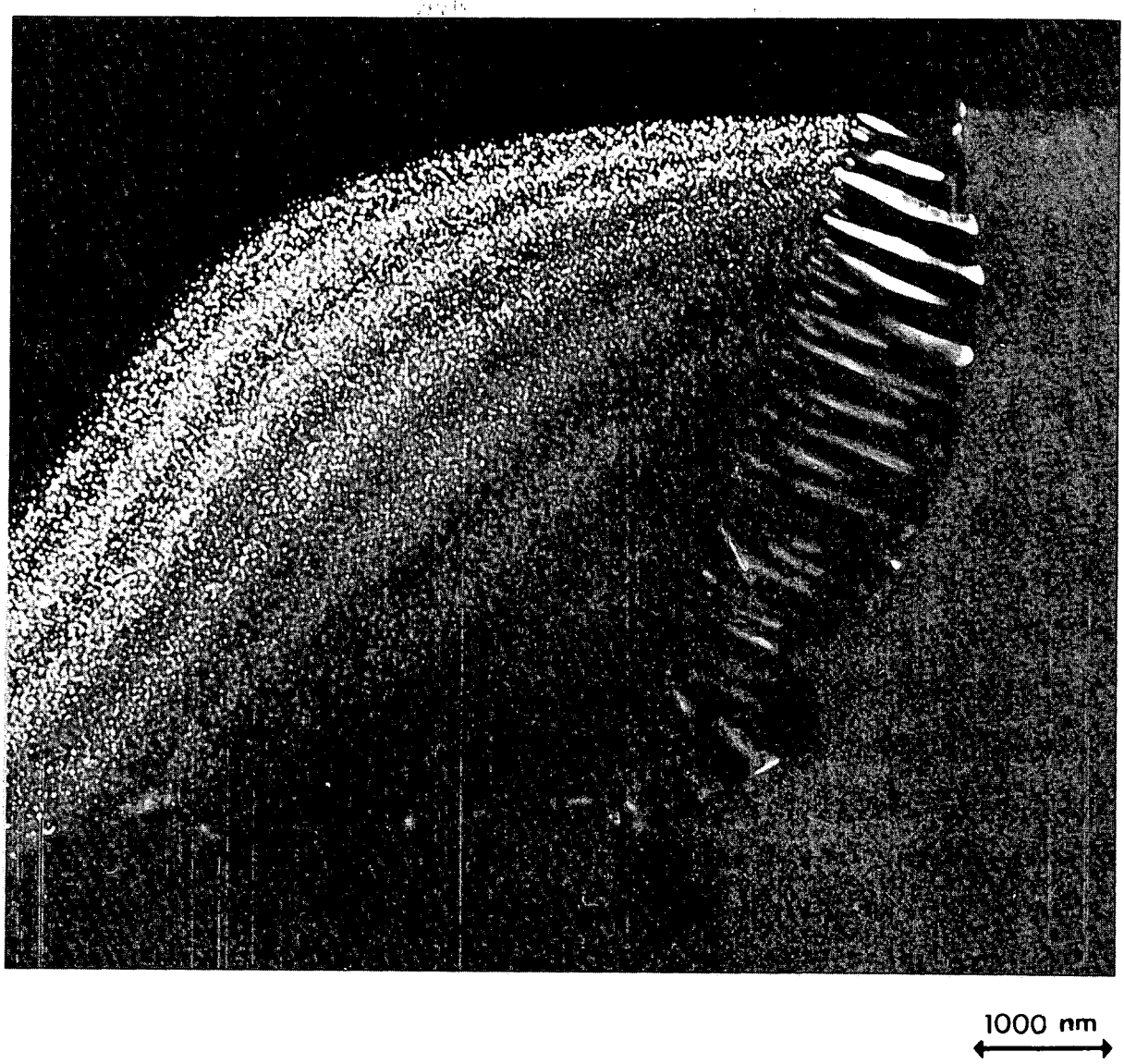

FIGURE 126. Gamma prime precipitation in alloy D21-B1.

full strength capabilities. Increasing the chromium content generally decreases the Ti and Al matrix solubilities, thereby increasing the volume fraction of the γ' strengthening phase.

The Series B alloys are presently under irradiation in the EBR-II irradiation test AA-XII. The follow-on EBR-II test containing the Series C alloys, AA-VI, is now under construction and is scheduled for Run 89 insertion.

10.3.4 γ'/γ'' Strengthened Alloys

The compositions of the Series B and C alloys of the γ'/γ'' strengthened class are shown in Table 37, together with those of the counterpart commercial (Inconel 706, Inconel 718) and developmental (D68) alloys.

Alloy D68 was selected after considerable study[9] as the candidate developmental alloy of this class of materials. The 100 hour/650°C rupture strength of alloy D68 is approximately five percent lower than that of Inconel 706, presumably because of the lower chromium content. This material, however, does swell a factor of two less than its commercial counterpart under 1 MeV electron irradiation. The microstructural behavior of alloys of this type is critically dependent upon the Nb, Ti and Al levels. For example, it is not possible to produce γ'' in these composition ranges if the alloy contains more than 0.5% aluminum. Alloy MD27, one of the first attempts at establishing the composition range for D68, exemplifies the potential for phase instability if the proper balance of alloy constituents is not maintained, as seen in Figure 127.

The developmental effort in the D68 class of alloys was continued in order to discover the lower level of nickel content for this alloy class and to design an alloy which can be treated to produce the "envelope structure". This morphology, which consists of an envelope of γ'' phase completely covering the γ' precipitates, has the advantage of an increased resistance to overaging. This structure should mitigate against degradation of in-reactor mechanical strength.

In alloy D68, the γ' phase precipitates prior to γ'', which is a necessary but not sufficient condition for the production of the envelope structure. Alloy D68-B1 was constructed to increase the time between the TTT curves for the γ' and γ'' phases by increasing the (Ti+Al)/Nb ratio. Transmission microscopy analysis of aged D68-B1 confirms that this time was increased from approximately one-half hour to 24 hours, yet the envelope structure was still not obtained. As Figure 128 reveals, however, there is a definite tendency for γ'/γ'' association in this material. Alloys D68-B3 and D68-B4 contain additions of molybdenum to increase the lattice mismatch between the austenite and the gamma prime phase. The lattice strains developed around the γ' should enhance the precipitation of the γ'' due to the tetragonality of the latter structure.

The principal drawback of the Inconel 706/D68 type of alloys is their relatively high neutron absorption cross-section. Although the high strength and low swelling of these alloys are expected to completely overshadow this disadvantage, there is still a strong incentive to reduce the neutron absorption cross-section via alloying optimization. Alloys D68-B2 and D68-B5 were designed to discover the lower limit of nickel content for this alloy class. TEM examination of the first of these alloys reveals the presence of both the γ' and γ'' phases, so the nickel content of γ'' strengthened alloys can be decreased at least to 37 percent. Stress rupture testing of D68-B2 confirms that the strength level of

TABLE 37

COMPOSITIONS* OF γ'/γ''-STRENGTHENED ALLOYS

Alloy Series	Designation	Fe	Ni	Cr	Mo	Nb	Si	Mn	Zr	Ti	Al	C	B	Other
Commercial	Inconel 706	Bal	41.5	16.0	-	2.9	0.18	0.18	-	1.75	0.2	0.03	-	
	Inconel 718	Bal	52.5	19.0	3.0	5.1	0.18	0.18	-	0.9	0.5	0.04	-	
Developmental	D68	Bal	45.0	12.0	-	3.6	0.4	0.26	0.05	1.8	0.4	0.03	0.005	
Series A	MD25	Bal	37.0	12.0	-	3.0	0.5	-	0.05	3.5	2.5	0.05	0.005	
	MD26	Bal	37.0	12.0	-	3.0	0.5	-	0.05	2.5	2.5	0.05	0.005	
	MD27	Bal	37.0	12.0	-	4.0	0.5	-	0.05	0.8	0.6	0.05	0.005	
Series B	D68-B1	Bal	45.0	12.0	-	3.0	0.3	0.2	0.05	1.6	0.5	0.03	0.005	
Series C	D68-C1	Bal	37.0	12.0	-	2.9	0.3	0.2	0.05	1.75	0.3	0.03	0.005	
	D68-C2	Bal	37.0	12.0	2.0	2.9	0.5	0.2	0.05	1.75	0.3	0.03	0.005	
	D68-C3	Bal	45.0	12.0	3.0	3.0	0.5	0.2	0.05	1.6	0.5	0.03	0.005	
	D68-C4	Bal	34.0	12.0	-	2.9	0.5	0.2	0.05	1.7	0.3	0.03	0.005	
	D68-C5	Bal	39.0	16.0	-	2.9	0.45	0.2	0.05	1.75	0.2	0.03	0.005	

*Compositions in weight percent

FIGURE 127. Phase instability observed in alloy MD27.

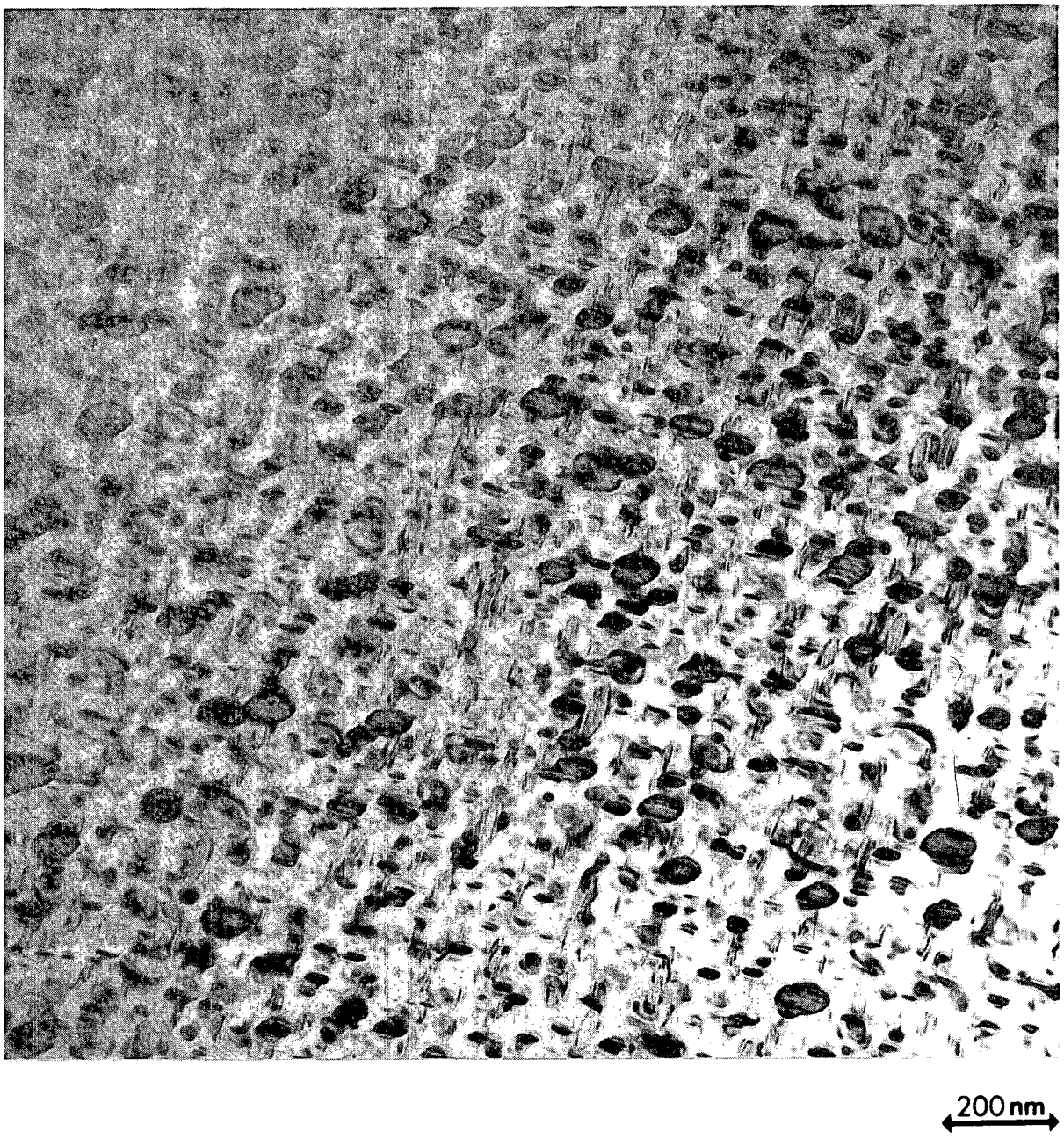

FIGURE 128. Bright field image of γ' and γ'' in D68-B2.

this alloy is identical to that of the candidate alloy D68; i.e., a 650°C/100 hour rupture stress of 586 MPa. These recent data were incorporated in the modified version of the Nb, Ti, Al and Mo range figure for the γ'/γ'' strengthened alloys shown in Figure 129. The 34 percent nickel alloy, D68-B5, will be investigated during the next reporting period.

Decreasing the nickel content also spreads the γ' and γ'' TTT curves in alloy D68-B1. Because of this increased TTT separation, the 37 percent nickel content may prove to be an ideal level for molybdenum additions to increase the γ/γ' mismatch and thereby enhance the envelope structure formation. Alloy D68-B3 will be examined to assess the feasibility of this concept.

All the intermediate nickel alloys employing γ'/γ'' strengthening are expected to be prone to transformation to delta or eta phases at temperatures in the range of 750 to 950°C. These phases usually nucleate in the grain boundaries, but nucleation at carbide precipitates (as shown in Figure 130) is also common. The thermomechanical treatment employed for D68 and Inconel 706 was designed to precipitate delta in the grain boundaries. This retards grain boundary sliding and increases the rupture strength. Recent postirradiation examination of Inconel 718 reveals that the γ' and γ'' are stable phases and do not decompose during irradiation in the presence of delta phase.

10.3.5 Conclusions

The specification of alloy compositions for ordering quantities of prime candidate alloy tubing for Cycle 1 FFTF testing is subject to certain basic constraints, primary among these being that the composition specified not be greatly different from that of the initial candidate alloy composition. This is intended to ensure that there will be no unexpected deviation of alloy properties from those determined through the EBR-II irradiation testing phase. Potential alloy improvements identified in this and similar investigations will be exploited to an extent consistent with the programmatic constraints. Modifications which fall outside these bounds must be de-emphasized in the near term and re-evaluated at a later stage in the program when further data are available and the opportunity exists for further improvements to the primary alloy(s) and possible backup alloys.

Specific conclusions pertaining to near-term alloy modifications are as follows:

1. A reduction in the molybdenum content of alloy D11 leads to improved phase stability and enhanced stress-rupture properties. The D11-B1 modification represents a desirable adjustment to the composition of this candidate alloy.

2. Gamma-prime precipitation strengthening of alloy D9 does not appear feasible, and further small additions of titanium and aluminum are expected to be deleterious to the swelling resistance of this alloy.

3. The optimum titanium and aluminum concentrations for both alloys D21 and D25 are approximately 3.3 Ti and 1.7 Al. These concentrations afford the proper balance between strength and ductility and do not lead to phase instabilities. Those phase instabilities which have been observed in D21 and D25 appear to be correctable by reductions in molybdenum and/or silicon content. Slight increases in chromium content also are expected to be beneficial.

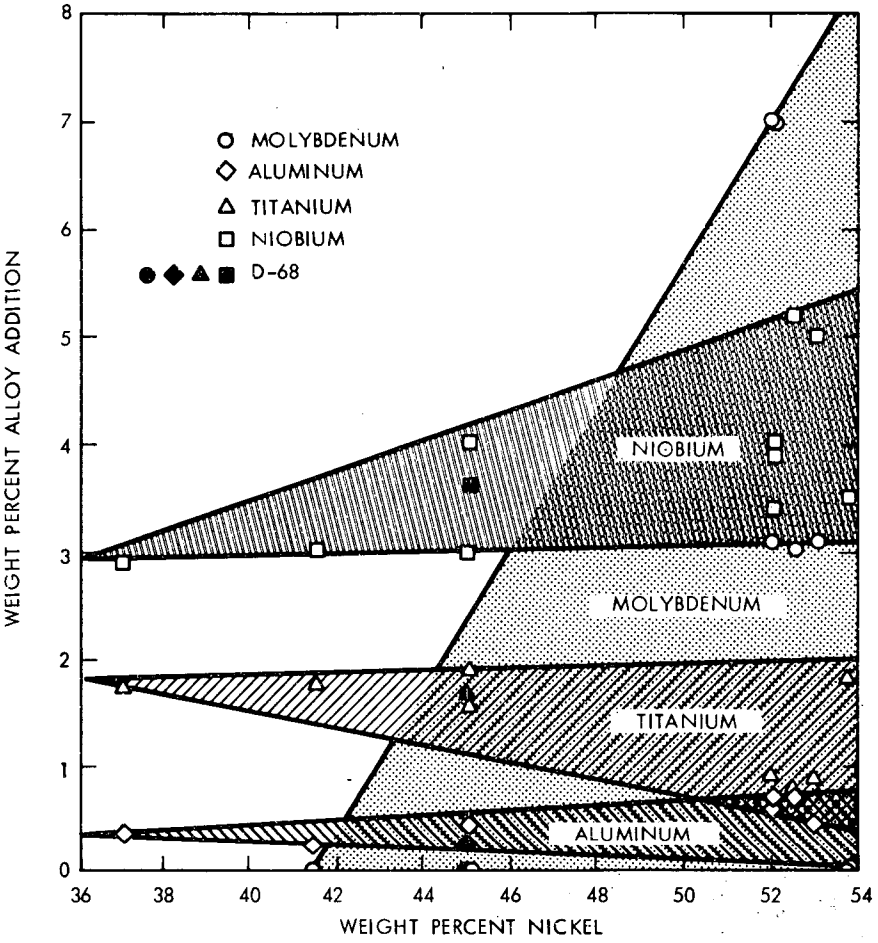

FIGURE 129. The expanded composition range of the γ'/γ'' strengthened alloys based on the new data from the Series B and C alloys. Shaded areas indicate allowed compositions.

FIGURE 130. Delta phase precipitation on carbides in the γ'/γ" class of alloys.

Further conclusions can be drawn regarding the more long-term developmental effort:

1. The nickel content of γ'/γ'' strengthened alloys such as D68 can be lowered to 37% without degradation of mechanical properties. The combination of reduced nickel content and increased (Ti+Al):Nb ratio may make it possible to achieve the desired envelope precipitate structure.

2. The fabricability of alloy D66 should be substantially improved by increasing the titanium content and decreasing aluminum.

10.4 EXPECTED ACHIEVEMENTS IN THE NEXT REPORTING PERIOD

To facilitate the June 1977 selection of the leading candidate alloys, there must be an intensive effort over the next two reporting periods to define the optimum compositions. This includes the postirradiation examination of the candidate alloys from the AA-I and AA-VII reactor tests, phase stability tests, limited creep rupture testing and charged-particle irradiations of the most promising modified alloys.

10.5 REFERENCES

1. Alloy Development Program Monthly Status Letter, November, 1976, TC-124-30, p. 5.

2. Korenko, M. K., Alloy Development Program Quarterly Technical Progress Letter, TC-160-10 (7-9/1976), p. 24.

3. Caplinger, W. H., Alloy Development Program Quarterly Technical Progress Letter, TC-160-8 (1-3/1976), p. 134.

4. Revision 5 Swelling Equation, Nuclear Systems Materials Handbook; also see Shiels, S. A., and Bagnall, C., Alloy Development Program Quarterly Technical Progress Letter, TC-160-8 (1-3/1976), p. 270.

5. Cummings, W. V., Korenko, M. K., Powell, R. W., and Thomas, L. E., Alloy Development Program Quarterly Technical Progress Letter, TC-160-11 (10-12/1976).

6. Korenko, M. K., Alloy Development Program Quarterly Technical Progress Letter, TC-160-6 (7-9/1975), p. 114.

7. Johnson, R. A., and Lam, N. Q., Phys. Rev. B, 13 (May, 1976), p. 4364.

8. Kossowsky, R., and Bajaj, R., Alloy Development Program Quarterly Technical Progress Letter, TC-160-8 (1-3/1976), p. 119.

9. Merrick, H. F., and Korenko, M. K., Alloy Development Program Quarterly Technical Progress Letter, TC-160-6 (7-9/1975), p. 53.

CHAPTER II.

ANALYTICAL STUDIES

I. THEORY OF PARTICLE REDISTRIBUTION IN AN IRRADIATION ENVIRONMENT

M. Baron, A. Chang and M. L. Bleiberg
Westinghouse Advanced Reactors Division

1.1 OBJECTIVE

The objective of this work is to develop analytical methods for treating the behavior of precipitation-strengthened alloys under irradiation.

1.2 SUMMARY

A new theory of particle redistribution in an irradiation environment is proposed based on the physical ideas of Nelson et al. The theory is a natural extension of the L-S-W approach to thermal coarsening.

An equation governing the kinetic evolution of the particle size distribution is derived. It is solved for the equilibrium (i.e., displacement dose independent) distribution and together with the conservation of solute, provides a theoretical characterization of the equilibrium state. It is shown that due to solute resolution, the equilibrium state is characterized by the existence of a maximum stable radius and an amount of solute in dynamic solution which is in excess of the equilibrium thermal concentration for the irradiation temperature. The equilibrium distribution has a universal form independent of the initial aging treatment. It is shown that in order to simulate the kinetics of particle redistribution of neutron irradiated materials at temperatures above 575°C, simulation experiments should be carried out at lower temperatures than the neutron irradiation temperature.

The kinetics of the maximum particle size are discussed and it is shown that the relaxation to the equilibrium value is exponential with displacement dose. The asymptotic form of the time dependent particle size distribution is discussed using the dynamic scaling hypothesis. It is proven that for such doses for which dynamic scaling holds, the relaxation kinetics of the average particle size to the equilibrium value is also exponential with total displacement dose.

1.3 ACCOMPLISHMENTS AND STATUS

1.3.1 Introduction

The stability of strengthening phases in an irradiation environment is an important consideration in the development of alloys for use in LMFBRs. It is well known[1] that when excess interstitials and vacancies are introduced by irradiation the diffusion of solute is enhanced. As a consequence, precipitation reactions as well as the redistribution of equilibrium phases can be considerably accelerated. The nucleation and growth of particles of minor phases during irradiation can lead to depletion of swelling inhibitors[2] from solid solution causing excessive accelerated swelling. Furthermore, massive coarsening of precipitates would lead to deterioration of mechanical properties[3].

It is important to note that the data base documenting the effect of high fluence fast neutron exposure on precipitation and redistribution of phases in structural materials is limited. Thus simulation of neutron damage by heavy charged particle bombardment of structural materials is often employed. For the simulation experiments to be a useful guide to the effects of neutron irradiation, the precipitate morphologies obtained in the respective irradiation environments must be correlated. This correlation is obtained by using particle size distributions and related quantities as a quantitative measure of irradiation effects.

As an aid for interpretation of experiments it is useful to have a kinetic theory describing the temporal evolution of particle size distributions and related quantities such as particle concentration, average radius and volume fraction of precipitate. The purpose of this report is to provide such a theory and to illustrate its usefulness by applying it to the case of in-reactor exposure of alloys strengthened by γ' precipitates.

1.3.2 Mathematical Formulation

1.3.2.1 Diffusion Coefficient for Solute. In an irradiation environment the diffusion coefficient of solute may be defined as

$$\tilde{D}_s = D_v C_v + D_i C_i \qquad [1]$$

where D_v and D_i are the vacancy and interstitial diffusion coefficients and C_v and C_i are the steady state vacancy and interstitial concentrations. Equation [1] requires that solute be able to migrate through the lattice both by interstitial as well as by vacancy mechanisms.

Under most irradiation conditions the build-up time toward steady state with respect to interstitial and vacancy concentrations is short compared to the time of the experiment. Thus the steady state vacancy and interstitial concentrations may be calculated by solving the two rate equations[4]

$$k_v^2 D_v C_v + \alpha C_v C_i - K_v^{eff} = 0 \qquad [2]$$

$$k_i^2 D_i C_i + \alpha C_v C_i - K_i^{eff} = 0 \qquad [3]$$

where α is the recombination rate K_v^{eff}, K_i^{eff} are the effective defect production rates for interstitials and vacancies respectively allowing for correlated I-V recombination following collapse of a cascade. Note that at a temperature at which the sinks present in the system, namely dislocations, precipitates and voids can emit vacancies the effective production rate of vacancies differs from that of interstitials.

Also contributing to the difference between K_v^{eff} and K_i^{eff} is the fact that cascade collapse leads to a transient nucleation of vacancy loops[5] which modifies the effective production rate of mobile vacancies capable of annihilation at other sinks. Furthermore K_i^{eff} may differ from K_v^{eff} because of interstitial and or vacancy binding at impurities. The quantities k_v^2 and k_i^2 are the total sink strengths determined by the action of all the sinks present in the system and are defined as in Reference 5.

Solution of Equations [2] and [3] and substitution into Equation [1] yields the following expression for the diffusion coefficient of solute

$$\tilde{D}_s = \left(\frac{K_v^{eff}}{k_v^2} + \frac{K_i^{eff}}{k_i^2}\right) \Phi\ (\eta,\delta,\varepsilon) \qquad [4]$$

where the recombination function $\Phi(\eta,\delta,\varepsilon)$ is defined as

$$\Phi(\eta,\delta,\varepsilon) = \frac{2}{2\varepsilon(1+\delta)+1}\ \frac{1}{\eta}\ \{[(1+\varepsilon\eta)^2+\eta]^{1/2} - 1 + \delta\varepsilon\eta\} \qquad [5]$$

and

$$\eta = \frac{4\alpha K_i^{eff}}{D_i D_v k_i^2 k_v^2} \qquad \varepsilon = \frac{K_v^{eff} - K_i^{eff}}{4K_i^{eff}} \qquad \delta = \frac{k_i^2 - k_v^2}{k_i^2 + k_v^2} \qquad [6]$$

The function $\Phi(\eta,\delta,\varepsilon)$ is plotted in Figure 131(a) and 131(b) for a range of η values and for selected values of δ and ε. In Figures 132(a) and 132(b) the diffusion coefficient of solute is plotted at several temperatures as a function of sink strength for dose rates characteristic of heavy ion and neutron irradiations. Using the data shown in Figures 131(a), 131(b), 132(a) and 132(b) and the values of D_v and α/D, shown in Table 38, Arrhenius plots of D_s were constructed from Equation [4]. These are displayed in Figures 133(a) and 133(b). Also shown in Figures 133(a) and 133(b) is a plot of the thermal diffusion coefficient of solute in austenitic Fe-Cr-Ni alloys using Q = 2.9 eV and a pre-exponential factor of 0.37 cm^2/sec[14]. These figures show the relative radiation enhancement of the diffusion coefficient for typical neutron and Ni-ion irradiation conditions. As an important application of Equation [4] the temperature shift for ion and neutron irradiations which is necessary for simulation of precipitate behavior is calculated in Section 1.3.4.3 below.

1.3.2.2 Kinetic Equations for Particle Size Distribution Function. A statistical assembly of spherical particles having a range of sizes can be described by the probability density function f(R,t). This function is defined such that f(R,t)dR is the number of particles per unit volume having radii between R and R+dR at time t. If f(R,t) can be predicted, various observable quantities can be calculated. For example

$$N_p = \int_0^\infty f(R,t)dR$$

$$\bar{R} = \frac{\int_0^\infty R\ f(R,t)dR}{\int_0^\infty f(R,t)dR} \qquad [7]$$

$$\Delta V/V = \frac{4\pi}{3} \int_0^\infty R^3 f(R,t)dR$$

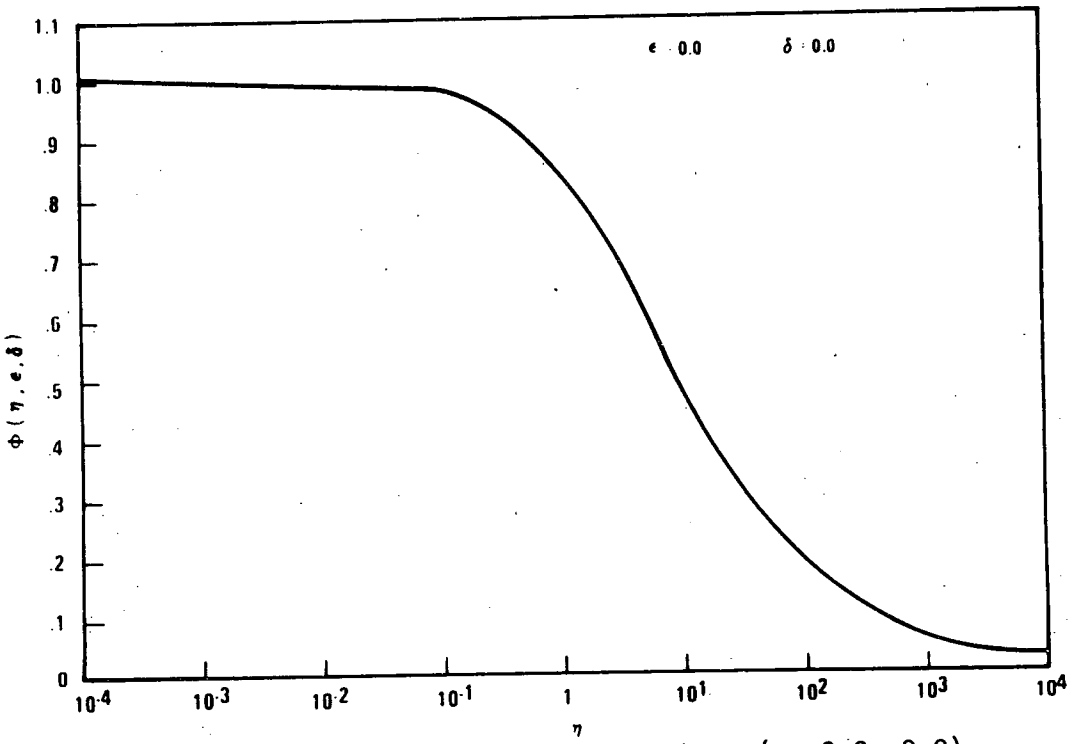

FIGURE 131(a). The recombination function $\Phi(\eta, 0.0, 0.0)$.

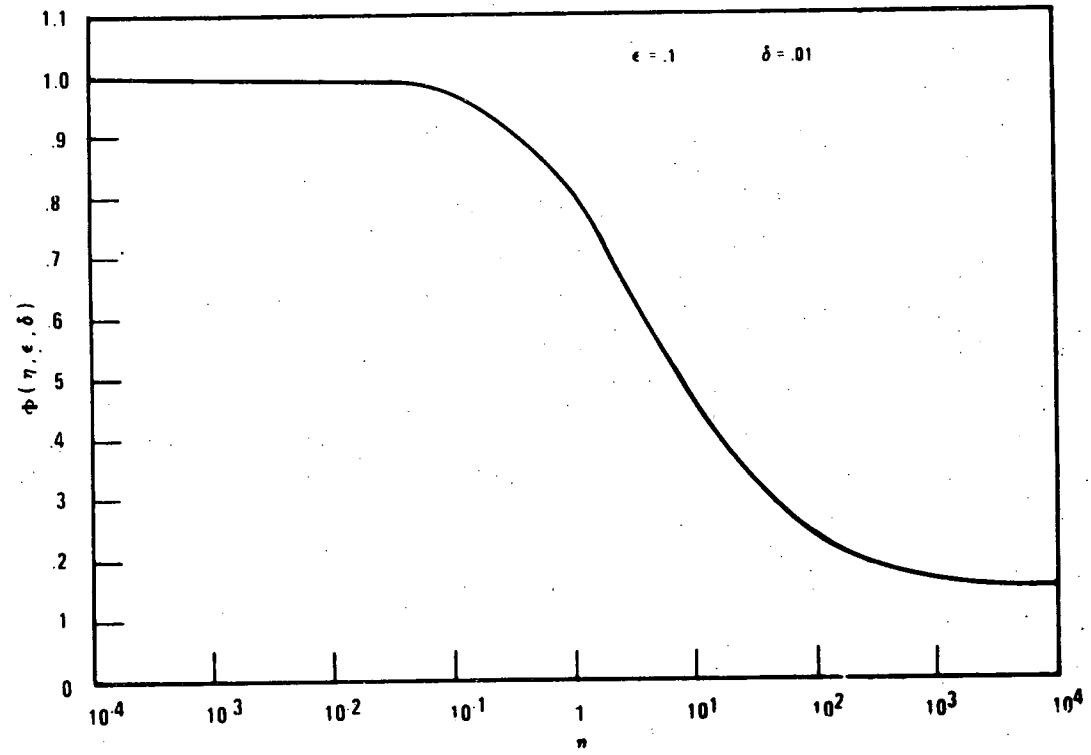

FIGURE 131(b). The recombination function $\Phi(\eta, .01, .1)$.

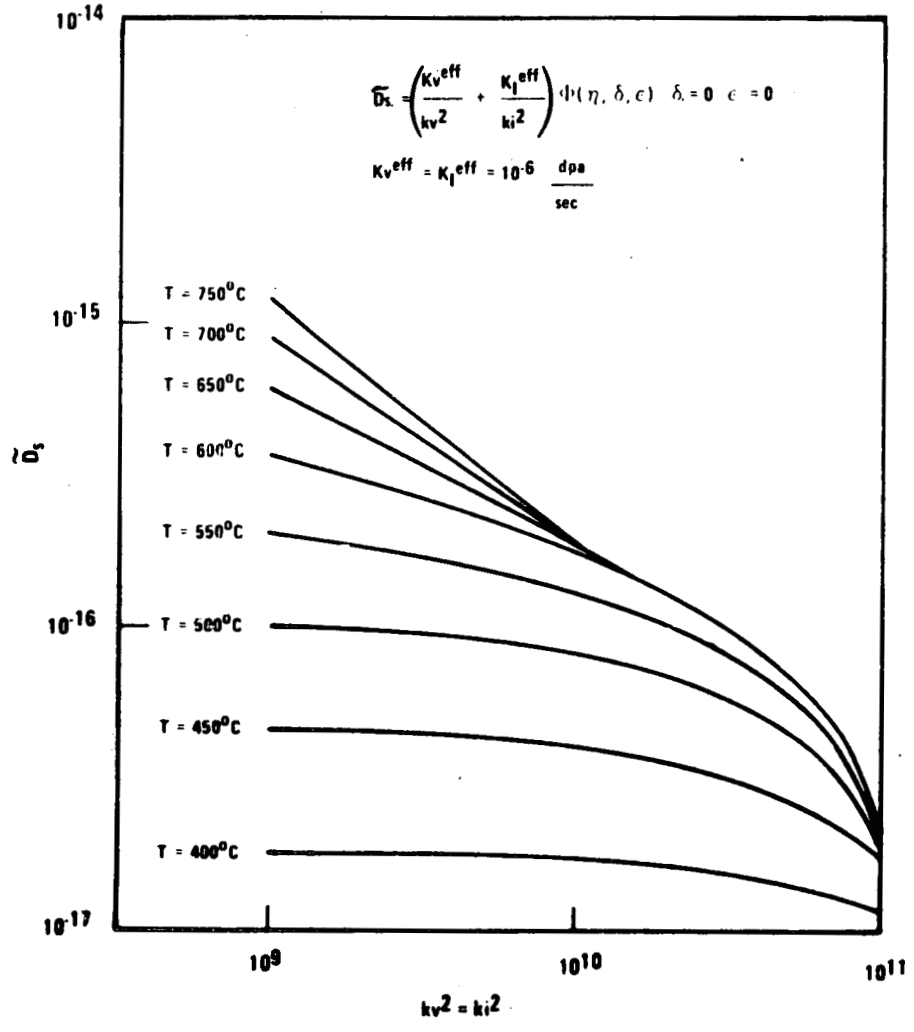

FIGURE 132(a). The diffusion coefficient of solute as a function of sink strength and temperature for a dose rate characteristic of neutron irradiations.

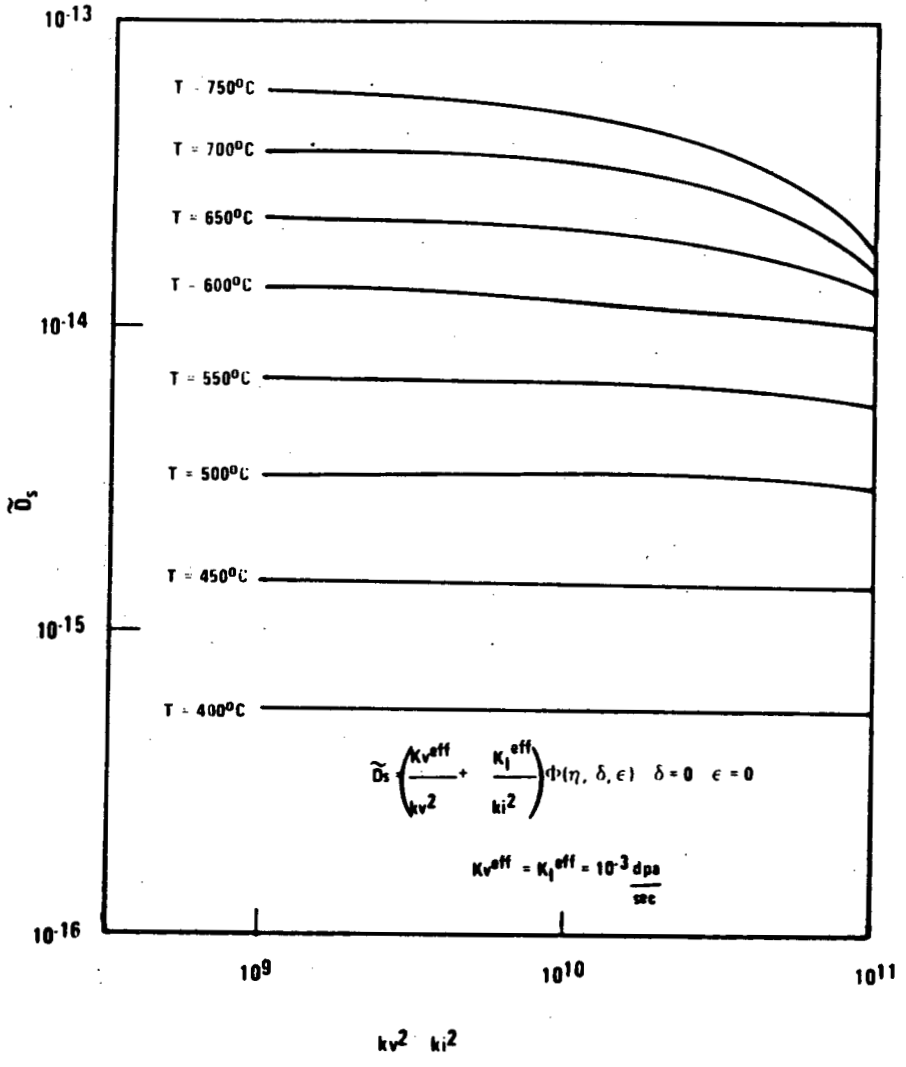

FIGURE 132(b). The diffusion coefficient of solute as a function of sink strength and temperature for a dose rate characteristic of Ni-ion irradiations.

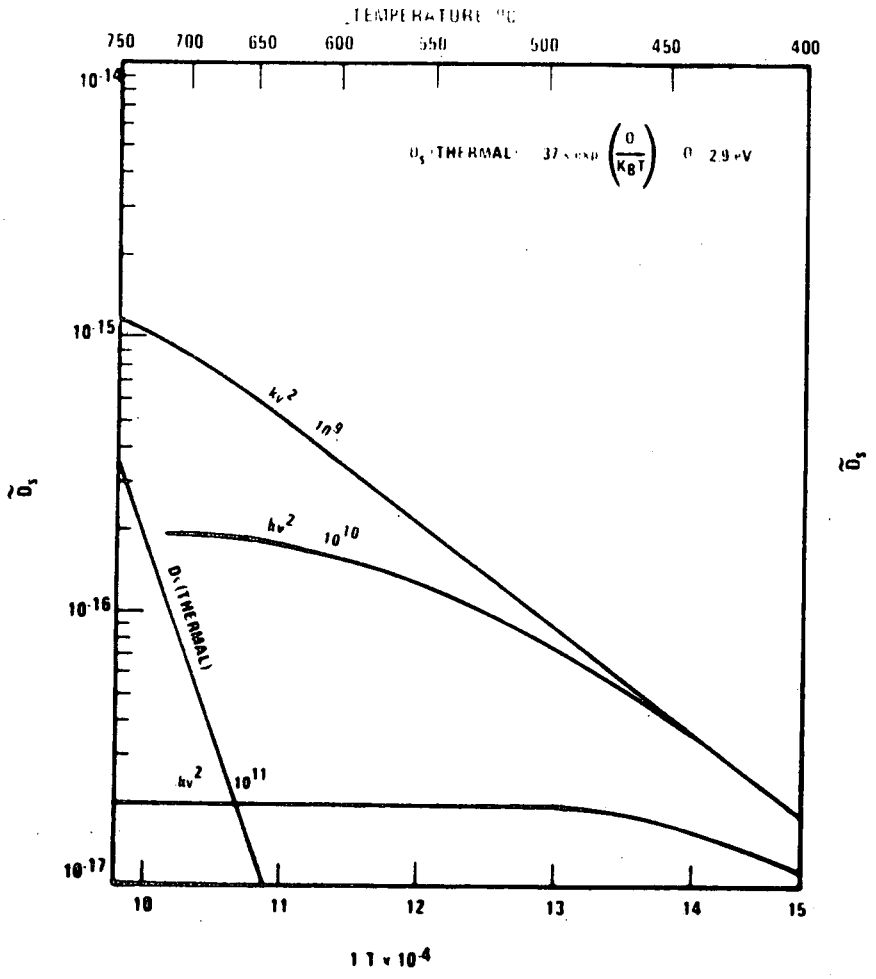

FIGURE 133(a). Arrhenius plot of diffusion coefficient of solute for a dose rate characteristic of neutron irradiation K = 10^{-6} dpa/sec, for various sink strengths.

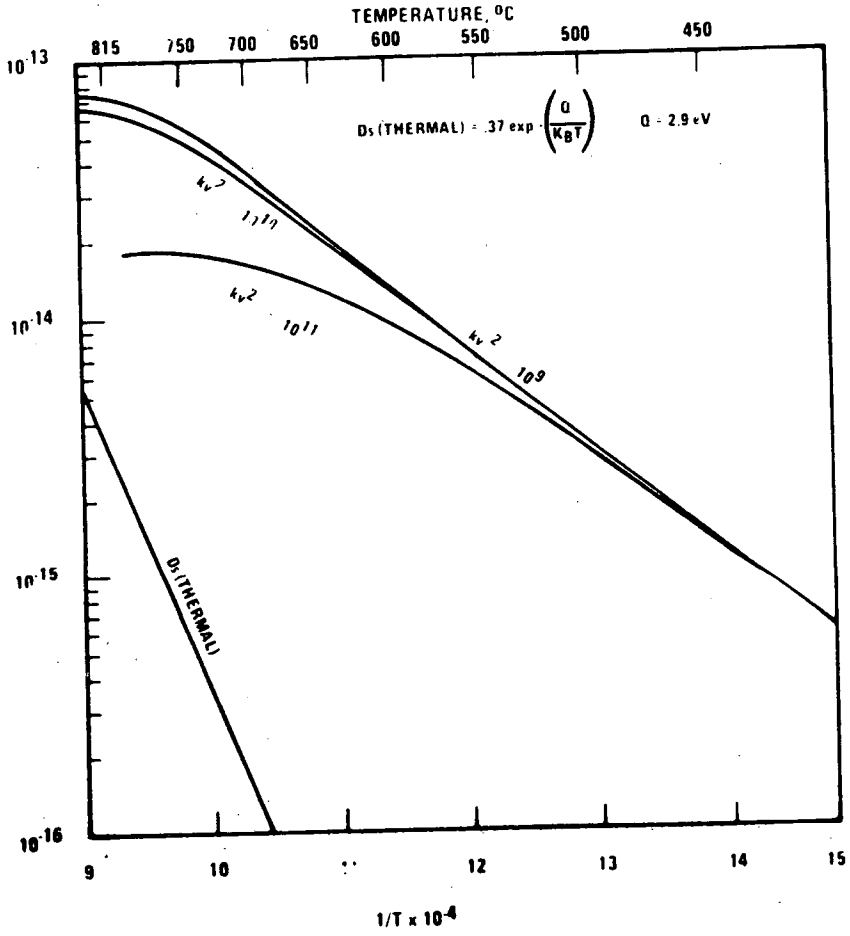

FIGURE 133(b). Arrhenius plot of diffusion coefficient of solute for a dose rate characteristic of Ni-ion irradiations k = 10^{-3} dpa/sec, for various sink strengths.

where N_p is the number of particles per unit volume, $\bar{R}$ is the average radius of the distribution and $\Delta V/V$ is the volume fraction of precipitate.

The kinetic development of f(R,t) is uniquely determined once the growth law for individual particles of the distribution is known. In Appendix A we show that in a radiation environment the continuity equation for f(R,t) in size space is of the Fokker-Planck type[6] and may be written as

$$\frac{\delta f}{\delta t} = -\frac{\delta}{\delta R}\left[<(\Delta\dot{R})>f\right] + \frac{1}{2}\frac{\delta^2}{\delta R^2}\left[<(\Delta\dot{R}^2)>f\right] \qquad [8]$$

where $<(\Delta\dot{R})>$ is the rate at which a particle of radius R is growing (or shrinking) and $<(\Delta\dot{R})^2>$ is the rate at which the radius of a particle of radius R fluctuates due to the irradiation. Note that in a thermal environment the second term is usually unnecessary since the motion of a particle of radius R is strictly regular[7] in dimension space. As the fluctuations in particle radius are due to random diffusion of solute to and away from the particle due to cascade damage, to a first order approximation it seems appropriate to set*

$$<(\Delta\dot{R}^2)> = \left(\frac{3a}{R}\right)\tilde{D}_s \qquad [9]$$

and

$$<(\Delta\dot{R})> = \frac{\tilde{D}_s}{C_p^s R}\left[\Delta(t) - \frac{\alpha}{R}\right] \qquad [10]$$

where C_p^s is the atomic fraction of solute in the precipitate, $\Delta(t)$ the supersaturation, $\alpha = 2\sigma\Omega/k_B T\, C_\infty$ is the Lifshitz Slyozov parameter where σ is the surface energy, Ω the atomic volume of solute in the matrix, k_B is Boltzman's constant, T the temperature and C_∞ is the solubility limit of solute in the matrix at equilibrium.

To complete the theory the continuity equation has to be supplemented by the conservation of solute which will be written as[7]

$$C_s = \Delta(t) + C_p^s \frac{4\pi}{3}\int_0^\infty R^3 f(R,t)\, dR \qquad [11]$$

where C_s is the atomic fraction of solute above the solubility limit in the alloy, $\Delta(t)$ and C_p^s are the supersaturation in the matrix and the atomic fraction of solute in the precipitate.

The unknown functions are f(R,t) and $\Delta(t)$. They must be determined by solving the continuity equation in size space (Equation [8]) and the conservation condition (Equation [11]) of solute. In this investigation the solution of the kinetic equations will be presented for the equilibrium distribution and for displacement doses larger than the nucleation dose, i.e., when the solute supersaturation has been essentially relieved. Thus

*See Appendix A

the kinetic solutions apply when solute redistribution can be considered to take place at a constant volume fraction. The case where the volume fraction is increasing due to nucleation from solution requires a separate investigation. The equilibrium distribution is of course universal and independent on whether the volume fraction was changing as equilibrium was approached.

1.3.3 Solutions of the Kinetic Equations

1.3.3.1 Equilibrium Solutions. The equilibrium properties of precipitation strengthened alloys under irradiation have been discussed by Nelson et al[8] (N-H-M). Based on a particle growth law and the conservation of solute N-H-M arrive at some important conclusions. They predict that in an irradiation environment a constrained equilibrium state will arise in which the enhanced diffusion of solute to particles and their subsequent growth due to the enhanced diffusion rate will be balanced by the resolution rate of solute from the particles into the solution due to cascade damage[8]. As a consequence, the constrained equilibrium state under irradiation will differ from the one attainable at the same temperature in a thermal environment. The difference is in the appearance of a maximum particle size under irradiation at equilibrium. In a thermal environment, at equilibrium, there is of course no maximum stable size, due to particle coarsening.

The existence of a maximum critical particle size under irradiation at equilibrium is of considerable interest and importance with respect to the use of precipitation strengthened alloys in LMFBR. It implies that degradation of mechanical properties due to overaging in reactor can be minimized if the maximum critical size at equilibrium can be kept low enough, such that the particles still provide effective barriers at which dislocations can be pinned.

Unfortunately, the theory proposed by N-H-M does not provide a sufficiently detailed description of the kinetics of γ' redistribution under thermal conditions (i.e., if one sets the dose rate equal to zero in the N-H-M equations). Thus it is suspected that with respect to γ' redistribution under irradiation, it may be lacking in detail even though it contains most of the important physical ideas. Equations [8] and [11] together with [9] and [10] provide the necessary tools to describe both the constrained equilibrium as well as the kinetics of particle redistribution in a radiation environment. In addition they reduce to the thermal coarsening equations in the appropriate limit.

In constrained equilibrium in a radiation environment the set of equations to be solved is

$$\frac{1}{2}\frac{\delta^2}{\delta R^2}\left[\left(\frac{3a}{R}\right)\tilde{D}_s f_\infty\right) - \frac{\delta}{\delta R}\left[\frac{\tilde{D}_s}{C_p^s R}\left(\Delta_\infty - \frac{\alpha}{R}\right)f_\infty\right] = 0 \qquad [12]$$

together with the boundary condition

$$C^s = \Delta_\infty + \frac{4\pi}{3} C_p^s \int_0^\infty R^3 \, f_\infty(R)\,dR \qquad [13]$$

where $f_\infty(R)$ is the equilibrium distribution function and Δ_∞ is the equilibrium supersaturation in dynamic solution. Note that in a radiation environment Δ_∞ does not have to vanish, although, of course, in a thermal environment $\Delta_\infty = 0$ at equilibrium. In order to solve Equation [12] another boundary condition is needed, which states that $f_\infty(R)$ vanishes as $R \to 0$ thus

$$\lim_{R \to 0} f_\infty(R) = 0 \qquad [14]$$

Consideration of the fundamental solutions of Equation [12] in Appendix B proves that in order to satisfy the solute conservation condition Equation [13] there must exist a maximum radius R_{max} such that $\lim_{R \to R_{max}} f_\infty(R) = 0$ and $f_\infty(R) = 0$ for $R \geq R_{max}$ for otherwise $f_\infty(R)$ will be exponentially divergent as $R \to \infty$. It turns out that a solution which satisfies Equation [12] and the boundary conditions Equations [13] and [14] can be written

$$f_\infty(R) = \begin{cases} f_\infty^0 \dfrac{x^{1}\ \alpha'\alpha''\ e^{\alpha' x}\ [1 - \frac{\gamma(\alpha'\alpha'' + 1,\ \alpha' x)}{\gamma(\alpha''\alpha' + 1,\ \alpha)}]}{\int_0^\infty x^{1-\alpha'\alpha''}\ e^{\alpha' x}\ [1 - \frac{\gamma(\alpha''\alpha' + 1,\ \alpha' x)}{\gamma(\alpha''\alpha' + 1,\ \alpha')}]dx} & , 0 \leq x \leq 1 \\ 0 & , x \geq 1 \end{cases} \qquad [15]$$

where $x = \dfrac{R}{R_{max}}$, $\alpha'' = \dfrac{\alpha}{R_{max}\ \Delta_\infty}$, $\alpha' = \dfrac{2R_{max}\ \Delta_\infty}{3C_p^s\ a}$, $\alpha' = 2 + \alpha'\alpha''$ [16]

Note that $\alpha''\alpha' = 2\alpha/3C_p^s a$, is a parameter which is independent of R_{max} or Δ_∞, $\gamma(\alpha''\alpha' + 1, \alpha' x)$ is the incomplete gamma function defined as

$$\gamma(\alpha''\alpha' + 1, \alpha' x) = \int_0^{\alpha' x} e^{-t}\ t^{\alpha'\alpha''}\ dt$$

This function is discussed and tabulated in Reference 9.

Note too that in order to satisfy the boundary condition of Equation [14], the range of variation of $\alpha''\alpha'$ is limited by $0 < \alpha'\alpha'' < 1$. The function $P_{\alpha'}(x)$ defined by

$$P_{\alpha'}(x) = \begin{cases} \dfrac{x^{1-\alpha'\alpha''}\ e^{\alpha' x}\ [1 - \frac{\gamma(\alpha''\alpha' + 1,\ \alpha' x)}{(\alpha''\alpha' + 1,\ \alpha')}]}{\int_0^1 x^{1-\alpha'\alpha''} e^{\alpha' x}\ [1 - \frac{\gamma(\alpha''\alpha' + 1,\ \alpha' x)}{\gamma(\alpha''\alpha' + 1,\ \alpha')}]\ dx} & , 0 \leq x \leq 1 \\ 0 & , x \geq 1 \end{cases} \qquad [17]$$

is a universal probability of distribution function normalized to unity, i.e, $\int_0^\infty P_{\alpha'}(x)dX = 1$ depending on a single parameter α'.

Equation [16] and the condition $0 < \alpha'\alpha'' < 1$ limit the parameter α' to the range $2 < \alpha' < 3$. The universal probability distribution $P_{\alpha'}(x)$ is plotted in Figure 134 for selected values of α' in the allowable range. It is important to note that the probability distribution $P_{\alpha'}(x)$ does not contain any arbitrary adjustable parameters. If all necessary ancillary data for an alloy system are known then $\alpha'\alpha'' = 2\alpha/3\ C_p^s a = 4\sigma\Omega C_\infty/3k_b T C_p^s a$ can be uniquely

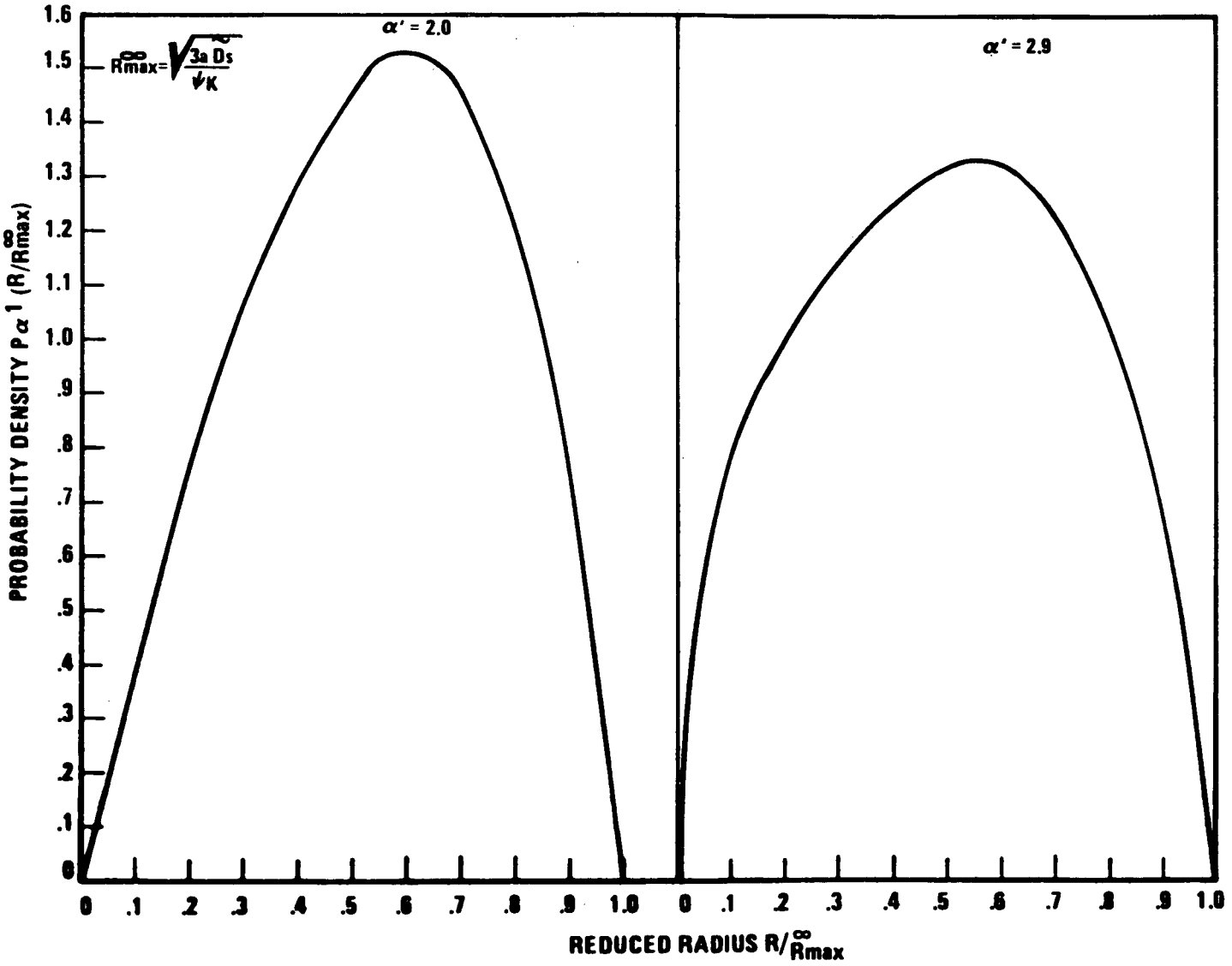

FIGURE 134. Universal constrained equilibrium distribution.

calculated. Once $\alpha'\alpha''$ is known α' can be calculated from the relationship $\alpha' = 2+\alpha'\alpha''$. Thus all parameters defining $P_{\alpha'}(x)$ are fixed by the ancillary data. The constant f_∞^0 in Equation [15] can now be expressed as a function of R_{max} and the concentration of solute in dynamic solution Δ_∞ using [13] and [17] and is given by

$$f_\infty^0 = \frac{3}{4\pi} \frac{(C^S - \Delta_\infty)}{C_p^S R_{max}^4 \int_0^1 x^3 P_{\alpha'}(x)\, dx} \qquad [18]$$

With these results at hand the concentration of particles per unit volume, the average radius and the volume fraction are given by

$$N_p = \int_0^\infty f_\infty(R)dR = R_{max} f_\infty^0 = \frac{3}{4\pi} \frac{(C^S - \Delta_\infty)}{C_p^S R_{max}^3 \int_0^1 x^3 P_{\alpha'}(x)dx} \qquad [19]$$

$$\bar{R} = R_{max} \int_0^1 x P_{\alpha'}(x)dx \qquad [20]$$

$$\frac{\Delta V}{V} = \frac{(C^S - \Delta_\infty)}{C_p^S} \qquad [21]$$

Finally, to complete the description of the constrained equilibrium state one must determine either R_{max} or Δ_∞, since if one is known the other can be computed from Equation [16].

An independent relationship between R_{max} and Δ_∞ can be found using an argument due to N-H-M. At equilibrium, the rate at which solute is drawn to the particle of maximum size by diffusion must exactly equal the rate at which solute is forced back into the matrix as a result of cascade damage for this particle. Otherwise, R_{max} would depend on time even in equilibrium. Thus for R_{max} the following condition must prevail

$$\frac{\tilde{D}_s \Delta_\infty}{C_p^S R_{max}} \left(1 - \frac{\alpha}{R_{max} \Delta_\infty}\right) = \psi K \qquad [22]$$

where K is the displacement rate and ψ is the dissolution parameter introduced by N-H-M. Using Equations [16] and condition [22] it can be shown that

$$\Delta_\infty = (3C_p^S a + \alpha) \sqrt{\frac{\psi K}{3a\tilde{D}_s}}, \quad R_{max} = \sqrt{\frac{3a\tilde{D}_s}{\psi K}} \qquad [23]$$

Substitution of [23] into [19], [20] and [21] yields the directly measurable parameters as a function of the ancillary data

1.3.4 Discussion of Equilibrium Solutions

1.3.4.1 Characterization of the Equilibrium State. These results imply that due to solute resolution a new equilibrium state is set up by the irradiation (as predicted by N-H-M). The complete characterization of this equilibrium state is as follows.

1. Particle size distributions assume the universal form given by Equation [17].

2. There exists a maximum stable particle radius given by

$$R_{max} = \sqrt{\frac{3a\tilde{D}_s}{\psi K}} \qquad [23]$$

The average particle radius is given by

$$\bar{R} = \sqrt{\frac{3a\tilde{D}_s}{\psi K}} \int_0^1 x \, P_{\alpha'}(x)dx$$

3. The amount of solute remaining in dynamic solution is

$$\Delta_\infty = (3C_p^s a+\alpha)\sqrt{\frac{\psi K}{3a\tilde{D}_s}} \qquad [23"]$$

and the constrained equilibrium volume fraction

$$\left(\frac{\Delta V}{V}\right)_\infty = \frac{C^s - \Delta_\infty}{C_p^s} = \frac{C^s - \left[(3C_p^s a+\alpha)\sqrt{\frac{\psi K}{3a\tilde{D}_s}}\right]}{C_p^s} \qquad [21']$$

4. The total particle concentration per unit volume can be calculated from

$$(N_p)_\infty = \frac{3}{4\pi}\left(\frac{\psi K}{3a\tilde{D}_s}\right)^{3/2} \frac{\left[C^s - (3C_p^s a+\alpha)\sqrt{\frac{\psi K}{3a\tilde{D}_s}}\right]}{\int_0^1 x^3 P_{\alpha'}(x)dx} \qquad [19']$$

1.3.4.2 Kinetic Consequences. Inasmuch as all alloy systems would tend to approach the constrained equilibrium state independent of their initial starting condition some rather general statements can be made.

A. If the initial state of the alloys prior to irradiation is characterized by a concentration of solute in solution which is higher than Δ_∞ [and as a consequence by a volume fraction of precipitate phase which is lower than $(\Delta V/V)_\infty$] then during exposure to irradiation the concentration of solute in solution will decrease [correspondingly the volume fraction of precipitate will increase]. This process will continue up to the point where the concentration of solute in dynamic solution will be exactly equal to Δ_∞ [and the volume fraction of

precipitate to $(\Delta V/V)_\infty$]. Subsequently only a redistribution of particle sizes will occur such that the particle size distribution will assume the universal distribution predicted by Equation [17]. Once the constrained equilibrium distribution is set up no further change will occur. For that condition the maximum particle radius, the concentration of solute in dynamic solution, the precipitate volume fraction and particle concentration can all be predicted from Equations [23'], [23"], [21'] and [19'].

B. If the initial state of the alloy prior to irradiation is characterized by a concentration of solute in solution which is lower than Δ_∞ [and as a consequence by a volume fraction of precipitate which is higher than $(\Delta V/V)_\infty$] then during exposure to irradiation the concentration of solute in solution will <u>increase</u> [correspondingly the volume fraction of precipitate will decrease]. In this case too the system will eventually again relax to the universal constrained equilibrium state.

Thus, depending on the initial state of the alloy in reference to the universal constrained equilibrium state, both particle growth as well as dissolution are possible. N-H-M[8] report some observations on aged Ni-Al systems irradiated with Ni ions which conform to possibility B. Potter, et al[10], report the result of Ni ion irradiation on solution annealed Ni-Al alloys which conform to possibility A. More specifically, however, Chang, et al, showed experimental confirmation of these ideas in nickel ion bombardment and neutron irradiated γ'#1 alloys[15].

1.3.4.3 <u>Application to Simulation Studies</u>. Note that the maximum radius at equilibrium as well as the amount of solute in dynamic solution depend only on the quantity $\tilde{D}_s/\psi K$ (Equations [23'] and [23"]). It follows that the condition to simulate the same equilibrium state with neutron and charged particle irradiations is

$$\left(\frac{\tilde{D}_s}{\psi K}\right)_{\text{charged particle}} = \left(\frac{\tilde{D}_s}{\psi K}\right)_{\text{neutron}} . \qquad [24]$$

In practice it is expected that a temperature shift in charged particle irradiations will be necessary in order to force the validity of Equation [24]. Using some simplifying assumptions, the temperature shift can be estimated as follows. In Equation [4] assuming that $\varepsilon = \delta \tilde{\sim} o$ then the values of D_s are as shown in Figures 132(a) for neutron and 132(b) for Ni-ions as described in Section 1.3.2.1 above.

The values of ψ neutron and ψ charged particle can be estimated from the work of Sigmund, et al[12], and Marwick[13]. The average energy transferred to the P-K-O by a 1 MeV neutron in Fe-Ni-Cr alloys is about 40 keV whereas the average energy transferred to the P-K-O for a 4 MeV Ni^+ ion is about 0.4 keV. The cascade size resulting from a neutron collision involving the transfer of 40 keV is about 5 nm whereas the cascade size appropriate for charged particle irradiations is about 1 nm. If it is assumed that $\psi \tilde{\sim}$ cascade size, appropriate approximate values for ψ are ψ neutron = 4 nm, ψ charged particle = 2 nm. N-H-M use a ψ value of 10 nm which appears to be too high for the γ'#1 alloys. In Figure 135 the quantity $(\tilde{D}_s/\psi K)$ is plotted for neutrons and charged particles for (kv^2) charged particle = 10^{10} and (kv^2) neutron = 10^{11}. In Figure 136 the temperature shift for charged particle irradiations is plotted versus neutron irradiation temperature. Note that for the parameters chosen, the shift is positive below about 575°C and negative above this temperature.

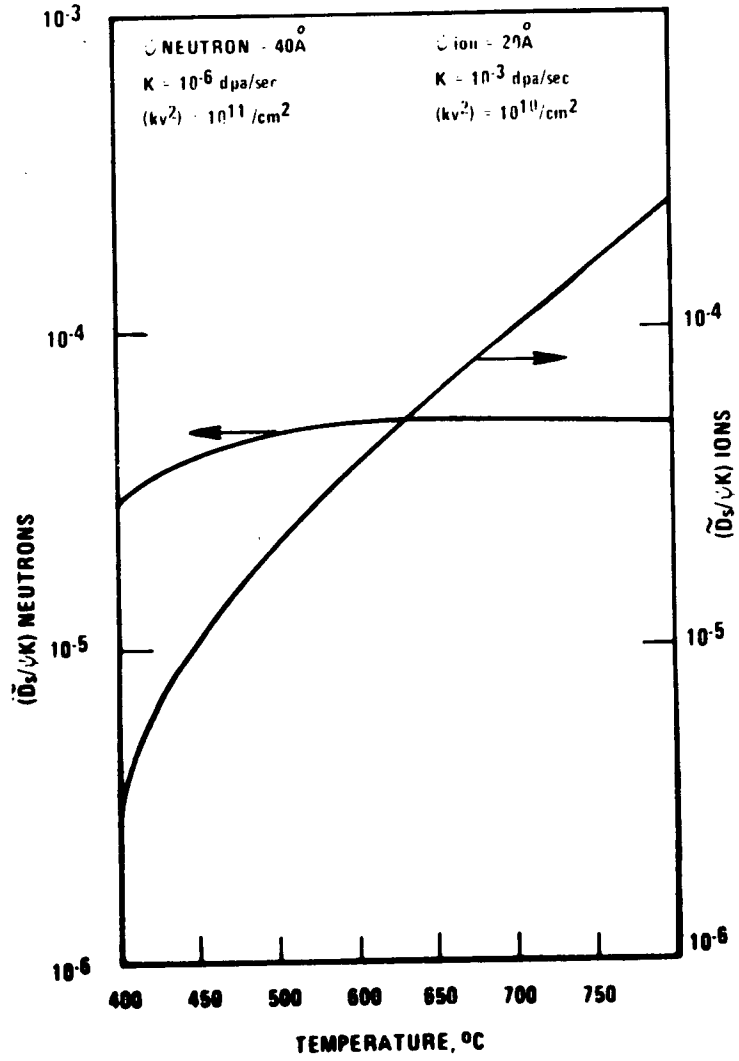

FIGURE 135. The quantity $\tilde{D}_s/\psi K$ for neutron and charged particle irradiations.

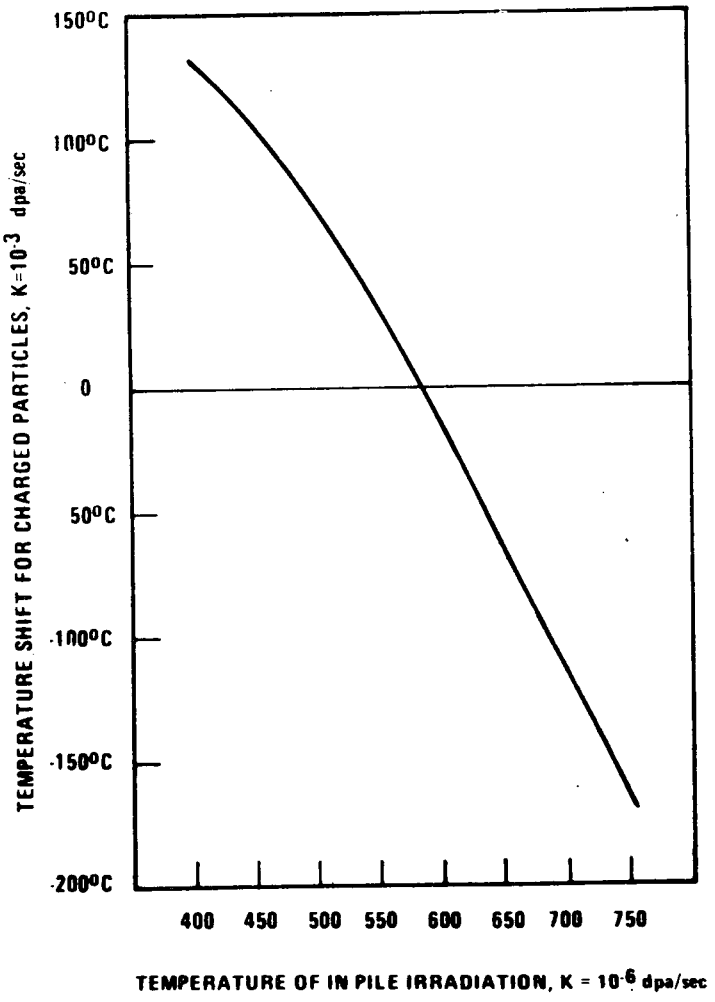

FIGURE 136. Temperature shift for charged particles, K = 10^{-3} dpa/sec.

Another consequence to simulation studies is as follows. In those systems where swelling response is controlled by second phase particles one would expect simulation studies to be conducted at a lower temperature than neutron irradiations since one must simulate precipitate redistribution in order to simulate swelling response. This seems to occur in alloy E48 where the temperature shift between ion bombardment and neutron irradiations is negative[11].

1.3.5 Time Dependent Solutions

1.3.5.1 The Dynamic Scaling Hypothesis. The solution of Equation [8] subject to arbitary initial conditions with the boundary condition [11] can in general be only achieved by numerical means. However, asymptotic solutions to Equation [8] can be derived if one assumes the dynamic scaling hypothesis to be valid. The dynamic scaling hypothesis is a simple assumption regarding the asymptotic form of the distribution f(R,t) for high displacement doses (i.e., long irradiation exposure times). Thus, it is postulated that the general form of f(R,t) can be written in the scaled version

$$f(R,t) = \begin{cases} L(t)\, h(x) & x \leq 1 \\ 0 & x > 0 \end{cases} \qquad [25]$$

where L is a function of time alone and h depends only on $x = R/R_{max}(t)$ where $R_{max}(t)$ is the maximum radius at time t. There are two necessary requirements to have solutions of the form of Equation [25]. The first requirement is that the amount of solute in the precipitate phase be large compared to the amount of solute in solution, i.e., the size redistribution occurring under irradiation can be considered to occur at constant volume fraction. This assumption should be valid both for solution annealed as well as aged alloys after the nucleation dose has been considerably exceeded.

The second requirement for solutions of the form [25] is that the product $R_{max}(t)$ $\Delta(t)$ be equal to a constant which is independent of irradiation dose.

Note that in the L-S-W theory in the asymptotic limit $R_{max}(t)\ \Delta(t) = 3/2\ \alpha$, i.e., the product of the maximum radius and the amount of excess solute in dynamic solution is independent of time as well as the diffusion coefficient. In an irradiation environment

$$R_{max}(t)\ \Delta(t) = R^{\infty}_{max}\ \Delta_{\infty} = 3C^{S}_{p}a+\alpha \qquad [26]$$

It is remarkable that Equation [26] is independent of any kinetic constants, such as the diffusion coefficient or the displacement rate, although, R^{∞}_{max} and Δ_{∞} depend on the irradiation parameters. In Table 38 the constant α is calculated at a temperature of 600°C for experimental alloy E42 containing γ' precipitates (it is assumed that $C^{\infty} = 20$ at. % and $\alpha = 40$ erg/cm^2, a = 0.357 nm). It is seen that at 600°C $\alpha < 3C^{S}_{p}a$. Assuming $\Delta_{\infty} = 1$ at. % it follows from Equation [26] that $R^{\infty}_{max} = 50$ nm. If $\Delta_{\infty} = 2$ at. %, then $R^{\infty}_{max} = 25$ nm. In general, the larger amount of solute which can be kept in dynamic solution, the smaller will be the maximum size at equilibrium.

TABLE 38

ANCILLARY CONSTANTS FOR ALLOY E42

$\sigma = 40$ erg/cm^2	$a = 3.57\mathring{A}$	$C_p^s = 25$ at.%
$C_\infty = 20$ at.%	$\alpha = .6\mathring{A}$ at 600°C	
$\alpha'\alpha'' = \frac{2\alpha}{3 C_p^s a} \tilde{=} .5$	$\alpha' = 2+\alpha'\alpha'' = 2.5$ at 600°C	
$\tilde{D}_{thermal} = .37 \exp(-\frac{Q}{k_B T})\ [\frac{cm^2}{sec}]$		$Q = 2.9$ eV
$D_v = .6 \exp(-\frac{Q}{k_B T})\ [\frac{cm^2}{sec}]$		$Q = 1.6$ eV
$\frac{\alpha}{D_i} = 4 \times 10^{16}[\frac{1}{cm^2}]$		

It follows that the stability of γ' precipitates will be enhanced if the concentration of Ti and Al in dynamic solution can be made to increase. A possible way to increase the concentration of Ti and Al in dynamic solution is to add minor elements which tend to form clustering reactions with Ti and Al atoms. Since Ti and Al are oversized atoms in Fe-Cr-Ni matrices the addition of an undersized minor element such as Si could enhance γ' precipitate stability if Si can be kept in dynamic solution.

The construction of a solution of the form of Equation [25] is laborious and will be presented in a subsequent report. Here the discussion will be centered on the kinetics of the maximum particle radius.

The equation of motion for R_{max} is

$$\frac{dR_{max}}{dt} = \frac{\tilde{D}_s}{C_p^s R_{max}} [\Delta(t) - \frac{\alpha}{R_{max}(t)}] - \psi K \qquad [27]$$

This equation can be easily integrated if $\Delta(t) R_{max}(t) = \Delta_\infty R_{max}^\infty$. One derives

$$\ln(\frac{1+x}{1-x}\ \frac{(1-x_o)}{(1+x_o)}) - 2(x-x_o) = 2\ \frac{\psi K}{R_{max}^\infty}\ (t-t_o) \qquad [28]$$

where Kt_o is the displacement dose at which the dynamic scaling hypothesis first becomes valid and

$$x \equiv \frac{R_{max}(t)}{R_{max}^\infty}\ ,\quad x_o \equiv \frac{R_{max}(t_o)}{R_{max}^\infty}$$

Two limiting predictions of Equation [28] are obvious. First, note that if $x_o > 1$ then for such displacement doses that $x > 1$

$$R_{max}(\phi) = R_{max}^{\infty}(\phi) - \psi(\phi-\phi_o) \qquad [28']$$

(ϕ denotes the displacement dose.)

Thus, if the maximum radius is plotted versus displacement dose the decrease in the maximum radius will be linear and the slope of the curve will be the dissolution parameter ψ. Note that Equation [28'] is expected to be valid only in a limited displacement dose range, larger than ϕ_o, but shorter than the saturation dose necessary to drive the system to equilibrium.

Secondly note that if $X_o \ll 1$ then for such displacement doses that $X<1$, expansion of the logarithmic term in Equation [28] up to third order yields

$$R_{max}^3(\phi) - R_{max}^3(\phi_o) = 3\psi(R_{max}^{\infty})^2 \phi = 9a \tilde{D}_s t \qquad [28"]$$

Note the similarity between Equation [28"] and the analogous equation based on L-S-W theory

$$R_{max}^3(t) - R_{max}^3(t_o) = \frac{2}{3}\alpha D t \qquad [28"']$$

It should however be stressed that Equation [28"] has a validity only over a limited displacement dose range whereas [28"'] is valid asymptotically for all time.

In Figures 137(a) and 137(b) the kinetics of the relaxation of $R_{max}(t)$ to its equilibrium value is plotted versus displacement dose.

Note also that for such values of the displacement dose for which $R_{max}(t)$ approaches R_{max}^{∞} the relaxation to the equilibrium value is exponential with displacement dose. On the basis of Equation [28] it can be shown that when $R_{max} \tilde{\sim} R_{max}^{\infty}$

$$R_{max}(\phi) = R_{max}^{\infty} - 2\frac{(R_{max}^{\infty} - R_{max}(\phi_o))}{R_{max}^{\infty} + R_{max}(\phi_o)} \exp 2\left(1 - \frac{R_{max}(\phi_o)}{R_{max}^{\infty}}\right)$$

$$\exp - \left[\frac{2\psi}{R_{max}^{\infty}}(\phi-\phi_o)\right] \qquad [29]$$

Whenever dynamic scaling holds it can be shown that the kinetics of the average particle size are identical to the kinetics of the maximum size up to a time independent proportionality constant. Thus, using [25]

$$\bar{R} = \frac{\int_0^{\infty} Rf(r,t)dR}{\int_0^{\infty} f(R,t)\,dR} = R_{max}(t)\,\frac{\int_0^1 uh(u)du}{\int_0^1 h(u)du} \qquad [30]$$

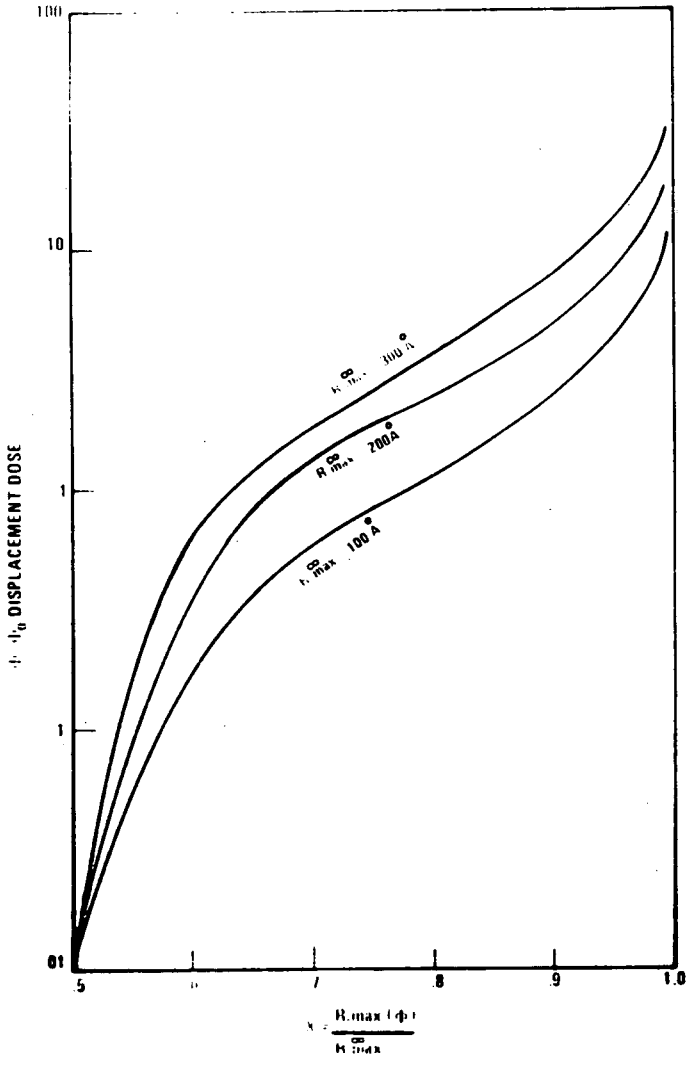

FIGURE 137(a). The dose dependence of the maximum (or average) particle radius in the dynamic scaling regime, illustrating particle growth.

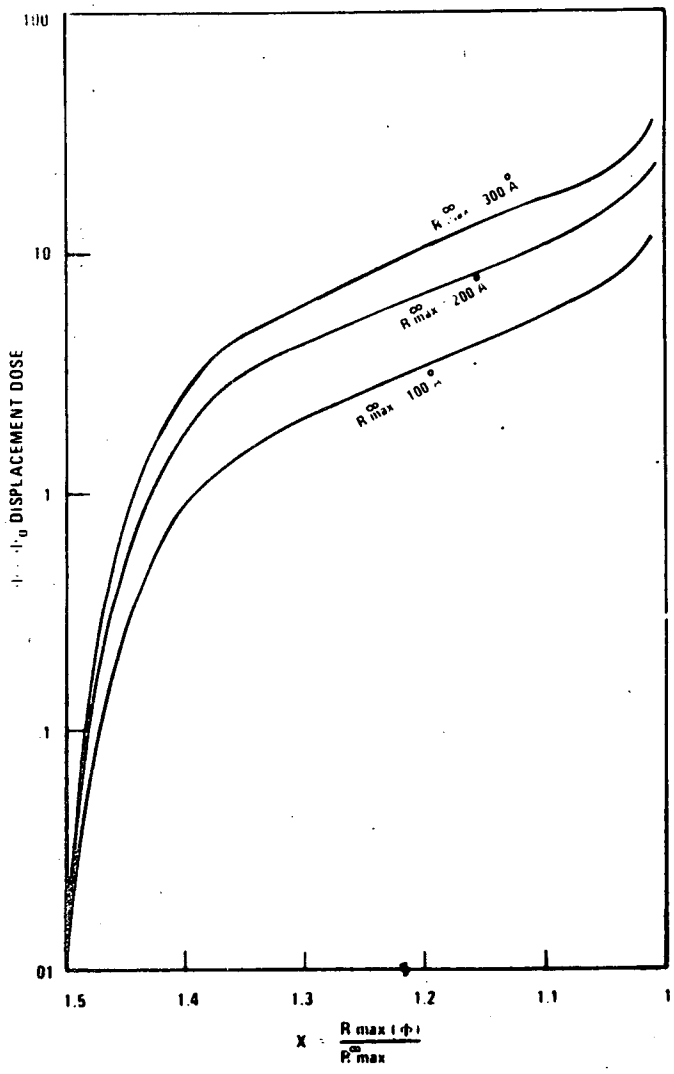

FIGURE 137(b). The dose dependence of the maximum (or average) particle radius in the dynamic scaling regime, illustrating solute redistribution.

Since the integrals appearing on the left hand side of [30] are independent of time one can write $\bar{R}$ = (const) $R_{max}(t)$. Thus the displacement dose dependence of R_{max} is identical to $\bar{R}$.

It can further be shown that to first order the function h(x) can be approximated by $f_\infty(x)$ where f_∞ is the equilibrium distribution. Thus in the asympotic regime formulas [19] to [21] hold to a first approximation with R_{max} replaced by $R_{max}(t)$.

1.3.6 Conclusions

1. A new theory of particle size redistribution in an irradiation environment is proposed based on the physical ideas of Nelson, et al[8]. The theory reduces to the L-S-W[7] approach to coarsening in the limit of zero displacement rate.

2. A complete theoretical characterization of the equilibrium state is provided by the equilibrium particle size distribution function, the number of particles/cm^3, the average and the maximum radius.

3. It is shown that both particle growth as well as dissolution are possible in an irradiation environment. The conditions under which either one will occur are calculated.

4. It is shown that irrespective of the initial starting condition an equilibrium state is approached at high doses which is characterized by a maximum particle size and an amount of solute in dynamic solution which is in excess of the solubility limit. Formulae are given for these quantities in terms of thermodynamic and kinetics constants. It follows that the infinite particle coarsening which occurs in a thermal environment will not occur under irradiation but the maximum particle size will saturate.

5. A necessary criterion is given for simulation of particle redistribution for in pile irradiations by charged particle bombardment. Using relevant assumptions it is shown that the temperature shift should be negative above 575°C. This contrasts with the case of void simulation where the temperature shift is positive. Thus in those systems where second phase particles control swelling response it is expected that the shift in peak swelling temperature could be negative. This appears to be the case in alloy E48.

6. The dynamic scaling hypothesis is formulated and necessary conditions for its validity are given. The kinetics of the maximum and average particle size are calculated based on dynamic scaling. Various special cases of the kinetic law governing the relaxation kinetics of the maximum (or average) particle size to their equilibrium values are discussed.

1.4 EXPECTED ACHIEVEMENTS IN THE NEXT REPORTING PERIOD

Using the dynamic scaling hypothesis, kinetic data generated by recent neutron and charged particle irradiations will be evaluated.

1.5 REFERENCES

1. Dienes, G. J., and Damask, A. C., J. Applied Physics, 29, 12, 1713 (1958).

2. Johnston, W. G., et al., "The Effect of Metallurgical Variables on Void Swelling," O. E. Report No. 76CRD019, January, 1976.

3. Kelly, A., and Nicholson, R. B., "Precipitation Hardening," Progress in Materials Science, Vol. 10, Pergamon Press, N.Y (1963).

4. Brailsford, A. D., and Bullough, R., J. Nucl. Material, 44 (1972), 121.

5. Bullough, R., et al., Karlsruhe Conf. on Irradiation Behavior of Fuel Cladding and Core Component Materials (1974), p. 1.

6. Chandrasekhar, S., Rev. Mod. Phys. 15, 1 (1943).

7. Lifshitz, I. M., and Slyozov, V. V., J. Phys. Chem. Solids, 19, 1/2, 35 (1961) and Wagner, C., Z. Elektrochemie, 65, 581 (1961).

8. Nelson, R. S., et al., J. Nucl. Material, 44, 318 (1972).

9. Handbook of Mathematical Functions, edited by M. Abramowitz and Irene A. Stegan, N-B-S Applied Math. Series 55, June 1974.

10. Potter, D. I., and Hoff, H. A., in "Fundamental Aspects of Radiation Damage in Metals," Gatlinburg Conference, October, 1975, CONF-751006-P2, Vol. II (1092).

11. Chickering, R. W., and Diamond, S., Alloy Development Program Quarterly Technical Progress Letter, TC-160-8 (1-3/1976), and Thomas, L. E., in Annual Information Meeting, National Advanced Alloy Development Program, TC-721, p. 114.

12. Sigmund, P., et al., Rad. Effects, 11 (1971), 39.

13. Marwick, A. D., AERE-R-7745, May, 1974.

14. Chang, A. L., and Baron, I. M., W-ARD Topical Report, "Pre-Irradiation Characterization of WARD γ'#1 Fe-Cr-Ni Experimental Alloys for LMFBR," to be published.

15. Chang, A. L., Baron, M., Chickering, R. W., and Bleiberg, M. L., "Neutron Irradiated γ'#1 Alloys in AA-IX Experiment," this quarterly report.

APPENDIX A

In a thermal environment the growth law for a particle of radius R can be written as[8]

$$\frac{dR}{dt} = \frac{D_s}{C_p^s R}\left[\Delta(t) - \frac{\alpha}{R}\right] \qquad [A1]$$

Equation [A1] predicts that at any given time t particles whose radius R>Rc = $\alpha/\Delta(t)$ will grow and particles whose radius R<Rc will shrink. Thus given the radius of a particle at any time its subsequent time evolution can be determined uniquely by solving Equation [A1] subject to an appropriate boundary condition. In reference 8 such behavior is termed regular. In an irradiation environment two modifications are necessary in Equation [A1].

First, the diffusion coefficient of solute will differ from the thermal diffusion coefficient due to the introduction of excess vacancies and interstitials thus $D_s \rightarrow \tilde{D}_s$ where $\tilde{D}_s$ can be calculated from Equation [4]. The second modification of Equation [A1] is more fundamental. In an irradiation environment a particle of radius R>Rc can shrink due to cascade damage events in the manner described by Nelson, et al. Thus a particle of radius R>Rc can lose solute by resolution of solute and the growth or shrinkage of particles becomes irregular and subject to fluctuations related to the irradiation conditions. Furthermore due to random

excess vacancy and interstitial fluxes a particle of radius R<Rc can grow due to non-Gibbsian solute flow. These effects can be described by adding a random fluctuating term to Equation [A1]. Thus one writes

$$\Delta R = \frac{\tilde{D}_s}{C_p^s R} [\Delta(t) - \frac{\alpha}{R}] \Delta t + \phi(\Delta t) \qquad [A2]$$

where the random function $\phi(\Delta t)$ describes the fluctuations.

The physical meaning of Equation [A2] is that the change in a particle's radius during time Δt can be written as a sum of two terms. The first term describes the systematic diffusional flow of solute and the second the fluctuating part. Such a decomposition is expected to be a valid representation because the high displacement rates under irradiation cause the function $\phi(\Delta t)$ to vary rapidly compared to the variations in R. In other words during a time Δt the change in R is small whereas the function $\phi(\Delta t)$ could undergo several fluctuations during Δt. An immediate consequence of [A2] is that the radius of a particle at time t cannot be predicted uniquely if its radius at an earlier time is known. One can say that the growth or dissolution become irregular and as a consequence all one can ask for is the probability that the radius of the particle is R at time t.

The continuity equation for the probability distribution f(R,t) can be derived from Equation [A2] by standard arguments as in Reference 6, if suitable assumptions are made on the statistics of the fluctuation $\phi(\Delta t)$.

It will be assumed that the statistics underlying the fluctuation $\phi(\Delta t)$ is gaussian and

$$\begin{aligned} &1.\ \langle\phi(\Delta t)\rangle = 0 \\ &2.\ \langle\phi^2(\Delta t)\rangle = (\frac{3a}{R})\ \tilde{D}_s\ \Delta t \end{aligned} \qquad [A3]$$

where $\langle\rangle$ denotes the average with respect to the gaussian distribution. Equation [1] states that positive or negative fluctuations are equally likely to occur. Equation [2] provides an order of magnitude estimate for the second moment of the fluctuation. Only those solute atoms which are within a thin surface layer can contribute to particle size fluctuations, to first order, therefore one expects $\langle\phi^2(\Delta t)\rangle$ to be directly proportional to the surface to volume ratio of the particle, the diffusion coefficient and the time interval Δt.

Using [A2] and [A3] and the methods in reference 6 the continuity equation for f(R,t) turns out to be of the Fokker-Planck type

$$\frac{\delta f}{\delta t} = -\frac{\delta}{\delta R}(\langle\dot{\Delta R}\rangle f) + \frac{1}{2}\frac{\delta^2}{\delta R^2}[\langle(\dot{\Delta R})^2\rangle f]$$

where

$$\langle\dot{\Delta R}\rangle = \frac{\tilde{D}_s}{C_p^s R}[\Delta(t) - \frac{\alpha}{R}]$$

and

$$\langle(\dot{\Delta R})^2\rangle = (\frac{3a}{R})\ \tilde{D}_s$$

APPENDIX B

In this appendix the existence of a maximum finite particle size at equilibrium is proved. The proof is based on the continuity Equation [12] and the boundary condition [13].

The two fundamental solutions of Equation [12] are

$$\psi_1 = R\left(1 - \frac{2\alpha}{3C_p^s a}\right) \exp\left(\frac{2\Delta_\infty R}{3C_p^s a}\right) \qquad [B1]$$

and

$$\psi_2 = \psi_1 \gamma\left(1 + \frac{2\alpha}{3C_p^s a}, \frac{2\Delta_\infty R}{3C_p^s a}\right) \qquad [B2]$$

The general solution of Equation [12] is a linear combination of ψ_1 and ψ_2. In order to satisfy the conservation of solute [13] there must exist a cutoff R_{max} above which the solution of Equation [12] vanishes identically for otherwise the integral over a linear combination of ψ_1 and ψ_2 appearing in [13] will be divergent and [13] could not be satisfied. Thus a unique consequence of Equation [12] and [13] is the existence of a maximum radius at equilibrium.

2. NEUTRON IRRADIATED γ' #1 ALLOYS IN AA-IX EXPERIMENTS

A. L. Chang, M. Baron and R. W. Chickering
Westinghouse Advanced Reactors Division

2.1 OBJECTIVE

The objectives of the present study are to characterize the microstructure of the neutron-irradiated γ'#1 alloys and to analyze these data along with the Ni-ion simulation data for the optimization of γ'-strengthened advanced alloys for LMFBR applications.

2.2 SUMMARY

Alloys E40 and E42 aged at 815°C for 36.5 hours were neutron irradiated to 2.7 x 10^{22} n/cm^2 (E>0.1 MeV) at 593°C in EBR-II. TEM examination showed void swelling of 0.34% for E40 and 0.27% for E42. The radiation-induced small γ' particles were found to populate in the matrix between the original γ' particles, on dislocations and voids. Alloy E42, containing C, Si and B, showed a larger increase in γ' volume fraction under irradiation than E40. Ribbon-shaped and rod-shaped γ' precipitates were also observed in E42 similar to that observed after Ni-ion bombardment simulation. These precipitates were found to be associated with dislocations.

Gamma prime volume fraction data showed that under irradiation a larger amount of solute can be kept in solution than that under thermal equilibrium. Experimental determinations of the supersaturation and maximum radius in both neutron and Ni-ion experiments confirm the validity of the "dynamic scaling" hypothesis of the new theory of particle redistribution under irradiation. These results show that the new theory prepared by Baron, et al, provides a framework for using Ni-ion simulation techniques for predicting in-reactor precipitation kinetics.

2.3 ACCOMPLISHMENTS AND STATUS

2.3.1 Introduction

The parameters governing the void swelling resistance and phase stability of γ' strengthened Fe-Ni-Cr alloys are important in the selection of candidate alloys for LMFBR fuel cladding and duct materials.

The γ'#1 alloys were specifically designed for investigation of such metallurgical parameters. Thermal aging kinetics studies[1] and Ni-ion bombardment simulation[2,3] on γ'#1 alloys have been described in previous quarterly reports. This is part of a series of reports on the neutron irradiation of γ'#1 alloys in AA-IX experiment. The solution treated and aged (STA) E40 (Fe-15Cr-35Ni-2Ti-1.5Al) and E42 (Fe-15Cr-35Ni-2Ti-1.7Al-0.04C-0.69Si-0.015B) specimen presently investigated belong to subcapsule J (2.7 x 10^{22} n/cm^2, E>0.1 MeV, at 593°C), pin B-213, subassembly X-216b, Row 2 of EBR-II.

The first part of this report will describe the experimental observations of the void swelling and γ' precipitates morphology. The emphasis will then be focused on finding the solute supersaturation under irradiation at 593°C in E42. This supersaturation data along with the maximum particle radius will be compared to the theoretical value. Similarly, Ni-ion irradiated E42 and E48 data will also be analyzed in terms of the same theoretical framework.

2.3.2 Experimental Procedures

The experimental details of the AA-IX experiment were described in TC-160-9[4]. After irradiation to a dose of 2.7 x 10^{22} n/cm^2 (E>0.1 MeV) at 593°C, the specimen rods were sectioned to 225 μm thick disks in the W-R&D hot cell and jet-electropolished in 20% perchloric acid, 80% acetic acid solution at room temperature for TEM examination. TEM characterization of void, dislocation and γ' structures was carried out in the stereoscopic mode.

2.3.3 Microstructural Observations

2.3.3.1 Pre-Irradiation Microstructures. Alloys E40 and E42 were solution treated at 1150°C for one hour and aged at 815°C for 36.5 hours prior to neutron irradiation in EBR-II. According to the thermal aging kinetics studies[1], this heat treatment gives 9.3 volume percent spherical γ', 38 nm in average size, 2.56 x 10^{15} (particles/cm^3) in concentration for E40 and 6.9 volume percent γ', 43.5 nm in average diameter and 1.28 x 10^{15} (particles/cm^3) for alloy E42. Cellular γ' along grain boundaries were observed in both E40 and E42. MC carbide and grain boundary precipitates (M_6C, $M_{23}C_6$ and Laves phase) were observed in E42.

2.3.3.2 Void Swelling. Figure 138 shows the void morphology of E40. The void swelling was found to be 0.34%. The average void size was found to be 60.5 nm with void concentration of 3.0 x 10^{13} (voids/cm^3). Figure 139 shows that E42 has 0.27% void swelling, 43 nm average void diameter and 4.36 x 10^{13} (voids/cm^3) void concentration. The void swelling data measured by TEM is consistent with that of Thomas[4] for neutron irradiated E40 at 510°C and 649°C. Figure 140 is a reproduction of Reference 4 with the addition of the present 593°C data points. There is a constant difference between void swelling data measured by TEM and density change by immersion density measurements which cannot be attributed to densification due to precipitation alone. It was estimated that the densification is about two to three times greater than that which can be attributed to the observed precipitation.

2.3.3.3 Precipitates Morphology. The morphology of the irradiated γ' particles is shown in Figure 141 and Figure 142 for E40 and E42 respectively. It is noted that the original γ' particles due to pre-irradiation heat treatment remained spherical with Frank dislocation loops within the particle.

The small γ' particles precipitated during irradiation are dispersed in the matrix between the original particles, along dislocations and on void surface. In the case of E42, ribbon-shaped γ' precipitates were observed as shown in Figure 142. It is suggested that this could be due to the build-up of a (Ti+Al) atmosphere around a dislocation. The low contrast of the ribbon-shaped γ' in superlattice dark field mode suggests that the precipitate is not fully ordered and hence without a well-defined interface. Rod-shaped γ' with strong contrast were also observed in E42 as shown in Figure 142. These rod-shaped γ' precipitates

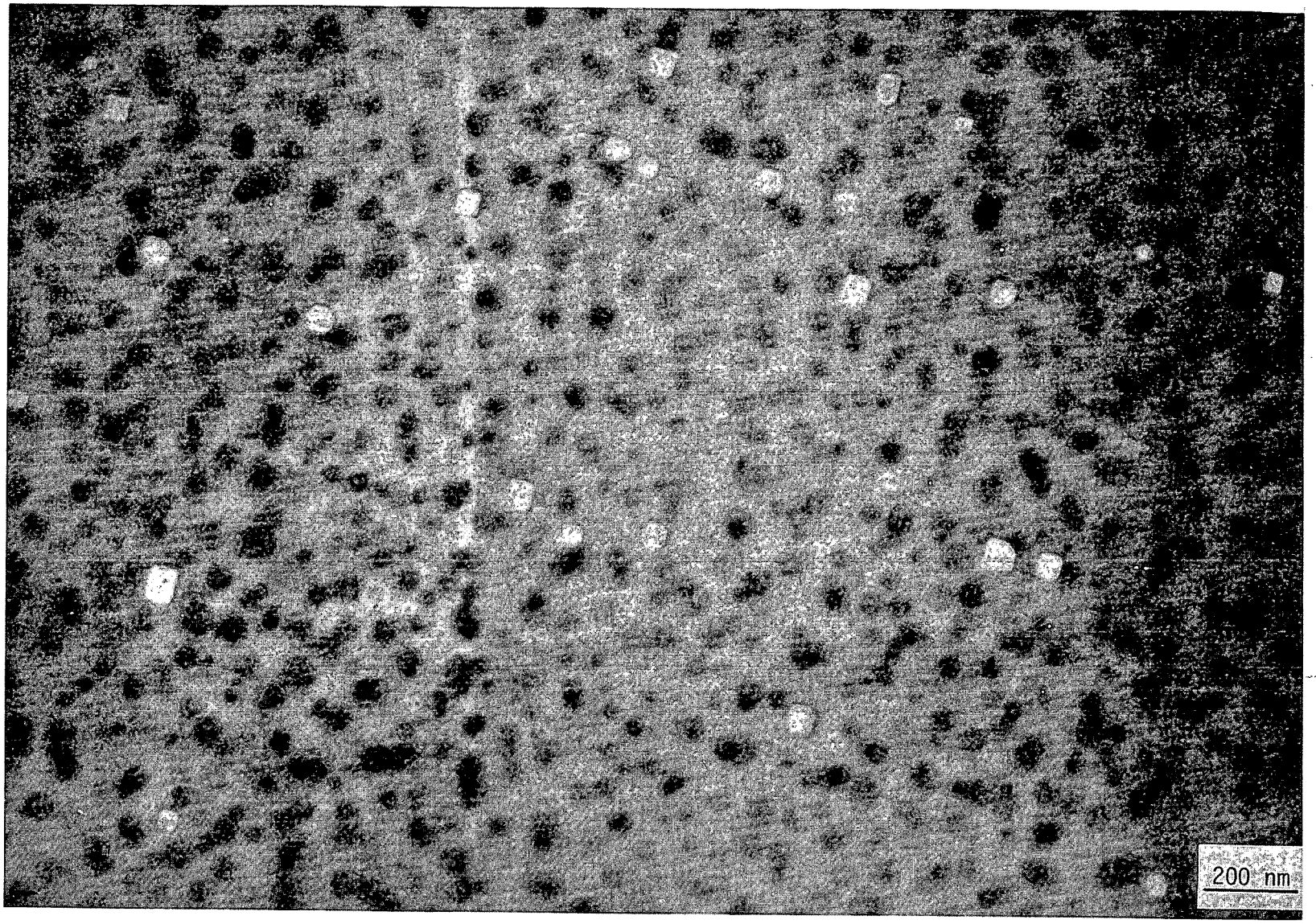

FIGURE 138. Void morphology of E40 after 2.7 x 10^{22} n/cm^2 at 593°C.

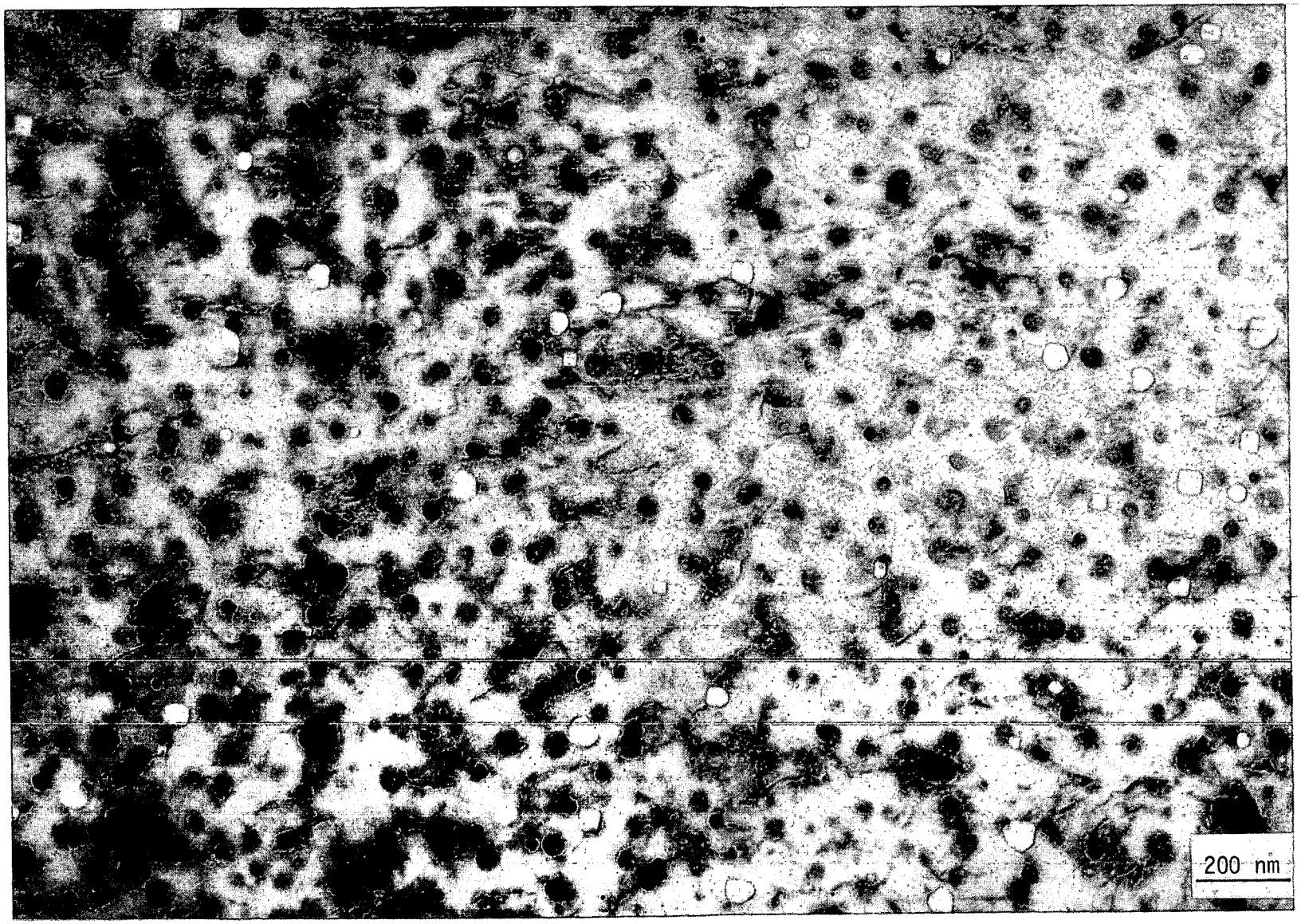

FIGURE 139. Void morphology of E42 after 2.7 x 10^{22} n/cm^2 at 593°C.

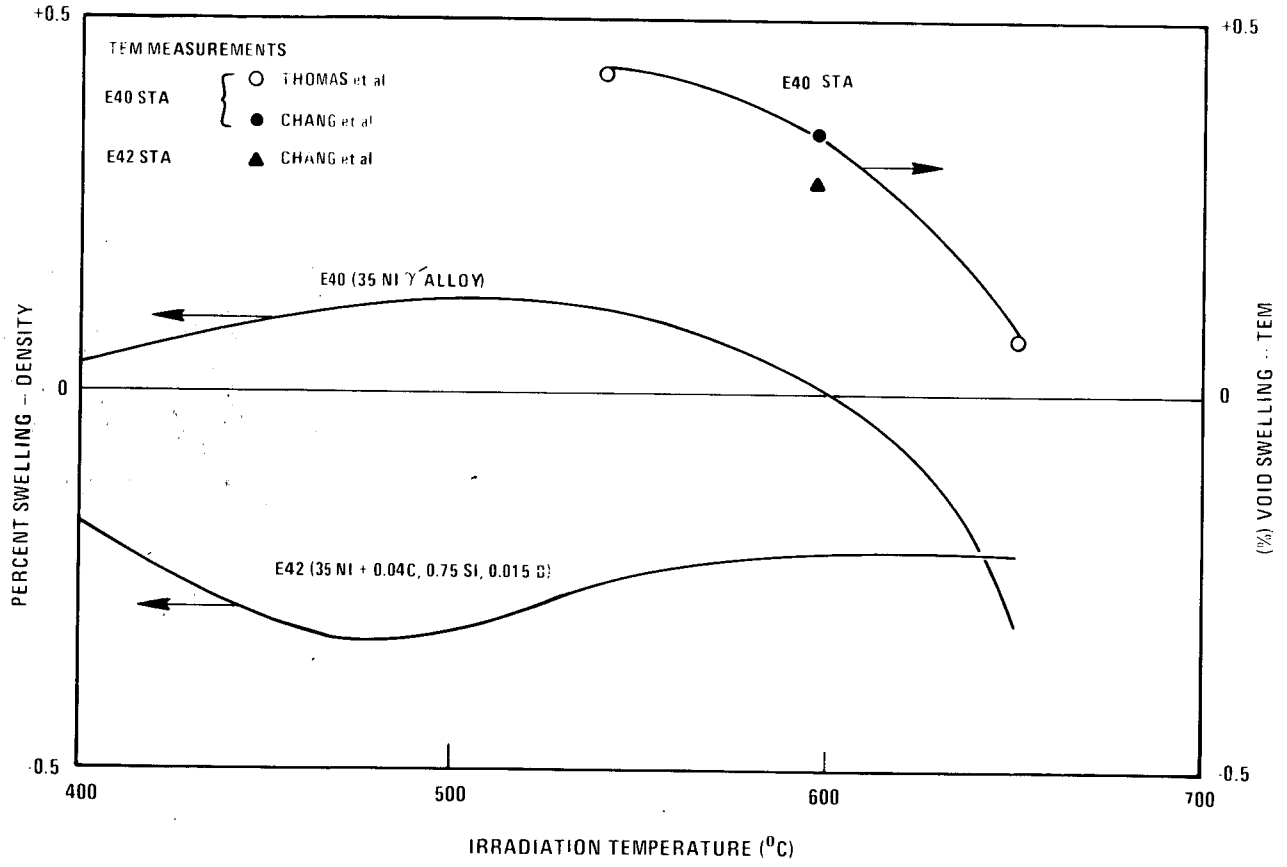

FIGURE 140. Temperature dependence of void swelling and density changes of E40.

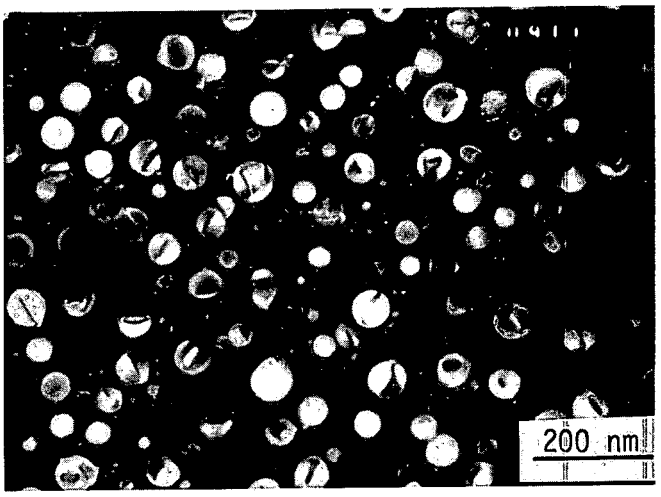

FIGURE 141. Superlattice dark field micrograph of γ' in E40 after 2.7×10^{22} n/cm^2 at 593°C.

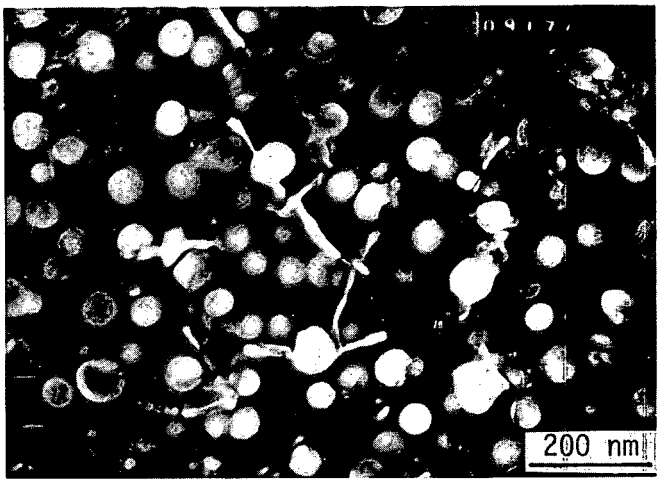

FIGURE 142. Superlattice dark field micrograph of γ' in E42 after 2.7×10^{22} n/cm^2 at 593°C.

are associated with dislocations. There appears to be a denuded zone of small γ' particles around these rod-shaped γ' precipitates. Small γ' particles with the configuration resembling a string of pearls were formed early in the irradiation on dislocations which are no longer present after irradiation.

Cellular γ' present before irradiation were also observed along grain boundaries in both E40 and E42 as shown in Figure 143 and Figure 144 respectively. Grain boundary precipitates (probably M_6C, $M_{23}C_6$ and Laves phase) and MC type carbides were observed in E42 but not in E40 due to the residual elements as shown in Figure 144. The small precipitates associated with voids observed in E42 after Ni-ion irradiation at 600°C reported by Chang, et al, were not observed after neutron irradiation at 593°C.

The γ' size distributions of neutron irradiated E40 and E42 are shown in Figures 145 and 146 respectively. In both cases, a double-peaked size distribution was observed with the small particles peaking at about 4.5 nm and large particles broadening their size distributions.

The microstructural data of neutron irradiated and pre-irradiation E40-36 and E42-36 are tabulated in Table 39.

TABLE 39

MICROSTRUCTURAL DATA OF NEUTRON IRRADIATED AND PRE-IRRADIATION E40-36 AND E42-36

Alloy	Void Swelling (%)	Average Void Size (nm)	Void Density (#/cm^3)	γ' Volume Percent (%)	Avg. γ' Diameter Size (nm)	Large γ' Concentration (#/cm^3)	Dislocation Density (cm/cm^3)
E40-36 J(0T)	0.34	60.5	3.0×10^{13}	9.9	S = 4.5 L = 46	1.46×10^{15}	1.4×10^{10}
E42-36 J(2T)	0.27	43	4.4×10^{13}	10.2	S = 4.5 L = 54	1.09×10^{15}	2.0×10^{10}
E40-36	-	-	-	9.3	38	2.56×10^{15}	-
E42-36	-	-	-	6.9	43.5	1.28×10^{15}	-

2.3.4 Discussion

2.3.4.1 Analysis of Neutron Irradiated Data. At this low fluence, the void swelling data of E40 and E42 are similar except that the average void size of E42 is significantly smaller than that of E40 (43 nm as compared to 60.5 nm). This could lead to a lower swelling rate for E42 at higher fluences if the void number density of these two alloys remains comparable.

The morphological evolution of the γ' precipitates under irradiation differs from that of the thermal double aging treatment according to the new theory of particle redistribution under irradiation formulated by Baron, et al[5]. It is suggested that there is a radiation-induced dissolution term in addition to the usual thermal growth term for the particle growth law. This will lead to the existence of an equilibrium maximum particle radius and a higher solute supersaturation under irradiation. Furthermore, it is predicted that under irradition the value of the product of the solute supersaturation and the maximum γ' particle radius should equal to the equilibrium value (which remains unchanged under further irradiation) if the system is within the so-called "dynamic scaling" region.

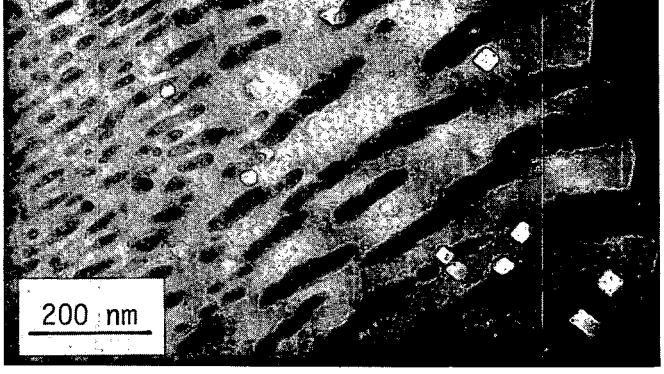

FIGURE 143. Cellular γ' morphology of E40 after 2.7 x 10^{22} n/cm^2 at 593°C.

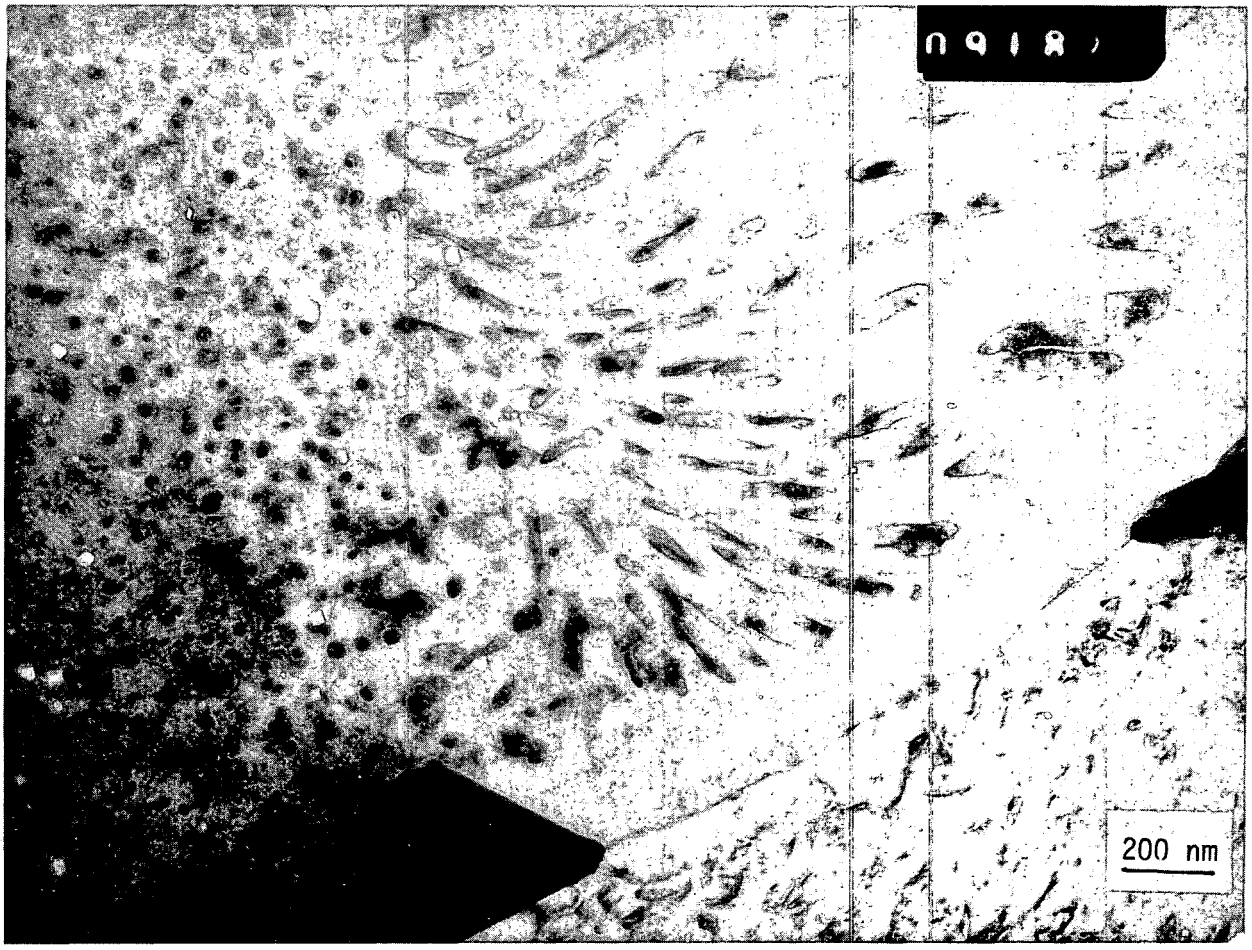

FIGURE 144. Cellular γ' morphology of E42 after 2.7 x 10^{22} n/cm^2 at 593°C.

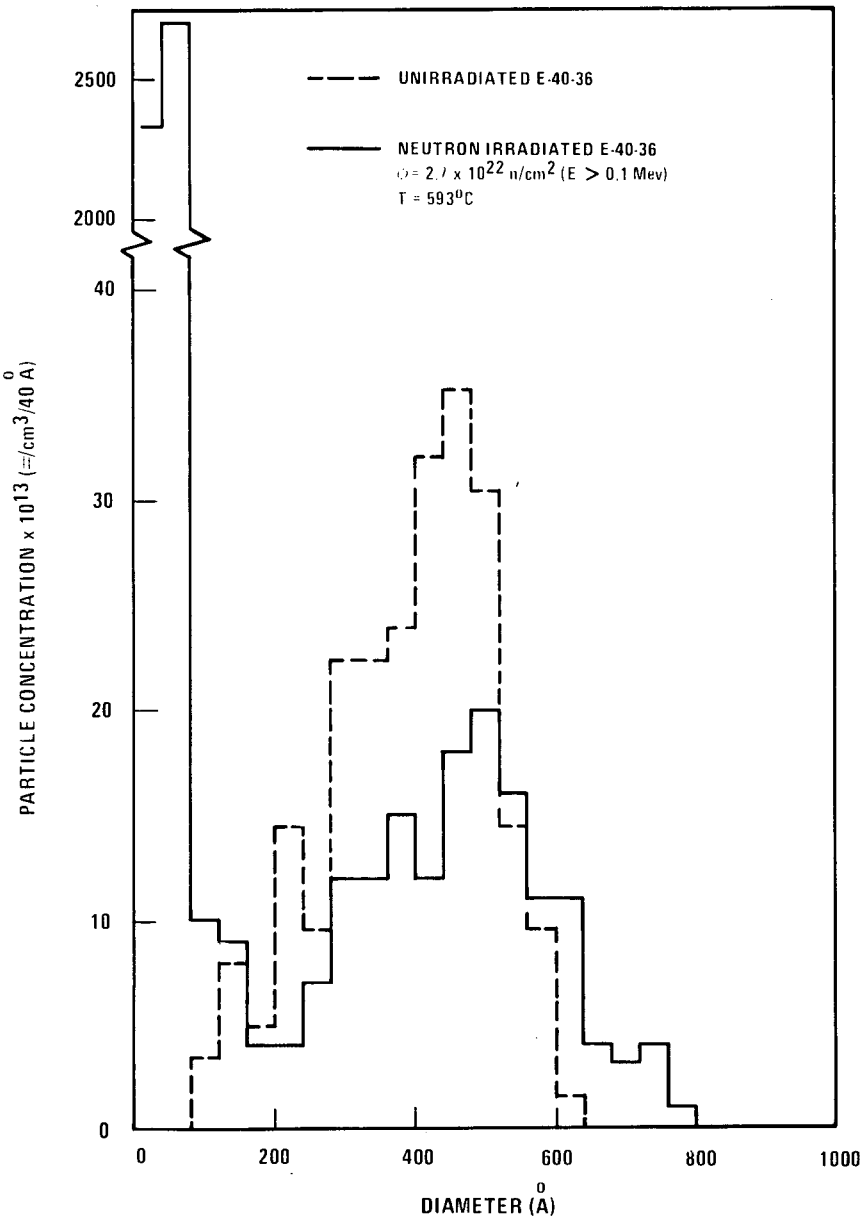

9460-2

FIGURE 145. Gamma prime particle size distribution of unirradiated and irradiated E40-36 after 2.7 x 10^{22} n/cm^2 at 593°C.

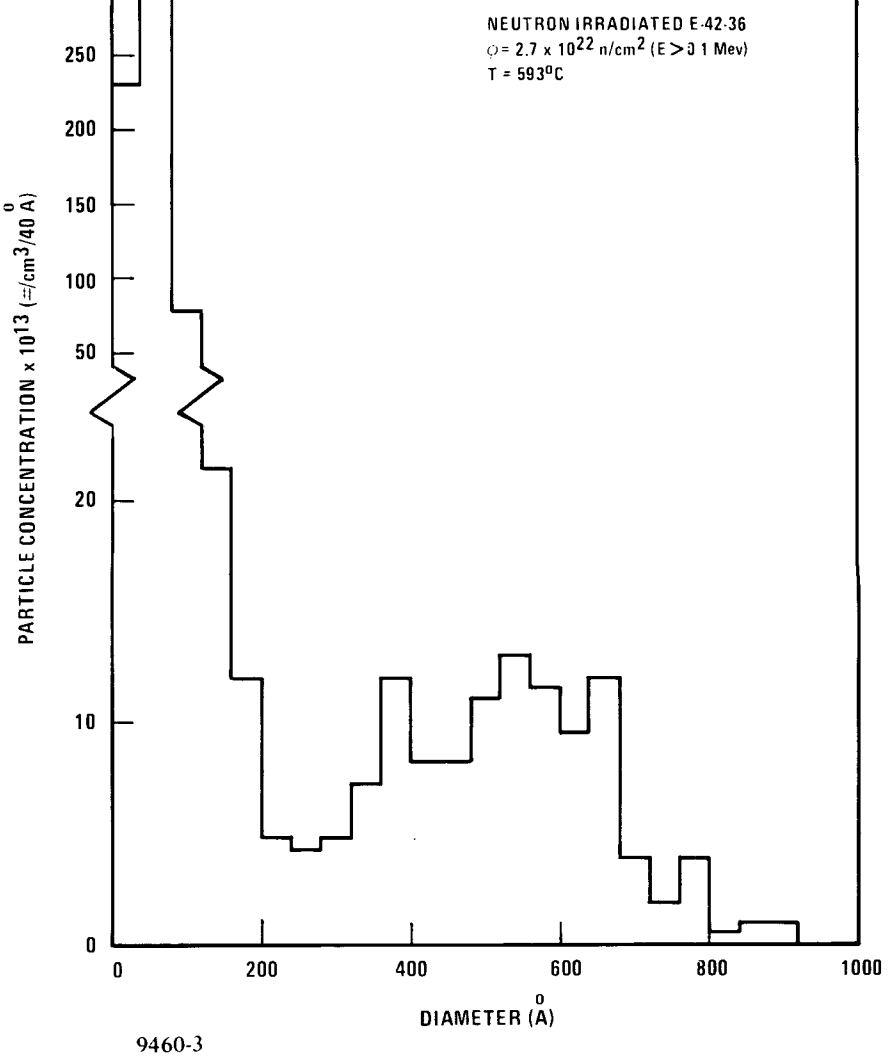

FIGURE 146. Gamma prime particle size distribution of irradiated E42-36 after 2.7 x 10^{22} n/cm^2 at 593°C.

In order to check whether the supersaturation of γ' forming solute was enhanced by the irradiation, it is necessary to compare the amount of γ' precipitation under irradiation to that under similar thermal double aging treatment. These double aged samples were solution treated at 1150°C for one hour, aged at 815°C for 10 hours and double aged at 593°C for various lengths of time ranging from 1,000 hours to 3,000 hours. Table 40 lists the γ' morphological data of the double aged E42-10 at 593°C. Comparing the 10.2% γ' volume percent in neutron irradiated E42 (about 2,160 hours at 593°C) to the 11.7 to 12.8% γ' volume percent in double aged E42 (between 1,000 to 3,000 hours at 593°C), it is evident that more γ' precipitation is observed in thermally double aged sample than that in the irradiated one.

TABLE 40

MICROSTRUCTURAL DATA OF DOUBLE AGED E42-10 AT 593°C

Alloy Condition	Avg. γ' Size (nm)	γ' Volume Percent (%)	Large γ' Concentration (#/cm^2)	$\overline{RN}_p$ (cm^{-2})
E42-10	28.5	6.5	4.11×10^{15}	5.8568×10^9
E42-10 1,000 hr at 593°C	S = 7.2 L = 33	11.7	4.47×10^{15}	7.3755×10^9
E42-10 3,000 hr at 593°C	S = 9.7 L = 39	12.8	3.57×10^{15}	6.9615×10^9

From the kinetic data of the thermally double aged E42-10 at 593°C listed in Table 40, it is concluded that the depletion of the supersaturation does not follow the usual $t^{-1/3}$ law for the single aging treatment. This is evident from the fact that the concentration of the large γ' particles stayed almost unchanged during the first 1,000 hours at 593°C while the volume fraction changed from 6.5% (after 10 hours at 815°C) to 11.7%. This implies that the solute supersaturation was depleted mostly by growth of already existing large particles. The growth law and depletion of supersaturation for the double aging treatment can be described as[6]:

$$\frac{d\bar{R}}{dt} = \frac{D_s \Delta(t)}{C_p^s \bar{R}} \qquad [1]$$

$$\frac{d\Delta(t)}{dt} = -4\pi D_s (\bar{R} N_p) \Delta(t) \qquad [2]$$

where

$\bar{R}$ = average radius of large particles

C_p^s = solute atomic fraction in precipitate

$\Delta(t)$ = supersaturation of solute in solution

N_p = number density of large particles (#/cm^3)

D_s = diffusion coefficient of solute

It was determined in E42 that $(\bar{R}N_p)$ stays almost constant during the entire double aging treatment as shown in Table 40. Therefore Equation [2] reduces to:

$$d \ln \Delta(t) = -4\pi D_s \langle \bar{R}N_p \rangle dt \qquad [3]$$

where $\langle \bar{R}N_p \rangle = 6.7313 \times 10^9$ (cm^{-2}) is the time average of $(\bar{R}N_p)$. Equation [3] can be integrated to yield

$$\Delta(t) = \Delta(0)e^{-4\pi D_s \langle \bar{R}N_p \rangle t} \qquad [4]$$

Experimental measurements of γ' volume fraction in E42 as a function of double aging time lead to the following relationship for the decay of the supersaturation

$$\Delta(t) = (1.584 \times 10^{-2}) \exp -(\lambda t) \qquad [5]$$

where $\lambda = 4.766 \times 10^{-7}$ sec^{-1}. Comparing [4] and [5] it is found that $\Delta(0) = 1.584 \times 10^{-2}$ and that the diffusion coefficient is given by

$$D_s = \frac{4.7663 \times 10^{-7}}{4\pi \times 6.7313 \times 10^{9}} = 5.63 \times 10^{-18} \text{ cm}^2/\text{sec}$$

and

$$V^{\infty} = \frac{\Delta(0)}{C_p^s} + V(0) = 0.1284$$

This value of the diffusion coefficient compares favorably with the one calculated from the aging studies of γ'#1 alloys[7]. It therefore appears that for double aging conditions Equations [1] and [2] provide a satisfactory description of the growth of large particles from solution.

These double aging data can be used to analyze the neutron irradiation data. After 2.7×10^{22} n/cm^2 at 593°C for about three months in EBR-II, E42-36 was found to increase its γ' volume percent from 6.9% to 10.2%. The supersaturation of the neutron irradiated E42-36 can be calculated:

$$^{*}\Delta = (V^{\infty} - V^{*})\, C_p^s = (12.84 - 10.2) \times 10^{-2} \times 0.25 = 0.0066$$

The maximum particle radius of the neutron irradiated distribution was measured to be:

$$R^{*}_{max} = 45 \text{ nm}$$

and

$$(\Delta^{*} R^{*}_{max})_{\text{Neutron Irr.}} = 0.297 \text{ nm}$$

The value of $(\Delta^{*} R^{*}_{max})$ should be equal to $(3a\, C_p^s + \alpha)$ if the evolution of particle redistribution is in the so-called "dynamic scaling" stage, according to the new theory where α is the L-S-W parameter[5]. The reader is referred to Section II.1 of this quarterly report by Baron and Chang (preceding paper) for details of this theory. From this theory the equilibrium value of the product of the supersaturation and the maximum γ' particle radius is:

$$(\Delta^{\infty}R^{\infty}_{max})_{Theoretical} = C^s_p(3a + \frac{\alpha}{C^s_p}) = 0.295 \text{ nm}$$

where

$$(\frac{\alpha}{C^s_p})_{E42 \text{ at } 593°C} = 0.1096 \text{ nm}^{\dagger}$$

a = lattice parameter = 0.357 nm

The theoretical value of $(\Delta^{\infty}R^{\infty}_{max})$ of 0.295 nm is in excellent agreement with the experimentally measured values of 0.297 nm from the neutron irradiation in alloy E42.

This is an experimental confirmation of the "dynamic scaling" hypothesis of the theory for neutron irradiation.

2.3.4.2 Interpretation of Ni-Ion Simulation Data. The Ni-ion simulation data on γ' morphological change can also be analyzed in terms of this theory. For the case of Ni-ion simulation experiments of E42-10 at 600°C, the solute supersaturation after 100 dpa can be calculated to be[2]:

$$(\Delta^{*}_{Ni^+})_{E42-10} = (V^{\infty} - V^{*})\, C^s_p = (12.84-8.3) \times 10^{-2} \times 0.25 = 0.01175$$

The maximum γ' particle radius of the Ni-ion irradiated E42-10 after 100 dpa at 600°C was measured to be[2]:

$$R^{*}_{max} = 25 \text{ nm}$$

and

$$(\Delta^{*}R^{*}_{max})_{Ni\text{-ion Irr.}} = 0.294 \text{ nm}$$

This value of $(\Delta^{*}R^{*}_{max})$ is also in excellent agreement with the theoretical value 0.295 nm.

In another simulation experiment, alloy E48 (aged at 815°C for 36 hours) was Ni-ion irradiated to 165 dpa at 750°C with dose rate 7.35×10^{-3} (dpa/sec). Similar analysis shows that:

$$(\Delta^{*}_{Ni^+})_{E48-36} = (V^{\infty} - V^{*})C^s_p = (14.306-7.22) \times 10^{-2} \times 0.25 = 1.7715 \times 10^{-2}$$

and

$$R^{*}_{max} = 19.5 \text{ nm}$$

---

†See Reference 7

$$(\Delta^* R^*_{max})_{\text{Ni-ion Irr.}} = 0.3454 \text{ nm}$$

for alloy E48-36 at 750°C.

The theoretical equilibrium value was calculated to be:

$$(\Delta^\infty R^\infty_{max})_{\substack{\text{Theoretical} \\ \text{E48 at 750°C}}} = C^s_p(3a + \frac{\alpha}{C^s_p}) = 0.3411 \text{ nm}$$

where

$$(\frac{\alpha}{C^s_p})_{\text{E48 at 750°C}} = 0.2934 \text{ nm}^\dagger$$

Again, the excellent agreement between the experimental value 0.3454 nm and theoretical equilibrium value 0.3411 nm indicates that the γ' particle size distribution under irradiation is evolving according to the "dynamic scaling" scheme and is approaching the equilibrium distribution. Table 41 lists the γ' microstructural data of Ni-ion irradiated and pre-irradiation E48-36 and E42-10. Examination of the data listed in Table 41 shows that the average γ' particle diameter of E48-36 decreased from 42 nm to 22 nm and the γ' volume fraction also decreased from 7.70% to 7.22% in the Ni-ion irradiated E48-36. These observations confirm that the effect of dissolution of the oversized γ' particles to an equilibrium average size does occur under irradiation as predicted by the theory[5]. Figure 147 shows schematically the change of average γ' particle diameter as a function of dose for Ni-ion irradiated E42-10 at 600°C and E48-36 at 750°C. The fact that the average γ' size of E42-10 after 100 dpa Ni-ion irradiation does not change suggests that the equilibrium γ' diameter for E42 at 593°C is around 36 nm. Although there is an apparent growth of γ' particles under neutron irradiation from 43.5 nm to 54 nm after 2.7×10^{22} n/cm^2 at 600°C in E42-36, we predict that further neutron irradiation would decrease the average size to around 36 nm, the same equilibrium size as shown schematically in Figure 140.

2.3.4.3 Estimation of Dissolution Parameter. The dissolution parameter, Ψ, can be estimated from the equilibrium maximum radius, R^∞_{max}, in terms of the following relation:

$$R^\infty_{max} = \sqrt{\frac{3a\tilde{D}_s}{\psi K}}$$

where

$\tilde{D}_s$ = diffusion coefficient of solute under irradiation

K = dose rate (dpa/sec)

---

†See Reference 7.

TABLE 41

GAMMA PRIME MICROSTRUCTURAL DATA OF Ni-ION IRRADIATED AND PRE-IRRADIATION E48-36 AND E42-10

Alloy Condition	Average γ' Diameter (nm)	γ' Volume Percent (%)	γ' Concentration (#/cm^3)	$(\frac{\alpha}{C_p^s})$(nm)
E48-36 (165 dpa at 750°C)	22	7.22	1.0478×10^{16}	0.2934
E48-36 (unirradiated)	42	7.70	1.654×10^{15}	0.2934
E42-10 (102 dpa at 600°C	S = 10 L = 36	8.30	S = 7.10×10^{15} L = 5.20×10^{15}	0.1096
E42-10 (unirradiated)	31.5	6.5	5.47×10^{15}	0.1096

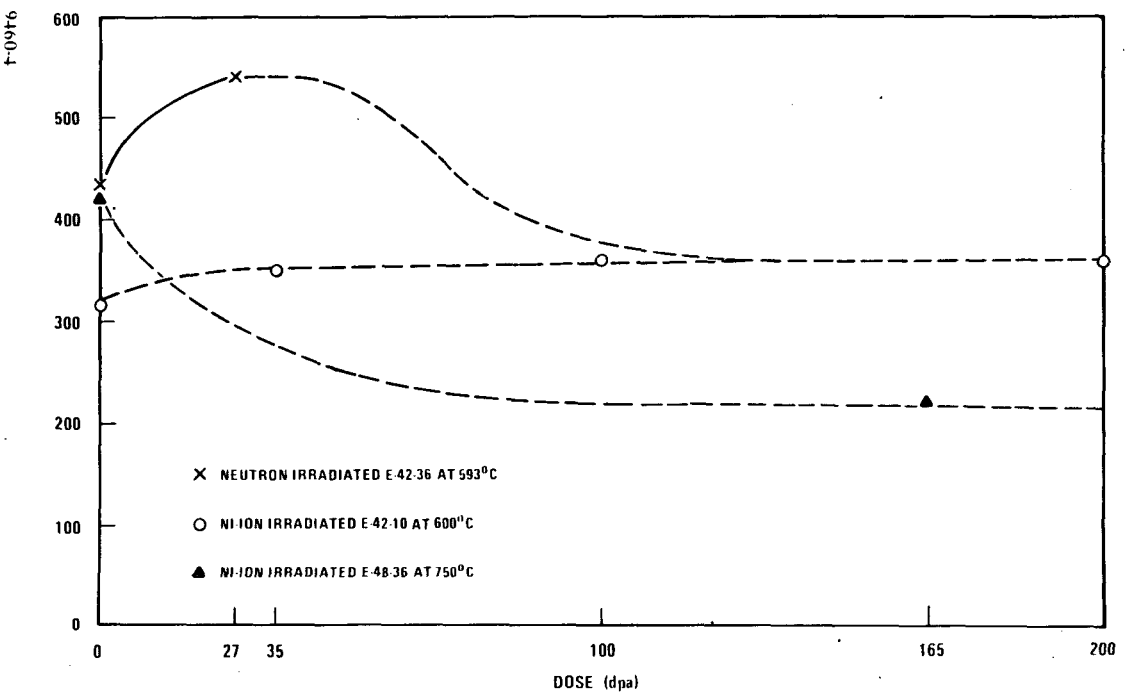

FIGURE 147. Schematic representation of the average γ' particle size as a function of dose.

The diffusion coefficient, $\tilde{D}_s$, under irradiation can be calculated by using the appropriate values of the dose rate and the sink density[5] and they are listed below:

$\tilde{D}_s$(cm^2/sec)	T(°C)	k(dpa/sec)	ρ(cm/cm^3)	Irradiation
1.8×10^{-14}	750	10^{-3}	10^{11}	Ni-ion
9.5×10^{-15}	600	10^{-3}	10^{11}	Ni-ion
2.0×10^{-17}	600	10^{-6}	10^{11}	Neutron

The dissolution parameters were estimated to be:

ψ(750°C, Ni^+ Irr.) ≡ 6.9 nm
ψ(600°C, Ni^+ Irr.) ≡ 1.6 nm
ψ(600°C, Neutron Irr.) ≡ 3.5 nm

The cascade size resulting from the 4 MeV Ni-ion irradiation is about 1 nm while the cascade size resulting from 1 MeV neutron irradiation is about 4 nm[8,9]. The estimated dissolution parameters 1.6 nm for Ni-ion and 3.5 nm for neutron seem to be reasonable as compared to the cascade size at 600°C. The fact that R^{∞}_{max} (750°C) is smaller than R^{∞}_{max} (600°C) suggests that the dissolution parameter could increase faster than $\tilde{D}_s$ with increasing temperature.

2.3.5 Conclusions

1. TEM examination of the neutron irradiated alloys E40-36 and E42-36 showed 0.34% and 0.27% void swelling respectively.

2. Irradiation-induced smaller γ' particles were found between original large γ' particles on dislocations and void surfaces.

3. Higher amounts of solute were left in solution under both neutron and Ni-ion irradiation. The product of supersaturation and maximum particle radius for both neutron and Ni-ion irradiation was found to be very close to the theoretical value.

4. It is expected that further neutron irradiation would decrease the average γ' particle size from the present value 54 nm to about 36 nm.

5. Dissolution parameters were estimated to be comparable with the cascade sizes at 600°C.

6. Present analysis provides a framework for correlating the Ni-ion simulation data with the in-reactor kinetics of phase redistribution effects in Fe-Ni-Cr based alloys.

2.4 EXPECTED ACHIEVEMENTS IN THE NEXT REPORTING PERIOD

Examination of the other alloys in the AA-IX experiment will continue. Emphasis will be placed on the consequence of the variation of compositions and the pre-irradiation heat treatment conditions and irradiation temperatures.

2.5 REFERENCES

1. W-ARD contributions to Alloy Development Program Quarterly Technical Progress Letters, TC-160-3 (10-12/1974), p. 136; TC-160-4 (1-3/1975), p. 237; TC-160-5 (4-6/1976), p. 288; TC-160-7 (10-12/1975), p. 144, and TC-160-8 (1-3/1976), p. 199.

2. Ibid., TC-160-6 (7-9/1975), p. 202, 223, 238; TC-160-10 (7-9/1976).

3. Ibid., TC-160-6 (7-9/1975), p. 223.

4. Thomas, L. E., Ibid., TC-160-9 (4-6/1976); Annual Information Meeting, National Alloy Development Program, 10/20/74, TC-721, p. 114.

5. Baron, I. M., and Chang, A. L., "Particle Redistribution under Irradiation", this quarterly report.

6. Ham, F. S., J. Phys. Chem. Solids, Vol. 6, p. 335-351 (1958).

7. Chang, A. L., and Baron, I. M., W-ARD Topical Report, "Pre-Irradiation Characterization of W-ARD γ'#1 Fe-Cr-Ni Experimental Alloys for LMFBR," to be published.

8. Sigmund, P., et al, Rad. Effects, 11, p. 39 (1971).

9. Marwick, A. D., AERE-R-7745, May 1974.

3. ELECTRON IRRADIATION OF SOLUTION ANNEALED 316 FOR THE USP EXPERIMENT

R. W. Powell
Hanford Engineering Development Laboratory

3.1 OBJECTIVE

The Unified Simulation Program (USP) has two principal objectives. First, it is intended to provide verification of the ability of simulation experiments to duplicate in-reactor swelling behavior. Second, the USP experiment will provide guidance for performing and interpreting simulation experiments on previously neutron-irradiated (preconditioned) specimens.

3.2 SUMMARY

High Voltage Electron Microscope (HVEM) electron irradiations were performed on SA 316 from heat M2783. Steady-state swelling rates were determined to be 0.90%/dpa(e) and 0.66%/dpa(e) at 650 and 600°C, respectively. In both cases, the void shapes tended toward spheres as the irradiations progressed. The growth rate of a void attached to a precipitate was found to be significantly higher than the average. It is concluded that such a phenonemon may occur extensively in some alloys and contribute to high steady-state swelling rates.

3.3 ACCOMPLISHMENTS AND STATUS

3.3.1 Introduction

The Unified Simulation Program is composed of several elements, including HVEM electron irradiations and nickel ion bombardments of solution annealed 316, cold worked 316, preconditioned solution annealed 316, preconditioned cold worked 316 and preconditioned Nimonic PE16. These experiments allow comparison of swelling rates determined from relatively high fluence neutron irradiations with the swelling rates determined from simulation studies.

Specimens of AISI 316 stainless steel from heat M2783 have been selected for a major portion of the USP experiment, for two principal reasons. First, material which has been neutron irradiated to approximately 8×10^{22} n/cm^2 (E>0.1 MeV) is available for use in simulation studies. This is the highest-fluence source of preconditioned (i.e., neutron irradiated) specimens currently available. Second, swelling data for this material exist at an even higher fluence, and this permits a comparison to be made of swelling during simulation experiments (i.e., no prior neutron irradiation), swelling during preconditioned simulation experiments (i.e., previously neutron irradiated specimens) and swelling during neutron irradiation. The work reported here deals with the first phase of the experiments involving HVEM electron irradiation of SA 316.

3.3.2 Experimental Procedure

The initial specimen preparation steps were performed by GE-FBRD. Disks were cut from solution annealed tubing of 316 (heat M2783) and ground flat on both sides. One surface

was then prepared for helium injection and helium was deposited to a depth of approximately 0.0026 mm at a nominal concentration of 5 appm. HEDL completed final specimen preparation for HVEM irradiation.

Transmission electron microscopy specimens were prepared with the examination midplane at a depth of approximately 0.0013 mm from the injected surface by electropolishing at approximately 10°C. This distance from the original surface was chosen to avoid any damage produced by the initial specimen preparation steps and to remain in the helium-containing zone. Some dislocation tangles were evident at this depth but were easily avoided when choosing the area to be irradiated. The presence of helium was verified by observing black spot damage under strong diffracting conditions at the start of HVEM examination.

A displacement rate of 9.1 dpa(e)/hour was employed for a total irradiation time of two hours. Micrographs were taken at time intervals to provide typically seven data points per irradiation. Thickness of the void layer was determined from stereo pairs taken halfway through the irradiation.

Void analyses were performed using the analyzing system "TRUNC" developed by L. E. Thomas[1]. This computer-based system accounts for void orientation and the degree of truncation in the void shape to more accurately define the void volume. All micrographs were taken near the [110] direction and a range of void shapes was estimated for each micrograph. The reported swelling values have been corrected for void volume fraction.

3.3.3 Results

HVEM irradiations have been performed at 600 and 650°C and analyses have been completed. Figures 148 and 149 describe the swelling as a function of dose for each of the irradiations while Figure 150 shows the corresponding variation of average void diameter with dose. Figure 151 depicts the change in void density with displacement damage.

The observed steady-state swelling rate is greater at 650°C than at 600°C. The steady-state swelling rate of 0.90%/dpa(e) at 650°C is within the range of rates reported by Gelles, Guthrie and Berting[2] for similar HVEM irradiations on the cold-worked condition of the same heat of 316. The rate of 0.66%/dpa(e) found at 600°C is lower, although not significantly, than the swelling rate determined by Gelles, et al[2] at the same temperature for cold-worked material. Comparison of these rates with neutron irradiation results on the same heat of 316 will be performed after the temperature dependence of swelling during HVEM irradiation has been determined.

The void sizes and void densities for the two irradiations show the typical variation of these parameters with dose. As shown in Figure 150, the average void diameter continually increases with dose while the void densities (Figure 151) initially increase due to void nucleation or increased void visibility (with increasing size) and then decrease due to void coalescence.

Examples of void coalescence are seen in Figure 152 in which the process occurred during examination, when the displacement rate was very low. The time elapsed between Figures 152(a) and 152(c) was less than five minutes. Note that the void centers have moved closer together and the void shapes have become more rounded during coalescence.

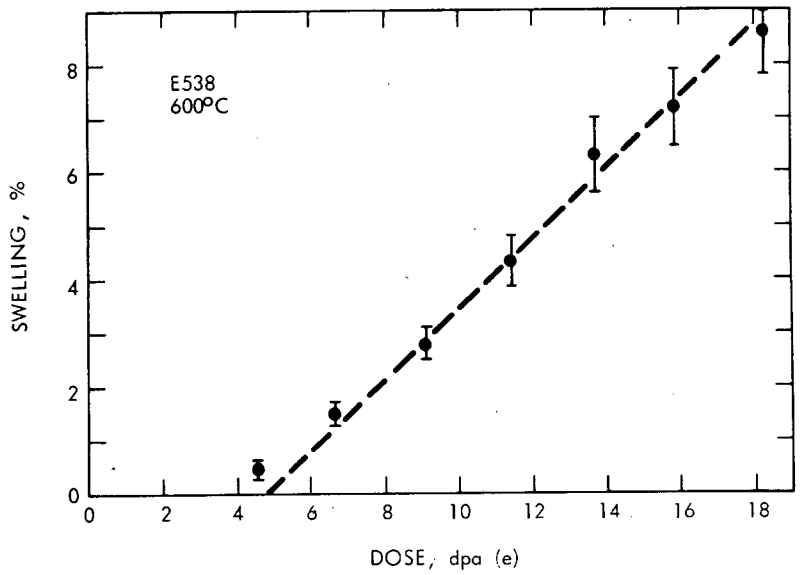

HEDL 7701-103.1

FIGURE 148. Swelling as a function of displacement damage in solution annealed 316 stainless steel (heat M2783) during HVEM electron irradiation at 600°C.

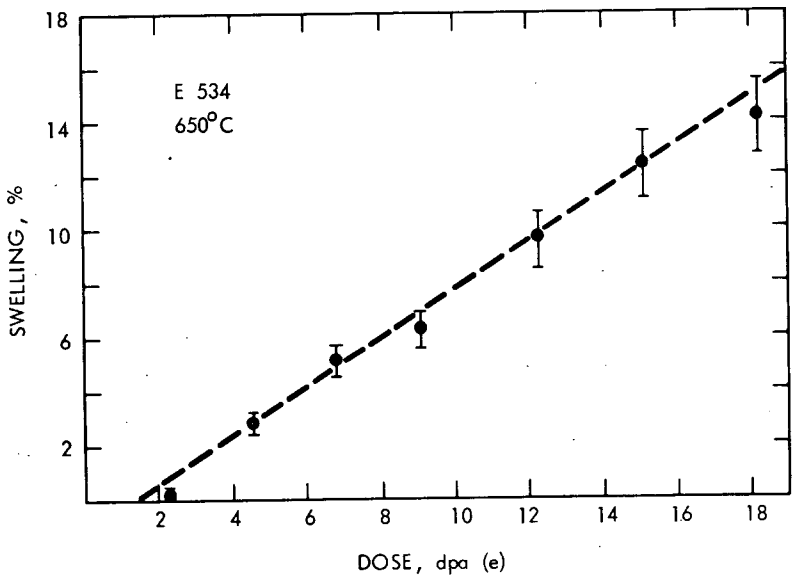

HEDL 7701-103.2

FIGURE 149. Dose dependence of swelling in heat M2783 for HVEM electron irradiation at 650°C.

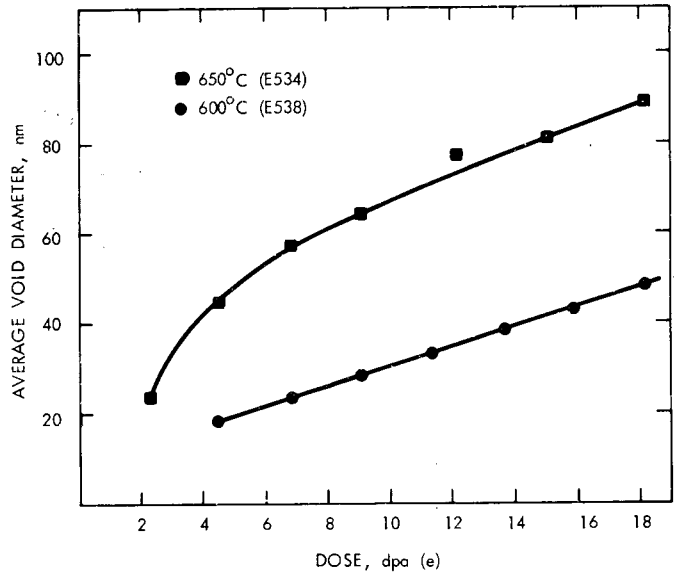

HEDL 7701-103.3

FIGURE 150. Variation of average void size during HVEM irradiation of 316 stainless steel at temperatures of 600 and 650°C.

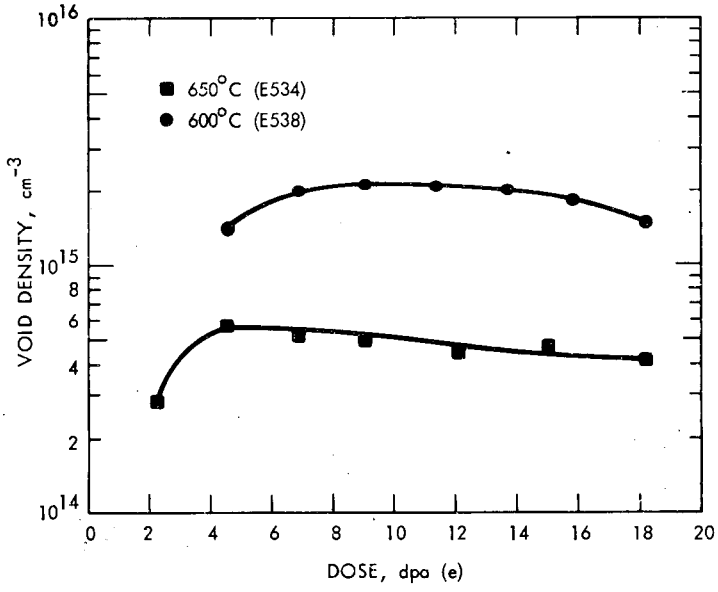

HEDL 7701-103.4

FIGURE 151. Void density variation with displacement damage during HVEM electron irradiations at 600 and 650°C.

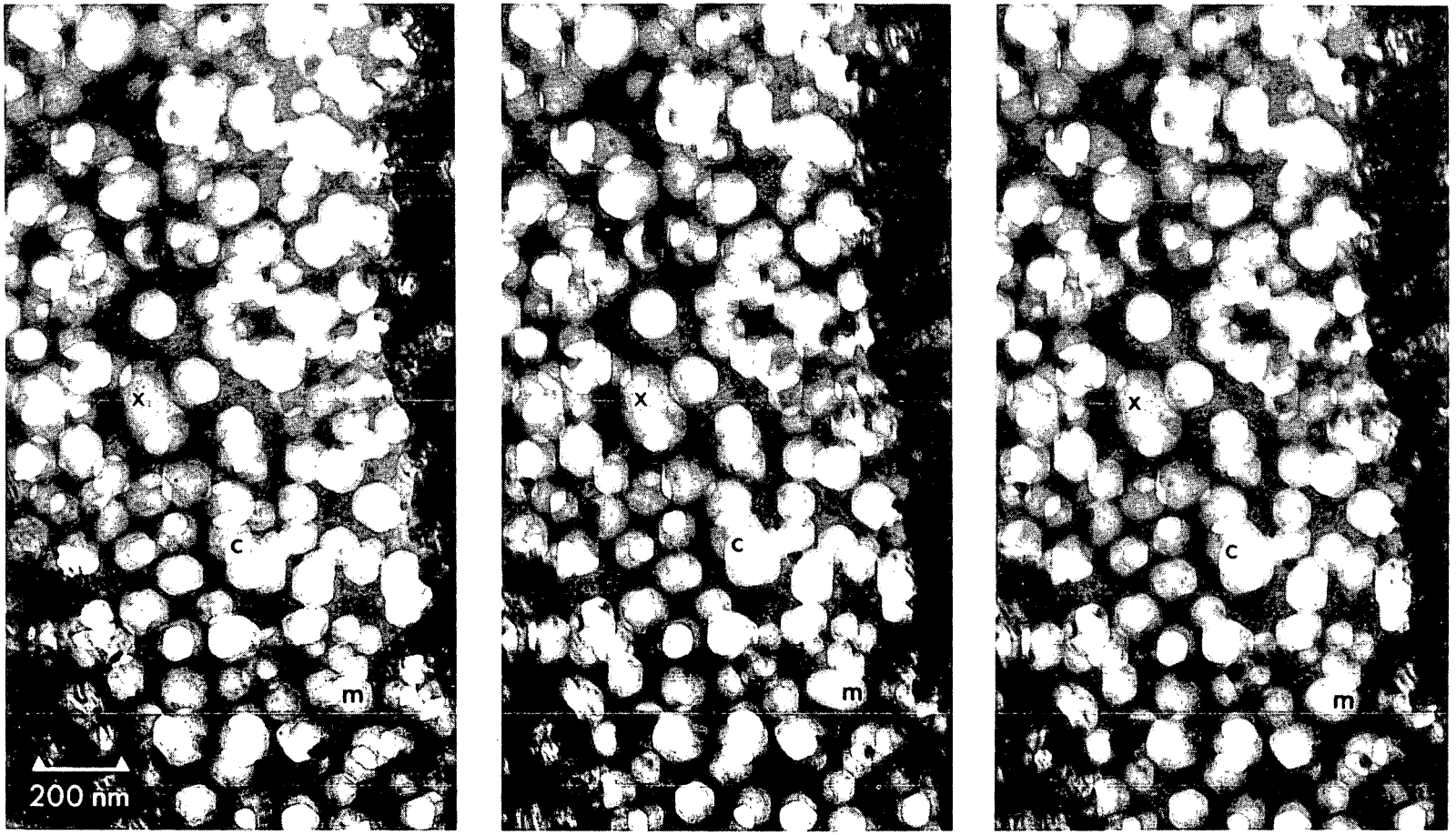

(a) (b) (c)

FIGURE 152. Time sequence showing void coalescence occurring during examination. Base temperature was 615°C. Coalescence events are designated with letters.

Other processes involving precipitates were observed. An association between a void and precipitate (probably a carbide) was observed during irradiation of E534 and was followed for a series of micrographs. This is illustrated in Figure 153 where it is apparent that the void associated with the precipitate is not only the largest void but also has a greater growth rate than the other voids. This observation is important since extensive occurrence may greatly increase the swelling rate of the alloy. This may explain the high swelling observed in neutron-irradiated A-286 where extensive void-precipitate association occurs, and may also explain high swelling in 316 during neutron irradiation at 600°C. It also seems apparent from this series of micrographs that the void formed at (or in) the pre-existing precipitate rather than vice versa. In addition, the fact that a portion of the strongly diffracting precipitate loses contrast as the void grows indicates that the precipitate is changed by the void growth process.

In voids which were not associated with precipitates, void growth appeared to affect the degree of void truncation. In each of the two HVEM irradiations performed on 316 for the USP experiment, the void shape changed from a slightly truncated cube ($f \tilde{=} 0.9$ in Reference 1) at low dose to a more highly truncated cube ($f \cong 0.5$) at higher doses. This change with dose is illustrated in Figures 153(b) and 153(c). Such a change probably occurs as a result of an increased importance of the surface energy (increased truncation reduces the ratio of surface area to volume) and may simply be a consequence of a changing void size. However, it is possible that the void shape is determined by kinetic processes rather than thermodynamics. For example, the relative contributions of surface diffusion (on the void surface) and lattice diffusion may control the void shape. In this case, the displacement rate may be an important parameter in determining void shape or void size when greater truncation occurs. Kinetically determined void shape may also explain the shape change which occurs during coalescence (surface diffusion may become more important than bulk diffusion).

3.3.4 Conclusions

The HVEM electron irradiations of solution-annealed 316 stainless steel (heat M2783) have led to the following conclusions:

1. The steady-state swelling rates for heat M2783 at 600 and 650°C lie within the range of values observed for the 20% CW condition and the solution annealed conditions.

2. The void shape in annealed 316 progresses during HVEM irradiation from a slightly truncated cube to a shape which is equally well defined as a {111} truncated cube or a {100} truncated octahedron.

3. Void formation at (or in) certain precipitates results in a higher steady-state swelling rate due to increased void growth rates.

3.4 EXPECTED ACHIEVEMENTS IN THE NEXT REPORTING PERIOD

Additional HVEM irradiations will be performed on this material to establish the temperature dependence of the swelling rate. Irradiations will also be performed for neutron-irradiated material in the cold-worked condition. Neutron-irradiated cold-worked tubing has been received from GE and specimen preparation is in progress.

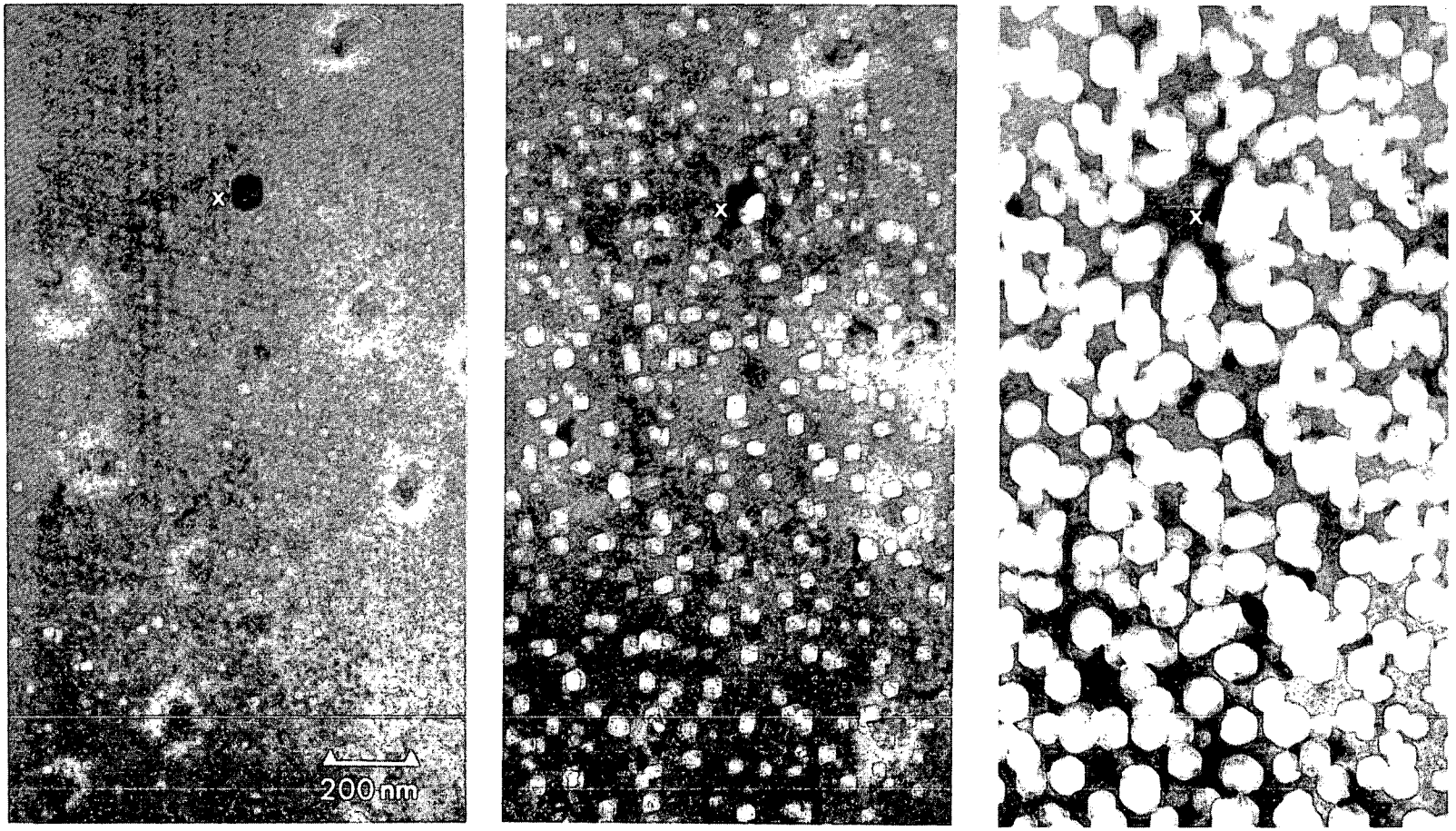

(a) (b) (c)

FIGURE 153. Irradiation sequence at 650°C showing accelerated void growth at a precipitate. Also note the change in void shape between (b) and (c).

3.5 REFERENCES

1. Thomas, L. E., Annual Information Meeting, National Alloy Development Program, October 20, 1976, TC-721, p. 544.

2. Gelles, D. S., Guthrie, G. L., and Berting, F. M., Reference Core and Structural Materials Quarterly Report, TC-675-2 (7-9/1976), 1-170.

4. PREPARATION OF ION BOMBARDMENT SPECIMENS FROM NEUTRON IRRADIATED TUBING

L. J. Turner and P. S. Sklad
Oak Ridge National Laboratory

4.1 OBJECTIVE

The Unified Simulation Program of which this work is a part is designed to establish a correlation between neutron, ion and electron damage in 316 stainless steel.

4.2 SUMMARY

In order to prepare ion bombardment disks from the M2783 316 tubing irradiated in the X-098 experiment, a shielded facility has been set up to permit spark cutting of disks from the tube wall. Grinding and polishing of the curved disks is accomplished semi-automatically in a rotary turret containing four disks held under vacuum. Techniques for the final polishing stages have been worked out. Difficulties are being experienced with the initial rough grinding stage.

4.3 ACCOMPLISHMENTS AND STATUS

4.3.1 Introduction

A description of the USP is provided elsewhere in this document. Ion and electron irradiations are to be carried out on both virgin and neutron irradiated TEM disks prepared from both solution annealed and cold worked tubing. During ion bombardment, five disks are clamped firmly against a thermalizer block which is heated directly by a broad electron beam. To ensure that each disk is maintained at the same temperature it is important that the disks should be flat, parallel-sided and of the same thickness to within 15 μm. In addition to these requirements it is essential that the preparation technique does not introduce deformation and that the surface to be bombarded should be smooth enough for accurate surface profilometry. In addition this surface will eventually form one surface of a TEM specimen. The neutron irradiated material is in the form of tubes 5 cm long, 6.35 mm diameter with a 0.38 mm thick wall. Each tube has a total activity of 20 R hr^{-1} at a distance of 5 cm. To minimize handling problems it has been decided to spark cut disks 3 mm diameter from the tube wall and to develop a technique for reducing the curved disk to a flat specimen meeting the requirements described above. A rotary turret polisher is under development and is described below.

4.3.2 Experimental Procedure

The equipment described here is being developed to prepare ion bombardment specimens from neutron irradiated material in an out-of-cell facility, and to minimize exposure to the operator by working semi-automatically. A low speed metallographic polishing wheel is used fitted with a "Whirlimet" attachment which permits specimens to be rotated in the opposite sense to the polishing wheel. The normal "Whirlimet" polishing head is removed and replaced with a stainless steel rotary turret which holds four disk specimens. A general

view of the arrangement is shown in Figure 154. An exploded view of the rotary turret is shown in Figure 155. To avoid mounting with epoxy or other adhesives, the disk specimens are held in place by a vacuum. Four hollow pistons are used [Figure 155(a)] located on a 6.4 cm diameter circle at 90° spacing. They are constructed to allow a differential pressure to hold the disks in place and at the same time to permit differential loading. Each piston is fitted with a return spring which also acts to bias the pressure applied to the disks. Vacuum is applied to the piston internally through the shaft and is monitored at a control panel. To control the turret vacuum a pressure-demand type regulator and two solenoid valves are used. This allows the negative pressure to be controlled to within 12 mm Hg. The vacuum is provided by a carbon vane dry-type rotary vacuum pump using a liquid/air separator to prevent liquid from entering the pump.

The turret is mounted on a central shaft [Figure 155(b)] using two double sealed combination radial and thrust ball bearing assemblies [Figure 155(c)] modified from the "Whirlimet" attachment. Polishing rate is monitored using two dial gauges mounted opposite each other and in contact with the tops of the pistons. The turret and shaft assembly are supported by a strut [Figure 155(e)] which also allows the turret to be moved vertically.

Disks are loaded by raising the "Whirlimet" attachment on its hinged mounting plate (Figure 156) and setting the vacuum regulator to maintain a negative pressure of 63.5 mm Hg at the turret. Disks are then inserted using a vacuum tweezer. When polishing is complete, the unit is again tilted vertically and the vacuum regulator set to provide full vacuum (400 mm Hg) causing the disks to protrude from the base of the turret. The disks are removed with vacuum tweezers. The entire unit is housed in a shielded glove box; active particles are flushed from the polishing unit into a suitable container for disposal.

The preparation sequence involves initial grinding on 600 grit paper to obtain a parallel sided disk. This is followed by removal of about 50 μm of material from the side to be bombarded by polishing with 0.3 μ Al_2O_3 on nylon cloth. The next step is a 0.5 μm diamond polish to remove ~10 μm. This removes any remaining surface damage and produces a good surface for subsequent TEM. It is not certain yet whether or not the 0.5 μm diamond stage is necessary although the amount of electropolishing should be minimized to maintain as smooth a surface as possible for profilometry. Initial trials with the equipment have demonstrated the ease of loading and unloading of disks. Uniform polishing rates producing good surfaces have been achieved with the Al_2O_3 and diamond polishing media. Some difficulty is still being experienced with the 600 grit grinding stage using disks spark cut from tubes, mainly due to the curved geometry of the samples. Several alternative types of grinding wheel are currently being experimented with. The possibility of giving the disks a preliminary grinding in a hand held jig to establish a flat on the convex side of the specimen is also being investigated.

4.4 EXPECTED ACHIEVEMENTS IN THE NEXT REPORTING PERIOD

It is anticipated that the difficulties with the initial grinding will be resolved and that preparation of all the disk specimens for USP will be prepared. A second turret is being fabricated so that one unit may be used exclusively for the fine polishing stage.

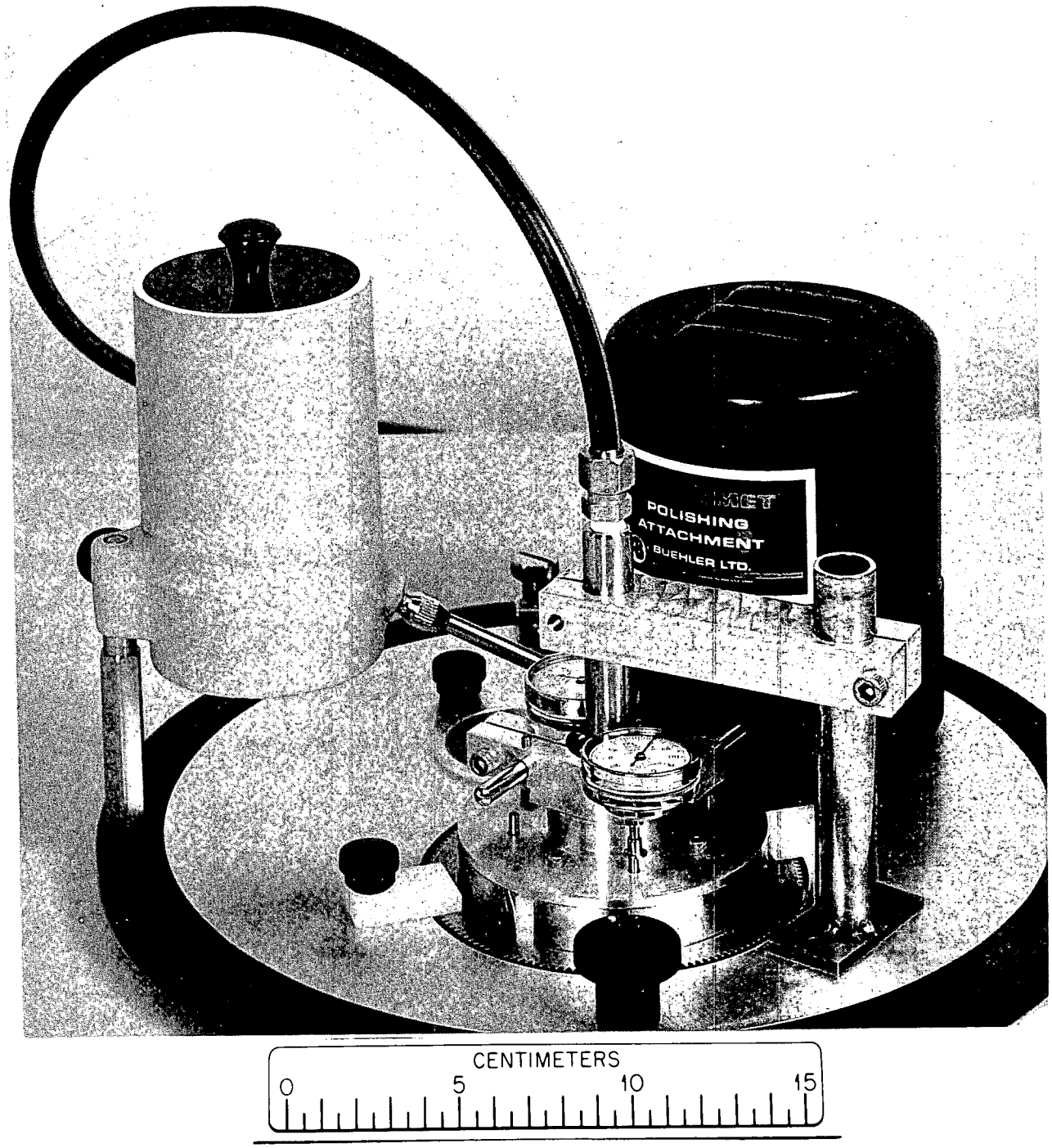

FIGURE 154. Rotary turret in position on "Whirlimet".

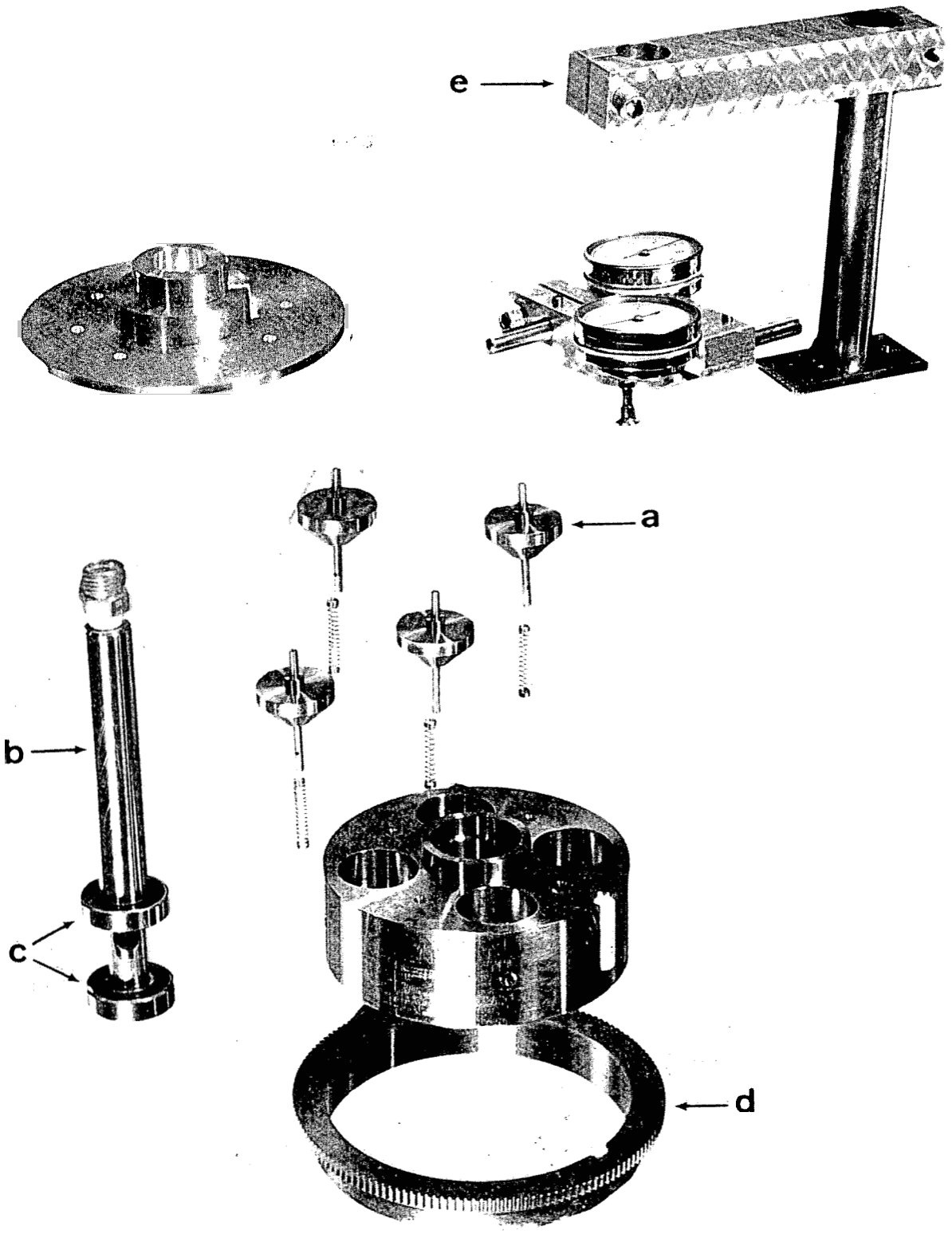

FIGURE 155. Exploded view of rotary turret.

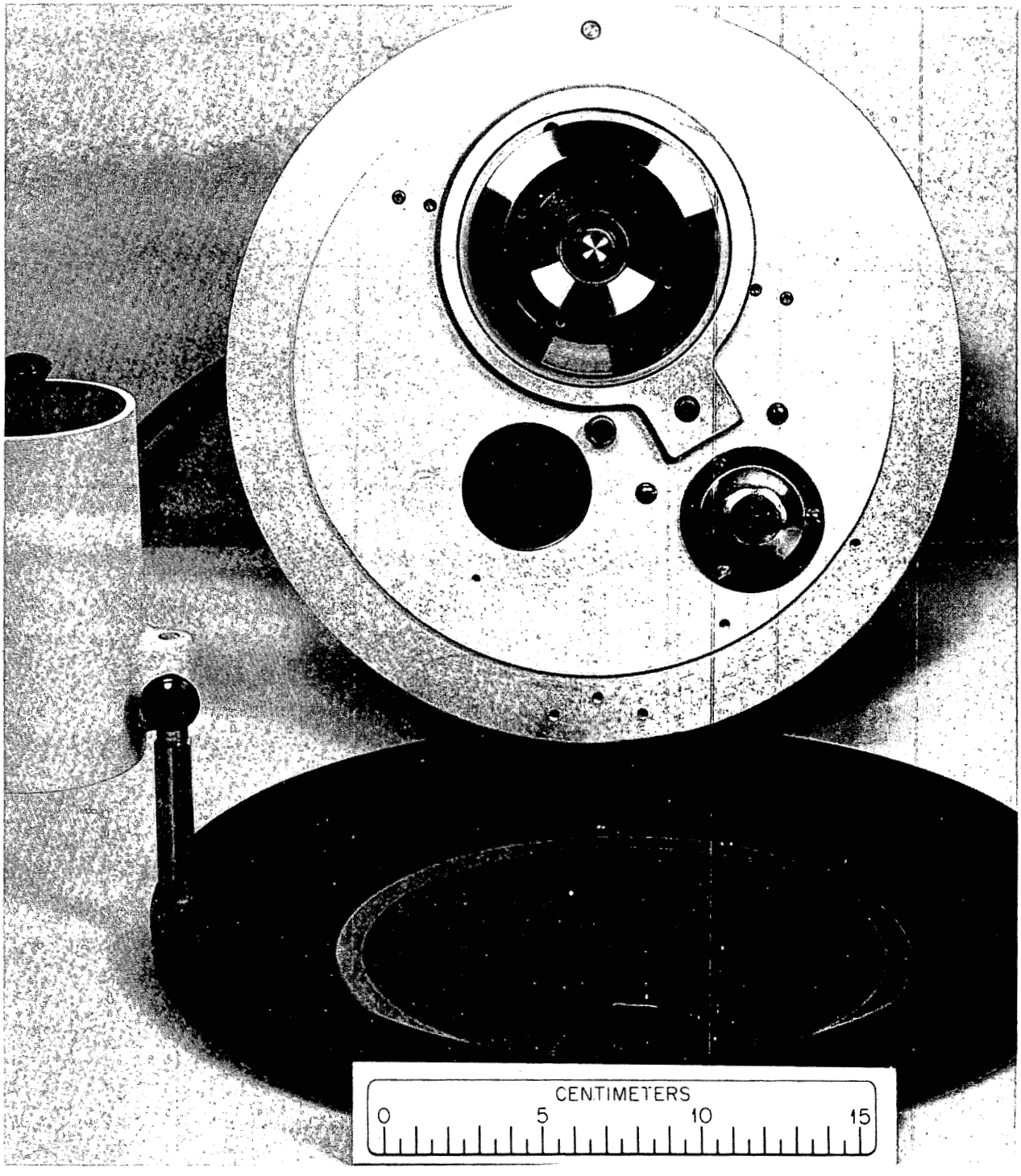

FIGURE 156. Rotary turret raised in loading position.

5. NEAR-SURFACE DEFORMATION OF USP SPECIMENS

F. M. Berting, F. A. Garner and M. H. Brady
Hanford Engineering Development Laboratory

5.1 OBJECTIVE

The object of this effort is to assess the level of deformation existing in the solution annealed 316 stainless steel specimens which will be bombarded with charged particles as part of the Unified Simulation Program.

5.2 SUMMARY

The specimen preparation procedure employed in the USP experiment leads to extensive near-surface damage which is easily removed by electrochemical techniques. Transmission electron microscopy observations confirm the presence of surface deformation but show that no damage due to mechanical polishing reaches to or beyond the depth picked for irradiation damage characterization.

5.3 ACCOMPLISHMENTS AND STATUS

5.3.1 Introduction

A technique for preparing flat undeformed foils from thin-wall tubular specimens was described previously[1]. Specimens produced by this method will be employed in the Unified Simulation Program (USP) in which both unirradiated and neutron-preconditioned 316 stainless steel will be subjected to charged-particle bombardment. Although the specimens are not deformed during the process of producing flat specimens from thin-walled tube sections, the abrasive polishing employed can lead to damage near the specimen surface. This damage layer must therefore be removed. The fact that the majority of the specimens will be radioactive precludes the use of unshielded ion sputtering devices to remove the damage layer.

One of the proposed specimen preparation techniques for the unirradiated specimens involves the electrolytic dimpling of the specimen surface to a depth of 15 μm. This will allow removal of the damaged layer adjacent to the region which is to be irradiated and which was previously uniformly preinjected with helium to a depth of 24 μm. The charged particles used in the irradiation then penetrate the new surface of the dimpled region. In order to verify the validity of this technique, it must be shown that the original near-surface damage does not extend beyond the 15 μm depth.

5.3.2 Experimental Procedure

Eight disk specimens of coarse-grained solution annealed Type 316 stainless steel from heat M2783 were provided by GE-FBRD from control (unirradiated) tubular material similar to that irradiated in the X-098B subassembly[2]. The disks were prepared according to the method outlined in Reference 1; i.e., spark cut from a tubular section and reduced to a flat disk by abrasive grinding. A 150 μm thick layer from the back surface of each disk was removed

by 320-grit grinding, followed by 600-grit deburring. A 75-100 μm thick layer from the front surface was removed by sequential grinding with 320, 400 and 600-grit paper, followed by 1-micron diamond and 0.05-micron alumina polishes. The final as-prepared thicknesses of the eight samples ranged from 160 to 185 μm. Disk diameters ranged from 2.95 to 3.0 mm. No helium was implanted in these disks. An additional 25 identical specimens were prepared for planned electron irradiation, but these specimens had 5 appm helium implanted in one surface.

Four of the specimens were used to calibrate the rate of dimpling so that any desired dimple depth could be achieved. Three specimens were then prepared by standard electropolishing techniques to allow observation of a layer at the original surface, one at the 15 μm depth and one at a 75 μm depth. The first two specimens required use of stop-off lacquer to preserve the surface at the desired depth.

5.3.3 Results

The front surface of the specimen illustrated in Figure 157 was very heavily worked, as had been anticipated. At a depth of 15 μm the specimen was essentially undamaged although there were areas such as that shown in Figure 158(a) where the specimen clamping procedures required for the stop-off lacquer application and removal process led to dislocation arrays typical of thin foil mechanical damage. To ensure that this damage was not a remnant of the surface damage, three helium-implanted specimens were observed in the HVEM prior to electron irradiation[3]. Handling procedures involved in the use of stop-off lacquer were not employed in the preparation of these specimens; preparation relied on the prior calibrated dimpling process to ensure perforation of the foil at the 15 μm depth. No appreciable damage was observed at this depth, although isolated clusters of dislocations typical of the preparation technique were found. Representative microstructure from this depth is shown in Figure 158(b).

At the 75 μm depth, no lacquer handling procedures were employed and the dislocation densities were typical of that found in annealed 316 specimens used in previous experiments. Figure 159 illustrates a higher than average but still small dislocation density found at this depth, i.e., a dislocation density that can be found in isolated regions in an otherwise undamaged specimen.

5.3.4 Discussion

In the charged-particle irradiation of annealed unirradiated material, the elimination of the first 15 μm of depth ensures irradiation of essentially undamaged material. Local high density dislocation tangles are few and easily avoided. In heavy ion irradiation of this material, the isolated regions characterized by a high dislocation density will be irradiated as well as the undamaged areas, so that the experimenter must make observations in regions typical of the overall specimen. The dislocation density in the damaged atypical regions does not approach that of the 20% cold worked condition, however, and probably will be of little consequence.

In the irradiation of cold-worked unirradiated material, the surface preparation damage will probably not contribute substantially to the existing high dislocation density and indeed its effect should decrease with depth at a faster rate. The reactor irradiated specimens require no helium implantation and can be directly thinned to the central layer of the disk. Much of the surface damage produced during specimen preparation will automatically be removed.

FIGURE 157. Highly damaged surface of annealed 316 stainless steel specimen resulting from mechanical abrasion.

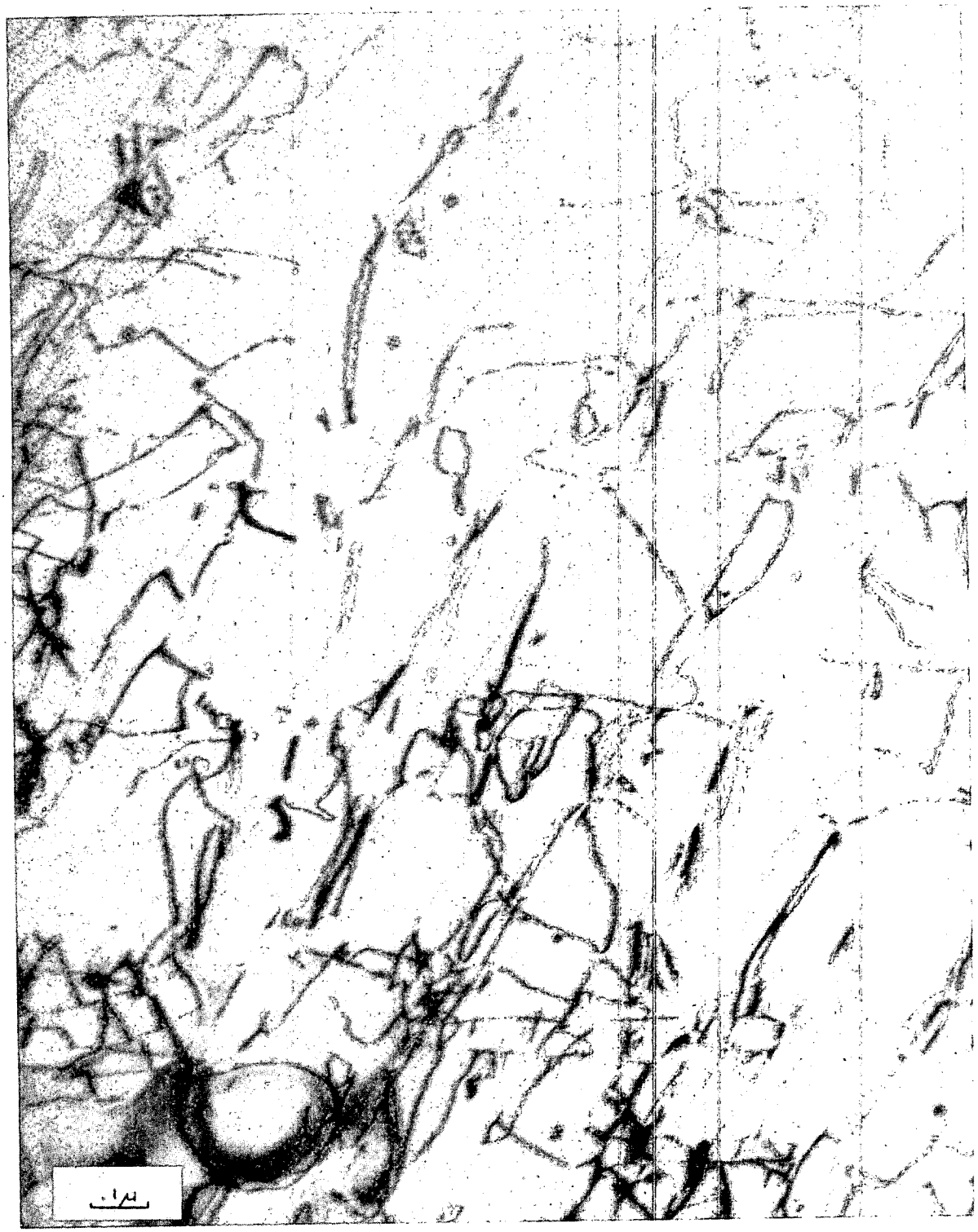

FIGURE 158(a). Atypical dislocation arrays found in a layer 15 μm from the original specimen surface introduced by the lacquer application and removal process.

FIGURE 158(b). Typical dislocation arrays found in a layer 15 μm from the original surface of a helium-injected specimen on which stop-off lacquer was not used during preparation.

FIGURE 159. Dislocation microstructure observed in isolated regions at a depth of 75μ m from the initial surface of a specimen of solution annealed 316 stainless steel. Most of the areas were relatively free of dislocations.

5.4 EXPECTED ACHIEVEMENTS IN THE NEXT REPORTING PERIOD

No further work is planned on this subject. Other activities related to the USP experiment will proceed.

5.5 REFERENCES

1. Lauritzen, T., and Darlin, E. S., "Unified Simulation Program: II. Preparation of Bombardment Foils from Tubular Specimens," Alloy Development Program Quarterly Technical Progress Letter, TC-160-10 (7-9/1976), pp. 127-135.

2. Lauritzen, T., and Kenfield, T. A., "Unified Simulation Program: I. Characterization of Control and Preconditioned Material," Alloy Development Program Quarterly Technical Progress Letter, TC-160-10 (7-9/1976), pp. 121-126.

3. Powell, R. W., this report.

6. SOLUTE REDISTRIBUTION UNDER IRRADIATION IN 20% CW 316 SS

S. Diamond, J. J. Schreuer,* R. Bajaj and R. Kossowsky*
Westinghouse Advanced Reactors Division

6.1 OBJECTIVE

The purpose of this work is to determine whether solute redistribution occurs during heavy ion bombardment of alloys and whether such redistribution can appreciably affect the void swelling in the alloys.

6.2 SUMMARY

Comparative Auger electron spectroscopic profiles were made on an irradiated and unirradiated section of a Ni ion irradiated 20% CW 316 SS sample to determine the extent of solute redistribution with depth in the alloy. It was shown that the bombarding Ni ions were deposited deeper into the sample (900 nm from the Ion Entry Surface, I.E.S.) than the position of the peak displacement damage region (780 nm from the I.E.S.). There is a pronounced Ni depletion near the I.E.S. and an increase in Cr and Fe concentration which could affect the swelling in this region of the sample. Thus, the composition of the alloy is essentially unchanged from the bulk composition from about 250 nm up to and including the peak damage region. Therefore, the measured swelling due to Ni^+ ion bombardment in this region of the foil is characteristic of an alloy of the given composition.

6.3 ACCOMPLISHMENTS AND STATUS

6.3.1 Introduction

Recent observations have indicated that substantial redistribution of the constituent elements of an alloy can occur during ion bombardment at elevated temperatures[1]. Segregation has been shown to occur near external surfaces and near or on the surfaces of radiation-induced voids within the material. Johnston[1] has demonstrated that an element present in low concentration (Si, 0.7%) can determine or strongly influence the redistribution of the major elements (those present in high concentrations, >15% i.e., Fe, Ni and Cr).

In order to more fully characterize the ion-irradiated alloys in the Alloy Development Program, Auger electron spectroscopy was employed to profile the concentration of the major elements of a Ni-ion bombarded 20% CW 316 stainless steel sample through the entire damage range.

The 316 SS sample was one of a group of sheet samples including several commercial, developmental and experimental alloys which were Ni-ion irradiated on edge at ORNL at 600°C to a peak damage of ∿250 dpa at a dose rate of 20-30 dpa/hour. The details of the sample

*Westinghouse R & D Center

configuration, preparation, He injection (to 5 appm), and irradiation have been reported earlier[2]. Since step height measurements were to be made to determine the swelling of the alloys, a mask shielding the central portion of each sample from the ion beam was mounted on the holder. This produced an irradiated and an unirradiated region on which comparative Auger profiles could be made. During the Auger measurements, the 316 SS specimen was isolated by covering the adjacent samples with a set of adjustable Ta masks.

Profiles of concentration vs. depth were achieved by sequential argon ion sputtering with a beam of about 3 mm diameter and a current density of ~180 $\mu A/cm^2$. This corresponds to a sputtering rate of about 10 nm/min. at a 2kV accelerating voltage. Sputtering was interrupted approximately every ten minutes and full Auger spectra were taken in the irradiated and unirradiated regions of the sample. The analyzing electron beam current density was 50 $\mu A/cm^2$ with a diameter of 30 μm at an accelerating voltage of 5 kV. The electron spectrometer used is of the cylindrical mirror analyzer type with a fixed relative energy resolution of 0.6% $\Delta E/E$.

6.3.2 Data Analysis

Normalized signal strengths (NS) were calculated from the data for the following elements: Cr(527 eV), Fe(703 eV), Ni(848 eV). The energies in parentheses refer to the Auger transitions used. The presence of C and O prohibit the interpretation of the NS as absolute atomic fractions but the relative changes of the NS with depth for a given element may be taken as the relative variation of the amount of that element as a function of depth in the sample. The range of values obtained for the unirradiated section, give an indication of the scatter to be expected for each element in a homogeneous sample.

Normalized signal strengths (NS) are obtained from the peak to peak heights (PPH) of one transition for each major constituent in the sample as follows:

$$NS = \frac{\left(\frac{PPH \times SCALE}{STD \times SENS}\right)}{\Sigma\left(\frac{PPH \times SCALE}{STD \times SENS}\right)}$$

where the Σ is over all elements, and

SCALE, SENS: Scale factors for STD and PPH respectively

STD: the peak to peak height of the pure element transition as obtained from the standard[3]

PPH: the peak to peak height for the element in this sample.

The results of the Auger composition profiling are shown in Figures 160-162. In Figure 160 the calculated energy deposition curve for 4 MeV Ni-ions in 316 SS is shown with the measured Ni profile in the sample for both the irradiated and unirradiated regions. It is apparent that the bulk of the bombarding Ni ions which have been employed to induce the radiation damage in this simulation experiment have been deposited deeper into the sample (900 nm from I.E.S.) than the position of the peak displacement damage region (780 nm from I.E.S.). These data confirm the assumption that the composition of the alloy is essentially unchanged from the bulk composition from about 250 nm up to and including the shallower portion of the

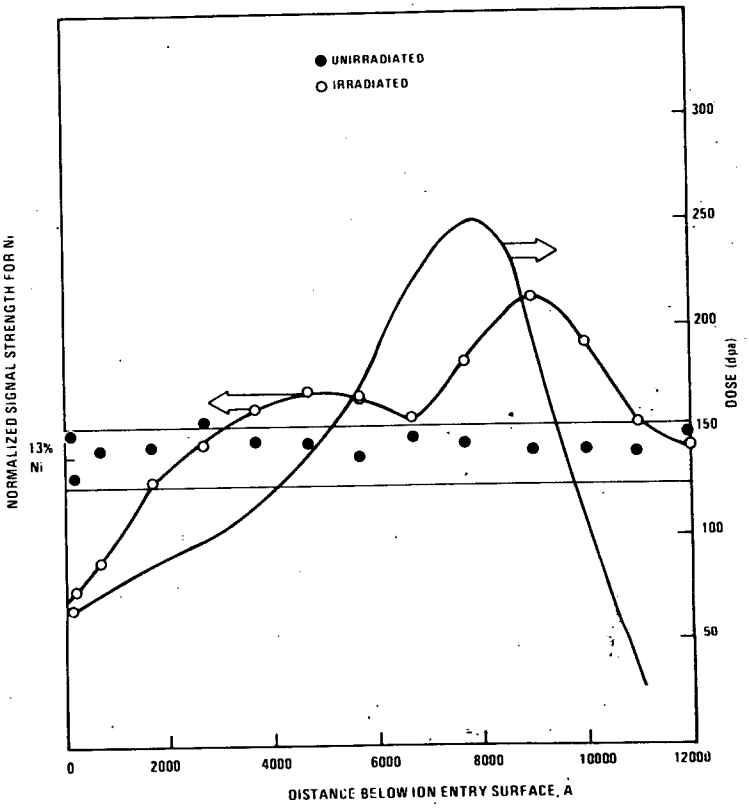

FIGURE 160. Energy deposition curve and Auger composition profile for Ni in Ni-ion irradiated and unirradiated 20% CW 316 SS.

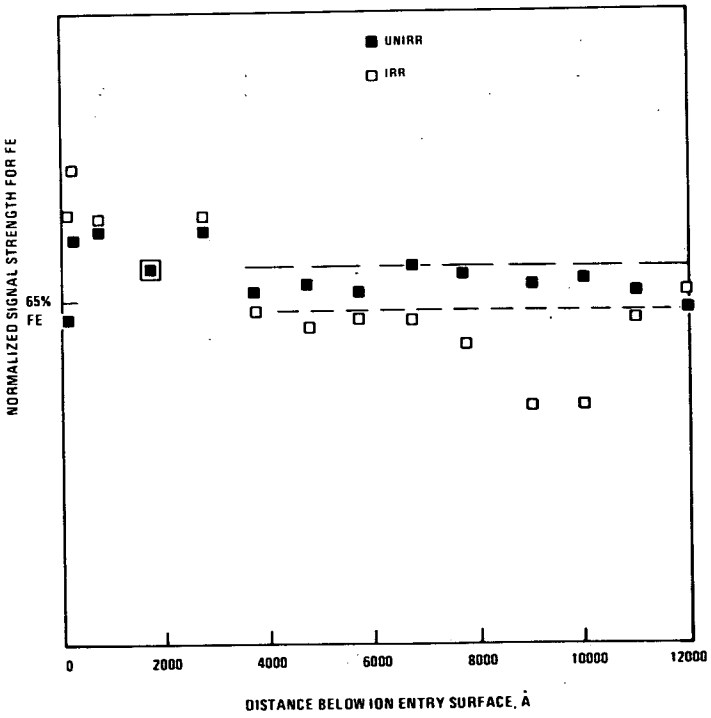

FIGURE 161. Auger composition profile for Fe in Ni-ion irradiated and unirradiated 20% CW 316 SS.

peak damage region and the measured swelling in this region of the foil is representative of an alloy of the given composition. However, there is a strong indication of a Ni depletion in the near I.E.S. region (<250 nm) of the ion-irradiated section of the sample. There appears to be a concomitant increase in the Fe and Cr compositions in this same region (Figures 161 and 162) but their variations with depth in the near surface region are not as clear as in the case of Ni. The Mo concentration displayed essentially no change with depth at >170 nm from the I.E.S. The signal strength from Si was not sufficient to permit profiling with an acceptable level of accuracy.

It thus appears that solute redistribution may indeed occur during heavy ion bombardment of alloys and may be a function of composition, particularly in the vicinity of the I.E.S. Comparisons between the profiles from alloys of different compositions and the same alloys in different metallurgical conditions, and improvements in instrumental sensitivity, where possible, must be made to fully determine the extent of the solute redistribution and its impact on swelling. However, nickel ion bombardment studies of swelling are representative of the bulk material in 316 stainless steel in the region from 250 nm to the peak swelling depth of 780 nm.

6.4 EXPECTED ACHIEVEMENTS IN THE NEXT REPORTING PERIOD

This completes the work on this task.

6.5 REFERENCES

1. Johnston, W. G., Turkalo, A. M., and Morris, W. G., Annual Information Meeting, National Alloy Development Program, TC-721, October 20, 1976, p. 471.

2. Bajaj, R., and Chickering, R. W., Alloy Development Program Quarterly Technical Progress Letter, TC-160-7 (10-12/1975), p. 79.

3. Handbook of Auger Electron Spectroscopy, Physical Electron Industries, Inc., Edina, MN.

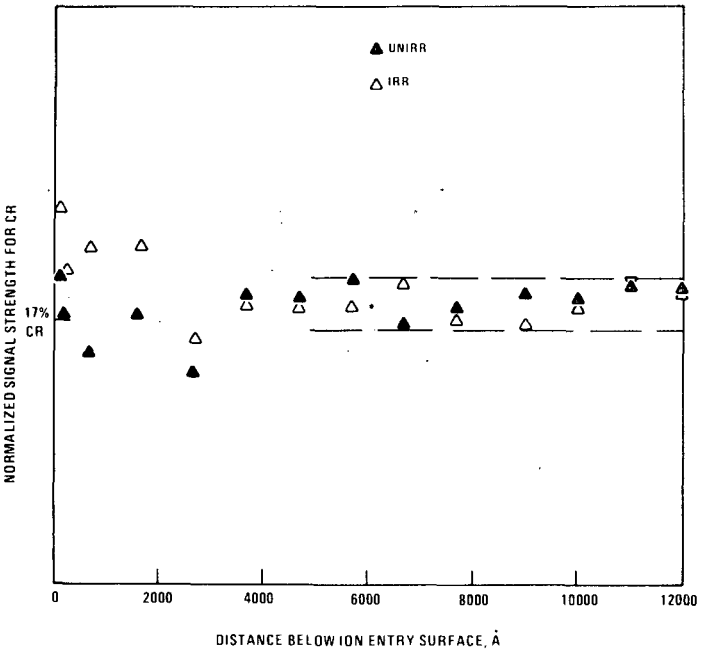

FIGURE 162. Auger composition profile for Cr in Ni-ion irradiated and unirradiated 20% CW 316 SS.

7. DESIGN AND ANALYSIS OF INTERCORRELATION EXPERIMENTS

F. A. Garner
Hanford Engineering Development Laboratory

7.1 OBJECTIVE

The object of this report is twofold. First, to present a compilation and distillation of all recent data and analyses which impact the understanding of phenomena involved in charged particle simulation and extrapolation of neutron-induced swelling to higher atomic displacement levels. Second, to describe the experimental plan and schedule of an intercorrelation program based on the charged particle irradiation of three alloys previously irradiated with neutrons.

7.2 SUMMARY

An experimental program, designated the Unified Simulation Program, has been designed to determine the optimum irradiation conditions for simulating neutron-induced swelling in various alloys. The experimental rationale, schedule and status of the program are outlined. The program employs for starting material both unirradiated and neutron-preconditioned specimens of Nimonic PE16 and the M2783 and LS-1 heats of 316 stainless steel. Based on analysis of recently acquired data, it is concluded that except for very simple alloys the temperature shift and dose equivalency concepts are more complex than previously modeled. It is anticipated, however, that the use of preconditioned specimens will allow the modified application of these concepts to more complex alloys.

7.3 ACCOMPLISHMENTS AND STATUS

7.3.1 Introduction

With increasing experience and data on neutron and charged particle irradiation studies, it has become apparent that there are many factors, some of which were previously unrecognized, which influence swelling. Some of these factors impact charged particle simulation and the neutron environment to a different extent, influencing strongly the conduct and interpretation of the simulation experiment. Those factors recognized to date have been characterized as "atypical variables" and are discussed in several recent review articles[1-3]. Armed with the increased understanding of charged particle simulation results, the Alloy Development Program has embarked on an irradiation program designed to use both low fluence neutron data ($\leq 8 \times 10^{22}$ n/cm^2) and simulation experiments to provide guidance in the selection of "prime candidate" advanced alloys for testing in FFTF.

With the increased understanding of the factors which influence swelling, there has also developed a new set of questions concerning the optimum irradiation conditions to be employed in the simulation experiments. The Unified Simulation Program (USP) has been developed to provide answers to these questions and to permit extension of low fluence reactor swelling data to higher displacement levels by utilization of data from charged particle irradiation experiments.

7.3.2 Background

The major considerations previously believed to be important in the selection of charged particle irradiation conditions are the temperature shift and dose equivalency concepts[1]. The temperature shift arises as a consequence of the accelerated displacement rate and involves an upward shift in the temperature regime of swelling. The dose equivalency concept appears at first glance to be independent of dose rate and to be a consequence of the differences in energy deposition characteristics for various bombarding species. As shown in the following sections, neither of these concepts are as simple as they were first imagined to be. The expectation that there exists a correlation defining an equivalence between two disparate irradiation environments requires a careful definition of what constitutes equivalence.

7.3.3 Theoretical Estimates of the Temperature Shift in Very Simple Materials with Zero Incubation Periods

Consider first a simple single phase material which undergoes no phase transformations or elemental redistributions. This material has diffusion coefficients D_V and D_I for vacancies and interstitials, and diffusion is governed by activation energies which are not sensitive to the elemental identity. These restrictions apply to either a pure metal or an alloy in which all atoms are considered to behave identically. It is also assumed that atomic displacement events occur in the same manner at all displacement rates and no incubation periods are involved in the swelling behavior. For these restrictive conditions, Westmoreland et al[4] have compiled the following set of temperature shift formulas arising from the Brailsford and Bullough[5] rate theory of swelling.

For "low temperatures" where the swelling rate increases with increasing temperature, a temperature shift can be defined if it is assumed that recombination events are the predominant sink for point defects and if "equivalent" or identical swelling is obtained at temperatures and dose rates for which the ratio of the vacancy sink loss rate to recombination rate is constant[4]. This requires $\dot{d}_1/D_{V1} = \dot{d}_2/D_{V2}$ or

$$\left(\frac{1}{T_2} - \frac{1}{T_1}\right) = \left(k_B/E_V^m\right) \ln\left[\left(\dot{d}_1/\dot{d}_2\right)\left(\kappa_{i,2}^2/\kappa_{i,1}^2\right)\left(\kappa_{V,2}^2/\kappa_{V,1}^2\right)\right] \qquad [1]$$

where T is the absolute temperature, k_B is the Boltzmann's constant, E_V^m is the vacancy migration energy, $\dot{d}$ is the displacement rate and κ^2 is the total microstructural sink strength for a particular point defect.

Brailsford and Bullough[5] defined a low temperature cut-off temperature T_s for swelling and derived a slightly simpler expression

$$\left(\frac{1}{T_{s,2}} - \frac{1}{T_{s,1}}\right) = \left(k_B/E_V^m\right) \ln\left[\left(\dot{d}_1/\dot{d}_2\right)\left(\kappa_{V,2}^2/\kappa_{V,1}^2\right)\right] \qquad [2]$$

They also developed temperature shift formulas for the peak swelling temperature T_p, and high temperature cut-off of swelling, T_f. These formulas require the assumptions that the vacancy concentration at the void surface equals the thermal equilibrium value, and also that the fraction of dislocation density in loops is identical for "equivalent" temperatures and dose rates. Then

$$\left(\frac{1}{T_{p,2}} - \frac{1}{T_{p,1}}\right) \approx \left\{k_B/(E_v^f + 2E_v^m)\right\} \ln\left[(\dot{d}_1/\dot{d}_2)(\kappa_{v,2}^2/\kappa_{v,1}^2)\right] \quad [3]$$

$$\left(\frac{1}{T_{f,2}} - \frac{1}{T_{f,1}}\right) \approx \left\{k_B/(E_v^f + E_v^m)\right\} \ln\left[(\dot{d}_1/\dot{d}_2)(\kappa_{v,2}^2/\kappa_{v,1}^2)\right] \quad [4]$$

where E_v^f is the vacancy formation energy.

In an earlier formulation[6] based on a high temperature limit where swelling goes to zero, it was assumed that the vacancy sink strengths are identical, giving

$$\left(\frac{1}{T_2} - \frac{1}{T_1}\right) = \left\{k_B/(E_v^f + E_m^f)\right\} \ln\left(\dot{d}_1/\dot{d}_2\right) \quad [5]$$

Note that Equations [1] - [5] always have two elements in common despite the fact that equivalency is defined differently in each. The temperature shift can be defined in terms of a displacement rate ratio and another term containing sink strengths and various activation energies. This latter term varies across the temperature regime of swelling, however. Even under the restrictive assumptions made here, the temperature shift is not constant for all portions of the swelling regime. This variability is compounded by the fact that the temperature shift formula is expressed in terms of an inverse temperature difference, rather than $(T_2 - T_1)$. This means that the temperature shift in each part of the swelling regime varies as a function of the initial displacement rate $\dot{d}_1$.

It should also be noted that temperature shift formulas [1] - [4] contain ratios of some or all of the microstructural sinks for point defects. No statement has yet been made which requires that the sinks evolve in the same manner at all displacement rates.

If one of the primary restrictive conditions is removed (that which requires that all elements in the metal contribute equally to the defect diffusivities), the temperature shift phenomenon becomes even more complicated. Realizing that vacancy diffusion involves an exchange of vacancies and lattice atoms, it is possible to visualize the lattice of a simple solid solution alloy to consist of a number of interpenetrating skeletons, each possessing a partial diffusion coefficient. If one elemental component, designated A, has a lower partial diffusion coefficient than the other elemental component B, then the lattice exists partly of a skeleton of slowly diffusing matrix atoms A, and vacancies migrate to sinks predominantly by exchanging lattice sites with the fast diffusing substitutional species B. Therefore the presence of element B in small amounts exerts a disproportionately large influence on vacancy diffusion, and results in a reduction of the vacancy concentration which is a major component of the driving force for void nucleation and growth[7]. If the diffusivities of the various elements are governed by different activation energies, then the relative influence of element B at higher temperatures will be changed, a factor which will distort the temperature dependence of swelling at the higher dose rate relative to that at the low rate, and which will add additional complications to interpretations of the temperature shift phenomenon.

In Figure 163 the temperature dependence of partial diffusivities in nickel for Ni, Fe and Si atoms are shown. It should be noted that the silicon partial diffusivity is two to three orders of magnitude greater than that of the matrix nickel atoms; therefore one atomic

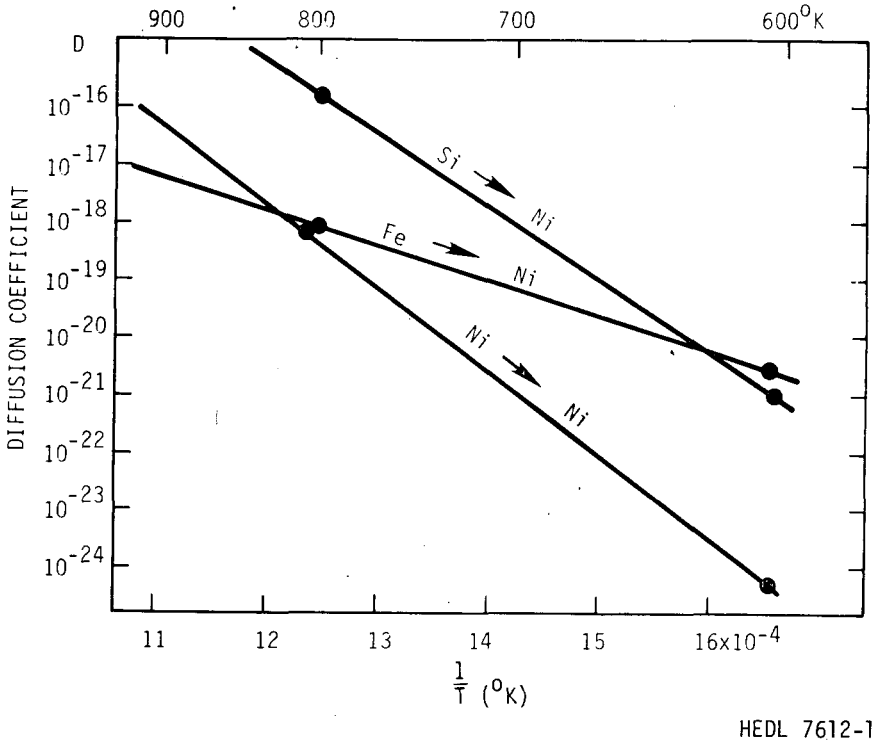

FIGURE 163. Partial diffusion coefficients of Si, Fe and Ni in nickel[7].

percent silicon can exert one to ten times as much influence on diffusion as can the matrix atoms. It is expected that this trend will also occur during irradiation. While the relative diffusivities of silicon and nickel change rather slowly with temperature, the relative diffusivity of iron to silicon and nickel changes drastically with temperature.

An additional complication arises if migrating vacancies or interstitials encounter elements which have strong attractions or high binding energies for point defects. It has been predicted that at constant displacement rate, the peak swelling temperature will decrease if the interstitial-solute complex is mobile[8], and increase if the complex is immobile[9]. Lam and Johnson predict that binding and related segregation effects at reactor displacement rates will differ from those at simulation displacement rates[10], influencing not only the peak swelling temperatures and temperature shift, but also changing the magnitude of the peak swelling for a given dose. A model describing the effect of both partial diffusivities and defect binding on void nucleation is presented elsewhere[11].

As more of the restrictive conditions are relaxed, the temperature dependence of swelling and the description of temperature shifts become more involved. Even in very simple alloys, phase changes can occur under irradiation which change the composition and diffusivities of the matrix components. Silvertre and coworkers[12] report that at high concentrations of iron, high purity Ni-Fe alloys form plate-shaped precipitates if Ni_3Fe at low fast neutron fluences which changes the matrix composition and leads to an increase of the swelling resistance of the alloys. Most alloys of commercial interest contain or can develop a variety of stable and metastable phases which are sensitive to both thermal and radiation environments. Changes in matrix composition accompany these phase changes and lead to a different swelling

behavior. Wilkes and coworkers[13] note that the presence of radiation-induced point defects results in a free energy increase, which differs from phase to phase, and this may cause the formation of new phases and changes of composition in existing phases. There will be also temperature shifts involved in the rate at which these phase changes occur.

7.3.4 Theoretical Estimate of the Temperature Shift During the Void Incubation Period

In the previous section, the temperature shifts were defined for the case of a constant dislocation microstructure, while the actual microstructure undergoes an evolution which is most pronounced during the void incubation period. There is no *a priori* reason to expect that the temperature shift relevant to the incubation behavior is the same as that of the steady-state void growth regime. One example should suffice to demonstrate this point. Employing the radiation-assisted nucleation theory of Russell[14], the nucleation rate of vacancy clusters can be defined as

$$J_n^v = Z' \quad \beta_n \, N_o \exp\left(- \Delta G_n'/k_B T\right) \quad , \qquad [6]$$

where Z' is the Zeldovich factor, β_n is the vacancy arrival rate at clusters of size n, N_o is Avogadro's number and $\Delta G'_n$ is the kinetically modified free energy barrier to nucleation. If the definition of equivalency requires a temperature shift such that a given level of void nucleation occurs at the same displacement level regardless of displacement rate, then the nucleation rates should obey the following relationship

$$J^v_{n,1} = (\dot{d}_1/\dot{d}_2)\, J^v_{n,2} \quad . \qquad [7]$$

This in turn requires that

$$\frac{\phi_2}{\phi_1} \frac{Z'_1}{Z'_2} \frac{\beta_{n,1}}{\beta_{n,2}} = \frac{\exp\left(\Delta G_{n,2}/k_B T_2\right)}{\exp\left(\Delta G_{n,1}/k_B T_1\right)} \quad . \qquad [8]$$

Examination of Equation [8] shows that Z', β_n and ΔG_n all vary as complex functions of temperature for even the simplest assumptions made about microstructures. Although rather complex temperature shift formulas for the nucleation period could perhaps be derived, computer calculations will be relied on to demonstrate the complexities involved. Powell[15] has calculated the void nucleation rates shown in Figure 164 for a restrictively simple alloy with an initially low dislocation density. It should be noted in Figure 164 that the equivalence requirement of Equation [7] results in a temperature shift which is variable with temperature and approaches zero at low temperature. The nucleation rate is quite sensitive to surface energy and the time-dependent microstructural densities[15] which in turn are strongly temperature-dependent. It is therefore not unreasonable to expect that a temperature shift formula derived from Equation [8] would include the stacking fault and surface energies, parameters not included in Equations [1] - [-5].

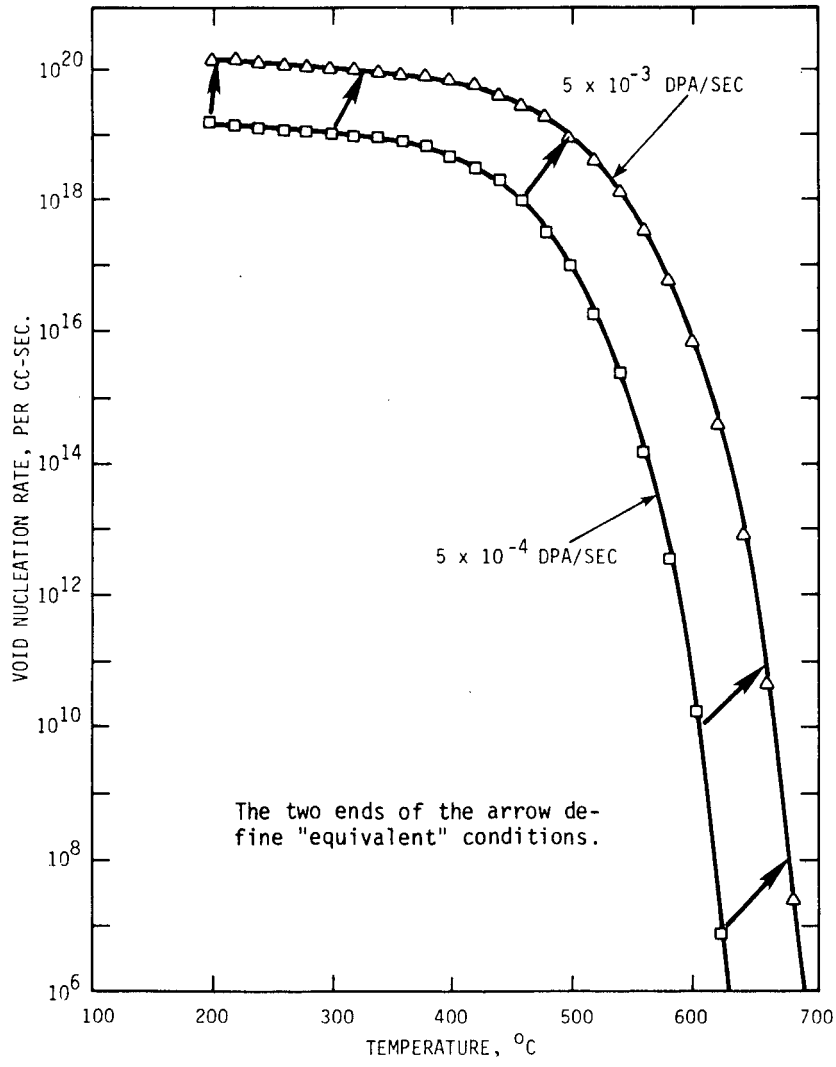

HEDL 7612-168.1

FIGURE 164. The effects of temperature and displacement rate on void nucleation rates calculated by Powell (15) for a simple alloy. Note that the temperature shift defined implicitly by Equation [17] changes with temperature.

7.3.5 Experimental Determinations of the Temperature Shift

From the above sections one can gain a partial idea of the complexity of the processes involved in the temperature shift phenomenon. In effect, there are numerous superimposed temperature shifts, one for each rate-sensitive process. There has only been one experiment to date in which all major features of a temperature shift have been conclusively demonstrated and in which the only variable was the displacement rate (other less conclusive experiments are discussed in later sections), that by Westmoreland and coworkers[4], who irradiated high purity nickel at two different dose rates using 2.8 MeV Ni^+ ions. The peak displacement rates were $\sim 7 \times 10^{-2}$ dpa/sec and $\sim 7 \times 10^{-4}$ dpa/sec; yielding a ΔT_p of $\sim 75°C$ for two orders of magnitude change in the displacement rate, as seen in Figure 165. Note in this figure that the peak swelling did not remain constant, however, in contradiction to the assumptions concerning equivalence made earlier.

Since the Westmoreland experiment most closely fits the restrictive assumptions made in the theoretical section, some of the other assumptions made about microstructure can be tested. Having assumed that the defects are partitioned between the various sinks in the same manner at equivalent temperatures, then the densities of dislocations and other microstructural features should shift in the same manner.

$$\left.\begin{aligned} \rho_d\,(\phi_1, T_1) &= \rho_d\,(\phi_2, T_1 + \Delta T) \\ \rho_v\,(\phi_1, T_1) &= \rho_v\,(\phi_2, T_1 + \Delta T) \end{aligned}\right\} \quad \text{for } \phi_1 t_1 = \phi_2 t_2 \quad . \qquad [9]$$

Figure 166 shows that there was indeed a shift of approximately the same magnitude in the microstructural densities, but the correspondence is not total. The discrepancy between the peak swelling values is troublesome, however, in that it conflicts with the simple definitions of equivalence and temperature shift. The discrepancy may well grow larger for the three to five orders of magnitude difference in displacement rates available in charged particle and reactor irradiations. A temperature shift of $\sim 200°C$ has been observed due to approximately five orders of magnitude difference in the displacement rate achieved in the neutron irradiation in the Oak Ridge Research Reactor and 4 MeV nickel ion bombardment of pure nickel[16]. One must conclude that the temperature shift continues to increase with increasing displacement level.

In another simple alloy system, Fe-25Ni-15Cr, the ADIP experiment has determined that ΔT_p appears to be $\sim 160°C$ for the approximately four orders of magnitude differences in displacement rate involved in this experiment[17]. (The exact ΔT_p cannot be determined until a better defined peak swelling temperature at higher fluence in EBR-II is obtained.) The data from this experiment tend to agree with the data of Westmoreland[4] and confirm a peak temperature shift ΔT_p° of 30-40°C per order of magnitude difference in displacement rate for simple systems. However, in a Ni^+ ion irradiation of Type 316 stainless steel the peak swelling temperature at 1.7×10^{-2} dpa/sec is only $\sim 650°C$[18], while recent X-098 neutron data at 1×10^{-6} dpa/sec indicate that the peak occurs at $\sim 590°C$[19]. This suggests a ΔT_p of $\sim 60°C$, where one of twice that magnitude was expected. One can construe from this that the

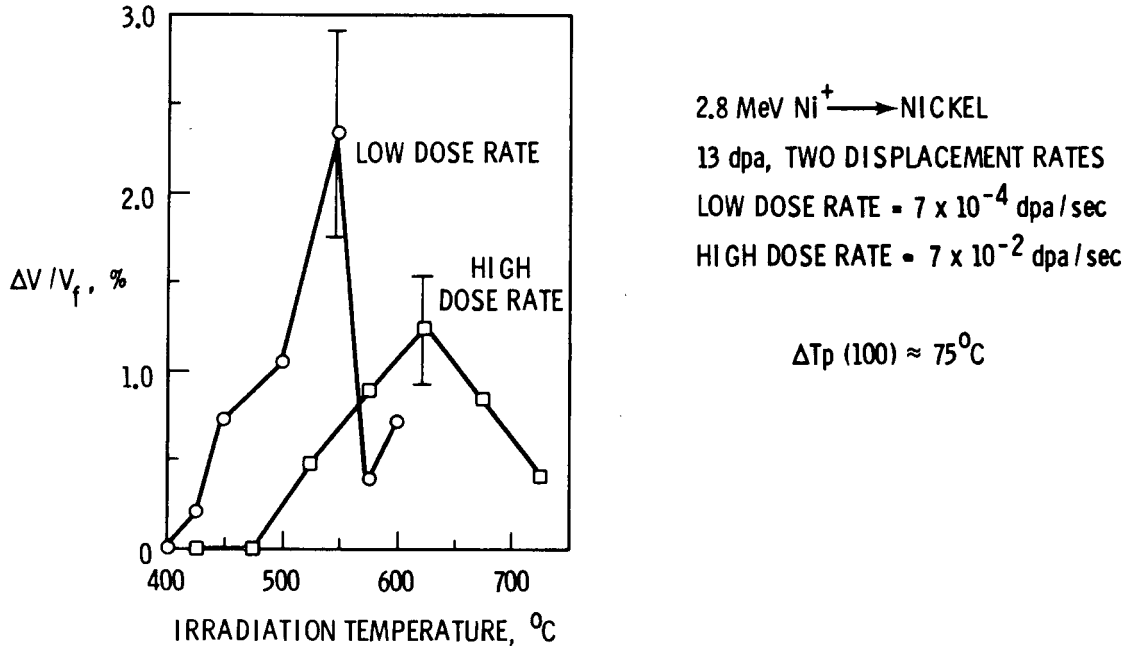

FIGURE 165. Temperature shift observed in ion irradiation of nickel at two displacement rates(4).

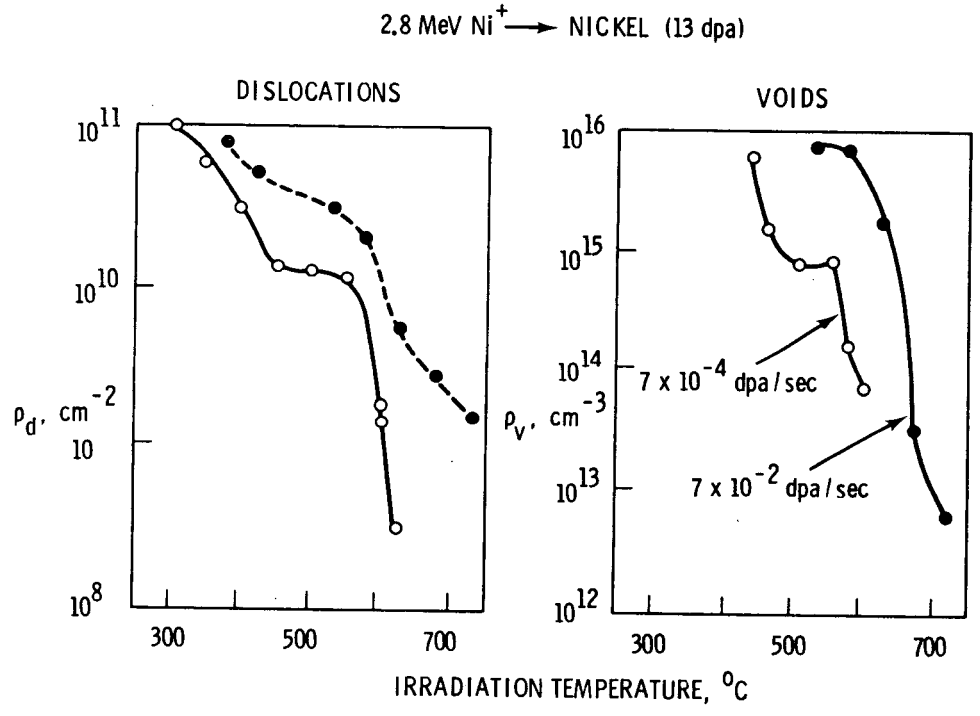

FIGURE 166. Shift of microstructure with displacement rate observed in the experiment described in Figure 165.

temperature shift magnitude is either dependent on the material identity or that the experimental determination of ΔT_p is even more complicated than previously expected. The following sections explore the complications recognized to date.

The first such complication was demonstrated in the ADIP experiment[17] where it was shown that the measurement of temperature shifts from comparisons of total swelling in various irradiations at a given fluence were often invalid, since the incubation period of swelling in simulation experiments was observed to be quite sensitive to experimental techniques and uncontrollable variables. The temperature dependence of the steady state swelling rates was determined to be the best quantity from which to determine the temperature shift. Total swelling can be used to derive an estimate of the temperature shift, however, if relatively large levels of swelling (>2%) are involved. Several previous attempts to study the temperature shift phenomenon have been thwarted by the low levels of swelling involved. Labbe and coworkers[20,21] irradiated copper in thermal reactors at dose rates ranging from 2×10^{13} to 2.8×10^{14} n/cm^2-sec and fluences from 5 to 8×10^{20} n/cm^2 and found no measurable temperature shift. The peak swelling declined slightly with increasing flux, as shown in Figure 167. Because all swelling values were low, 0.4% or less, it is inferred that incubation behavior was rate-sensitive and dominated throughout the experiment.

Glowinski and coworkers[22] compared the temperature dependence of swelling in copper irradiated with 0.5 MeV Cu^+ ions at constant irradiation time but at two different dose rates (3×10^{-4} and 3×10^{-3} dpa/sec). Although the total dose varied from 3 to 30 dpa, the peak swellings were relatively large, as shown in Figure 168, and imply a temperature shift of 50°C per decade of flux. Due to the differences in dose and the fact that only one data point is non-zero for the lower dose irradiation, the data from this experiment must be assessed as being insufficient for measurement of the temperature shift.

More recently Menzinger and Sacchetti[23] employed 46.5 MeV Ni^+ ions to irradiate nickel at 6.7×10^{-3} and 3.3×10^{-4} dpa/sec. These experiments are judged to be rather inconclusive. The results do indicate a temperature shift, the measurement of which is complicated by a double peak in the temperature dependence of swelling, a subject to be discussed in more depth in a following section. Sacchetti[24] continued these experiments with 316 stainless steel and for the factor of twenty difference in displacement rate measured a temperature shift of 100°C at 18 dpa, as shown in Figure 169. Using Equation [1] with constant sink densities, Sacchetti calculated a value of E_v^m of 1.5 eV. Such a calculation illustrates the danger involved in using low fluence data. The excessively large temperature shift measured is a consequence of measuring incubation behavior, since at higher fluences the peak swelling obviously occurs at higher temperatures, as is also shown in Figure 169. The activation energy therefore cannot be calculated from this data set. Sacchetti's data at 18 dpa do demonstrate that there is a shift in the microstructure with rate, however, as can be seen in Figure 169(c). This shift is comparable to the behavior shown in Figure 166.

To this point it has been assumed that the peak temperature shift ΔT_p can be measured at a sufficiently large fluence without interference from experimental perturbations. There are at least two factors which can thwart such a measurement, however. These are surface effects and displacement gradient effects.

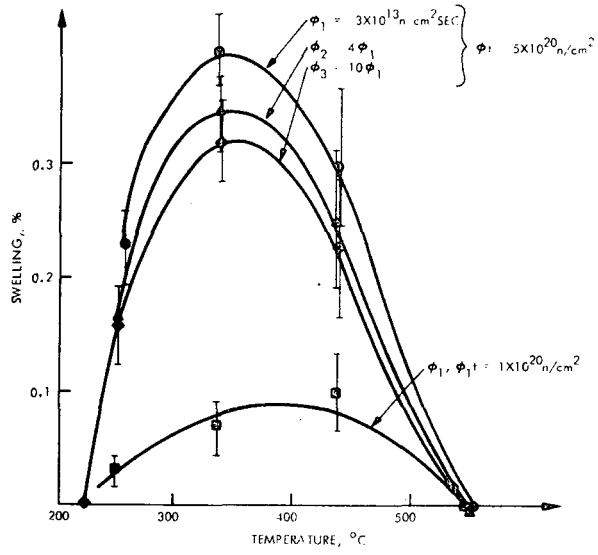

FIGURE 167. The absence of a temperature shift in copper at a constant neutron fluence as observed by Labbe and coworkers(20,21). An apparent temperature shift occurs due to accumulated fluence, as shown in comparison of the top and bottom curves. The incubation fluence appears to increase at higher displacement rates.

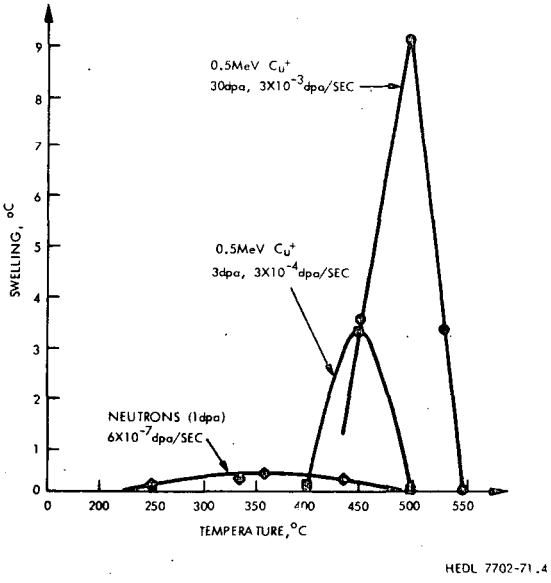

FIGURE 168. Temperature shift demonstrated by Glowinski and coworkers(22) in neutron and ion irradiation of copper. Each curve is at a different displacement level, however. Note that the neutron-induced swelling covers a larger temperature range at a lower dose than does the ion-induced swelling at a higher dose. The high temperature side of the ion curves may be depressed by surface effects at these low displacement rates.

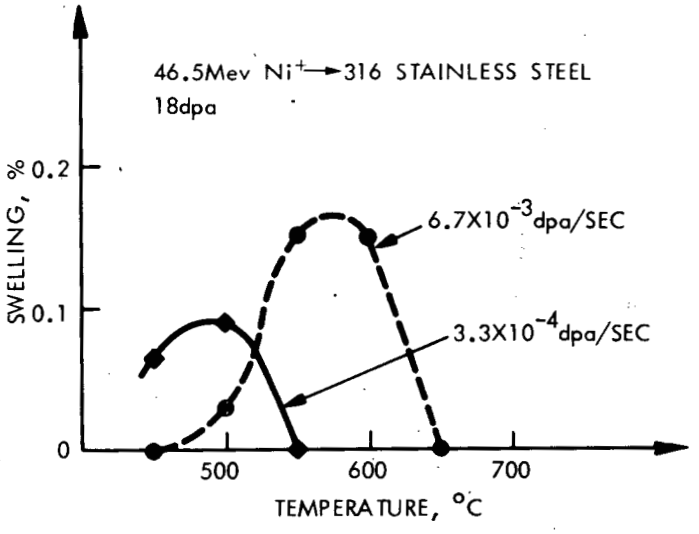

FIGURE 169(a). Temperature dependence of ion-induced swelling in 316 stainless steel at different rates and total damage levels(24).

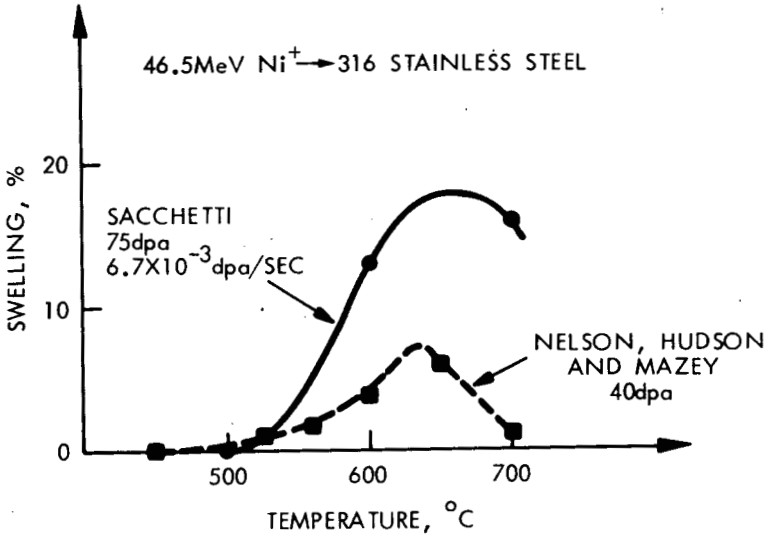

HEDL 7702-71.2

FIGURE 169(b). The dotted curve is drawn from Reference 31 and confirms that the peak swelling temperature at 6.7 x 10^{-3} dpa/sec lies above the 580°C value determined from Figure 169(a).

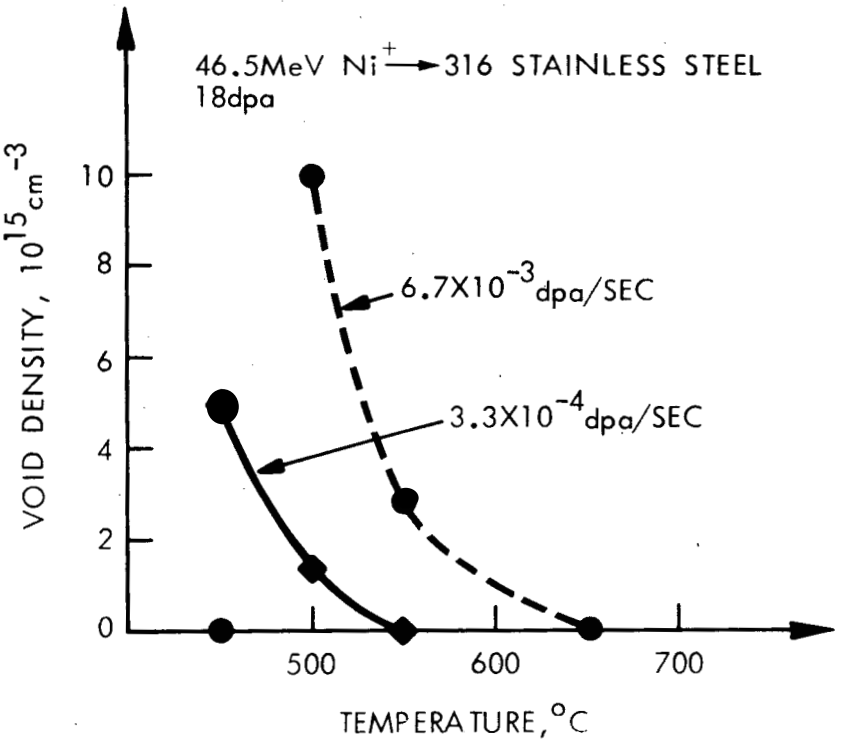

HEDL-7702-71.3

FIGURE 169(c). Temperature dependence of void density at 18 dpa in ion-irradiated 316 stainless steel showing temperature shift of void density with displacement rate(24).

7.3.6 Surface Effects

The proximity of free surfaces to the irradiated zone distorts defect and microstructural profiles from that expected from displacement vs. depth calculations. This consideration becomes important at higher temperatures where swelling is depressed at greater depths. The peak swelling temperature is thus moved downward, below that expected in an environment free from surface influence. Figure 170(a) demonstrates this effect in 200 keV C^+ irradiations of Type 304 stainless steel, where the damage occurs in the first 0.2 μm below the surface. Shimada[25] found a peak swelling temperature of 625°C in 8 x 10^{-3} dpa/sec irradiations without preinjection of helium, but addition of 30 ppm helium led to an extension of swelling to higher temperatures with T_p ∿700°C. The addition of helium allowed the surface influence on nucleation to be reduced and the peak swelling temperature to be better defined. At low temperatures the swelling was identical, even though the void population was enhanced by helium at all temperatures [Figure 170(b)].

Referring back to Figure 168 note that at 1 dpa the neutron induced swelling in copper extends over a range of ∿250°C, while at 3 and 30 dpa the 0.5 MeV Cu^+ ion-induced swelling covers only 100-125°C. Equations [1]-[5] all predict an extension of the swelling regime with increasing displacement rate, so this observation requires some explanation. It appears that the short range of the copper ions is insufficient to overcome the strong influence of the front surface at higher temperatures. The ion induced swelling profiles are therefore unrepresentative of that which would evolve in bulk material at these displacement rates. This effect precludes the use of low energy self-ions for confident intercorrelation studies. Delaplace and coworkers demonstrated the surface-related suppression of swelling of 200 KeV self-ions relative to that of 500 KeV ions as shown in Figure 171. The suppression at 200 KeV occurs first in mean void size and later in void density. Note that at 500 KeV a reduction in mean void size occurs above 650°C, a behavior uncharacteristic of bulk-representative void growth experiments.

For 3-5 MeV Ni^+ ion irradiations, the argument is usually advanced that the surface influence in the 0.3-1.0 μm range is minimal, and therefore the description of the temperature dependence of swelling is not affected. Figures 172 and 173 demonstrate that this argument is not necessarily correct. Blamires and Worth[26] have shown that the use of 4.2 MeV Fe^+ and 46.5 MeV Ni^+ ions at the same displacement rate yields identical swelling behavior at low temperatures. At high temperatures, however, the swelling diverges considerably and a 50°C discrepancy in the determination of T_p results. From this one may conclude that the surface influence at ∿10^{-3} dpa/sec in ion irradiations of 300 series stainless steels at 650°C and above is still very strong in the 0.6-0.8 μm range, the region where the specimens irradiated at 4.2 MeV were examined. Note in Figure 175(a) that the void denuded zone width at grain boundaries and the front surface in these experiments at 650-700°C was ∿0.4 μm.

Several studies[4,27-29] have shown that the influence of the surface extends beyond the denuded zone and that reduced swelling occurs to a depth equal to twice the denuded zone width, as shown in Figures 174(a) and 174(b). The mechanism of reduction varies between various irradiations, sometimes being manifested in void size reductions[2,27] and sometimes in perturbations of void number density[28,29] as shown in Figure 176.

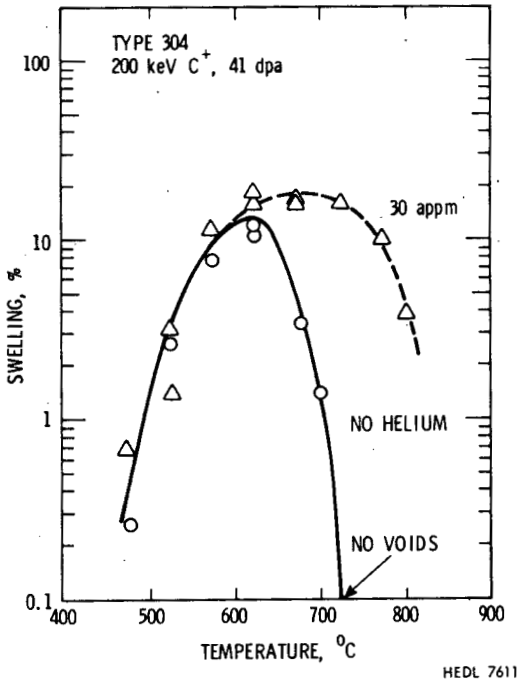

(a)

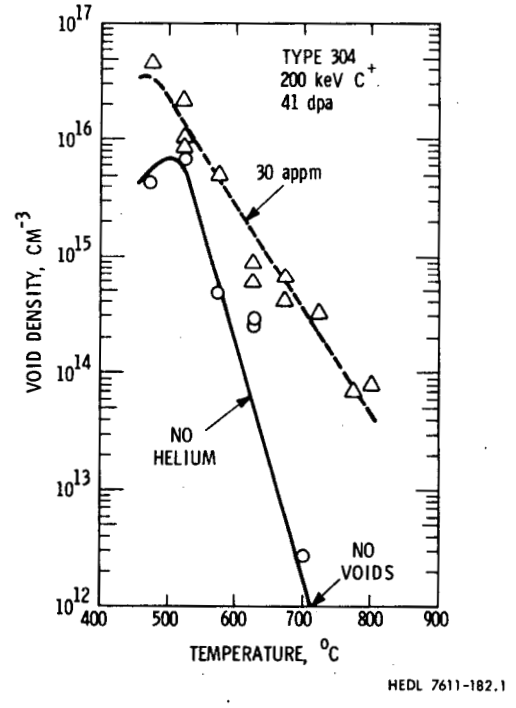

(b)

FIGURE 170. Demonstration by Shimada and coworkers(25) that the peak swelling temperature may be obscured in simulation experiments if void nucleation is depressed by surface effects at high temperatures. At low temperatures the swelling is insensitive to the void density and its dependence on helium content.

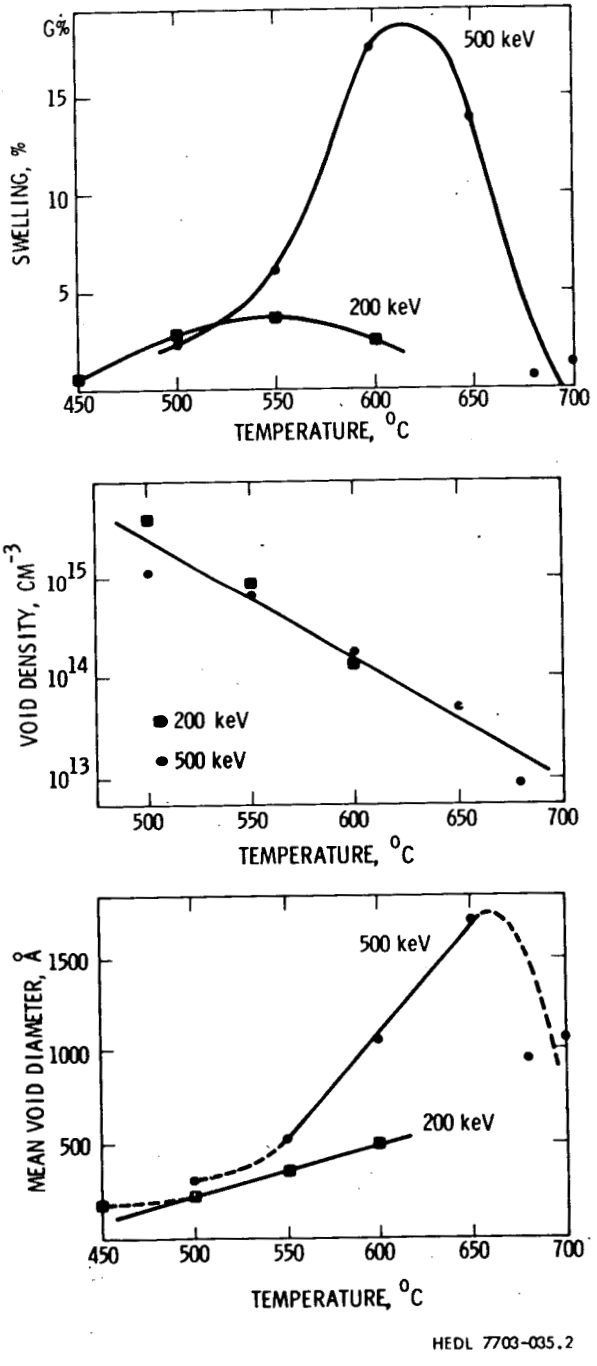

FIGURE 171. The variation with ion energy at 25 dpa of swelling, void density and mean void size observed in low energy Ni^+ ion irradiations of pure nickel(55). Note that the effect of the surface first occurs in the mean void size and later in the void density.

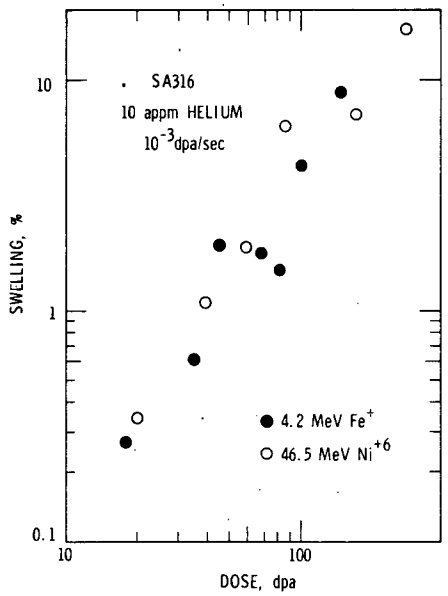

HEDL 7612-38.1

FIGURE 172. Demonstration by Blamires and Worth that at 525°C the swelling behavior for shallow and deep penetrating ions is identical(26).

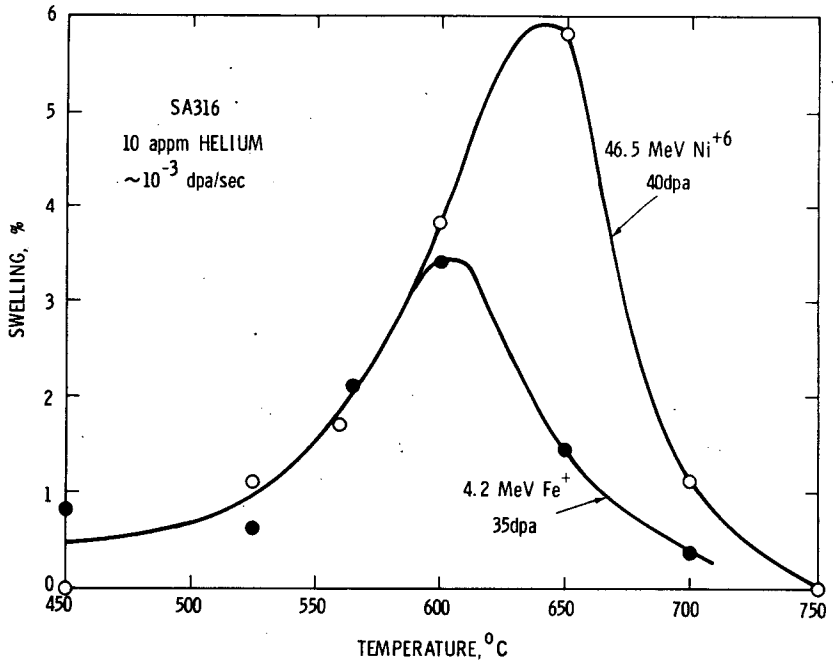

HEDL 7612-38.2

FIGURE 173. The effect of surface influence on ion-induced swelling. At higher temperatures the data of Blamires and Worth(26) show that the effect of the surface depresses the swelling at 4.2 MeV, yielding a low estimate of the peak swelling temperature.

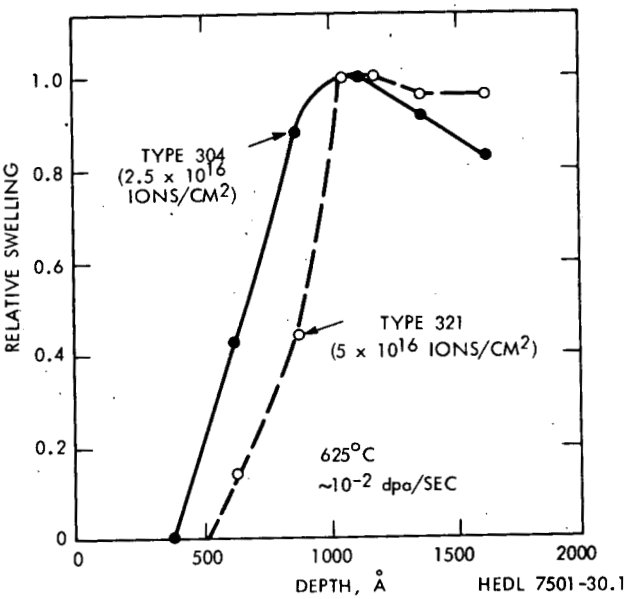

FIGURE 174(a). Demonstration by Johnston and coworkers[28] that the effect of the surface on total swelling extends to a depth twice the denuded zone depth. The void number densities are relatively unaffected in the depressed zone, however.

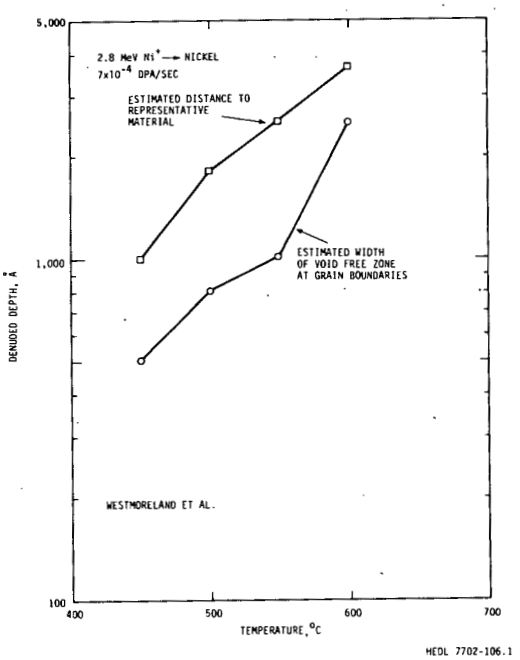

FIGURE 174(b). A factor-of-two criterion for the surface effect demonstrated by Westmoreland and coworkers(4) in ion irradiation of nickel.

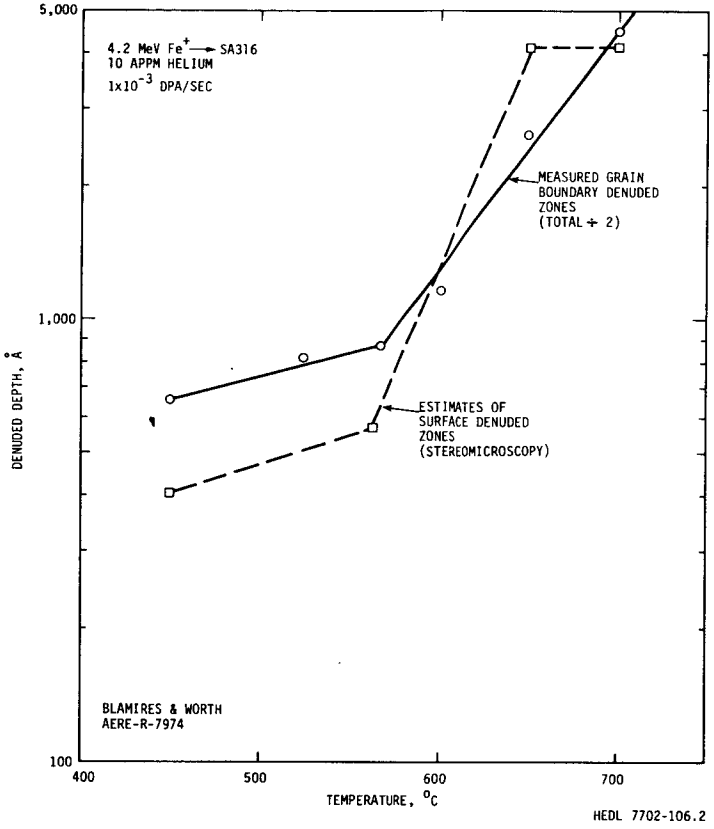

FIGURE 175(a). Denuded zone measurements at grain boundaries and front surfaces in annealed 316 stainless steel with 4.2 MeV Fe^+ bombardment(26).

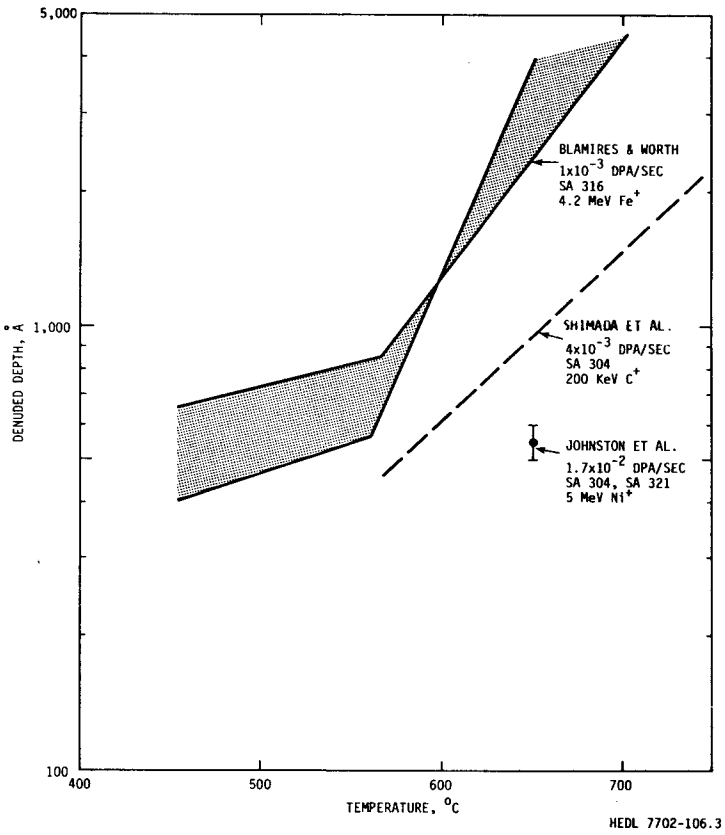

FIGURE 175(b). Denuded zone measurements observed in ion irradiations of 300 series stainless steels at various displacement rates. At 650°C an inverse square-root dependence on displacement rate appears to be justified.

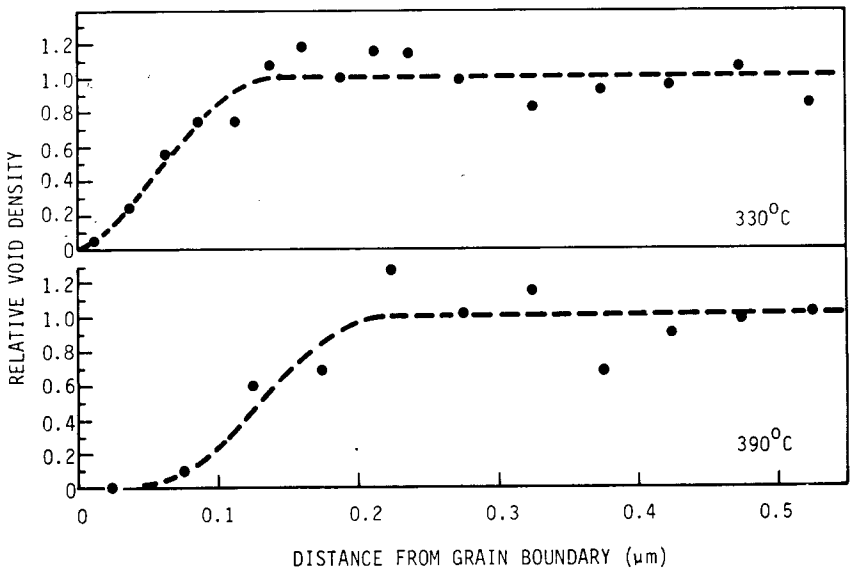

HEDL 7612-168.6

FIGURE 176. Surface effects on swelling. Norris(29) found that in HVEM irradiation of pure nickel the surface influence was expressed primarily in a suppression of the void number density.

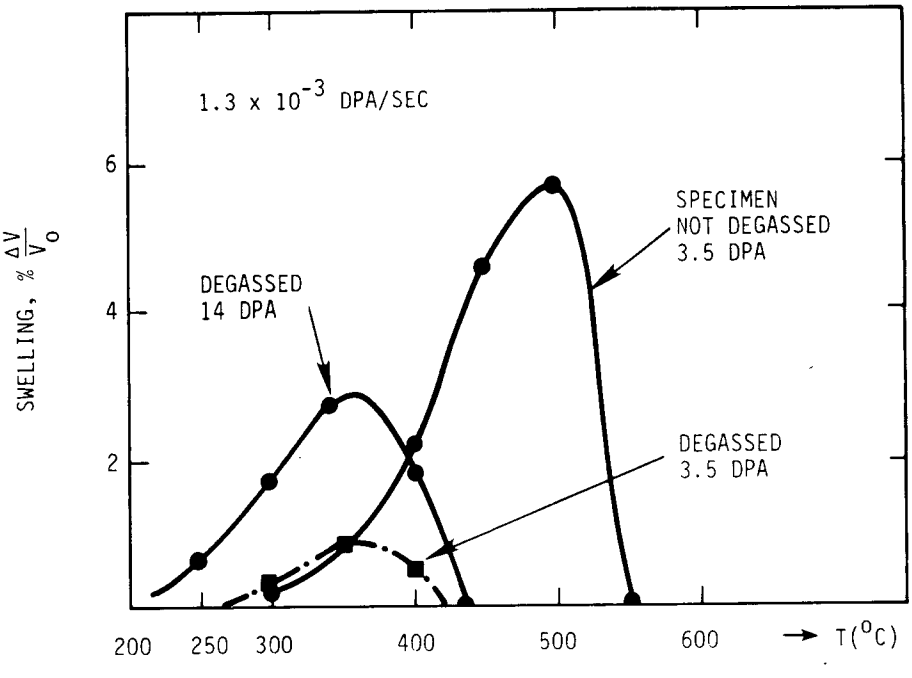

HEDL 7612-168.3

FIGURE 177. Effect of gas atoms on swelling near surfaces. Glowinski(30) demonstrated that the presence of gas atoms in electron-irradiated copper extended the range of swelling to higher temperatures. Note that the surface-induced suppression without gas is a permanent feature, persisting at least to 14 dpa.

A most convincing demonstration of the effect of surfaces on void nucleation can be seen in the work of Glowinski[30] (Figure 177) where the irradiation of thin copper foils with 1 MeV electrons yielded a cessation of swelling at 450°C in degassed foils at intermediate and high doses, whereas a specimen at intermediate dose which was not degassed yielded swelling to 550°C. At low temperature, the behavior of the two kinds of foils was identical. The high-temperature influence of the surfaces on void nucleation was obviously overcome by the presence of dissolved gas in the second experiment. There is no guarantee, however, that in bulk material the swelling regime may not extend to temperatures even higher than that observed in Figure 177.

It appears that the suppression of void nucleation upon gas removal at higher temperatures is related to factors in addition to those which determine the denuded zone width. Shimada and coworkers[36] recently reported that the denuded zone width of helium-injected 304 stainless steel was smaller than that of uninjected steel. From this result it can be inferred that a relationship exists between gas content and denuded zone width. This conclusion overlooks the fact that the denuded width was measured from the specimen surface to the equator of the nearest void. The mean void size decreases with helium content as shown in Figure 178(b)[25], and in reality if void nucleation occurs the properly defined denuded width is independent of helium content.

Figures 174(b) and 175(b) indicate a near-identical and strong dependence on temperature of denuded zone width during ion bombardment, in agreement with earlier electron irradiation results[27]. Figure 175(b) also indicates that the denuded width decreases with increasing displacement rate. Whereas Garner and Thomas[27] predicted that the denuded width L_{DZ} would vary with flux to the -1/2 power, others[32,33] have predicted that $L_{DZ} \sim \phi^{-1/4}$. At 650°C the data in Figure 175(b) on 300 series stainless steels support the $\phi^{-1/2}$ dependence and allows an estimate to be made of the surface affected depth, $L_S = 2\ L_{DZ}$, at any temperature and displacement rate. As an example, consider the recent ORNL ion irradiation experiments[34] conducted with 4 MeV nickel ions at a peak displacement rate of 5×10^{-3} dpa/sec. Microscopy specimens from such irradiations would be extracted from a depth of 0.5 to 0.6 μm. The $L_S = 2\ L_{DZ}$ criterion would be exceeded at 750 to 770°C and the TEM measurement of the bulk-representative peak swelling would be precluded if it existed above this temperature range.

If the temperature dependence for these irradiations were to be determined with step height measurements, however, such as reported by Rowcliffe and Gessel[35], then the effect of the surface would perturb the measurements at lower temperatures. This is a consequence of the fact that step height measurements are composed of the integrated strains from all depths which include the regions affected by the surface.

7.3.7 Displacement Gradient Effects

As reported earlier by Garner and Guthrie[37] the presence of displacement rate gradients along the ion trajectory leads to a distortion of the swelling vs. depth profile. This phenomenon was designated the "internal temperature shift" and was found by Johnston and coworkers[28] to have a considerable impact on the interpretation of step height measurements. As shown in Figure 179 the swelling vs. depth profile becomes increasingly distorted at temperatures away from that of the peak swelling rate. Figure 180 indicates that the integrated distortion is expressed in the step height measurement as a substantial deviation in the swelling calculated from TEM measurements and that determined by step height measurements.

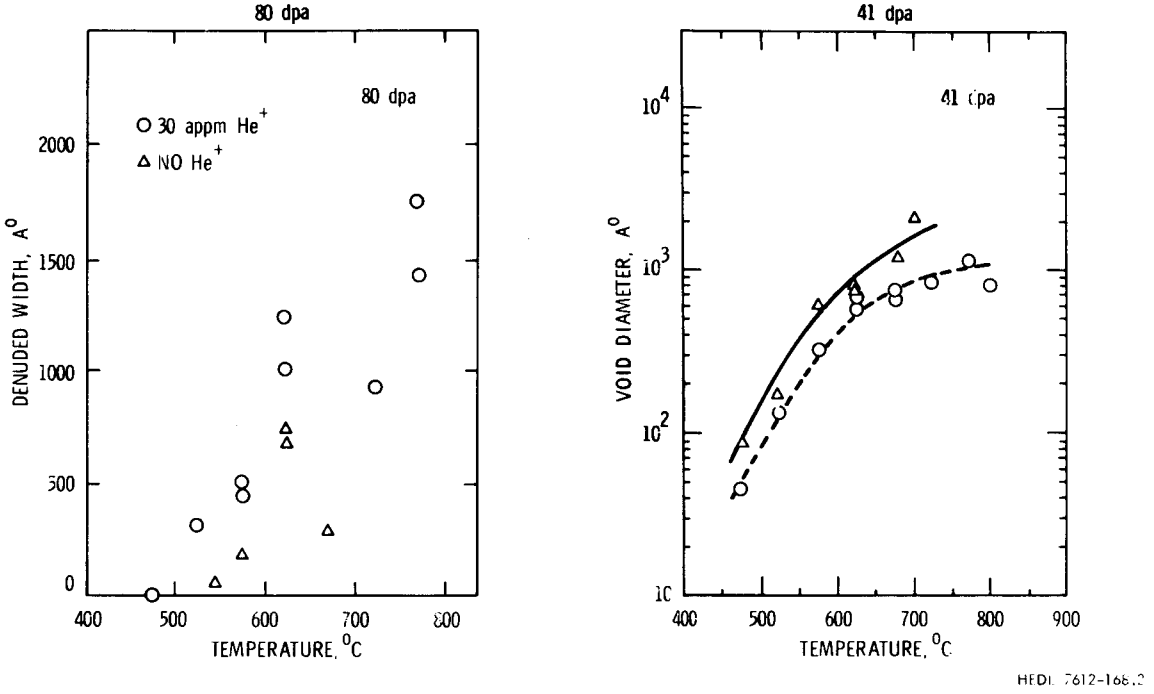

(a) (b)

FIGURE 178. Effect of helium on denuded zone width. In (a) Shimada and coworkers(36) draw an incorrect conclusion that helium increases the denuded zone width. From another publication(25), Figure 178(b) shows that the void size changes substantially with helium, yielding misleading measurements when based on void equators rather than nearest void surfaces.

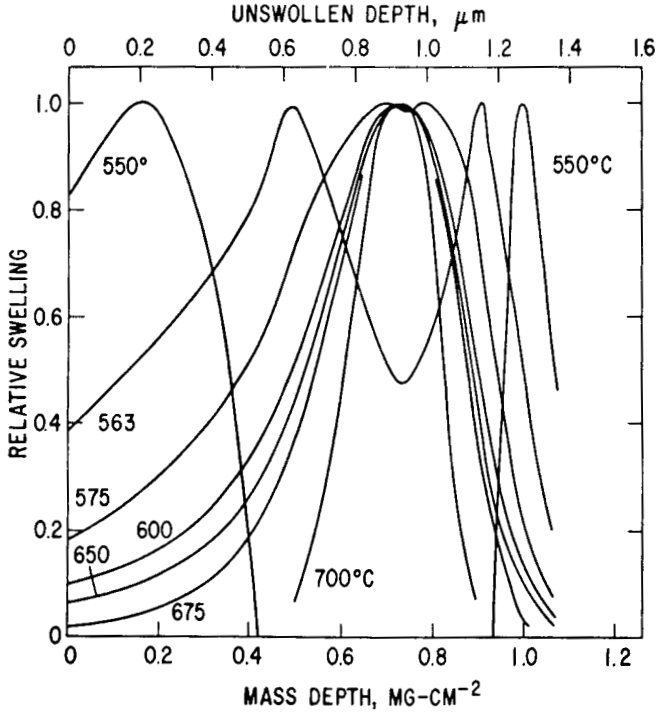

FIGURE 179. Normalized swelling profiles computed by Johnston(28) showing swelling profile distortion arising from displacement rate gradients.

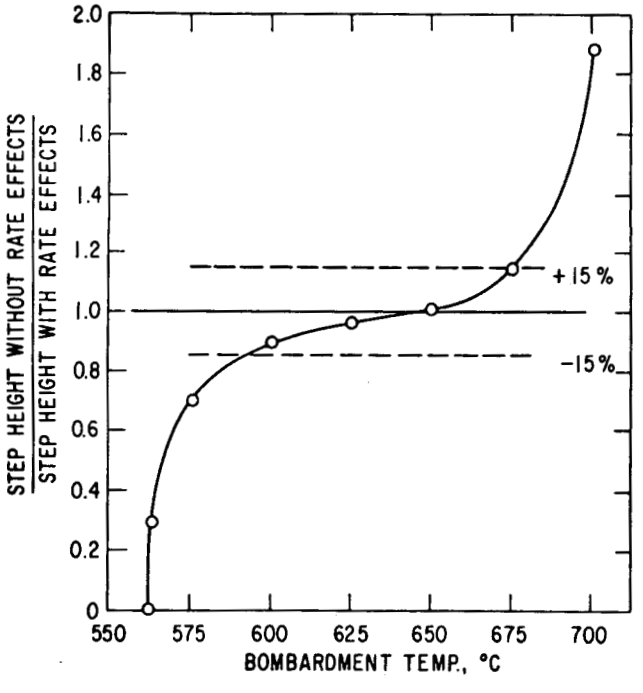

FIGURE 180. Ratios of the step heights calculated with and without taking into account the variation of displacement rate along the ion range [Johnston and coworkers(28)].

It is concluded therefore that determinations of the temperature dependence of swelling from step height measurements involve substantial perturbations by displacement gradient and surface effects, and that TEM observations are desirable whenever possible. If the surface effect can be minimized, step heights can be used to determine the peak swelling temperature but not the full temperature dependence. If a complex multiple-peak temperature dependence of swelling is exhibited by the irradiated material, step height data may be inadequate to determine any measure of the temperature dependence of swelling.

The presence of displacement rate gradients also leads to swelling rate gradients and associated stress states that are large and atypical of the neutron environment. It has been proposed that this will lead to a reduction in swelling[38-40]. Consequently, the concept of dose equivalency between ions and neutrons, and possibly the temperature dependence of swelling measured in simulation experiments may be affected.

7.3.8 The Dose Equivalency Concept

In the early stages of the intercorrelation effort, it was assumed that the temperature shift occurred as a straightforward displacement of the swelling regime in temperature, without change in distribution, range or magnitude[41]. It was recognized, however, that these assumptions were quite optimistic and additional data were required for substantiation. Any change in magnitude of swelling therefore was thought to be contained in the dose equivalency concept, as shown in Figure 181. The rationale employed[42] in describing the dose equivalency concept involved only the relative calculational uncertainties of atomic

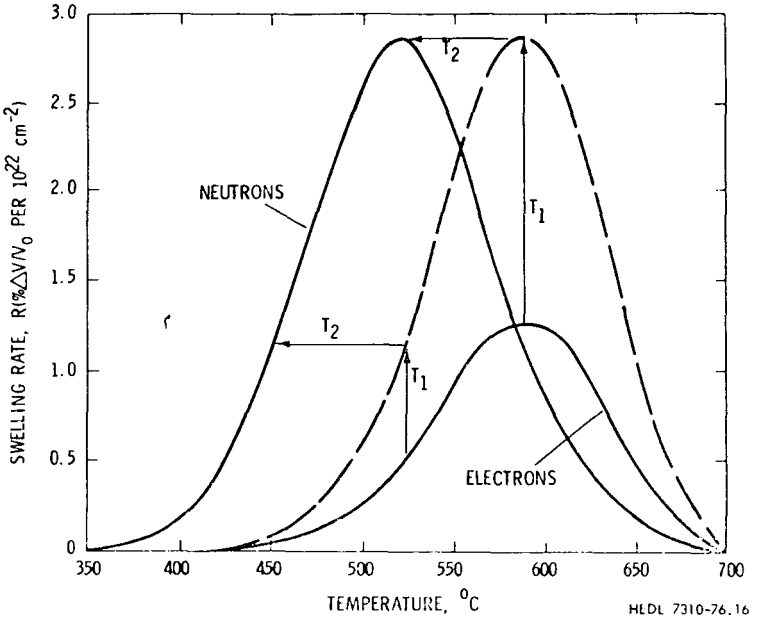

FIGURE 181. Schematic illustration of method used to correlate electron and neutron swelling rates. T_2 represents the temperature shift and T_1 the relative dose equivalency. Reproduced from Laidler(41).

displacements for various bombarding particles and the fractional survivability of the defects in each displacement cascade or event. No allowance was made for the possibility that from purely displacement rate considerations the swelling profile might change in magnitude or shape.

From the previous sections, it has been shown that the swelling profile can change if the microstructure evolves differently with fluence at the higher rate, if phase changes occur in a different manner, or if the activation energies for diffusion of the various elements are substantially different. If the experimenter opts for measurements of the shift in peak swelling temperatures (ΔT_p) and displacement equivalencies based on comparison of swelling rate magnitudes (previously designated K-factors)[42], then the measured K-factor must include contributions from three categories of phenomena which determine its magnitude:

a. Differences in the deposited energy and defect production characteristics, as well as the experimenter's ability to calculate these parameters.

b. Contributions which compensate for those material parameters which violate the assumptions implicit in a simple temperature shift model.

c. Experimental perturbations related to displacement gradients, surface effects, stress effects and other unidentified phenomena.

The evaluation of experimentally determined K-factors therefore requires analysis of each of the three categories of contributions. Although stress effects are inherent in the simulation technique and are unavoidable, surface effects can be minimized by conducting the experiments at the greatest depth possible and by increasing the displacement rate. Since the ion energies available are usually fixed by the irradiation facility, the maximum feasible beam current must be employed. Displacement rate gradient effects can be converted from disadvantage to advantage by measuring not only the step height but also the peak swelling by TEM whenever feasible. Comparison of the two measurements yields additional insight on the processes involved.

The only procedure envisioned to date which allows discrimination of category (b) contributions involves the use of very simple alloys, where many of the restrictive temperature shift assumptions still apply. Measurement of K-factors for such a system supplies the best estimate of category (a) contributions. Comparison of K-factors for more complex systems with that of the simple system then yields an estimate of the category (b) contributions.

7.3.9 Evaluation of Data Derived from Simple Alloys

The most relevant data fields for this purpose are those of Westmoreland et al[4] and the ADIP experiment[17], which will be evaluated in retrospect to determine whether they yield estimates of the category (a) contributions to the dose equivalency.

The data of Westmoreland and coworkers[4] (Figure 165) show that the 2.8 MeV Ni^+ data yield a clear temperature shift in the total swelling of ∿35°C per decade of flux, hereafter designated ΔT_p°. The swelling rates were not measured in these experiments, however. The data are judged to be sufficient to estimate the temperature shift since reasonably large swellings were measured and most data points are non-zero. On the other hand no conclusions

can confidently be developed on whether the difference in peak magnitude is due to a rate effect on incubation or represents different steady-state swelling rates. It appears, however, that the incubation fluence may have been larger at the higher temperatures where the high dose rate experiment was conducted. For a 2.8 MeV Ni^+ ion energy, TEM examination is concentrated in the 0.4 to 0.6 μm range, and using Figure 174(b) and the $2L_{DZ}$ and $\phi^{-1/2}$ criteria, the high dose rate experiment should not have been perturbed by surface effects. The low dose rate experiment, however, should have exhibited surface perturbations at 580°C and above. Therefore the low dose rate experiment just barely escaped being dominated by surface effects.

In the ADIP experiment[17] the ion-induced displacement rates ranged from 5×10^{-3} to 2×10^{-2} dpa/sec, and helium was preinjected, both of which precluded surface-related complications. Because the peak swelling temperatures and rates per dpa were the same for all three ion energies employed, 2.8, 3.5 and 5.0 MeV, considerable confidence is given to the experimental technique employed. Since all experiments involved TEM rather than step height measurement, displacement gradient effects should not have perturbed the measurements. The determination of the K-factor ratio describing the relative dose equivalency between Ni^+ ions and neutrons must await the measurement of neutron-induced swelling at higher fluences. For the present it is assumed that nickel ions and neutrons have fully equivalent damage characteristics. Therefore it is assumed that $K_{Ni^+}/K_n = 1.0$, although a value of 0.5 has been predicted based on considerations of stress affected swelling[38]. The ADIP experiment yielded a K-factor ratio of $K_e/K_{Ni^+} = 6.4$ for electrons. The sensitivity of the high temperature electron irradiation results to specimen preparation technique[17] indicated that the electron irradiation experiment operated just under the high temperature surface-affected limit, however. The value of $K_e/K_{Ni^+} = 6.4$ most probably represents the category (a) contributions, which describe the irradiation environment rather than the material response. As shown in Table 42, the composition of the alloy is essentially pure Fe, Ni and Cr, all of which have near-identical self-diffusion activation energies in ternary alloys, 63 ± 3 Kcal/mole. Due to the very low level of minor elements with smaller activation energies, the ADIP alloy results can be interpreted as being representative of a simple alloy, wherein $\Delta T_p^\circ \simeq 35°C$ per decade in flux and $K_e/K_{Ni^+} = 6.4$. Another way of stating this latter ratio is that $1\ dpa_e = 6.4\ dpa_{Ni^+}$.

TABLE 42

COMPOSITION OF PHASE I ADIP ALLOY (WEIGHT PERCENT)

Fe	Ni	Cr	C	Cu	Si	Mn	N_2	O_2
60.1	25.04	14.80	0.01	0.02	0.02	0.005	0.0028	0.0154

7.3.10 Intercorrelation Experiments on Complex Alloys

In more complex alloys the identity and stability of the various phases control the distribution of minor elements, many of which have activation energies for diffusion which are greatly different from that of Fe, Ni and Cr. Typical minor elements of this nature are C, Si, Al and Ti. It is therefore expected that the details of the temperature distribution of swelling will change in response to both the accelerated displacement rate and pre-irradiation thermomechanical treatments. A consensus has not yet developed, however, on how an

"equivalent" irradiation temperature should be selected for such alloys. Suggestions based on various experimental and theoretical viewpoints range from ΔT_p° = 35°C per decade, to zero, and even to negative values where precipitation kinetics are thought to be the dominant concern.

If one focuses on the strong temperature dependence of point defect supersaturations, however, it is difficult to envision that the material characteristics can completely overwhelm and reverse the impact of the irradiation-induced production of point defects, a viewpoint which argues for a positive ΔT_p. Although the ΔT_p° = 35°C per decade figure is felt to best represent the irradiation environment's contribution, various experimental results support lower values in 316 stainless steel. If the current neutron-induced swelling equation[19] for 316 stainless steel is accurate, the ion data of Johnston[18] yield a ΔT_p of only 60°C for an increase of 1.7 x 10^4 in displacement rate, while the data of Rowcliffe and Gessel[35] yield a higher ΔT_p, 85°C, for a lower factor of 5 x 10^3 increase in displacement rate. Not only are these numbers inconsistent with each other, but they are low with respect to predictions based on the ADIP and pure nickel experiments. It should be noted that the two experiments proceeded on different heats of material, neither of which was involved in the data base from which the swelling equation was developed.

The data of Rowcliffe and Gessel[35] are the first U.S. ion data which confirm the double peaked behavior often seen in U.S., U.K. and French fuel pins made with 316 stainless steel. As shown in Figure 182, the double peaked behavior persists to very high fluence levels[45] (17.2% burnup = 1.2 x 10^{23} n/cm^2 E>0.1 MeV), and arises from a complex

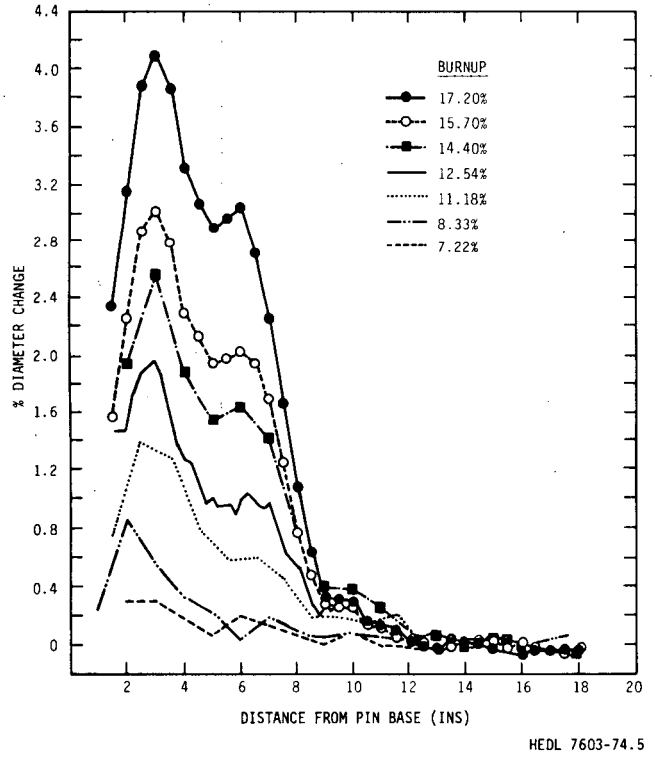

FIGURE 182. Diameter change profiles of U.K. fuel pin 1684 at various burn-up levels, showing double-peaked swelling behavior in 20% CW M316(45).

temperature dependence of the steady state swelling rate[46]. The peak swelling rate was determined to be about 1.45%/10^{22} n cm^{-2}, a rate substantially below the 2.63%/10^{22} n cm^{-2} measured on the M2783 heat of 316 steel[19].

Gelles[47] determined a peak electron-induced swelling rate for the M2783 heat at ~1.2 ± 0.1%/dpa_e but he was unable to extend the irradiations to sufficiently high temperatures to observe the decline of the swelling rate at high temperatures. Similar results have been reported for other heats of 316 steel[48]. This implies that $K_e/K_n \cong (2.6/1.2) \cong 2.2$ for this heat of steel. Only if $K_{Ni}+/K_n$ were 0.34 would this result be consistent with the result of the ADIP experiment. Korenko and Gelles[49] have accepted the possibility that $K_{Ni}+/K_n$ ~0.5, but found that the K-factor ratios appear to be different for each alloy class.

The variability in alloy response to irradiation may indeed be different for each alloy or alloy class. For example, some materials exhibit much more complex temperature dependencies in neutron environments than is the case for 316 stainless steel. In Figure 183 are shown the diameter change profiles observed in a U.K. fuel pin cladding of 20% CW FV548[45]. If the fluence profile were factored into the analysis, the double-peaked behavior would become even more pronounced. As shown in Figure 184 the complexity of the temperature response of Nimonic PE16 at constant fluence is strongly dependent on the heat identity and preirradiation thermomechanical treatment.

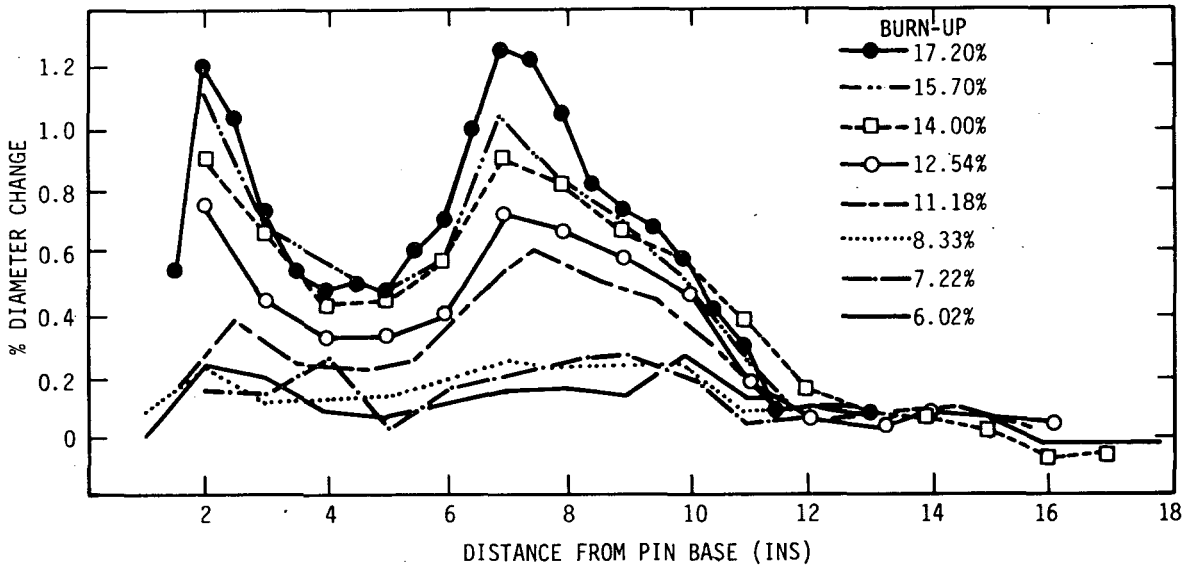

FIGURE 183. Diameter change profiles of U.K. fuel pin 1822 at various burn-up levels, showing pronounced double-peaked swelling behavior in 20% CW FV548 (45).

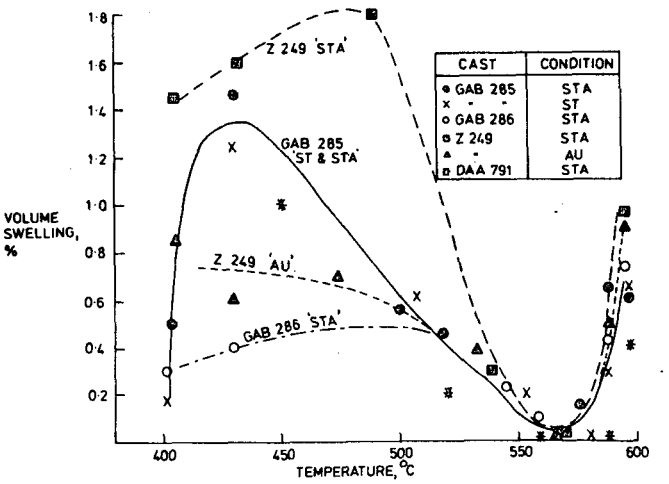

FIGURE 184. Neutron-induced swelling of several casts of PE16 at 30 dpa_n (6 x 10^{22} n/cm^2, E>0.1 MeV)(50).

7.3.11 Experimental Basis for the USP Experiment

From the foregoing discussions it is obvious that any intercorrelation experiment must proceed with no material variability in the various irradiations. For a definitive experiment the neutron-induced swelling rate must be well defined, however. The only material for which there is a confident description of the neutron-induced swelling rate behavior[19] is the M2783 heat of annealed and cold-worked 316 stainless steel. Fortunately there exists archive unirradiated material, and the irradiated microstructures have been examined in detail[51,52].

The complexity of the temperature shift and dose equivalency phenomena pose many problems for any intercorrelation experiment on this material, however. In order to investigate the factors which control the response of swelling in the disparate neutron and charged particle environments, the Unified Simulation Program (USP) experiment will employ "reactor-preconditioned"[53] material, and will compare the swelling and microstructural response of both the "virgin" and "preconditioned" M2783 heats during charged particle irradiation. A central feature of the experiment is the possibility that the simulation will be improved if the charged particle irradition proceeds on a microstructure which is exactly that produced in-reactor at "equivalent" temperatures.

Since the magnitude of the temperature shift is not known in advance, specimens preconditioned at a series of reactor irradiation temperatures will be irradiated with charged particles over a range of temperatures thought to cover the possible temperature shift; all are positive and non-zero shifts. The major effort will proceed on annealed M2783 rather than cold-worked material to ensure the unhindered extraction of microstructural data. The starting fluence is ~9 x 10^{22} n/cm^2 (E>0.1 MeV) while the target neutron fluence to be simulated is 14 x 10^{23} n/cm^2, a fluence already attained by reactor irradiation alone.

The advantages of preconditioning are rather obvious in light of the previous discussions. Since the temperature shift for nucleation is often different from that of void growth, it is best to bypass the nucleation stage entirely. The influence of the surface on void incubation is also avoided. Any phase changes, elemental segregation or redistribution effects are either over or well in progress. Most importantly, however, because the dislocation densities at the start of the charged particle irradiations are identical to those at the end of the neutron irradiation, one partial but important requirement of the simple temperature shift concept is satisfied. If the microstructure subsequently evolves with increasing charged particle fluence in a manner inconsistent with that observed for the high neutron fluence case, then direct comparisons of the differences and their consequences can be made.

The definition of "equivalent" swelling temperatures will involve both quantitative and subjective judgments. In attaining the target swelling, ranging from 2 to 18%, the irradiation must proceed at known swelling rates and yet not develop "uncharacteristic" microstrucrures. In other words, the dislocation and loop density must remain characteristic of the simulated neutron environment, and no "excessive" nucleation of voids should occur in a manner uncharacteristic of the simulated environment.

7.3.12 Phase I Experiments

Anticipating the complexity of the temperature dependence of the various USP alloys, the program participants have elected to define initially only a partial irradiation matrix. Using step height information gained from the first irradiation series, judgments will then be made on further irradiation conditions. In the Phase I experiment, for example, a full temperature dependence of the swelling of virgin SA316 (M2783 heat) at 100 dpa will be obtained in an attempt to determine the location and number of swelling peaks. The fluence dependence of swelling will then be determined at those temperatures which are deemed to be the most important. The information gained from these irradiations will then be used to determine the irradiation conditions for the preconditioned specimens.

A mixture of TEM and step height measurements will be employed in the evaluation of the specimens. Microstructural information is best gained from specimens with a low level of swelling, while step heights are unreliable for such applications. Electron microscopy of thin foil specimens with $\geq$20% swelling is subject to large errors, however. Step height measurements reflect only the additional swelling induced by charged particle bombardment, while TEM techniques measure the total accumulated swelling.

The various Phase I irradiations are described in more detail in the following sections.

Phase I.A. Virgin Annealed M2783 Heat of 316 Stainless Steel. Charged particle irradiations are to span the full temperature range of swelling, to doses sufficient to reach the target levels of swelling. The full temperature distribution of swelling will be determined at 100 dpa; dose dependencies will be established at selected temperatures. Five appm helium will be uniformly deposited to 0.95 mils to overcome nucleation and surface related problems. The ion irradiations will proceed at the maximum feasible rate, $\sim 8 \times 10^{-3}$ dpa/sec,

thus minimizing surface problems. Comparison of the electron irradiation results will be made with irradiation results of virgin cold worked M2783 performed earlier by Gelles[47]. Irradiations are to be performed by GE and HEDL. Judicious use of step height measurements will be employed to reduce TEM requirements, particularly where the swelling levels are too large for TEM data extraction.

Phase I.B. Preconditioned Annealed M2783 Heat. Nominal neutron irradiation temperatures are 450, 520 and 600°C at doses of 8-9 x 10^{22} n/cm^2 (E>0.1 MeV). Charged particle irradiations will proceed at four temperatures for each reactor temperature, spanning a ΔT_p range of 50 to 160°C, with sufficient dose levels to determine the swelling rate and to reach the target swelling levels. Irradiations are to be performed by HEDL and the W-ARD/ORNL team (4 MeV Ni^+).

Phase I.C. Preconditioned 20% Cold Worked M2783 Heat. The nominal neutron irradiation temperature is 600°C at 9 x 10^{22} n/cm^2 (E>0.1 MeV). The major purpose of this experiment is to test the effect of preconditioning on void nucleation. Whereas most voids have already nucleated prior to Ni^+ irradiation in the Phase I.B. experiment, the density of voids in the cold worked material at the 9 x 10^{22} level is one or more orders of magnitude below that found at 1.4 x 10^{23} n/cm^2. Charged particle irradiations are to proceed at four temperatures spanning a ΔT_p range of 50 to 160°C, with sufficient dose levels to determine the swelling rates and to reach the target swelling levels. GE and HEDL will perform the irradiations.

7.3.13 Phases II and III

These portions of the experiment are exploratory in nature since no neutron-induced swelling rates are available and the materials involved have exhibited swelling behavior more complex than that of 316. The LS-1 heat of 316 stainless steel has shown pronounced differences in neutron, ion and electron irradiations, differences which appear to be related to phase instabilities[34,54]. Phase II will explore the effect of preconditioning on charged particle irradiations of this material. The material will be removed from the B-113 capsule irradiated at a temperature of 540°C to a low fluence in EBR-II. ORNL and HEDL will conduct the irradiations.

Phase III of the experiment involves the irradiation of preconditioned STA Nimonic PE16 specimens and the comparison of swelling results with those from previously conducted virgin irradiations on the same heat of material. The neutron irradiation temperatures are 550, 600 and 650°C, with the neutron fluence developed in EBR-II in the X-223 (AA-I) subassembly ranging up to 5 x 10^{22} n/cm^2. HEDL and the W-ARD/ORNL team will conduct the charged particle irradiations.

7.3.14 USP Schedules and Status

Unified Simulation Program schedules and status are shown in Table 43.

TABLE 43

USP SCHEDULE AND STATUS

	Scheduled Completion
I. M2783 PHASE OF EXPERIMENT	
A. Specimen Preparation	
1. Virgin SA 316 specimens prepared from archive tubing (GE)	Complete
2. Helium implantation in virgin specimens (GE)	Complete
3. GE forwards virgin specimens for electron irradiation at HEDL	Complete
4. GE forwards virgin specimens for ion irradiation at ORNL	Complete
5. Thinning of HEDL specimens to helium bearing layer	Complete
6. Determination of depth dependence of dislocation density (HEDL)	Complete
7. Transfer of hot CW 316 tube from EBR-II to GE	Complete
8. Sectioning of hot CW 316 tube at GE	Complete
9. GE forwards 1/3-section of hot CW 316 tube to HEDL	Complete
10. Preparation of hot CW 316 specimens for ion (GE) and electron studies (HEDL)	Complete
11. GE forwards hot CW 316 specimens for ion bombardment to ORNL	Complete
12. Transfer of hot SA 316 tubes from EBR-II to ORNL	Complete
13. Preparation of hot SA 316 specimens from tubes for both ion and electron irradiations (ORNL and W-ARD)	*1/30/77
14. Forward hot SA 316 specimens for electron irradiation from ORNL to HEDL	*2/15/77
B. Irradiation Schedule	
1. Testing, shakedown and calibration of ion irradiation facility (ORNL)	Complete
2. Start ion irradiations, SA 316 virgin first (ORNL, W-ARD)	*+ 12/15/76
3. Complete virgin irradiation with ions (ORNL, W-ARD)	*1/30/77
4. Complete hot irradiation with ions (ORNL, W-ARD)	3/30/77
5. Start electron irradiations on virgin specimens (HEDL)	1/15/77
6. Complete electron irradiations on virgin and hot CW specimens (HEDL)	3/30/77
7. Complete electron irradiations on hot annealed specimens (HEDL)	6/30/77
C. Analysis and Documentation	
1. Complete TEM analysis on ion bombarded virgin material (W-ARD, GE, ORNL)	5/30/77
2. Complete TEM analysis on ion bombarded hot material (W-ARD, GE, ORNL)	9/30/77
3. Complete counting and analysis of all HVEM irradiations (HEDL)	9/30/77
4. Complete intercorrelation and documentation (all labs)	12/30/77
II. NIMONIC PE16 PORTION OF EXPERIMENT	
1. HEDL forward archive specimens to W-ARD	Complete
2. Remove PE16 rods from AA-I (HEDL)	Complete
3. Prepare disk specimens at HEDL	Deleted
4. Forward rod specimens to W-ARD	Complete
5. W-ARD prepare surface of disk and forward to ORNL	4/1/77
6. HEDL supply documentation on B-109 preconditioned PE16 HVEM irradiations	Complete
7. ORNL completes ion irradiations	6/1/77
8. W-ARD and ORNL complete full range TEM evaluation and analysis	9/30/77
9. HEDL completes HVEM irradiations and analysis (start 6/30/77)	9/30/77
III. LS-1 PORTION OF EXPERIMENT	
1. HEDL provides LS-1 specimens to ORNL	2/29/77
2. ORNL completes ion irradiation and analysis	5/15/77
3. HEDL completes HVEM irradiation and analysis	5/15/77

*Behind schedule, +New starting date, 3/7/77

7.4 EXPECTED ACHIEVEMENTS IN THE NEXT REPORTING PERIOD

The USP experiment will proceed and results of the initial irradiations will be reported.

7.5 REFERENCES

1. Garner, F. A., and Laidler, J. J., "Review of Factors Relevant to Intercorrelation Experiments," Proceedings of Workshop on Correlation of Neutron and Charged Particle Damage, Oak Ridge, TN, June 4, 1976.

2. Laidler, J. J., Garner, F. A., and Thomas, L. E., "Simulation Experiments with the High Voltage Electron Microscope," Proceedings of ASM Materials Science Seminar, Radiation Damage in Metals, November 9-10, 1975, Cincinnati, OH.

3. Johnston, W. G., "Void Swelling Profiles Produced by Charged Particle Experiments," Ibid., Ref. 1.

4. Westmoreland, J. E., Sprague, J. A., Smidt, F. A., Jr., and Malmberg, P. R., Radiation Effects, 26, 1-16 (1975).

5. Brailsford, A. D., and Bullough, R., J. Nucl. Mat., 44, 121 (1972).

6. Bullough, R., and Perrin, R. C., in Irradiation Effects on Structural Alloys for Nuclear Reactor Applications, ASTM STP 484, p. 317 (1970).

7. Venker, H., and Ehrlich, K., J. Nucl. Mat., 60, 347-349 (1976).

8. Okamoto, P. R., Lam, N. Q., and Wiedersich, H., "Effect of Defect Trapping and Radiation-Induced Solute Segregation on Void Swelling," Ibid., Ref. 1.

9. Koehler, J. S., J. Applied Phys., 46, 2423 (1975); also Schilling, W., and Schroeder, K., "The Physics of Irradiation Produced Voids," R. S. Nelson (editor), AERE-R7934, p. 212 (1975).

10. Lam, Nghi Q., and Johnson, R. A., Nucl. Mat., 20, 121 (1976).

11. Garner, F. A., and Brager, H. R., "The Combined Influence of Silicon and Cold Work on Neutron-Induced Swelling in 316 Stainless Steel," HEDL TC-675-3.

12. Silvestre, G., Silvent, A., Regnard, C., and Sainfort, G., J. Nucl. Mat., 57, 125-135 (1975).

13. Wilkes, P., Liou, K. Y., and Lott, R. G., Rad. Effects, 29, 249-251 (1976).

14. Russell, K. C., Acta. Met., 19, 753 (1971).

15. Powell, R. W., "The Predicted Effects of Experimental and Material Parameters on Void Nucleation," TC-160-1, p. 360-377.

16. Packan, N. H., Ibid., Ref. 1.

17. Garner, F. A., et al., "Summary Report on Alloy Development Intercorrelation Program Experiment," TC-160-9, pp. 117-134.

18. Johnston, W. G., Rosolowski, J. H., and Turkalo, A. M., Nickel Ion Bombardment of Types 304, 316 and 321 Steels: Comparison with Fast Reactor Swelling Data, ASTM STP 529, pp. 213-227.

19. Garner, F. A., et al., "Revision 5 Swelling Correlation for 20% CW 316 Stainless Steel," TC-675-2, pp. 1-186 to 1-199.

20. Labbe, M., and Poirier, J. P., J. Nucl. Mat., 46, 86 (1973).

21. Labbe, M., Brebec, G., and Poirier, J. P., J. Nucl. Mat., 49, 223-234 (1974).

22. Glowinski, L. D., Lanore, J. M., Fiche, C., and Adda, Y., J. Nucl. Mat., 61, 41-52 (1976).

23. Menzinger, F., and Sacchetti, F., J. Nucl. Mat., 57, 193-197 (1975).

24. Sacchetti, F., J. Nucl. Mat., 64, 115-120 (1977).

25. Shimada, M., Nakahigashi, S., and Terasawa, M., "Swelling of Type 304 Stainless Steel," to be published, advance copy supplied by M. Shimada.

26. Blamires, N. G., and Worth, J. H., "Comparison of 4.2 MeV Fe^+ and 46.5 MeV Ni^+ Irradiation for the Study of Void Swelling," AERE-R-7974 (1975).

27. Garner, F. A., and Thomas, L. E., Production of Voids in Stainless Steel by High Voltage Electrons, ASTM STP 529, pp. 303-323 (1973).

28. Johnston, W. G., Rosolowski, J. H., and Turkalo, A. M., J. Nucl. Mat., 62, 167-180 (1976).

29. Norris, D. I. R., J. Nucl. Mat., 40, 66-76 (1971).

30. Glowinski, L. D., J. Nucl. Mat., 71, 8-21 (1976).

31. Nelson, R. S., Hudson, J. A., and Mazey, D. J., "The Physics of Irradiation Produced Voids," Consultant Symposium, Harwell (U.K.), R. S. Nelson (editor), September 1974.

32. Foreman, A. J. E., Rad. Effects, 14, 175 (1972).

33. Konobeev, Yu. V., Subbotin, A. V., Bykov, V. N., and Tscherbak, V. I., Phys. Stat. Sol. (a), 29, K121 (1975).

34. Bloom, E. E., Stiegler, J. O., Rowcliffe, A. F., and Leitnaker, J. M., "Austenitic Stainless Steels with Improved Resistance to Radiation-Induced Swelling," accepted for publication in Scripta Met.

35. Rowcliffe, A. F., and Gessel, G. R., "The Effect of Heat Treatment and Hot Hardness on Alloys D9 and D11," Alloy Development Program Information Meeting, October 1976 (TC-721), pp. 526-539.

36. Shimada, M., Nakahigaski, S., and Terasawa, M., Rad. Effects, 25, 283 (1975).

37. Garner, F. A., and Guthrie, G. L., "The Influence of Displacement Gradients on the Interpretation of Charged Particle Simulation Experiments," CONF-750989 (March 1976).

38. Garner, F. A., Wire, G. L., and Gilbert, E. R., "Stress Effects in Charged Particle Simulation Experiments," TC-160-5, p. 416.

39. Garner, F. A., "Evidence for Stress Affected Swelling in HVEM Irradiations," TC-160-7, p. 101.

40. Garner, Effect of Crystalline Orientation on Swelling-Induced Stress States," TC-160-7, p. 124.

41. Laidler, J. J., "Development of a Stress Free Swelling Design Equation," HEDL TC-29.

42. Garner, F. A., "Intercorrelation Activities," TC-160-3, pp. 100-115.

43. Perkins, R. A., et al., Met. Trans. 4, 2535-2538 (1973); also pp. 1665-1668.

44. Alloy Development Program Monthly Status Letter, TC-124-31, p. 8, item A3.

45. Butler, J. K., and Sloss, W. M., "Recent Results from Fuel Pin Diameter Measurements," USAEC/UK Information Exchange Meeting on Fast Reactor Fuel Elements and Structural Materials, Richland, WA, November 4-14, 1975.

46. Garner, F. A., "Analysis of U. K. Fuel Pin No. 1684," TC-675-1, p. 1-190.

47. Gelles, D. S., "The Effect of Heat-to-Heat Variations Due to Melting Technique on HVEM Induced Swelling in AISI 316," TC-675-2, p. 1-170.

48. Garner, F. A., Mastel, B., and Gelles, D. S., "Temperature Dependence of Swelling in Electron Irradiated 316 Stainless Steel," TC-675-3.

49. Korenko, M. K., and Gelles, D. S., "HVEM Irradiations of the Candidate Developmental Alloys," TC-160-9, p. 41.

50. Watkin, J. S., and Standring, J., U.S./U.K. Fast Reactor Exchange Meeting (November 1975).

51. Brager, H. R., et al., "Immersion Density and TEM of Highly Irradiated 20% Cold Worked Type 316 Stainless Steel, (X-098)," HEDL TC-646, p. 1-114.

52. Kenfield, T. A., Bell, W. L., and Appleby, W. K., "TEM Characterization of Void Swelling in Type 316 Stainless Steel at Fluences to 1.4 x 10^{22} n/cm^2, E>0.1 MeV," TC-675-2,

53. Garner, F. A., Laidler, J. J., Mastel, B., and Thomas, L. E., "Influence of High Voltage Electron Microscope Irradiation on Neutron-Produced Microstructures in Stainless Steels," ASTM STP 570, pp. 433-448.

54. Bates, J. F., et al., "Evaluation of the Swelling Behavior of Neutron-Irradiated LS-1," TC-160-7, p. 31.

55. Delaplace, J., Azam, N., Le Naour, L., Lott, M., and Fiche, C., Journal De Physique, Colloque C5, Tome 34, C5-11 (1973).

CHAPTER III.

COOLANT COMPATIBILITY STUDIES

1. SODIUM COMPATIBILITY TESTS OF ADVANCED CLADDING ALLOYS

R. P. Anantatmula, P. A. White, L. E. Chulos, R. R. Rake and J. L. Bevan
Hanford Engineering Development Laboratory

1.1 OBJECTIVE

The objective of this activity is to compare the corrosion behavior in liquid sodium of candidate cladding alloys. The prime candidate alloys will be tested at longer exposure times, and under conditions more nearly prototypic of an LMFBR core.

1.2 SUMMARY

Electron microprobe analysis of samples from Run 3B, STCL-4 indicated the general surface depletion of Ni, Cr, Al, Ti, Si and Mn and enrichment of Fe and Mo near the surface.

Corrosion rates obtained from the weight loss data of samples from Run 4B, STCL-4 indicated alloy D21 to have the lowest corrosion rate, similar to D25 of Run 3, STCL-4, followed by D68 and D9. The corrosion rate of D68 is even lower than that of the reference AISI 316.

Optical metallography of as-received developmental alloys D9, D21 and D68 of Run 4, STCL-4 revealed the presence of carbides and annealing twins in alloys D21 and D68. The structure of alloy D9 consisted of deformation bands and a few carbide precipitates similar to as-received D11.

1.3 ACCOMPLISHMENTS AND STATUS

1.3.1 Introduction

Electron microprobe analysis of alloy samples from Run 3B, STCL-4 has been completed. Corrosion rates have been evaluated from the weight loss data of 2,500-hour sodium-exposed developmental alloys D9, D21 and D68. Optical metallography has been performed on as-received alloys D9, D21 and D68.

1.3.2 Experimental Procedure

The sodium compatibility tests on the developmental alloys D9, D21 and D68 have been carried out in STCL-4. The test conditions were the same as those for Run 3, STCL-4. The experimental methods and data acquisition procedures have been described elsewhere[1].

1.3.3 Results and Discussion

1.3.3.1 Electron Microprobe Data of Run 3B, STCL-4 Alloys. The variation in composition (weight percent) with respect to the distance (μm) from the exposed surface in the depleted zone is plotted for each element comprising the alloy.

The composition profiles of alloy D11 are shown in Figures 185 and 186. Depletion of Ni, Si and Mn at the surface can be noted from the figures. This result agrees well with the scanning electron microscopy (SEM) data reported earlier[2] for this alloy. It

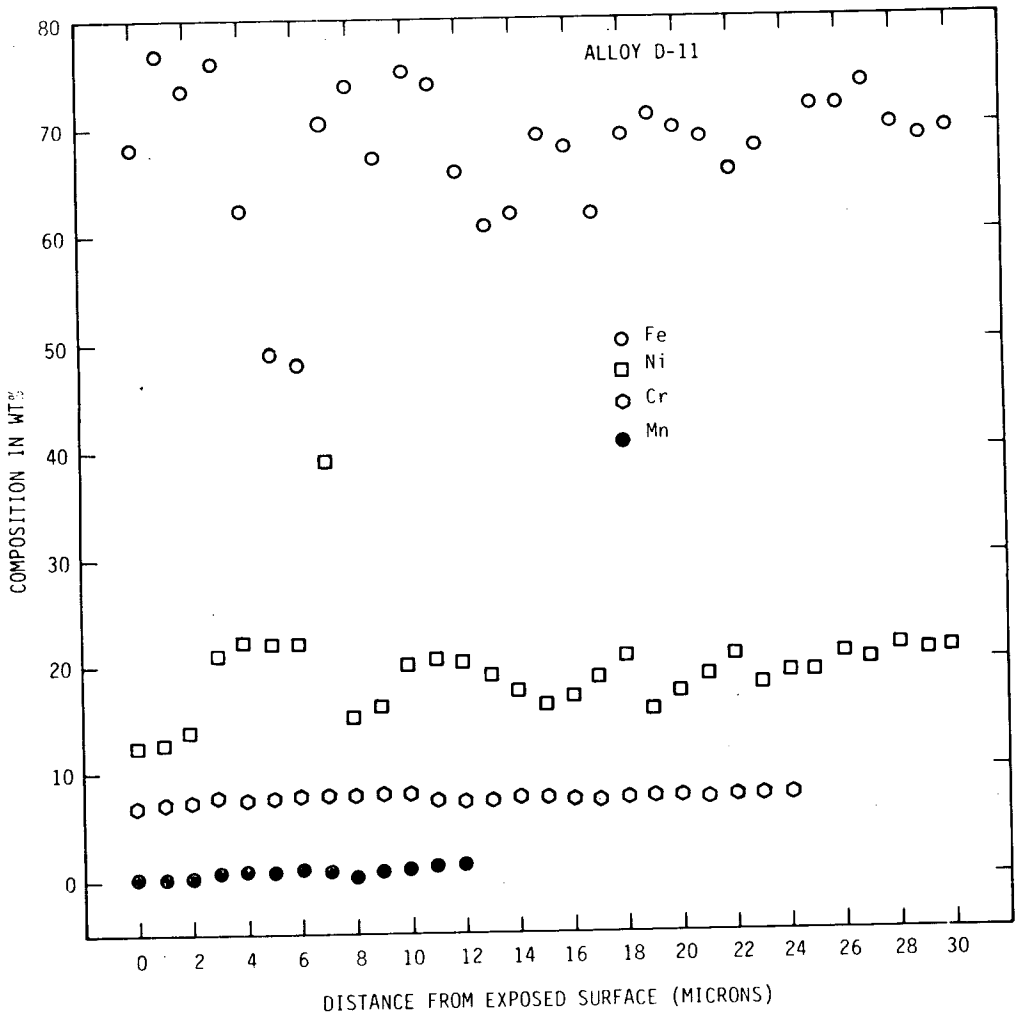

HEDL 7701-43.1

FIGURE 185. Concentration profile of alloy D11.

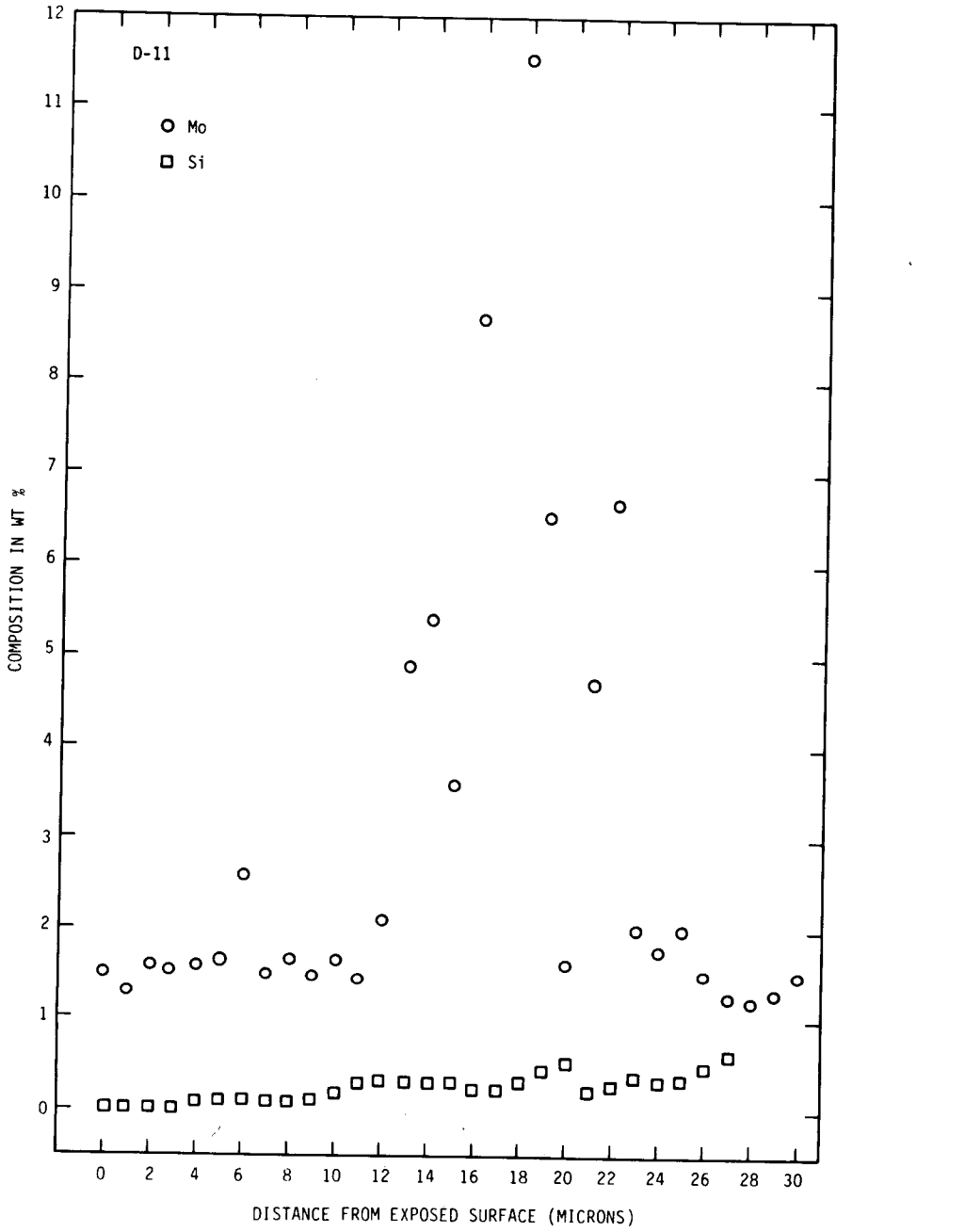

FIGURE 186. Concentration profile of alloy D11.

can be seen from Figure 186 that there is a maximum in the molybdenum profile. This is a result of the probe traversing across the Laves phase particles precipitated during the exposure to sodium[2].

The composition profiles of alloy D25 are given in Figures 187 and 188. As seen from the figures, the elements Cr, Al, Mn and Si seem to be surface depleted. These data are in fair agreement with the SEM data for this alloy and are also similar to that of A-286, the commercial alloy tested in Run 1, STCL-4. This similarity between D25 and A-286 can be expected since the alloys have similar compositions. Laves phase precipitation during the sodium exposure led to a peak in the concentration profile of molybdenum in this alloy also as in the case of D11.

The electron microprobe data of alloy D66 are illustrated in Figures 189 and 190. This alloy displayed the highest corrosion rate and the microprobe profiles indicate a surface depletion of Ni, Ti, Cr, Al and Si. There is enrichment near the surface of Mo and Fe. The data are in excellent agreement with the SEM data reported earlier. As with the alloys D11 and D25, there is an additional Mo peak indicating the precipitation of Laves phase during the thermal aging due to sodium exposure.

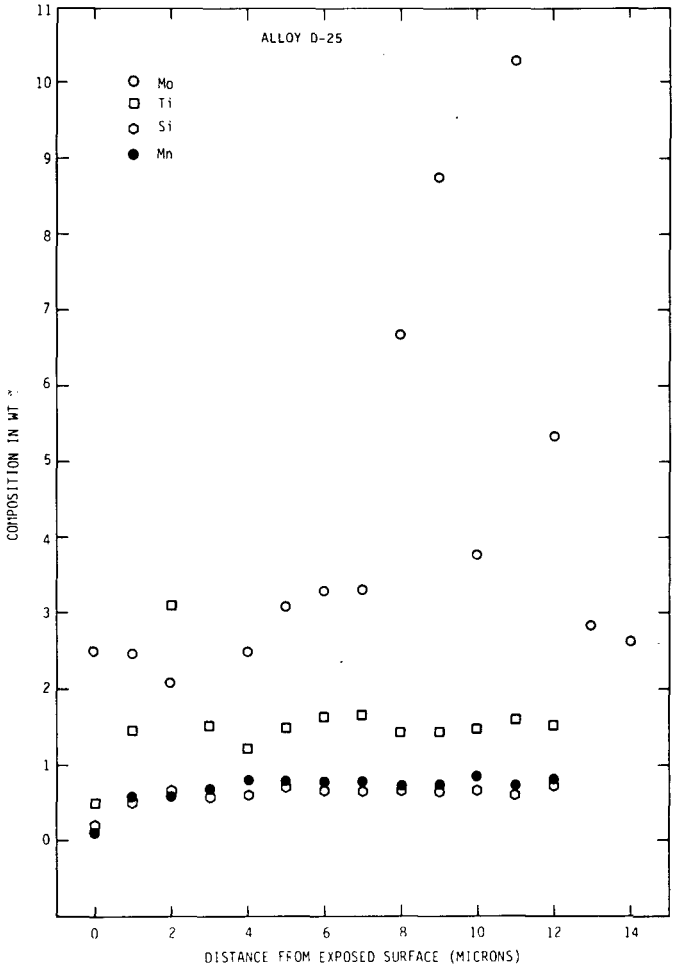

HEDL 7701-43.3

FIGURE 187. Concentration profile of alloy D25.

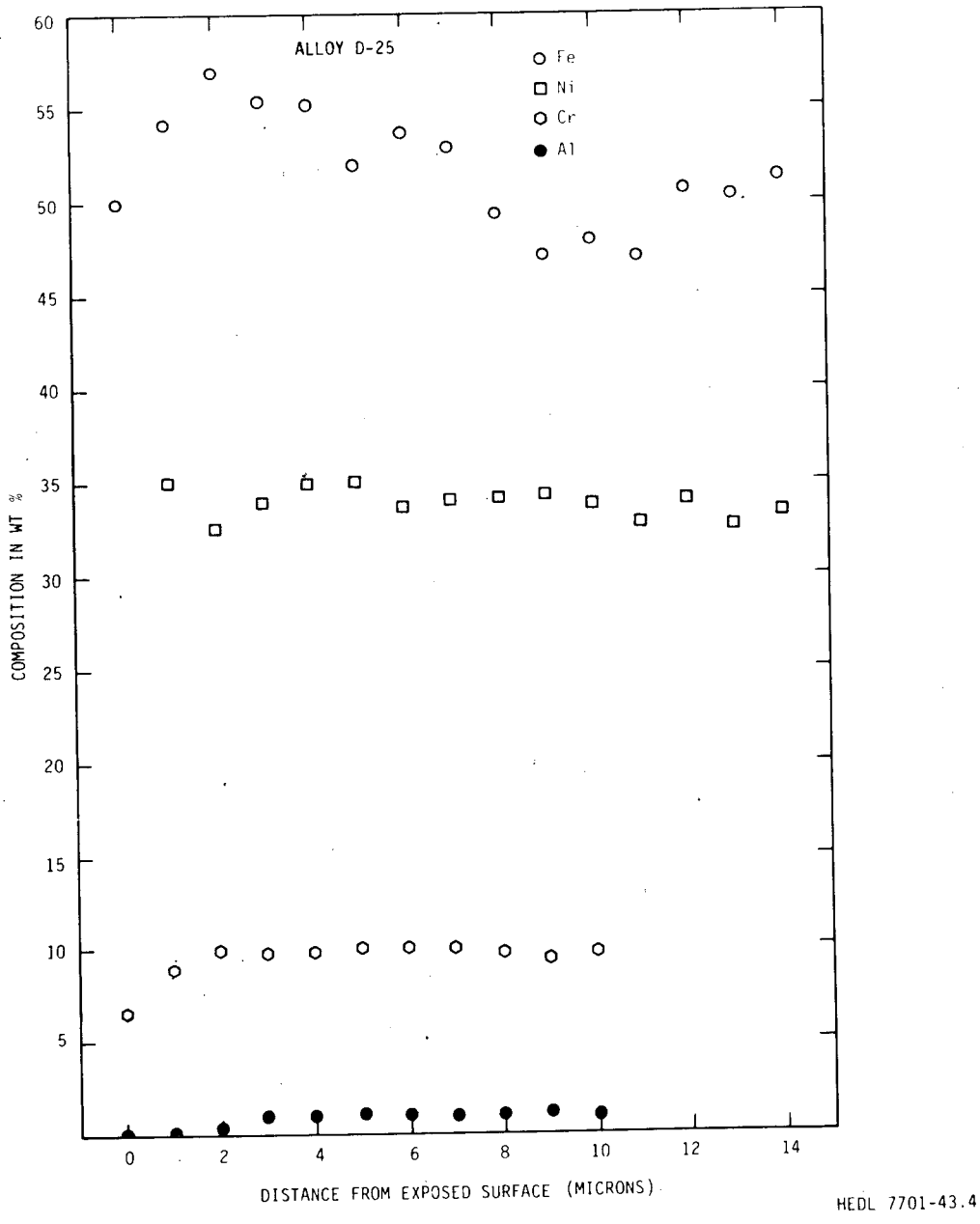

FIGURE 188. Concentration profile of alloy D25.

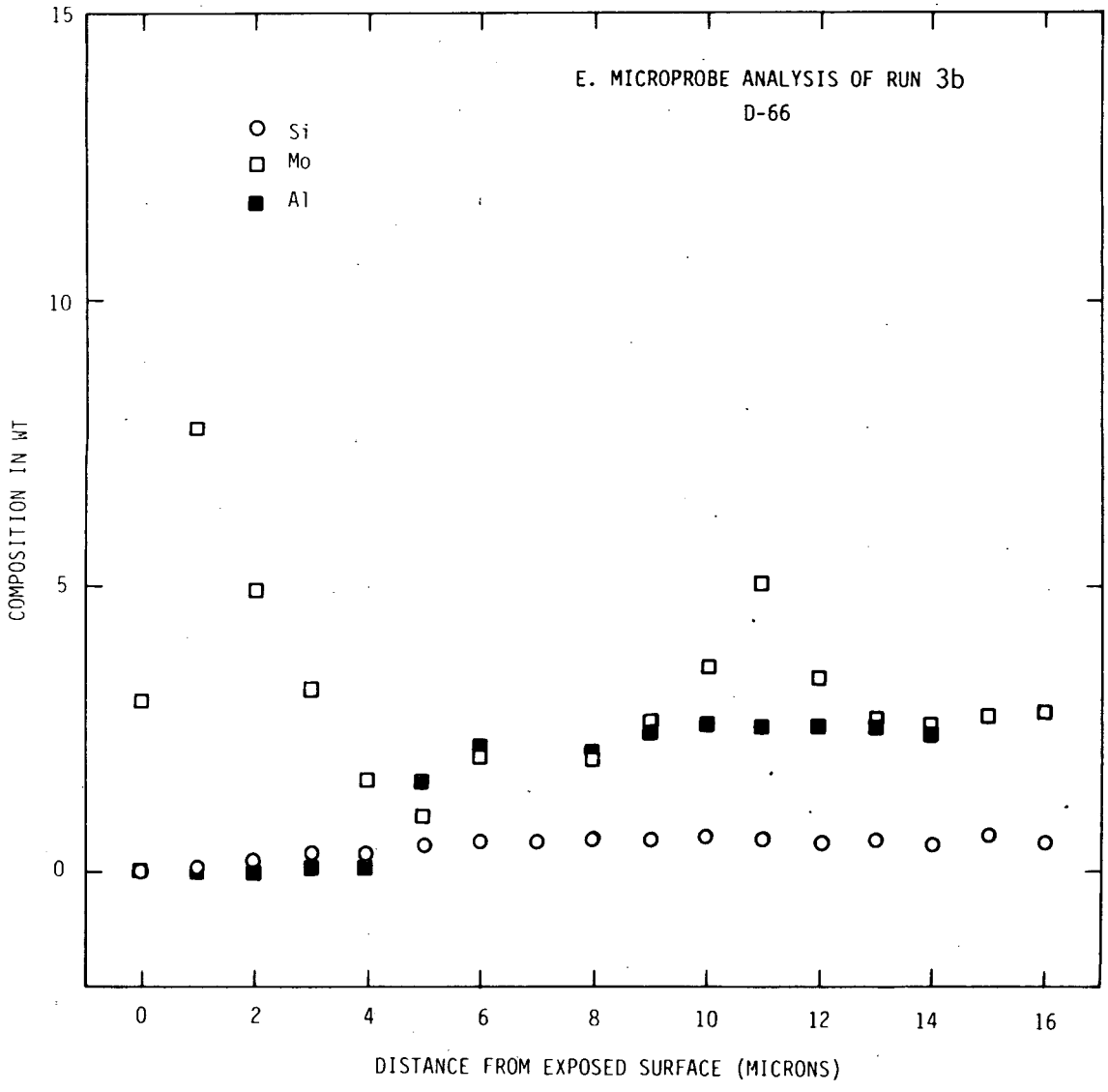

FIGURE 189. Concentration profile of alloy D66.

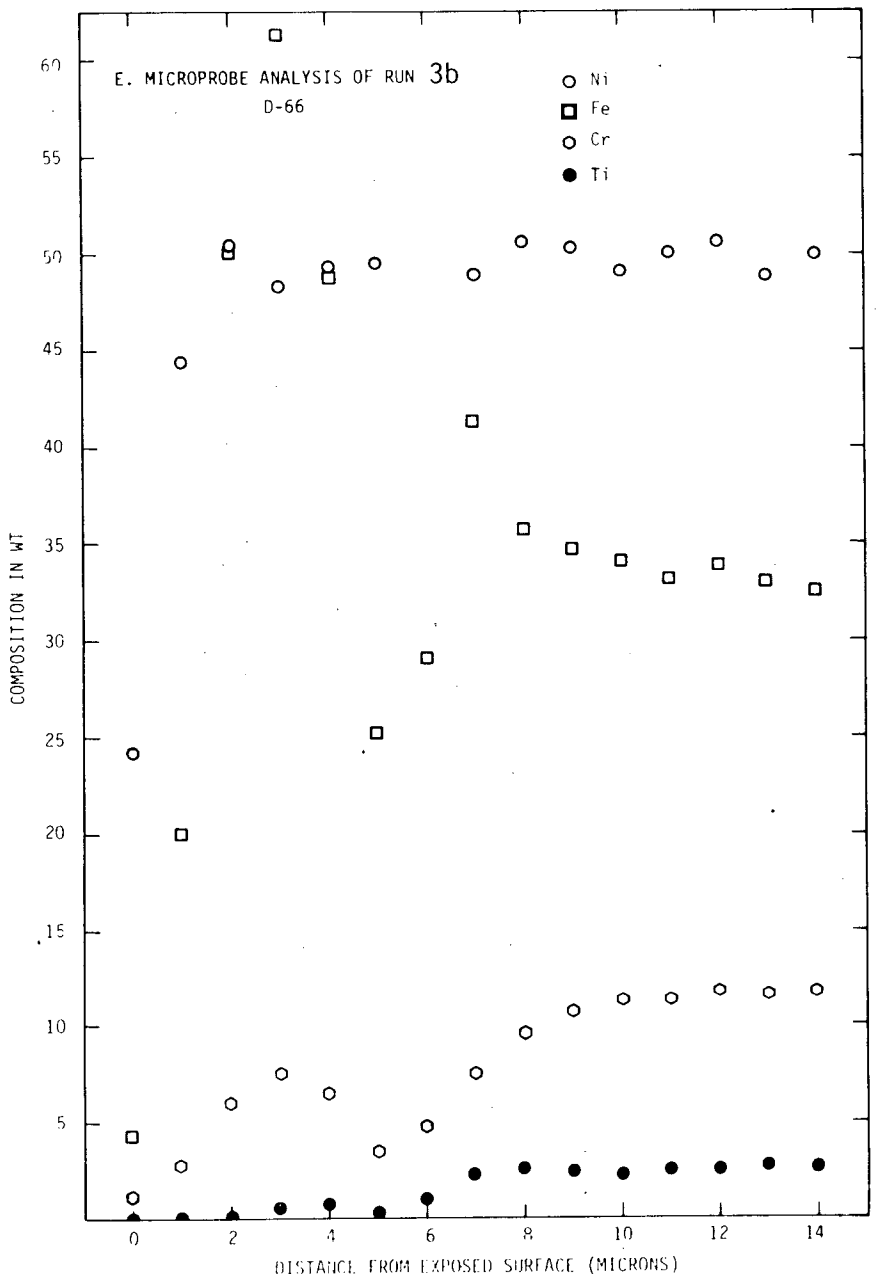

FIGURE 190. Concentration profile of alloy D66.

1.3.3.2 Corrosion Data of Run 4B, STCL-4. This was a 2,000-hour run which included samples of developmental alloys D9, D21 and D68 and the reference AISI 316. These samples have been reinserted in the loop from Run 4A, which concluded after 500 hours. The test conditions for Run 4B were identical to those for Run 4A, i.e., 700°C, 1 ppm oxygen and 6 m/s sodium velocity.

The cumulative 2,500-hour corrosion data are given in Table 44. Equivalent yearly corrosion rates have been computed and listed in the table along with the downstream position parameter for each sample. All the alloys tested display the downstream effect. The average corrosion rates computed from Table 44 are listed in Table 45 for each alloy. Once again, the data in Table 45 point out that the corrosion rate of an alloy exposed to liquid sodium does not depend on its nickel content.

TABLE 44

CUMULATIVE (2,500 HOURS) CORROSION DATA OF ADVANCED CLADDING ALLOYS OF RUN 4, STCL-4, 700°C, 1 ppm OXYGEN, 6 m/s SODIUM VELOCITY

			Equivalent Corrosion Rate		
	Specimen	Material	L/D	W(μg/mm²)	Microns/yr
	E61	AISI 316	25.00	35.30	15.5
	109	D9	30.67	40.60	17.8
	121	D21	36.30	18.00	7.9
	168	D68	41.95	29.29	12.8
	E69	AISI 316	53.24	31.28	13.7
	209	D9	58.96	38.12	16.7
	221	D21	64.58	15.07	6.6
	268	D68	70.27	28.34	12.4
	E71	AISI 316	81.51	30.34	13.3
	309	D9	87.26	34.05	14.9
	321	D21	92.90	12.80	5.6
	368	D68	98.53	25.09	11.0
Flow	E76	AISI 316	109.65	22.83	10.0

TABLE 45

AVERAGE VALUES OF CUMULATIVE CORROSION DATA SAMPLES OF RUN 4, STCL-4

Material	Wt% Ni	Equivalent Corrosion Rate Microns/yr
AISI 316	12	13.1
D9	14.5	16.5
D21	25	6.7
D68	45	12.1

As for Run 3 data, least squares analysis has been performed on the Run 4 data. The data were fitted to a linear equation, $R = a_1 t + b_1$, and a logarithmic equation, $\log R = a_2 \log t + b_2$, where R is the weight loss in μg/mm², t is the test time in 1,000-hour units, a_1(μg/mm² 10^3 hours), b_1(μg/mm²), a_2 and b_2 are constants. The values of the constants, a_1, b_1, a_2, and b_2 along with their standard error estimates are given in Table 46. Equivalent yearly corrosion rates have been computed from the equations and also listed in Table 46.

TABLE 46

LEAST-SQUARES ANALYSIS OF CORROSION DATA
OF CLADDING ALLOYS OF RUNS 4A AND 4B, STCL-4

Material	Equation $R = a_1 t + b_1$			Equation $\log R = a_2 \log t + b_2$		
	a_1 $\mu g/mm^2$ $10^3 hr$	b_2 $\mu g/mm^2$	Equivalent Corrosion in One Year, μm	a_2	b_2	Equivalent Corrosion in One Year, μm
AISI 316	10.49 ±1.33	3.12 ±2.40	12.0	0.75 ±0.07	1.17 ±0.02	9.4
D9	16.70 ±1.03	-4.35 ±4.32	17.7	0.62 ±0.04	1.33 ±0.01	10.3
D21	5.84 ±0.77	0.69 ±1.39	6.5	0.90 ±0.09	0.82 ±0.03	5.8
D68	9.48 ±0.63	3.84 ±1.13	10.8	0.72 ±0.03	1.15 ±0.01	8.4

Although the linear rate of AISI 316 (12 μm/yr) is less than that predicted by the Bagnall-Jacobs correlation[3], it is higher than the value obtained for Run 3, STCL-4[2]. As mentioned earlier, the corrosion rate of AISI 316 is steadily increasing with increasing service life of the loop. The corrosion rate of alloy D21 is the lowest and is approximately the same as that reported for alloy D25 of Run 3, STCL-4. This is perhaps not surprising since both the alloys have similar compositions and heat treatments. The linear rate of D9 is the highest of all the alloys studied in Run 4. However, the logarithmic rate is about the same as for alloy D11 of Run 3, STCL-4, which also has undergone the same heat treatment as D9. The decrease in logarithmic rate is due to a fairly large reduction in corrosion rate after the first 500 hours of exposure. The linear as well as the logarithmic corrosion rate of alloy D68 are both less than that for reference AISI 316.

1.3.3.3 Metallography of As-received Alloys D9, D21 and D68. Optical metallography was performed on longitudinal sections of as-received developmental alloys D9, D21 and D68. The alloys have been heat treated according to the heat treatments listed in Table 47. The observed microstructures have been illustrated in Figures 191, 192 and 193. The microstructure of alloy D9 (Figure 191) consists of a few carbide (MC) precipitates with deformation bands running across the grains. This structure is essentially similar to that of D11 reported earlier[2], which had received the same heat treatment. The carbides can be seen in the form of short stringers. As seen in Figure 192, the structure of D25 shows more extensive carbide precipitation (in the form of stringers of globules) than in D9 and the grain structure resembles that of a solution annealed and aged material. A few annealing twins can also be noted in the structure. The increase in carbide precipitation can perhaps be attributed to the much higher titanium content of alloy D21. The microstructure of D21 is quite similar to that of D25 which has similar composition and had received the same heat treatment[2]. Optical micrographs of as-received D68 are given in Figure 193. Here again we see globular or blocky precipitates of carbides that are intermediate in number between that of D9 and D21. Similar to D21, the grain structure is typical of a solution annealed and aged material, with a few annealing twins.

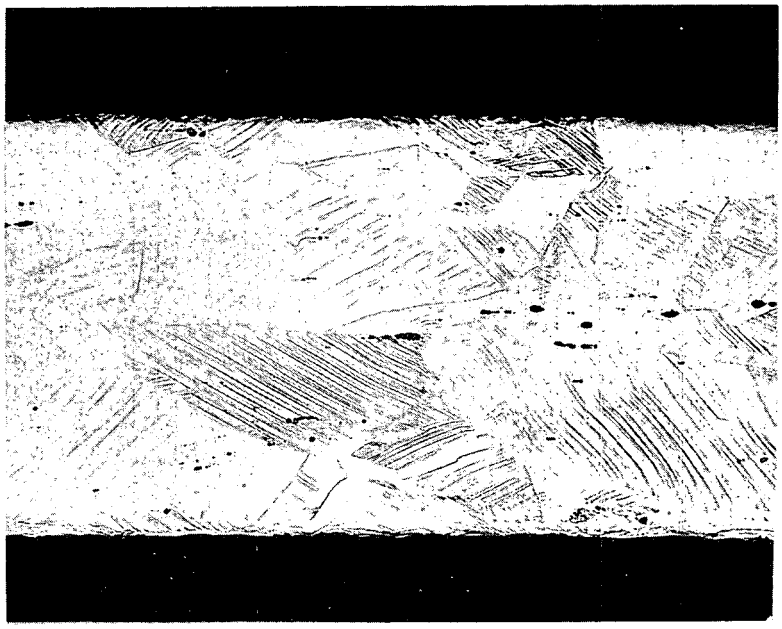

(a) 120 μm

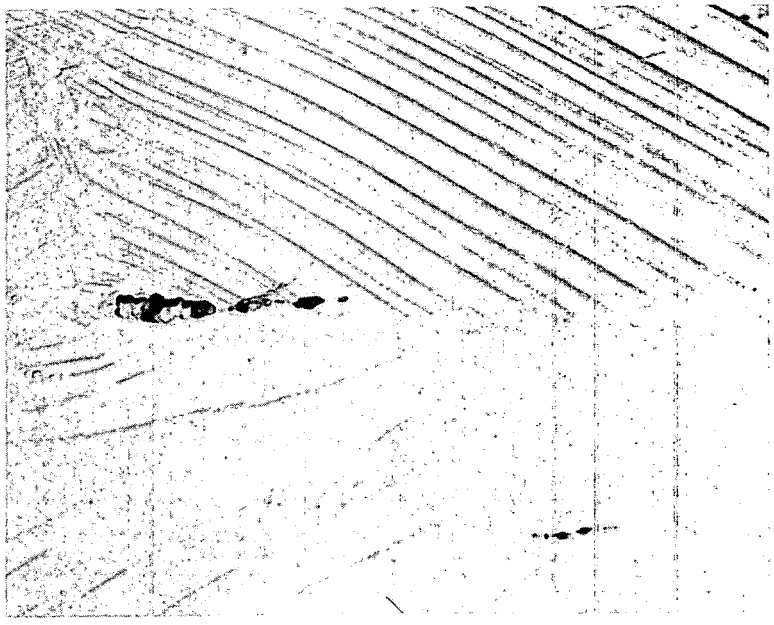

(b) 30 μm

FIGURE 191. Optical micrographs of as-received D9.

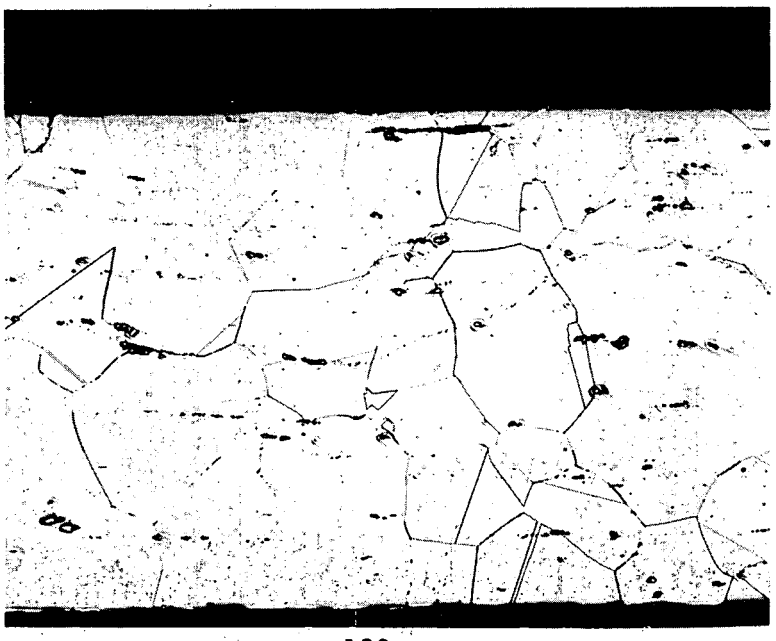

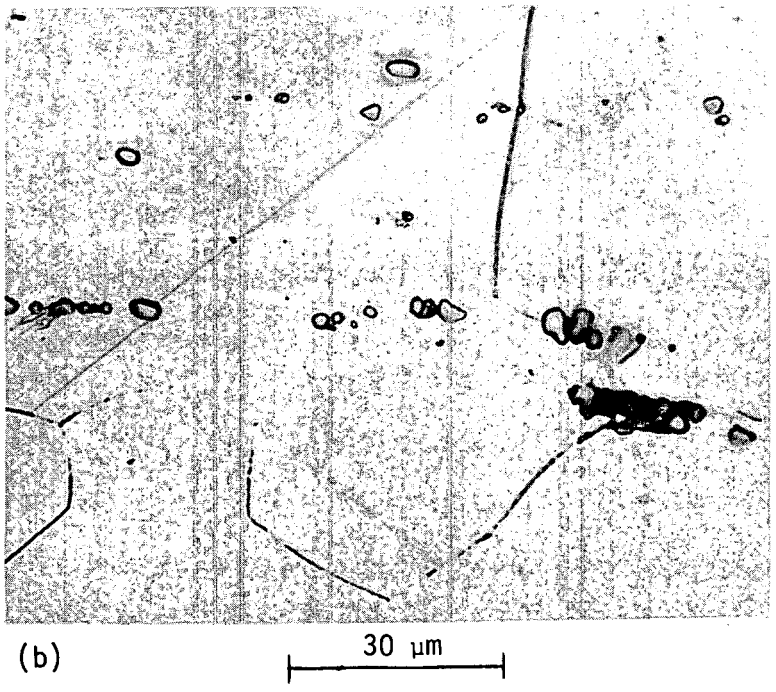

FIGURE 192. Optical micrographs of as-received D21.

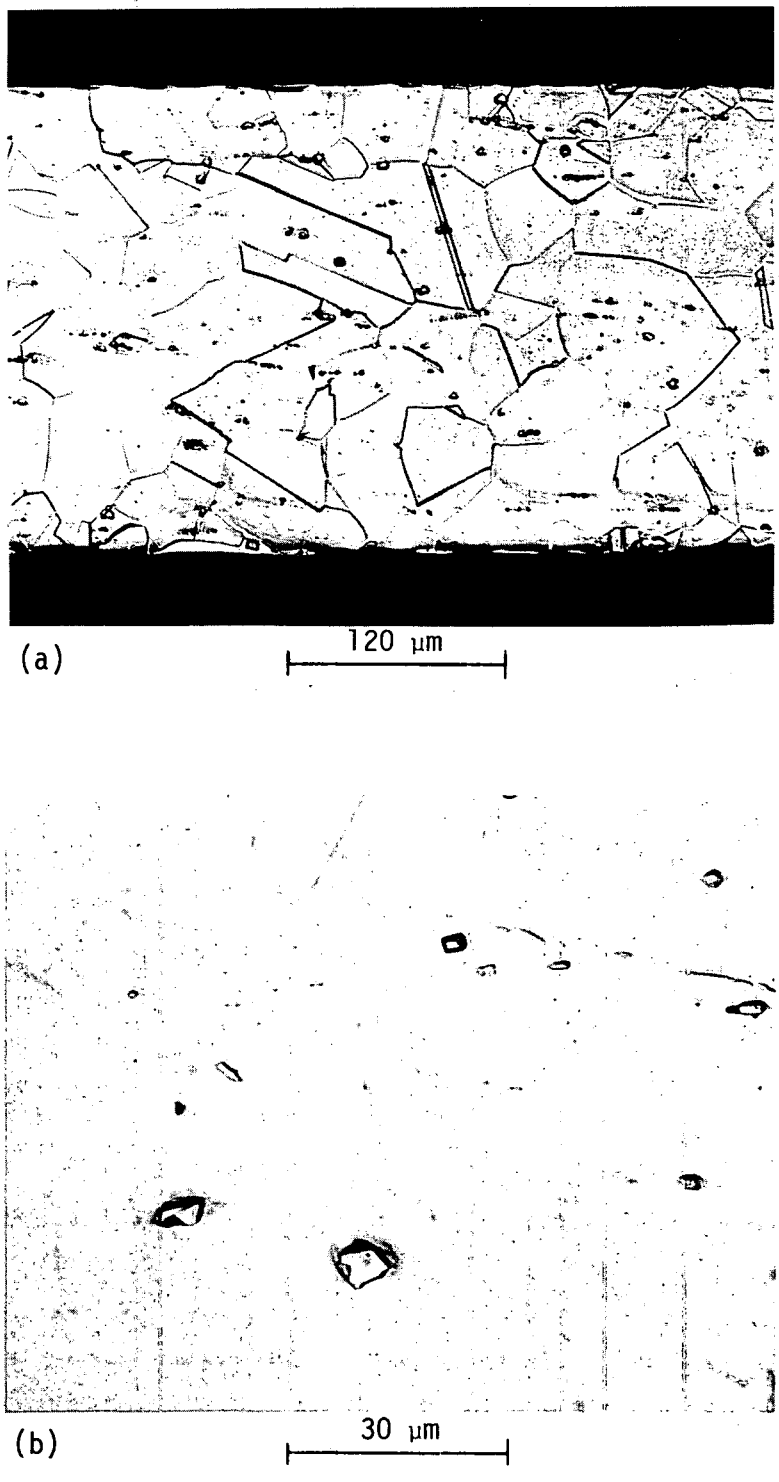

FIGURE 193. Optical micrographs of as-received D68.

TABLE 47

THERMOMECHANICAL TREATMENTS FOR ALLOYS D9, D21 AND D68

Alloy	Thermomechanical Treatment
D9	1100°C/.25 hr/air cooled and 25% cold work
D21	1050°C/.5 hr/air cooled and 700°C/24 hr/air cooled
D68	1050°C/.5 hr/air cooled and 800°C/2 hr/ furnace cooled to 625°C/12 hr/air cooled

1.3.4 Conclusions

The corroded surfaces of alloys D11, D25 and D66 are generally depleted of Ni, Cr, Al, Ti, Si and Mn and enriched with Fe and Mo. The as-received alloys D9, D21 and D68 contained stringers of carbides, the amount dependent upon the amount of titanium in the alloy. The structures are similar to those observed for Run 3, STCL-4 alloys of the same heat treatments and similar compositions. Based on the existing 2,500-hour data, excellent swelling properties, and absence of sigma phase in long term thermal aging tests, alloys D21 and D25 seem to be strong candidates for cladding purposes. Although alloys D9 and D68 have good sodium corrosion characteristics, additional sodium testing and optical metallography of sodium exposed materials is needed to firmly establish the viability of these alloys for cladding applications.

1.4 EXPECTED ACHIEVEMENTS IN THE NEXT REPORTING PERIOD

1. Complete optical metallography, scanning electron microscopy and electron microprobe analysis of sodium-exposed alloys D9, D21 and D68.

2. Start Run 5, STCL-4 with new samples of D9, D66 and D68 on Stringer I, and developmental alloy sheet samples on Stringer II, and continue testing.

3. Complete a detailed report on the sodium compatibility of developmental alloys studied so far.

1.5 REFERENCES

1. Brehm, W. F., Chulos, L. E., McGuire, J. C., Leaf, A. C., and Colburn, R. P., "Techniques for Studying Corrosion and Deposition of Radioactive Materials in Sodium Loops," IAEA Specialists' Meeting, Dimitrovgrad, USSR, IWGFR-7 (1976).

2. Alloy Development Program Quarterly Technical Progress Letter, TC-160-10 (7-9/1976), p. 167.

3. Bagnall, C., and Jacobs, D. C., W-ARD-NA-3045-23, May 1975.

4. Alloy Development Program Quarterly Technical Progress Letter, TC-160-10 (7-9/1976), p. 64.

2. CORROSION OF CANDIDATE ALLOYS UNDER HIGH HEAT INPUT CONDITIONS

S. A. Shiels, C. Bagnall and R. E. Witkowski*
Westinghouse Advanced Reactors Division

2.1 OBJECTIVE

The objectives of this work are: (a) to measure the corrosion rates of candidate alloys under high heat input conditions utilizing the ITF; (b) to determine the effect of system structural materials on the measured corrosion rates; and (c) to characterize sodium exposure-induced chemical and structural changes within the test alloys.

2.2 SUMMARY

The corrosion rates of Nimonic PE16, Inconel 706 and alloy A-286 did not change significantly over a period of 6,000 hours, suggesting that the equilibrium corrosion rate had been reached early in the cumulative exposure period. The corrosion rate of Type 316 SS dropped slightly between four and six thousand hours. Molybdenum-coated Nimonic PE16, which was expected to show negligible corrosion, corroded at a rate equivalent to 6 μm/yr (0.24 mpy) at an L/D position of 100.

Studies of the corroded surfaces of Type 316 SS and Nimonic PE16 were performed. The PE16 surface, while still covered with molybdenum-rich modules, was almost totally depleted of nickel and chromium after 6,000 hours, suggesting that the surface is ferritic.

2.3 ACCOMPLISHMENTS AND STATUS

2.3.1 Corrosion Measurements: Run #ITF-11

Run #ITF-11, a 2,000 hour run at 700°C, was completed at the end of October. Certain specimens accumulated up to 6,000 hours exposure at the end of this run while others reached 2,000 and 4,000 hours total exposure time. The specimen loading sequence is given in Table 48, loop operating conditions in Table 49, and corrosion data in Table 50.

Data from the 6,000 hour exposure specimens are compared with earlier 2,000 and 4,000 hour data from the same specimens in Table 51. Note that a third mandrel was inserted immediately downstream of mandrel No. 1. This has resulted in an overall increase in L/D for the specimen assembly which has moved the downstream samples even further downstream. This gives rise to a slightly smaller value for the slope of the line, however the effect on the zero L/D extrapolation is minimal.

The Nimonic PE16, A-286 and Inconel 706 alloys do not show any significant change in corrosion behavior with time as shown in Table 51 and graphically in Figure 194. The corrosion rate of the Type 316 SS continues to fall. How much of the decrease is due to

* Westinghouse Research Laboratories

TABLE 48

SPECIMEN LOADING SEQUENCE

Mandrel #1[1]		Mandrel #2[3]		Mandrel #3[1]	
E-26	T316SS	X-14	M-813	E-62	T316SS
E-43	T316SS	X-27	M-813	E-103	T316SS
57-1	A-286	75-M1	Mo-coated PE16	57-4	A-286
57-2	A-286	75-M2	Mo-coated PE16	57-5	A-286
80-1	Inconel 706	E-87	T316SS	80-4	Inconel 706
80-2	Inconel 706	E-100	T316SS	80-5	Inconel 706
75-1	PE16	57-7	A-286	75-4	PE16
75-2	PE16	57-8	A-286	75-5	PE16
57-3	A-286	80-7	Inconel 706	E-105	T316SS
80-3	Inconel 706	80-8	Inconel 706	57-6	A-286
75-3	PE16	75-7	PE16	80-6	Inconel 706
89-22[2]	330SS	75-8	PE16	75-6	PE16
		89-16	330SS	89-27[2]	330SS
		89-35	330SS		

Flow

(1) Previously exposed in ITF Run #9 and ITF Run #10
(2) Previously exposed in ITF Run #10
(3) New Specimens

TABLE 49

LOOP OPERATING CONDITIONS
(RUN #ITF-11)

T. max	700°C
Flow Velocity	4.76 m/s
Oxygen	0.95 ppm av.
Duration	2,008.9 hr

TABLE 50

RUN #ITF-11 CORROSION DATA

Specimen Number	Location (cm)	L/D	Area (cm^2)	ΔW (mg)	Corrosion Rate/Year (mg/dm^2)	(μm)	(mils)
A. Cumulative Exposure Time 6,077.9 hours							
T316SS							
E-26	5.6	20.4	1.90	20.73	1573	19.7	0.77
E-43	6.6	25.4	1.90	18.63	1414	17.7	0.70
E-62	106.2	357.7	1.92	14.64	1099	13.7	0.54
E-103	107.4	364.0	2.32	15.69	975	12.2	0.48
E-105	114.8	400.5	2.32	12.49	777	9.7	0.38
A-286							
57-1	7.6	30.4	1.94	24.32	1808	22.8	0.90
57-2	8.6	35.4	1.97	23.40	1721	21.7	0.86
57-3	14.0	60.7	1.94	20.01	1487	18.8	0.74
57-4	108.5	369.0	1.94	9.53	708	8.9	0.35
57-5	109.5	374.0	1.95	9.58	709	9.0	0.35
57-6	115.8	405.5	1.94	6.77	503	6.4	0.25

TABLE 50. RUN #ITF-11 CORROSION DATA (continued)

Specimen Number	Location (cm)	L/D	Area (cm^2)	ΔW (mg)	Corrosion Rate/Year (mg/dm^2)	(μm)	(mils)
Inconel 706							
80-1	9.7	40.4	1.92	31.30	2353	29.2	1.15
80-2	10.9	47.6	1.92	31.50	2365	29.4	1.16
80-3	15.0	65.7	1.98	28.40	2068	25.6	1.01
80.4	110.5	379.0	1.92	11.76	884	11.0	0.43
80-5	111.5	384.0	1.92	10.55	792	9.8	0.39
80-6	116.8	410.5	1.91	8.18	618	7.7	0.30
Nimonic PE16							
75-1	119.0	50.7	1.85	23.79	1854	22.6	0.89
75-2	191.0	54.4	1.84	22.85	1791	21.8	0.86
75-3	14.0	70.7	1.85	22.53	1756	21.4	0.84
75-4	112.5	389.0	1.85	10.39	810	9.9	0.39
75-5	113.5	394.9	1.85	9.10	709	8.7	0.34
75-6	118.1	416.7	1.85	8.59	670	8.2	0.32
B. Cumulative Exposure Time 4,069.4 hours							
Alloy 330SS							
89-22	17.0	75.7	1.92	39.71	4455	55.7	2.20
89-27	118.9	420.5	1.89	25.74	2934	36.7	1.44
M-813							
X-14	21.8	86.9	1.87	17.03	3870	48.4	1.90
X-27	22.9	91.9	1.88	15.30	3462	43.3	1.70
Mo-Coated PE16							
75-M1	23.9	96.9	1.86	2.89	661	6.3*	0.25*
75-M2	24.9	101.9	1.86	2.64	604	5.7*	0.23*
T316SS							
E-87	25.9	106.9	1.92	7.17	1588	19.3	0.70
E-100	26.9	111.9	1.90	7.04	1576	19.7	0.78
A-286							
57-7	27.9	116.9	1.95	7.22	1575	19.9	0.78
57-8	29.0	121.9	1.95	6.92	1510	19.1	0.75
Inconel 706							
80-7	30.0	126.9	1.95	8.31	1813	22.5	0.89
80-8	31.0	131.9	1.93	8.52	1878	23.3	0.92
Nimonic PE16							
75-7	32.0	136.9	1.86	7.02	1605	19.6	0.77
75-8	33.0	141.9	1.85	6.98	1605	19.6	0.77
Alloy 330SS							
89-16	34.0	146.9	1.89	22.68	5105	63.8	2.50
89-35	35.0	151.9	1.88	22.18	5019	62.7	2.50

* Density of molybdenum taken as 1030 kg/m^3.

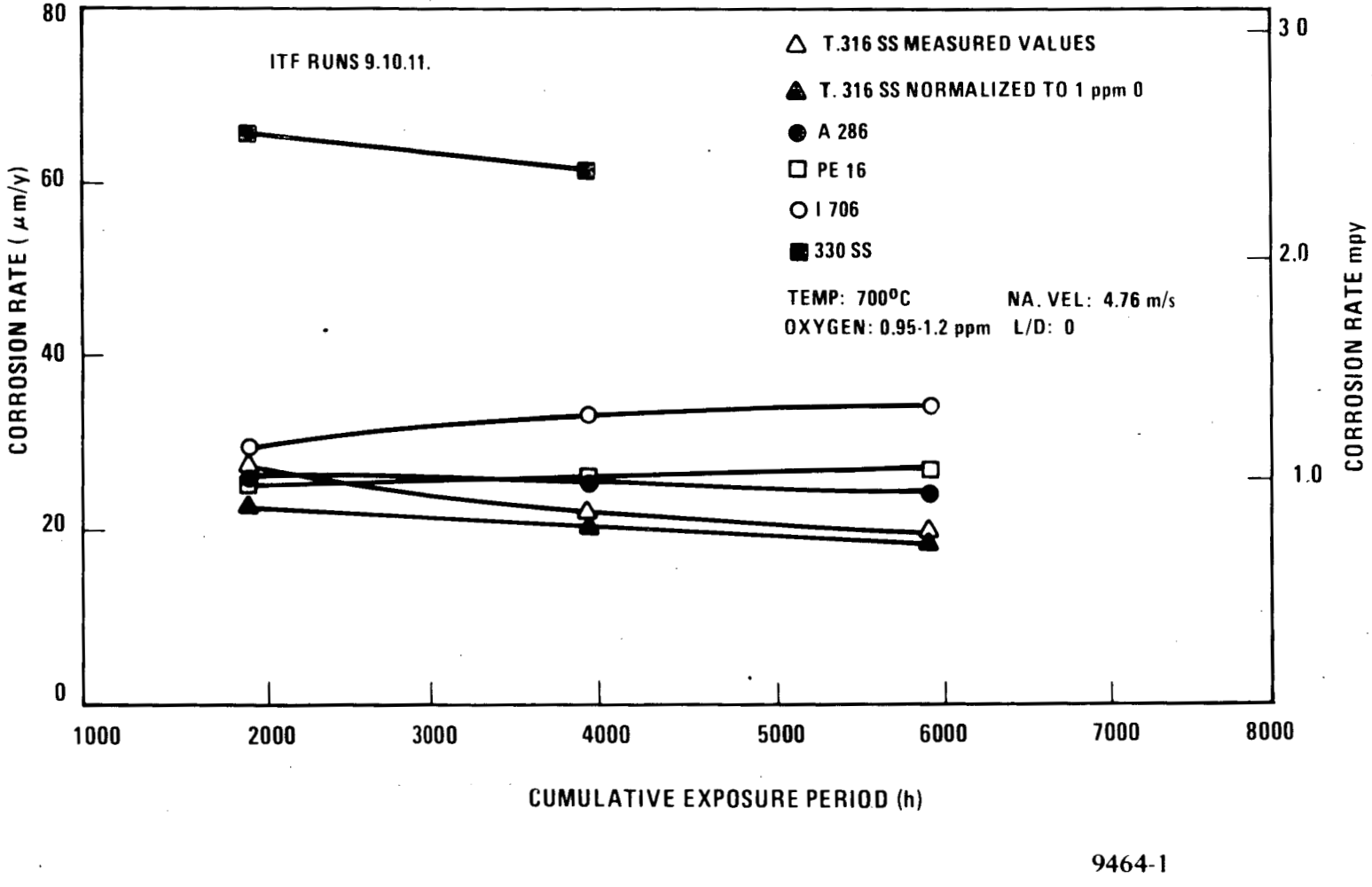

FIGURE 194. Corrosion rates of advanced alloys vs. exposure time at 700°C (ITF Runs 9, 10, 11).

TABLE 51

CORROSION RATES AS A FUNCTION OF EXPOSURE TIME

Run No.	Cumulative Time (Hours)	Corrosion Rate at 0 L/D μm/y	Corrosion Rate at 75 L/D μm/y	Downstream Slope
T316SS				
ITF-9	2009	27.2 (22.6)*	24.1 (20.1)*	-7.2×10^{-4}
ITF-10	4017	22.1 (20)*	19.8 (19.4)*	-6.5×10^{-4}
ITF-11	6078	19.4 (18.4)*	17.5 (16.7)*	-5.9×10^{-4}
Inconel 706				
ITF-9	2009	29.7	23.6	-1.3×10^{-3}
ITF-10	4017	33.0	25.7	-1.5×10^{-3}
ITF-11	6078	33.5	25.4	-1.4×10^{-3}
A-286				
ITF-9	2009	25.4	19.4	-1.5×10^{-3}
ITF-10	4017	24.9	19.6	-1.4×10^{-3}
ITF-11	6078	23.6	19.1	-1.3×10^{-3}
Nimonic PE16				
ITF-9	2009	24.9	20.3	-1.2×10^{-3}
ITF-10	4017	25.7	20.8	-1.2×10^{-3}
ITF-11	6078	26.2	21.6	-1.2×10^{-3}
Alloy 330				
ITF-10	2009	65.8	60.7	-4.5×10^{-4}
ITF-11	4069	61.0	55.9	-5.3×10^{-4}

* Bracketed value normalized to 1 ppm O_2.

uncertainties in oxygen level measurements cannot be resolved. The values for Type 316 SS are also shown normalized to 1 ppm oxygen using the average oxygen levels reported for each run.

The corrosion rate of alloy 330 has decreased only slightly between 2,000 hours and 4,000 hours from an extrapolated zero L/D value of 66 to 61 μm/y. No further 700°C tests will be performed on this alloy.

The middle mandrel held a selection of alloys all of which were previously unexposed. Two new materials were included, M-813 and molybdenum-coated PE16. Alloy M-813, located at about 90 L/Ds corrodes at a rate of ~46 μm/y. Insufficient data were available to allow extrapolation to zero L/D. Assuming that the downstream slope is similar to that for alloy 330, the zero L/D value might be expected to be about 50-55 μm/y.

The molybdenum-coated PE16 corroded at a rate of about 6 μm/y at L/D = 100 which was higher than anticipated. Preliminary tests in WHIRL-1 had shown virtually no weight change after 500 hours. If the relationship between enhancement factor and downstream position discussed in the previous quarterly is valid[1], then the molybdenum-coated material will show a steep downstream slope which could put the zero L/D value anywhere between 12 and 25 μm/y.

The other samples from this mandrel were Type 316 SS, A-286, Inconel 706 and Nimonic PE16. When the values given in Table 50 were compared with the interpolated values from Run #ITF-9, they were found to be marginally higher. This may simply be a result of run-to-run scatter, or due to the fact that the new specimens are located downstream of previously exposed material. Conceivably the sodium reaching the new specimens is less saturated than it would be had all of the upstream specimens been new.

2.3.2 Corrosion Measurements: Run #ITF-12

The start up of Run #ITF-12 has been delayed until the beginning of January because of the unavailability of new specimens. Specimens were not received until mid-December. Advantage was taken of the unscheduled downtime to make some minor modifications to the facility. These modifications included the design and fabrication of a high velocity (~5 m/s) insert for the ITF secondary heater. This will allow about four specimens to be exposed at 550°C.

Several changes in specimen inventory will be made for this run. Alloys A-286 and 330 will be dropped from the 700°C exposure program. The Nimonic PE16 and the Inconel 706 will be exposed for an additional 2,000 hours. New material will include double aged Inconel 706 (as opposed to the solution annealed material currently under test), cast M-813 (the current material is a powder product) and a selection of similar metal electron beam weldments.

2.3.3 Scanning Electron Microscopy (SEM) of Specimens from ITF Runs 9, 10 and 11

SEM characterization of Type 316 SS and Nimonic PE16 exposed to flowing sodium in runs 9, 10 and 11 has been completed. A total sodium exposure time of 6,000 hours at a temperature of 700°C was realized. SEM instrument operation parameters and specimen handling techniques, as previously detailed, were used throughout this study[2].

2.3.3.1 Type 316 SS. The sodium corroded surface features of this alloy revealed two distinct differences from the structures observed on specimens exposed in WHIRL-1 for 6,000 hours[3]. First, as shown in Figure 195, there was no evidence of the characteristic Mo-rich nodules. A comparison of the two 6,000 hour x-ray spectra indicated that the surface of the ITF specimen contained about 55% less chromium, while nickel in both cases was at background level (≤1%). The approximate surface compositions for the ITF and WHIRL-1 specimens may therefore be estimated as 96Fe-3Cr-1Ni and 93Fe-5.5Cr-1(+)Ni respectively.

The corroded surface was not, however, featureless. Isolated areas covered with steps or swirls, resembling in many cases contoured terracing, were observed scattered across the surface of the columnar, ferrite grains. These structures were noted previously by Berkey and Whitlow[3], who suggested that they were formed by an atomic dissolution sodium corrosion process which was dependent on the crystallographic orientation of the grains. In the present case, the "steps" appeared to be 100-200 nm high; that is, a block of b.c.c. structure many atomic planes thick.

2.3.3.2 Nimonic PE16. The OD surface morphology and electron excited x-ray (EDAX) spectrum generated from a 100X rastered area is shown in Figure 196. The nodular, coral-like corrosion features and micron size holes previously noted for this alloy after a 2,000 hour run (#1b) in the W-RL WHIRL-1 sodium loop facility are clearly visible[4]. The

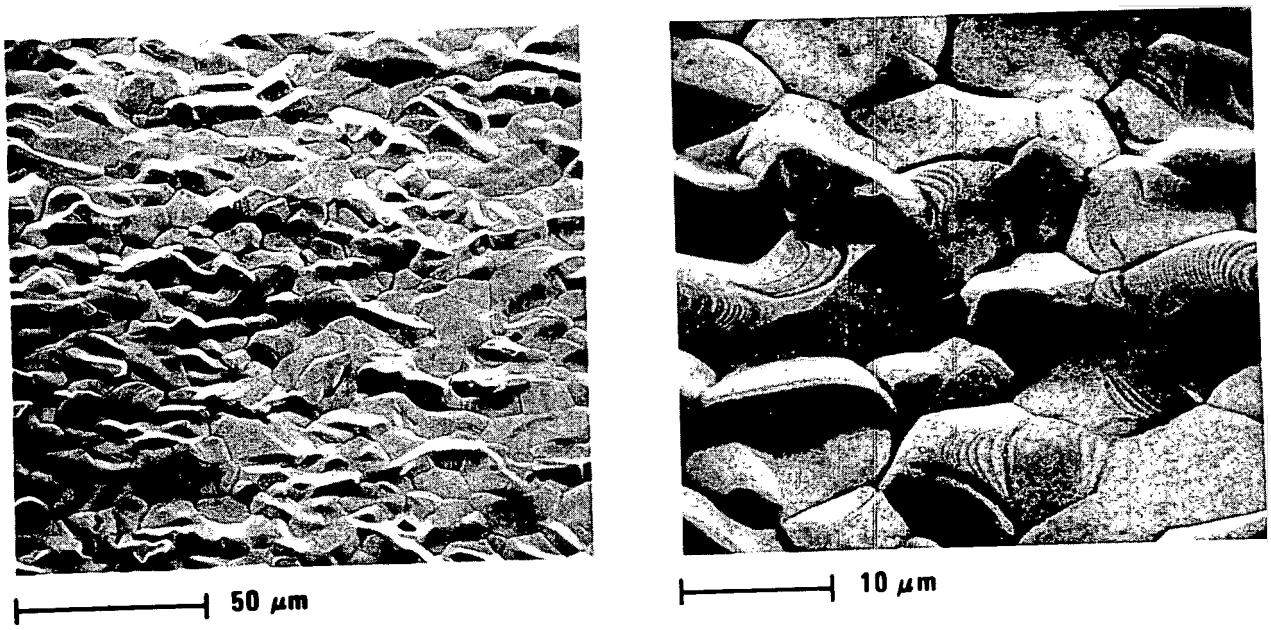

(A) Na EXPOSED, 6000 Hr., 700°C

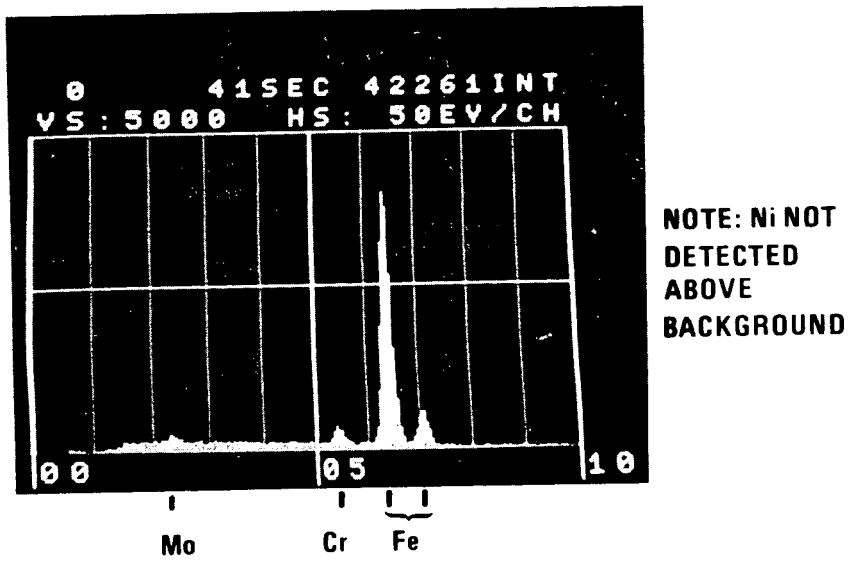

(B) ELECTRON EXCITED X-RAY SPECTRUM (100 X RASTERED AREA)

FIGURE 195. Surface morphology and chemistry of Type 316 SS exposed to sodium at 700°C (ITF Runs 9, 10, 11).

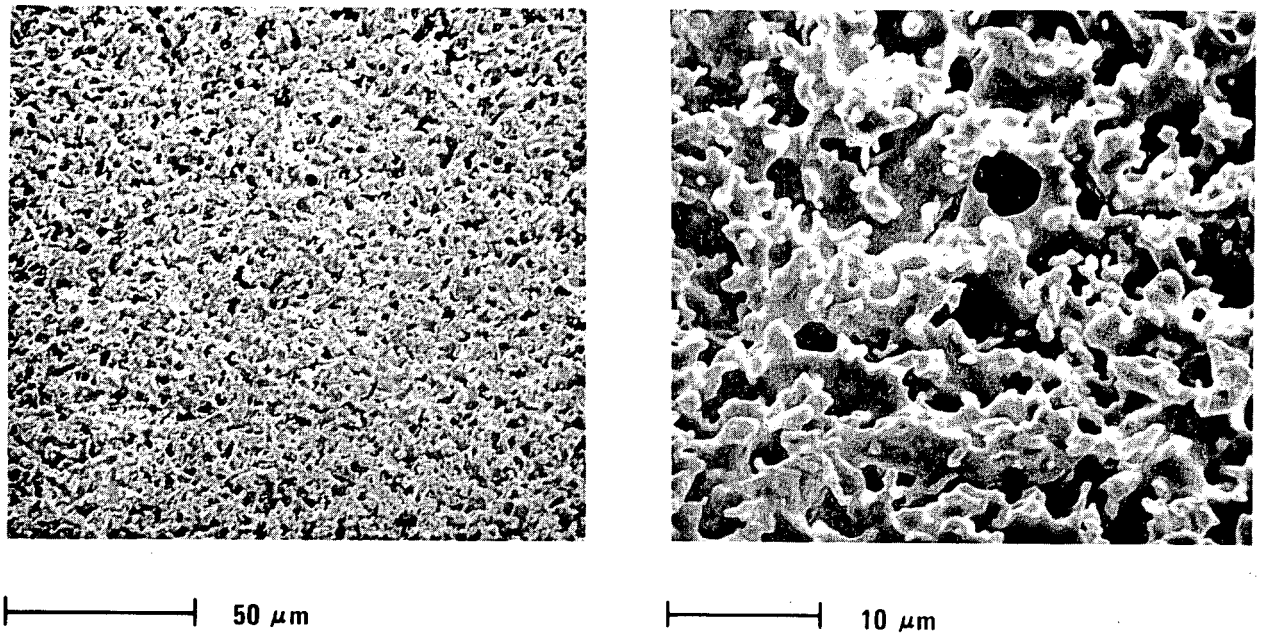

(A) Na EXPOSED 6000 Hr., 700°C

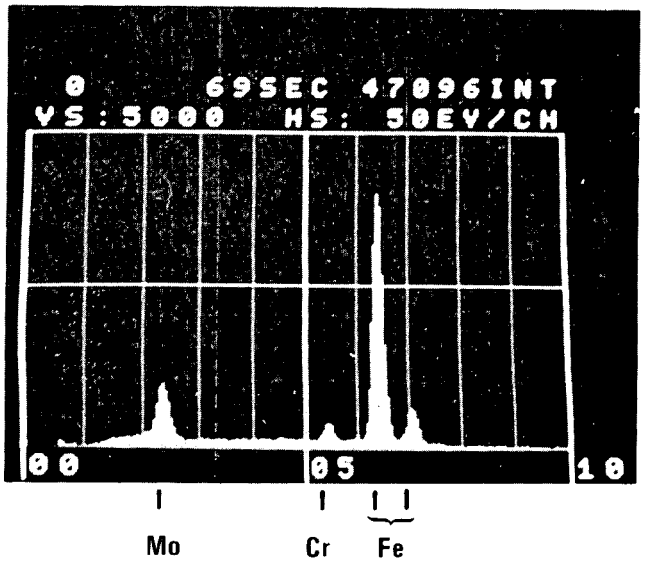

(B) ELECTRON EXCITED X-RAY SPECTRUM
(100 X RASTERED AREA)

FIGURE 196. Surface morphology and chemistry of Nimonic PE16 exposed to sodium at 700°C (ITF Runs 9, 10, 11).

EDAX spectrum clearly shows that, while an enhancement of the Mo is most evident when compared with a similar spectrum generated from the as-received material, the elements Ti, Cr and Ni are significantly depleted. In fact, the Ti and Ni peaks are no longer detectable above the background signal. While the spectrum generated from a 100X rastered area presents an average surface elemental composition, a more detailed "spot" analysis provides an indication of the composition of individual features.

Figure 197 presents a detailed analysis of the nodular, coral-like features and illustrates the marked difference in Mo composition when compared with the matrix material. Although the corrosion-resistant nodules were again found to be rich in Mo, unlike the specimen exposed in WHIRL-1 (Run #1b)[5] Ni concentration was below the detection limit (<1%).

2.3.4 Discussion

Exposures up to 6,000 hours show that the alloys tested must be close to their equilibrium corrosion conditions. Overall changes in corrosion rate over the 6,000 hour time period were small, varying between 1 and 4 μm/y. The order of corrosion resistance has changed slightly since the initiation of the tests and is now Type 316 SS, A-286, Nimonic PE16, Inconel 706, with alloys such as M-813, alloy 330 and Inconel 718 showing very high corrosion rates. The commercial alloys Inconel 706 and Nimonic PE16 will be exposed a further 2,000 hours before being phased out of this portion of the test program.

It has become evident during the course of the sodium compatibility task that microstructure appears to play an important role in deciding the manner in which a material corrodes. The importance of testing material with the correct microstructure is now well recognized. Accordingly new Inconel 706 and M-813 specimens, more typical of the materials proposed for use, will be exposed in the next series of runs.

It was pointed out in section 2.3.1 that specimens exposed for 2,000 hours in Run #ITF-11 corrode at rates slightly higher than the original 2,000 hours data from run #ITF-9 would predict. The possibility that these specimens were being influenced by the behavior of the pre-exposed upstream specimens was suggested. It should also be recognized, however, that this may simply represent specimen-to-specimen scatter and that the cumulative data to 6,000 hours are statistically rather limited having all been generated on the same specimens.

2.3.5 Work in Progress

Specimens for Run #ITF-12 have been prepared and loaded into ITF. Start up procedures have been initiated. The run will be a 2,000 hour run terminating in March-April 1977.

Detailed SEM and electron probe analysis is now being planned in order to study the possible effects of localized chemistry variation on corrosion behavior. Metallography on Run #ITF-11 samples has started.

2.4 EXPECTED ACHIEVEMENTS IN THE NEXT REPORTING PERIOD

Run #ITF-12 will be close to completion at the end of the reporting period.

Analytical work on selected samples will be completed. All metallography on Run #ITF-11 specimens will be completed.

FIGURE 197. Detailed SEM analysis of node formation present on sodium-exposed Nimonic PE16 (ITF Runs 9, 10, 11).

50 μm

(A) Na EXPOSED, 6000 Hr., 700°C

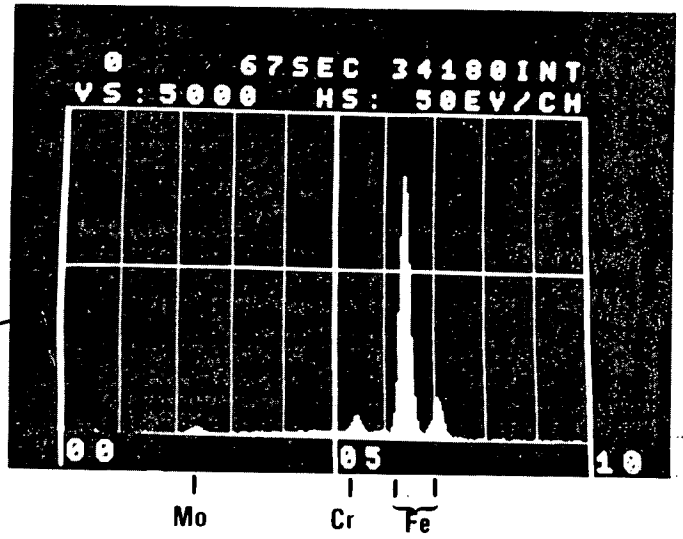

(B) SPOT ANALYSIS. MATRIX

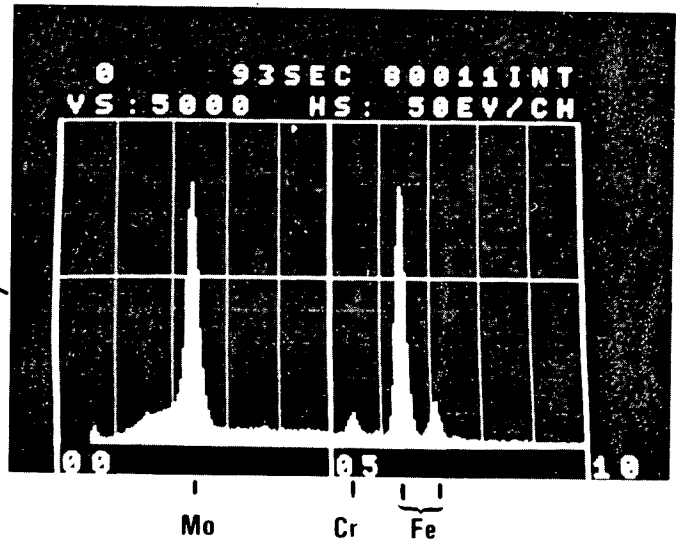

(C) SPOT ANALYSIS, NODE FORMATION

Contributions will be made to the first drafts of two papers; one covering the corrosion rate data and the other the structural information.

2.5 REFERENCES

1. Shiels, S. A., Bagnall, C., and Schrock, S. L., "Corrosion of Candidate Alloys under High Heat Input Conditions," Alloy Development Program Quarterly Technical Progress Letter, TC-160-10 (7-9/1976).

2. Keeton, A. R., Witkowski, R. E., and Berkey, E., "Corrosion Studies of Advanced Cladding Alloys," Ibid, TC-160-5 (4-6/1975).

3. Keeton, A. R., Witkowski, R. E., and Berkey, E., "Corrosion Studies of Advanced Cladding Alloys," Ibid, TC-160-10 (7-9/1976).

4. Berkey, E., and Whitlow, G. A., "Microstructural and Compositional Changes in Sodium Exposed Stainless Steel by Scanning Electron Microscopy," Chem. Aspects of Corrosion and Mass Transfer in Liquid Sodium: Proceedings of the Symposium, S. Jansson, Ed., Detroit, 1971.

5. Keeton, A. R., Witkowski, R. E., and Berkey, E., "Corrosion Studies of Advanced Cladding Alloys," Alloy Development Program Quarterly Technical Progress Letter, TC-160-6 (7-9/1975).

3. CORROSION STUDIES OF ADVANCED CLADDING ALLOYS

A. R. Keeton, R. E. Witkowski and Edgar Berkey
Westinghouse Research Laboratories

3.1 OBJECTIVE

The object of this work is to determine corrosion rates of candidate materials in sodium at specified conditions of time, temperature, sodium flow rate and oxygen level, and to characterize sodium exposure-induced chemical and structural changes within the test alloys.

3.2 SUMMARY

Modifications of WHIRL-1 were completed and a 90-hour check run was conducted to test effectiveness of modifications. These modifications included the addition of a new specimen holder between the main heater discharge and the original specimen holder and the isolation of the vanadium wire equilibration device (VWED) on a separate economizer.

The addition of a new specimen holder allows double the number of specimens to be tested at one time and provides a greater hydraulic L/D range for the specimens. The isolation of the VWED on a separate economizer allows operation of this unit without disturbing the oxygen and hydrogen meters and provides thermal protection for the VWED control valves. The check run verified that all test parameters, including sodium flow velocity, can be met for the next series of corrosion tests.

3.3 ACCOMPLISHMENTS AND STATUS

Operation of the vanadium wire equilibration device (VWED) previously required isolation of the oxygen and hydrogen meters in WHIRL-1 to prevent excessive temperatures at these meters. This was undesirable because oxygen and hydrogen monitoring is useful while operating the VWED. In addition, valving these meters in and out of the system provided greater opportunity for damaging a meter. Also, because of the location of the VWED control valves and the high operating temperature of the VWED (750°C), a malfunction occurred twice during the past 10,000 hours of loop operation in which a valve could not be opened because of self-welding.

For these reasons, WHIRL-1 was modified as shown in Figure 198 to isolate the VWED on a separate economizer. Control valves LMV-6 and 7 are located on the loop side of the economizer to prevent exposure to excessive temperatures.

Corrosion rate analysis of previous tests in WHIRL-1 indicated the desirability of having each test contain more test specimens over a wider hydraulic L/D range for more accurate evaluation. This was accomplished by the addition of a new specimen holder between the main heater discharge and the original specimen holder as shown in Figure 199. The two specimen holders are identical except for the mechanical end closure, thus doubling the number of specimens for each test. The hydraulic L/D range is also extended with L/D values of 32 to 105 for the first specimen holder and 168 to 241 for the second specimen holder.

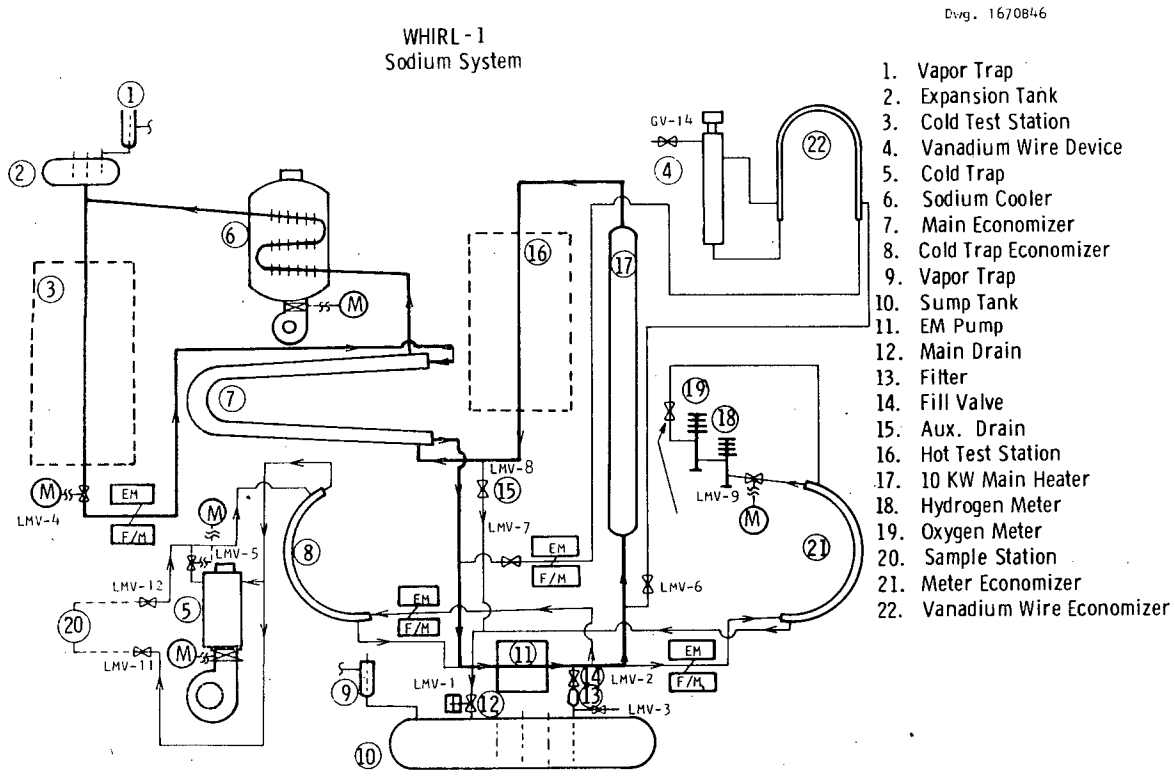

FIGURE 198. WHIRL-1 Sodium system as modified.

Dwg.6401A08

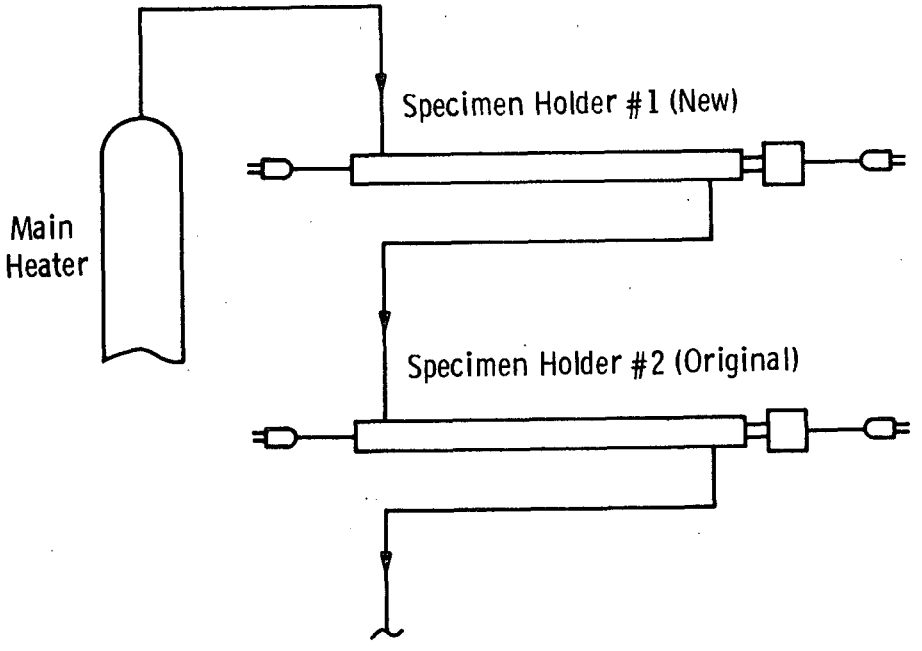

FIGURE 199. Schematic arrangement for specimen holders in WHIRL-1 hot test station.

A check-out test was conducted after the loop modifications to insure that WHIRL-1 could meet program requirements. Operating conditions were the same as required for the next series of tests scheduled for WHIRL-1:

Specimen temperature (both specimen holders) 600°C ± 5

Cold leg temperature 425°C ± 5

Sodium flow by test specimens 5-6 m/s

Sodium oxygen level 1 ppm ± .2

The test system was operated for 90 hours and met all of the test objectives.

3.4 EXPECTED ACHIEVEMENTS IN THE NEXT REPORTING PERIOD

Test Run #3, a 4,000 hour test of materials M-813, Nimonic PE16, Inconel 706, 330 SS and 316 SS, including weldments, will be initiated. An intermediate shutdown at 2,000 hours for weight change analysis will be accomplished.

SEM and electron probe measurements will be completed on Inconel 706 and 310 and 330 SS exposed to sodium for 6,000 hours at 700°C in ITF; SIMS and Auger spectroscopy studies will be initiated on selected materials.

4. THE INFLUENCE OF THERMAL AGING AND SODIUM CORROSION ON THE STABILITY OF AISI TYPE 310S AND ALLOY 330 AT 700°C

C. Bagnall,[1] and R. E. Witkowski[2]
[1]Westinghouse Advanced Reactors Division
[2]Westinghouse Research Laboratories

4.1 OBJECTIVE

(Not provided)

4.2 SUMMARY

(Not provided)

4.3 ACCOMPLISHMENTS AND STATUS

4.3.1 Introduction

Stainless steels AISI 310 and 330 were developed principally for operation in an air environment at temperatures up to 1150°C. In comparison to the composition of Type 304 SS (Table 52), the higher chromium level provides greater oxidation resistance, while the increase in nickel reduces the differential thermal expansion between alloy and oxide and so reduces spalling under cyclic conditions.

TABLE 52

COMPARISON BETWEEN TYPE 304 SS AND THE ADVANCED CLADDING CANDIDATE ALLOYS, TYPE 310 SS AND ALLOY 330

	w/o							wppm			
Alloy	Fe	Cr	Ni	Mo	Mn	Si	Cu	C	N	S	P
Type 304SS	71	18	8	-	2.0	1.0		800		30	45
Type 310SS	52.90	24.97	19.34	0.3	1.58	0.47	0.32	680*		200	280
Alloy 330	41.95	18.87	36.03	-	1.54	1.28	0.23	580		110	220

* Type 310 SS normally contains 2500 ppmC. The low carbon version, Type 310S, with 800 ppm max C is closer to the above composition.

The following discussion compares the behavior of these two candidate duct materials in and out of a sodium environment at 700°C.

4.3.2 Type 310S Stainless Steel

The composition of this 20% cold worked tubing led to an extremely unstable microstructure at 700°C. The transformations that took place in both sodium and vacuum environments after exposure periods up to 6,000 hours are described below.

The as-received microstructure of Type 310S is shown in Figure 200. With a light etch at low magnification, the abnormally high density of inclusions may be observed in the transverse and longitudinal sections. Further examination revealed that some of these apparent "inclusions" were in fact casting defects (shrinkage porosity) drawn out during

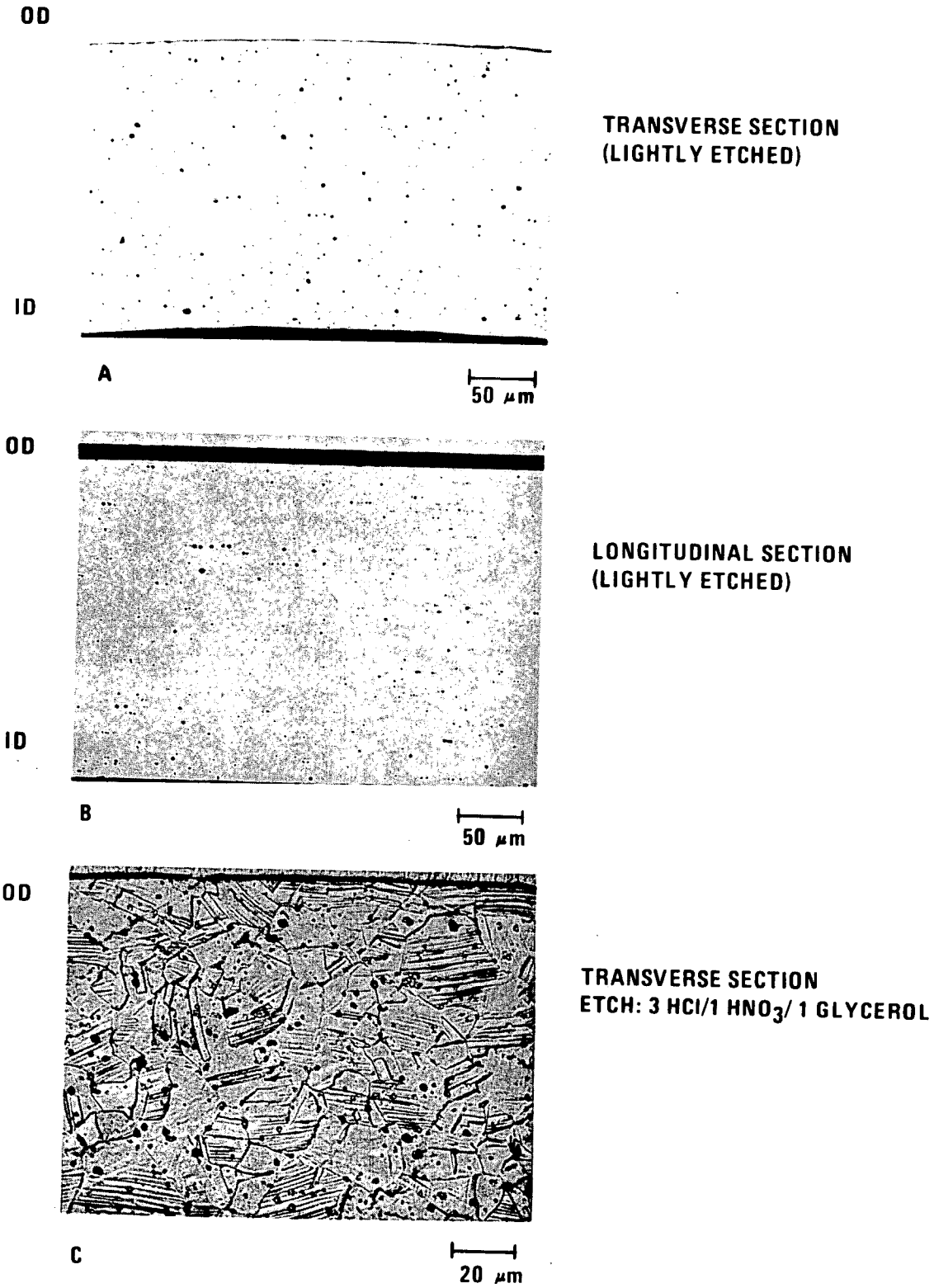

FIGURE 200. Twenty percent CW Type 310S stainless steel: as-received microstructure.

tube fabrication. At higher magnification, the fully etched microstructure revealed the effects of cold working. Prominent deformation bands and many examples of bent annealing twins were evident.

The effect of a 500-hour sodium exposure in WHIRL-1 is shown in Figure 201. With the matrix slightly defocused, the structural changes induced by sodium at the O.D. can be discerned. Selective removal of certain elements within the surface grain boundaries are measured to a depth of ∿10 μm. This corrosion behavior, also observed in Type 316 SS, should not be confused with the complete leaching out of grain boundaries noted in Inconel 718 and to a lesser extent in Nimonic PE16. Also visible in this micrograph are the many examples of casting defects.

At higher magnification [Figure 201(b)], the early effects of exposure at 700°C may be observed. The initial austenitic structure has begun an unusual transformation to sigma. The original grains, surrounded by broadening boundaries can be seen "dissolving" into large islands of sigma, leaving behind a new austenitic matrix.

After 2,000 hours exposure (Figure 202), the most striking feature is the extent and degree of sigma formation throughout the structure; between 25 and 28 volume percent is occupied by this phase.

The microstructures were double etched, first with Glycergia then with Murakami's solution*, used by many investigators attempting to distinguish carbide, ferrite and sigma by color (dark, yellow and blue respectively). However, phase identification by this technique is unreliable since the color of the (oxidized) particle is dependent on etch-application technique and the exact chemical composition of the phase. The latter fact was used to advantage in the present study since it permitted a clear picture of the depth to which composition was influenced by corrosion. In Figure 202(a), the various effects of sodium exposure may be distinguished; selective removal of certain alloy elements from grain boundaries at the surface, some redissolution of sigma in the matrix immediately below the surface, and the "coloring" of the zone in which alloy modification has occurred. This zone, about 40 μm wide was distinguished by a blue coloration of the sigma with Murakami's etch. In Figure 202(b), at higher magnification, the transition of "blue" to "yellow" sigma is not abrupt but takes place over a region in which particles clearly have a "cored" composition; that is, a chemical gradient from edge to center.

The width of this zone of depletion is of interest, since the diffusion rate of the corroding species (chiefly, Cr, Ni and Mn) may be calculated. The total depth of a diffusion profile, X, is given approximately by the expression:

$$X = 2\sqrt{Dt} \qquad [1]$$

where D is the diffusion coefficient of the diffusing species and t is the time. Hence, the diffusivity of the corroding element(s) is approximately 5.5×10^{-13} cm^2sec^{-1}. In comparison to Cr diffusion in Types 316 SS at 700°C ($\sim 10^{-14}$ cm^2sec^{-1}), and Ni ($\sim 10^{-15}$ cm^2sec^{-1}) this

* $10gK_2FeCN+10gKOH$ in 100 ml H_2O

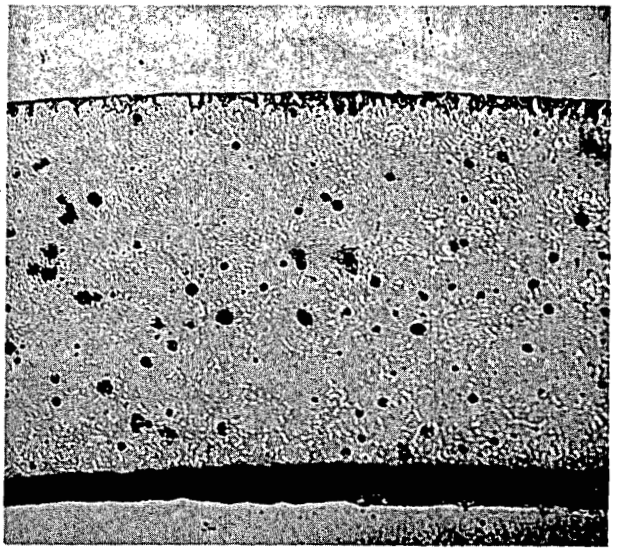

NOTE: SODIUM ATTACK AT OD, INCLUSIONS AND POROSITY IN MATRIX

A) TRANSVERSE SECTION

50 μm

ETCH: 3 HCl/ 1 HNO_3/ 20 H_2O

NOTE: AUSTENITE TRANSFORMATION TO PRODUCE SIGMA

B) TRANSVERSE SECTION

20 μm

FIGURE 201. Twenty percent CW Type 310S stainless steel: 700°C/500 hour sodium exposure (WHIRL-1).

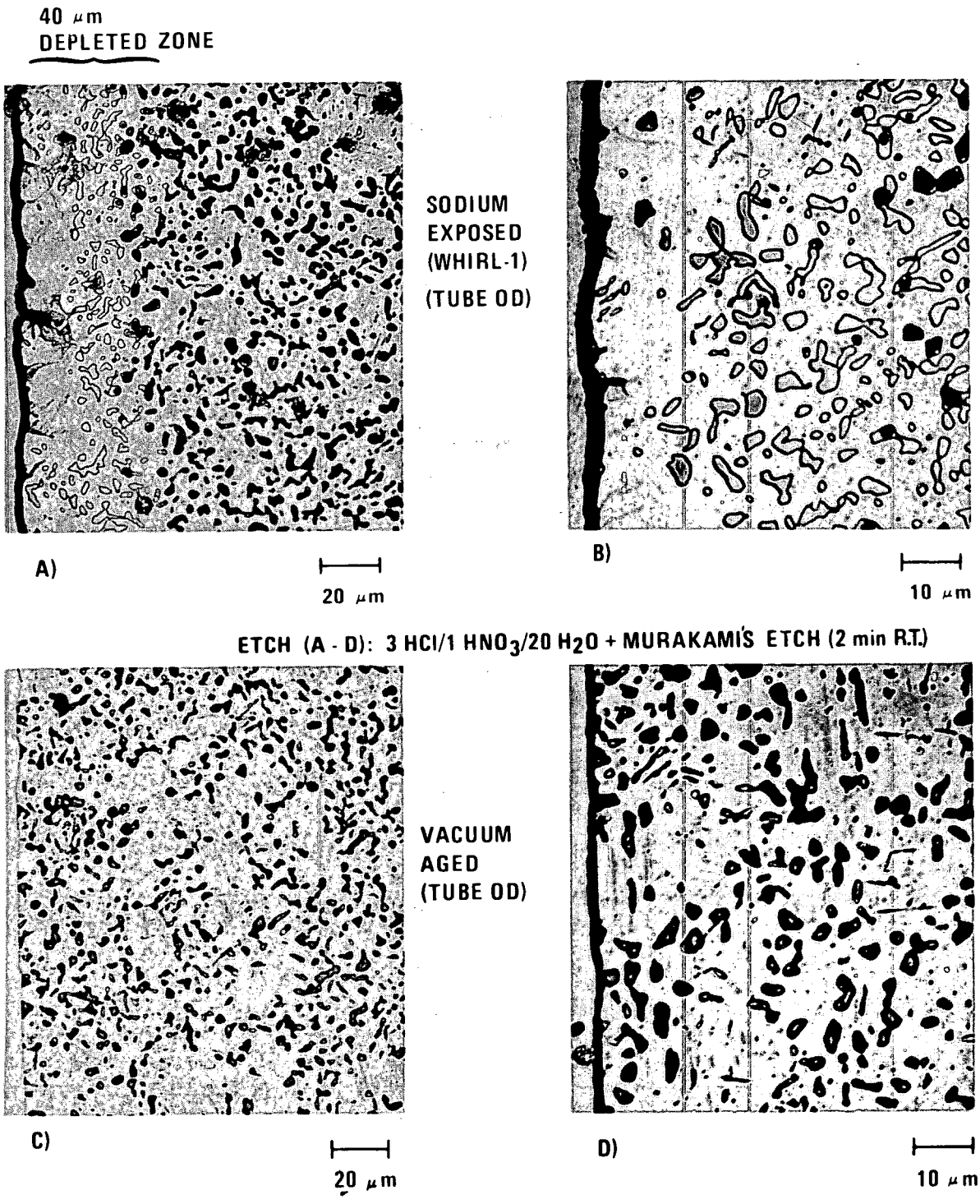

FIGURE 202. Twenty percent CW Type 310S stainless steel: a comparison of 700°C/2,000 hour exposures in sodium and in vacuum.

result is somewhat high. However, the nickel content of an alloy has been shown to have a strong influence on the diffusivity of substitional elements, and this may account for the higher rate in Type 310 SS.

It should be noted that the "yellow" phase was identified as sigma and not ferrite in two ways. First, the specimen was etched in 10% chromic acid; both blue and yellow particles were uniformly and rapidly attached [See Figure 204(a). This reagent reacts with sigma, but has no effect on ferrite. Secondly, several specimens were tested with a strong magnet; all showed minimal response. Unlike ferrite, sigma is not a magnetic phase.

It is also evident that carbon depletion has occurred at the sodium exposed surface. In comparing Figures 202(c) and 202(d) with 202(a) and 202(b), it will be noted that there are in general many more carbides present in the vacuum aged material, some clearly formed along the deformation bands of the original structure. Carbides, however, are markedly absent in the depleted zone of the sodium exposed specimen.

A more complete development of the microstructure was observed in a specimen aged at 700°C for 4,000 hours (Figure 203). Dilute chromic acid etch was used to enhance other matrix precipitation, albeit at the expense of a relatively severe attack on the sigma islands. Carbides were observed, growing on the deformation bands of the original cold worked structure [Figure 203(c)]. It is clear that carbide nucleation occurred before the matrix transformation at about 500 hours, and this would be anticipated. The formation of the parallel carbide stringers within the more heavily deformed grains, prevented the growth of sigma in these confined areas.

The tubing no longer has a formal grain structure, but more closely resembles the products obtained from a eutechtoid reaction in which the original polycrystalline single phase gives way to an integral mixture of two new solids. In this case, however, the reaction is occurring within a miscibility gap in which the original solid undergoes an ordering reaction as one new second phase (sigma), is produced.

The effect of 6,000 hour sodium exposure in WHIRL-1 is illustrated in Figure 204. At low magnification, it can be seen that corrosion has occurred on both the O.D. and I.D. of the tube. A comparison of the wall dimensions of Figure 203(a) and Figure 204(a) (taken at the same microscope settings) provides a useful check on the corrosion measurements calculated from specimen weight loss. The average wall thinning was estimated at 7.42%. For a 250 μm wall tube, this amounts to 19 μm in 6,000 hours, or 27 μm/y. The metallographic specimen was exposed at L/D = 60, and gave a calculated corrosion rate of 27 μm/y, in agreement with the above value.

The depleted zone depth after 6,000 hours in sodium has increased considerably. In Figure 204(b), the 40 μm "blue" zone observed after 2,000 hours [see Figure 202(a)], is now essentially free of precipitate. Behind this surface band, sigma with a blue coloration after treatment with Murakami's etch extended for an additional 30 μm. Using Equation [1], with the value of D calculated after 2,000 hours, the predicted depth, X, after 6,000 hours is equal to 69 μm, in excellent agreement with the measured value.

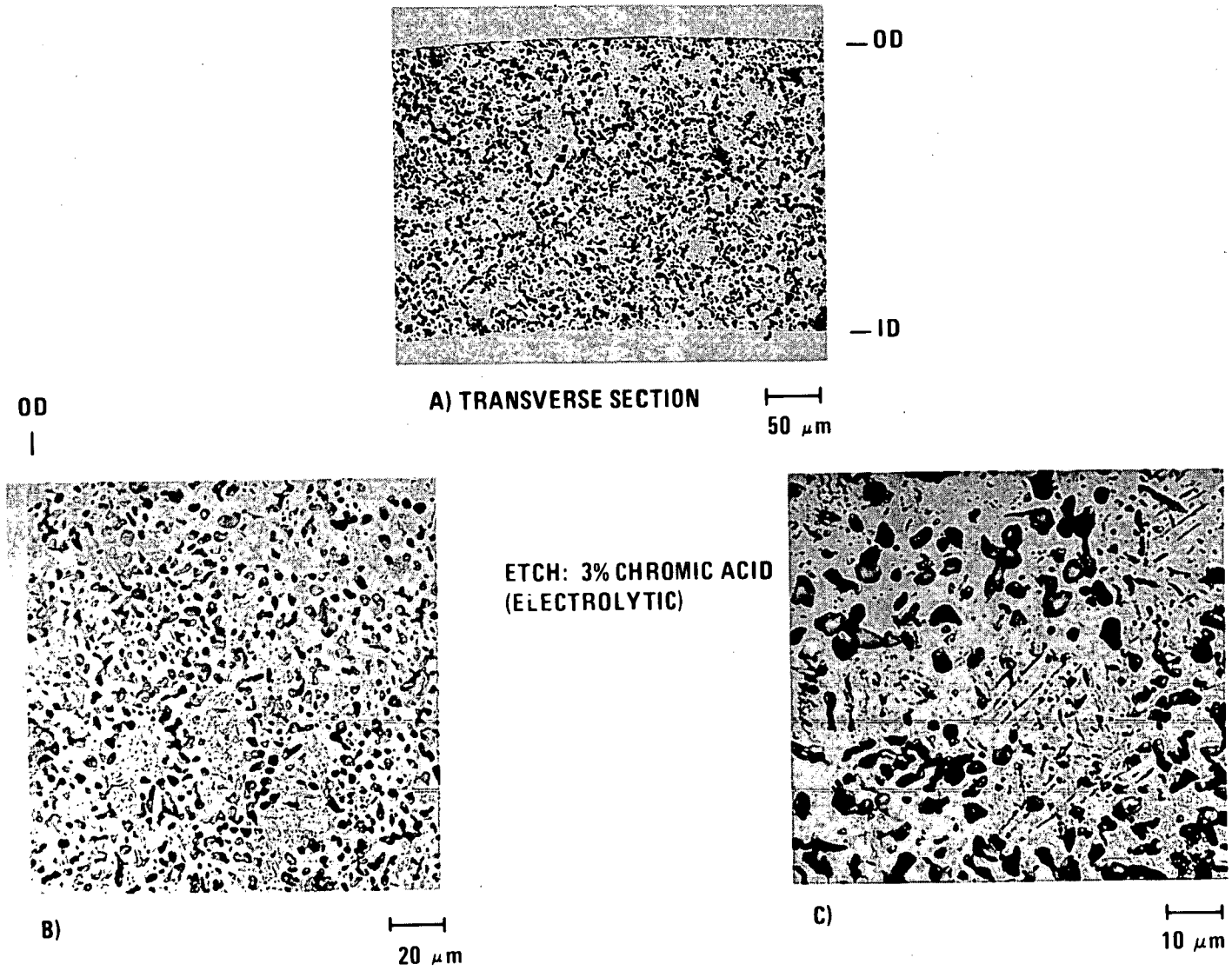

FIGURE 203. Twenty percent CW Type 310S stainless steel, vacuum aged at 700°C/4,000 hours.

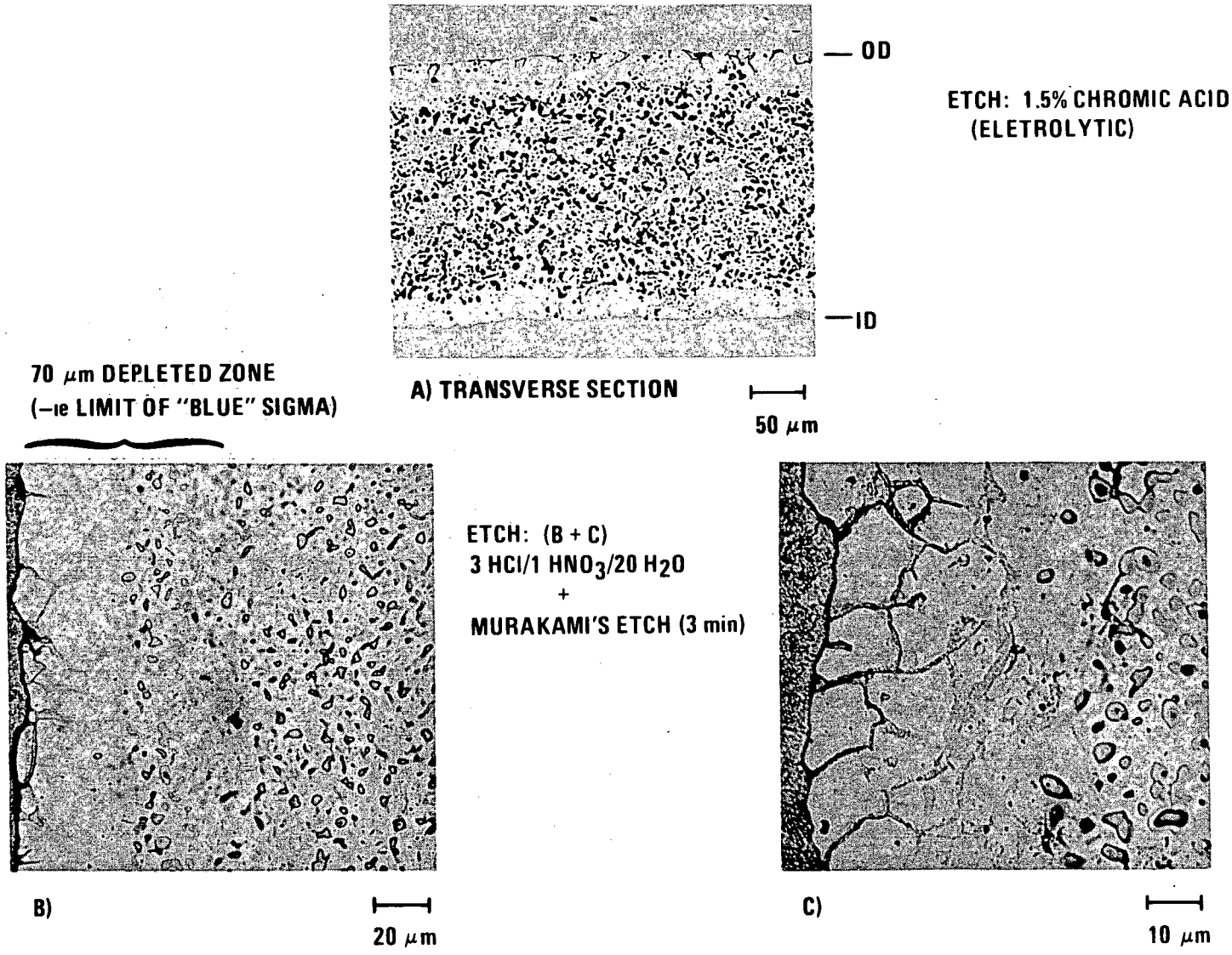

FIGURE 204. Twenty percent CW Type 310S stainless steel, sodium exposed at 700°C, 6,000 hours (WHIRL-1).

The continuing process of sigma dissolution within the depleted zone may be observed in Figure 204(c). As corrosion progresses the net composition of this zone is moving further and further away from a two-phase region (i.e., away from the miscibility gap) and a polycrystalline structure is beginning to return.

The features of the sodium corroded surface as observed in the scanning electron microscope are illustrated in Figure 205. A generally uniform pattern of attack was established after 2,000 hours, with blocky, somewhat angular regions interspersed with smoother, shallow areas in which slight grain boundary etching has occurred. With increasing exposure time, the development of small micron-sized angular holes was noted. These holes were sparsely scattered across the surface, and although these were angular in character, suggesting the complete removal of a precipitate or particle, there was no evidence for the presence of any second phase over the surface examined.

Some significant changes in surface composition were monitored, as shown graphically in Figure 205. The most noteworthy was the change in the Cr-Fe ratio from 0.725 to 0.300 over the 6,000 hour exposure period. In terms of concentration, this would represent a change in chromium from the initial 25% to about 10%. The change in the Ni:Fe ratio, 0.250 to 0.113, indicates a drop from 19% to about 8.5%. It is evident that the original austenitic character of the material at the tube surface has been almost entirely lost as a result of the sodium exposure.

A comparison of x-ray microprobe traces taken in a radial direction across the tube wall of 4,000 hours aged and 6,000 hours sodium exposed specimen confirmed qualitatively that the elements Cr, Ni and Mn have been depleted. In addition, however, a significant surface gradient was noted for silicon. This is shown schematically in Figure 206. At present these data are not quantitative; several alloy standard specimens are required to allow for the change in instrument response to a minor constituent, in an alloy whose basic composition is itself changing. However, a clear trend is evident. At the surface of the sodium corroded sample, the silicon concentration was reduced to about half its initial level with depletion extending back into the bulk for about 50-70 μm. This profile corresponds with the depleted zone observed in the microstructure [Figure 204(b)] and may account for the compositional difference indicated by the reaction of sigma phase with Murakami's etch. The "peaks," most evident on the vacuum aged profile, appeared to coincide with the casting defects noted earlier, suggesting that the holes themselves or the area around the holes contained a silicate or similar compound.

4.3.3 Alloy 330

The as-received structure of alloy 330 [Figure 207(a)] differed in several respects from Type 310 SS. Although of similar grain size (ASTM 7-8), there was less evidence of cold work, fewer inclusions and only occasional spherical porosity. The generally irregular grain structure (as opposed to polygonized) and the presence of second phase particles scattered throughout the matrix suggest that the annealing treatment (1065°C/1 hr/WQ) was not sufficient to return the material to a single phase condition, and that only partial recrystallization occurred.

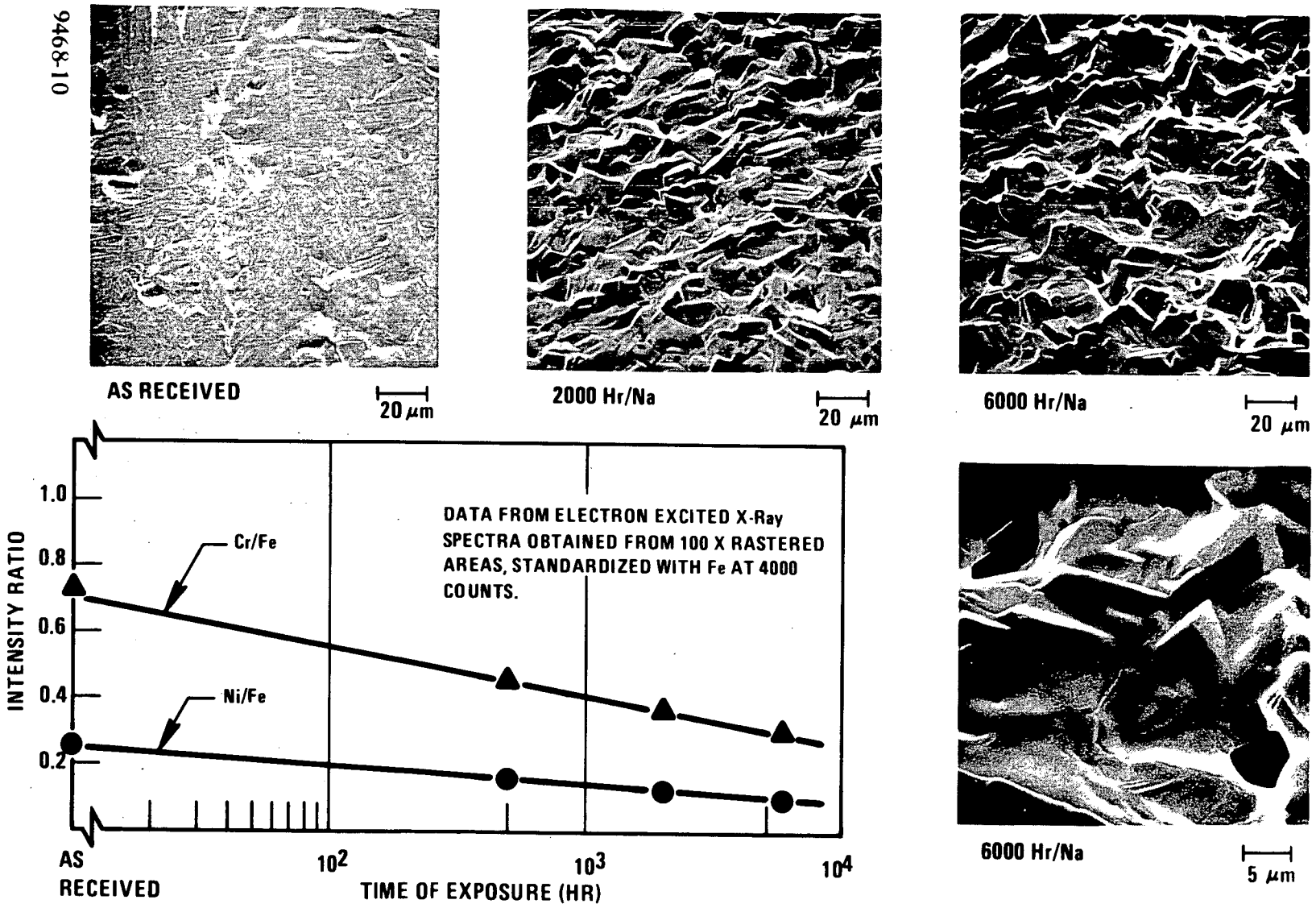

FIGURE 205. Surface features and compositional changes in Type 310S exposed to sodium at 700°C (WHIRL-1).

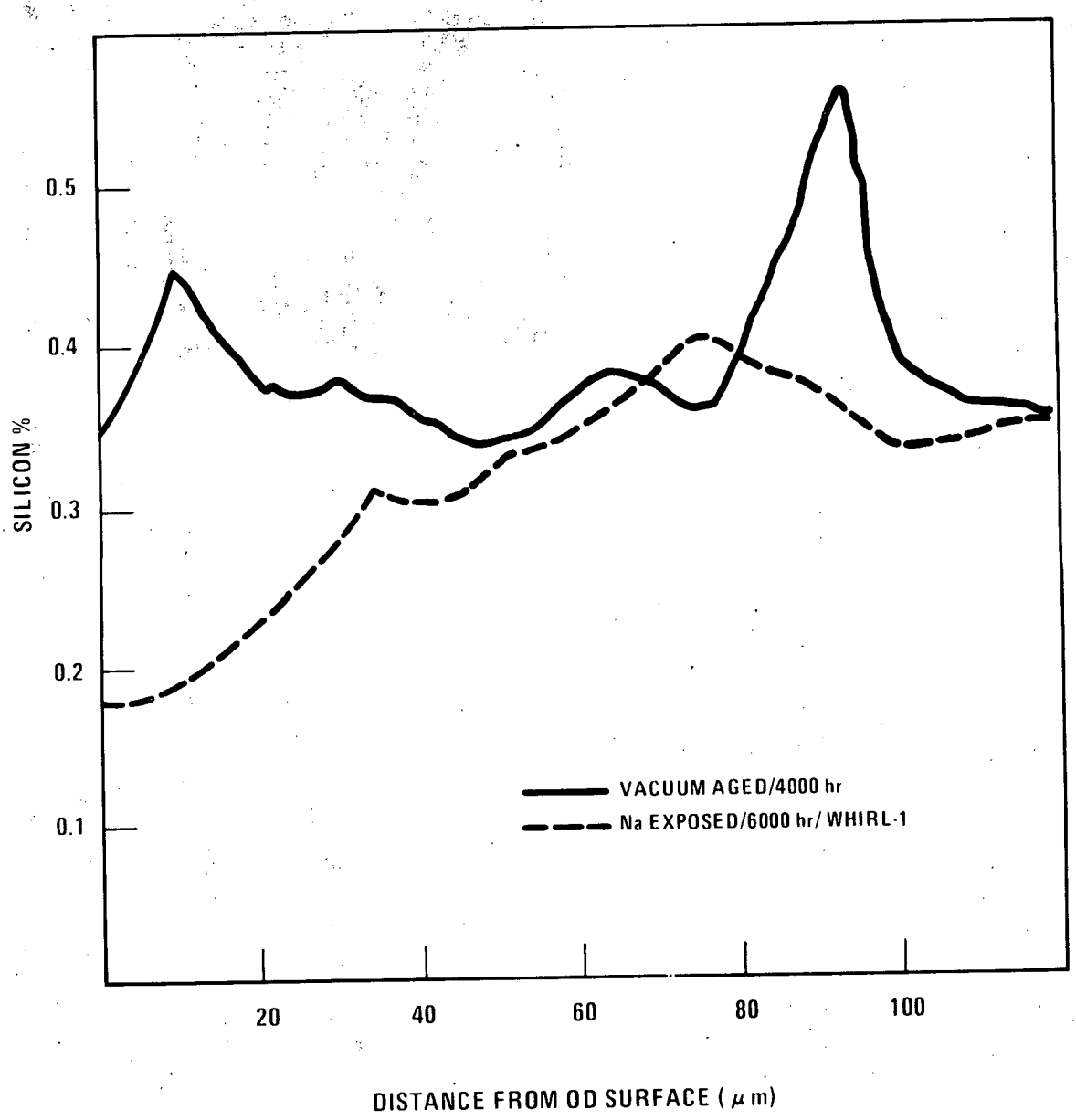

9468-14

FIGURE 206. Comparison of silicon surface profiles before and after sodium exposure.

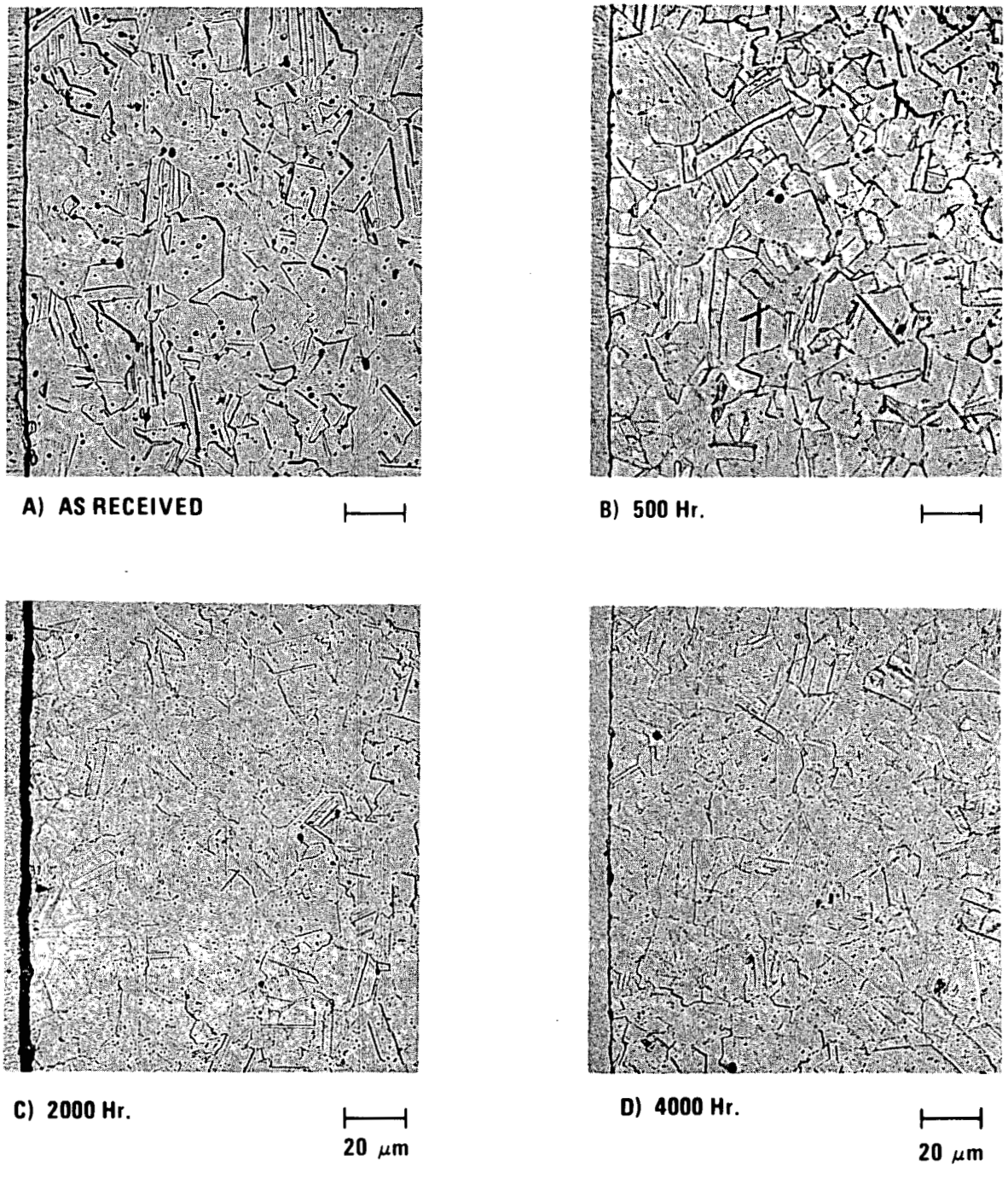

FIGURE 207. Microstructural development of alloy 330 at 700°C.

After 500 hour aging at 700°C [Figure 207(b)], the structure contained additional random precipitation; this is most probably carbide. However, after 2,000 hours [Figure 207(c)] these small spherical carbides were observed to be conforming to a distinct structural pattern, apparently decorating original grain boundaries, present prior to the solution anneal. Coupled with this phenomenon was the fact that there was no obvious precipitation occurring on the new grain boundaries. Furthermore, a considerable number of these boundaries appeared to have dissolved or were no longer resolved in the microscope. This effect was also noted in the specimen aged for 4,000 hours, as shown in Figure 207(d).

The structural changes due to sodium exposure are also very different from Type 310 SS. Unlike the mild, general surface attack observed on the latter alloy, the sodium appears to be leaching grain boundaries and channeling its way to a depth of 50-60 μm below the surface. The development of this attack is shown in Figures 208 and 209. There are many surface "pot-holes" with fine hair-line or crack-like grain boundaries leading down from the surface, or laterally away from corrosion "caverns" well within the tube wall. The surface attack is morphologically similar in many respects to that of Type 310, however, the increased development of holes is very evident. Although the initial Ni content was almost twice that of Type 310 (36 vs. 19%), selective removal of this element in particular reduced its concentration to about 10% after 6,000 hours exposure in WHIRL-1. An even more severe depletion was noted after only 4,000 hours exposure in the high dT/dL environment of ITF (Figure 210) where Ni was estimated to be at about the 2% level.

Undoubtedly, the formation of a labyrinthian surface structure enhances the mass transfer process since the sodium-wetted surface is increased and small, partially isolated, volumes of metal are more readily depleted of their alloy constituents.

The reason for the development of such holes in a given material is unclear, but when they do form, metal loss occurs largely from below the surface and is not reflected as wall thinning. Dimensional measurements made on the specimen exposed for 6,000 hours in WHIRL-1, for example, provided the surprising result of a corrosion rate equivalent to only 8.9 μm/y, as compared with 35 μm/y calculated from weight change measurements at this specimen location of L/D = 66. Almost 75% of the weight loss has therefore occurred below the tube surface.

4.3.4 Discussion

In earlier aging studies of Type 310 SS, White and LeMay[1] observed an entirely different transformation sequence from that observed in the advanced alloy tubing. In annealed material, containing 0.11C and 0.75Si, they noted sluggish grain boundary carbide formation at 650°C with very little sigma identified after 900 hours. At 750°C, intergranular carbide precipitation was heavier, and some intragranular sigma was observed, but up to 900 hours, there was no evidence of widespread intermetallic formation.

A comprehensive mechanical property/aging program of a low carbon heat of Type 310 SS very similar to the advanced cladding material (0.07C, 0.46Si) was conducted by Emmanuel[2]. The behavior of cold worked and annealed specimens was investigated over the 540-930°C temperature range for periods up to 1,000 hours. He found that sigma forms directly from the austenite, that it forms more rapidly and over a wider temperature range in cold worked than in annealed material and that impact strength was the most sensitive indicator

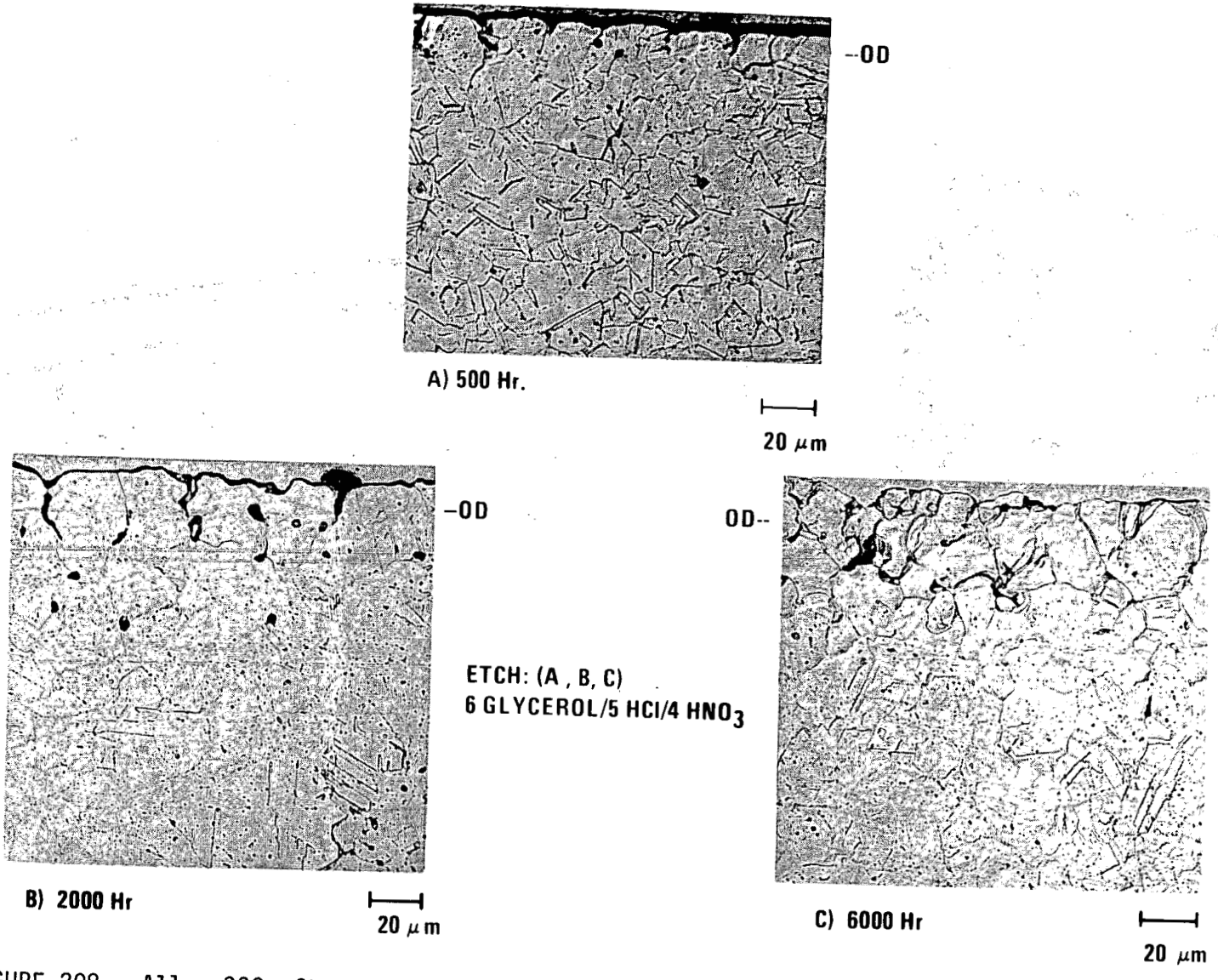

FIGURE 208. Alloy 330 after exposure to sodium at 700°C (WHIRL-1).

9468-3

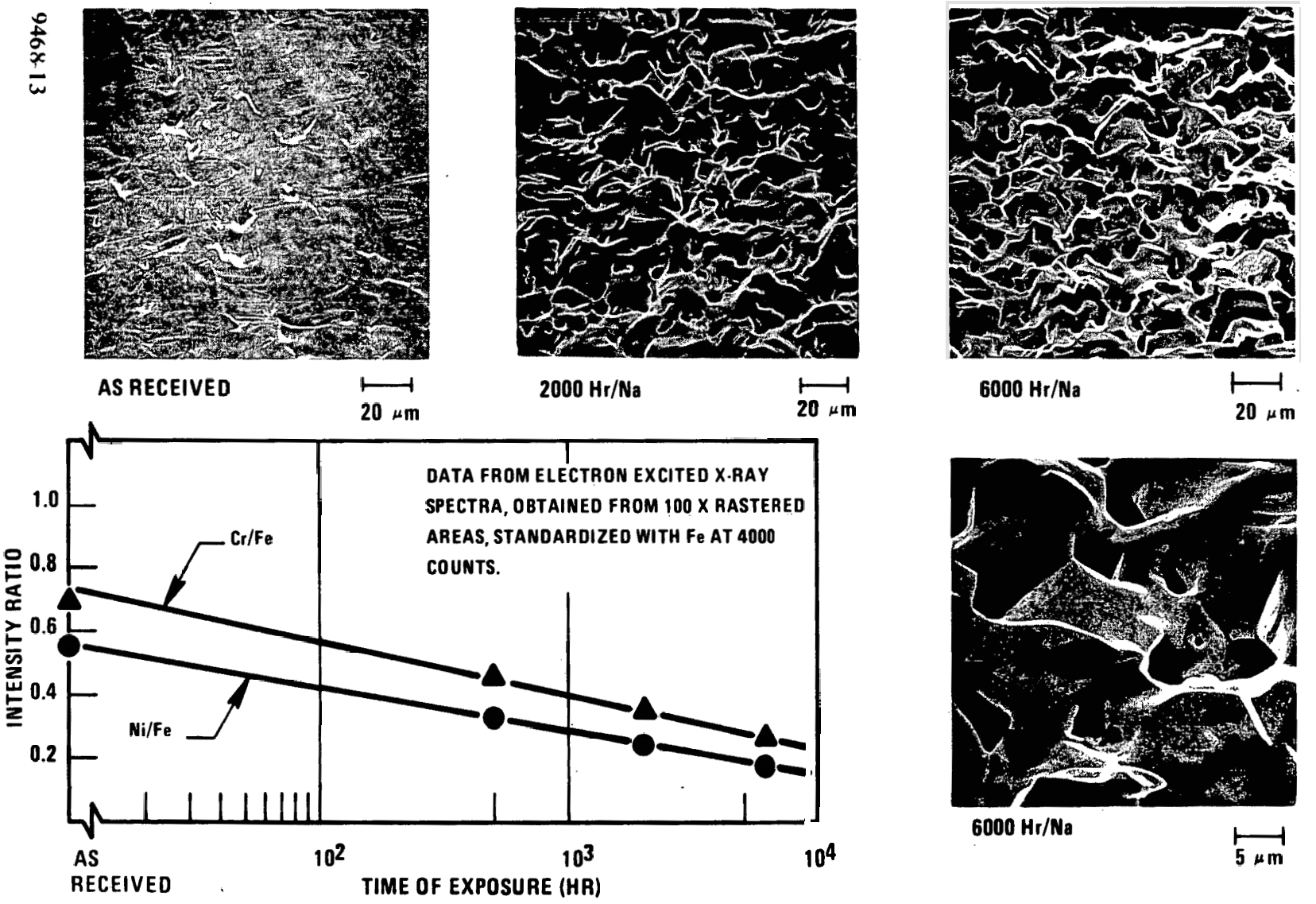

FIGURE 209. Surface features and compositional changes in alloy 330 exposed to sodium at 700°C (WHIRL-1).

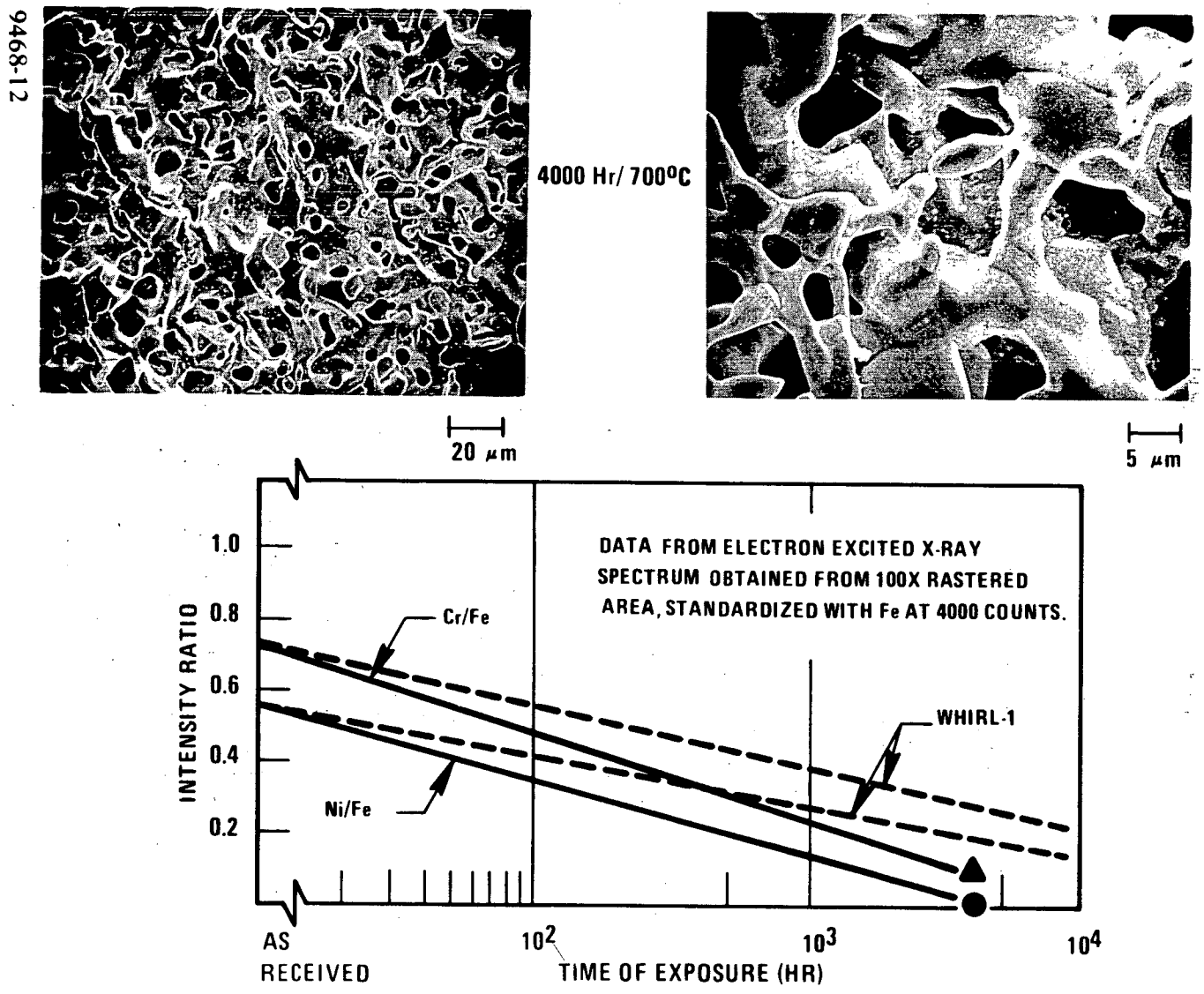

FIGURE 210. Surface features and composition of alloy 330 after exposure in ITF.

for the presence of sigma. However, the amount of sigma formation at 700°C, although described as "heavy" and greater than 8%, was not reported to the levels of ~25% as measured in the present advanced cladding material. No mention was made of any widespread breakdown and transformation of austenite after 500 hours at 700°C.

Dulis and Smith[3] examined structures in a series of annealed austenitic steels, including AISI Type 310 (0.07C, 0.58Si) and Type 314 (25Cr, 20Ni, 0.18C, 2.3Si). After aging at 700°C/3,000 hours, they measured 10% sigma in the Type 310 specimen, with a structure very close to the (cold worked) cladding material after 2,000 hours at the same temperature. The higher silicon alloy produced the same amount of sigma in 1,000 hour/760°C, but the particles were in general much larger.

Foley and Krivobok[4] developed Cr-Ni-% sigma plots for annealed and cold worked commercial alloys at 650°C, 800°C and 900°C. They also produced a companion set of triaxial figures showing the variation of Charpy impact values with composition after 100 and 3,000 hours aging. A curve showing the effect of sigma on impact values is reproduced in Figure 211. The figure demonstrates that about 5% sigma is required to "embrittle" the steel (impact data < 15 ft-lb). The authors point out that significant loss of impact properties was observed even after 100 hours aging. This could not be attributed to sigma, but was probably due to carbide formation. Subsequent additional deterioration, however (having given sigma time to form), was almost certainly the result of the presence of this latter phase.

Foley and Krivobok also indicated that silicon enhanced the formation of sigma, and, for their three test temperatures, demonstrated the effect of changing the silicon content from 0.2% to 0.7%.

However, sigma formation is also strongly affected by carbon concentration. Since carbon acts in the opposite sense to silicon, some net effect of these two elements should be taken into account. This was attempted with the data presently available. From the results compiled in Table 53, a plot of sigma versus the Si:C ratio was constructed (Figure 212). With a ratio of 6 or less, the amount of sigma produced appears to be low at about 3%.

TABLE 53

SIGMA, CARBON AND SILICON DATA FOR 25Cr-20Ni STEELS

Reference	Carbon w/o	Silicon w/o	Si:C Ratio	Initial Alloy Condition	Aging		
					Time (hr)	Temp. (°C)	% Sigma
This Program	0.068	0.47	6.91	CW	2000	700	25
(1)	0.110	0.70	6.36	A	900	750	3-5*
(2)	0.070	0.46	6.57	CW	1000	700	~10
(3)	0.070	0.58	8.28	A	3000	700	10+
(3)	0.180	2.30	12.70	A	1000	760	10+
(4)	0.050	0.20	4.00	CW	3000	675	3
(4)	0.050	0.70	14.00	CW	3000	675	10

* Estimated

The foregoing discussion and review of literature data suggests that with suitable compositional adjustments, the amount of sigma phase formed at 700°C could be controlled to a tolerable level in Type 310 SS.

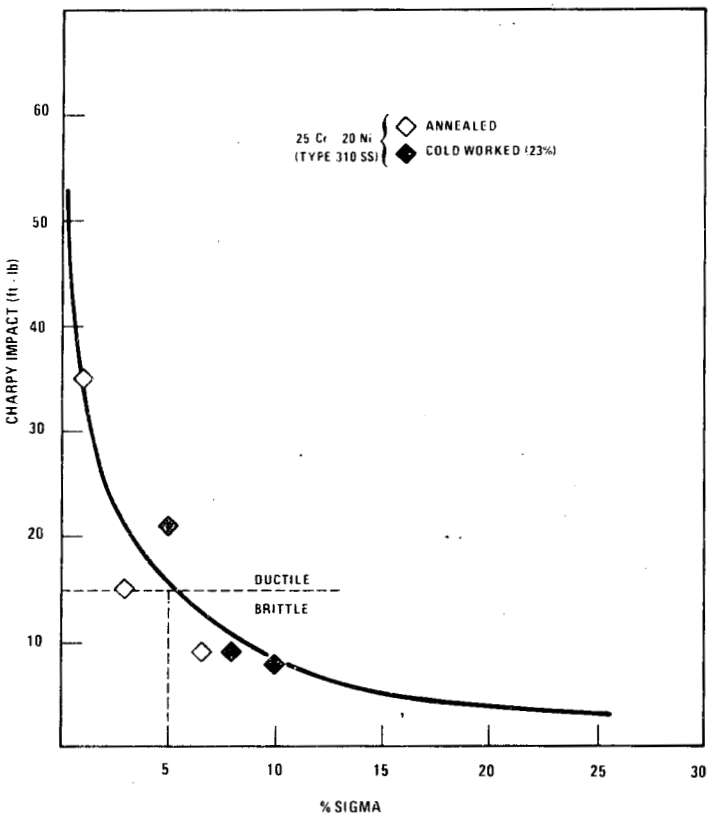

FIGURE 211. The effect of sigma on impact properties, for austenitic steels in the range (25-30)Cr, (20-35)Ni (Charpy Keyhole Specs, Ref. 4).

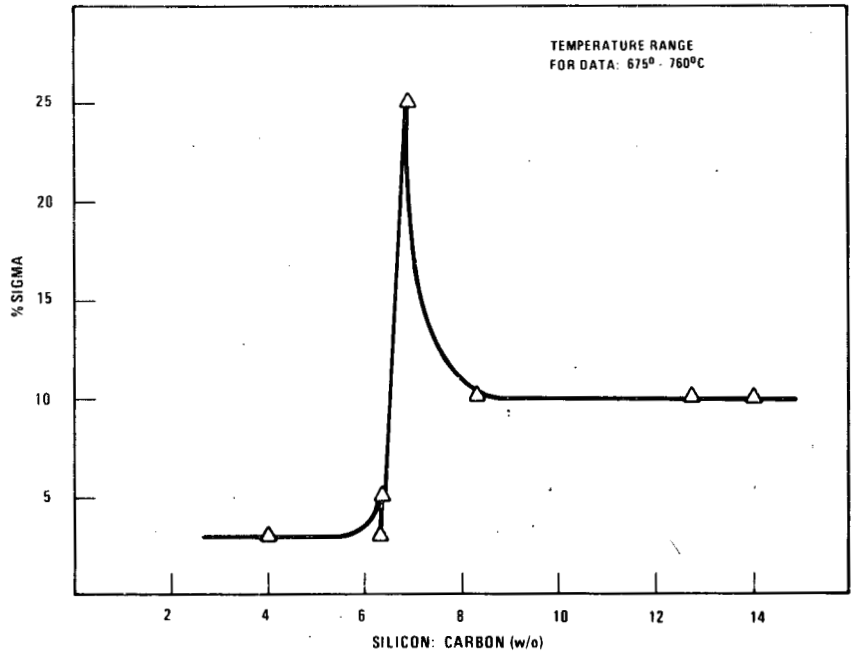

FIGURE 212. Sigma formation in 25Cr-20Ni steel as a function of Si:C ratio.

Although sigma formation is not normally anticipated in alloy 330, Foley and Krivobok[4] showed that this was also dependent on silicon content. If the silicon level is high enough (~3%), the sigma will form in this alloy also, to about 3 or 4%, within a very limited temperature range (600-675°C).

The presence of, or tendency to form sigma in either alloy is not, however, the major issue for consideration for reactor application of these two alloys. The edge alloy 330 holds over Type 310 SS in view of its superior swelling properties, is clearly lost when sodium corrosion behavior is taken into account. Both alloys are corroding at a prohibitively high level at 700°C; this would not only affect the mechanical integrity of a component, but it also gives rise to concern for the volume of radioactive corrosion product released to the sodium system.

Corrosion studies are continuing at W-RL on alloy 330 at 600°C in the hope that the corrosion rate will fall to a tolerable level at this lower temperature.

4.4 EXPECTED ACHIEVEMENTS IN THE NEXT REPORTING PERIOD

(Not provided)

4.5 REFERENCES

1. White, W. E., and LeMay, L., "Metallographic Observations on the Formation and Occurrence of Ferrite, Sigma Phase and Carbides in Austenitic Stainless Steels, Part I: Studies of AISI Type 310 Stainless Steel," Metallography, Vol. 3, No. 1 (March, 1970), Elsevier.

2. Emmanuel, G. N., "Sigma Phase and Other Effects of Prolonged Heating at Elevated Temperatures on 25 Percent Chromium - 20 Percent Nickel Steel," Symposium on the Nature, Occurrence and Effects of Sigma Phase, June 1950, ASTM Special Technical Publication No. 110.

3. Dulis, E. J., and Smith, G. V., "Identification and Mode of Formation and Resolution of Sigma Phase in Austenitic Chromium-Nickel Steels," Ibid.

4. Foley, F. B., and Krivobok, V. N., "Sigma Formation in Commercial Ni-Cr-Fe Alloys," Metal Progress, May 1957.

CHAPTER IV.

STATUS OF EBR-II IRRADIATION TESTS

1. STATUS OF EBR-II IRRADIATION TESTS

The status of advanced alloy irradiation tests in EBR-II, as of the end of December, 1976, is shown in Table 54.

TABLE 54

STATUS OF EBR-II IRRADIATION TESTS

Experiment	General Description	Subassembly Designation	Reactor Position	Status: 12/30/76*		Remarks
				Accumulated MWD	Est. Peak Fluence, 10^{22} n/cm^2 (E>0.1 MeV)	
AA-Ia	Swelling in Commercial Alloys	X-157C	4D2	21,398	5.28	Irradiation completed
AA-I	Swelling in Candidate Commercial Alloys	X-223C	2F1	26,297	7.41	Next discharge end of Run 87
AA-IIa	Mechanical Properties of Candidate Commercial Alloys	X-260B	4D3	17,078	4.22	Discharge at end of Run 87
AA-IIb		X-269	4C2	8,324	2.06	1st discharge end of Run 89
AA-IIc		X-263	4E2	19,737	4.87	1st discharge end of Run 87
AA-III	In-Reactor Stress-Rupture, Candidate Alloys	-	-	0	0	Planned for INCOT position, Run 89
AA-IV	AA-II Backup	-	-	0	0	Backup test
AA-V	AA-VIII Backup	-	-	0	0	Backup test
AA-VI	Swelling in Modified (Series C) Alloys	-	-	0	0	Run 89 insertion scheduled
AA-VII	Swelling in Candidate Developmental Alloys	X-223C	2F1	16,863	4.75	Next discharge end of Run 87
AA-VIIIa	Mechanical Properties of Candidate Developmental Alloys	X-295	-	0	0	Run 87B insertion scheduled
AA-VIIIb		X-261B	-	0	0	Run 89 insertion scheduled
AA-VIIIc		X-296	-	0	0	Run 87B insertion scheduled
AA-IX	Fundamental Studies on Void Nucleation and Alloy Stability	X-216B	2D1	9,550	2.68	Irradiation completed
AA-X	Mechanical Properties of Solid Solution Developmental Alloys	X-287	-	0	0	Run 87A insertion scheduled
AA-XI	Swelling Suppression Through Compositional Synergisms	X-216D	2D1	13,934	3.93	1st discharge end of Run 92
AA-XII	Swelling in Modified (Series B) Developmental Alloys	X-223C	2F1	5,440	1.55	1st discharge end of Run 87

* End of Run 86A